# Advanced Gasoline Turbocharged Direction Injection (GTDI) Engine Development

# End of Project Technical Report

# Ford Motor Company

**Recipient:** Ford Motor Company
**Award Number:** DE-EE0003332

**Working Partners:** Ford Motor Company (Ford) and Michigan Technological University (MTU)
**Cost-Sharing Partners:** Ford and MTU

Contact: Dr. Terrance Wagner, 313-805-9879, twagner3@ford.com
DOE Manager: Ralph Nine, 304-285-2017, RALPH.NINE@NETL.DOE.GOV

**Project Title:** Advanced Gasoline Turbocharged Direction Injection (GTDI) Engine Development

**Project Period:** October 1, 2010 - December 31, 2015
Date of Report: December 31, 2015

## Project Objectives:

Ford Objectives:

- Demonstrate 25% fuel economy improvement in a mid-sized sedan using a downsized, advanced gasoline turbocharged direct injection (GTDI) engine with no or limited degradation in vehicle level metrics.
- Demonstrate vehicle is capable of meeting Tier 2 Bin 2 emissions (modified to Tier 3 Bin 30) on the FTP-75 cycle.

MTU Objectives:

- Support Ford Motor Company in the research and development of advanced ignition concepts and systems to expand the dilute / lean engine operating limits.

## Background:

This program was undertaken in response to US Department of Energy Solicitation DE-FOA-0000079, resulting in a cooperative agreement with Ford and MTU to demonstrate improvement of fuel efficiency in a vehicle equipped with an advanced GTDI engine.

Ford Motor Company has invested significantly in GTDI engine technology as a cost effective, high volume, fuel economy solution, marketed globally as EcoBoost technology. Ford envisions additional fuel economy improvement in the medium and long term by further advancing EcoBoost technology.

The approach for the project was to engineer a comprehensive suite of gasoline engine systems technologies to achieve the project objectives, and to progressively demonstrate the objectives via concept analysis / computer modeling, single-cylinder and multi-cylinder engine testing on engine dynamometer, and vehicle-level testing on chassis rolls. The technologies included:

- Aggressive engine downsizing in a mid-sized sedan from a large V6 to an I4.
- Medium and long term advanced EcoBoost technologies:
  - Dilute combustion with cooled exhaust gas recirculation and advanced ignition.
  - Lean combustion with direct fuel injection and advanced ignition and aftertreatment systems.
  - Boosting systems with active and compounding components.
- Advanced friction reduction technologies, engine control strategies, cooling systems, and NVH countermeasures for use of an I4 engine in place of a V6 engine.

Targets to enable achievement of the overall project objectives were established at the engine level for full load steady state performance, transient response from part load to full load, fuel consumption, emissions, and combustion stability over a mini-map of steady state test points at part load, and emissions during a transient cold start.

## Summary of Results:

All project objectives were met or exceeded.

### Full Load Performance

Status vs. targets for full load steady state engine performance and transient time-to-torque (TTT) on the multi-cylinder engine dynamometer are shown in Figure 1. As shown, the engine meets the full load performance targets at all engine speeds and the transient TTT target at 1500 rpm. Meeting the targets of 20 bar BMEP at 2000 to 4500 rpm and 80kW/L at 6000 rpm was challenging at 11.5:1 compression ratio and required detailed parameter optimization to balance compressor outlet temperatures, peak cylinder pressures, turbine inlet temperatures, oxygen blowthrough during overlap, and other critical constraints.

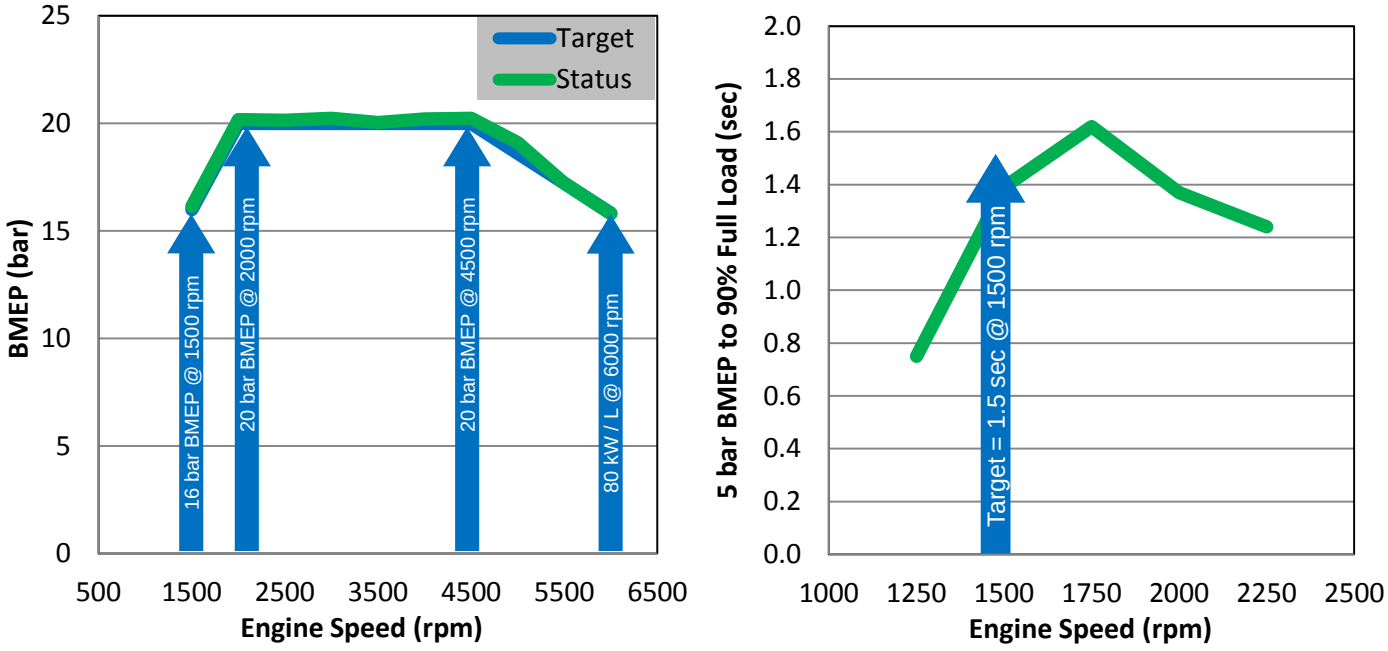


***Figure 1 - Status vs. target full load BMEP (left) and transient time-to-torque (right) for 2.3L GTDI DOE engine.***

As shown in Figure 2, the engine operates at stoichiometry up to 3500 rpm at full load for good on-road fuel consumption. Also, the engine operates with typical GTDI combustion phasing (50% mass fraction burned location between 25-30° aTDC) across the speed range, which indicates a good balance of attributes which affect engine knock.

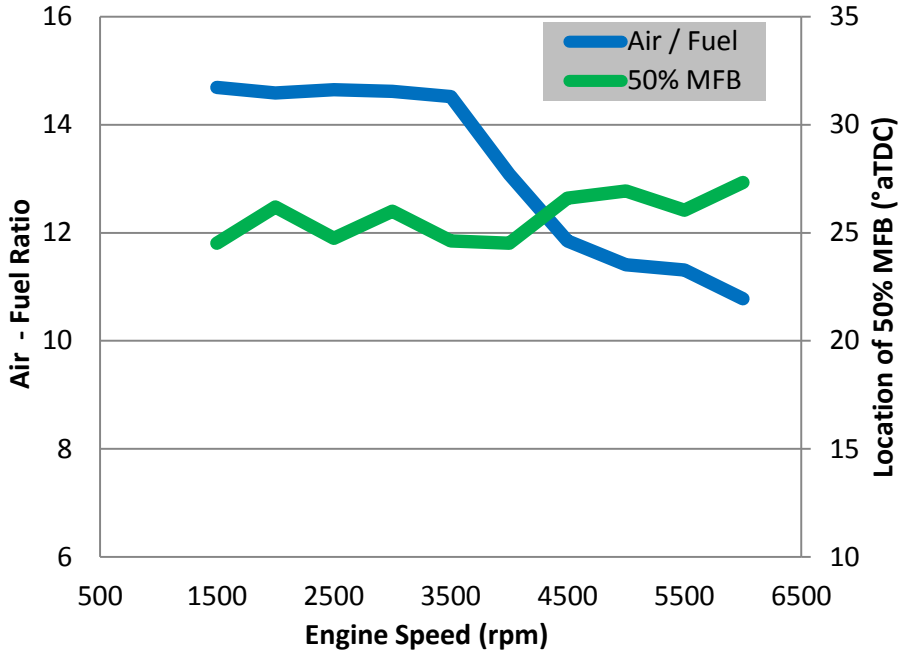


***Figure 2 - Air-fuel ratio and combustion phasing vs. engine speed at full load for 2.3L DOE engine.***

The full load target curve was defined using a Ford analytical toolset to match the performance metrics of the baseline 2010 3.5L Taurus / Fusion. The analytical toolset captures the effects of the naturally-aspirated torque before boost is generated, the transient time-to-torque, and the boosted full load torque, and was developed specifically for EcoBoost powertrain matching. It was not possible to construct a fair vehicle level performance comparison, since the baseline 2010 3.5L Taurus / Fusion certified at the 4250 ETW weight class, whereas the build-from vehicle for this project was a 2013 Fusion certified at the 3875 ETW weight class, plus other differences in the vehicles such as frontal area/aerodynamics and parasitic losses. Since the engine meets the full load targets determined using the analytical toolset, it can be assumed that the performance metrics of the baseline vehicle with the 2.3L DOE powertrain would match those of the baseline vehicle with the baseline powertrain.

## Emissions

Emission targets for the project were met at both the engine and the vehicle level.

Optimization of 20°C cold start emissions was first conducted at the engine level, and included both steady state cold fluids development and transient cold start development. As shown in Table 1, the engine meets the transient cold start emissions targets which were derived from the tailpipe standards. Performance vs. the targets is evaluated at an exhaust heat flux to the catalyst during the cold idle period after the engine start that achieves ~350°C catalyst mid-bed temperature at 20 seconds after engine start.

***Table 1 - Transient engine test cold start emissions compared to the SULEV30 targets.***

| Cold Start Attribute | Units | Target[1] | Status |
|---|---|---|---|
| 0-20s Cumulative FGHC + FGNOx | mg | 227 | 224 |
| 0-20s Cumulative Particulate Mass (PM) | mg | 3.0 | 1.3 |

Consistent with the multi-cylinder engine transient emissions testing on engine dynamometer, the vehicle results measured on chassis dynamometer with an aftertreatment system aged to full useful life (FUL) meet the SULEV30 emissions standards, as shown in Table 2. The results include bags 1, 2, 3, and highway as well as all assisted direct start (ADS) stop-start events. The innovative transverse central direct injection combustion system developed during the project exceeds expectations with regard to PM emissions. In 2013, the project objectives transitioned from Tier 2 Bin 2 to Tier 3 SULEV30 emissions, and both are shown in Table 2 for reference.

***Table 2 - Vehicle emission results with catalysts aged to FUL compared to the SULEV30 standards.***

| Tailpipe Standards | Tier 2 Bin 2 | SULEV30 | Status |
|---|---|---|---|
| NMOG | 10 mg / mi | -- | -- |
| NOx | 20 mg / mi | -- | -- |
| NMOG + NOx | -- | 30 mg / mi | 25 mg / mi |
| PM | 10 mg / mi | 3 mg / mi | 1 mg / mi |

**Fuel Economy**

The brake specific fuel consumption (BSFC) of the engine measured on engine dynamometer at nine mini-map speed / load points is shown in Figure 3. The BSFC of the engine is 1.3% to 4.3% better than the targets at these speed-load points, and is substantially better than a comparator 2.0L GTDI engine.

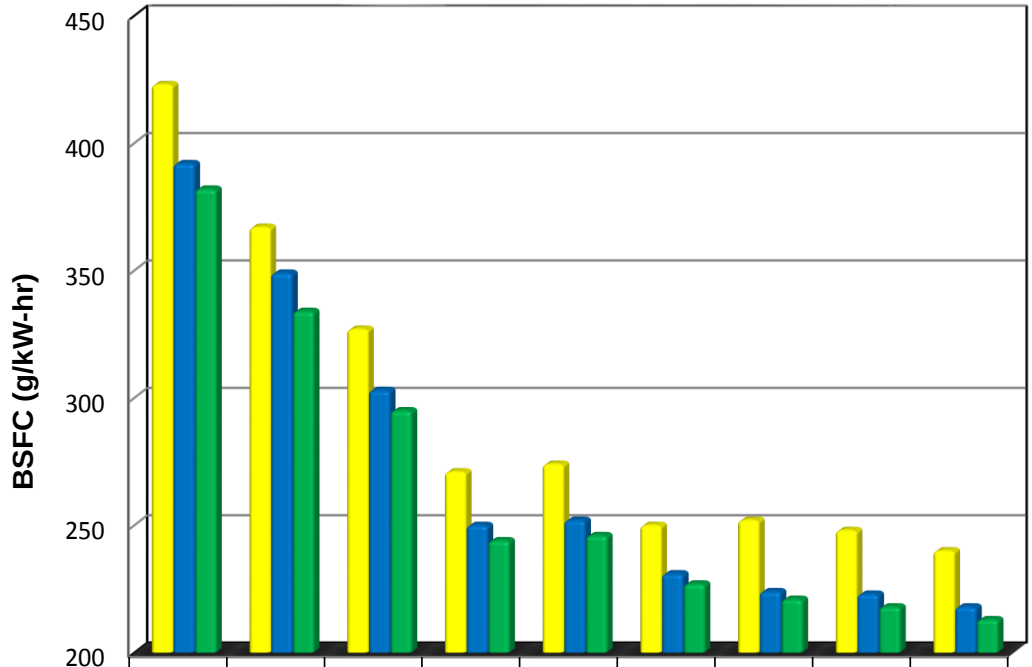


| | 1000 / 1.5 | 2000 / 2.0 | 1500 / 2.62 | 1500 / 5.0 | 2000 / 5.0 | 3000 / 7.5 | 1500 / 9.0 | 2000 / 9.0 | 2500 / 14.0 |
|---|---|---|---|---|---|---|---|---|---|
| 2.0L GTDI | 423 | 367 | 327 | 271 | 274 | 250 | 252 | 248 | 240 |
| DOE Target | 392 | 349 | 303 | 250 | 252 | 231 | 224 | 223 | 218 |
| DOE Status | 382 | 334 | 295 | 244 | 246 | 227 | 221 | 218 | 213 |

***Figure 3 - BSFC status vs. targets and reference 2.0L GTDI engine for mini-map test points.***

Consistent with the mini-map data, the vehicle results measured on chassis dynamometer meet the 25% M-H fuel economy improvement target, as shown in Table 3.

***Table 3 - M-H vehicle fuel economy results.***

| | **Fuel Economy (mpg)** | **Improvement (%)** |
|---|---|---|
| 2010 3.5L V6 Taurus / Fusion | 27.78 | Baseline |
| | | |
| DOE Adv GTDI 2.3L I4 Fusion – Measured on chassis rolls | 34.30 | 23.5% |
| Measured residual balance shaft friction correction | 0.34 | - |
| Measured powertrain weight save | 0.13 | - |
| | | |
| **DOE Adv GTDI 2.3L I4 – Measured Total** | **34.77** | **25.2%** |

The combined M-H fuel economy required two adjustments as shown in Table 3 and described below.

The engine was designed with an integrated balance shaft-oil pump module. Because the vehicles were equipped with active engine mounts, the balance shafts were not needed for acceptable NVH. Hence the counterweights were machined from the balance shafts for the vehicle engines. The shafts remained due to the oil pump design constraint of the integrated balance shaft-oil pump module. The residual balance shaft friction was measured on component dynamometer and converted to a vehicle level fuel economy effect of 1% M-H fuel economy or 0.34 mpg.

Additionally, downsizing from a 3.5L V6 to a 2.3L I4 GTDI engine yields a 75 pound powertrain weight save. The 2010 Taurus / Fusion was certified at 4250 lb ETW. The next lower weight class is 4000 lb ETW, and coast-down coefficients exist only for discrete weight classes. Thus, the vehicle level fuel economy improvement for decreasing from 4250 to 4000 lb ETW was measured on chassis rolls and pro-rated for a 75 pound powertrain weight save, resulting in a net effect of 0.13 mpg.

## Project Overview:

The objective of the project was to demonstrate 25% fuel economy improvement in a mid-sized sedan using a downsized, advanced GTDI engine with no or limited degradation in vehicle level metrics, while meeting Tier 2 Bin 2 emissions (modified to Tier 3 Bin 30) on the FTP-75 cycle. MTU provided support to Ford in the research and development of advanced ignition concepts and systems to expand the dilute / lean engine operating limits. Milestone timing and budget periods for the project are shown in Figure 4.

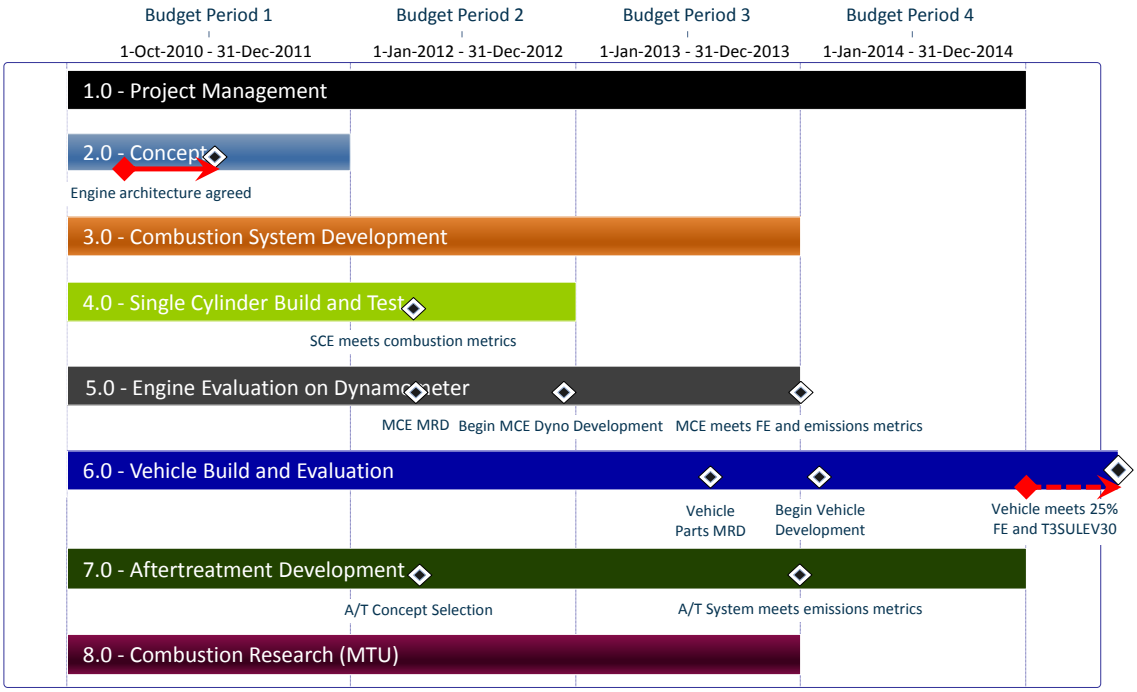


***Figure 4 - Milestones and budget periods for the project.***

The project objectives were progressively demonstrated via concept analysis, computer modeling, single and multi-cylinder engine testing, and vehicle testing. Initial fuel economy benefits projected for the engine and vehicle architecture and system assumptions are shown in Figure 5.

| Architecture / System Assumption | % Fuel Economy | |
|---|---|---|
| 3.5L V6 ⇨ 2.3L I4 High Expansion Ratio Architecture | + | **15.6% - Engine Architecture / Downsizing** |
| 583 ⇨ 565 $cm^3$ Displacement / Cylinder | ~ | |
| 1.07 ⇨ 0.93 Bore / Stroke | ~ | |
| 10.3:1 ⇨ 11.5:1 Compression Ratio | + | |
| PFI ⇨ Transverse Central DI | - | |
| iVCT ⇨ Electric tiVCT | + | |
| Split, Parallel, Cross-Flow Cooling & Integrated Exhaust Manifold | + | **7.8% - Engine & As-Installed Systems** |
| Variable Displacement Oil Pump & Roller Bearing Cam Journals | + | |
| DAMB ⇨ Compact RFF Valvetrain | + | |
| 3.5L V6 ⇨ 2.3L I4 Idle & Lugging Limits | - | |
| Torque Converter Pendulum Damper & Active Powertrain Mounts | + | |
| Assisted Direct Start, ADS | + | |
| Electric Power Assisted Steering, EPAS | + | |
| Active Wastegate | + | **4.4% - Air Path / Combustion** |
| Low Pressure, Cooled EGR System | + | |
| Lean NOx Aftertreatment, LNT + SCR | + | |
| Torque Converter & Final Drive Ratio | + | **0.2% - Engine Match** |
| **Total** | **28.0** | |

***Figure 5 - Architecture and system assumptions with projected fuel economy benefits.***

A surrogate 1.8L single cylinder engine (SCE) was used to conduct combustion system verification testing, provide data for correlation to detailed multi-dimensional engine simulation (MESIM) analyses, and select injector and spark plug specifications for subsequent build of a new 2.3L SCE. A schematic of the innovative transverse central direct injection system developed through SCE testing and MESIM analyses is shown in Figure 6. On the new 2.3L SCE, combustion system verification testing was completed to ensure that the combustion system met the target metrics, including fuel consumption, combustion stability, and emissions of NOx, CO, and PM. Testing included part-load points at lean and stoichiometric conditions, air-fuel ratio sweeps, injection timing sweeps, cooled EGR sweeps, and cam timing sweeps. The effects of split fuel injection strategies on the cold start emissions of the engine were also investigated.

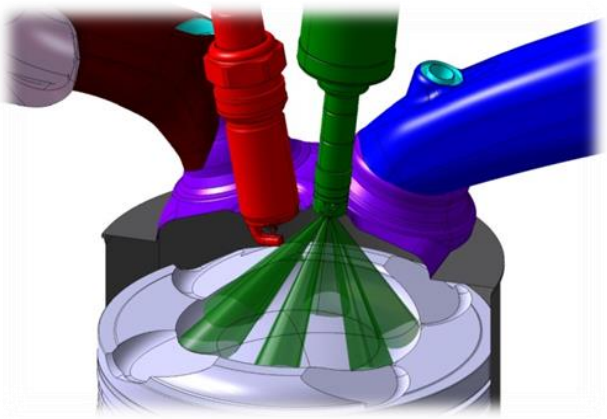

***Figure 6 - Pictorial of transverse central DI injection system.***

Following development of the combustion system, a new 2.3L I4 engine was designed. A picture and design highlights of the engine are shown in Figure 7.

- Displacement / Cylinder = 565 $cm^3$
- Bore & Stroke = 87.5 & 94.0 mm
- Compression Ratio = 11.5:1
- Bore Spacing = 96.0 mm
- Bore Bridge = 8.5 mm
- Deck Height = 222 mm

- Transverse central DI + ignition w/ intake biased multi-hole injector
- Advanced boosting system + active wastegate
- Low pressure, cooled EGR system
- Composite intake manifold w/ integrated air-water charge air cooler assembly
- Split, parallel, cross-flow cooling with integrated exhaust manifold
- Integrated variable displacement oil pump / balance shaft module
- Compact RFF valvetrain w/ 12 mm HLA
- Roller bearing cam journals on front, all other locations conventional
- Electric TiVCT

***Figure 7 - 2.3L GTDI DOE engine.***

A total of twelve multi-cylinder engines were built for various tasks, as shown in Figure 8.

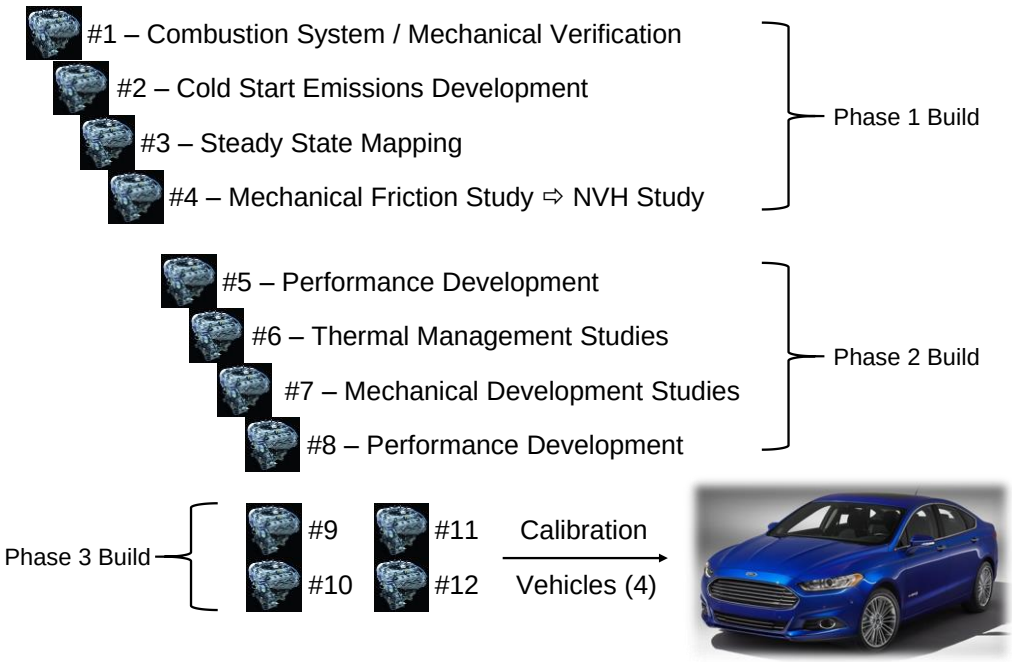


***Figure 8 - Multi-cylinder engine builds and tasks.***

Engine #1 was used for combustion system and mechanical verification testing on engine dynamometer, including partial and full factorials for optimum attributes, part-load fuel consumption and emissions, full-load performance, and advanced engine systems control (e.g. advanced boost system, electric TiVCT). Engine #2 was used for optimization of cold start emissions, including steady state cold fluids development and transient cold start development.

Engine #3 was used for steady state engine mapping, incorporating AutoTest control for autonomous engine mapping. Principal tasks included: a) electric TiVCT cam timing optimization, b) DI fuel injection timing optimization, c) DI fuel rail pressure optimization, d) naturally aspirated air charge throttle sweeps, e) boosted air charge scroll / wastegate control sweeps, f) full load performance BLD / MBT spark sweeps, and g) preliminary “auto” calibration. Mapping validation testing and additional detailed mapping factorials were completed as required to ensure accuracy. Vehicle calibration support testing was also conducted, including verification of multiple software releases and feature functionality.

Engine #4 was used for total engine and successive component removal friction testing, and then rebuilt for subsequent NVH testing and mechanical development studies. Engine #7 was also used for mechanical development studies. Engines #5 and #8 were used for full load performance development. Performance development studies included speeds sweeps, load sweeps, charge air temperature sensitivity surveys, and fuel research octane number sensitivity surveys. Engine #6 was used for thermal management studies, including detailed metal temperature and heat rejection surveys. Engines #9, 10, 11, and 12 were used for vehicle builds and vehicle calibration and optimization of fuel economy, emissions, driveability, and performance.

As part of this project, the feasibility of incorporating stratified charge lean burn at light-medium load operating conditions to improve fuel economy was investigated. The stratified charge concept utilized “micro-stratification”, where a small fraction of the fuel is injected late in the compression stroke to create a close to stoichiometric charge near the spark plug for good ignitability and initial flame development.

It is well known that a three-way catalyst (TWC) cannot reduce $NO_x$ under lean conditions. While urea injection is a recognized enabler for $NO_x$ emissions compliance during lean operation, such an approach places a burden on the consumer to maintain the urea system. In contrast, the work conducted during this

project considered two passive approaches for lean $NO_x$ control which do not require customer maintenance: a lean $NO_x$ trap + selective catalytic reduction (LNT/SCR) system and a passive SCR system in which the $NH_3$ for the SCR catalyst is generated from reduction of the feedgas $NO_x$ on the upstream TWC during rich operation. After a detailed investigation, the TWC+LNT/SCR approach was dismissed due to the inability to desulfate the LNT in the underbody location as required to maintain effectiveness at high mileage. Thus, efforts were focused towards the passive TWC+SCR system, which was less sensitive to the effects of sulfur poisoning. After system design was completed, projections based on detailed accounting indicated that the M-H fuel economy benefit of the passive TWC+SCR system was only 0.8%. This was due to limited opportunities for lean operation due to competing technologies, penalties for enrichment to generate $NH_3$, and penalties due to the weight of the additional SCR converter. The resulting fuel economy value was low relative to other technologies under consideration. As a result, lean burn was excluded from the vehicle phase of the project.

Four 2013MY Fusion vehicles were procured for the vehicle calibration phase of the project. Powertrain-vehicle integration tasks were completed on these four vehicles, including removal of the existing powertrain, preparation for the new powertrain, preparation for new advanced integrated and supporting powertrain systems, and installation of the new powertrain. Initial vehicle calibration tasks included basic startability (crank, run-up, cold / warm idle stability) and basic driveability (tip-in / tip-out stability, acceleration / deceleration stability, transmission scheduling). Vehicle calibration then focused on achieving the fuel economy and emissions project objectives. Main vehicle calibration features are listed in Table 4. Vehicle controls and calibration releases supporting the calibration tasks were ongoing throughout the vehicle phase of the project.

***Table 4 - Vehicle calibration features.***

| Feature | Status |
|---|---|
| Air Charge | ● |
| Fuel Control | ● |
| Spark & Knock Control | ● |
| Torque Model & Control | ● |
| Boost – Scroll / Wastegate / CBV | ● |
| Cold Start & Warm Up | ● |
| Stop / Start | ● |
| Electric tiVCT | ● |
| Cooling & Lubrication | ● |
| Torque Converter Schedule & Control | ● |
| Shift Schedule & Control | ● |
| Low Pressure Cooled EGR | ● |

◐ Functional h/w & s/w verification complete. 'Safe' vehicle calibration.

◔ Development calibration with full transient control.

● Mature transient calibration. Refinement only as necessary for attribute balancing.

MTU provided support to Ford in the research and development of advanced ignition concepts and systems to expand the dilute / lean engine operating limits, as shown in Table 5. This research is documented in three SAE papers and four PhD theses.

***Table 5 - Combustion research areas and deliverables for MTU.***

| Research Area | | Deliverables | Pressure Vessel | Engine Dyno |
|---|---|---|---|---|
| 1 | Advanced Ignition – Ignition and Flame Kernel Development | Gain insight to the fundamental physics of the interaction of combustion system attributes & ignition system design variables relative to both design factors & noise factors; use results to develop an analytical spark discharge model. | ✓ | |
| 2 | Advanced Ignition – Impact on Lean and Dilute | Validate the findings from the pressure vessel & predictions of the resultant model on a mature combustion system, focusing on dilute & lean operating conditions. | | ✓ |
| 3 | Planer Laser Induced Fluorescence | Apply laser-based diagnostics to characterize multi-phase fuel / air mixing under controlled high pressure & temperature conditions; use data for CFD spray model development & spray pattern optimization. | ✓ | |
| 4 | Combustion Sensing and Control | Assess production viable combustion sensing techniques; detect location of 50% mass fraction burned & combustion stability for closed loop combustion control. | | ✓ |
| 5 | Advanced Knock Detection with Coordinated Engine Control | Compare stochastic knock control to various conventional control techniques. | | ✓ |
| 6 | Combustion Surface Temperature | Measure instantaneous temperatures of combustion chamber components under lean, dilute, & boosted operation to improve numerical models and reduce knock tendency. | | ✓ |

The combustion pressure vessel used for tasks 1 and 3 of Table 5 is shown in Figure 9. This vessel utilized dual fans / shrouds for wide range charge motion representing engine-like mean flow and turbulence intensity conditions.

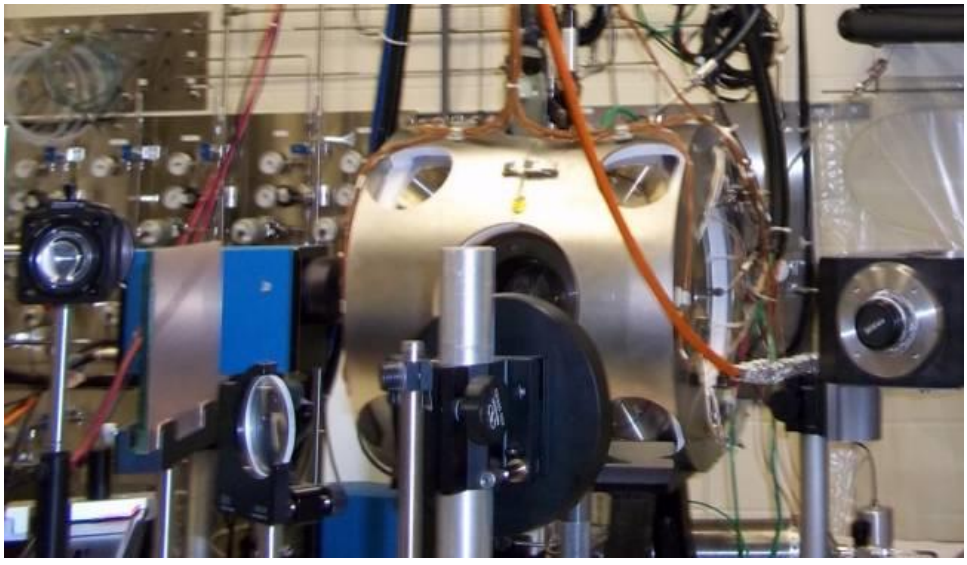

***Figure 9 - Combustion pressure vessel at MTU.***

# Technical Discussion

# Table of Contents


Concept Definition ..... 17
Architecture and System Assumptions ..... 17
Engine Targets ..... 19
Central DI Combustion System Optimization ..... 20
Transverse Central Direct Injection Description ..... 20
3D CFD Upfront Combustion System Optimization ..... 21
Single Cylinder Engine Build and Testing ..... 28
Multi-Cylinder Engine Component Design ..... 36
Cylinder Head ..... 36
Valvetrain ..... 41
Camshaft Drive ..... 44
Electric Variable Camshaft Timing ..... 46
High Pressure Air Intake System ..... 51
Boost System ..... 56
Fuel System ..... 59
Cylinder Block ..... 60
Oil Pump and Balance Shaft ..... 69
Piston, Piston Rings, and Connecting Rod ..... 72
Lubrication System ..... 77
Ignition System ..... 82
Covers and PCV System ..... 85
Low Pressure EGR System ..... 94
Cooling System ..... 101
Multi-Cylinder Engine Development ..... 103
Part Load ..... 103
Full Load ..... 136
Engine Mapping ..... 142
Steady State Emissions with Cold Fluids ..... 147
Transient Cold Start Emissions Development ..... 158
Vehicle Build and Calibration ..... 164
Aftertreatment Development ..... 168
Combustion Research (MTU) ..... 195
References ..... 230

# List of Tables

Table 1 - Transient engine test cold start emissions compared to the SULEV30 targets. 3
Table 2 - Vehicle emission results with catalysts aged to FUL compared to the SULEV30 standards. 4
Table 3 - M-H vehicle fuel economy results. 5
Table 4 - Vehicle calibration features. 9
Table 5 - Combustion research areas and deliverables for MTU. 10
Table 6 - Cold start emission targets. 19
Table 7 - Speed-load points for injector evaluation. 33
Table 8 - VCT Phasing Tests. 48
Table 9 - Cylinder block dimensions. 60
Table 10 - Rod analysis for bulking and fatigue safety factor. 75
Table 11 - Piston cooling jet benchmarking. 79
Table 12 - Transient cold start targets. 158
Table 13 - Emission targets and transient cold start attribute results. 163
Table 14 - Vehicle calibration features. 165
Table 15 - Vehicle emission results with catalysts aged to FUL vs. the SULEV30 standard. 166
Table 16 - Unadjusted M-H vehicle fuel economy results. 167
Table 17 - Combustion research areas and deliverables for MTU. 195

# List of Figures

Figure 1 - Status vs. target full load BMEP (left) and transient time-to-torque (right) for 2.3L GTDI DOE engine. 2
Figure 2 - Air-fuel ratio and combustion phasing vs. engine speed at full load for 2.3L DOE engine. 3
Figure 3 - BSFC status vs. targets and reference 2.0L GTDI engine for mini-map test points. 4
Figure 4 - Milestones and budget periods for the project. 6
Figure 5 - Architecture and system assumptions with projected fuel economy benefits. 6
Figure 6 - Pictorial of transverse central DI injection system. 7
Figure 7 - 2.3L GTDI DOE engine. 7
Figure 8 - Multi-cylinder engine builds and tasks. 8
Figure 9 - Combustion pressure vessel at MTU. 10
Figure 10 - Architecture/system assumptions and projected fuel economy improvements. 18
Figure 11 - Types of direct injection systems. Top view in the left images and side view of the velocity field and spray interaction in a central cross-section in the right images, 5000rpm/full load. 20
Figure 12 - Liner impingement comparison for side, longitudinal central, and transverse central DI systems at 2000 rpm and 5000 rpm full load. 21
Figure 13 - Side and top views of the 2.3L GTDI combustion system. The intake port is on the right. 22
Figure 14 - Tumble ratio evolution during the intake and compression strokes. 23
Figure 15 - Velocity (m/s) field in a cross-sectional plane through the intake port, 2000rpm/full load. 23
Figure 16 - Volumetric efficiency vs. tumble ratio for various engines. 23
Figure 17 - Injector spray patterns. 24
Figure 18 - Spray pattern optimization at 1500/5 bar, SOI=425° aTDC: mixing index, piston impingement, and liner impingement. 25
Figure 19 - Piston top showing fuel spray jets at 35 °bTDC (middle) and 30 °bTDC (right). 25
Figure 20 - Air-fuel ratio contours during CSER operation at CA=700°, 720°, and 740° aTDC for 2.3L engine with spray 6H34 (left) and 1.8L engine with spray 6H21 (right) at 1250 rpm. 26
Figure 21 - Piston impingement at CSER, 1250 rpm. 26
Figure 22 - Mixing index and piston impingement comparison between 2.3L GTDI DOE and other DI engines at part load and full load. 27
Figure 23 - Liner impingement comparison between 2.3L GTDI DOE and other DI engines at full load. 27
Figure 24 - Initial spray pattern 6H21 evaluation at part load in 1.8L SCE. 29

Figure 25 - Fuel injector spray pattern comparison at 1500 rpm/2.62 bar BMEP (left) and 1500 rpm/5 bar BMEP (right) in 2.3L SCE. 30
Figure 26 - Fuel injector spray pattern comparison at 2000rpm/9 bar BMEP in 2.3L SCE. 31
Figure 27 - CSER fuel injector spray pattern comparison for 50/50 (left) and 90/10 (right) split injection in 2.3L DOE SCE. 32
Figure 28 - NSCO, COV IMEP, and smoke data over a range of injection timings with injector 34A. 33
Figure 29 - NSCO, COV IMEP, and smoke over a range of injection timings at a 1500 RPM, 5.60 bar NMEP. 34
Figure 30 - SD of NMEP, smoke, and FGHC + FGNOx over a range of second injection timings at 1250 RPM, 1.90 bar NMEP with a split ratio of 50/50. Coolant and oil temperature 20°C. 35
Figure 31 - SD of NMEP, smoke and FGHC + FGNOx over a range of second injection timings at 1250 RPM, 1.90 bar NMEP with a split ratio of 90/10. Coolant and oil temperature 20°C. 35
Figure 32 - Combustion chamber with transverse central DI. 36
Figure 33 - Cylinder head cross-section and components. 36
Figure 34 - Cylinder head dry valley. 37
Figure 35 - Camshaft carrier. 37
Figure 36 - Integrated exhaust manifold. 37
Figure 37 - Split cooled water jacket. 38
Figure 38 - Coolant flow in the upper and lower cooling jackets. 38
Figure 39 - Critical cross-sections for cooling. 39
Figure 40 - CAE metal temperature predictions. 39
Figure 41 - Cylinder head HCF safety factors. 40
Figure 42 - Distance between fuel injector tip and spark plug center electrode. 40
Figure 43 - Fuel injector spray pattern. 40
Figure 44 - Intake port. 41
Figure 45 - Charge motion - fuel spray interaction. 41
Figure 46 - Valvetrain. 42
Figure 47 - Valvetrain dimensional layout. 42
Figure 48 - Minimum force between cam lobe and roller follower as predicted by dynamic model. 43
Figure 49 - Needle bearing at front of camshaft. 43
Figure 50 - Camshaft loads for bearing life calculation. 44
Figure 51 - Belt (left) and chain (right) layouts considered for cam drive. 44
Figure 52 - Segment of Borg Warner 3 x 2 Type 111 chain. 45
Figure 53 - Chain tension results of dynamic analysis. 45
Figure 54 - Chain snubber. 46
Figure 55 - Electric VCT mechanism and operating ranges. 47
Figure 56 - Variable cam timing control structure. 47
Figure 57 - Slip ring and chain sprocket of ElVCT. 47
Figure 58 - VCT response during tip-in at 1500 RPM engine speed. 48
Figure 59 - VCT response for intake retarding and exhaust holding position. 49
Figure 60 - VCT holding position. 49
Figure 61 - Vehicle random drive. 50
Figure 62 - Vehicle cold start at 0 $^{o}$F (-18 °C) ambient temperature. 50
Figure 63 - High pressure air induction system. 51
Figure 64 - Intake integrated charge air cooler top view. 51
Figure 65 - Isometric view of pre-throttle charge air cooler with end tanks. 52
Figure 66 - Aspect ratio of charge air coolers for low pressure drop. 52
Figure 67 - Low boosted volume for good transient response. 53
Figure 68 - Volumetric efficiency variation at peak power. 53
Figure 69 - Volumetric efficiency variation at 3500 rpm, 16.5 bar BMEP. 54
Figure 70 - Temperature distribution at runner inlets. 54
Figure 71 - Temperature distribution at remote charge air cooler entrance. 55
Figure 72 - Sealing and assembly for the intake manifold integrated charge air cooler. 55
Figure 73 - Electric wastegate actuator and four-bar linkage; EGR takeoff port. 56
Figure 74 - Binary flow turbine. 57
Figure 75 - Dynamometer test results showing engine transient torque response. 57

Figure 76 - Exhaust inlet gasket, support bracket, and heat shield. ..... 58
Figure 77 - Overview of turbocharger and related air ducts. ..... 58
Figure 78 - Direct injector high pressure fuel pump and fuel rail. ..... 59
Figure 79 - Direct injector fuel spray. ..... 59
Figure 80 - Cross bolted ladder frame main bearing caps and offset crankshaft. ..... 61
Figure 81 - PTWA coated cylinder bore wall definition. ..... 62
Figure 82 - Wet crank position sensor package definition. ..... 62
Figure 83 - Crankshaft sensor timing for offset crank package. ..... 63
Figure 84 - Open head deck showing cooling circuit and head oil drain features. ..... 63
Figure 85 - Critical pressure loading cases: crank angle and peak pressure. ..... 64
Figure 86 - Effect of saw cut depth on predicted cylinder block metal temperatures. ..... 64
Figure 87 - Fatigue factors for critical loading cases. ..... 65
Figure 88 - Block bore saw cut stress conditions. ..... 66
Figure 89 - Bore distortion analysis. ..... 66
Figure 90 - Excite loads for bulkhead analysis. ..... 67
Figure 91 - Fatigue factor analysis for bulkhead. ..... 67
Figure 92 - Piston oil jet flow control and block packaging. ..... 68
Figure 93 - Cylinder block views. ..... 68
Figure 94 - BSM-OP (integrated balance shaft module and oil pump) side view. ..... 69
Figure 95 - BSM-OP bottom view. ..... 69
Figure 96 - BSM-OP chain drive. ..... 70
Figure 97 - BSM-OP drive and gear train. ..... 70
Figure 98 - Oil pump intake and discharge. ..... 71
Figure 99 - Oil intake for lubrication, tensioner, and oil pump switching. ..... 71
Figure 100 - Oil pump solenoid and connector. ..... 72
Figure 101 - Benchmarking of piston K factors. ..... 72
Figure 102 - Calculated piston temperatures. ..... 73
Figure 103 - Calculated piston fatigue safety factors. ..... 74
Figure 104 - Analysis of piston skirt and pin boss contact pressures. ..... 74
Figure 105 - Ring tension benchmarking. ..... 75
Figure 106 - CAE analysis of rod fatigue safety factors. ..... 76
Figure 107 - Analysis of joint face separation. ..... 76
Figure 108 - Analysis of big end bore distortion. ..... 77
Figure 109 - Lubrication system schematic. ..... 78
Figure 110 - Oil module comparison. ..... 79
Figure 111 - AMEsim lubrication system analytical model. ..... 80
Figure 112 - Protection from failure modes with check valve function. ..... 80
Figure 113 - Oil pump flow and pressure requirements (left); oil pump actual performance (right). ..... 81
Figure 114 - Oil flow for sub-systems. ..... 81
Figure 115 - Ignition coil output characteristics. ..... 82
Figure 116 - Ignition coil drawing. ..... 83
Figure 117 - Spark plug firing end detail. ..... 83
Figure 118 - Spark plug drawing. ..... 84
Figure 119 - Sealing components for DOE engine. ..... 85
Figure 120 - Valve cover with integrated PCV/oil separators. ..... 86
Figure 121 - PCV system schematic. ..... 86
Figure 122 - High efficiency oil/PCV separator. ..... 87
Figure 123 - Valve cover surface normal velocity at 6000 rpm. ..... 88
Figure 124 - Front cover assembly. ..... 89
Figure 125 - Engine mount bracket. ..... 89
Figure 126 - Low friction micro-torq seal comparison to PTFE and sprung elastomeric seals. ..... 90
Figure 127 - Front cover NVH analysis results. ..... 91
Figure 128 - Front mount bracket velocity analysis. ..... 91
Figure 129 - Oil pan initial design concept and final design. ..... 92
Figure 130 - Oil pan NVH analysis. ..... 93

Figure 131 - Rear seal retainer. ..... 93
Figure 132 - 2.3L GTDI engine low pressure EGR system. ..... 95
Figure 133 - Low pressure EGR System with 2.3L GTDI engine. ..... 96
Figure 134 - EGR schedule extent sensitivity study. ..... 96
Figure 135 - Compressor outlet temperature study for two different EGR cooler sizes. ..... 97
Figure 136 - LP EGR system pressure drop analysis. ..... 97
Figure 137 - EGR cooler flow distribution study. ..... 98
Figure 138 - LP EGR pre-compressor mixing study. ..... 98
Figure 139 - EGR cooler coolant flow requirement analysis. ..... 99
Figure 140 - EGR cooler internal coolant cavity CFD study. ..... 100
Figure 141 - EGR inlet tube thermo-mechanical stress analysis from Borg-Warner. ..... 100
Figure 142 - Cooling system schematics of high (top) and low (bottom) temperature loops. ..... 102
Figure 143 - 2.3L DOE BSFC status at mini-map points (top graph) and % BSFC difference compared to the targets (bottom graph). ..... 103
Figure 144 - 2.3L DOE engine % BSFC improvement from 0 to 15% EGR from multiple samples. ..... 104
Figure 145 - Flange view of exhaust entrance into turbine. ..... 105
Figure 146 - Top view of exhaust entrance into turbine. ..... 106
Figure 147 - Pumping loops at 2500 rpm/ 14 bar BMEP with the turbo scroll control valve open (black line) and closed (red line). ..... 106
Figure 148 - Turbo scroll control valve closed to open turbine in pressure decrease (top graph) and the corresponding pumping work (∆PMEP/IMEP) fuel benefit (bottom graph) at mini-map points. ..... 107
Figure 149 - Turbo scroll control valve closed to open CA50 improvement (top graph) and the corresponding %ISFC fuel benefit (bottom graph) at mini-map points. ..... 108
Figure 150 - Turbo scroll control valve closed to open sum of ∆PMEP/IMEP and CA50 % fuel consumption benefits. ..... 108
Figure 151 - Cut-away view of variable displacement oil pump (VDOP). ..... 109
Figure 152 - Oil pressure at mini-map points with all permutations of VDOP in HP/LP mode and oil squirters on and off. ..... 110
Figure 153 - VDOP HP to LP mode BSFC % improvement (red bars) and oil pressure reduction (blue bars) at selected mini-map points with the oil squirters on (top graph) and off (bottom graph). ..... 111
Figure 154 - Oil temperature at mini-map points with all permutations of VDOP in HP/LP mode and oil squirters on and off. ..... 112
Figure 155 - Oil squirter on to off BSFC % improvement (red bars) and oil pressure reduction (blue bars) at mini-map points with the VDOP in HP mode (top graph) and LP mode (bottom graph). ..... 113
Figure 156 - Proposed VDOP/oil squirter map. ..... 114
Figure 157 - Optimized results at 1500/5 bar with four combinations: [14.6:1 A/F and 0% EGR], [14.6:1 A/F and 15% EGR], [22:1 A/F, 15% EGR, micro-strat], and [26:1 A/F, 0% EGR, micro-strat]. ..... 117
Figure 158 - % BSFC benefit relative to 14.6:1 A/F, 0% EGR (top graph) and 14.6:1 A/F, 15% EGR (bottom graph). ..... 117
Figure 159 - Intake VCT sweeps at various levels of exhaust VCT and EGR to determine optimum stability cam timing. ..... 119
Figure 160 - EGR sweep at 1500 RPM, 0.7 bar BMEP. ..... 120
Figure 161 - EGR sweep at 1000 RPM, 0.12 EECLOAD, 0 torque. ..... 121
Figure 162 - 600 RPM, 0.7 bar BMEP with 0% EGR, spark sweeps with 0° intake and various exhaust cam retards. ..... 122
Figure 163 - Cam timing diagrams for 2.3L DOE engine. ..... 122
Figure 164 - EPA city cycle fuel usage contour plot from e-CVSP. ..... 123
Figure 165 - EPA highway cycle fuel usage contour plot from e-CVSP. ..... 124
Figure 166 - US06 cycle fuel usage contour plot from e-CVSP. ..... 124
Figure 167 - 1500/2.62 bar, 15% EGR, scroll closed full factorial intake and exhaust sweeps. ..... 125
Figure 168 - 2000/5 bar, 15% EGR, scroll closed full factorial intake and exhaust sweeps. ..... 126
Figure 169 - 2000/9 bar, 15% EGR, scroll open full factorial intake and exhaust sweeps. ..... 127
Figure 170 - 2500/14 bar, 15% EGR, scroll open full factorial intake and exhaust sweeps. ..... 128
Figure 171 - 1500/5 bar, 15% EGR, scroll open full factorial SOI and FRP sweeps. ..... 130
Figure 172 - 1500/5 bar, 15% EGR, scroll open full factorial SOI and FRP sweeps. ..... 131

Figure 173 - 2000/9 bar, 15% EGR, scroll open full factorial SOI and FRP sweeps. 132
Figure 174 - 2000/9 bar, 15% EGR, scroll open full factorial SOI and FRP sweeps. 133
Figure 175 - 2500/14 bar, 15% EGR, scroll open full factorial SOI and FRP sweeps. 134
Figure 176 - 2500/14 bar, 15% EGR, scroll open full factorial SOI and FRP sweeps. 135
Figure 177 - Full load BMEP and brake power vs. engine speed. 136
Figure 178 - Air-fuel ratio, turbine inlet temperature, combustion phasing, and smoke number vs. engine speed at full load. 137
Figure 179 - Valve timings, feedgas $O_2$, and combustion stability vs. engine speed at full load. 137
Figure 180 - IMEP, MAP, wastegate duty cycle, and peak pressure vs. engine speed at full load. 138
Figure 181 - Turbine inlet pressure, PMEP, turbocharger speed, and compressor outlet temperature vs. engine speed at full load. 139
Figure 182 - Optimization of VCT settings at 3000 rpm for best efficiency. 139
Figure 183 - Cylinder pressure pumping loop at 1500 rpm. 140
Figure 184 - Cylinder pressure pumping loop at 3000 rpm. 140
Figure 185 - Cylinder pressure pumping loop at 5000 rpm. 140
Figure 186 - Transient time-to-torque vs. engine speed. 141
Figure 187 - Mapping engine installed in dynamometer test cell. 142
Figure 188 - Initial and updated calibrations for intake cam advance vs. EEC Load. 143
Figure 189 - Difference in percent load between engine data and map vs. engine speed (left) and EEC Load (right). 145
Figure 190 - Difference in brake torque between engine data and map vs. engine speed (left) and EEC Load (right). 145
Figure 191 - Difference in exhaust backpressure and manifold pressure between engine data and regressed engine map. 146
Figure 192 - CA50 vs. EEC Load (air flow) for mapping data. 146
Figure 193 - 2.3L I4 DOE cam timing. 147
Figure 194 - SOI1 and fuel rail pressure sweep with single intake injection. 148
Figure 195 - EOI2 and SOI1 sweep with 50/50 split ratio. 149
Figure 196 - EOI2 and SOI1 sweep with 90/10 split ratio. 149
Figure 197 - EOI2 and SOI1 sweep with 70/30 split ratio. 150
Figure 198 - Intake and exhaust cam sweep with 70/30 split ratio. 151
Figure 199 - Heat flow (spark timing) sweep with 70/30 split ratio. 152
Figure 200 - Air-fuel ratio sweep with 70/30 split ratio. 153
Figure 201 - Split ratio and fuel ratio pressure sweep at 290/40 injection timing, -30/30 cam timing. 153
Figure 202 - Heat flow, scroll control valve and wastegate sweep. 154
Figure 203 - SOI1 and EOI2 sweep with 70/30 split ratio. 155
Figure 204 - Intake and exhaust cam sweep with 70/30 split ratio. 156
Figure 205 - Heat flow and cam timing sweep with intake only injection. 157
Figure 206 - Engine dynamometer transient cold start, neutral idle, drive idle, and drive away. 159
Figure 207 - Heat flow study with mass flow and spark timing swept between 15° to 24° aTDC. Heat flow units are in Watts/liter of engine displacement. 160
Figure 208 - Lambda sweep during the cold idle portion of the test. 161
Figure 209 - Cumulative feedgas HC and NOx vs. lambda during the 5 -15 sec period. 161
Figure 210 - Effect of wastegate and scroll control valve positions on catalyst midbed temperature at 20 seconds. 162
Figure 211 - Repeat of heat flow study with mass flow and spark timing swept between 15° to 24° aTDC. 162
Figure 212 - 2.3L engine with measurement instrumentation installed in a Fusion vehicle. 164
Figure 213 - Fusion vehicle on chassis rolls. 166
Figure 214 - TWC system specifications. 168

# Technical Discussion

## Concept Definition

A 2.3L I4 high expansion ratio engine architecture was selected to “right-size” the engine with future North American, high volume, CD-size (i.e. mid-size) vehicle applications. Assumptions were developed for the engine, transmission/vehicle, and aftertreatment to support the overall fuel economy, performance, and emission objectives. Detailed fuel economy, emissions, performance, and NVH targets were generated, and component assumptions were developed to achieve the targets, as well as to guide combustion system, single-cylinder engine, and multi-cylinder engine design and development. Cycle-based CAE analysis of the fuel economy contribution of critical technologies was completed to ensure that the vehicle demonstrates 25% weighted city / highway fuel economy improvement.

### Architecture and System Assumptions

Engine

The deck height and bore spacing of the new engine were based on an existing production Ford I4 engine. A high geometric compression ratio of 11.5:1 was specified to provide high expansion ratio for improved fuel economy in conjunction with a relatively long 260° intake camshaft duration to provide reduction of effective compression ratio (“Miller Cycle”) for acceptable knock behavior with 98 RON fuel. The engine was designed for a maximum cylinder pressure (mean + 3σ) of 100 bar and maximum exhaust gas temperature of 960°C. Key dimensions of the engine architecture are listed below:

- Displacement / Cylinder = 565 $cm^3$
- Bore and Stroke = 87.5 and 94.0 mm
- Compression Ratio = 11.5:1
- Bore Spacing = 96.0 mm
- Bore Bridge = 8.5 mm
- Deck Height = 222 mm

Engine assumptions are summarized below:

- Transverse central DI + ignition with intake biased multi-hole injector
- Advanced boosting system + active wastegate
- Low pressure, cooled EGR system
- Composite intake manifold with integrated air-water charge air cooler assembly
- Split, parallel, cross-flow cooling with integrated exhaust manifold
- Integrated variable displacement oil pump / balance shaft module
- 10 mm offset crankshaft
- Compact RFF valvetrain with 12 mm HLA
- Roller bearing cam journals on front, all other locations conventional
- Electric twin independent variable cam timing (TiVCT)

A transverse central direct injection combustion system was chosen to provide enhanced stratified charge capability with reduced cylinder liner and piston fuel wetting compared to other direct injection configurations. Enhanced stratified charge capability was deemed necessary for investigation of lean burn at part load and to enable more flexibility with split injection during the cold idle period for cold start emissions reduction.

Friction reduction actions included a 10 mm offset crankshaft, variable displacement oil pump, compact roller finger follower valvetrain with 12 mm hydraulic lash adjusters, front roller cam bearings, and active turbocharger wastegate (for reduced part load pumping work).

Low pressure cooled EGR was incorporated to provide dilution for improved fuel economy via reduced pumping and heat losses at lower speed-loads, and improved fuel economy via reduced knocking tendency and enrichment at higher speed-loads.

Electric TiVCT was chosen to provide cam position control independent of engine speed, oil pressure, and oil temperature, as well as good shifting velocity and shifting range capability.

An integrated exhaust manifold was incorporated to reduce enrichment requirements at high engine speed/load, reduce weight and cost, and provide improved packaging of the turbocharger in the engine compartment. A composite intake manifold with integrated air-water charge air cooler assembly was specified to provide good low speed transient response via low boosted volume, good high speed power via low pressure drop, minimum transport delay for low pressure cooled EGR, and good vehicle package.

Transmission / Vehicle

NVH countermeasures for use of an I4 engine in place of a V6 engine were incorporated in the project. These included a torque converter pendulum damper and active powertrain mounts to improve fuel economy via preservation of V6 idle and lugging limits by providing mitigation of the I4 firing frequency and 2nd order shaking force unbalance.

Assisted direct start (ADS) and electric power assisted steering (EPAS) were also included in the program to improve fuel economy.

Aftertreatment

Passive lean NOx aftertreatment consisting of a lean NOx trap (LNT) and selective catalytic reduction (SCR) system was included as part of the program for evaluation in conjunction with stratified charge lean burn as a means of improving part load fuel consumption.

## Fuel Economy Analysis

Cycle-based CAE analysis of the fuel economy contribution of the critical technologies is shown in Figure 10.

| Architecture / System Assumption | % Fuel Economy | |
|---|---|---|
| 3.5L V6 ⇨ 2.3L I4 High Expansion Ratio Architecture | + | **15.6% - Engine Architecture / Downsizing** |
| 583 ⇨ 565 $cm^3$ Displacement / Cylinder | ~ | |
| 1.07 ⇨ 0.93 Bore / Stroke | ~ | |
| 10.3:1 ⇨ 11.5:1 Compression Ratio | + | |
| PFI ⇨ Transverse Central DI | - | |
| iVCT ⇨ Electric tiVCT | + | |
| Split, Parallel, Cross-Flow Cooling & Integrated Exhaust Manifold | + | **7.8% - Engine & As-Installed Systems** |
| Variable Displacement Oil Pump & Roller Bearing Cam Journals | + | |
| DAMB ⇨ Compact RFF Valvetrain | + | |
| 3.5L V6 ⇨ 2.3L I4 Idle & Lugging Limits | - | |
| Torque Converter Pendulum Damper & Active Powertrain Mounts | + | |
| Assisted Direct Start, ADS | + | |
| Electric Power Assisted Steering, EPAS | + | |
| Active Wastegate | + | **4.4% - Air Path / Combustion** |
| Low Pressure, Cooled EGR System | + | |
| Lean NOx Aftertreatment, LNT + SCR | + | |
| Torque Converter & Final Drive Ratio | + | **0.2% - Engine Match** |
| **Total** | **28.0** | |

***Figure 10 - Architecture/system assumptions and projected fuel economy improvements.***

## Engine Targets

Engine performance targets were developed using CAE to support the objective of no or limited degradation in vehicle level metrics, assuming a 2.3L boosted I4 engine in place of the baseline naturally aspirated V6 engine. The performance related targets are as follows:

- Peak Power = 80 kW / L @ 6000 rpm
- Peak Torque = 20 bar BMEP @ 2000 – 4500 rpm
- Naturally Aspirated Torque @ 1500 rpm = 8 bar BMEP
- Peak Boosted Torque @ 1500 rpm = 16 bar BMEP
- Time-To-Torque @ 1500 rpm = 1.5 s
- As Shipped Inertia = 0.0005 kg-$m^2$ / kW

Targets for transient 20°C cold start feedgas emissions of HC, NOx, and PM for the first 20 seconds of the FTP test were derived from the tailpipe standards for Tier 2 Bin 2 (later transitioned to Tier 3 SULEV30), and are shown in Table 6. Performance vs. the targets is evaluated at an exhaust heat flux to the catalyst during the cold idle period after the engine start that achieves ~350°C catalyst mid-bed temperature at 20 seconds after engine start.

***Table 6 - Cold start emission targets.***

| Cold Start Attribute | Units | Target[1] |
|---|---|---|
| 0-20s Cumulative FGHC + FGNOx | mg | < 227 |
| 0-20s Cumulative Particulate Mass (PM) | mg | < 3.0 |
| 5-15s CSER stability (RMS_SDIMEP) | bar | < 0.350 |

Engine fuel consumption targets were developed for a steady state mini-map of nine speed-load points. These targets were cascaded based on analysis using Ford's corporate vehicle simulation program (CVSP), and are consistent with the engine technical content. Achieving the engine fuel consumption targets is necessary to deliver the engine portion of the 25% vehicle fuel economy improvement relative to the baseline V6. Feedgas emission targets for the same nine steady state mini-map points were specified for CO emissions to ensure good air-fuel mixing, and for PM emissions to ensure avoidance of excessive direct injection fuel wetting on the cylinder liner and piston.

# Central DI Combustion System Optimization

The 2.3L GTDI DOE engine combustion system was designed using an integrated approach between upfront 3D CFD modeling optimization, single-cylinder engine development, and multi-cylinder engine development. The combustion chamber, intake port, piston, and spray pattern were extensively developed and optimized upfront with 3D CFD modeling with the goals of good fuel/air mixing and combustion stability, minimal fuel wetting on the cylinder walls and piston, and good spark retard capability during the catalyst heating period following a cold start. Single cylinder engine testing revealed good part load mixing comparable to PFI benchmarks based on CO emissions. Low smoke emissions were also demonstrated over a wide range of injection timings for part load conditions. For the catalyst heating period termed cold start emissions reduction (CSER) at Ford, standard injection split ratios produced comparable emissions and stability as previous DI combustion system applications. The close spacing of the injector and spark plug further enabled new split injection CSER strategies (e.g., 90/10) that improved both emissions and stability. Finally, compatibility of the combustion system with an outwardly-opening solenoid injector (OOSI) showed potential to further reduce part load particulate emissions, as well as enabling lower criteria emissions during CSER compared with the multi-hole injector results.

## Transverse Central Direct Injection Description

Direct-injection (DI) combustion systems can be classified according to the injector location as side DI or central DI. The central DI combustion systems can be further classified as longitudinal central DI or transverse central DI. The 2.3L GTDI engine for this project is a transverse central DI combustion system. Figure 11 compares the three different types of combustion systems. The images show the spray in the cylinder at 5000 rpm/ full load, at CA = 500° aTDC (140° aTDC of the intake stroke). In the top views on the left, the green circle shows the injector location and the red arrow shows the position of the spark plug. The other two arrows show the direction of the air flow.

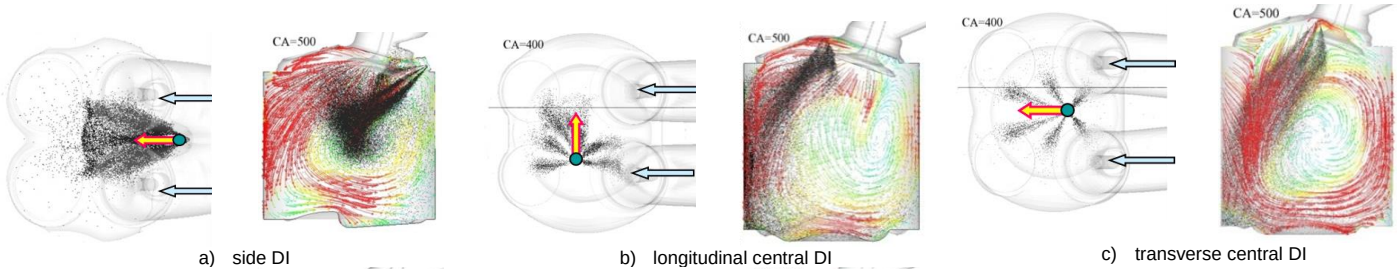


***Figure 11 - Types of direct injection systems. Top view in the left images and side view of the velocity field and spray interaction in a central cross-section in the right images, 5000rpm/full load.***

In the side DI combustion system, the injector is located on the side of the combustion chamber below the intake port and the spray jets are aligned with the intake airflow, as seen in Figure 11a. In these engines the piston has an asymmetrical bowl shaped to capture the spray jets during compression injection and direct rich mixture to the spark plug for good combustion stability during CSER. The central DI layout enables close placement of fuel injector and spark plug. In longitudinal central DI systems, the spark plug-injector axis is oriented longitudinally with the crankshaft axis and the central spray is across the air flow. Because of this arrangement, the airflow can deflect the spray jets as seen in Figure 11b, which can lead to an asymmetrical air-fuel mixture distribution in the cylinder and also increased liner impingement at high speeds. The piston impingement is generally lower in central DI engines than in side DI engines because the fuel spray has to travel a longer distance before it impinges on the piston. In a transverse central DI layout, such as the 2.3L engine for this project, the fuel injector and spark plug are aligned with the air flow from the intake port, as seen in Figure 11c.

Figure 12 compares the liner impingement in the three types of DI engines at 2000 rpm/full load and 5000 rpm/full load. The liner impingement quantifies the cumulative percentage of the injected fuel that impinges on the liner during an engine cycle. The trend in liner impingement between the three engines is different at 2000 rpm/full load and 5000 rpm/full load. At the lower speed operating condition, 2000 rpm/full load, the central DI engines have lower liner impingement than the side DI engine, and the transverse DI engine for this project

has slightly lower liner impingement than the longitudinal DI engine. The liner impingement in the side DI engine is larger than in the central DI engines at 2000 rpm because the intake air flow is weak and cannot block the spray penetration and since all jets are directed towards the exhaust side, most of them actually reach the liner and increase liner impingement. In the central DI engines fewer spray jets impinge on the liner at 2000 rpm. In longitudinal central DI engines the airflow bends part of the jets towards the liner and in transverse central DI engines the two front jets directed at the spark plug are the ones that impinge on the liner.

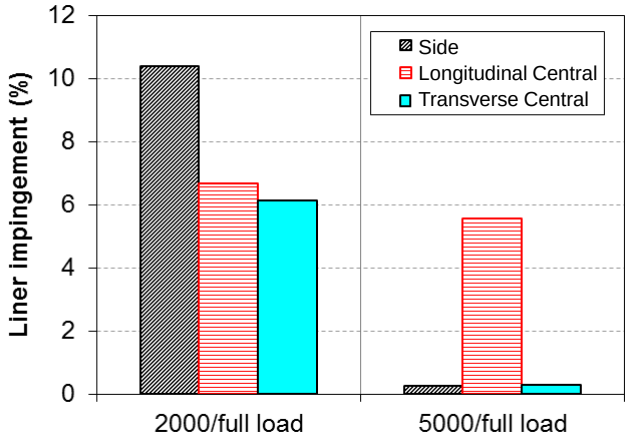


***Figure 12 - Liner impingement comparison for side, longitudinal central, and transverse central DI systems at 2000 rpm and 5000 rpm full load.***

Figure 12 shows large differences in liner impingement between the three engines at 5000 rpm/full load. At 5000 rpm/full load, the side DI and transverse central DI engines have lower liner impingement than the longitudinal central DI engine. In side DI engines, the spray jets are aligned with the airflow and at high speeds, such as 5000 rpm, the high velocity intake air blocks the spray from penetrating towards the exhaust side, as seen in Fig.1a, and minimizes liner impingement. In longitudinal DI engines, the spray jets are across the air flow and at higher engine speeds such as 5000 rpm, the high velocity intake air entrains and deflects the spray jets towards the liner, as seen in Fig. 1b, which increases liner impingement. In the transverse central DI layout of the 2.3L DOE engine, the fuel injector and spark plug are aligned with the air flow from the intake port. This allows the airflow to bend the spray jets downwards, as seen in Fig 1c, similarly to what happens in a side DI engine, which leads to reduced liner impingement. In conclusion, the transverse central DI layout combines the spray-airflow orientation advantage of the side DI layout with the central location advantage of the longitudinal DI layout.

## 3D CFD Upfront Combustion System Optimization

The combustion system of the 2.3L GTDI engine for this project was designed using an integrated approach between upfront 3D CFD modeling optimization, single-cylinder engine development, and multi-cylinder engine development. The combustion chamber, intake port, piston, and spray pattern were extensively developed and optimized upfront with 3D CFD modeling using the Ford internal 3-D CFD code MESIM and MESIM-Converge. MESIM is an extension of KIVA-3V (Amsden, 1997, 1999) with enhanced dynamic mesh moving algorithm (Yi and Han, 2001) and improvements in the multi-hole direct injection spray and film models (Han and Xu, 2004). MESIM was also updated with a level set method, G-equation based, combustion model linked to the chemical kinetics software CHEMKIN (Liang and Reitz, 2006, Liang et al., 2007). MESIM was successfully used at Ford Motor Company for the combustion system development and optimization of a light stratified-charge direct injection engine (Yi et al., 2000, 2002 and 2004; Han et al., 2002 and 2004), for the development of a spray-guided direct injection engine (VanDerWege et al., 2003, Iyer et al., 2004), and for the development of the 3.5L EcoBoost engine (Kapp et al., 2009, Yi et al, 2009, Iyer and Yi, 2009). The MESIM-Converge code was developed by incorporating Ford's leading spray and wall impingement models in the commercial CONVERGE CFD software (Richards et al., 2012) released by Convergent Science.

The combustion chamber, the intake port, piston top, and the exhaust port were discretized and the computational mesh moved dynamically following the valve lift profile and the piston motion. The flow and energy equations were solved coupled with a RNG k-ε turbulence model (Han and Reitz, 1995). Initial and boundary conditions were setup with the use of existing dynamometer data or with simulations from a zero-dimensional engine model, GESIM (Dai, 2005). At the inflow and outflow boundaries a constant pressure boundary condition was set. Simulations were initiated before intake valve opening (IVO) and were continued through the remainder of the exhaust stroke, the intake stroke, and the compression stroke. Simulations were performed at part load and full load operation, as well as at the catalyst heating mode CSER condition. The CSER simulations were run up to the spark timing of 20° aTDC. The main factors tracked during analysis were air-fuel mixing, turbulence intensity, spray impingement on surfaces, tumble ratio, trapped mass at full load, and the evolution of the rich cloud around the spark plug for CSER simulations.

## Tumble Motion

The intake port design determines the type of in-cylinder charge motion generated during the intake stroke. The intake port flow capacity for boosted combustion systems is not as important as for naturally aspirated engines, therefore there is an opportunity to use intake ports with higher charge motion. The in-cylinder charge motion generates turbulence that in turn affects burn rates, knock resistance and heat transfer. Lang et al. (2005) showed that higher charge motion intake port concepts give favorable results when used in the design of boosted engines. Hancock et al. (2008) showed that in order for their combustion system to obtain stable lambda 1 combustion the inlet port was designed for a high level of tumble. Bandel et al. (2006) indicated that a turbocharged engine could be designed with much less flow capacity for a much higher tumble than naturally aspirated engines. A high tumble motion is important for the generation of improved mixture preparation and reduced cylinder wall wetting. A high tumble intake port design enforces a well-organized stable motion and an optimized dissipation of the large-scale flow structures into turbulence. A more stable tumble flow results in higher turbulence intensity in the cylinder that leads to faster burn rates, a more stable combustion process (with low levels of COV of IMEP), and reduces fuel enrichment requirements at full load operating conditions. A fast and more stable combustion also reduces the tendency to knock. In addition, an enhanced tumble intake port improves dilution tolerance due to faster burn rates, and high dilution tolerance was one of the desired attributes of the 2.3L GTDI engine or this project. In conclusion, a higher tumble intake port improves mixture preparation, burn rates, knock resistance, combustion stability, and dilution tolerance. The port optimization strategy for the 2.3L GTDI DOE engine was to design a high tumble intake port. The main feature that generates tumble is a tumble step on the short side of the port, as seen in Figure 13.

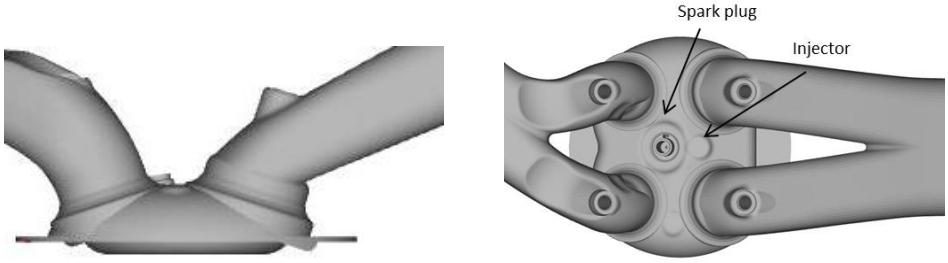


***Figure 13 - Side and top views of the 2.3L GTDI combustion system. The intake port is on the right.***

Figure 14 shows the tumble ratio evolution at 2000 rpm/full load, SOI=420° aTDC, FRP=150 bar. The tumble ratio shows the strength of the rotational motion in the cylinder and it is defined as:

$$TR = \frac{M_y}{I_y} = \frac{\sum_{cells} \rho_i V_i \left[ (z_i - z_{center}) u_i - (x_i - x_{center}) w_i \right]}{\frac{\pi N}{30} \sum_{cells} \rho_i V_i \left[ (z_i - z_{center})^2 + (x_i - x_{center})^2 \right]}$$

Where $M_y$ is the angular momentum about the y-axis; $I_y$ is the mass moment of inertia about the y-axis; N is the rotational speed; ($u_i$, $v_i$, $w_i$) are the velocity components at the cell i; ($x_{center}$, $y_{center}$, $z_{center}$) is the center of mass of the cylinder; ($x_i$, $y_i$, $z_i$) is the coordinate of cell i; $V_i$ is the volume of cell i; and $\rho_i$ is the density of cell i.

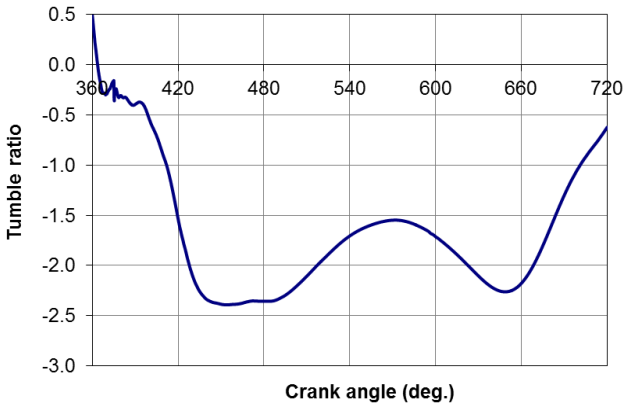


***Figure 14 - Tumble ratio evolution during the intake and compression strokes.***

Figure 15 shows the velocity field in a cross-sectional plane through the center of the intake port, during the intake stroke, at CA=480° aTDC. It can be seen that the flow separates over the tumble step in the intake port and enters the cylinder tangentially to the chamber head and the bottom of the exhaust valve. The 2.3L GTDI intake port generates a well-developed tumble motion that leads to good air-fuel mixing homogeneity.

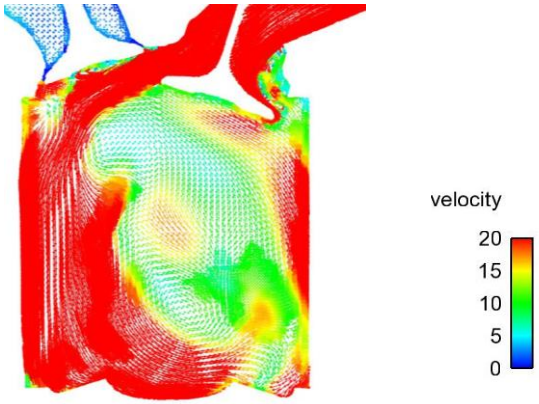


***Figure 15 - Velocity (m/s) field in a cross-sectional plane through the intake port, 2000rpm/full load.***

Figure 16 shows port volumetric efficiency versus tumble ratio for various engines. There is a trade-off between tumble motion and volumetric efficiency. The volumetric efficiency of the intake port decreases as tumble ratio increases because the tumble design features in the intake port, such as tumble steps, restrict the air flow. The Pareto front (pink line) shows the upper bound of the trend. The 2.3L GTDI DOE I4 engine exhibits a good volumetric efficiency vs. tumble ratio trade-off.

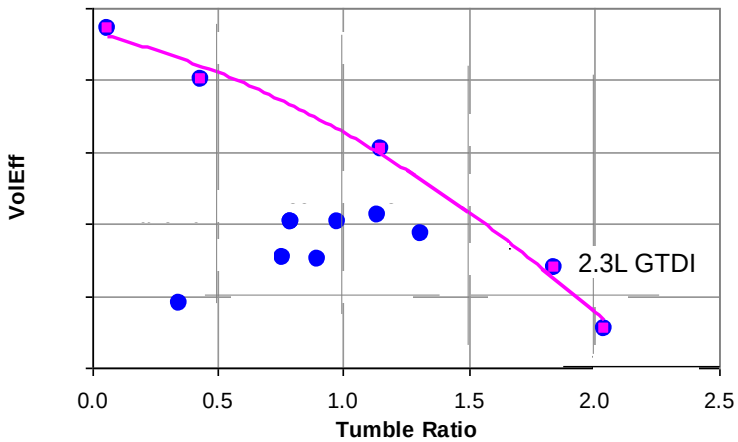


***Figure 16 - Volumetric efficiency vs. tumble ratio for various engines.***

## Spray Pattern Optimization

3D CFD modeling was extensively used upfront for spray pattern optimization. The goals of the spray pattern design are to deliver good mixture homogeneity for part load and full load operation, to minimize spray impingement on the piston for reduced smoke emissions, and to minimize spray impingement on the liner to avoid oil dilution issues. At the same time, the injector needs to be designed in conjunction with the piston bowl to guarantee that the piston bowl captures the fuel spray injected late in the compression stroke to deliver a fuel rich cloud around the spark plug for stratified-charge and cold start operation.

A sample of the six-hole and seven-hole spray patterns investigated is shown in Figure 17. In the top and side views, the intake ports are on the right side and the exhaust ports on the left side of the image. The spark plug is located between the two jets pointing towards the exhaust side, which are referred to as the spark plug jets. The six-hole spray pattern 6H21 is more compact than the other spray patterns, as seen in Figure 17. The top view images show that four of the spray jets in spray pattern 6H21 are angled more downward towards the piston compared to spray pattern 6H32. The four jets angled more downward are the two jets on the right, toward the intake side, and the two middle jets. The 3D CFD analysis indicates that spray pattern 6H21 has higher piston impingement, and the dynamometer data shows that it has higher smoke emissions, than the other spray patterns. The other spray patterns, 6H32, 6H34, 6H34A, and 7H38, were optimized starting with spray 6H21 and were designed to reduce piston impingement and improve performance. The two right jets and the two middle jets in spray 6H32 were raised 5 degrees compared to spray 6H21. The two middle jets in 6H34 were raised 5 degrees compared to spray 6H32. The two spray jets pointing towards the spark plug (towards the left) in spray pattern 6H34A were raised 5 degrees compared to spray 6H34 to improve the air-fuel mixture around the spark plug during stratified charge and cold start operation. Spray pattern 7H38 is one of the seven-hole spray patterns investigated and it has an additional central jet pointing towards the piston.

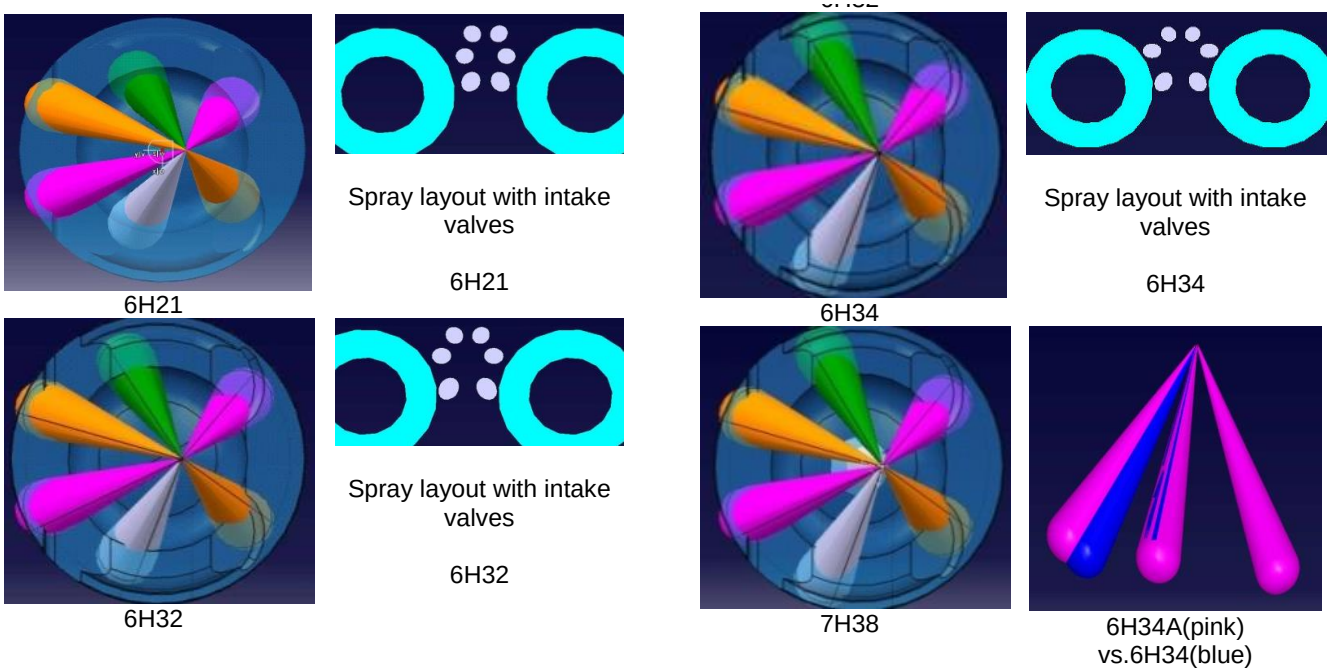


***Figure 17 - Injector spray patterns.***

Mixing index, piston impingement, and spay impingement are typical metrics used for spray optimization at part load and full load operation. The mixing index is a metric that shows the degree of air-fuel mixture homogeneity. A value of the mixing index below 0.045 at part load correlates with measured BSCO ~ 20 g/kW-hr. The piston and liner impingement are metrics that quantify the cumulative percentage of the injected fuel that impinges on the piston and liner, respectively, during a cycle. The spray pattern optimization was done by simulating several operating conditions: part load (1500 rpm/2.62 bar BMEP, 1500 rpm/5 bar BMEP, 1500 rpm/9 bar BMEP) and full load (2000 rpm/FL and 5000 rpm/FL) and cold start, CSER operation.

Figure 18 shows the results of a sample of seven spray patterns investigated at 1500 rpm/5 bar BMEP with SOI=425° aTDC. It can be noticed that the spray patterns investigated have good mixture homogeneity, with a mixing index lower than 0.045, which is the guideline recommended value for the mixing index calculated with MESIM. It is obvious that the spray pattern design has a large effect on piston impingement and liner impingement. It can be seen that spray pattern 6H21 has the highest piston impingement and consequently the lowest liner impingement among the spray patterns investigated. The desire to improve the performance of spray pattern 6H21, in particular to reduce piston impingement, led to the development and simulation of additional spray patterns. As can be seen in Figure 18, all subsequent spray patterns reduced piston impingement compared to spray 6H21. Raising four jets in spray pattern 6H32 reduced piston impingement compared to spray 6H21, and further raising the two middle jets in spray 6H34 further reduced piston impingement. The seven hole injector 7H38 spray pattern has the advantage of a lower liner impingement because there is less fuel flow in the two jets that impinge on the liner. However, the dynamometer data did not show a significant benefit for this injector.

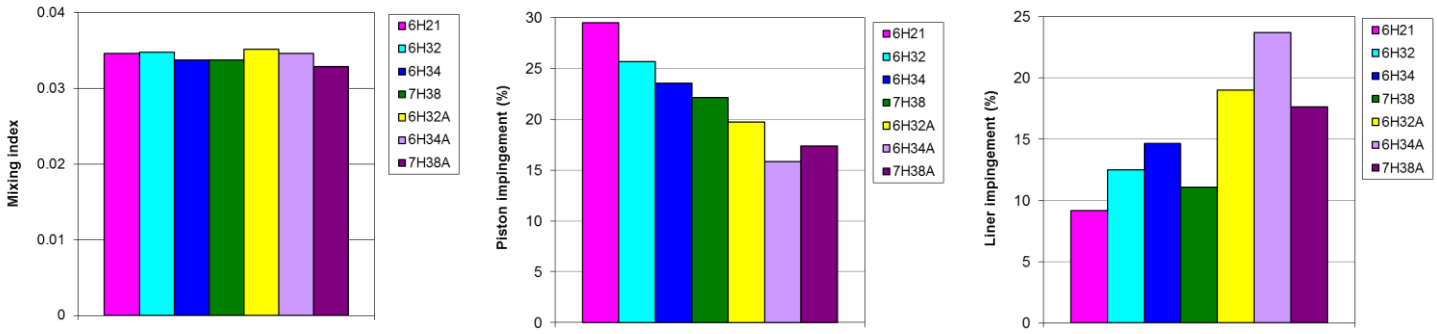


***Figure 18 - Spray pattern optimization at 1500/5 bar, SOI=425° aTDC: mixing index, piston impingement, and liner impingement.***

The spray jets pointing towards the spark plug were raised 5° in the refined spray patterns (6H32A, 6H34A, and 7H38A) in order to improve the fuel rich mixture around the spark plug during cold start operation and micro-stratification operation. Raising the two spark plug jets in these refined spray patterns leads to lower piston impingement but higher liner impingement, as a trade-off. The spray pattern recommended for the multi-cylinder engine was 6H34A. Spray pattern 6H34A was chosen because it generates lower piston impingement that will result in lower smoke emissions. The lower piston impingement will also allow an earlier fuel injection timing that will lead to improved mixture homogeneity and lower CO emissions at part load.

## Piston Optimization

Piston optimization is done mainly at CSER operation, the 5-15 second catalyst heating phase after a cold start. The 3D CFD CSER simulation is accomplished by using multiple cycles. The goal of piston optimization is to generate a rich fuel cloud around the spark plug at retarded spark timings, 15-20° aTDC. The 2.3L GTDI DOE piston top design is shown in Figure 19. During cold start operation a split injection strategy is used with the first injection during the intake stroke and the second injection during the compression stroke. The piston bowl is designed to capture the spray jets during the late compression stroke and generate a rich fuel cloud at spark timing. Figure 19 shows that the spray pattern and piston bowl work well together, and the bowl captures the spray jets injected late in the compression stroke.

***Figure 19 - Piston top showing fuel spray jets at 35 °bTDC (middle) and 30 °bTDC (right).***

Figure 20 shows the evolution of the air-fuel ratio in the central combustion chamber plane at crank angles 700° aTDC=20°bTDC, 720°=TDC, and 740° aTDC=20°aTDC, for the 2.3L engine with spray 6H34 and the1.8L engine with spray 6H21. Both designs generate a rich cloud around the spark plug at spark timing 20° aTDC, and this will ensure stable combustion during cold start operation. In this analysis, a 50/50 % split injection strategy is employed for the 2.3L engine case and a 30/70 % split injection strategy for the 1.8L engine case. In both strategies, the end of the second injection is at CA=680° aTDC=40° aTDC. The split injection strategy employed in the 1.8L engine analysis generates a richer fuel cloud around the spark plug because of the larger fuel mass injected in the second injection, 70%, compared to 50% for the 2.3L engine analysis. An important metric in cold start optimization is piston impingement. The piston impingement for the two cold start simulations shown in Figure 20 is plotted in Figure 21. It can be observed that the 2.3L engine has a lower total piston impingement at the end of the cycle than the 1.8L engine, which is desirable to reduce smoke emissions.

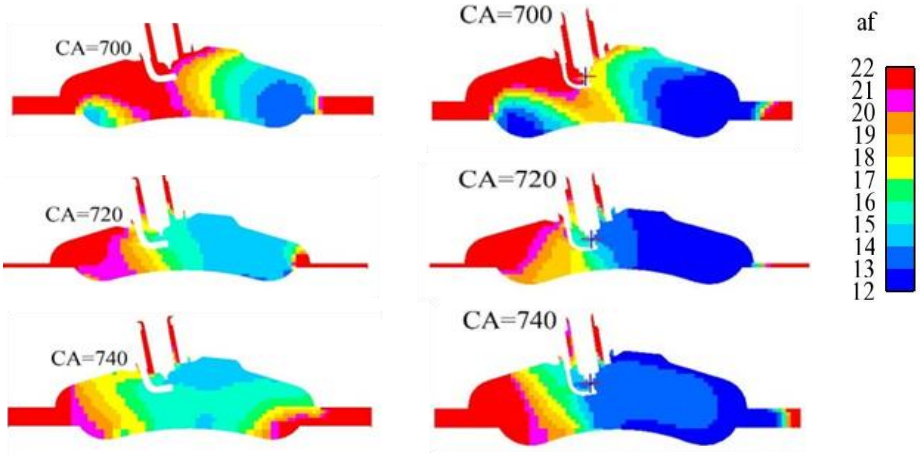


***Figure 20 - Air-fuel ratio contours during CSER operation at CA=700°, 720°, and 740° aTDC for 2.3L engine with spray 6H34 (left) and 1.8L engine with spray 6H21 (right) at 1250 rpm.***

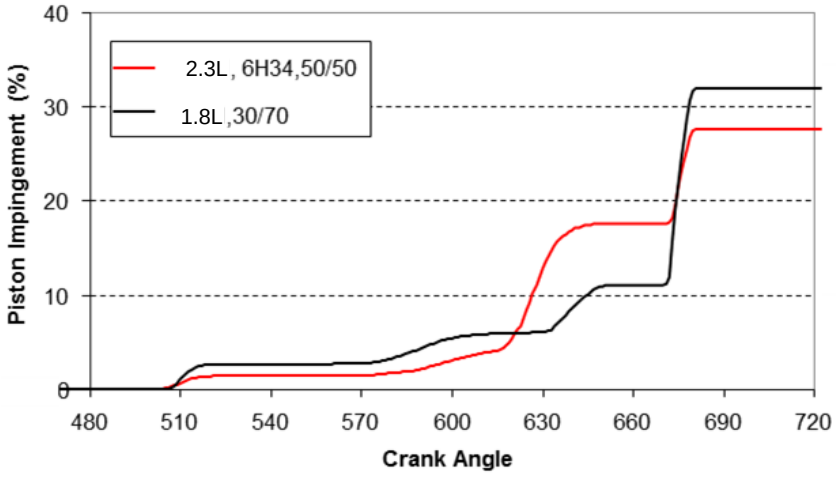


***Figure 21 - Piston impingement at CSER, 1250 rpm.***

In conclusion, the piston performs well at CSER. The spray jets are targeted in the bowl and generate a fuel rich cloud around the spark plug for good combustion stability. Detailed CSER calibration/optimization involving a wide range of parameters is done during single-cylinder and multi-cylinder engine development.

## Summary of Part Load and Full Load Modeling Assessment

During the development and optimization process of the 2.3L GTDI I4 DOE engine, part load and full load assessments with 3D CFD modeling were conducted and the results were compared to two side DI engines and two central DI engines.

Figure 22 shows a comparison between the 2.3L GTDI DOE engine and other DI engines at part load: 1500/2.62 bar BMEP, 1500/5 bar BMEP, and 1500/9 bar BMEP, and also at full load operation at 2000 rpm and 5000 rpm. It can be seen that the 2.3L DOE engine has a lower mixing index than the other engines at all part load and full load operating conditions investigated. A low mixing index indicates good air-fuel mixture homogeneity and will lead to lower CO emissions and reduced fuel consumption. Figure 22 also shows that the 2.3L GTDI DOE engine has lower or similar piston impingement compared to the other engines at part load and full load, and this will lead to reduced smoke emissions.

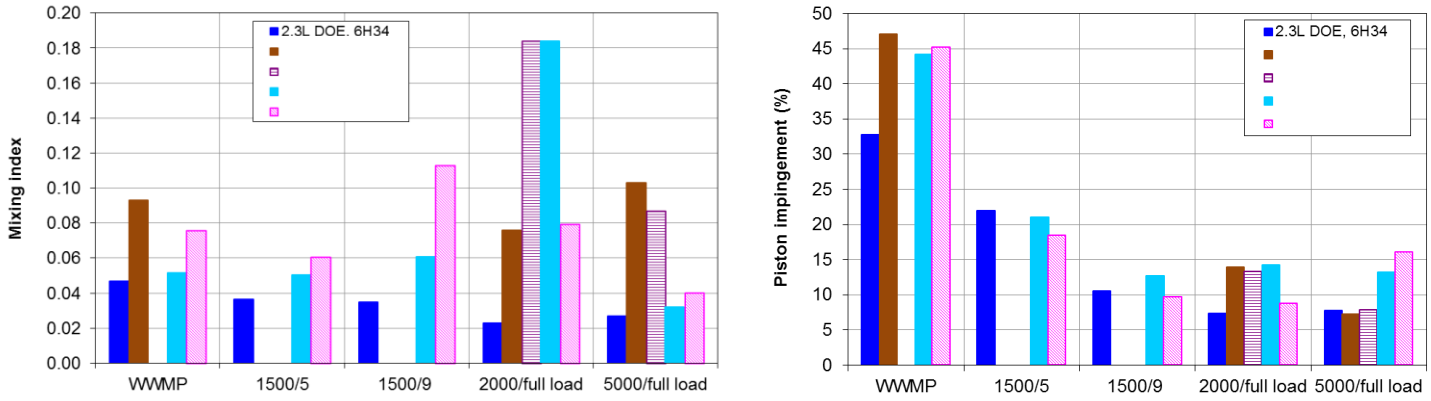


***Figure 22 - Mixing index and piston impingement comparison between 2.3L GTDI DOE and other DI engines at part load and full load.***

Figure 23 compares liner impingement at full load operation. The 2.3L GTDI engine has lower liner impingement than the other engines at full load operation and this will reduce the risk of oil dilution.

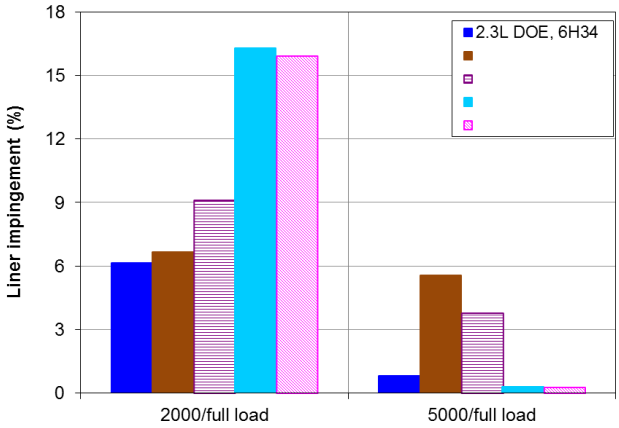


***Figure 23 - Liner impingement comparison between 2.3L GTDI DOE and other DI engines at full load.***

## Conclusions

The 2.3L GTDI DOE engine combustion system was designed using an integrated approach between upfront 3D CFD modeling optimization, single-cylinder dynamometer development, and multi-cylinder engine development. The combustion chamber, intake port, piston and spray pattern were extensively developed and optimized upfront with 3D CFD modeling with the goal of improved mixture preparation, good combustion stability, and minimal fuel-wall wetting. The 3D CFD part load and full load assessment demonstrated that the 2.3L GTDI DOE engine performed well in terms of mixing, piston impingement and liner impingement when compared to other engines. The piston top designed also performed well at CSER operation. The spray jets were targeted in the piston bowl and generated a fuel rich cloud around the spark plug that is needed for good combustion stability.

## Single Cylinder Engine Build and Testing

A surrogate single cylinder engine (SCE) representative of one cylinder of a 1.8L I4 engine was used to complete combustion system verification testing, provide data for correlation to the detailed MESIM analyses described previously, and select injector and spark plug specifications for a new SCE representative of one cylinder of the 2.3L DOE engine. This new SCE was designed and built to further develop and assess the performance of the hardware at part-load and cold start operating points. Table 3 lists engine parameters for the two phases of the SCE development.

***Table 3. Engine parameters of 2.3L GTDI and 1.8L GTDI***

| | 2.3L DOE | 1.8L DOE |
|---|---|---|
| **Fuel Injector Layout** | transverse central DI w/intake biased multi-hole injector | transverse central DI w/intake biased multi-hole injector |
| **Bore** | 87.5 | 80 |
| **Stroke** | 94 | 90 |
| **Compression ratio** | 11.5 | 11.5 |
| **Tumble ratio** | 1.8 | 1.8 |
| **Intake cam duration** | 260 | 260 |
| **Exhaust cam duration** | 224 | 224 |
| **Intake cam phaser range** | -20° to 40° BTDC | -20° to 40° BTDC |
| **Exhaust cam phaser range** | 55° to -5° ATDC | 55° to -5° ATDC |
| **Intake cam Lift (mm)** | 10 | 10 |
| **Exhaust cam lift (mm)** | 8.7 | 8.7 |
| **Ignition Coil** | 100 mJ Bosch | 100 mJ Bosch |

### Initial Fuel Injector Spray Pattern Evaluation

The 1.8L SCE engine was used to evaluate the early transverse central fuel injector spray patterns, which were all multi-hole designs. An early candidate spray pattern design with six holes was designated 6H21. In comparison to later designs the non-spark plug jets were lower, as depicted in Figure 17. For example, in comparison to pattern 32 the non-spark plug jets were all 5 degrees lower.

Figure 24 shows the results for spray pattern 21 at part load in the 1.8L SCE. This data was acquired with a dual retard cam timing strategy with high internal residual dilution, but without external cooled EGR. Evaluations are shown later for the 2.3L SCE with cooled EGR. The results shown in Figure 24 cover mixing, combustion stability, and smoke using metrics of NSCO, COV IMEP, and FSN over a range of SOI timings during the intake stroke. For this early spray pattern design, combustion stability was less than the 2% COV IMEP metric, but CO was higher than the target range of less than 20 g/kWh, indicating mixing improvements were needed at this point in the development. With a target of less than 0.1 FSN, smoke was also a challenge for this spray pattern. It is desirable to have low smoke for SOI timing as early as possible, since typically mixing improves as SOI is advanced. Good side DI engines have shown that this can be achieved for timings of 410 and earlier. For spray pattern 21 the smoke knee is occurring at timings later than 410 SOI, so changes to the spray pattern to reduce smoke were included in later designs.

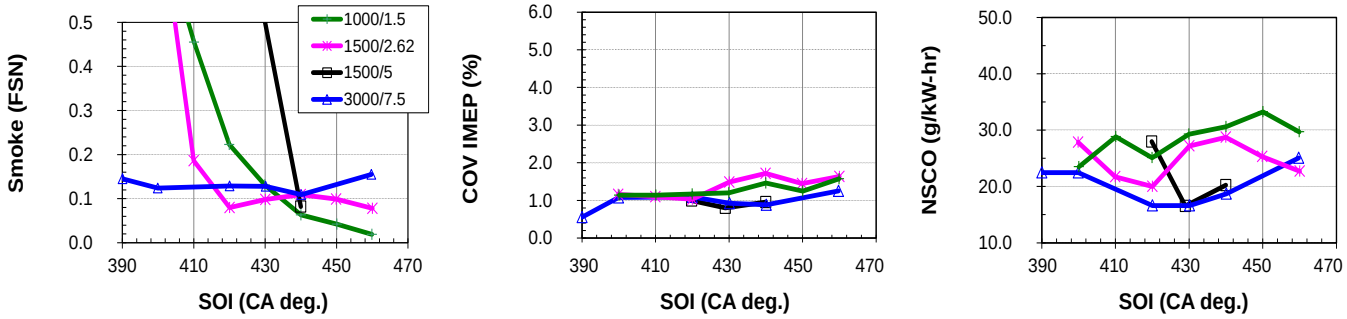


***Figure 24 - Initial spray pattern 6H21 evaluation at part load in 1.8L SCE.***

## Spray Pattern Optimization in 2.3L SCE at Part Load and Mid Load

As described previously, spray patterns 32, 34 and 38 were designed to improve on the performance of pattern 21. Pattern 32, a six hole arrangement, had the rear four jets (non-spark plug) raised 5 degrees to increase the spray length prior to piston impingement to reduce smoke emissions. Pattern 34 raised the middle jets an additional 5 degrees over 32 to further increase the spray length prior to impingement. Pattern 38, a 7 hole design, had the same spray coordinates as 34 with the addition of a central jet directed downward toward the piston. The flow rate for 38 was 15 cc/sec, the same as 34, so the individual sprays each have less flow resulting in lower momentum and penetration. This lower penetration is intended to decrease piston wetting. The “A” designation on a design is used when the two spark plug jets are raised 5 degrees. Directing the spray closer to the spark plug was found to improve lean combustion flame initiation and early flame growth, a finding from the micro-stratification and stratified charge development on the 1.8L DOE SCE engine.

Spray patterns 32A, 34, 34A and 38 were evaluated in the 2.3L DOE SCE. The spray patterns were manufactured by Magneti Marelli and evaluated with 3D CFD modeling at Ford, as described previously. They included hardware design improvements that Magneti Marelli designated as level IHP5. Part load results are shown in Figure 25 for 1500 rpm / 2.62 bar BMEP and 1500 rpm / 5 bar BMEP. Both speed load points were run using dual retard cam timing and 15% cooled EGR. All four injector designs demonstrated good mixing, achieving NSCO levels less than 20 g/kWh for SOI timings of 410 and earlier. Meeting the 2% COV IMEP target is more challenging with the highly dilute mixture created with dual retard cam timings and 15% external cooled EGR. Even given this more challenging environment, COV IMEP was 2% or less for optimized SOI timings. By raising the four rear jets and reducing piston impingement, all of these new designs achieved much earlier SOI timings prior to reaching the smoke knee as compared to pattern 21 run in the 1.8L DOE SCE. In particular, pattern 34A is able to run very early SOI timings without exhibiting the typical smoke knee.

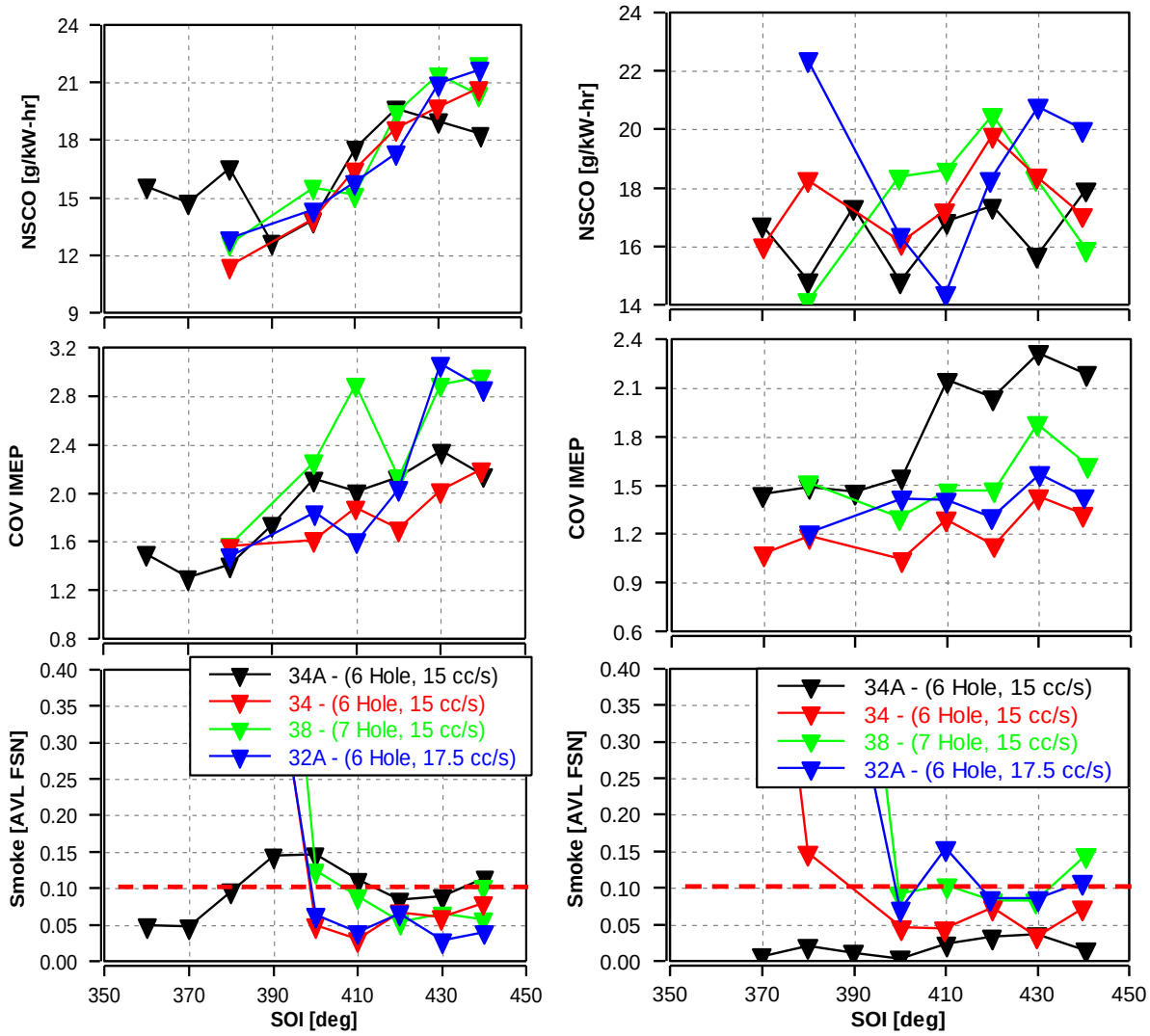


***Figure 25 - Fuel injector spray pattern comparison at 1500 rpm/2.62 bar BMEP (left) and 1500 rpm/5 bar BMEP (right) in 2.3L SCE.***

Figure 26 shows the smoke comparison for these fuel injector spray patterns at 2000 rpm / 9 bar BMEP at 150 bar fuel rail pressure (FRP) without cooled EGR. At this higher load operating point, smoke FSN exceeds 0.1 FSN for pattern 38 at 440 SOI, a very late injection timing. This is likely due to the center jet that is directed at the piston, since this is the main difference in comparison to spray pattern 34. While at this operating condition all injectors achieve acceptable mixing, stability, and gaseous emissions levels, patterns 34 and 34A enable earlier injection than patterns 32 and 38. Having a wider injection window enabled by patterns 34 and 34A is useful as loads become even higher to allow for the time needed to inject the required fuel mass.

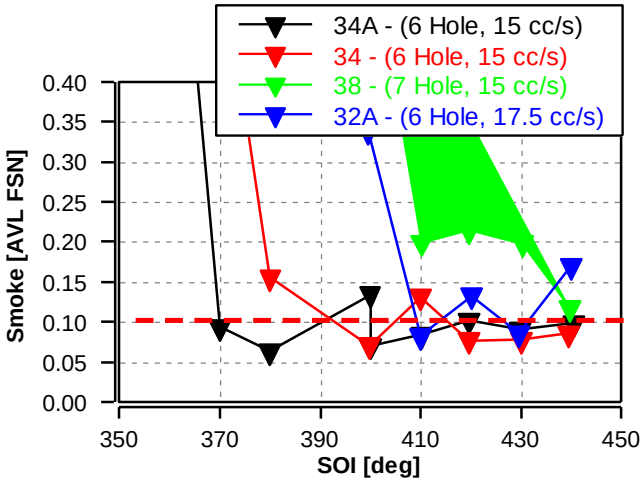


***Figure 26 - Fuel injector spray pattern comparison at 2000rpm/9 bar BMEP in 2.3L SCE.***

## Spray Pattern Optimization at CSER in 2.3L SCE

The 2.3L SCE was also operated at steady state operating conditions with the coolant and oil temperature at 20°C to simulate the 5-15 sec catalyst heating phase of the transient cold start procedure referred to as cold start emission reduction (CSER). The engine speed was held constant at 1250 rpm, load was maintained at 1.9 bar NMEP, exhaust heat flow was targeted at 6500 W/L, and fuel rail pressure was set at 100 bar. At this condition, a two-injection strategy was utilized to improve the combustion stability at retarded spark, high heat flux conditions. This strategy uses a first injection during the intake stroke to provide a largely homogeneous fuel/air background mixture at the time of spark. The second injection then occurs later in the compression stroke, producing a stratified fuel/air mixture near the spark plug prior to ignition. The richer mixture generated by the second injection near the spark plug improves the ignitability and initial flame development. The heat flux was held constant at 6,500 W/L during these tests by adjusting the airflow and spark timing, and the overall air-fuel ratio was kept slightly lean at 15:1. For each of the tests a sweep of the first injection timing was conducted at a fixed second injection timing to determine an optimal first injection timing. This timing was then held constant as the second injection was varied late in the compression stroke.

Figure 27 shows the fuel injector spray pattern comparison during simulated CSER conditions. The split ratio for the data shown on the left side of Figure 27 was 50/50 with the timing of the first injection optimized previously for each spray pattern and occurring late in the intake stroke. The second injection timing was swept to identify the optimal timing based on achieving targets for combustion stability and emissions. Spray patterns 34 and 34A achieved the lowest SD IMEP values, with the lowest value reached at 50° bTDC EOI2. SD IMEP was also below 0.4 bar for a 15° EOI2 range, and this is advantageous in minimizing operational difference that may result from production variation. Patterns 34 and 34A also allow the latest EOI2 timing prior to reaching the smoke knee. This allows operation at the lowest combined FGHC and NOx levels in comparison to pattern 38 where the smoke knee occurs prior to the lowest point and 32A where it occurs simultaneously, leaving no margin. The combined HC+NOx level for 34A was higher than the other fuel injectors for a given timing and this was due to higher FGNOx.

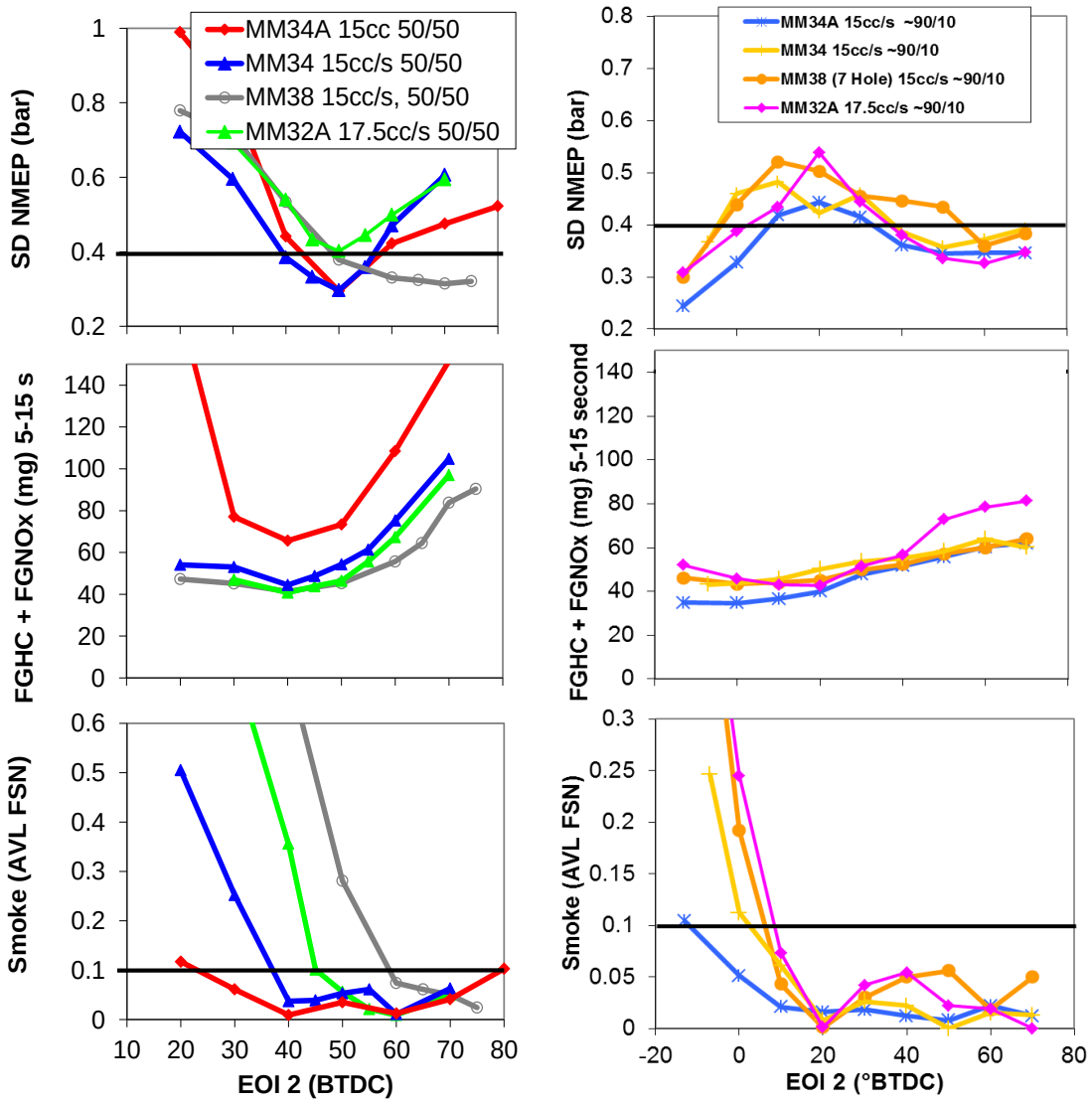


***Figure 27 - CSER fuel injector spray pattern comparison for 50/50 (left) and 90/10 (right) split injection in 2.3L DOE SCE.***

With the fuel injector centrally located creating a spray guided system, the characteristics needed to develop a stratified mixture are improved in comparison to side DI. This allowed additional operating strategies to be tested. A unique operating strategy tested for CSER was a 90/10 split ratio with 90 percent of the fuel injected in the intake stroke and 10 percent injected very late in the compression stroke or even early in the expansion stroke. The left side of Figure 27 shows the CSER fuel injector comparison for a 90/10 split ratio over a range of EOI2 timings. At early EOI2 timings all of the spray patterns achieve good combustion stability, low smoke, and acceptable HC+NOx emissions. Pattern 34A has a later smoke knee achieving even lower SD IMEP and HC+NOx emissions.

## Final Combustion System Assessment of 2.3L SCE

The following sections describe the results from steady-state dynamometer testing at a range of conditions. Each of the tests was run with two different injector technologies: (1) a multi-hole solenoid injector developed by Magneti Marelli and (2) an outwardly-opening solenoid injector known as “A-nozzle” developed by Delphi. Testing both of these injectors on the same SCE allows for a direct comparison of the technologies with fewer confounding factors than a multi-cylinder engine.

The Magneti Marelli multi-hole injector was equipped with the 34A spray pattern described earlier. This spray pattern was chosen based on the CFD simulations and the single-cylinder dynamometer testing described above on the 1.8L engine. The static flow rate of this multi-hole injector is 15 cc/s.

The Delphi outwardly-opening solenoid injector was selected based on previous engine testing which showed that the increase in PM that can be attributed to injector tip deposits is essentially eliminated with an outwardly-opening injector. Optical measurements of the spray also show that the penetration of the hollow-cone, sheet-like spray generated by this outwardly-opening injector is significantly reduced relative to a standard multi-hole injector. The reduced penetration also has the potential to reduce the amount of wall and piston impingement and, consequently, reduce the feedgas PM that is generated by the engine. The static flow rate of the outwardly-opening injector that was used in this study was 15 cc/s and the cone angle of the nozzle geometry was 75°.

## Summary of Part-Load Operation with Multi-Hole Injector

For each of the injectors described above, the 2.3L DOE single-cylinder engine was operated at the ten steady state part-load operating points listed in Table 7. These operating conditions include a range of engine speeds and loads, covering low-load operation up to a slightly knock-limited point (1500 RPM 9.60 bar NMEP).

***Table 7 - Speed-load points for injector evaluation.***

| Engine Speed (RPM) | NMEP (bar) | EGR (%) | Injection Pressure (bar) |
|---|---|---|---|
| 1000 | 2.00 | 15 | 100 |
| 1500 | 3.22 | 0 & 15 | 100 |
| 1500 | 5.60 | 0 & 15 | 100 |
| 1500 | 9.60 | 0 | 150 |
| 2000 | 2.60 | 15 | 100 |
| 2000 | 5.60 | 15 | 100 |
| 2000 | 9.60 | 0 | 150 |
| 3000 | 8.30 | 0 | 150 |

Results obtained at four of the operating conditions with 15% EGR with the 34A injector pattern are shown in Figure 28. The sampling of results shown in Figure 28 is representative of all ten operating conditions listed in Table 7. The main focus of the results for part-load operation are (1) NSCO as a surrogate for air-fuel mixing, (2) the COV of IMEP as a measure of combustion stability and (3) the measured Filter Smoke Number (FSN) to monitor the PM generated at each condition.

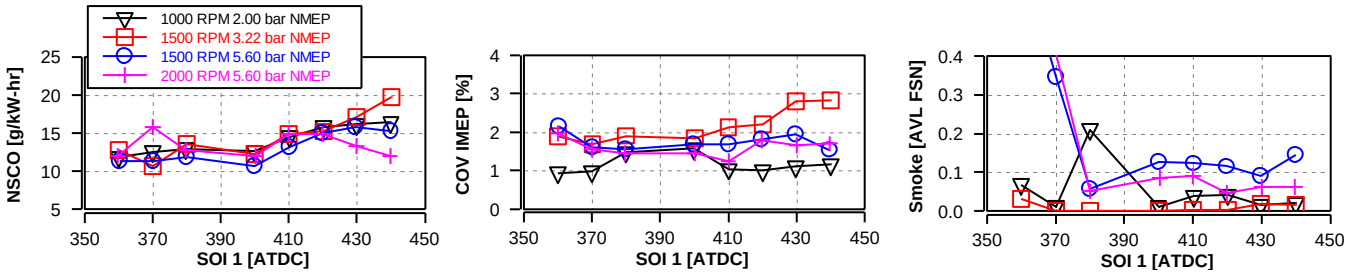


***Figure 28 - NSCO, COV IMEP, and smoke data over a range of injection timings with injector 34A.***

The results in Figure 28 show that the combustion chamber and port design of the 2.3L DOE engine provides good mixing with NSCO ranging from 10-15 g/kWh at the optimal injection timing for each condition. Additionally, the COV of IMEP in the range of injection timings between 370° and 410°ATDC remains at or below the 2% limit even with dual retard cam phasing and 15% cooled EGR. The smoke emissions as indicated by the FSN measurements show that an increase in smoke, often referred to as the smoke knee, occurs at injection timings between 370° and 410°ATDC depending on the operating condition. As will be

shown later, the smoke knee occurs earlier than a number of other engines, allowing for a wider range of injection timings with low PM emissions. At later injection timings (> 390° ATDC), the smoke decreases to near-zero levels for the low load conditions (1000 RPM/2.00 bar NMEP and 1500 RPM/3.22 bar NMEP). For the higher load conditions the smoke appears to asymptote to a value of roughly 0.1 FSN. This is likely due to injector tip coking that has been identified as an issue in previous studies.

## Comparison to Side DI and Outwardly-Opening Injector at Part Load

In this section, the results from the 2.3L DOE SCE with transverse central DI are compared with data acquired on a SCE with a side DI combustion chamber design. In addition, multi-hole and outward-opening injector technologies are also compared.

All of the part-load conditions were tested with both the Magneti Marelli multi-hole injector (spray pattern 34A) and the Delphi outward-opening solenoid injector (OOSI). The main parameters of interest are compared in Figure 29 at a single operating condition of 1500 RPM, 5.60 bar. The results in Figure 29 show that the NSCO and COV of IMEP are essentially the same for the Magneti Marelli 34A multi-hole injector and the Delphi OOSI injector at this condition. This similarity in mixing and combustion stability was also observed at the remaining of the operating conditions listed in Table 7 above. However, using the Delphi OOSI resulted in lower smoke emissions at injection timings later than 390° aTDC, possibly due to elimination of injector tip coking with the OOSI technology.

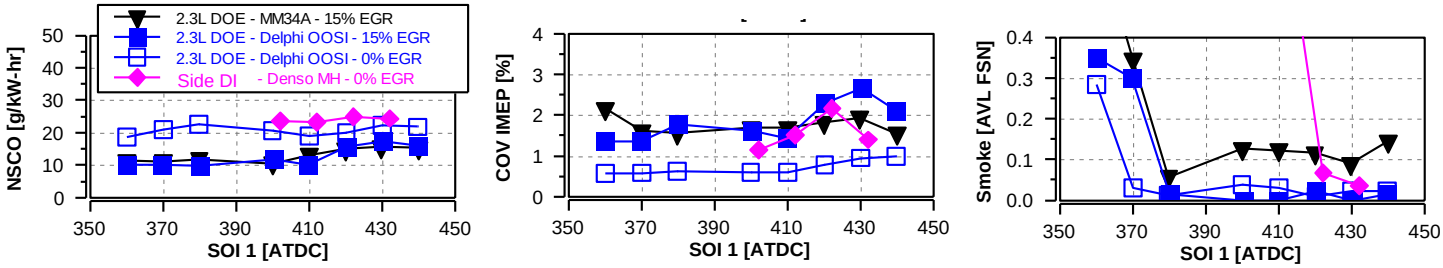


***Figure 29 - NSCO, COV IMEP, and smoke over a range of injection timings at a 1500 RPM, 5.60 bar NMEP.***

With regards to the comparison of the 2.3L DOE transverse central DI and the side DI engine, the main difference is observed in the engine-out smoke emissions. The smoke knee occurs at earlier injection timings for the 2.3L DOE relative to the side DI engine. This may be due to the fact that the injector tip-to-piston distance is increased from 28 mm in the side DI combustion chamber to 40 mm in the 2.3L DOE at a crank angle of 420° aTDC, which is the location of the smoke knee for the side DI combustion chamber. This increased distance gives the sprays more space to penetrate prior to impinging on the liner or piston surfaces. Both engines provide similar combustion stability and mixing (NSCO) at this 1500 RPM, 5.60 bar NMEP operating condition.

## Comparison to Outwardly-Opening Injector at Cold Fluids Conditions

Two different split ratios (ratio of the mass in the first injection to the mass in the second injection) were investigated, 50/50 and 90/10. The results for both split ratios are presented in the following sections.

50/50 Split Ratio

Figure 30 shows the main parameters of interest during the steady state cold fluids operating conditions over a range of second injection timings for a split ratio of 50/50 (injected fuel mass is split equally between the two injections) and cam timings of IVO/EVC = -30/10 aTDC. The results of the same test from a side DI SCE are also included for a split ratio of 70/30 to provide a comparison to a side DI combustion chamber design. The optimal second injection timing is highlighted for each engine configuration. The optimal timing was chosen based on balancing the combustion stability, smoke emissions, and the feedgas HC and NOx. Note that the optimal second injection timings for the 2.3L DOE engine with the Delphi OOSI and the side DI engine coincide for this split ratio.

The results in Figure 30 show that the combustion stability of the 2.3L DOE and the side DI single-cylinder engines is similar at these conditions with low smoke emissions at the optimal set of injection timings. However, the feedgas HC + NOx is higher for the 2.3L DOE single-cylinder engine regardless of the injector type. The Delphi OOSI does provide an incremental improvement in feedgas emissions for the 2.3L DOE design, approaching the levels observed for the side DI SCE.

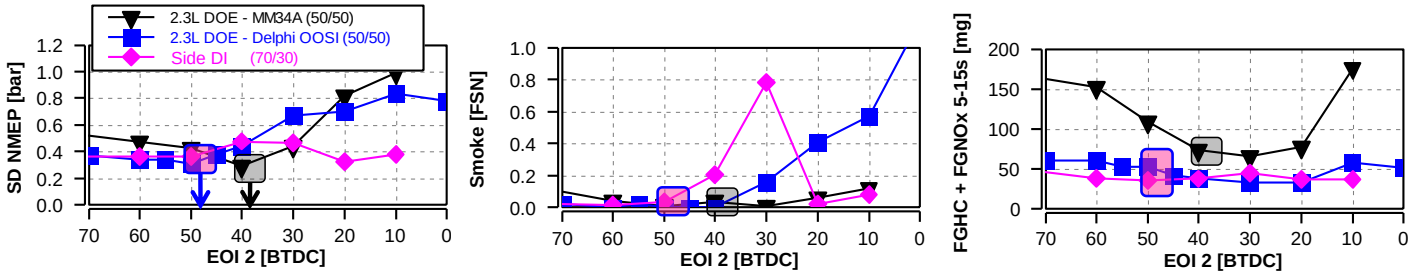


***Figure 30 - SD of NMEP, smoke, and FGHC + FGNOx over a range of second injection timings at 1250 RPM, 1.90 bar NMEP with a split ratio of 50/50. Coolant and oil temperature 20°C.***

90/10 Split Ratio

Figure 31 shows the results of the cold fluids testing over a range of second injection timings for a split ratio of 90/10 for the Magneti Marelli multi-hole injector and the Delphi OOSI in the 2.3L DOE SCE. The optimal second injection timings are again highlighted for both of the injector configurations. The side DI SCE was not tested at this split ratio and, therefore, data from this engine is not included in Figure 31. The 90/10 split ratio strategy provides improved combustion stability, which allows for increased overlap (IVO/EVC = -30/25) with stable combustion and, thus, increased residual.

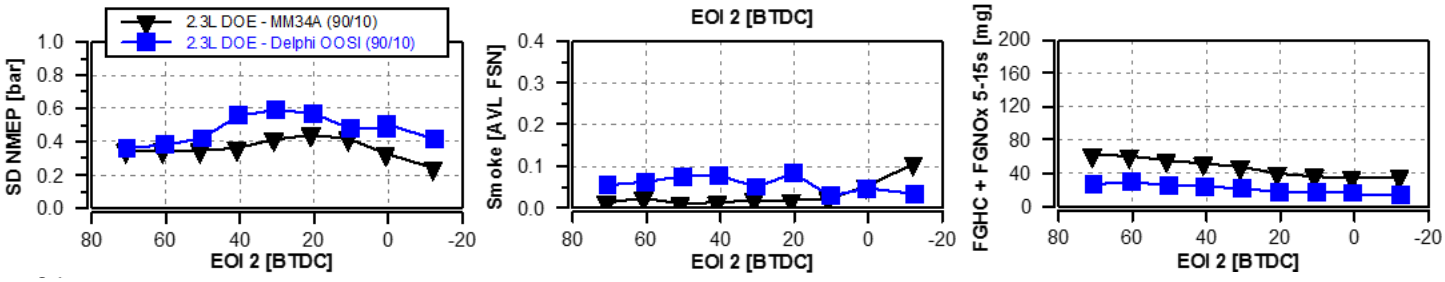


***Figure 31 - SD of NMEP, smoke and FGHC + FGNOx over a range of second injection timings at 1250 RPM, 1.90 bar NMEP with a split ratio of 90/10. Coolant and oil temperature 20°C.***

The increase in residual gas provides additional dilution which reduces burned gas temperatures and subsequently less NOx is generated. Therefore, the feedgas HC + NOx is reduced with the Magneti Marelli multi-hole injector by using a 90/10 split strategy, from roughly 80 mg for a split ratio of 50/50 to roughly 40 mg for a 90/10 split ratio. The Delphi OOSI provides an additional reduction in the feedgas NOx + HC to approximately 20 mg by significantly reducing the feedgas NOx emissions.

## Conclusions

Single cylinder engine testing exhibited good part load mixing comparable to PFI mixing benchmarks based on CO emissions. Low smoke emissions were also demonstrated over a wide range of injection timings for part load conditions. For CSER, standard injection split ratios produced comparable emissions and stability as previous DI combustion system applications. The close spacing of the injector and spark plug further enabled new split injection CSER strategies (e.g., 90/10) that improved both emissions and stability. Finally, A-nozzle (OOSI) injector compatibility of the combustion system showed potential to further reduce part load particulate emissions, as well as enabling lower criteria emissions at CSER compared with the multi-hole injector results.

# Multi-Cylinder Engine Component Design

## Cylinder Head

The cylinder head is a 4-valve per cylinder gasoline direct injection design with the fuel injector placement between the 2 intake valves and on a common centerline with the spark plug (Figure 32). This design is known as a transverse central direct injection layout.

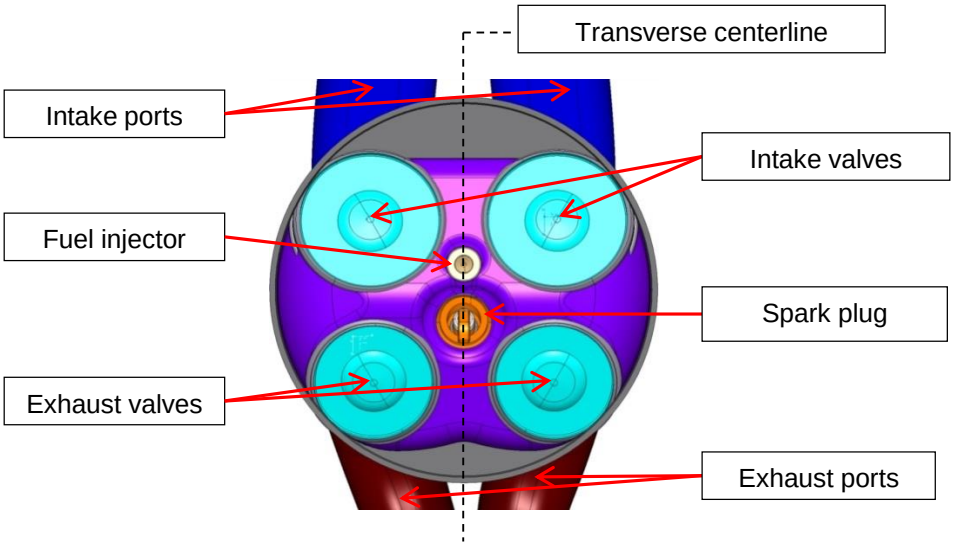


***Figure 32 - Combustion chamber with transverse central DI.***

The cylinder head utilizes a 153.6 mm distance between camshaft centerlines. This allows the packaging of the valvetrain, ignition, and fuel injection components between the intake and exhaust camshafts. Figure 33 illustrates the relationship between the camshafts, outboard lash adjuster roller finger follower (RFF) valvetrain, fuel injector, ignition coil, and spark plug.

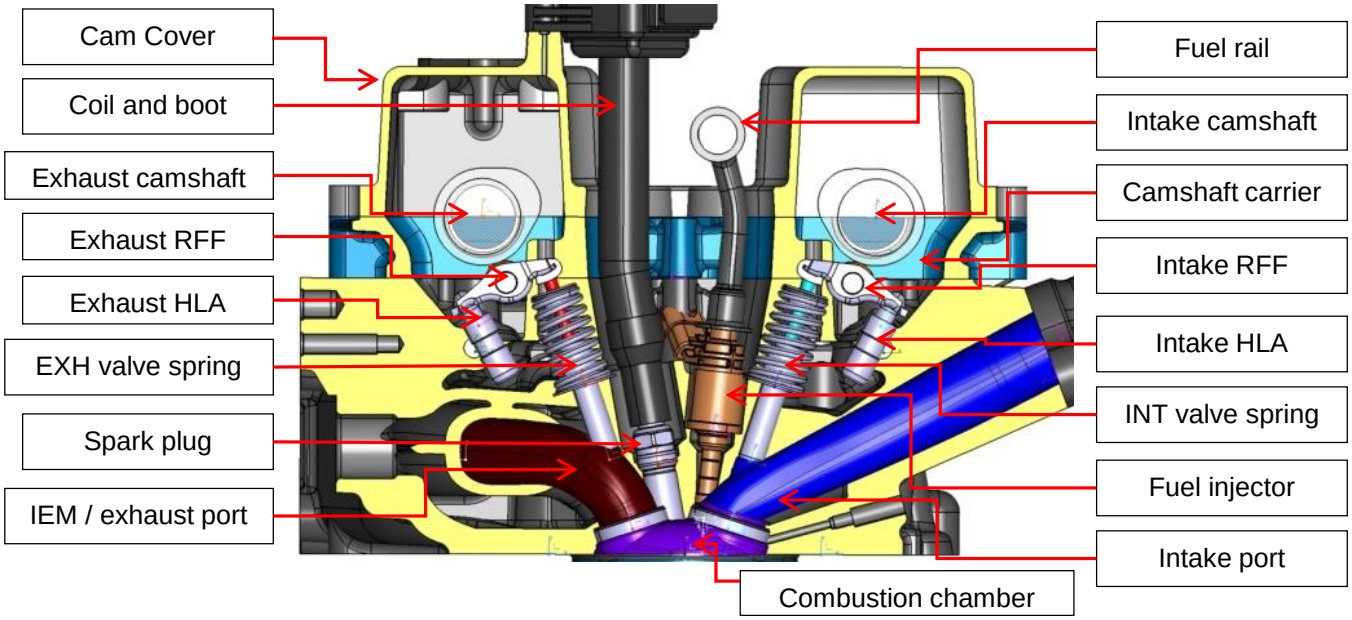


***Figure 33 - Cylinder head cross-section and components.***

Figure 34 illustrates the "dry" valley design that packages the fuel injection and ignition components. The camshaft carrier (Figure 35) is a separate component that mounts both camshafts and the mechanical fuel pump independently of the cylinder head. The dry valley design with the camshaft carrier allows oil to drain under the dry valley from the intake to the exhaust side without contaminating the fuel or ignition components. The carrier is doweled and fastened to the cylinder head. A press in place gasket seals the carrier to the cylinder head resulting in the dry valley.

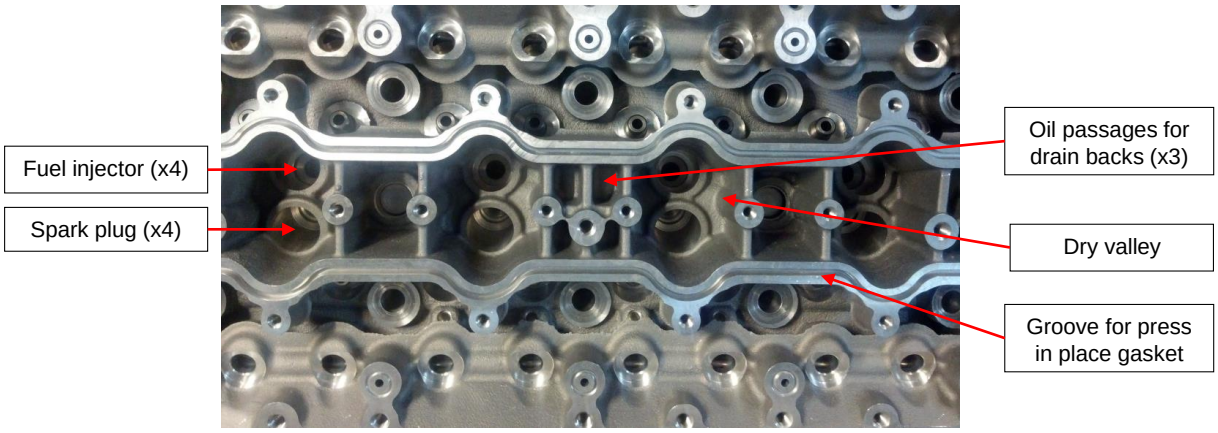


***Figure 34 - Cylinder head dry valley.***


***Figure 35 - Camshaft carrier.***

## Integrated Exhaust Manifold

The cylinder head was designed with an integrated exhaust manifold (IEM) which routes all four exhaust ports to exit at one point (Figure 36).

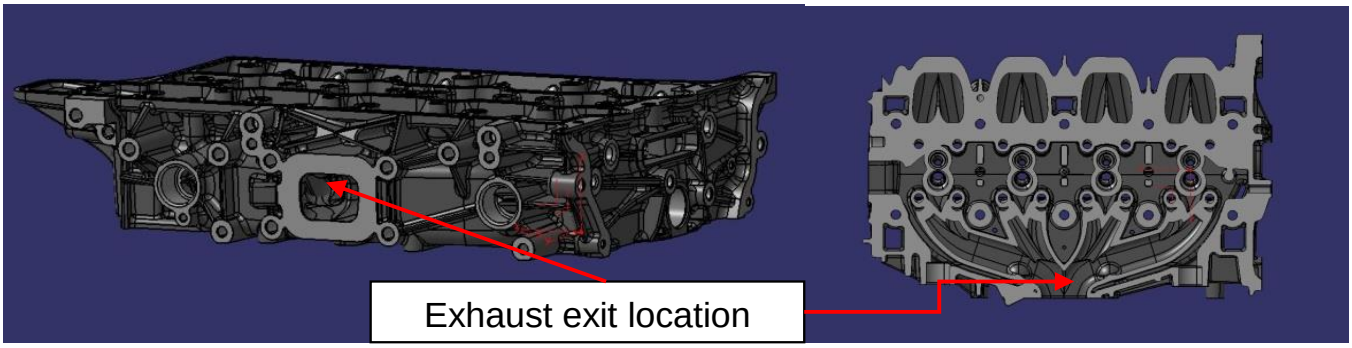


***Figure 36 - Integrated exhaust manifold.***

An IEM along with a transverse central DI combustion chamber presents several design challenges. The IEM and transverse combustion chamber require uniform cooling to reduce the possibility of a cylinder head structural failure over time due to excessive material temperatures combined with the mechanical loads created by the combustion process. This type of failure is referred to as a high cycle fatigue (HCF) failure. A safety factor for HCF failure is established analytically by using the engine cylinder pressure at full load and calculating the resultant stresses through an engine cycle at peak metal temperatures.

The cylinder head utilizes a split cooled water jacket (upper and lower, see Figure 37) to allow coolant in the lower jacket to flow from exhaust to intake uniformly over each combustion chamber while coolant in the upper jacket flows from front to rear (Figure 38). The intent of the cross flow design of the lower jacket is to allow the coolest coolant to flow to the hottest areas of the cylinder head first, which were assumed to be the exhaust side of the combustion chamber and the IEM exit location which interfaces with the turbocharger flange. The most difficult design challenge was cooling between the two exhaust/ports valves and the spark plug (Figure 39). The thickness of the coolant jacket, spark plug, and exhaust port walls is 4 mm, while the thickness of the combustion chamber wall is 8.5 mm.

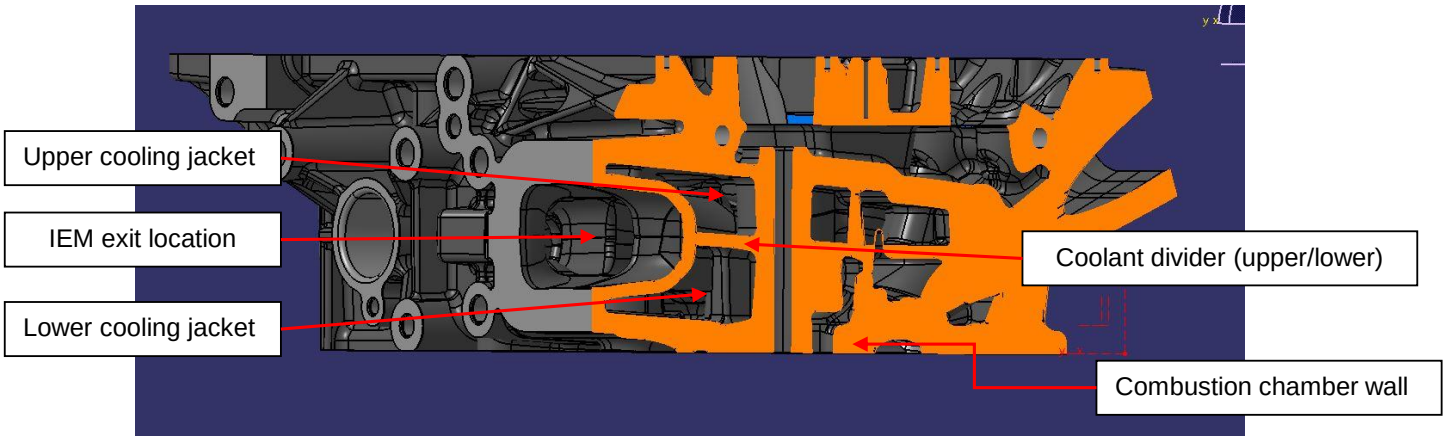


***Figure 37 - Split cooled water jacket.***

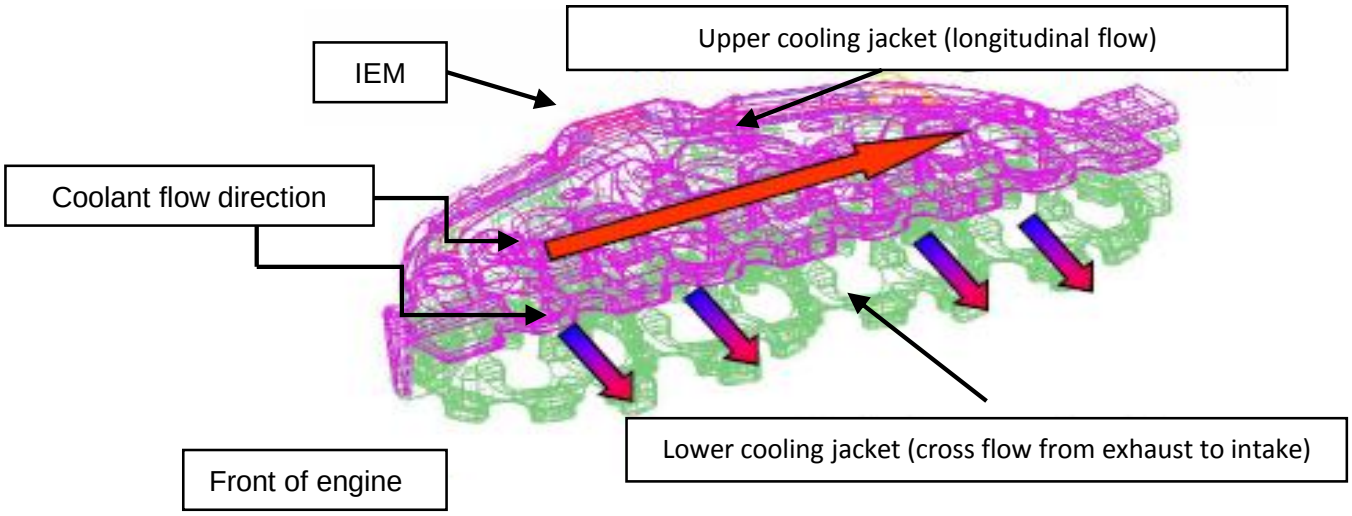


***Figure 38 - Coolant flow in the upper and lower cooling jackets.***

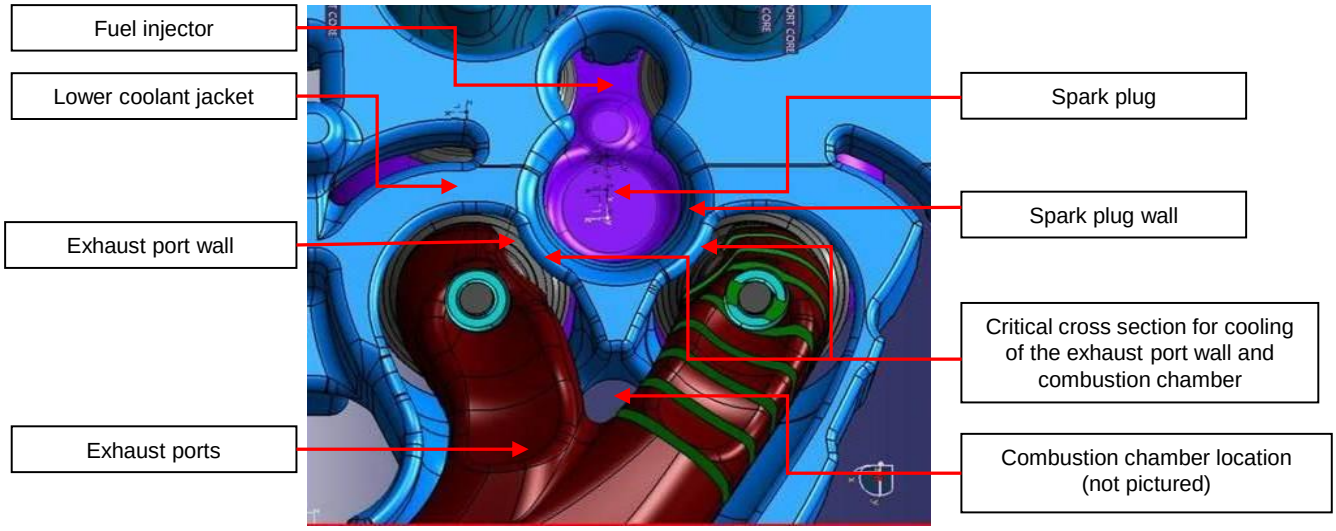


***Figure 39 - Critical cross-sections for cooling.***

Extensive computer aided engineering analyses were performed to develop the coolant jacket to achieve proper cylinder head cooling. The initial maximum material temperature target was not to exceed 260°C with a peak cylinder pressure of 125 bar. Note that the engine reaches only 100 bar as the maximum peak cylinder pressure. Figure 40 is a temperature profile determined using the analytical powertrain (AP) method.

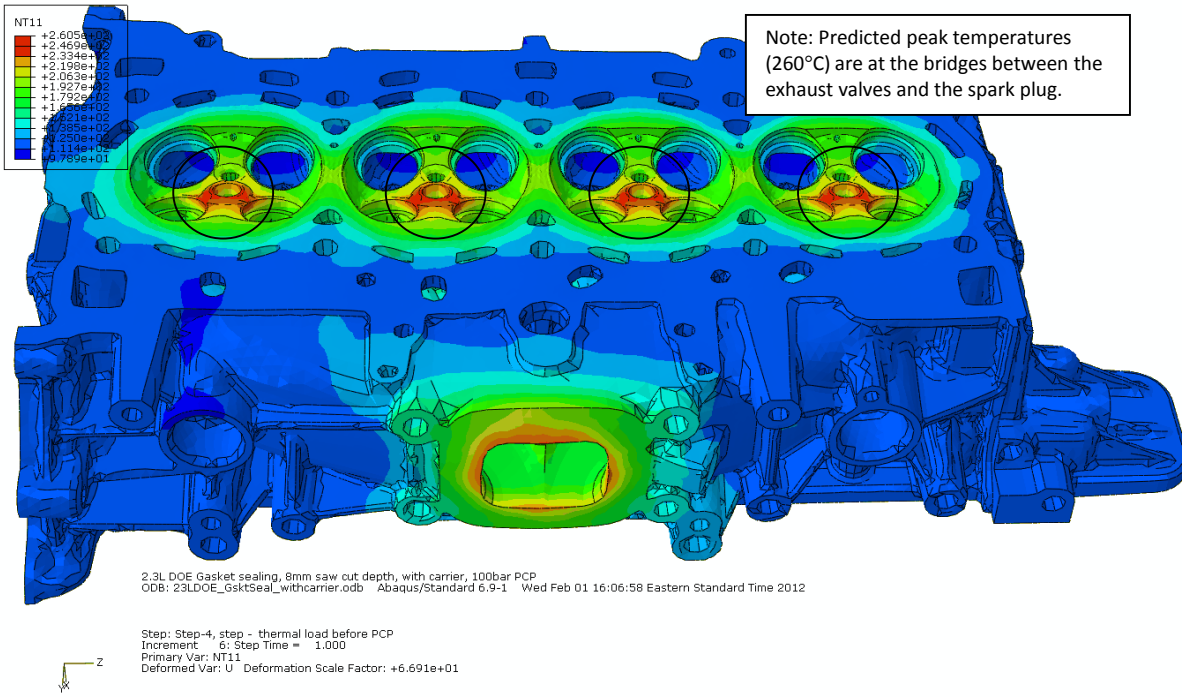


***Figure 40 - CAE metal temperature predictions.***

Using the temperature profile from the AP method, the HCF safety factor was calculated. The target was a minimum value of 1.2. Figure 41 show the minimum safety factor value of 1.6 at the bridge between the exhaust valves and spark plug which is the same location as the highest predicted peak temperatures.

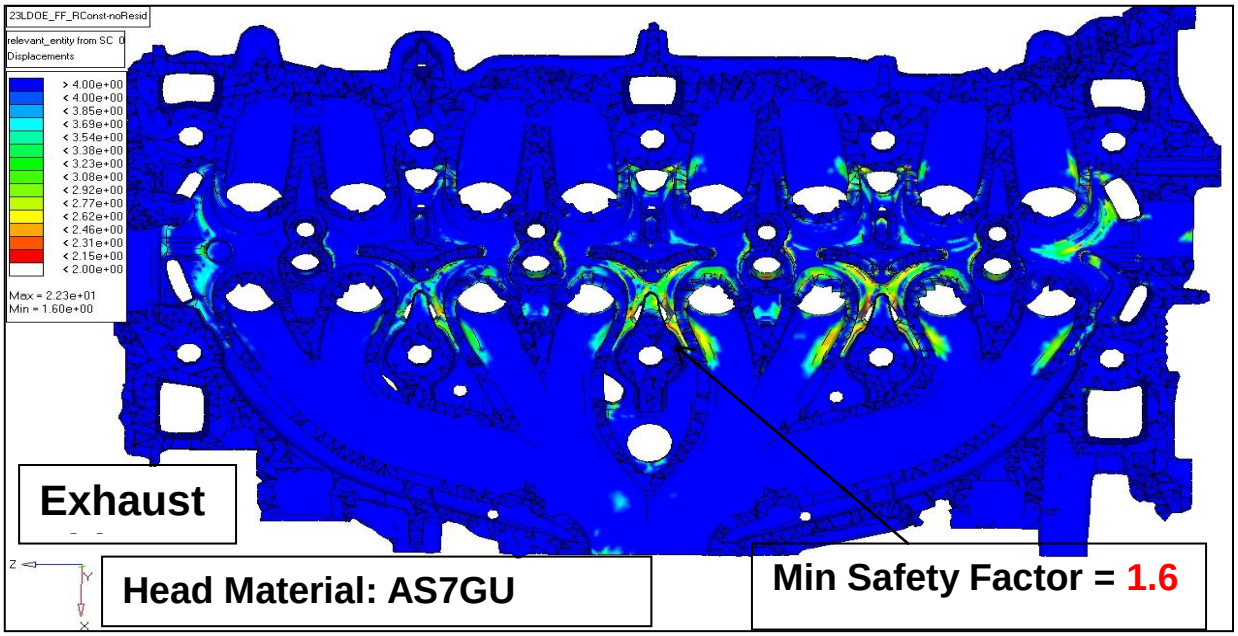


***Figure 41 - Cylinder head HCF safety factors.***

The geometrical relationship between the spark plug electrode and the fuel injector spray (see Figure 42 and Figure 43) is critical for stratified combustion which enables both greater spark retard during the cold idle after an engine start for fast catalyst light-off and the use of “micro-stratification” at part load for improved fuel economy. The design criteria for the distances along the x-axis and the y-axis from the spark plug electrode to the tip of the fuel injector are 13.0 to 14.0 mm and 1.5 to 2.5 mm, respectively. Both of these criteria were achieved in the cylinder head design.

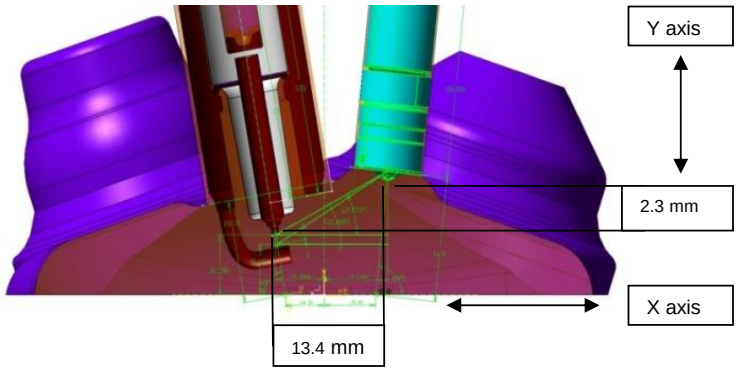


***Figure 42 - Distance between fuel injector tip and spark plug center electrode.***

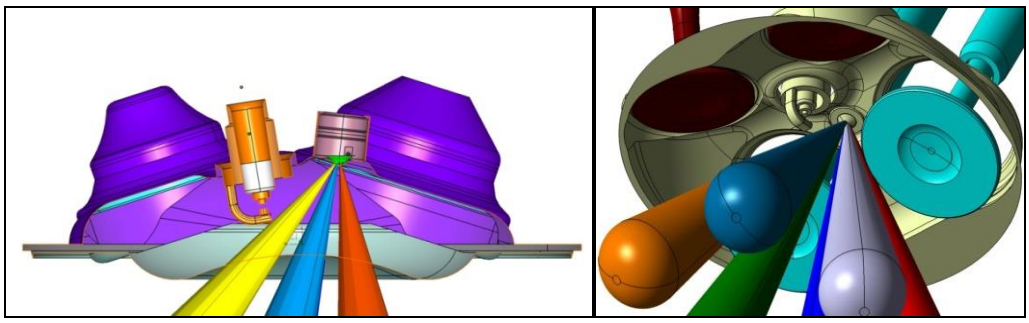

***Figure 43 - Fuel injector spray pattern.***

The intake port was designed to increase in-cylinder tumble charge motion by creating a ledge at the bottom of the intake port as it interfaces with the intake valve. Increased tumble charge motion improves both mixing of the air with the fuel spray and combustion characteristics. Figure 44 illustrates the intake port. Figure 45 illustrates the interaction of the air flowing from the intake port into the cylinder while mixing with the fuel.

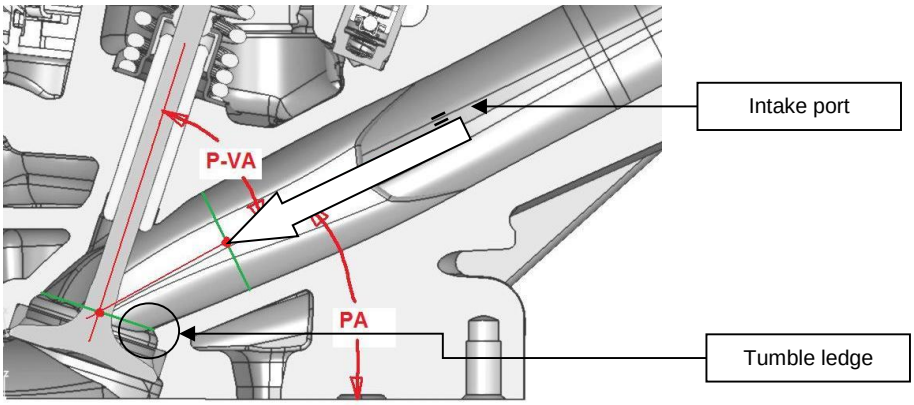


***Figure 44 - Intake port.***

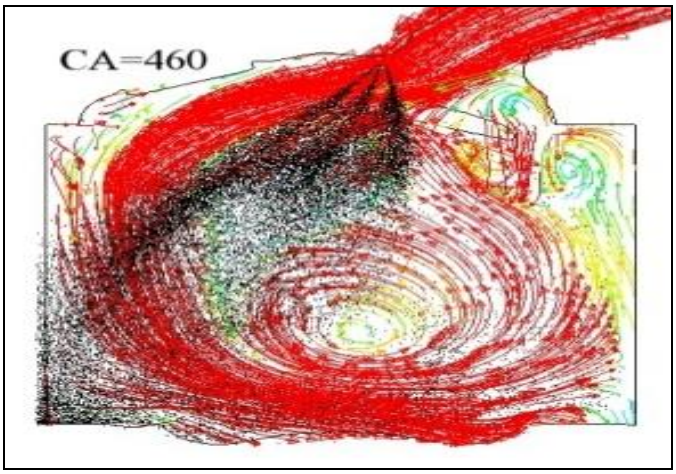


***Figure 45 - Charge motion - fuel spray interaction.***

In conclusion, the transverse central DI cylinder head design presented several challenges for combustion, durability, and cooling. Each challenge was met and validated through CAE analysis.

## Valvetrain

A standard 4-valve-per-cylinder configuration was selected to allow for sufficient valve flow area to achieve the full load performance objectives. A RFF layout with outboard lash adjusters yielded good packaging compatibility with the transverse central DI fuel injector and spark plug. An optimization routine was performed to select valve head diameters that fit within the chamber while setting the exhaust valve diameter to 90% of the intake valve diameter for best performance. The resulting valve sizes are 31.8mm for intake and 28.5mm for exhaust. The RFF, hydraulic lash adjuster, spring, stem seal, retainers and keepers are standard parts from another Ford engine with slight modifications. Premium valve seat and guide inserts were specified for the valve interfaces to the cylinder head. Figure 46 shows the valves packaged in the cylinder head along with the fuel injector and spark plug.

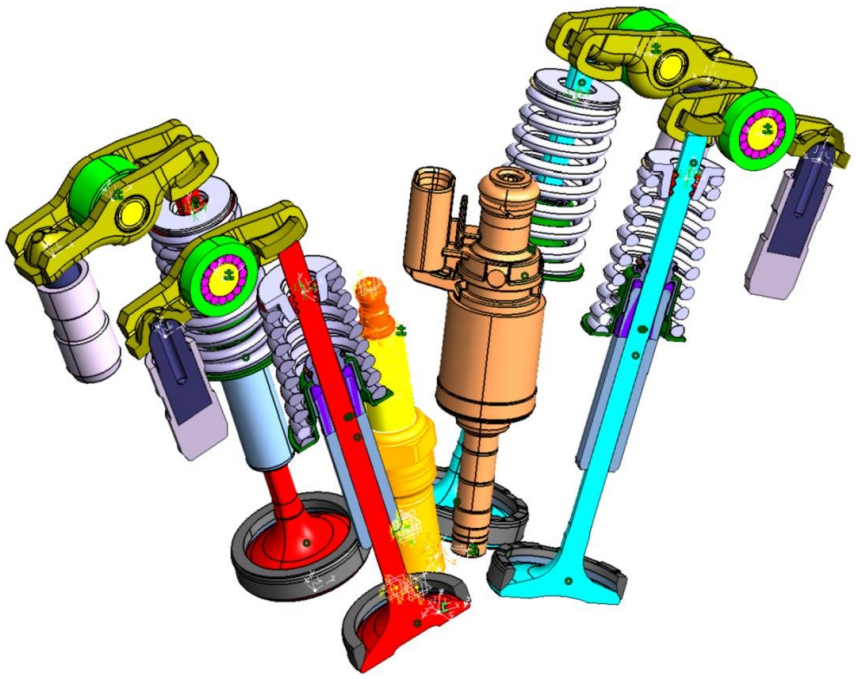

***Figure 46 - Valvetrain.***

The 2-dimensional valvetrain layout was designed using an in-house layout optimization tool called EDAT. The tool considers the desired valve angles and packaging constraints to propose the layout for all the components of the valvetrain and related cylinder head features. EDAT includes Ford design rules such as valve guide length to valve diameter ratio and pressure angles on the roller of the follower so that kinematic analysis of the layout was only needed as a matter of confirmation. The layout shown in Figure 47 represents the final configuration, with the exhaust valve shown to the left and the intake valve on the right.

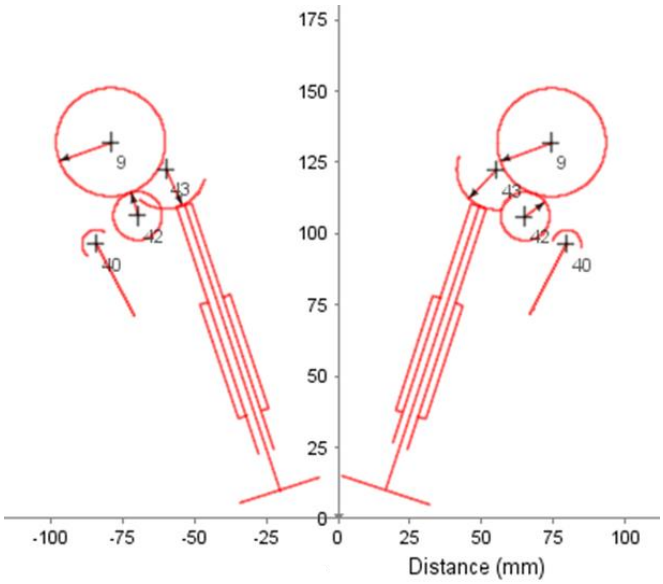


***Figure 47 - Valvetrain dimensional layout.***

A single-valve dynamic model was built using Ricardo Valdyn software to confirm that the stiffness of the components was sufficient to maintain control up to the target engine speed. Results of the model showed that valve seating velocity was below 0.5 mm/sec and camshaft contact force was above 100 N at all speeds up to 7000 rpm as shown in Figure 48. Confirmation measurements on a cylinder head test rig using laser measurement techniques found no stability issues.

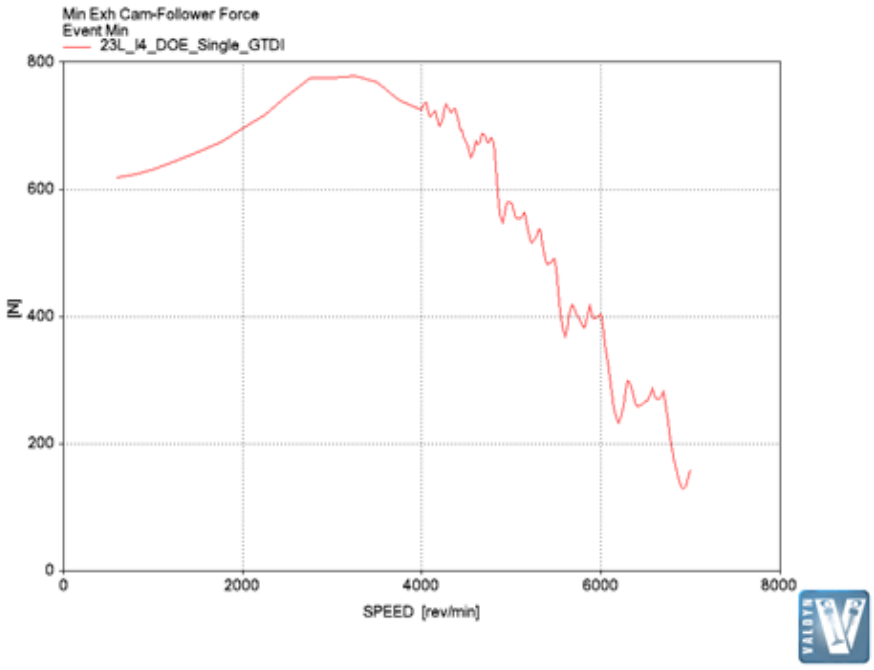


***Figure 48 - Minimum force between cam lobe and roller follower as predicted by dynamic model.***

Roller finger followers are inherently lower in friction than typical flat tappets with a sliding interface to the cam lobe. To further reduce friction, the front camshaft bearing uses a needle bearing in place of a plain hydrodynamic bearing. The front bearings are more highly loaded than the other locations due to the cam drive tension. Reduced valvetrain friction due to the roller bearings was expected to result in an improvement of fuel consumption of 0.1 to 0.2%, depending on the drive cycle. A bearing with 30 mm OD and 24 mm ID and 14 mm length was selected based on package and durability requirements. The bearing is captured on the assembled camshaft and cannot be serviced separately. The cage which aligns the needles extends past the outer race to position the bearing correctly with respect to the cam cap. Figure 49 shows the needle bearing installed on the camshaft.

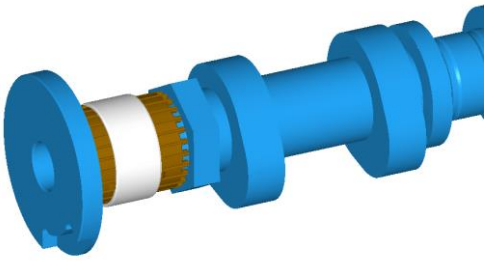

***Figure 49 - Needle bearing at front of camshaft.***

In order to ensure that the needle bearing would be sufficiently durable for series production, the bearing supplier performed a bearing life analysis. The input to the analysis included the dynamic camshaft loads at each lobe, bearing, and cam drive interface (Figure 50) for a variety of engine speeds. With peak loads predicted to not exceed 2000 N, the bearing life was determined to be 3200 hours, well in excess of the target.

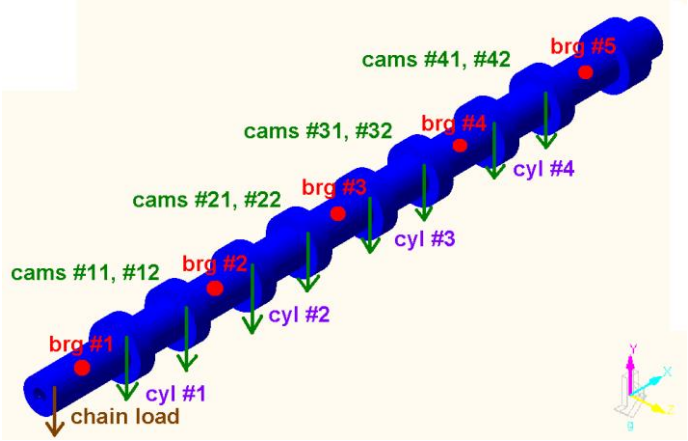


***Figure 50 - Camshaft loads for bearing life calculation.***

## Camshaft Drive

This engine uses a double overhead camshaft valvetrain. The main objectives for the cam drive are to provide accurate camshaft timing with low noise and low friction while minimizing the engine length. There are three main technologies used in the industry for gasoline engine cam drive systems: dry belt, belt-in-oil, and chain drive. Dry belt systems are difficult to use with variable cam timing phasers, and are not the most efficient for package space. Hence this type of camshaft drive was not considered for the 2.3L DOE engine.

Ford worked with Dayco to design a suitable belt-in-oil system and with Borg Warner on a chain drive system (Figure 51). Additional chain drive systems with innovative tensioner designs were also considered, but ultimately eliminated due to incompatibility with the front engine mount. The belt and chain systems were evaluated relative to several metrics including package (engine length), noise, friction, oil usage, cost, weight, and ease of layout modification for alternate camshaft positions. The chain was judged equivalent to the belt on many attributes and slightly worse for NVH and oil usage, but the significantly narrower width of the chain provided a significant advantage in helping meet the engine length constraint.

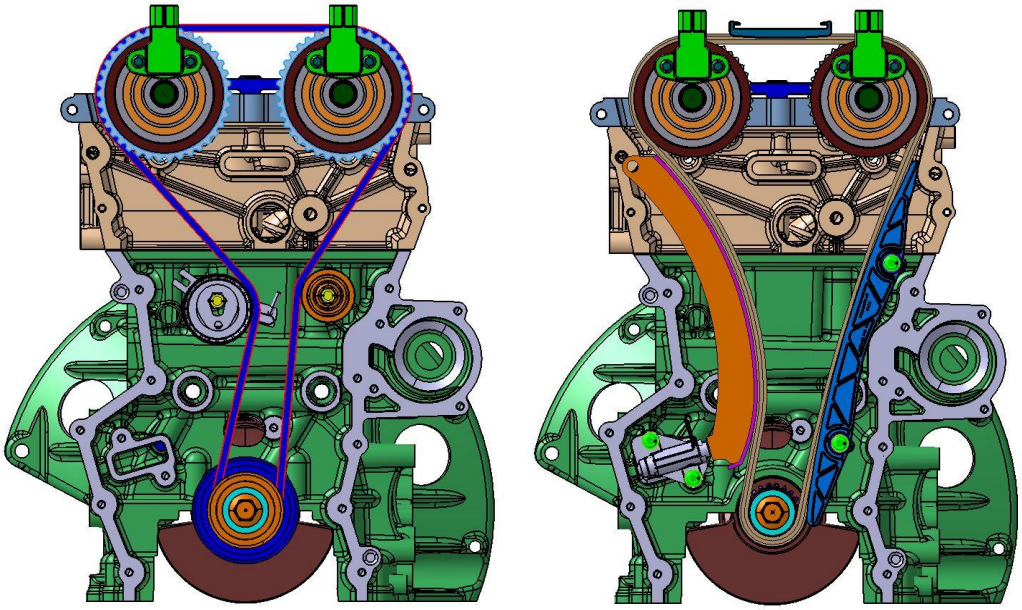

***Figure 51 - Belt (left) and chain (right) layouts considered for cam drive.***

The chain drive system contains the standard components for a DOHC inline engine: crank sprocket, cam sprockets (integrated with VCT actuators), hydraulic tensioner, composite tensioner arm, composite chain

guide, and chain. The chain is an 8mm pitch inverted tooth design that Borg Warner designates Type 111. It includes features to reduce friction and wear. To reduce friction, the links are made with a 3x2 plate configuration (Figure 52) which reduces the number of sliding interfaces compared to older designs which contain a greater number of thinner interlaced plates. The backsides of the links are not flat, but have a generous radius to reduce the contact area with the chain guide, but without imparting excessive contact stress. This results in lower frictional losses between the chain and guide. The chain tooth profile has been refined by Borg Warner to provide an optimal balance between NVH and link/sprocket contact stress.

***Figure 52 - Segment of Borg Warner 3 x 2 Type 111 chain.***

GTDI engines are known to produce more particulates than PFI engines, and some of the particulates are present in the engine oil. Particulates are known to accelerate chain wear which leads to chain elongation and cam timing error. The chain wear often occurs at the pin to plate interfaces. To counteract the more aggressive oil, this chain includes larger pin diameters with super finish aperture (SFA) links. Supplier bench testing has shown a wear improvement of 75% compared to traditional chain under severe engine oil conditions.

Dynamic analysis was performed on the cam drive system to ensure that chain loads and camshaft oscillations would not be excessive at any engine speed. Inputs to the simulation model included camshaft torsional values from a Valdyn multi-cylinder model and crankshaft torsional values from another dynamic model. The results showed that the chain loads (Figure 53) and tensioner plunger movement were well within the rated and design guide limits. One area of concern was the chain span between the two camshafts. Since the cams are 153.6 mm apart, there is a large unsupported span between them. To prevent uncontrolled chain movement in this span, a snubber was added above the chain (Figure 54). The snubber is installed with a clearance of 0.5 to 1 mm above the tight chain so that it is not constantly rubbing and imparting a friction load. Under conditions where the chain starts to deviate from the intended path, it contacts the snubber and is nudged back in line. The snubber consists of a nylon wear face snapped to a steel mounting bracket. The bracket is attached to the camshaft carrier with two bolts.

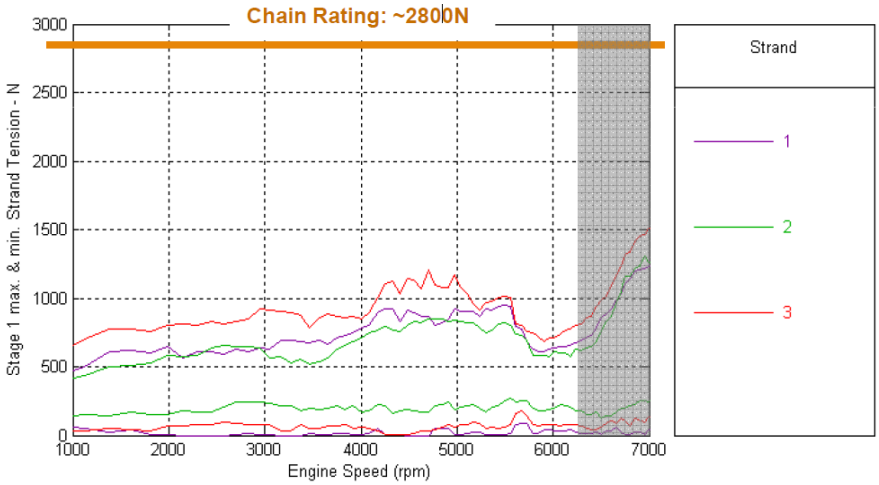


***Figure 53 - Chain tension results of dynamic analysis.***

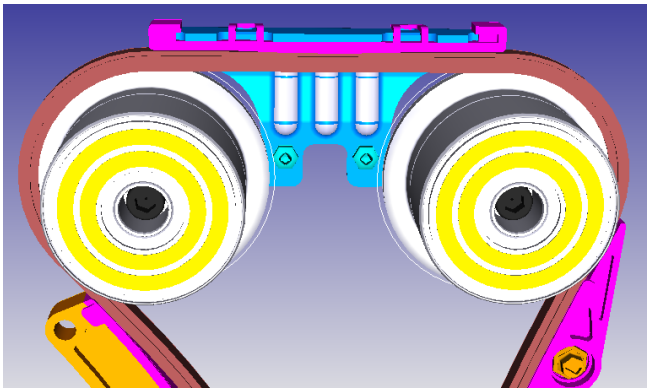

***Figure 54 - Chain snubber.***

## Electric Variable Camshaft Timing

Electric variable camshaft timing (el-VCT) uses a brush electric motor to actuate the cam phaser, instead of using high pressure engine oil. The motor rotational motion is transmitted to the camshaft via an Oldham type reduction gear mechanism that is mounted to the camshaft. In principle, the electric actuation allows the phaser to shift independently of oil pressure, temperature, and engine rpm. This functionality allows the cam to be positioned immediately after startup and with a wider operating window of conditions. Below is a list of possible uses to improve engine attributes.

- Emission reduction during startup.
- Rapid and consistent response during throttle tip-ins at low engine speed to assist turbocharger spool up.
- High compression heating via early intake valve closing during cold start for flexible fuel vehicle applications.
- Optimal valve timing for start-stop and Atkinson cycle applications.
- Reduction of oil pump size.

### Design Assumptions

Below are the el-VCT design and performance assumptions for the DOE engine and Figure 55 from the component supplier shows key design parameters and operating ranges.

- Range of authority: 60 °CA on both intake and exhaust
- Default positions: Full retard on intake full advance on exhaust
- Shifting velocity maximum: 300 °CA/sec
- Operating temperature range: -30 °C to 120 °C
- Engine speed range: 600 to 7000 rpm
- Battery voltage range: 9 to 16 V
- Power consumption: <1 A holding and <15 A peak at cold conditions
- Actuator type: DC brush motor + slip ring
- Gear ratio: 60:1

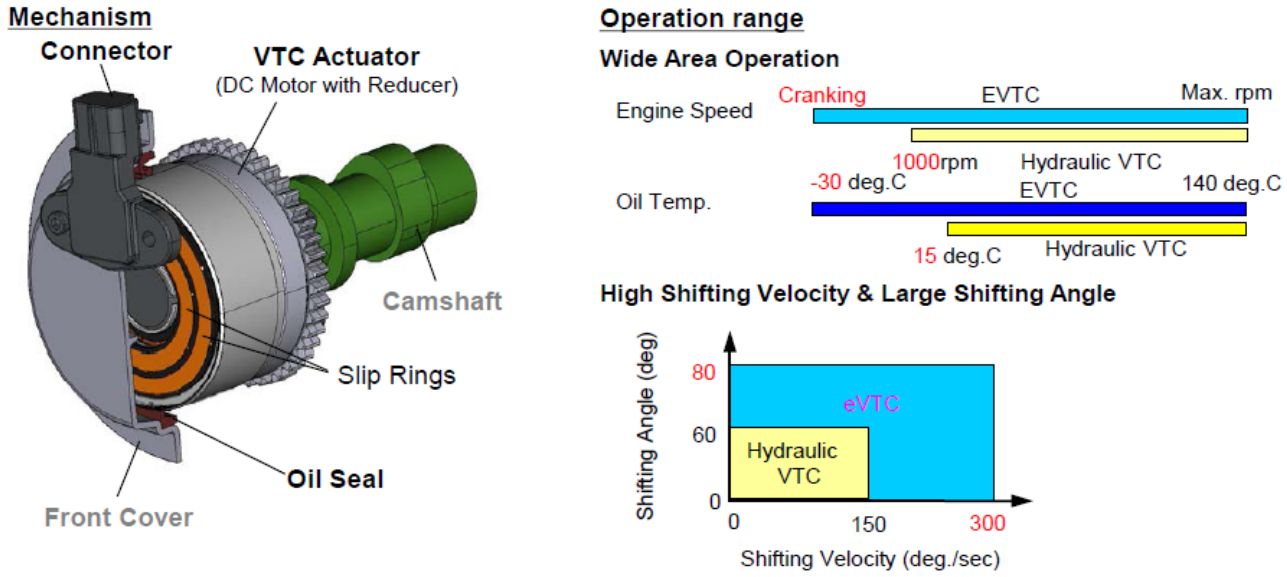


***Figure 55 - Electric VCT mechanism and operating ranges.***

## System / Component Summary

Figure 56 is the control structure for controlling and actuating the VCT. Control logic was created to provide a transfer function which takes the input from the PCM on the amount of phase angle and time to reach the target angle. The control logic and power electronics then provide appropriate current to the DC brush motor via the slip ring brush that is connected to the input shaft. The output shaft assembly, which is mounted to camshaft, has a gear reduction unit that multiplies the motor torque. The advantage of a brush motor is its low power consumption, as it only needs to operate during phase shifting and holding cam position that is other than the default position.

Since the design does not have a lock pin and internal sensor, the camshaft positions cannot be accurately tracked during initial startup. Therefore, the VCT units are positioned at full retard for the intake and full advance for the exhaust during shutdown. Then they are phased immediately to the desired positions after startup.

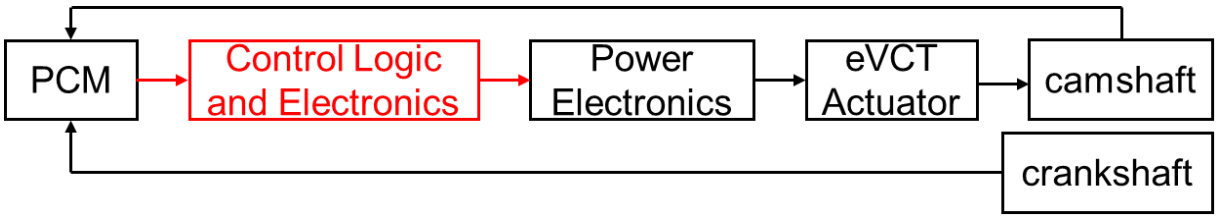


***Figure 56 - Variable cam timing control structure.***

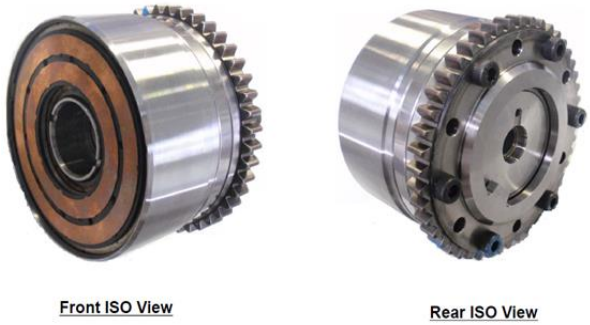


***Figure 57 - Slip ring and chain sprocket of ElVCT.***

## Engine Dynamometer Test Results

Tests at several speed load points as shown in Table 8 were conducted on an engine dynamometer to evaluate the response of the VCT units.

***Table 8 - VCT Phasing Tests.***

| Test | Results | Type | Intake Phasing | Exhaust Phasing |
|---|---|---|---|---|
| 1 | Figure 58 | 1500 rpm tip in | Auto advancing from fully retarded position | Auto advancing from fully retarded position |
| 2 | Figure 59 | 2000 rpm 5 bar | Retarding from fully advanced position | Holding |
| 3 | Figure 60 | 2500 rpm full load | Holding | Holding |

Test 1 is the evaluation for a tip-in at 1500 rpm engine speed. Figure 58 is a plot of the VCT positions during the tip-in. During the transient, the intake phasing rate was about 120 °CA/s and exhaust was about 100 °CA/s. Both VCT units were able to reach the target positions in less than 500 ms. The results also show that there was about 100 ms delay from the time of the PCM command to VCT movement.

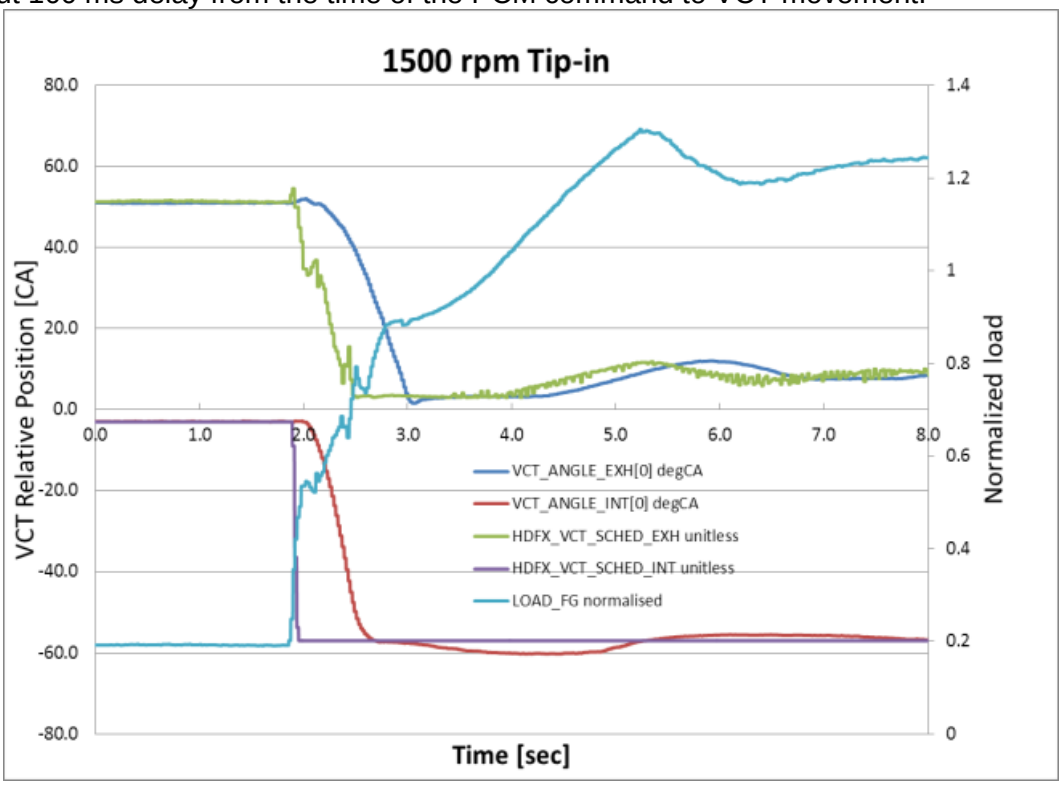


***Figure 58 - VCT response during tip-in at 1500 RPM engine speed.***

Figure 59 shows the results for Test 2 where the intake phaser was retarding from the full advanced position while the exhaust phaser was holding position. In this case, the phasing rate on the intake VCT was 150 °CA/s while the exhaust was able to hold its position to within +/- 1 °CA accuracy.

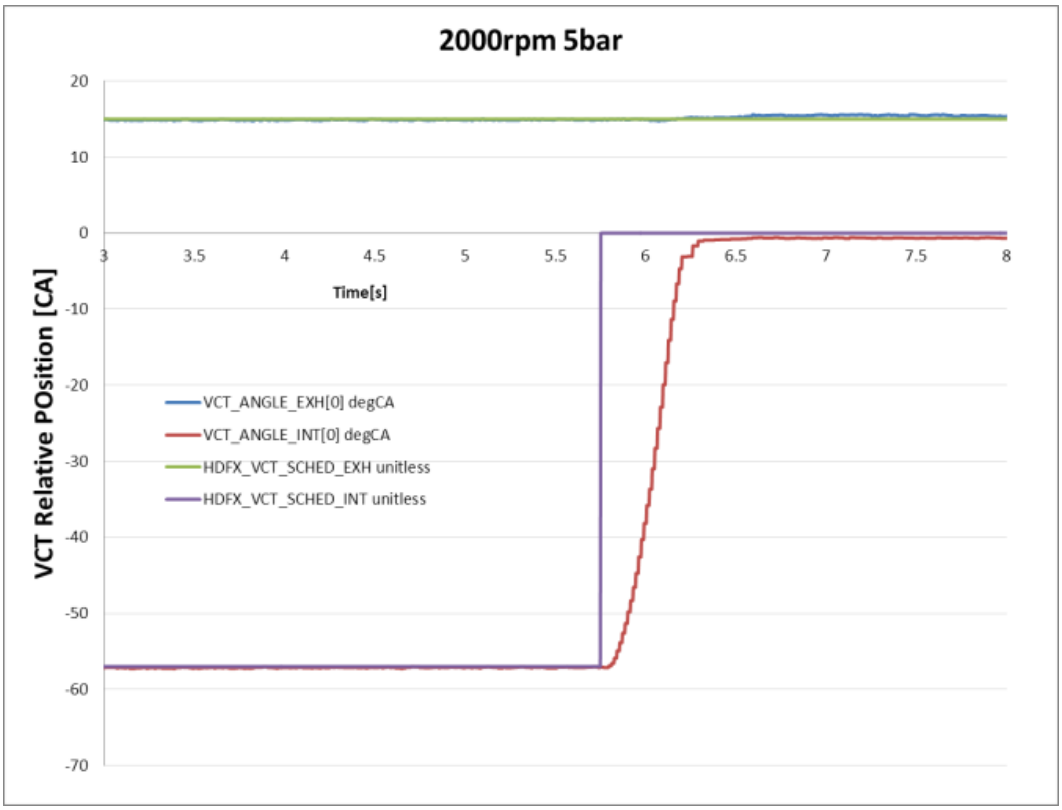


***Figure 59 - VCT response for intake retarding and exhaust holding position.***

Results plotted in Figure 60 for Test #3 at 2500 rpm full load shows that the phasers were able to hold cam positions to within 1 °CA accuracy at this condition.

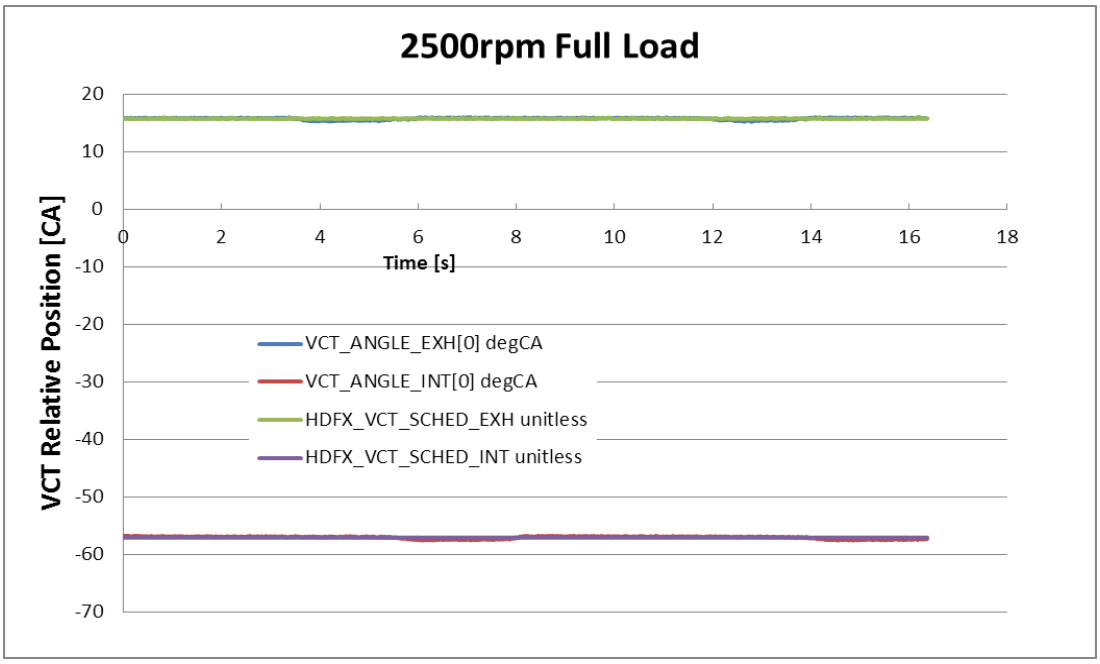


***Figure 60 - VCT holding position.***

## Vehicle Testing

Additional VCT phasing data were also taken on a running vehicle. The data shown in Figure 61 and Figure 62 were taken during a random drive and a cold start, respectively.

Figure 61 shows the engine speed went from 1000 to 2000 rpm during a low to mid-load transition. The initial positions of the cam phasers were full retard for the intake and full advance for the exhaust. Both VCT units were able to meet the commanded target positions throughout the random drive cycle as shown in the plot.

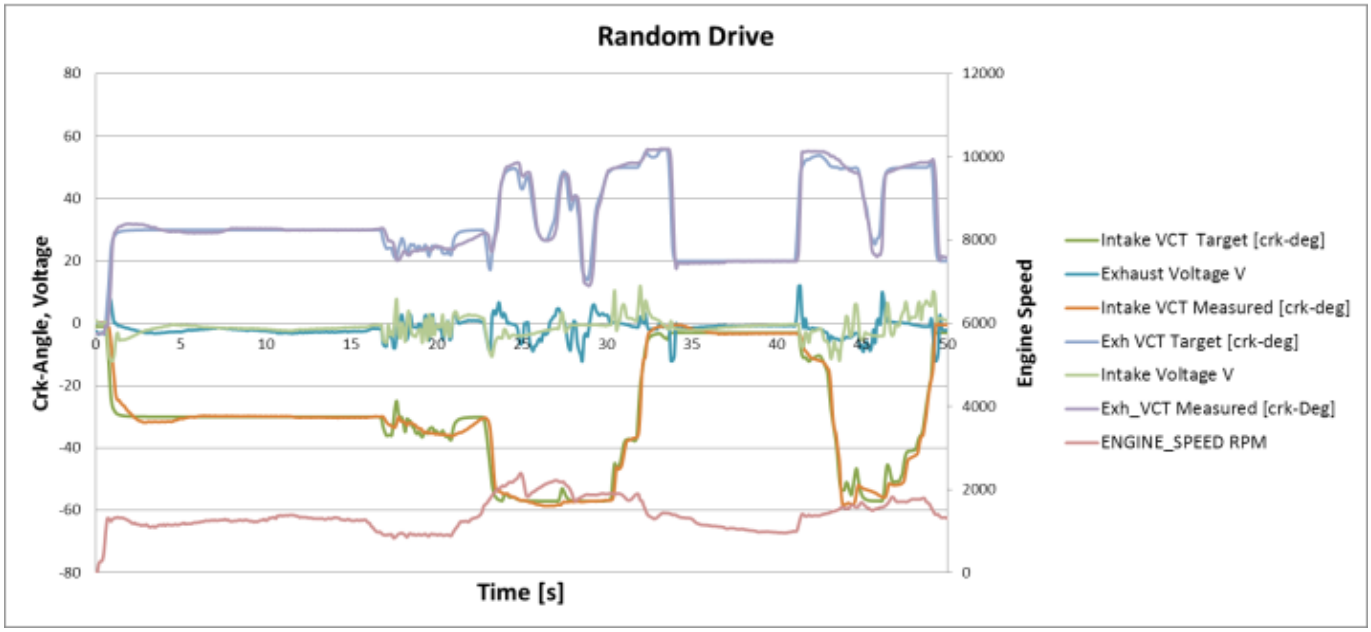


***Figure 61 - Vehicle random drive.***

Figure 62 shows the data taken during a vehicle cold start at 0 °F (-18 °C) ambient. At this temperature, the VCTs were not able to meet commanded cam positions during the first 5 seconds. The phasing speeds were about 10-15 °CA/s due to friction in the gear reduction unit and the valvetrain.

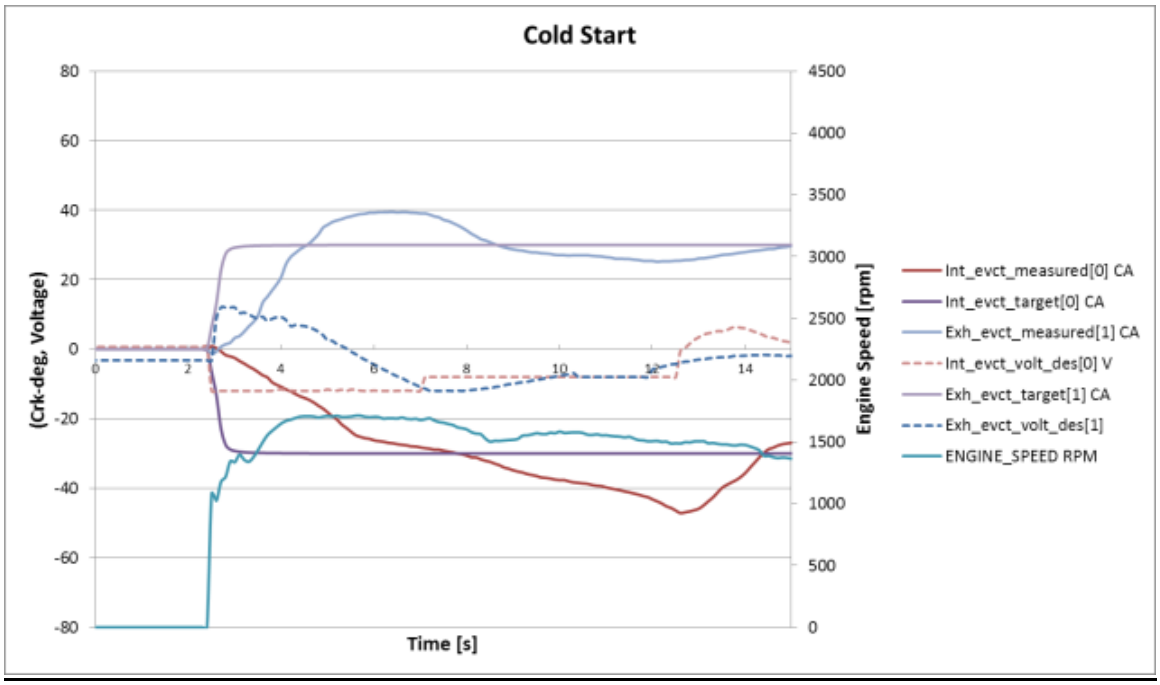


***Figure 62 - Vehicle cold start at 0 °F (-18 °C) ambient temperature.***

In summary, the electric VCT units were able to phase to commanded angles in both engine dynamometer and vehicle tests except during the vehicle 0 °F ambient temperature test. Due to the absence of a high resolution sensor in the VCT unit to track camshaft position during engine start, the intake camshaft was positioned at full retard on shutdown, resulting in non-optimal cam position on startup.

## High Pressure Air Intake System

The high pressure air path system on the engine encompasses the components from the turbocharger compressor outlet to the cylinder head flange. This includes all high pressure air charge ducting, charge air coolers (CAC), electronic throttle body, and intake manifold (Figure 63). The engine has a unique intake system with a dual water-to-air charge air cooler system. It consists of an integral water-to-air charge air cooler located in the intake manifold (Figure 64) and a separate pre-throttle water-to-air charge air cooler (Figure 65) to maximize cooling performance and protect the electronic throttle body from temperatures associated with low pressure exhaust gas recirculation (LP EGR) that could exceed its design limits.

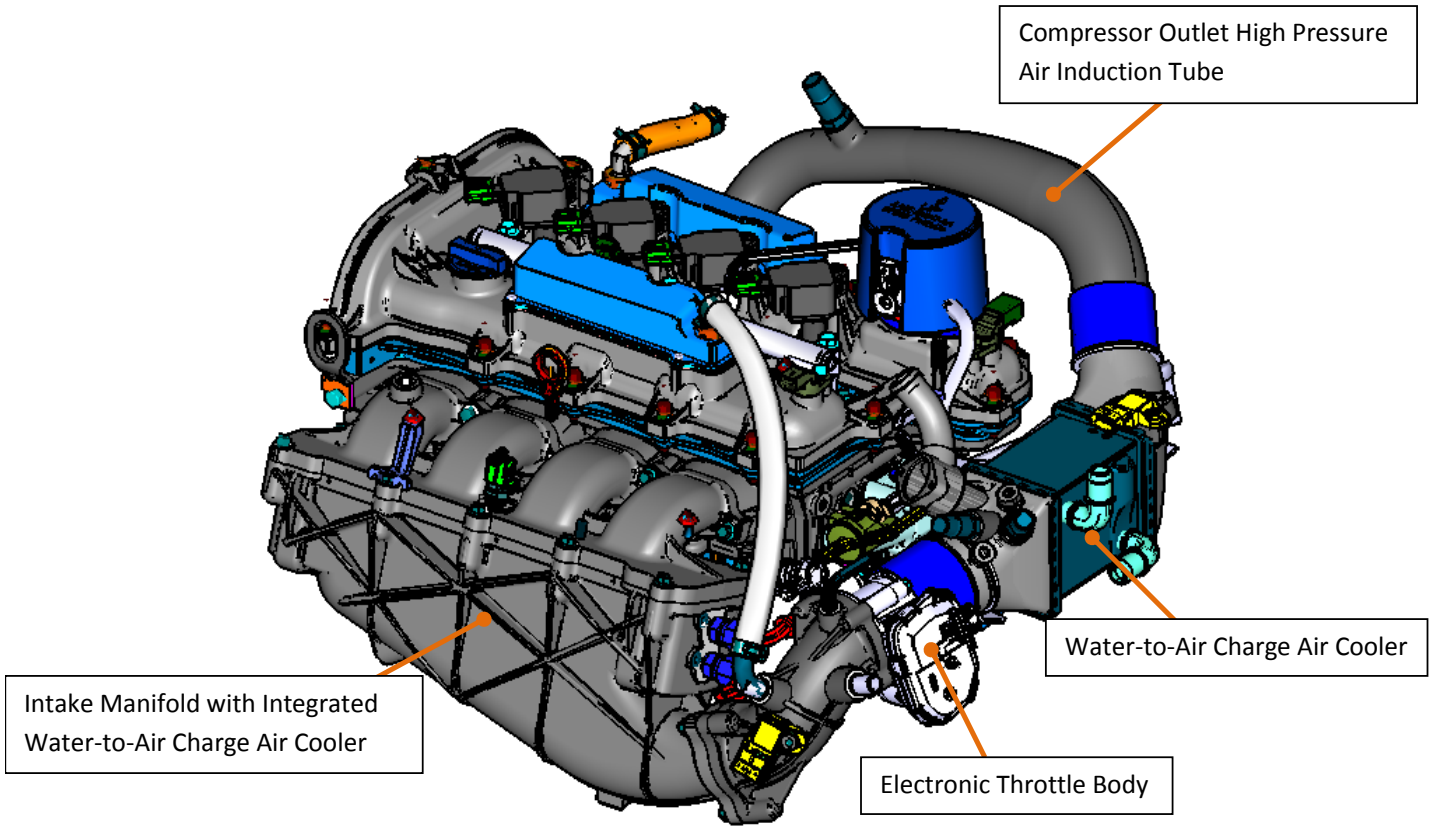


***Figure 63 - High pressure air induction system.***

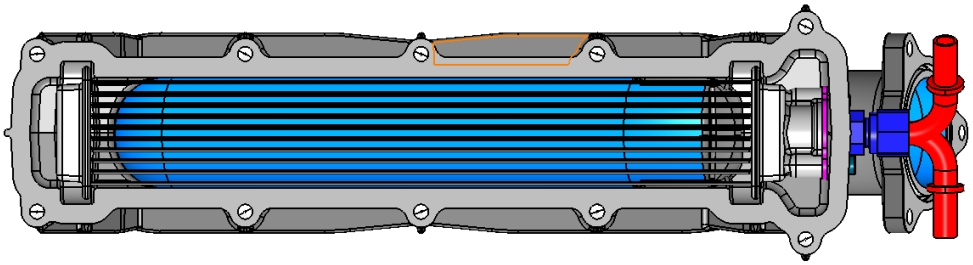

***Figure 64 - Intake integrated charge air cooler top view.***

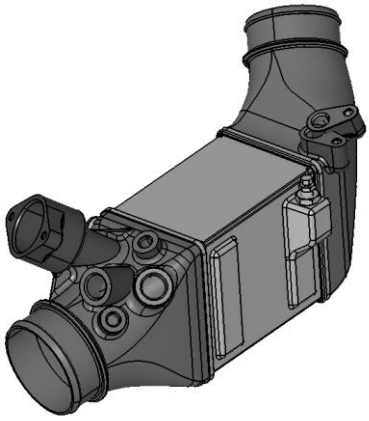

***Figure 65 - Isometric view of pre-throttle charge air cooler with end tanks.***

Providing a low overall pressure drop in the high pressure air path is necessary in order to meet the peak power requirement of 181 kW at 6000 rpm. Both charge air coolers have an aspect ratio with a large frontal face for airflow and reduced height, so there is an inherently small pressure drop with these designs. This ensures the system is not restrictive to meet the high speed power and delivers good cooling performance of manifold charge air. The charge air coolers and respective cross-sectional areas are shown in Figure 66.

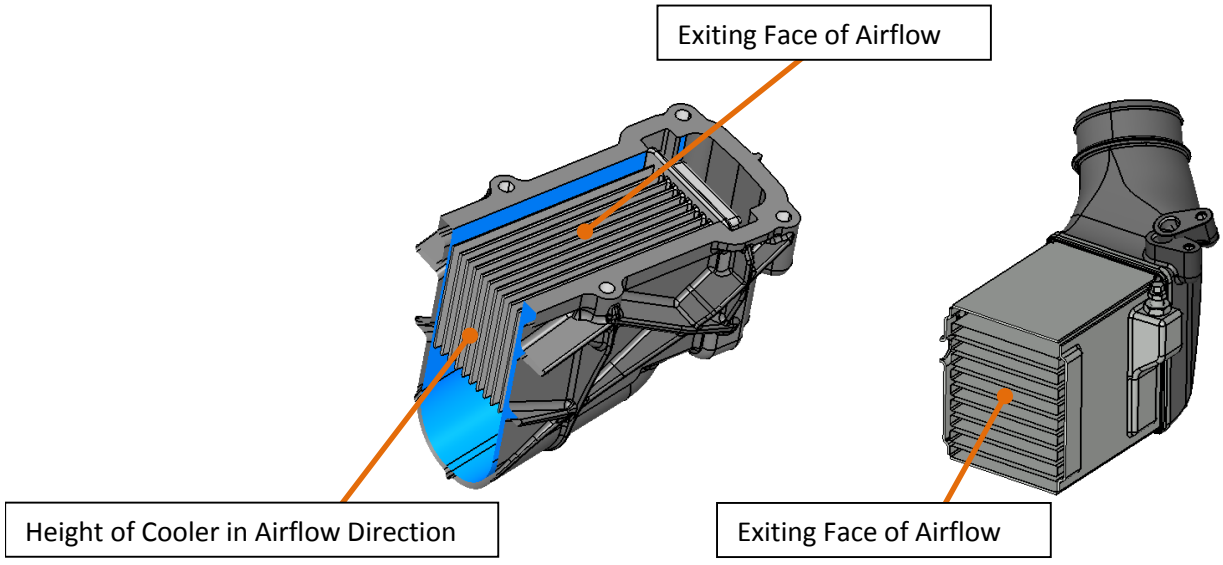


***Figure 66 - Aspect ratio of charge air coolers for low pressure drop.***

Another important design aspect of the system is low boosted volume via a very compact high pressure air path design to provide good torque response. This low volume is synergistic with low pressure exhaust gas recirculation (LP EGR) and minimizes the transport delay of EGR to further enhance its effectiveness. The design also provided favorable packaging in the engine compartment.

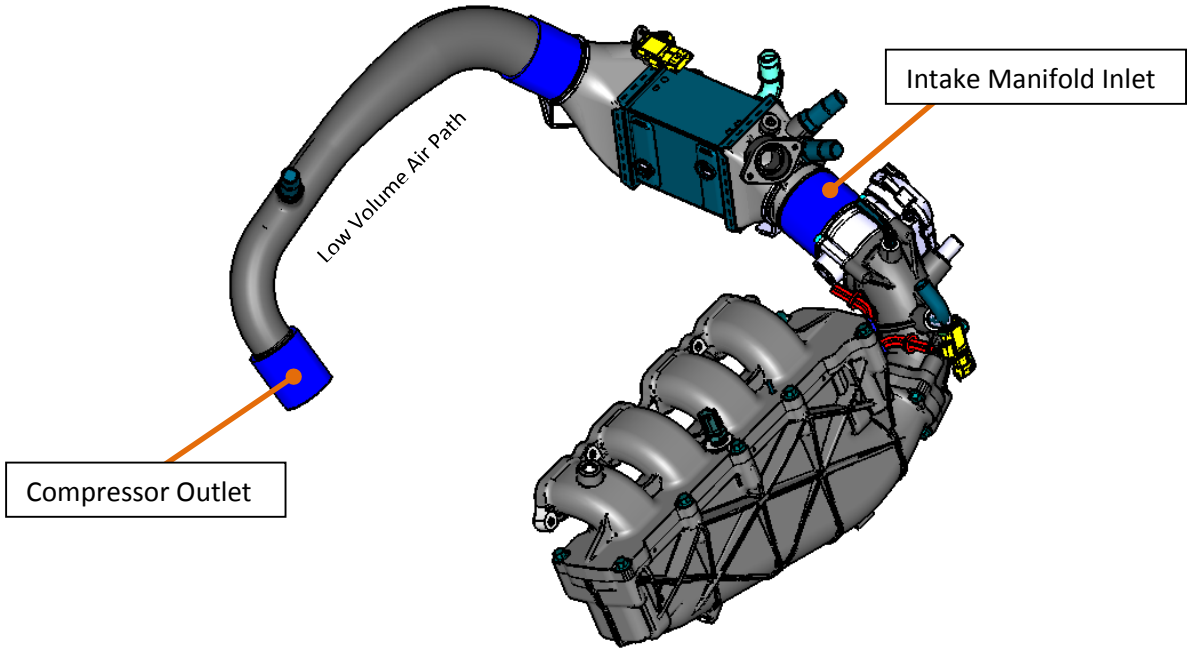


***Figure 67 - Low boosted volume for good transient response.***

Delivering the air charge evenly to each of the cylinders is an important objective of intake manifold design. The intake manifold designed for the engine delivers the intake air charge within +/-1% cylinder-to-cylinder at peak power (Figure 68), and within less than +/-1% at 3500 rpm, high load (Figure 69). This enables even A/F distribution between cylinders and also evenly distributed secondary gas (i.e. PCV, EGR).

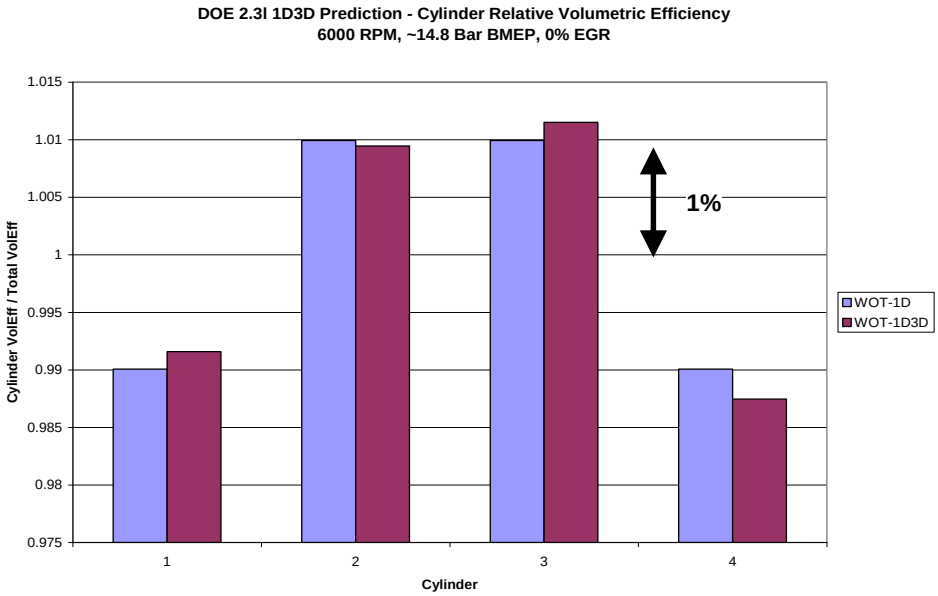


***Figure 68 - Volumetric efficiency variation at peak power.***

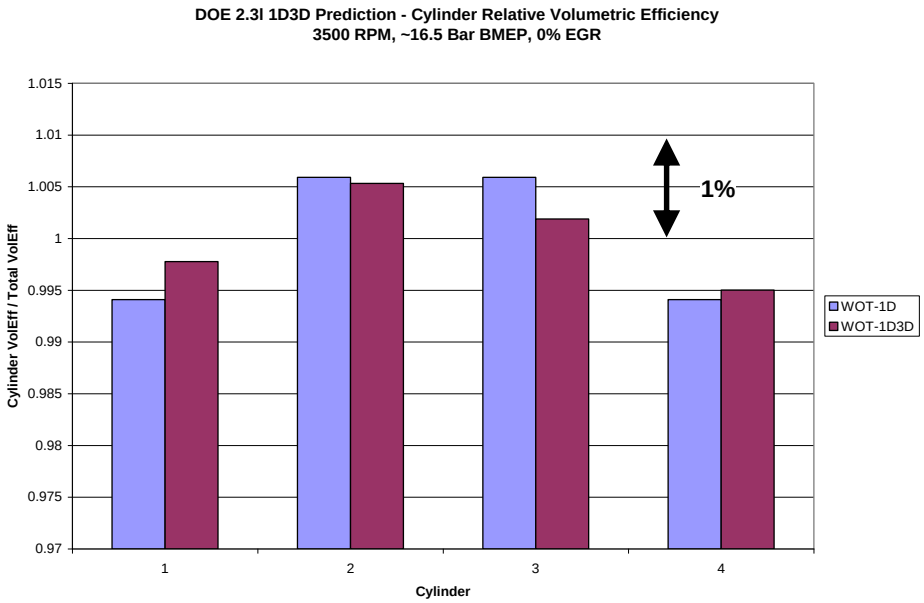


***Figure 69 - Volumetric efficiency variation at 3500 rpm, 16.5 bar BMEP.***

Along with even air charge delivered to the cylinders, it is also important to have even temperature distribution. The less than one percent variation in cylinder-to-cylinder volumetric efficiency is possible because the temperature distribution across the intake manifold is also within these bounds. The design of the intake manifold plenum is critical to distribute the flow evenly across the CAC core face, which enables more uniform cooling of the charge and hence more uniform temperature distribution and air distribution between cylinders. Even temperature distribution at the intake runner entries going to the cylinder head intake ports is shown in Figure 70. The pre-throttle CAC also delivers good face utilization at +/-8% (Figure 71).

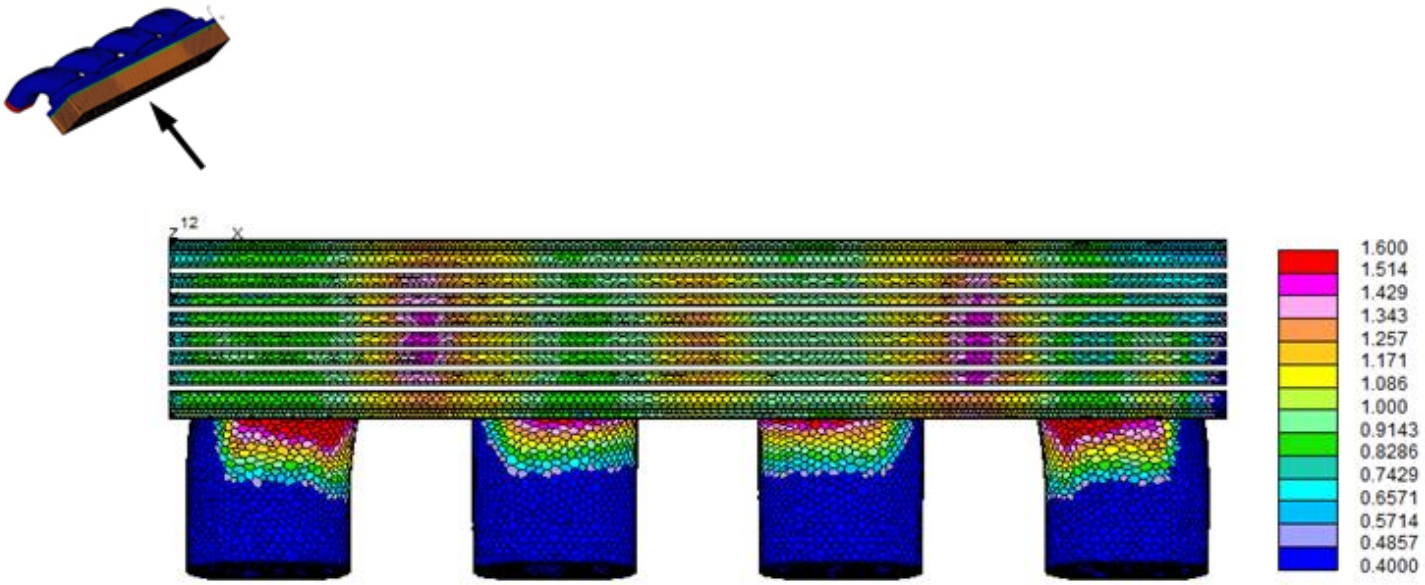


***Figure 70 - Temperature distribution at runner inlets.***

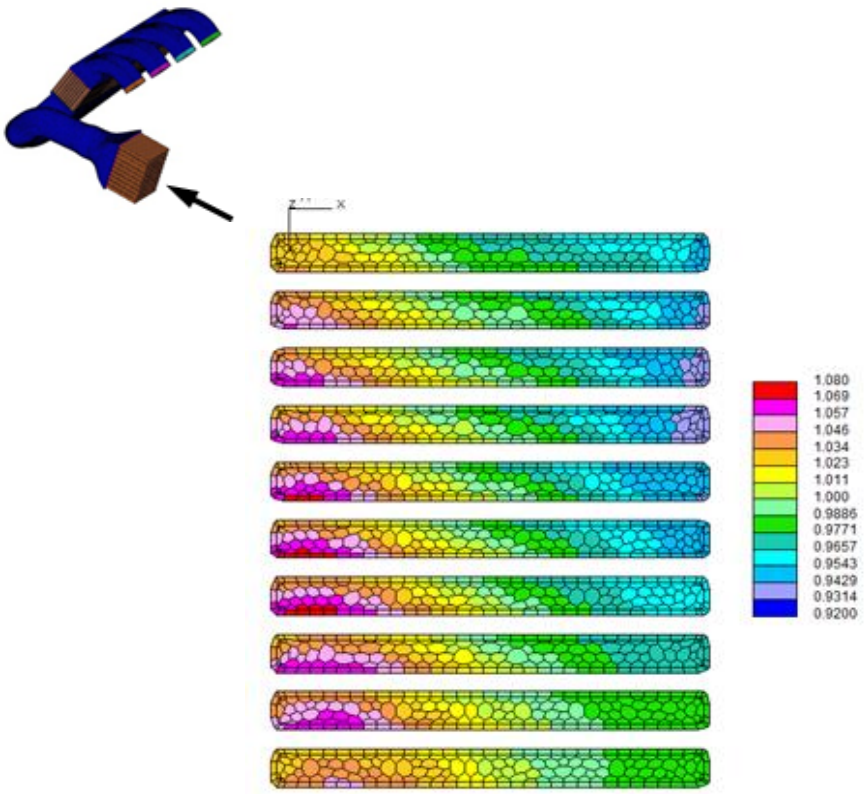


***Figure 71 - Temperature distribution at remote charge air cooler entrance.***

The assembly and sealing approach utilized for the intake manifold is shown in Figure 72. Isolation of the core from vibration, sealing boost to the atmosphere and internally, and good support to prevent leaks are incorporated in this design.

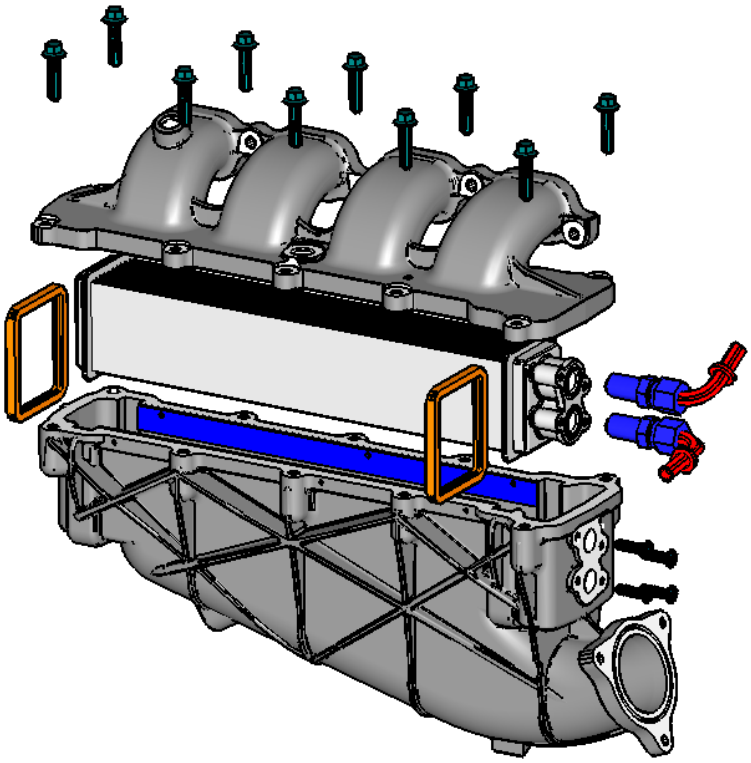

***Figure 72 - Sealing and assembly for the intake manifold integrated charge air cooler.***

## Boost System

The boost system must deliver pressurized air to the intake manifold in order to force enough air into the cylinders to achieve the engine performance targets. Turbocharging is an integral part of Ford's EcoBoost technology. Turbocharger sizing must be matched to the engine in order to deliver the objective torque at all engine speeds, and to minimize the time to reach target torque at low engine speeds. The main components that are specified during the matching stage include the compressor wheel diameter and trim, the turbine wheel diameter, and the scroll cross sectional areas. The turbocharger must minimize the exhaust backpressure, especially under non-boosted conditions. Additionally, the turbocharger for this engine needed to be robust to high exhaust gas temperatures on the turbine side, and EGR related contamination entering the compressor.

Ford worked closely with Borg Warner Turbo Systems to design and select a turbocharger to meet the program objectives. Three compressor wheel sizes ranging from 53 to 56mm with trims from 74 to 80% were considered. A GT Power 1-D engine model was extensively used to determine the surge margin at 1500 rpm, 16 bar BMEP as well as the choke margin at peak power for the various compressors. Ultimately a 55mm compressor wheel with 78% trim and a 51mm turbine wheel with 89% trim were selected for the program. Engine dynamometer testing confirmed that the engine was capable of achieving the target torque curve with the selected boost system.

Four technologies were applied to the turbocharger which were new to Ford. First, the turbine wastegate uses an electric actuator for precise control under all conditions. A rotary actuator with an integral position sensor moves the wastegate through a four bar linkage (Figure 73). When boost is not required, the wastegate is opened to minimize exhaust back pressure and pumping work. This functionality is known as active wastegate and accounts for approximately 0.5% fuel consumption improvement. When boost is required, the valve is controlled to a commanded position to achieve the desired boost.

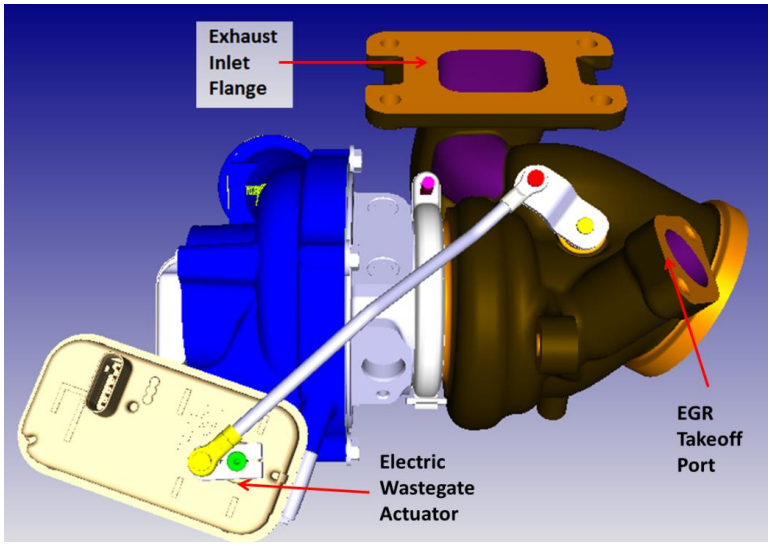


***Figure 73 - Electric wastegate actuator and four-bar linkage; EGR takeoff port.***

Second, the turbine housing includes a takeoff port for EGR (Figure 73). CFD was used to define the size, position, and orientation of the port to increase the pressure driving EGR through the system. The rotational momentum of exhaust gas exiting the turbine wheel was captured by the geometry of the EGR port to improve dynamic pressure to drive more EGR thereby minimizing the restriction required at the AIS throttle.

Third, the turbo was designed with a configuration known as "binary flow turbine" (Figure 74). This twin-scroll based design allows the turbine housing to act small under low flow conditions, and large under high flow conditions. All exhaust gas enters the turbine housing through a single inlet into the primary scroll. A valve

contained in the turbine housing can open to allow exhaust to flow into the secondary scroll as well when desired. The scroll control valve is controlled by an electric actuator similar to the wastegate actuator.

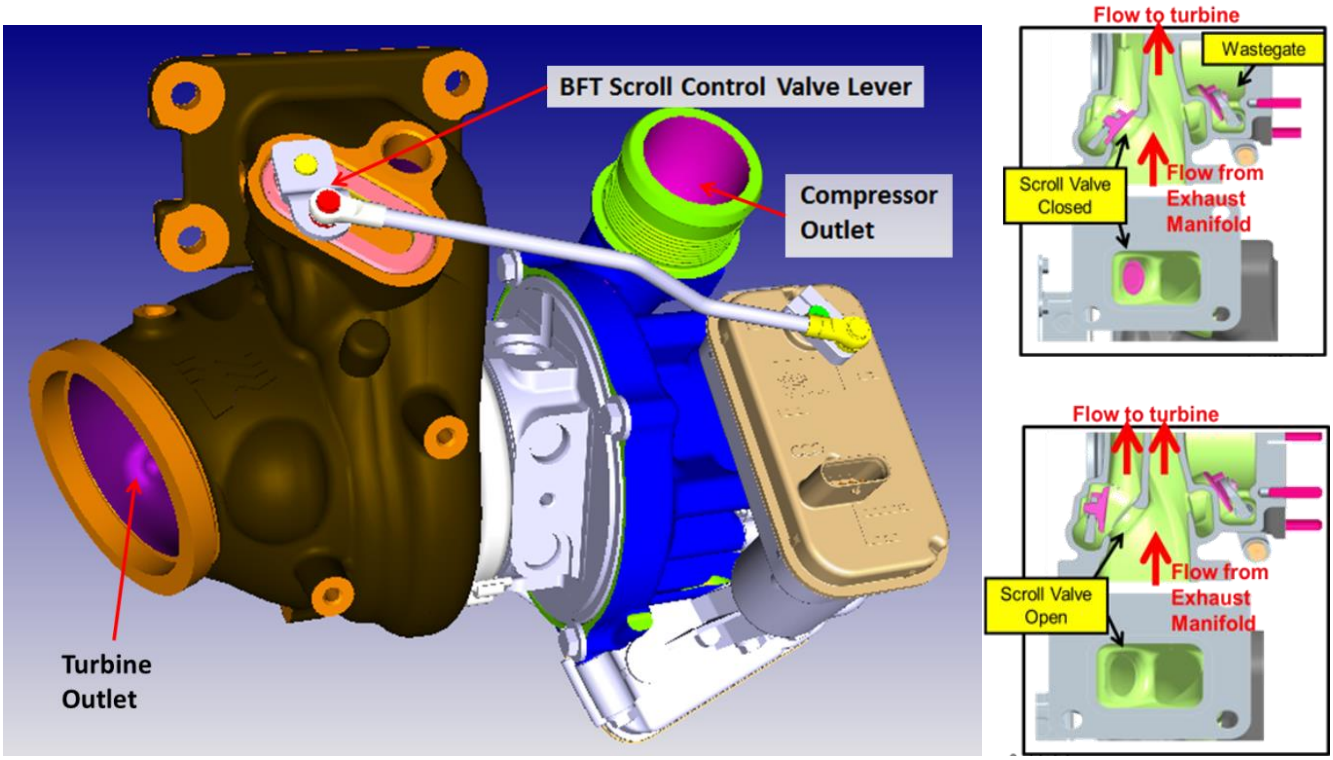


***Figure 74 - Binary flow turbine.***

Engine testing on dynamometer showed that the turbocharger was able to deliver the required boost levels in steady state conditions with the scroll control valve open at all speeds. At low engine speeds, the torque could also be achieved with the valve closed, and under transient conditions, the torque was able to build more quickly with the valve closed as shown in Figure 75.

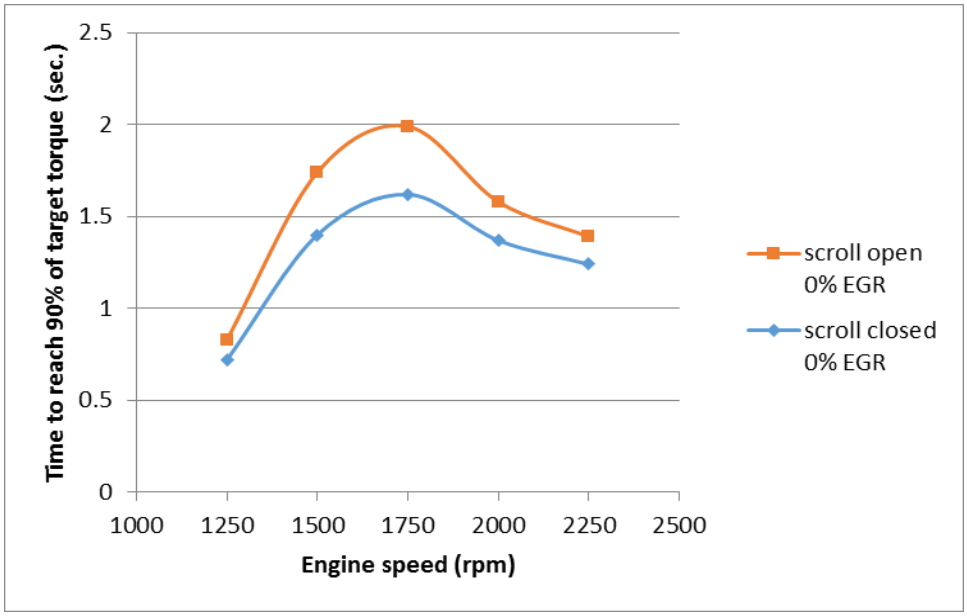


***Figure 75 - Dynamometer test results showing engine transient torque response.***

Finally, the compressor wheel includes a ceramic coating to prevent pitting and erosion in the presence of contamination which can be introduced with low-pressure loop EGR. The coating is much harder than aluminum and able to withstand impact from soot and small water droplets.

Additional specifications were selected to meet design objectives. The twin-scroll turbine housing is a premium high-nickel content alloy A5N material which can sustain inlet temperatures at 980°C with infrequent excursions to 1000°C. The gasket between the cylinder head exhaust outlet and the turbocharger inlet is a 3-layer stainless steel design from Dana. A stainless steel support bracket made from a bracket in production on a different engine was incorporated to stiffen the assembly which would otherwise only be supported by the exhaust inlet flange. Finally, in order to protect the electric actuators and other underhood components from radiated heat, a multi-layer aluminum heat shield was designed to be attached to the outside of the turbine housing. These items are pictured in Figure 76.

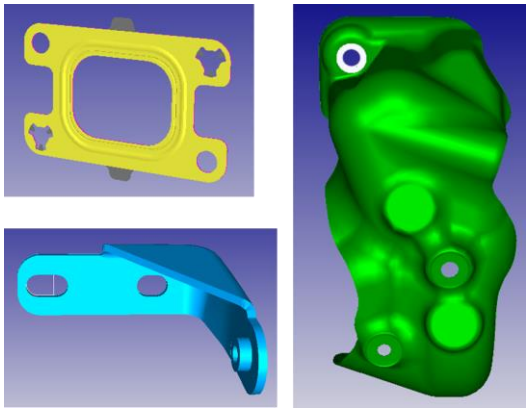

***Figure 76 - Exhaust inlet gasket, support bracket, and heat shield.***

The boost system also included high and low pressure air induction tubes, which were fabricated from aluminum for this project (Figure 77). An electric compressor recirculation valve prevents surge during throttle tip-out maneuvers. Two water-to-air charge air coolers were applied in series, with one upstream of the throttle body and a second integrated with the intake manifold.

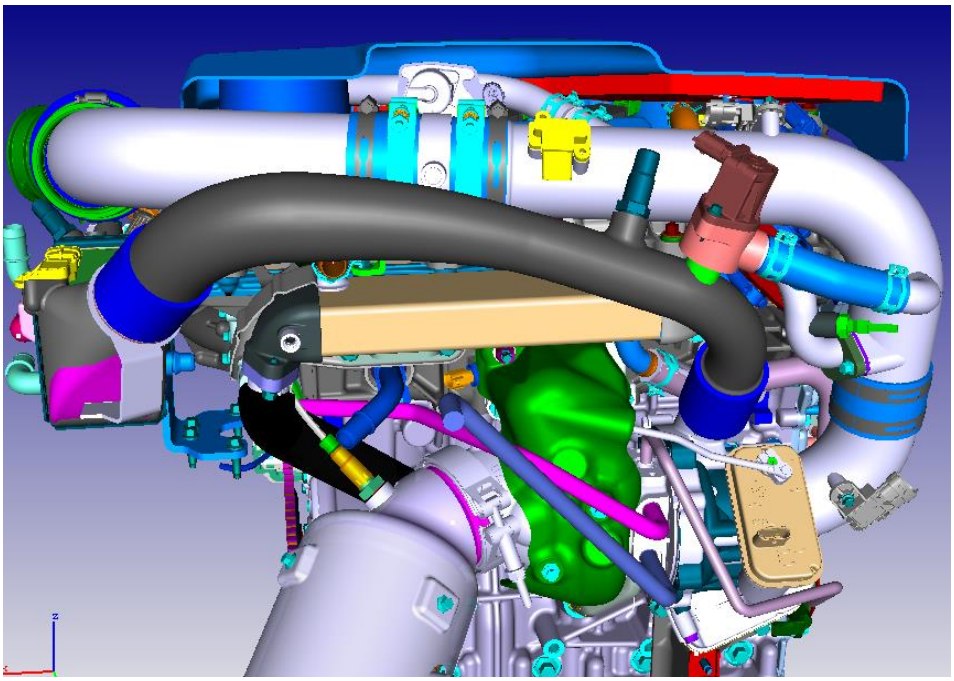

***Figure 77 - Overview of turbocharger and related air ducts.***

# Fuel System

## Design Objective

Design and develop a “Benchmark” fuel system to meet or exceed program targets for packaging, crash, cost, service, performance, and system robustness.

## Design Assumptions

- Compatible to 20MPa fuel system pressure. (PM reduction effort)
- Solenoid type multi-hole injector with stepped hole for deposit resistance
- Lower Q-stat flow rate (from 20cc to 17.5cc) for improved low pulse width performance
- Multiple injections per cycle capability – (Bosch & MM are benchmark)
- Minimum fuel mass delivered capable for micro-stratification and CSER injection – being evaluated
- Optimized targeting and reduced spray variability (Bosch & MM are benchmark)
- Reduced secondary injection or bounce via design improvements (Benchmark)

## System / Component Summary

The direct injection high pressure pump and fuel rail are shown in Figure 78. Unique features of the fuel rail are as follows:

- Three main rail bracket concept
- M8 home run bolts
- Captured high pressure line fitting and sensor housing
- Direct injector drop down tubes

A cross section of the cylinder head illustrating the direct injector location and fuel spray developed through MESIM analyses and SCE testing is shown in Figure 79.

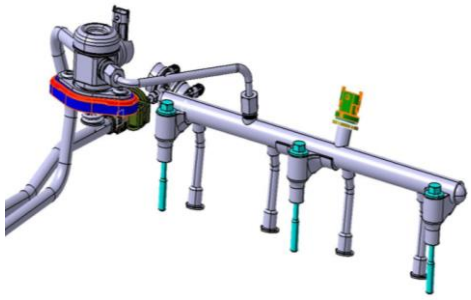

***Figure 78 - Direct injector high pressure fuel pump and fuel rail.***

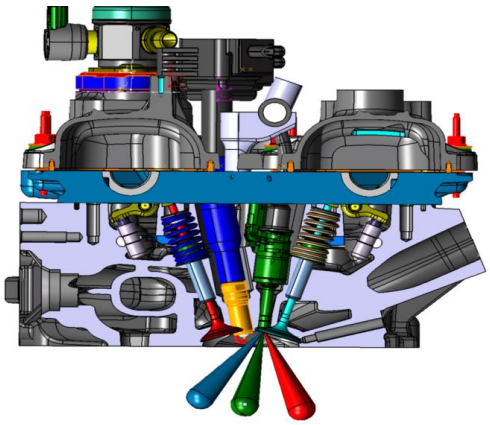

***Figure 79 - Direct injector fuel spray.***

### Design Verification Completed

The following fuel system analyses and studies were completed:

- Fuel rail modal analysis - Meets target of 600 Hz or greater for the first frequency response).
- Fuel system CAE stress analysis – Meets design targets.
- Fuel thermal distribution study – Meets design targets.
- Fuel rail pulsation study (air/ fuel distribution evaluation) – Meets design targets.
- Dyno testing completed.
- Vehicle evaluation testing completed.

## Cylinder Block

The 2.3L DOE engine assumptions included reduced friction for improved fuel economy. To achieve the engineering targets, an aluminum alloy cylinder block was designed to package within the current production 2.0L GTDI engine compartment in a CD391 (Fusion) vehicle. Key dimensions of the cylinder block are shown in Table 9.

***Table 9 - Cylinder block dimensions.***

| item | value | units |
|---|---|---|
| Cylinder Block | A380 HT T5 | HPDC Al alloy |
| Peak cylinder pressure | 125 GTDI & 100 MiGTDI | Bar (mean +3σ) |
| Bore Diameter | 87.5 (protect for 89) | mm |
| Stroke | 94 (protect for 96.5) | mm |
| Bore Spacing (Pitch) | 96 | mm |
| Deck Height | 222 | mm |
| Bore Bridge | 8.5 | mm |
| Crank Offset | 10 | mm |
| Saw cut (Bridge cooling) | 1.2 ±0.15 partial x 8 mm deep | mm |
| Open Deck Water Jacket | Target 85% ring travel | mm (split/parallel strategy) |
| PTWA cylinder bores | 4130 (8.9 mm bore wall) | Coating material type |
| MBC Ladder style w/side bolts | A380 HT T5 | HPDC Al alloy |
| Main Bearing Cap fastener | M11 x 1.5 PC 11.9 (inner) | mm (64kN proof load) |
| Cylinder Head fastener | M11 x 1.5 PC 11.9 | mm (64kN proof load) |
| Main Bearing Cap fastener | M9 x 1.25 PC 10.9 (side) | mm (38kN proof load) |
| OAL OF BLOCK | 433 (3 mm longer 2.3L c/o) | mm |

The lower end structure was targeted for powertrain friction reduction by packaging an offset crankshaft relative to the cylinder bore center for reduced piston skirt friction against the cylinder bore walls. CAE predicted 6-8% friction reduction. Powertrain bending and NVH were addressed by utilizing a cross bolted aluminum alloy ladder frame main bearing cap design to deliver best-in-class targets as compared to similar displacement in-line cylinder blocks, see Figure 80.

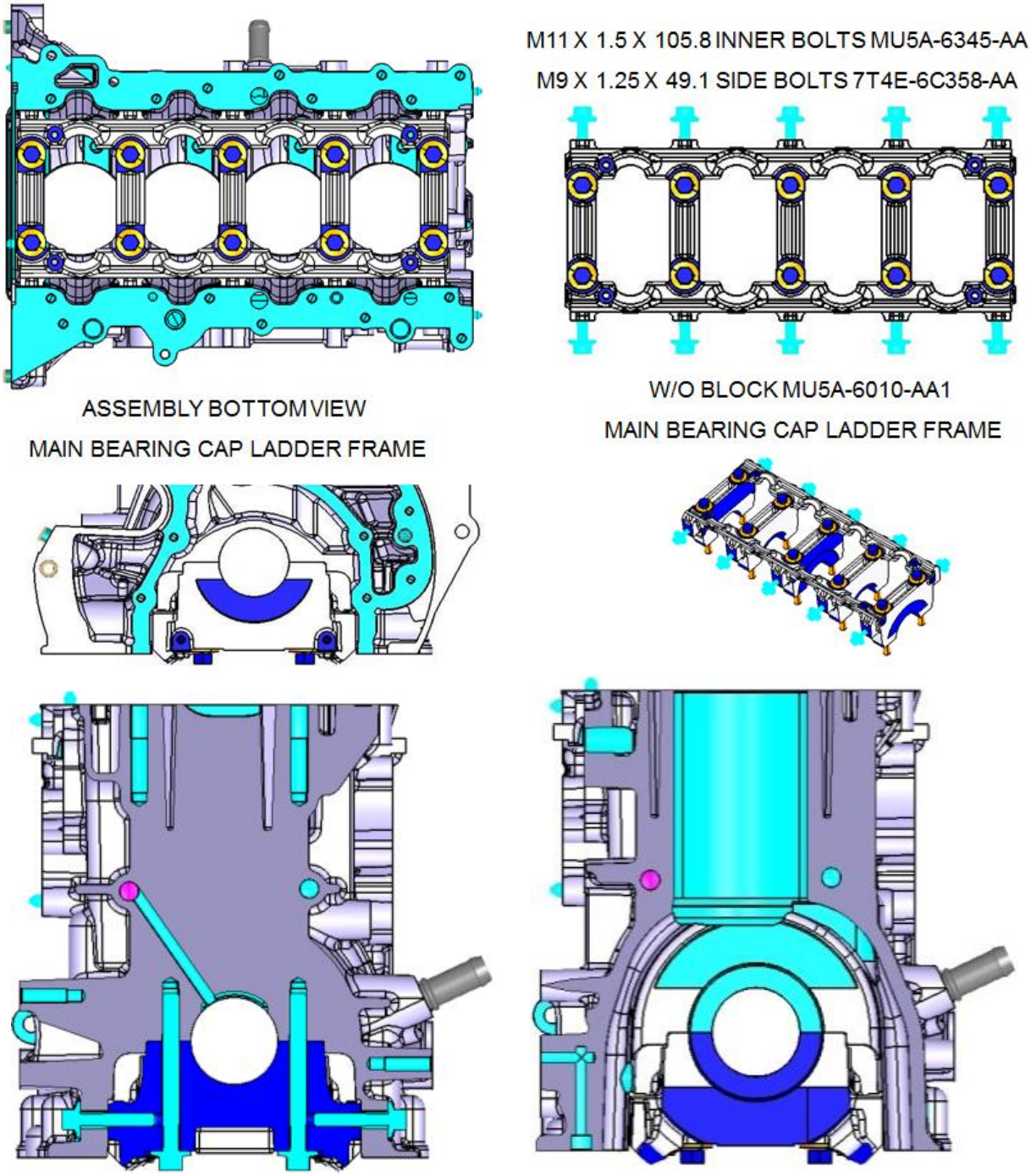


***Figure 80 - Cross bolted ladder frame main bearing caps and offset crankshaft.***

The cylinder bore configuration utilizes a partial plasma coating cylinder surface called plasma transferred wire arc (PTWA) instead of cast-in iron liners for weight reduction and improved heat transfer, see Figure 81.

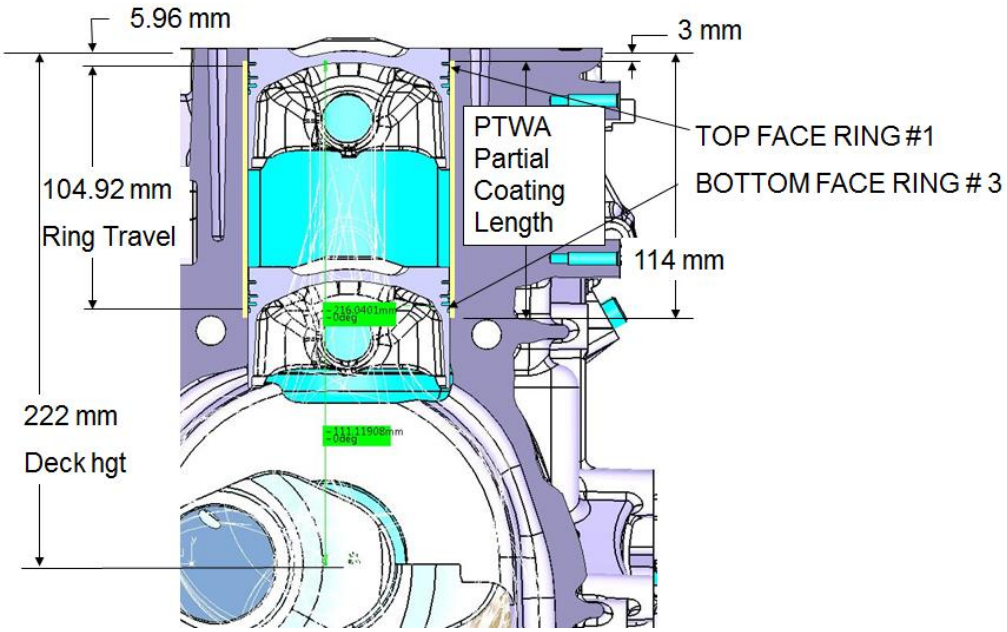


***Figure 81 - PTWA coated cylinder bore wall definition.***

A new location for the crank position sensor packaged in a low torsional distortion location found at the rear main bearing web allowing optimal signal response up to maximum engine speed, see Figure 82.

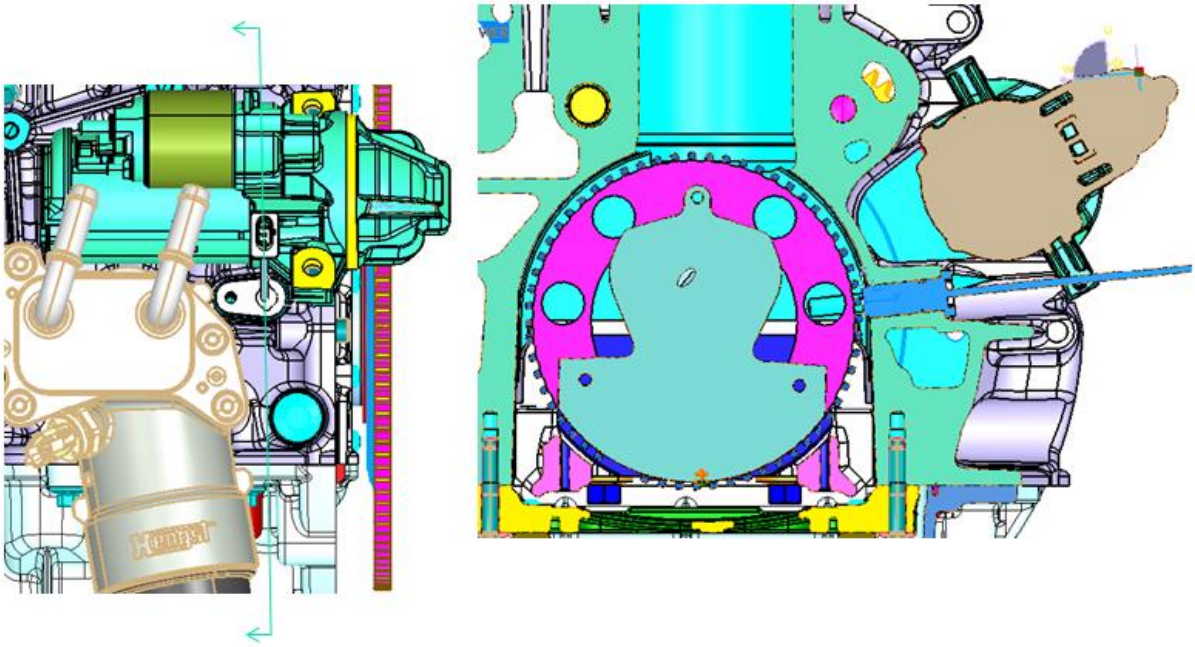

***Figure 82 - Wet crank position sensor package definition.***

The crank sensor is specifically timed to account for the offset crankshaft block design in the engine system, as shown in Figure 83.

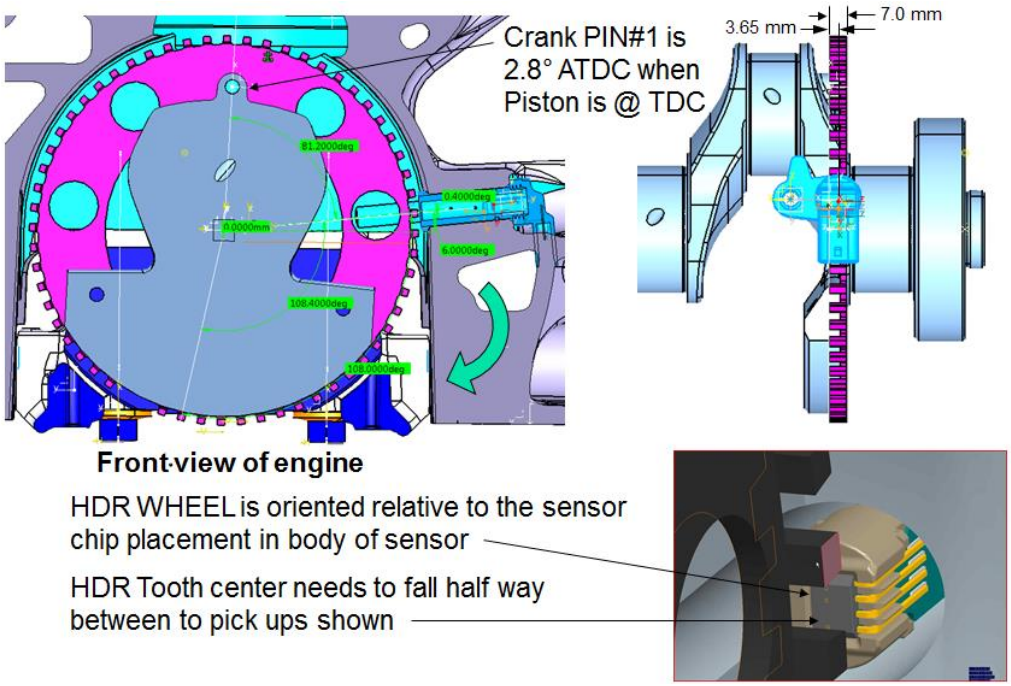


***Figure 83 - Crankshaft sensor timing for offset crank package.***

A key to optimizing thermal efficiency is to integrate a cooling circuit to allow crossflow in the cylinder head and split flow cooling between block and head. Additional features to improve heat transfer were to have an open deck water jacket with a constant flow across the inter bore bridge through a partial saw cut with coolant flowing from the block into the cylinder head lower water jacket. The coolant flow is controlled via a separate cylinder block thermostat located at the exit point that routes coolant back to the bypass housing (Figure 84).

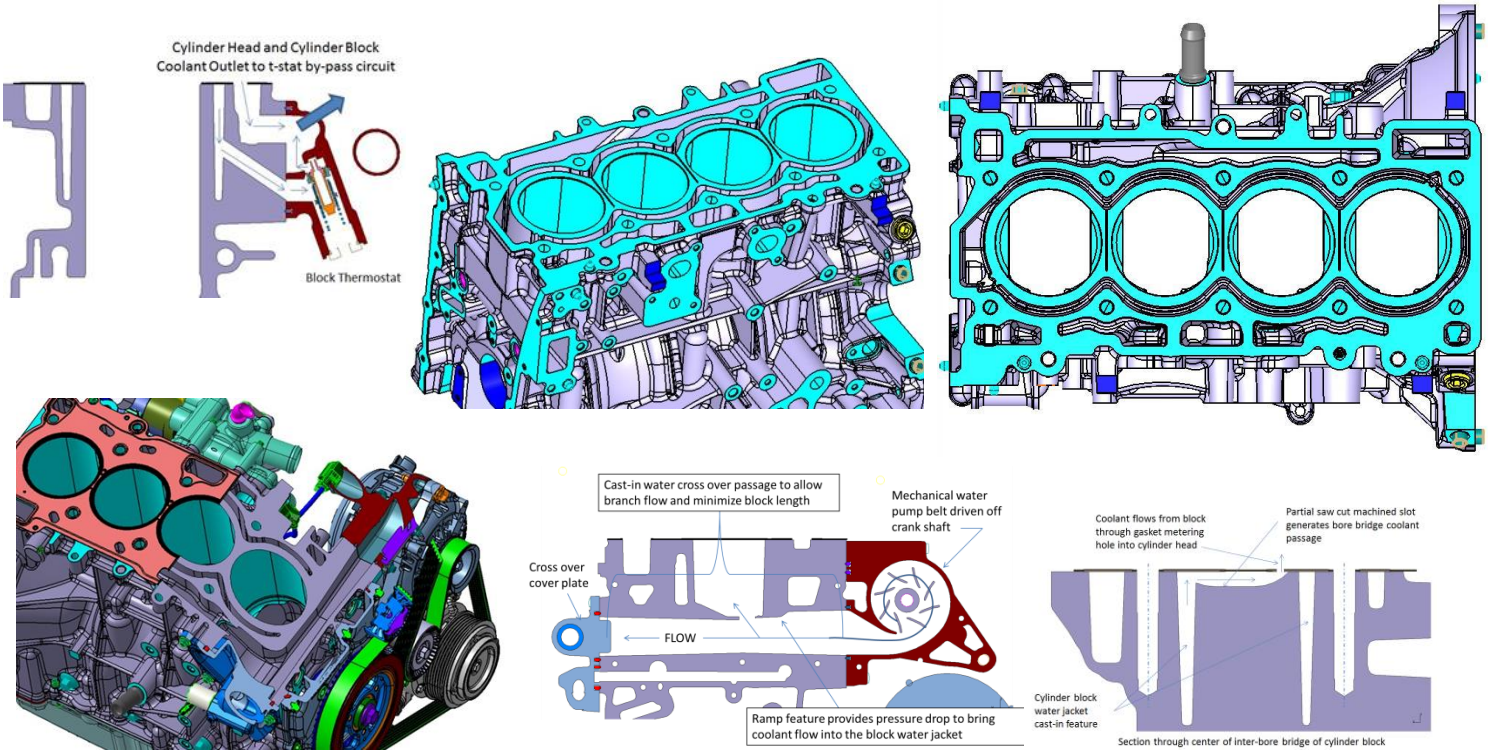


***Figure 84 - Open head deck showing cooling circuit and head oil drain features.***

Design analysis demonstrated the sensitivity of the cooling strategy and methods to overcome potential failure modes in the cylinder block. An example is the partial saw cut between cylinder bores. High cycle fatigue of the saw cut feature was affected by a delicate balance between stresses due to peak cylinder pressure and metal temperatures. The solution was found through the depth of the saw cut and a full fillet radius at the bottom to allow dissipation of the stress load concentration due to engine firing order cylinder pressures and thermal loading. The analytical walk is shown in Figure 85 through Figure 88. Crtiical load conditions were defined to help determine FF structural responses in key areas based on piston position with cylinder pressures during the combustion event. The CAE results predicted a high cycle fatigue issue in the saw cut region, yet no failures have occurred in all dyno tests to date.

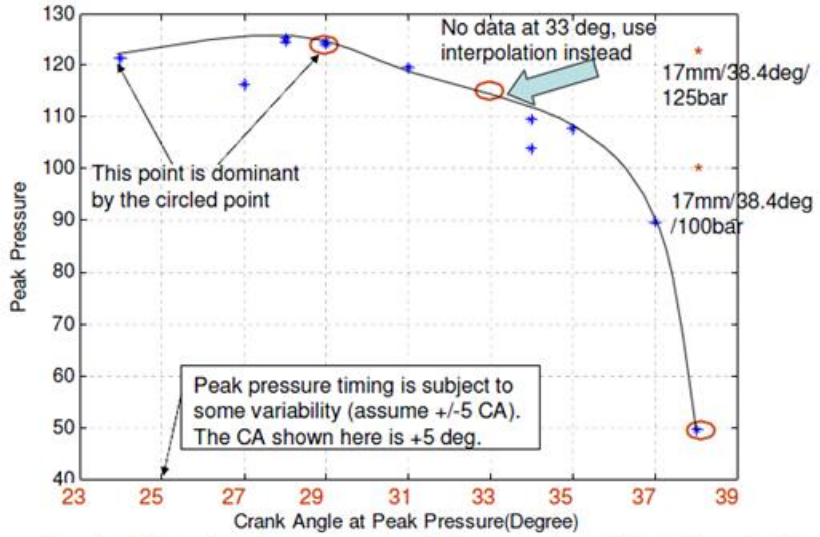


- Based on the crank angle-pressure enveloping curve shown above, three dominant critical cases (circled) are picked: 12mm/29deg/125bar, 14mm/33deg/113bar, 17mm/38.4deg/50ba
- Additionally, for sensitivity study purpose, three more cases are run: 7mm/14.5deg/125bar, 17mm/38.4deg/125bar, and 17mm/38.4deg/100bar

***Figure 85 - Critical pressure loading cases: crank angle and peak pressure.***

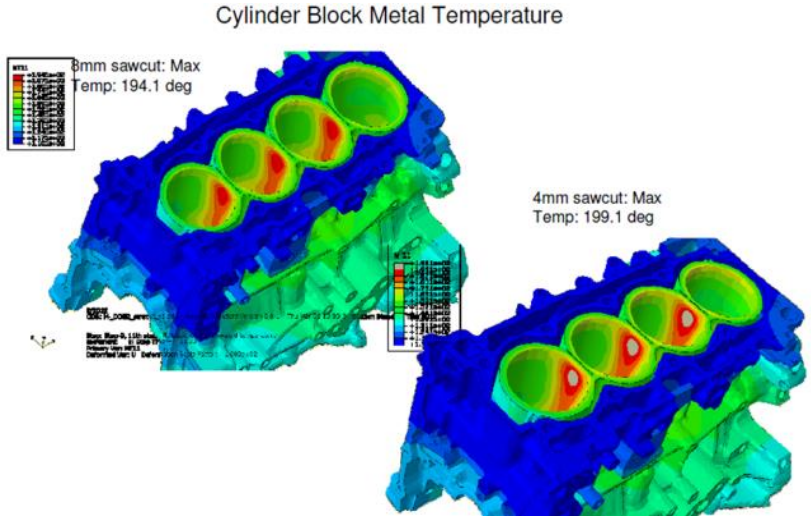


***Figure 86 - Effect of saw cut depth on predicted cylinder block metal temperatures.***

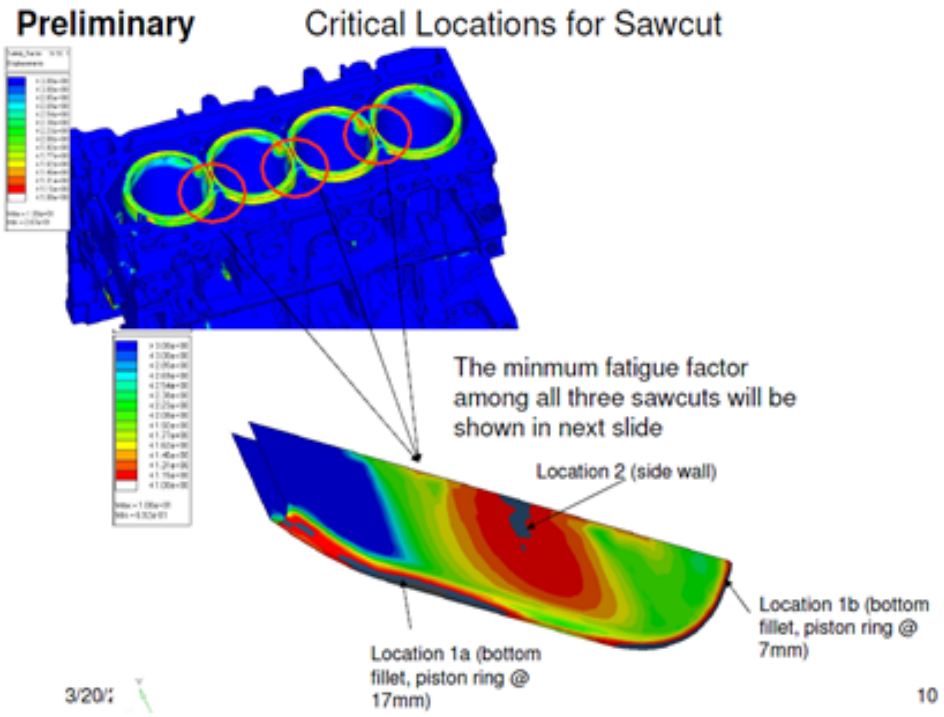


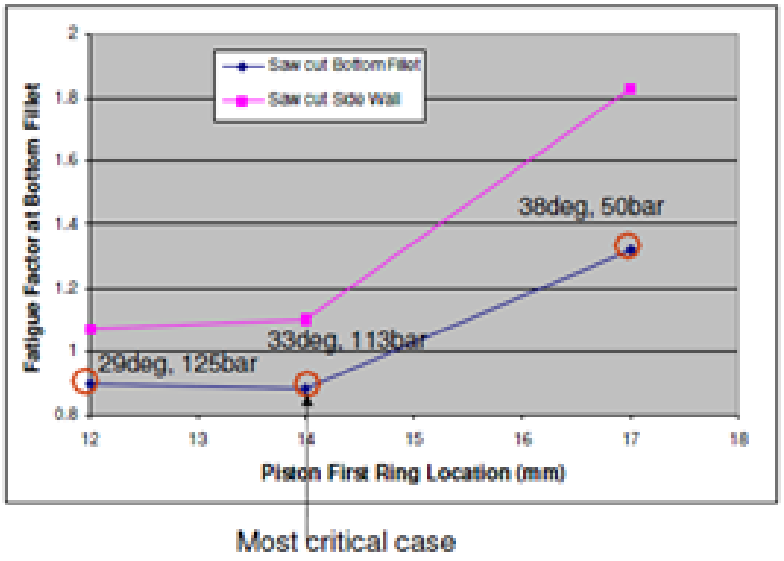


***Figure 87 - Fatigue factors for critical loading cases.***

- The fatigue factors are shown for critical loading combinations 20°/125 bar, 33°/113 bar, and 38°/50 bar. The fatigue factors for all other loading cases should be above the enveloping curve represented by the three points.

- Most critical case: 0.88 at 33° (14mm)/113 bar. This is 21% better than the original assumption, i.e., 38° (17 mm)/125 bar with FF=.073.

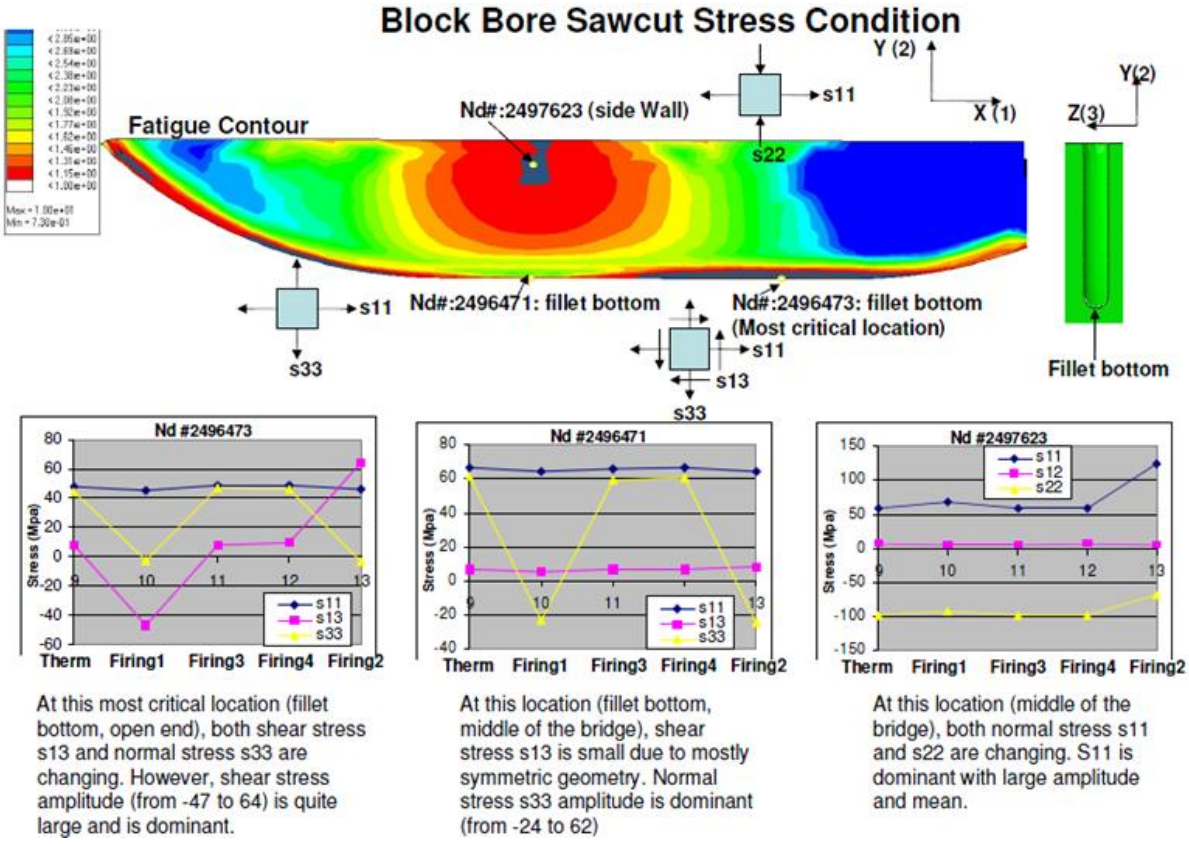


***Figure 88 - Block bore saw cut stress conditions.***

A detailed assembled bore distortion analysis was conducted and the predicted deformation matches the physical measured PAT gage data, as shown in Figure 89.

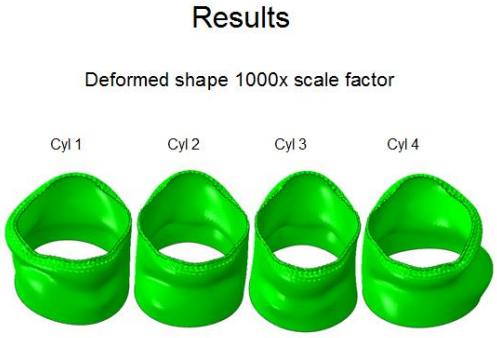


| | DOE 2.3 Max Value (um) | Location | PVS CTQs |
|---|---|---|---|
| Over All | 20.3 | Cyl 3 | |
| Cylindricity | 29 | Cyl 3,4 | |
| Roundness (Cir) | 20.1 | Cyl 3 | 50 |
| 2nd Order | 10.4 | Cyl 3 | 20 |
| 3rd Order | 2.5 | Cyl 1 | 10 |
| 4th Order | 2.7 | Cyl 1 | 8 |

All cylinder bores meet PVS CTQ's

***Figure 89 - Bore distortion analysis.***

Bulkhead analysis using the loading shown in Figure 90 as input demonstrated a concern for high cycle fatigue in the threaded region where the fatigue factor (FF) was 0.42 (Figure 91). This value is below the acceptance criteria in a GTDI combustion cycle at 125 bar (mean plus 3 sigma) peak cylinder pressure. The bulkhead was tested in the MTS fatigue fixture and passed 10 million cycles at 58 kN load with an average safety factor of 1.2 for eight samples tested, which is within engineering design guide targets.

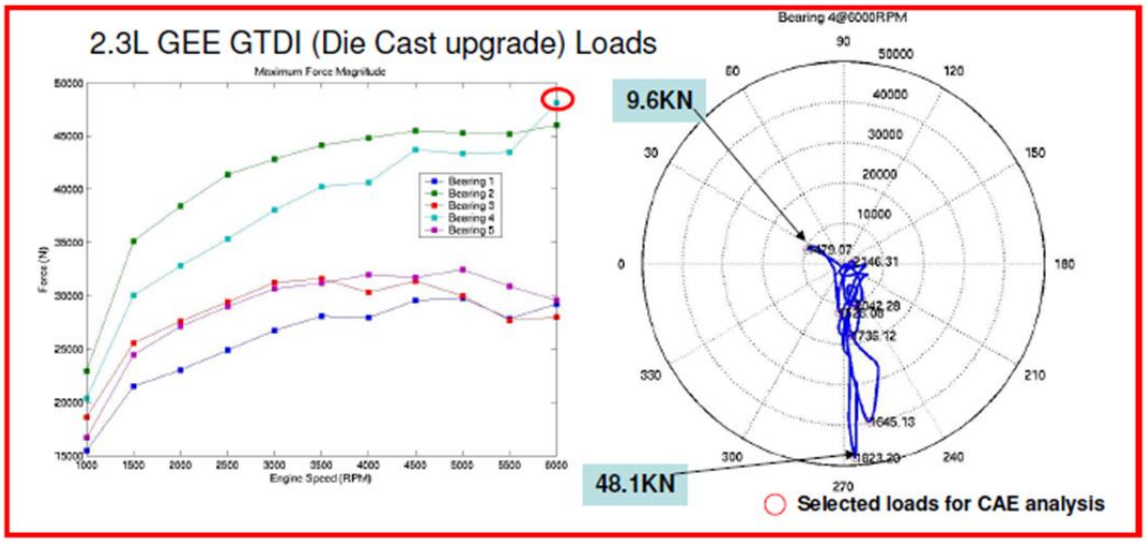


2.3L DOE GTDI Loads based on Miller Crankshaft/block (Reference only, Adapted from Mike Liu's report)

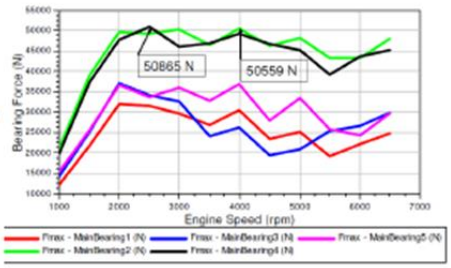


- 2.3L GEE GTDI loads are used for bulkhead analysis (120 bar peak firing pressure).
- Load on upper main bearing is not ignorable (9.6KN) and could lead to fatigue issue.



***Figure 90 - Excite loads for bulkhead analysis.***

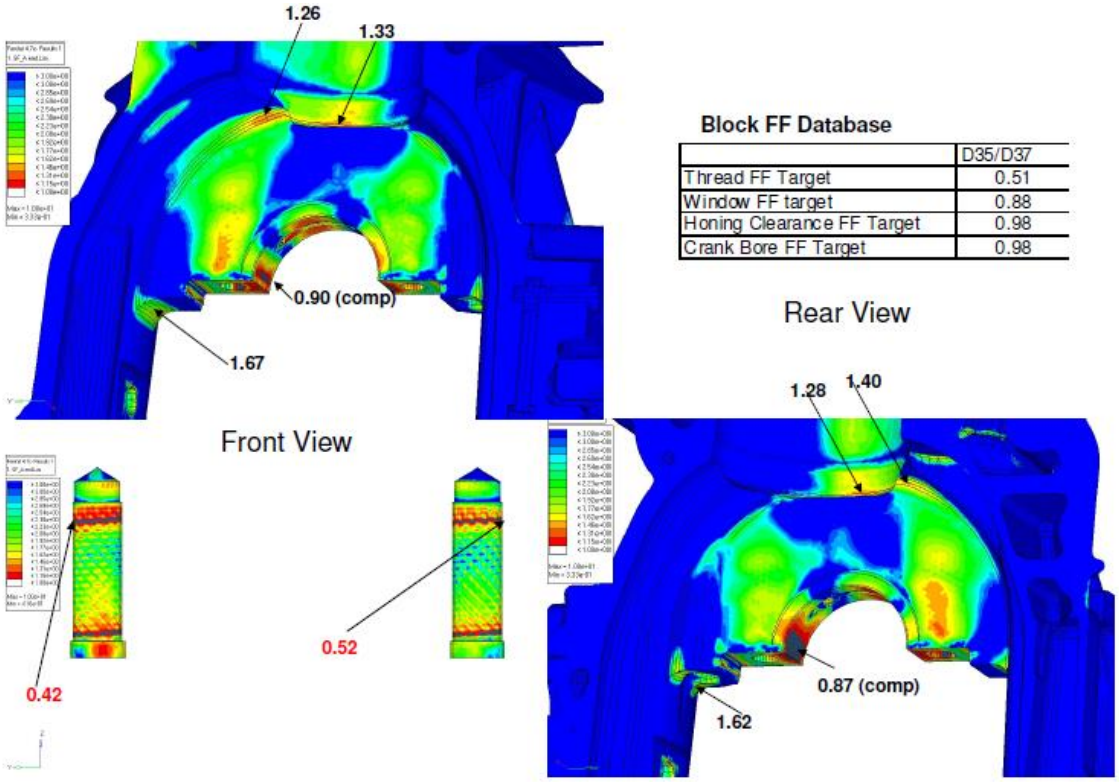


**Block FF Database**

| | D35/D37 |
|---|---|
| Thread FF Target | 0.51 |
| Window FF target | 0.88 |
| Honing Clearance FF Target | 0.98 |
| Crank Bore FF Target | 0.98 |

***Figure 91 - Fatigue factor analysis for bulkhead.***

US Patented technologies delivered a switched piston oil jet cooling system using a single solenoid valve to control oil flow to the piston oil jets mounted to the roof of the crank case for optimal trajectory targeting the underside of the piston crown center. The device also acts as a cylinder head coolant flow crossover cover plate on the left side of the block, see Figure 92.

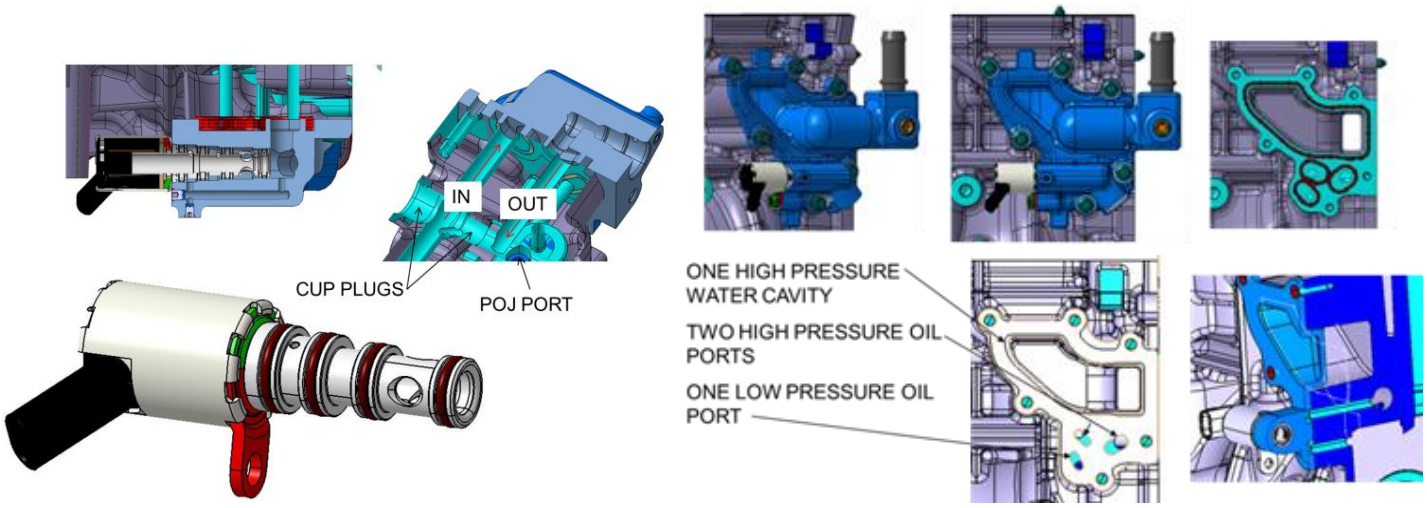


***Figure 92 - Piston oil jet flow control and block packaging.***

Views of the final cylinder block design are shown in Figure 93.

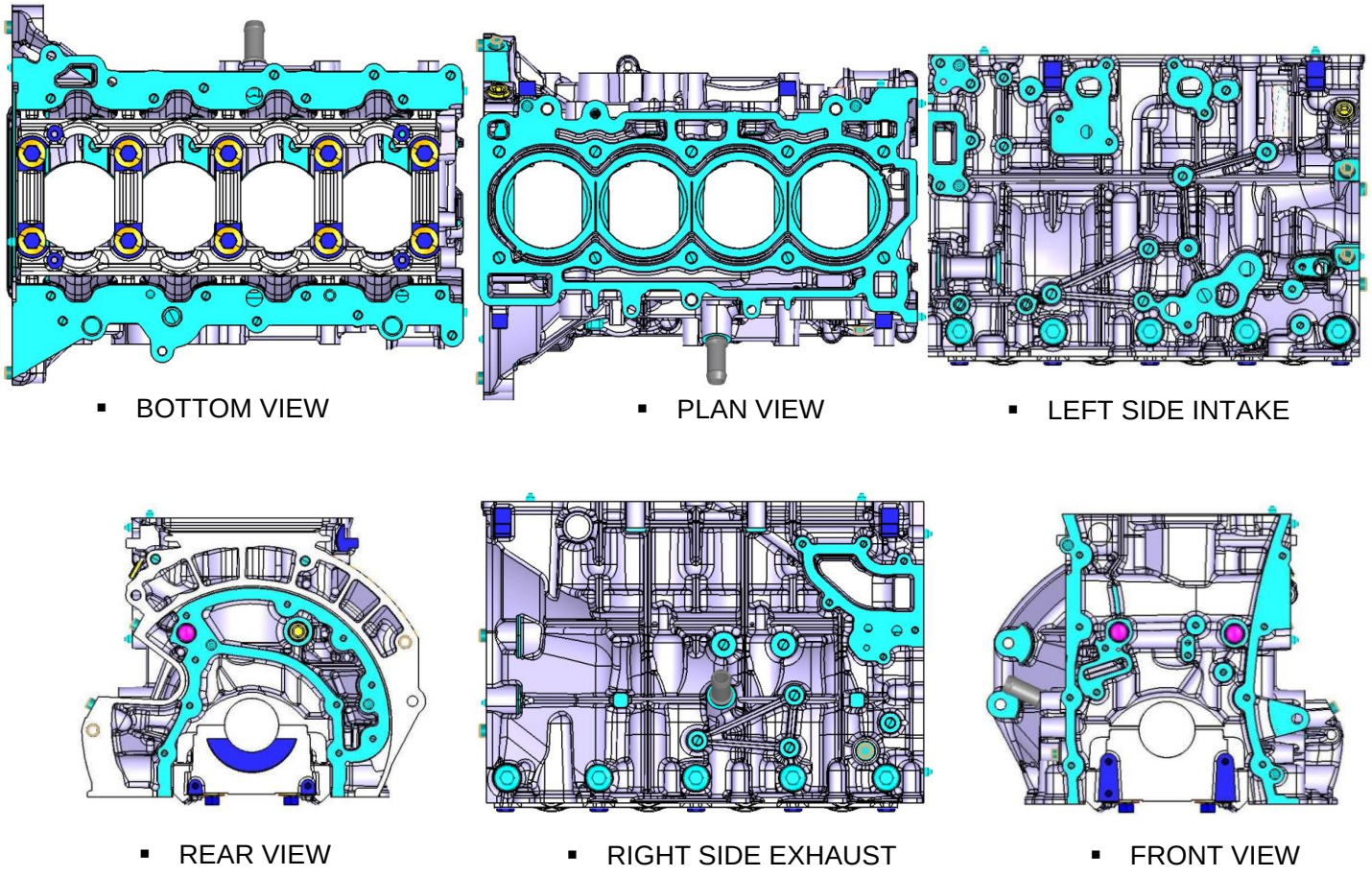

- BOTTOM VIEW
- PLAN VIEW
- LEFT SIDE INTAKE
- REAR VIEW
- RIGHT SIDE EXHAUST
- FRONT VIEW

***Figure 93 - Cylinder block views.***

## Oil Pump and Balance Shaft

The 2.3L engine has a vertical shaking force of 7,865 N at 5000 RPM due to the inherent 2nd order imbalance created by the reciprocating weight in an I4 engine. This value of shaking force is over the Ford target, and hence the engine requires either a balance shaft or active engine mounts. The balance shaft is discussed in this section, however, in the vehicle the counterweights of the balance shaft are machined off and active engine mounts are used instead.

The balancing mechanism in this I4 engine requires two shafts counter-rotating at twice engine speed with an imbalance of 3.6 kg mm each. The balance shafts are integrated with a two stage vane oil pump and bolted to the oil pan rail of the block as shown in Figure 94. The aluminum housing of the integrated balance shaft module and oil pump (BSM-OP) ties together the block side walls to improve the engine stiffness and NVH. The balance shaft is supplied by Metaldyne, the oil pump by Stackpole, and the chain drive by Borg Warner. The bottom view in Figure 95 shows the mounting locations to the block.

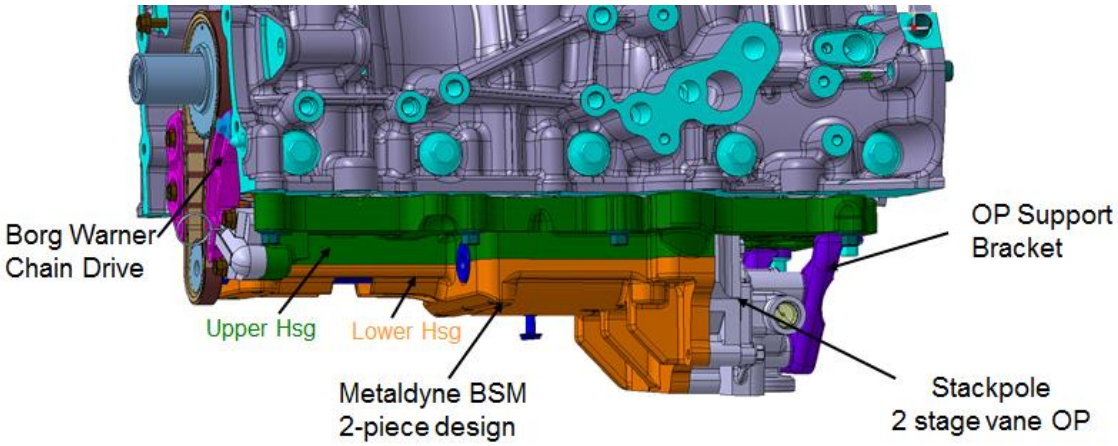


***Figure 94 - BSM-OP (integrated balance shaft module and oil pump) side view.***

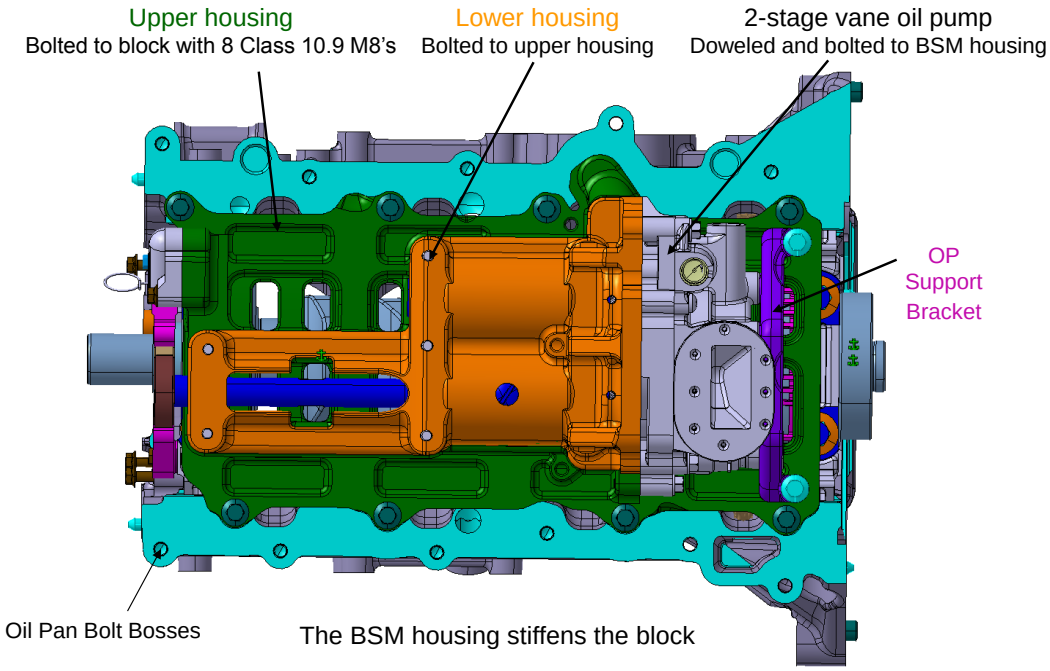


***Figure 95 - BSM-OP bottom view.***

Figure 96 shows the chain drive for the BSM-OP. The BSM-OP is driven at twice engine speed by a T107 4x4 silent chain from Borg Warner. In order to survive the high dynamics of the chain drive, a piston tensioner with a high flow pressure reactive vent (PRV) is required.

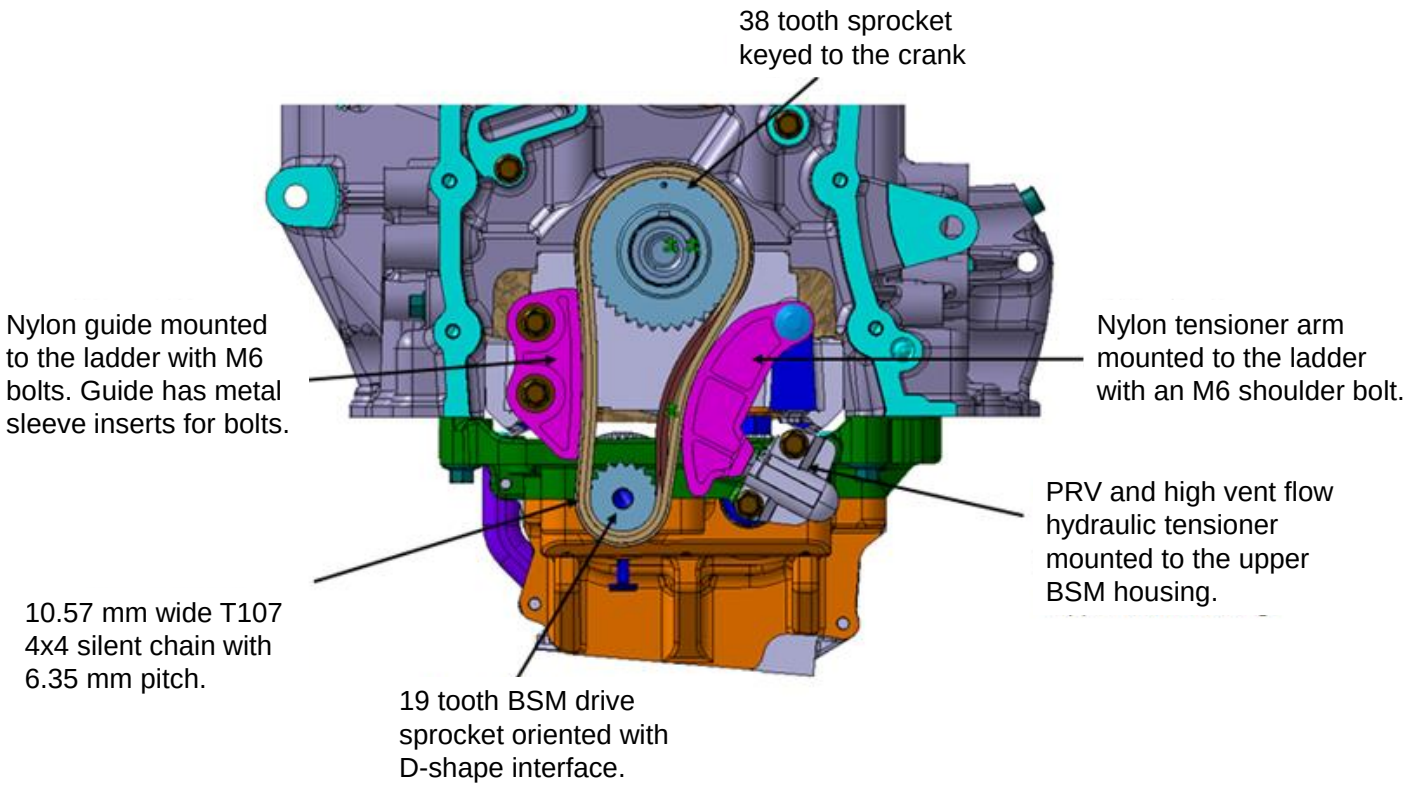


***Figure 96 - BSM-OP chain drive.***

The layout of the balance shaft and gear train is shown in Figure 97. The oil pump runs at engine speed with a step down gear set off the driven shaft. Running the oil pump off the driven shaft gives the driven shaft some resistance to prevent gear rattle.

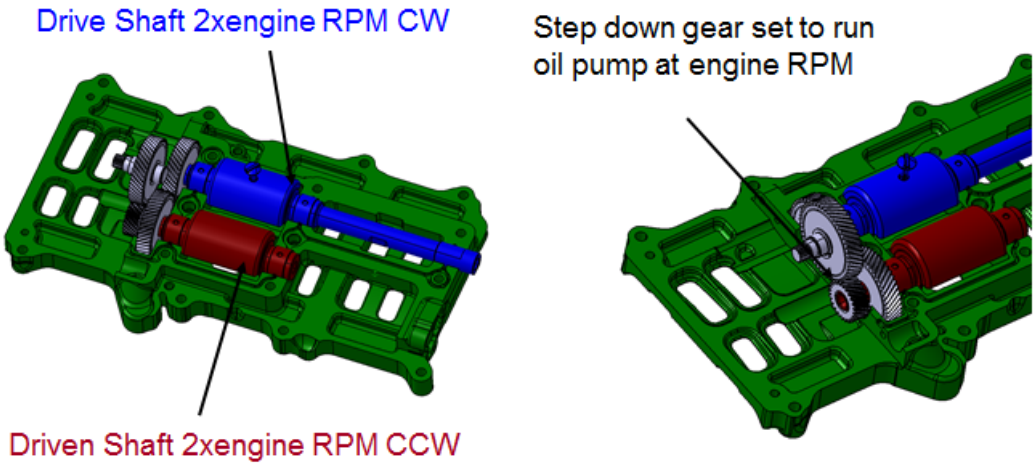


***Figure 97 - BSM-OP drive and gear train.***

The oil pump intake and discharge are shown in Figure 98. The oil pump stays in the high pressure mode by default. To switch to low oil pressure chamber #4 is filled with oil to change the volute position for low flow.

Oil Intake and Discharge

1. Oil is pulled through the oil pick up and into the vane oil pump.
2. Oil is pumped through the vane oil pump at low or high pressure.
3. Oil flows through the BSM housing to a pad on the oil pan rail.
4. The solenoid is activated and oil fills the chamber to force the volute to move to turn the oil pump to low pressure.

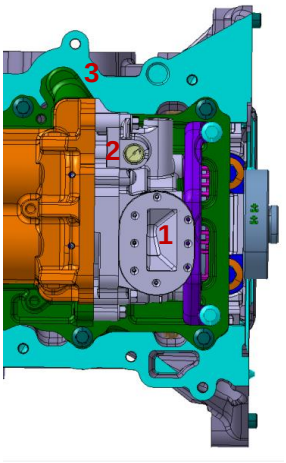


2 stage vane pump

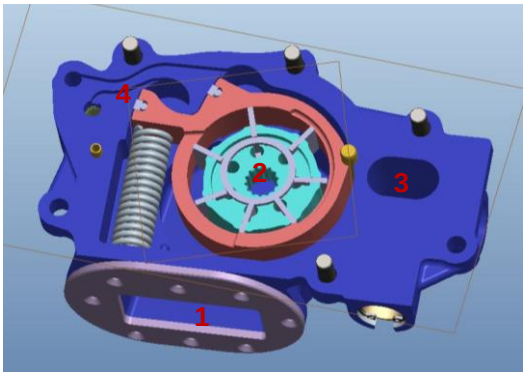


The spring forces the volute to the location where the OP discharges high oil pressure (default).

***Figure 98 - Oil pump intake and discharge.***

As shown in Figure 99, oil is discharged to the block oil pan rail through a pad on the BSM-OP housing. This pad also receives clean oil to feed the journals and tensioner. The oil is also used to fill the oil chamber #4 in Figure 98 if the solenoid is energized. This brings the oil pump to the low pressure state. Less energy is needed to turn the oil pump in the low pressure state, thereby improving the efficiency of the system.

Clean oil feeding up through the same pad on the oil pan rail has three purposes:

1. Lubricate the journals. All parts have standard journal bearings except two needle bearing units for testing. The front journal remains a standard journal bearing for clearance to the RWD oil pan.
2. Feed the tensioner.
3. Switch the OP from high to low pressure – dedicated oil line.
   a. When the solenoid is activated, it allows oil to turn the volute for low oil pressure.
   b. When the solenoid is not activated the volute goes to the default high oil pressure position.

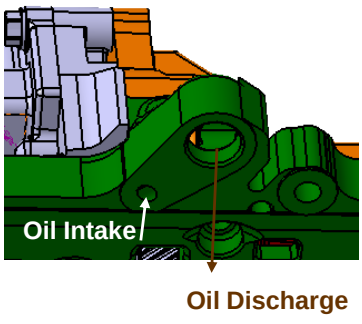


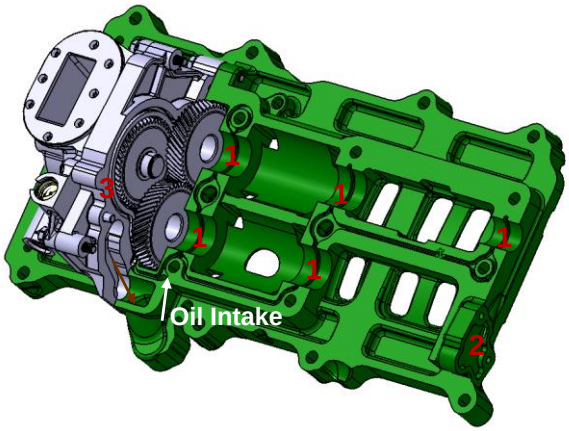


***Figure 99 - Oil intake for lubrication, tensioner, and oil pump switching.***

The solenoid used to control switching from low to high oil pressure is shown in Figure 100. The wire is schematically shown. It has a connector with an O-ring that is pushed through the block.

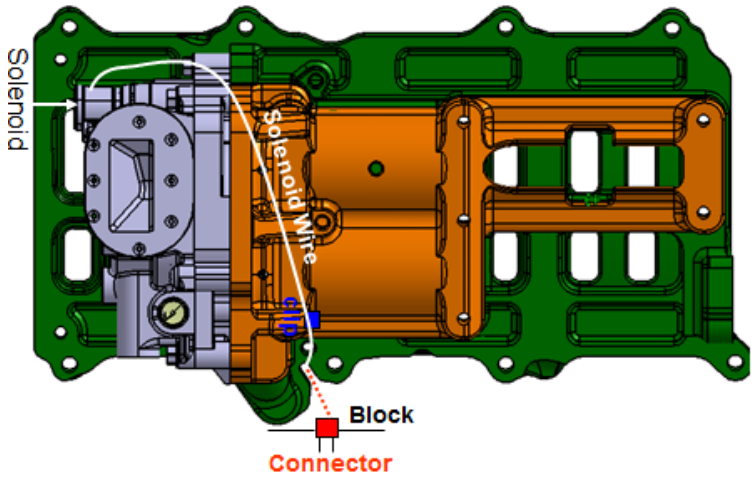


***Figure 100 - Oil pump solenoid and connector.***

## Piston, Piston Rings, and Connecting Rod

The design of the power cylinder assembly was driven largely by the expected peak cylinder pressures of approximately 100 bar, and by the peak rpm and lowest rpm at peak cylinder pressure. Considerable benchmarking was performed to help validate the design directions for the various components.

### Piston Design

A K-factor is used to normalize a piston weight regardless of bore size. It is a good method to assess design efficiencies and weights when comparing engines of similar cylinder pressure capability. Typical K-factors and benchmarking are shown in Figure 101. An aggressive 0.47 K factor was chosen as the design target, more similar to a performance oriented naturally aspirated application.

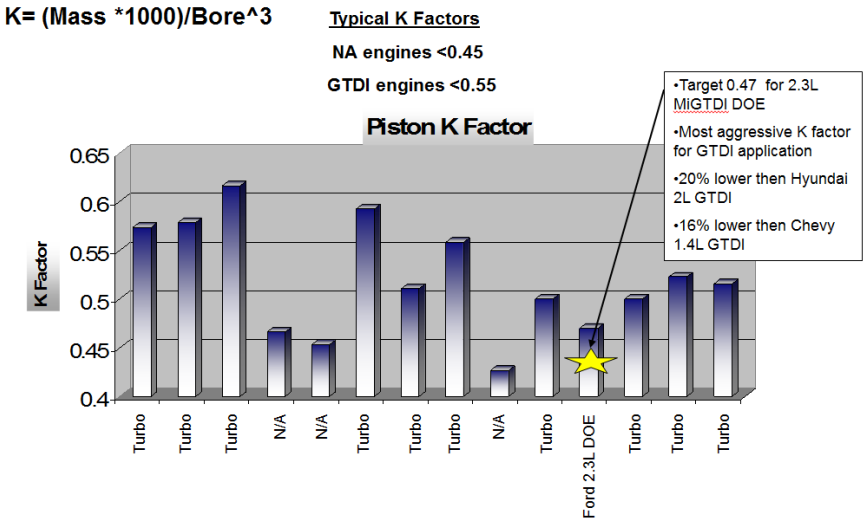


***Figure 101 - Benchmarking of piston K factors.***

Working with KUS as the supplier, multiple CAE analyses were performed to optimize the design geometry. First, a 3D temperature prediction model was generated as shown in Figure 102. As can be seen, the highest

temperatures are in the crown area. These elevated temperatures affect the fatigue strength capabilities of the aluminum and must be taken into account in the fatigue analysis. Fatigue safety factors were calculated through multiple design iterations until meeting all criteria for 500 hours at 100 bar cylinder pressures at 4000 and 6350 RPM. Results are shown in Figure 103.

Contact pressures as well as pressure profiles were also calculated for the piston pin bores and piston skirts. Results are shown in Figure 104. Piston pin bore analysis is critical for avoiding pin bore scuffing or crack initiation that would lead to piston failures. Piston skirts are analyzed to avoid cylinder bore wall scuffing from localized high contact pressures, as well as reducing NVH from excessive piston secondary motion. It is important to balance the NVH characteristics of the skirt shape with piston clearance and oil film development for the lowest possible friction to improve fuel economy.

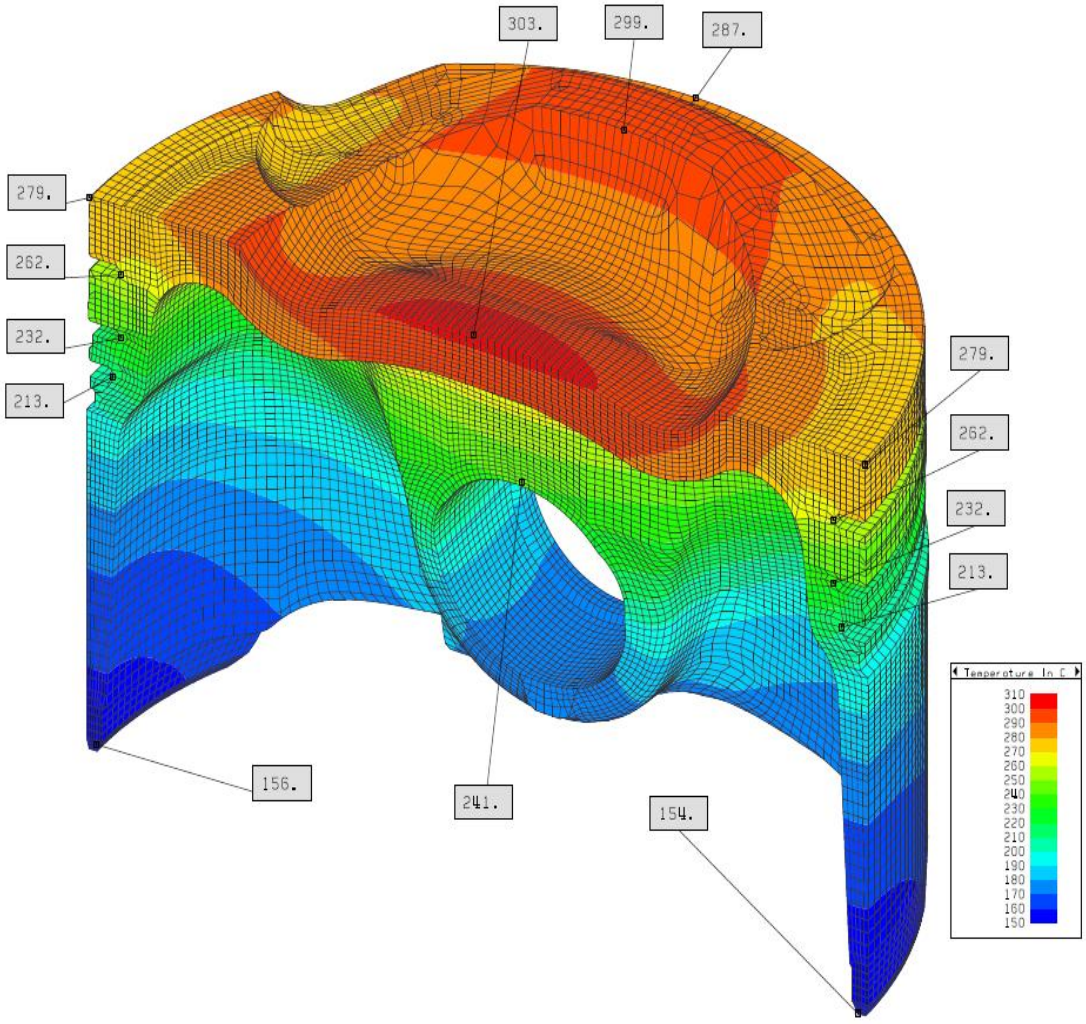


***Figure 102 - Calculated piston temperatures.***

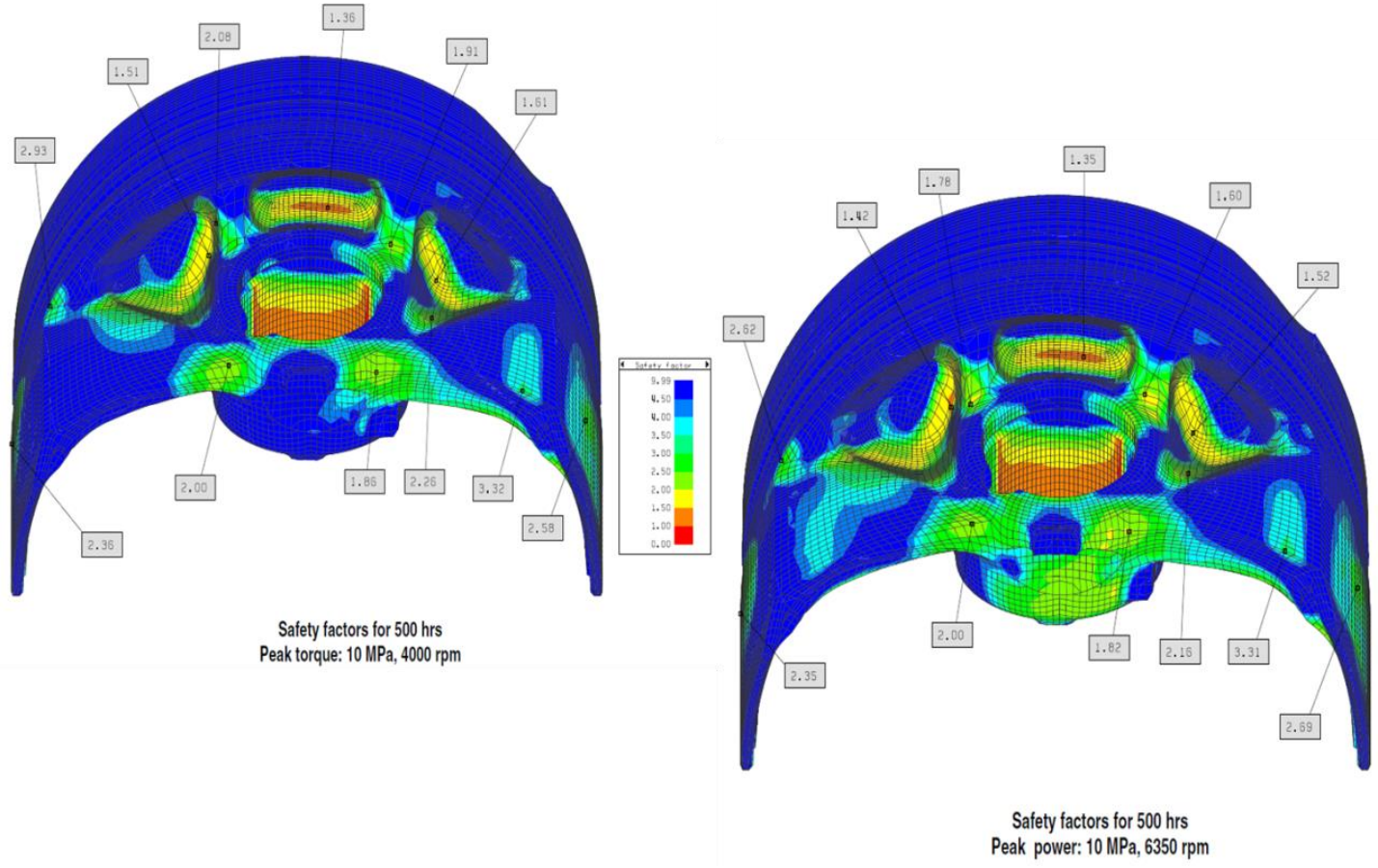


***Figure 103 - Calculated piston fatigue safety factors.***

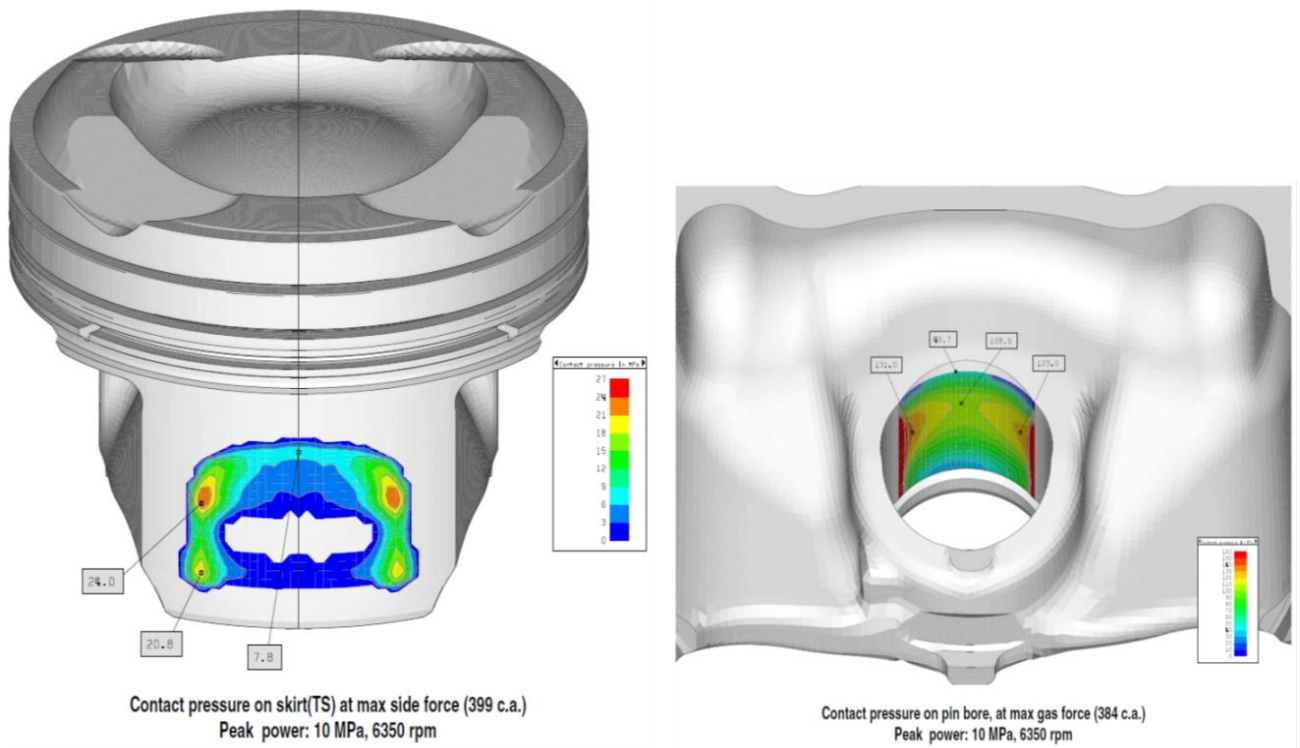


***Figure 104 - Analysis of piston skirt and pin boss contact pressures.***

## Ring Design

Special attention was given to the ring pack design and ring tensions as these details can have a significant effect on power cylinder friction. As shown in Figure 105, the 2.3L ring pack tensions are below all of the vertical benchmarked values. The final tension was chosen well below Hyundai's 2.0L GTDI but not as aggressive at the N/A 1.2L Hyundai or hybrid Toyota Prius (horizontal dashed lines). Inadequate ring tensions can result in increased blowby and oil consumption.

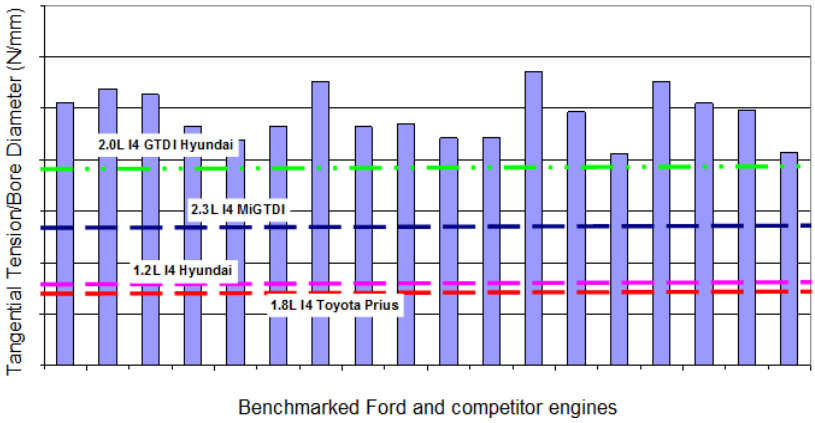


***Figure 105 - Ring tension benchmarking.***

## Rod Design

The connecting rod design is relatively conventional, but weight reduction was a high priority. The shank area calculations are shown in Table 10. The production intent material and the prototype billet 4340 steel are tracked to ensure that they meet both the yield safety factor for buckling and the fatigue safety factor. Multiple conditions are calculated to ensure capturing the worst case. The fatigue safety factor of the entire rod is calculated using CAE as final confirmation. The reduced cross section of the DOE connecting rod can be seen in comparison to the carryover 2.3L GTDI design in Figure 106.

**DOE MiGTDI 2.3L**
**Shank Stress Cyl Pressure Sweep Results**

| Assumptions: | |
|---|---|
| Displacement | 2.3L |
| Cyl Bore - | 87.5 mm |
| Pin Offset- | 0.5 mm |
| Stroke | 94 mm |
| Rod Length- | 145.10 mm |

| Rod Parameters | Dimension (mm) |
|---|---|
| Length | 145.10 |
| WST | 15.00 |
| WSB | 15.00 |
| TST | 12.00 |
| TWT | 2.50 |
| TFT | 3.75 |

| PM-HS170 | | |
|---|---|---|
| Tensile | Compressive | Fatigue |
| 1060 N/mm^2 | 810 N/mm^2 | 357 N/mm^2 |

| 4340 Steel | | |
|---|---|---|
| Tensile | Compressive | Fatigue |
| 965 N/mm^2 | 855 N/mm^2 | 386N/mm^2 |

| Eng Speed (RPM) | Peak Pressure(bar) | Peak Pressure(psi) | PM-HS170 | | 4340 Steel | |
|---|---|---|---|---|---|---|
| | | | YSF | FSF | YSF | FSF |
| 1000 | 38.17 | 553 | | | | |
| 1501 | 76 | 1102 | 1.33 | 2.36 | | |
| 1501 | 100 | 1450 | 1.01 | 1.88 | 1.07 | 2.00 |
| 2000 | 95.99 | 1392 | 1.06 | 1.92 | | |
| 2500 | 95.92 | 1391 | 1.08 | 1.90 | | |
| 3000 | 100.39 | 1456 | 1.04 | 1.81 | 1.10 | 2.00 |
| 3500 | 82.93 | 1203 | 1.30 | 2.08 | | |
| 4000 | 95.46 | 1385 | 1.14 | 1.82 | | |
| 4500 | 84.38 | 1224 | 1.34 | 1.97 | | |
| 5000 | 91.97 | 1333 | 1.25 | 1.80 | | |
| 5500 | 79.95 | 1160 | 1.53 | 1.95 | | |
| 6000 | 89.56 | 1299 | 1.39 | 1.74 | | |
| 6500 | 93.39 | 1355 | 1.37 | 1.64 | | |

***Table 10 - Rod analysis for bulking and fatigue safety factor.***

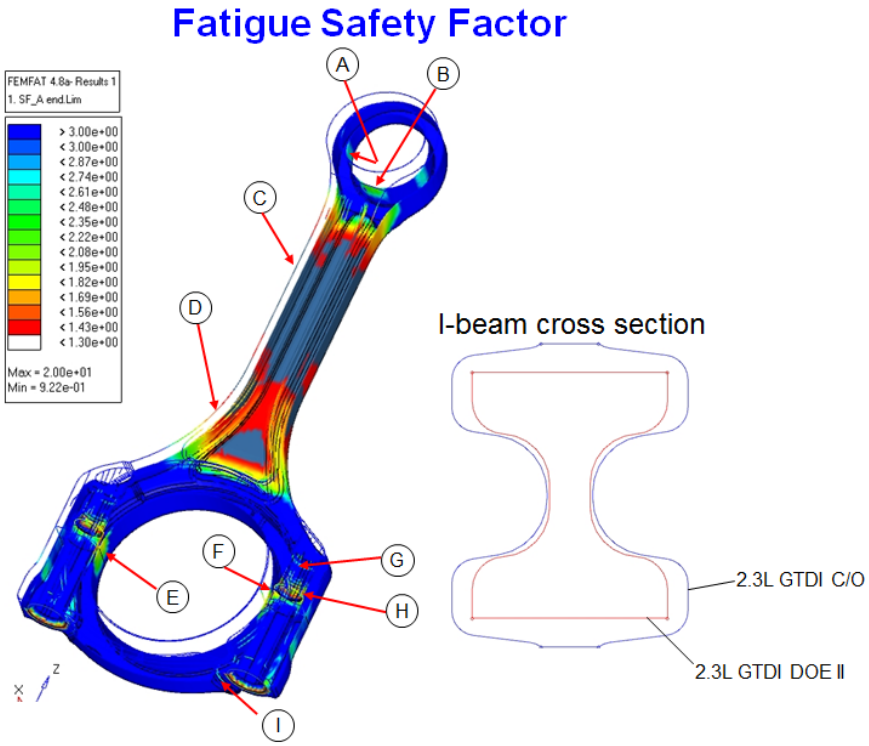


***Figure 106 - CAE analysis of rod fatigue safety factors.***

The small end of the rod is analyzed for piston pin bushing pressures and pin bending to avoid edge loading in the bushing. The top side is tapered to reduce mass as the inertia loads from the piston on the bushing at high engine speeds are lower than the compressive loads.

The large end is analyzed for the required fastener size and proper clamp load to avoid any loss of contact at the joint face which may result in fretting, see Figure 107. The connecting rods are heat treated and hardened to allow for cracking of the joint for a fracture split surface.

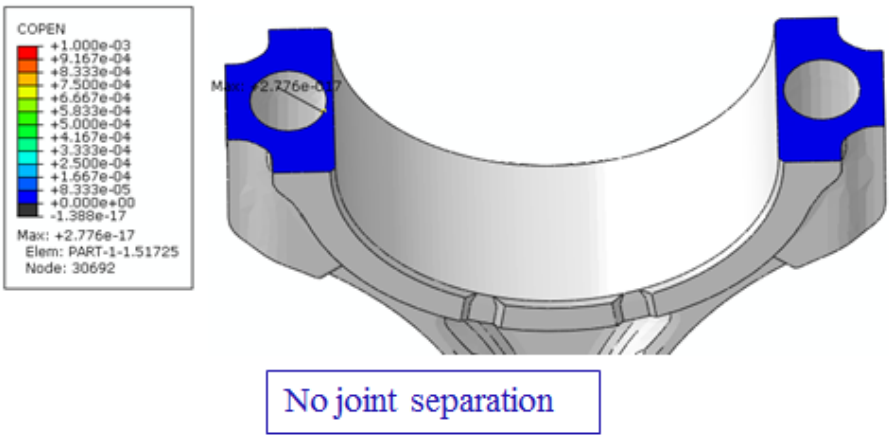


***Figure 107 - Analysis of joint face separation.***

Finally, the bore distortion of the big end was analyzed in CAE for all relevant conditions. Close attention is paid to the geometry after bearing assembly and bearing “crush” for optimal roundness and bearing clearance. Next, various loading conditions are analyzed, such as max pull, max compression and whipping of the rod due to its own inertia, see Figure 108.

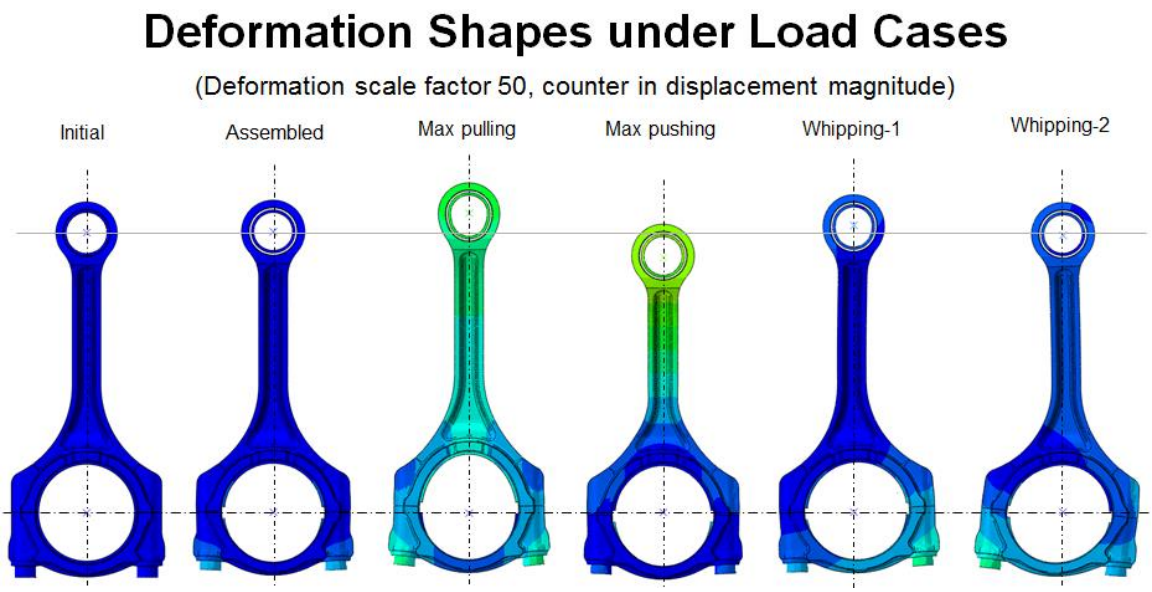


***Figure 108 - Analysis of big end bore distortion.***

## Lubrication System

The lubrication system for the 2.3L DOE engine was designed for the engine speed range of 650 rpm to 6500 rpm and for a maximum oil temperature of 140 °C. Under these engine operating conditions, the lubrication system needs to meet all sub-system performance requirements. A schematic of the lubrication system is shown in Figure 109. Two variable technologies were incorporated in the system:

1. A two stage active variable flow oil pump which provides both low and high engine oil pressure modes. This allows the oil supply pressure to be tuned for the specific engine oil flow requirements. Adjusting the oil pump flow output such that the supply pressure meets the lubrication system needs reduces the parasitic load on the crankshaft and provides a fuel economy benefit.
2. Solenoid controlled piston cooling jets whereby the jets can be turned on or off based on the engine requirements. Typically these jets are passively managed with oil pressure. The opening / flowing oil pressure threshold is set such that it is low enough to open with hot engine oil pressures across the engine speed range. This, however, means that the jets are open during cold starts when piston cooling is not necessary. If the jets can be switched off during cold starts, the piston and exhaust gas heat up more quickly, improving heat transfer to the catalyst.

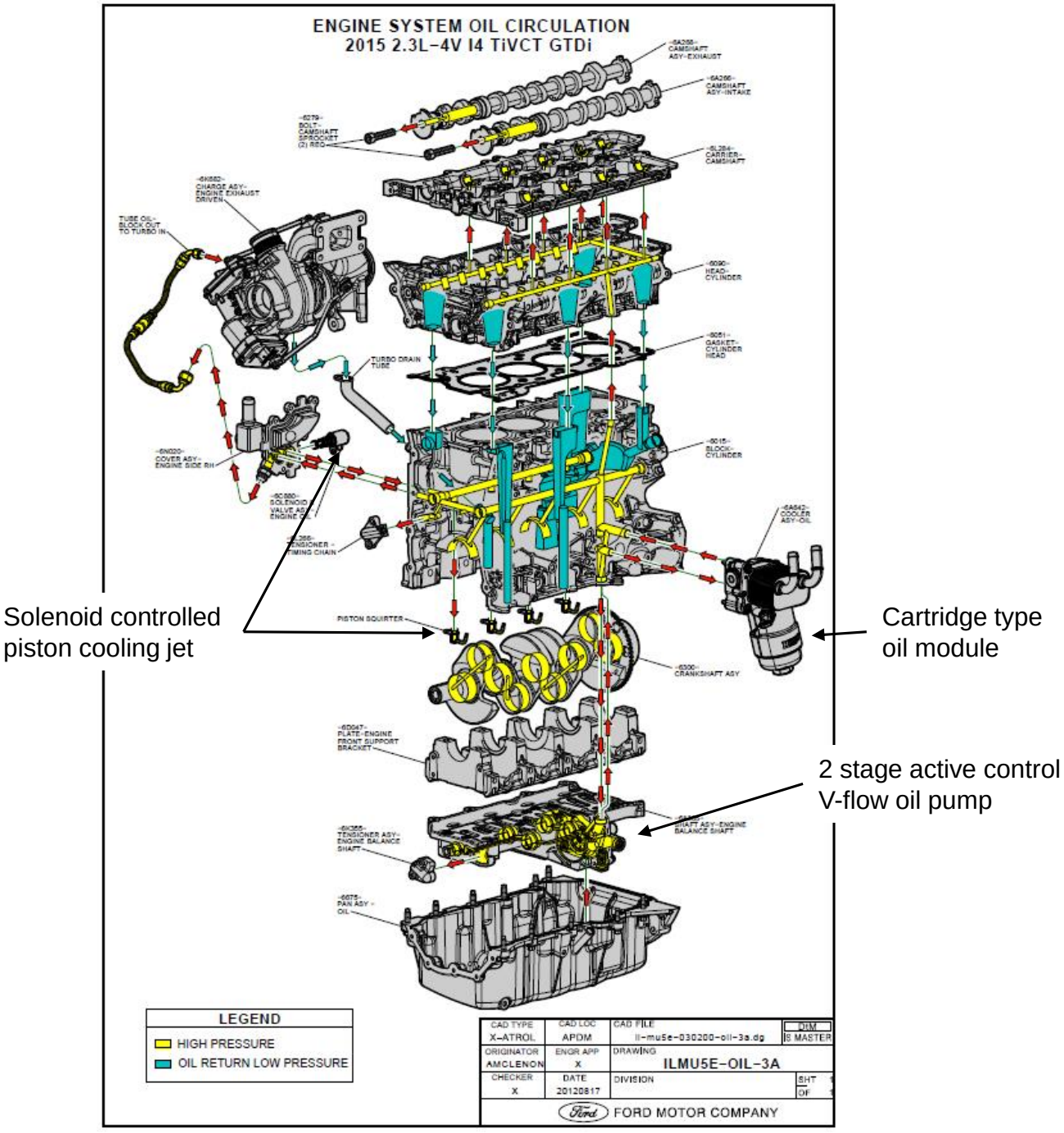


***Figure 109 - Lubrication system schematic.***

Benchmarking was performed on piston cooling jet and oil module designs comparing the performance, package, and cost. The piston cooling jet comparison is displayed in Table 11. Based on this comparison, the solenoid controlled piston cooling jet was chosen for the 2.3L DOE engine.

Based on the oil module performance comparison shown in Figure 110, the cartridge type oil module showed much lower pressure drop which could result in a smaller oil pump that potentially leads to fuel economy improvement. For this reason the cartridge type oil module was chosen for the 2.3L DOE engine.

## *Table 11 - Piston cooling jet benchmarking.*

| Piston Cooling Jet Design and Cost Bench Marking | | | | | | | | |
|---|---|---|---|---|---|---|---|---|
| | Bent Tube Cooling Jet Design | | | | | Bulk Head Piston Squirter Design | | |
| **Supplier** | A | | | | B | A | | C |
| | Tube only plus | Solenoid valve | Tube with ball mechanism | Tube with piston mechanism | Tube with ball mechanism | Ball mechanism | Piston mechanism | Ball mechanism |
| Design |  |  | |  | | |  | |
| Cross Section | | |  | 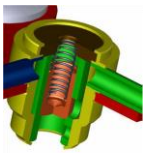 |  | 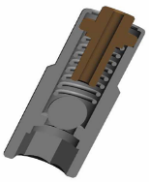 | 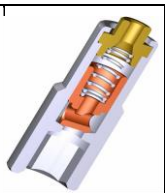 |  |
| Performance | Should be better than tube jet with piston mechanism | | N/A | See performance curve | See performance curve | See performance curve | See performance curve | See performance curve |
| Hysteresis | Hysteresis for this design can be eliminated | | N/A | 5psi | 3psi | 17 psi | 4psi | 10 psi |
| Usable flow 50 psi@ 250F | Should be close to or better than tube jet with piston mechanism | | N/A | Testing in process | 96% | 48% | 100% | 95% |
| Usable flow 70 psi@ 250F | | | N/A | Testing in process | 98% | 62% | 98% | 62% |
| Block requirement | Extra drilling for cooling jets and packaging the solenoid valve | | Extra drilling for cooling jets | | | No extra drilling in the block is required. It is usually installed at the back of main bearing cap | | |
| Control options for cooling jets | Using on/off solenoid to turn on and off solenoid based on engine load, speed and temperature | | 1)The main gallery pressure<br>2) Set low/high pressure mode using V-flow oil pump technology | | | 1)The main gallery pressure<br>2) Set low/high pressure mode using V-flow oil pump technology | | |
| Recommendation | Based on the cost, performance and engineering capability, supplier A bulk head design with piston mechanism should be the first choice. | | | | | | | |

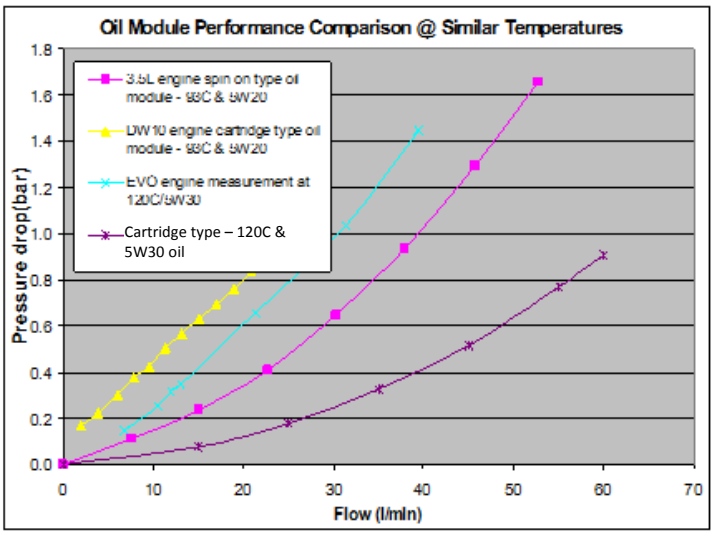


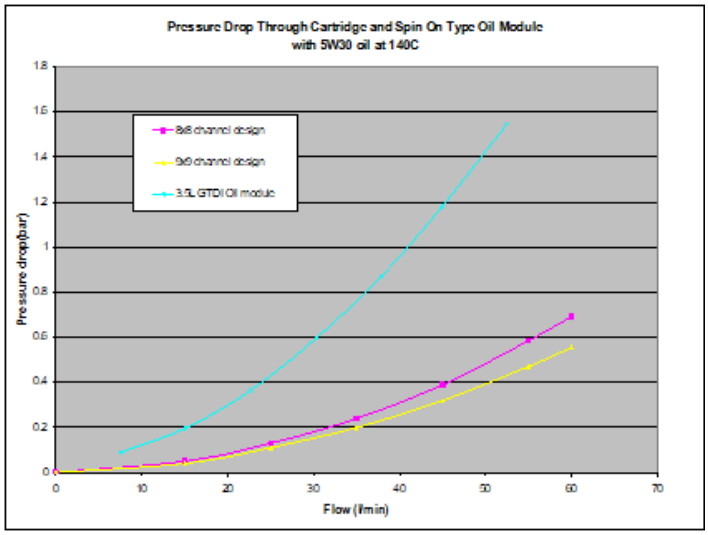


## *Figure 110 - Oil module comparison.*

## Design and Analysis

The lubrication system AMESim analytical model was developed for designing and analyzing the lubrication system to ensure the system design will meet all sub-system performance requirements and to determine the oil pump requirement for the supplier to deliver the oil pump design. A schematic of the model is shown in Figure 111.

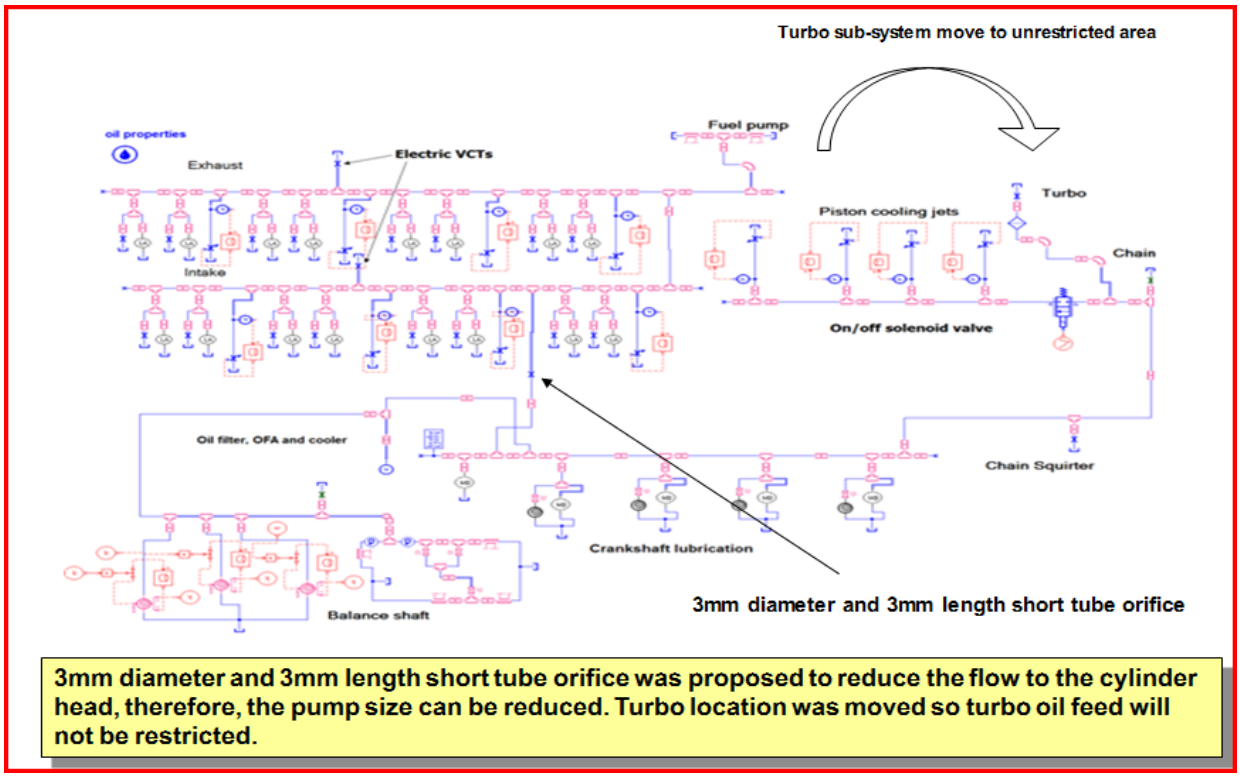


***Figure 111 - AMEsim lubrication system analytical model.***

The on/off solenoid valve controlled piston cooling jet system with check valve provided protection for the following two conditions (illustrated in Figure 112):

1. Protect bearings from failure at high oil temperature and low engine speed.
2. Protect piston from failure at maximum power conditions (5750 rpm).

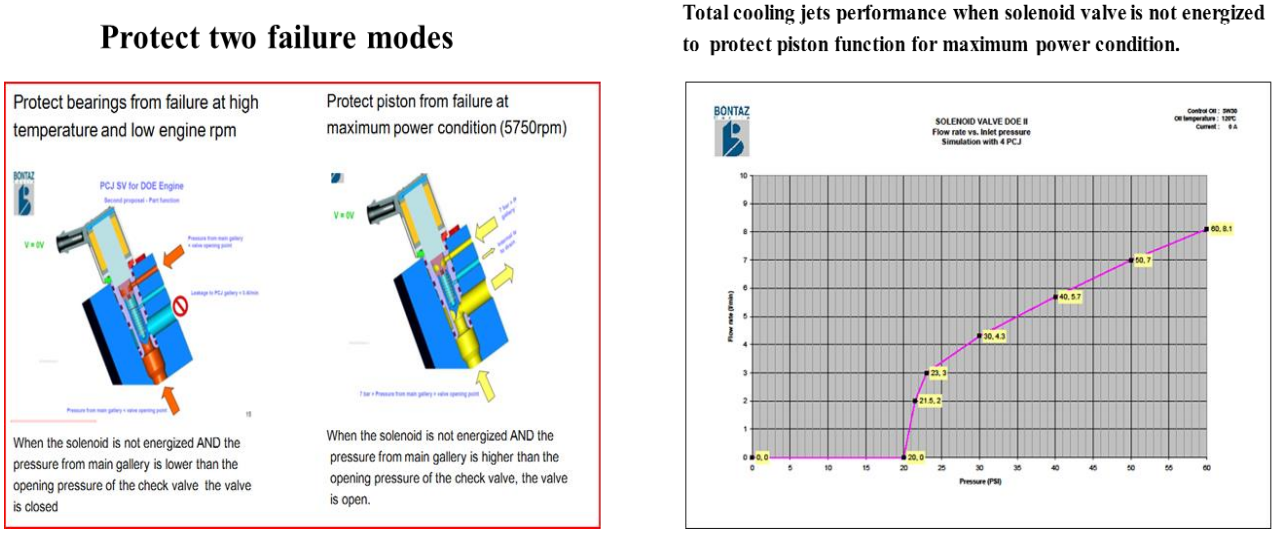


***Figure 112 - Protection from failure modes with check valve function.***

After the system analysis was performed, the required pump output, main gallery pressure, and total output flow were established for the oil pump supplier. The oil pump size of 16.4 cc/rev was designed by the supplier. The oil pump bench test results showed that actual performance satisfied the requirements very well, as shown in Figure 113.

**Oil pump flow and pressure requirements**

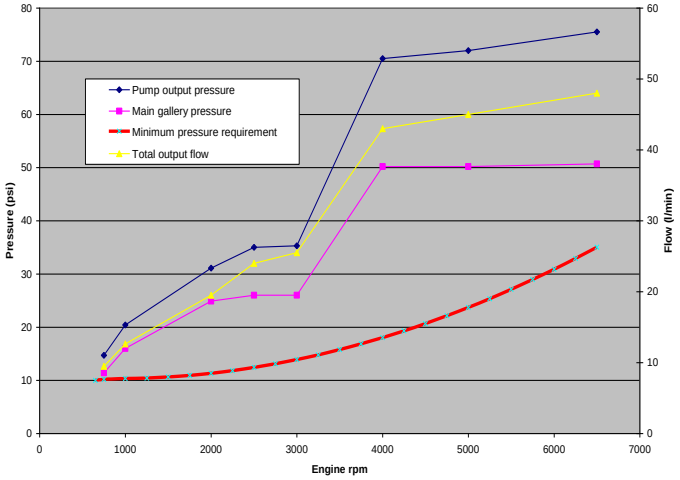


**Oil pump actual performance**

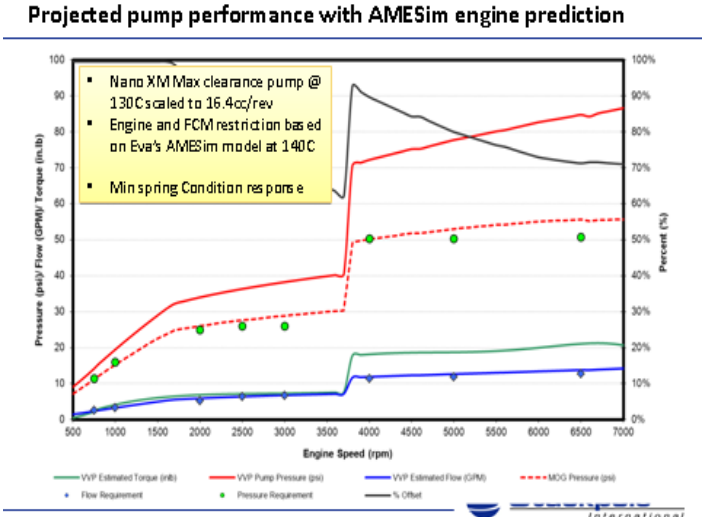


***Figure 113 - Oil pump flow and pressure requirements (left); oil pump actual performance (right).***

## Lubrication System Optimization

In order to optimize the lubrication system performance, all sub-system flow requirements were analyzed and the flow distribution among sub-systems was predicted. The results are displayed Figure 114.

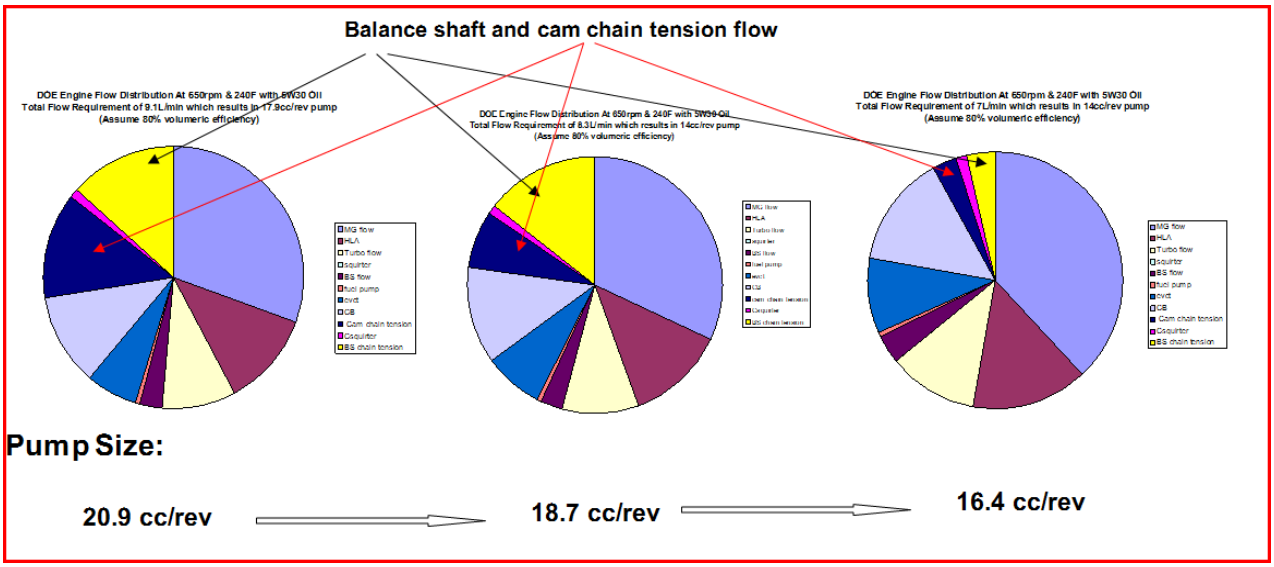


***Figure 114 - Oil flow for sub-systems.***

When the initial flow requirement of the chain tensioner was 2.4 l/min, the required oil pump size was 20.9 cc/rev. When the flow requirement was reduced to 1.8 l/min, the oil pump size was reduced to 18.7 cc/rev. After further discussion with the supplier and more analysis was done on the chain tensioner, the final 0.45 l/min flow was achieved. The final pump size of 16.4 cc/rev was determined, a 22% reduction from the initial design.

## Ignition System

Project assumptions for operating with high levels of charge dilution drove the need for an upgraded ignition system. The design constraints dictated that the components should be near term production feasible and meet the packaging requirements. Testing documented that the level of output needed to increase in terms of:

- Peak secondary current
- Peak available breakdown voltage
- Spark discharge duration
- Spark energy

Figure 115 compares the coil selected for the project to a production coil used on GTDI applications.

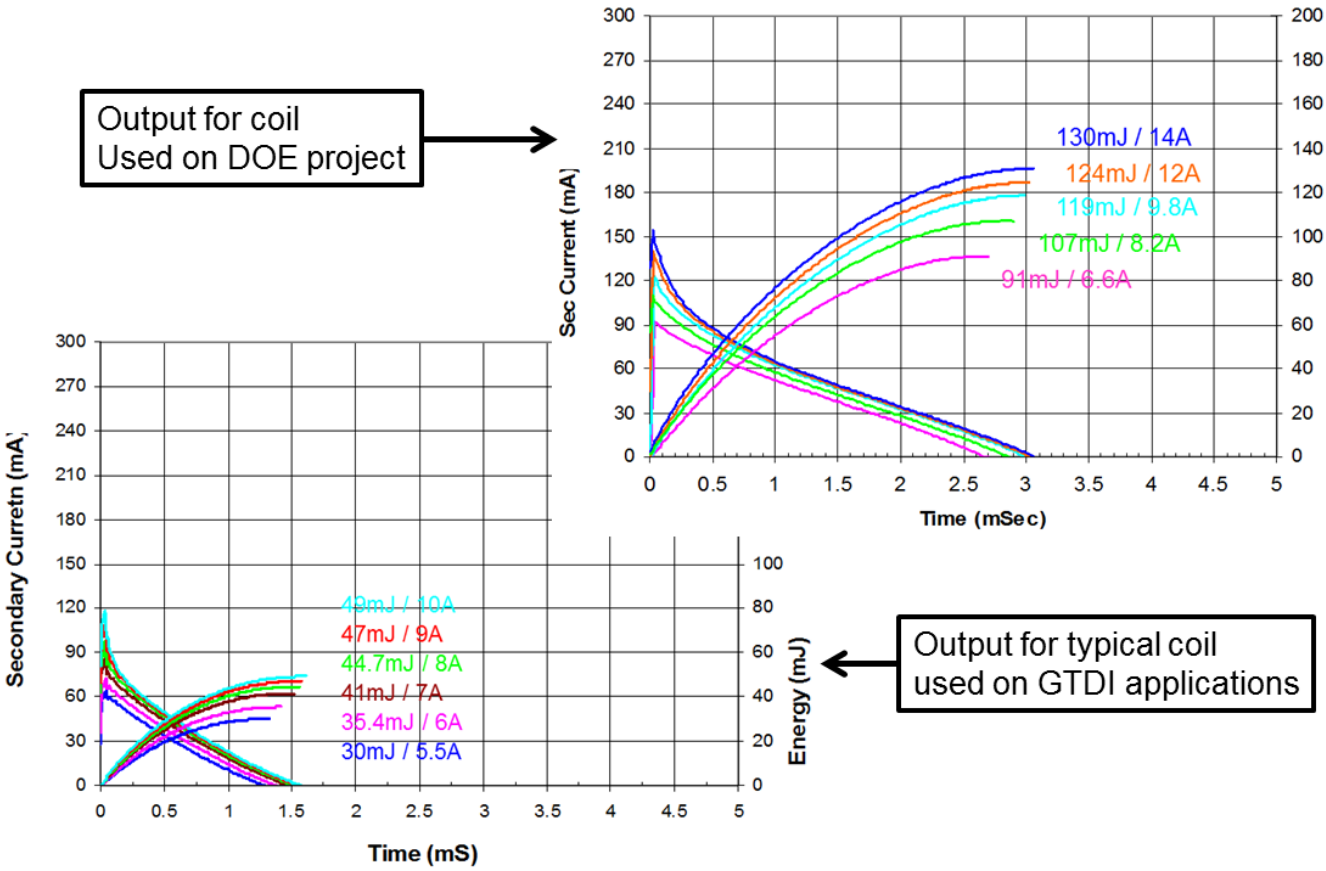


***Figure 115 - Ignition coil output characteristics.***

The electronics needed to control the ignition coil as specified are not normally used in production and needed to be integrated into the primary harness. Subsequently the electronics were qualified for production use and are capable of being packaged within the ignition coil housing. Figure 116 is the drawing of the coil used.

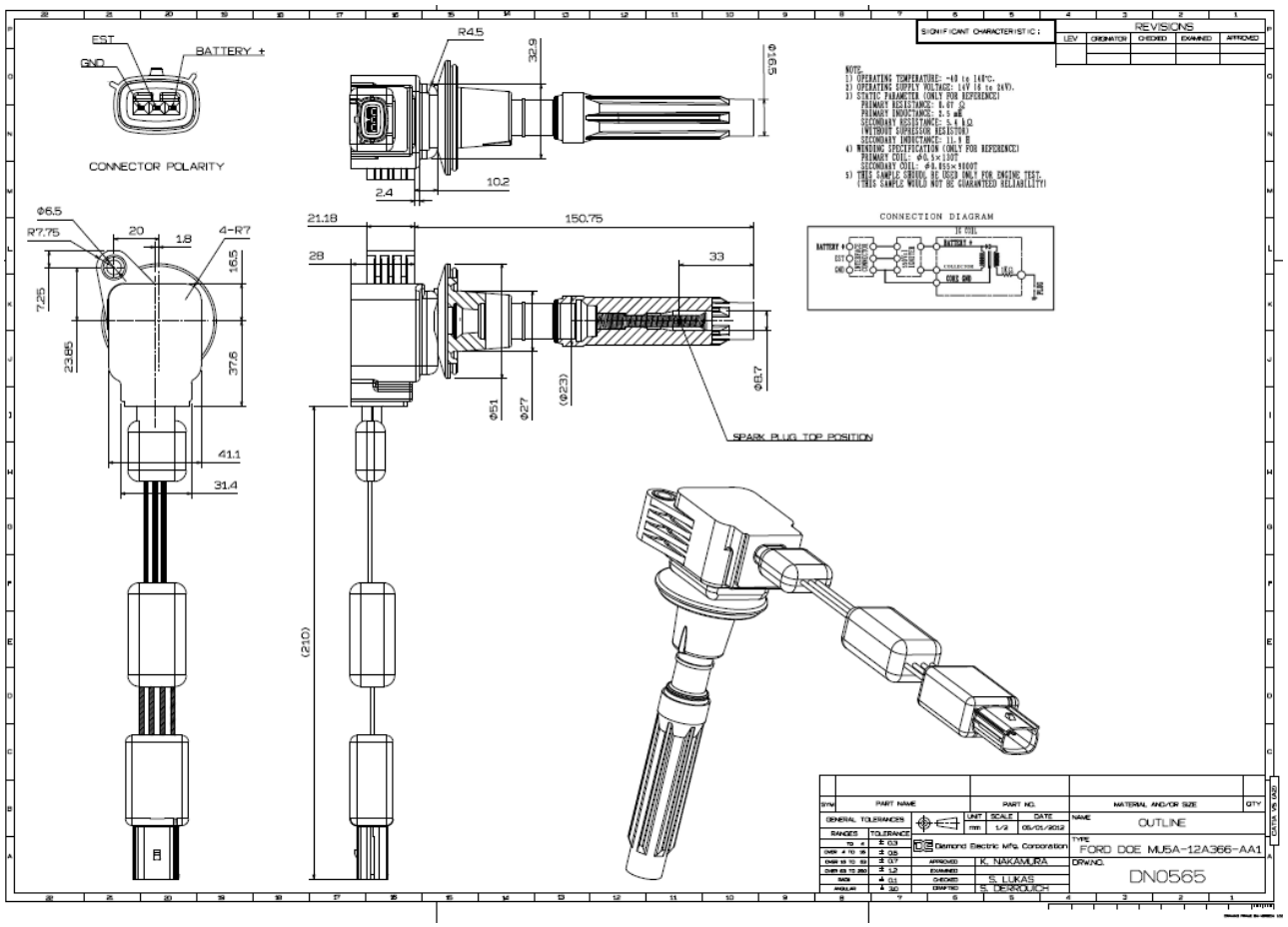


***Figure 116 - Ignition coil drawing.***

Several spark plug designs were evaluated to identify sensitivity to ignitability. The double fine wire geometry was determined to provide the best results in terms of combustion metrics. Figure 117 is a close up view of the spark plug geometry utilized. Figure 118 is the drawing released for the project.

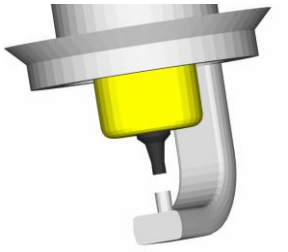

***Figure 117 - Spark plug firing end detail.***

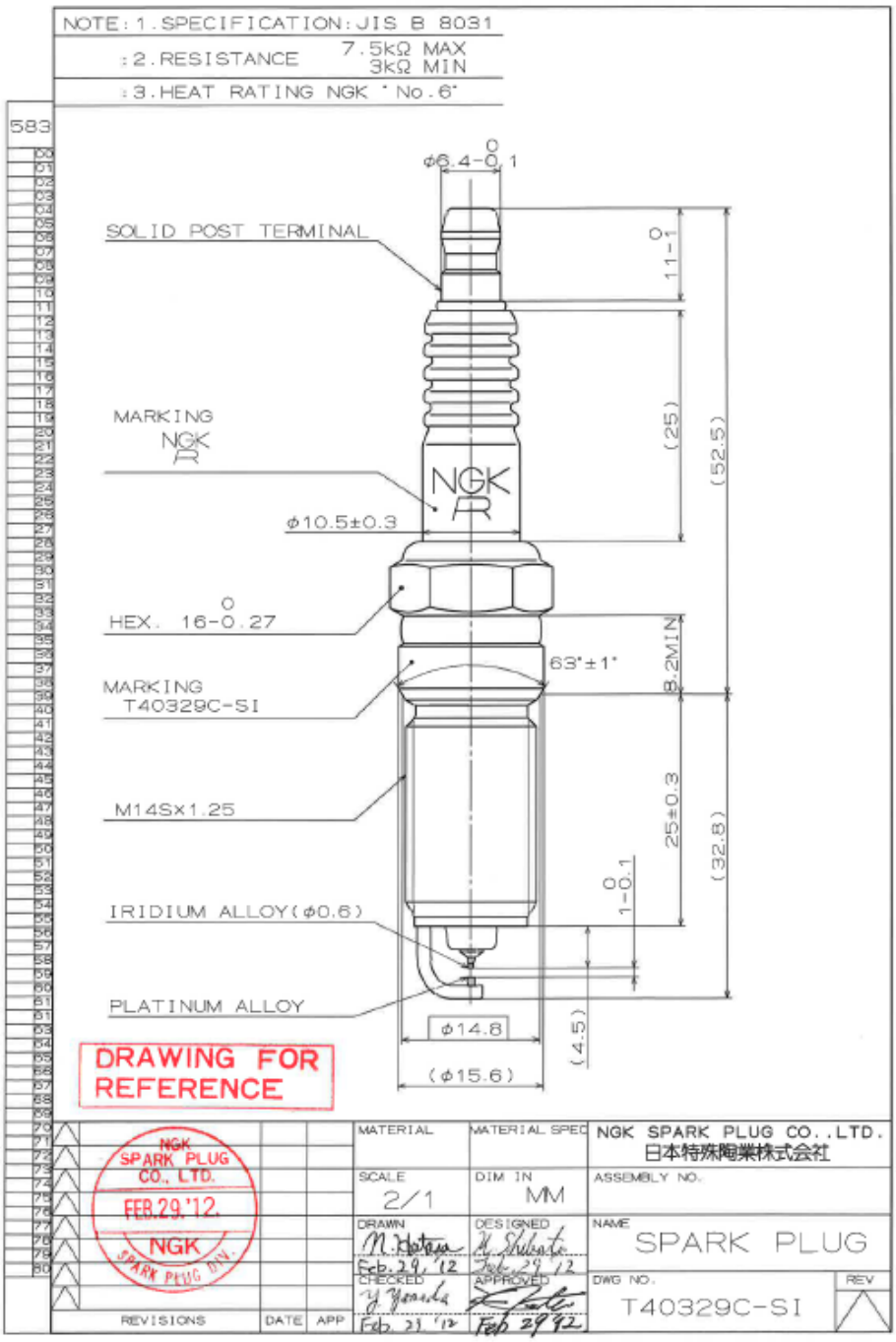


***Figure 118 - Spark plug drawing.***

## Covers and PCV System

Covers and sealing components for the 2.3L DOE engine are shown in Figure 119. For each cover, an initial design concept was used as a starting point for CAE iterations to improve the design. Topography software was also used to achieve consistent wall thickness, avoiding additional weight in areas that would not improve structural NVH characteristics.

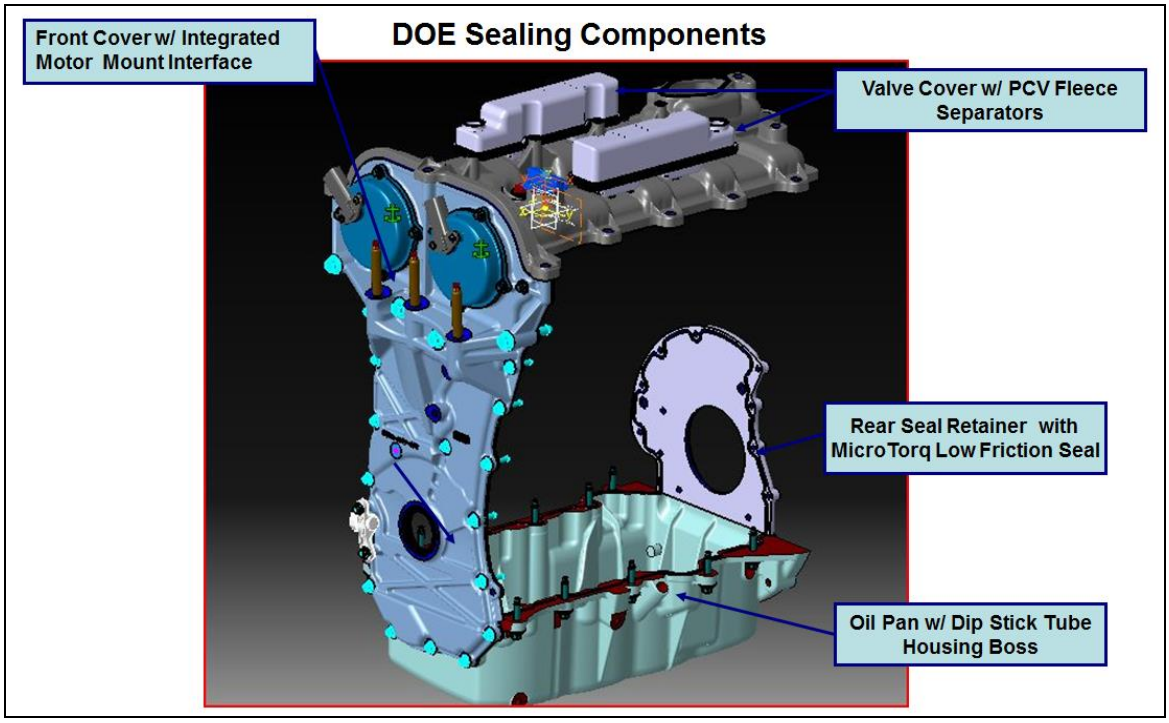


***Figure 119 - Sealing components for DOE engine.***

### Valve Cover/PCV System

The valve cover containing the positive crankcase ventilation (PCV) system is shown in Figure 120. A schematic of the PCV system is shown in Figure 121.

Design objectives for the valve cover and PCV system were as follows:

- Meet program NVH targets with a robust design.
- Incorporate oil separators internal to the valve cover.
- Provide oil separation meeting the GTDI engine oil carryover target of 1 g/scfm-hr while accepting flow variation from 0 - 110 l/min (3.9 cfm).
- Meet Ford blow-by requirements.
- Meet Ford control droplet distribution requirements at extraction points.
- Provide full ventilation PCV system both in boosted and non-boosted modes to prevent sludging and reduce $CO_2$ concentration inside the crankcase.

Design assumptions for the valve cover were as follows:

- Aluminum SAE J452 308 material.
- Fully isolated.
- Integrated full and part load PCV oil separators.
- Provision for attachment locations for spark plug coils.
- Provision for sealing surface for fuel pump pedestal mounting plate.

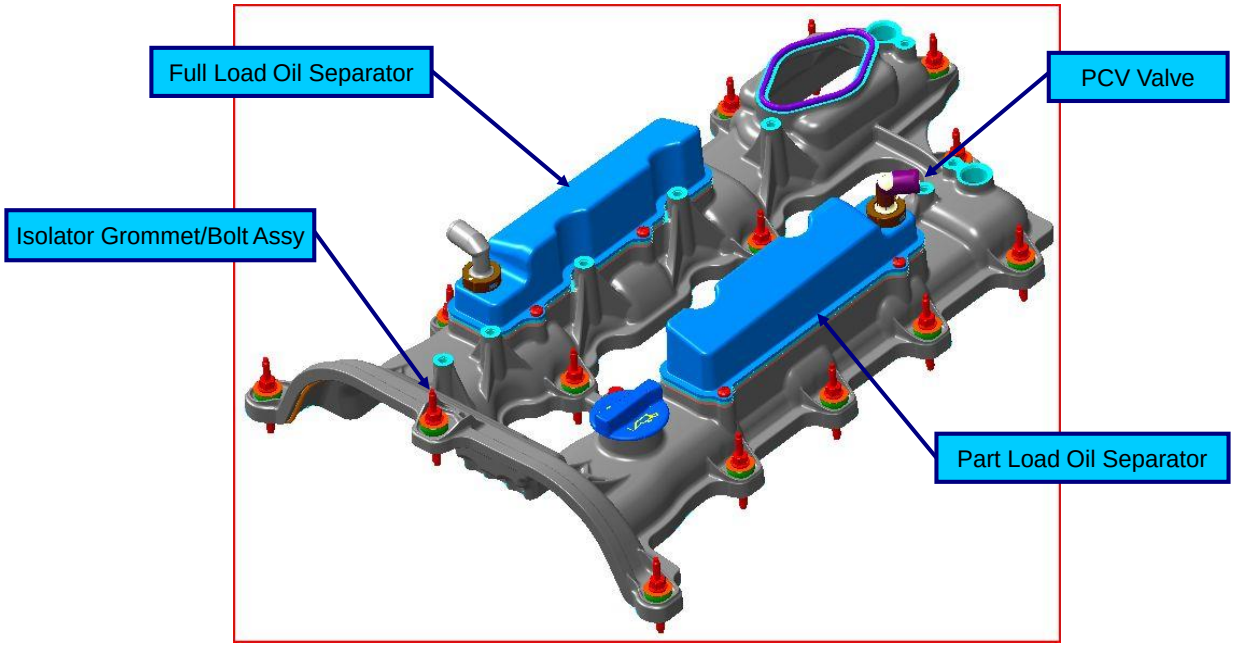


**Material: Aluminum – 356-T6**
**Fully Isolated for NVH Benefit**
**PCV Oil Separator – Nylon Composite PA6.6 with Fleece Media**

***Figure 120 - Valve cover with integrated PCV/oil separators.***

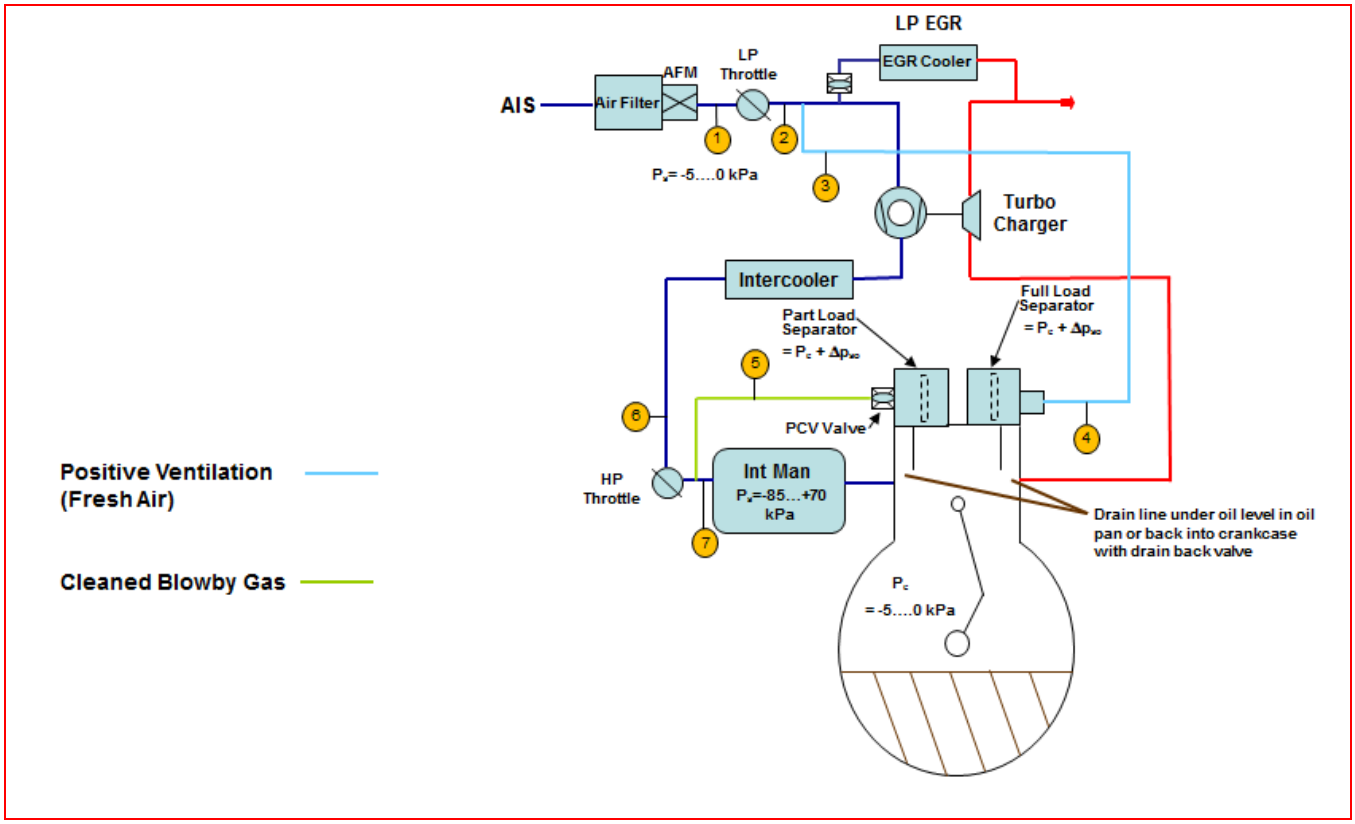


***Figure 121 - PCV system schematic.***

The valve cover incorporates highly efficient fleece media oil separators based on a production Ford V6 GTDI engine design. This reduced manufacturing cost dramatically by using existing tooling that was available to the prototype supplier. A description of the fleece media separator function provided by the supplier is shown in Figure 122.

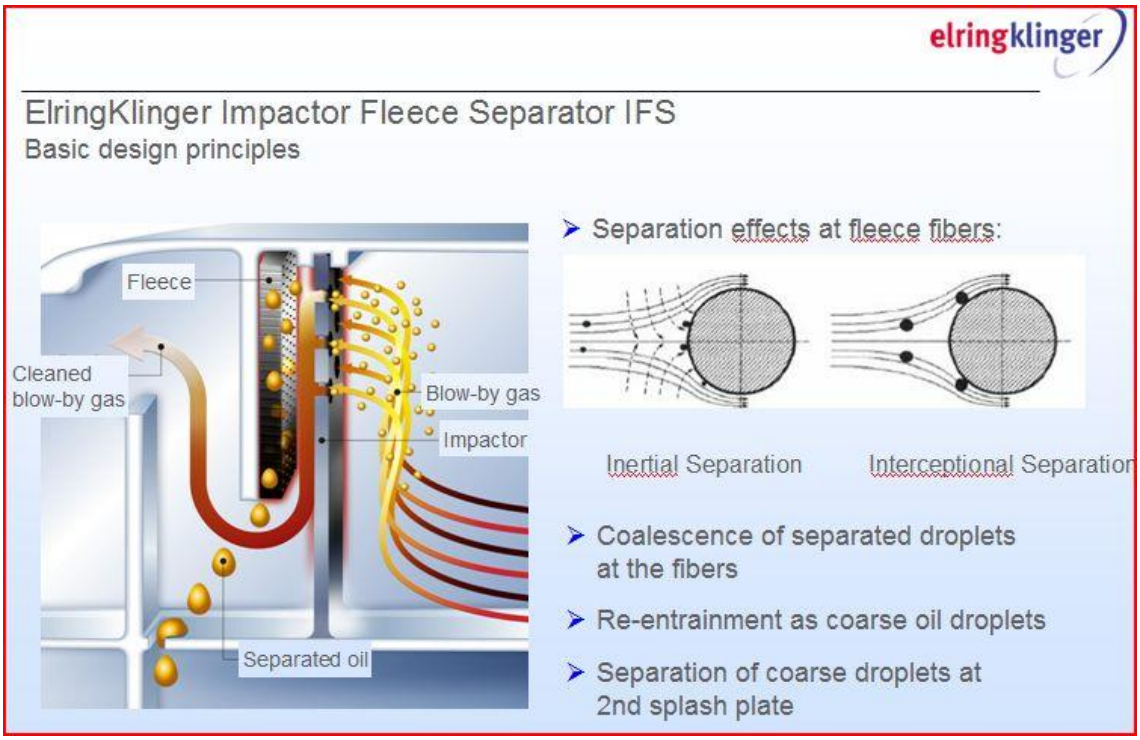


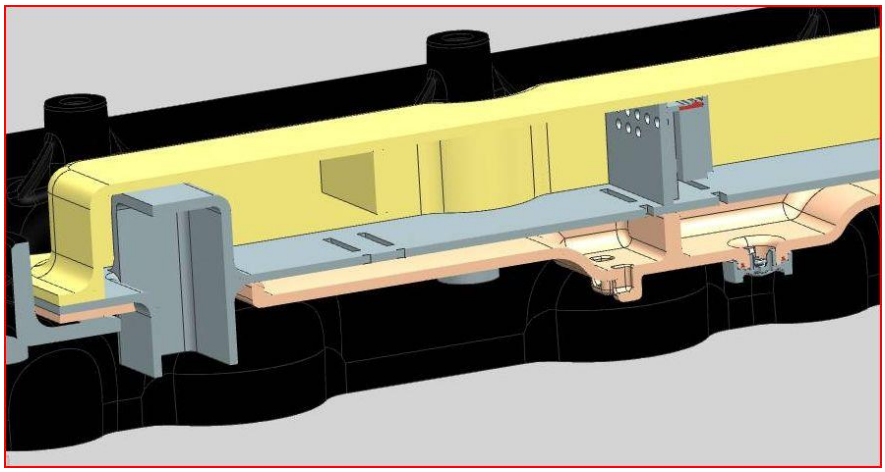

***Figure 122 - High efficiency oil/PCV separator.***

CAE iterations for the valve cover are shown in Figure 123. The valve cover met all NVH frequency and modal analysis targets. Oil consumption testing was planned but was not completed, however, none of the engines consumed an excessive amount of oil during engine dynamometer and vehicle testing.

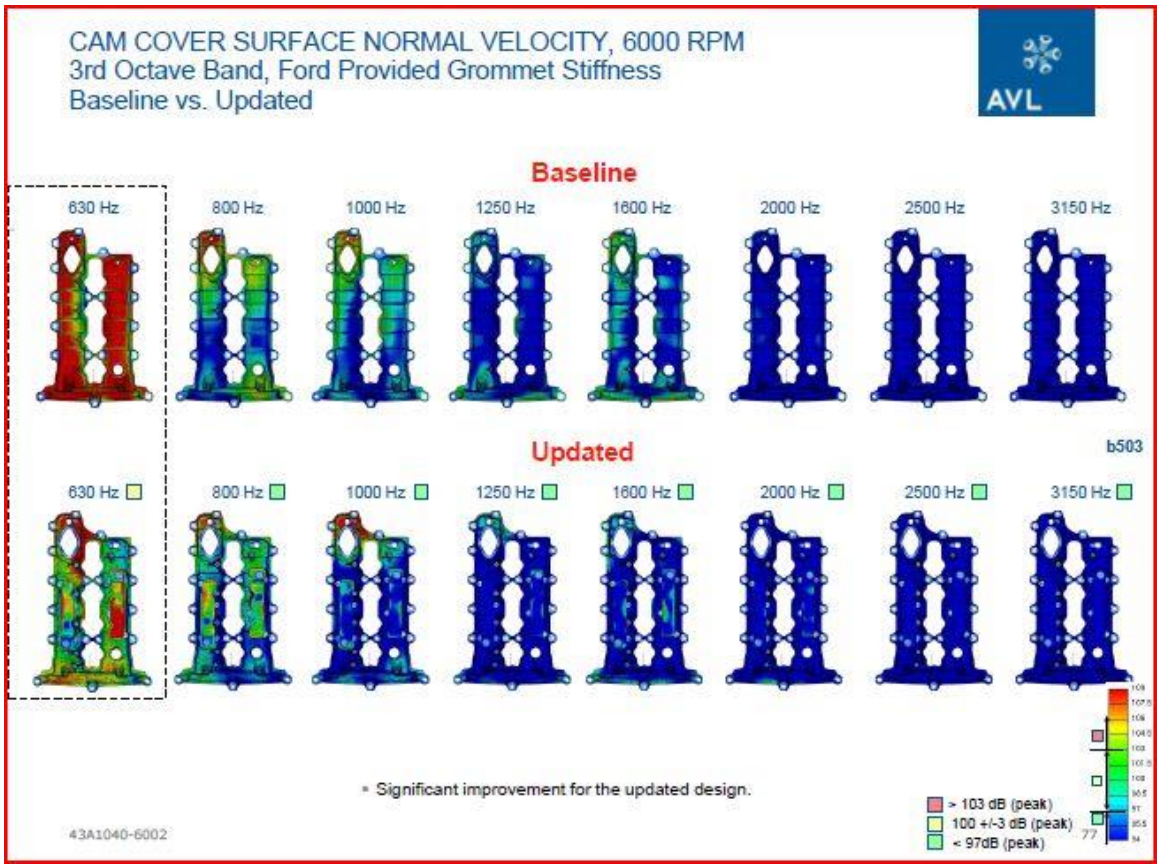


***Figure 123 - Valve cover surface normal velocity at 6000 rpm.***

## Front Cover

The front cover assembly and front engine mount bracket are shown in Figure 124 and Figure 125, respectively.

Design objectives for the front cover were as follows:

- Provide all necessary internal and external clearances.
- Follow the contour of the cover with ribs utilizing the minimum height to achieve NVH targets.
- Meet the program specific NVH targets with a robust design.
- Structurally integrate cover mounting bolt bosses with the required column strength within the sealing flange.
- Provide a nominal sealing land of ≥ 10 mm around the periphery of the cover.
- Provide a seal bore land ≥ 10mm for the dynamic crankshaft seal.

Design assumptions for the front cover were as follows:

- Aluminum SAE J452 308 material.
- Integrated motor mount interface location and attachment locations for elVCT covers.
- Protection for a crank position sensor.
- Incorporation of the new Federal Mogul MicroTorq low friction seal for crankshaft sealing.
- Doweling of the front cover to the cylinder block because it contains the dynamic crankshaft seal.

The front engine mount bracket was redesigned to accommodate new mounting boss locations. The new Federal Mogul MicroTorq low friction seal is described in Figure 126 provided by the supplier.

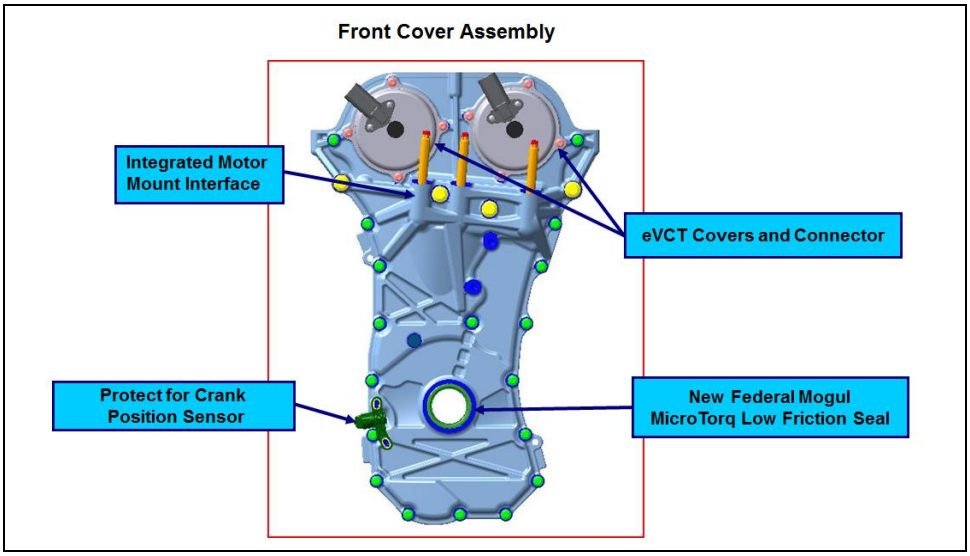


*Figure 124 - Front cover assembly.*

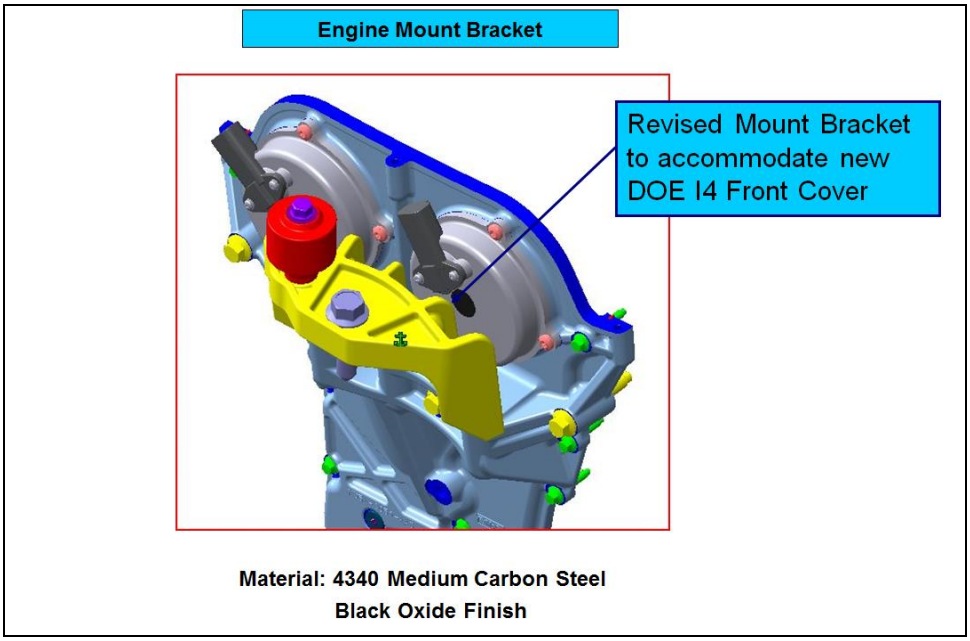


*Figure 125 - Engine mount bracket.*

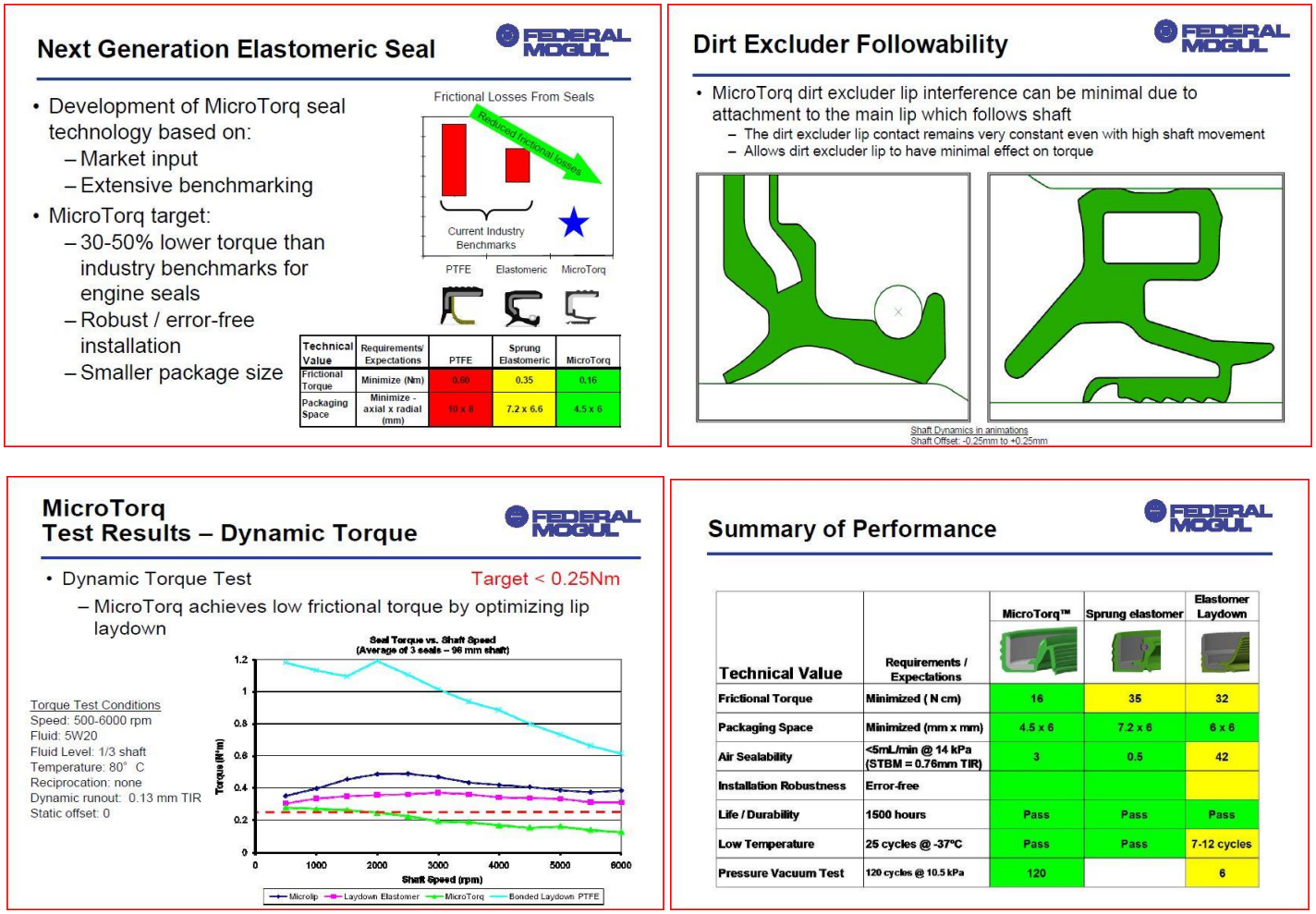


***Figure 126 - Low friction micro-torq seal comparison to PTFE and sprung elastomeric seals.***

CAE iterations for the front cover and engine mount bracket are shown in Figure 127 and Figure 128, respectively. Special emphasis was placed on the engine mount bosses, as they carry the primary engine loads to the vehicle frame. A steel engine mount bracket met all NVH frequency and modal analysis targets. The targets could not be met with aluminum.

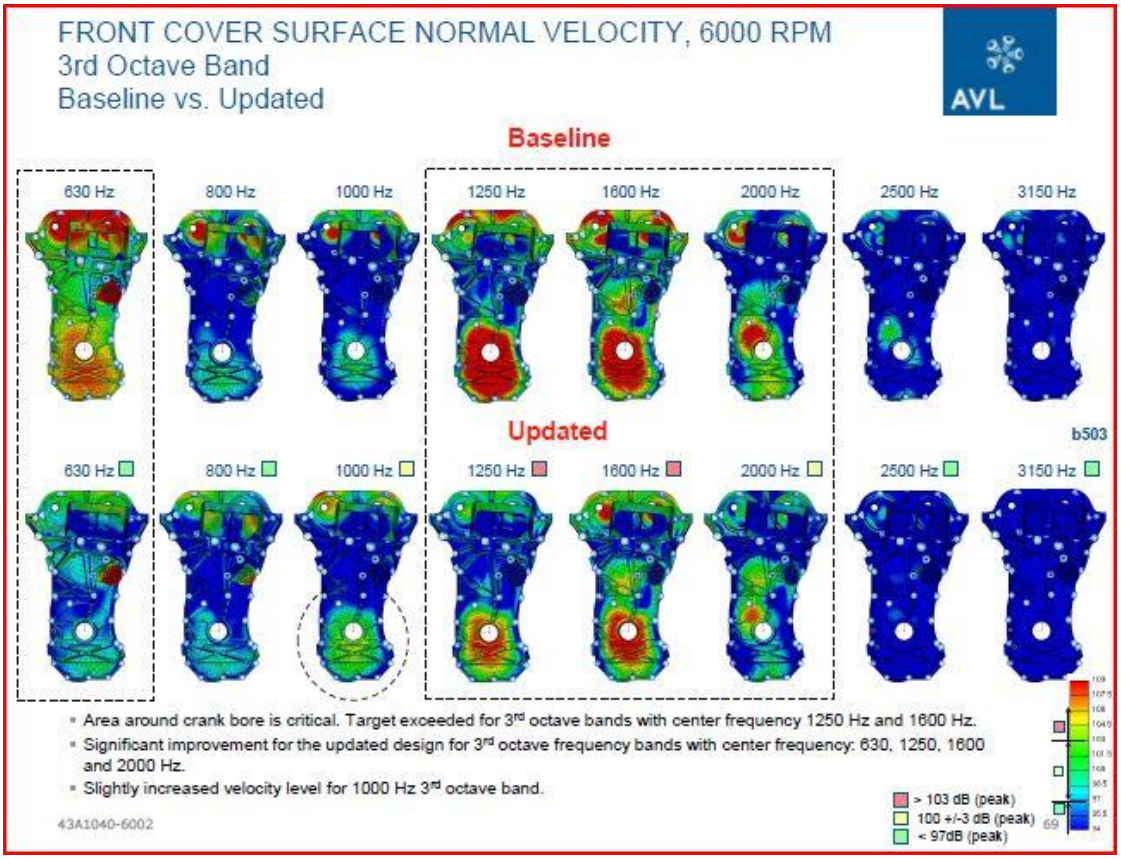


***Figure 127 - Front cover NVH analysis results.***

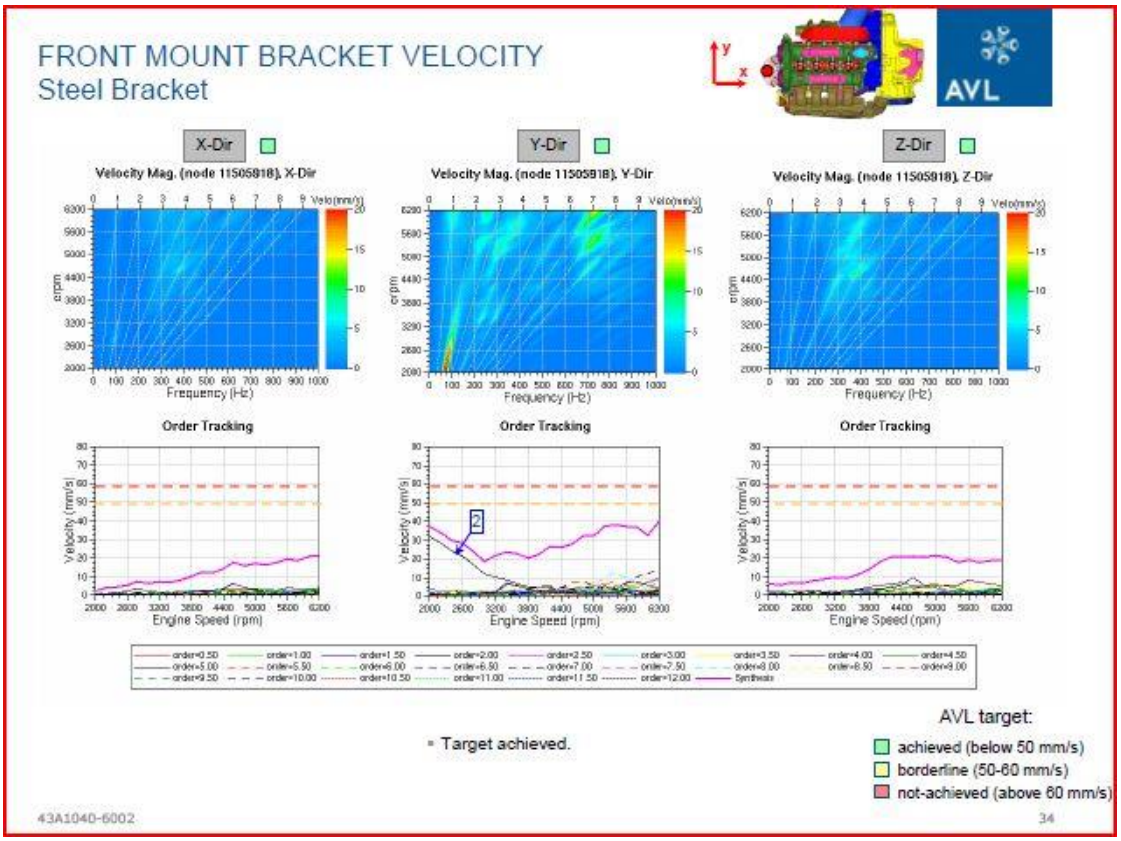


***Figure 128 - Front mount bracket velocity analysis.***

## Oil Pan

Design objectives for the structural oil pan were as follows:

- Meet the program specific NVH targets for powertrain bending.
- Provide service access for the transmission torque converter flywheel nut tool, unless access is provided through the starter motor opening.
- Provide a nominal static clearance of 20 mm between the surface of the oil and rotating components.
- Ensure the oil entrance within the screen and cover assembly remains submerged in oil in the sump.
- Package the Ford common drain plug.
- Adhere to the Ford corporate requirement for vehicle ground line clearances.

Design assumptions for the oil pan were as follows:

- Aluminum SAE J452 308 material.
- Incorporation of mounting locations for the transmission bell housing.
- Incorporation of a nominal sealing land of ≥ 10 mm for the sealing gasket.
- Provision for a dipstick mounting boss and attachment bosses for the air conditioning bracket.

The initial design concept and the final design of the oil pan are shown in Figure 129. CAE results for the oil pan are shown in Figure 130. Primary emphasis was placed on the bell housing interface, as this is the primary source for powertrain bending during engine operation. Emphasis was also placed on the bosses for the air conditioning bracket, an area that is highly loaded when the air conditioning is running. The oil pan was found to marginally meet all NVH frequency and modal analysis targets. Due to time constraints, further optimization was not performed and the parts were cast and machined.

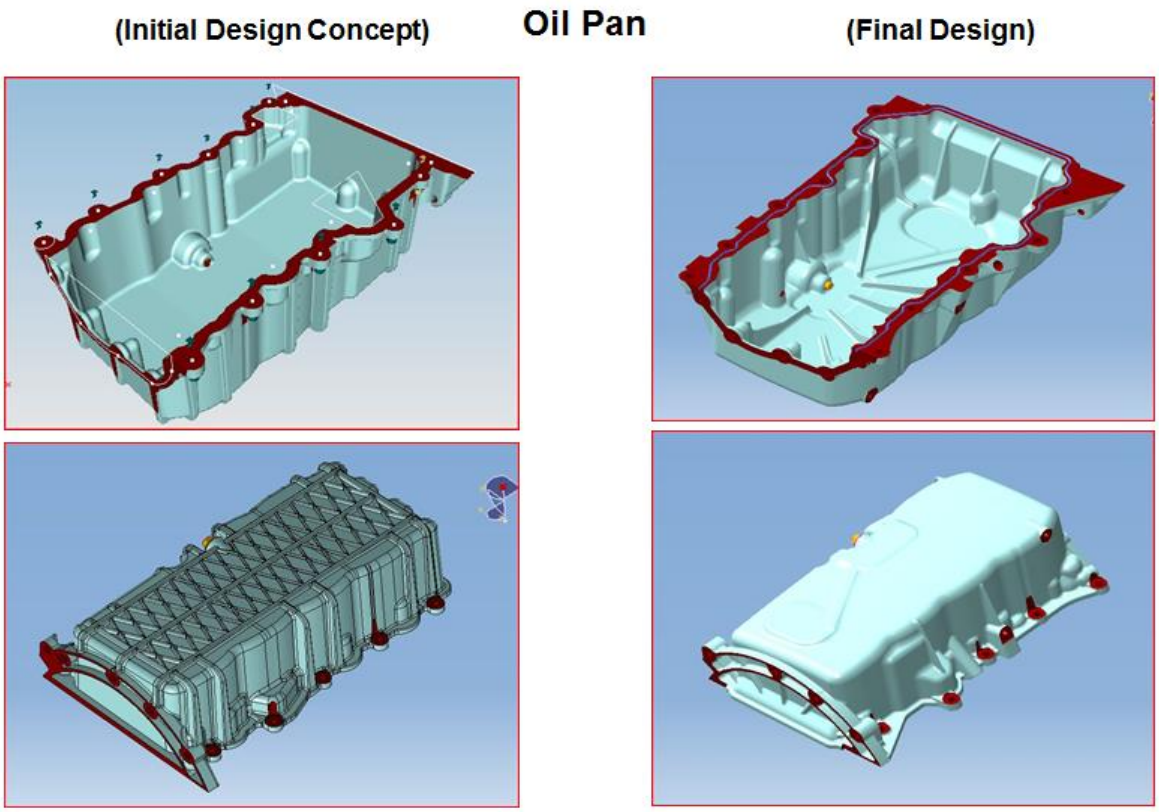


***Figure 129 - Oil pan initial design concept and final design.***

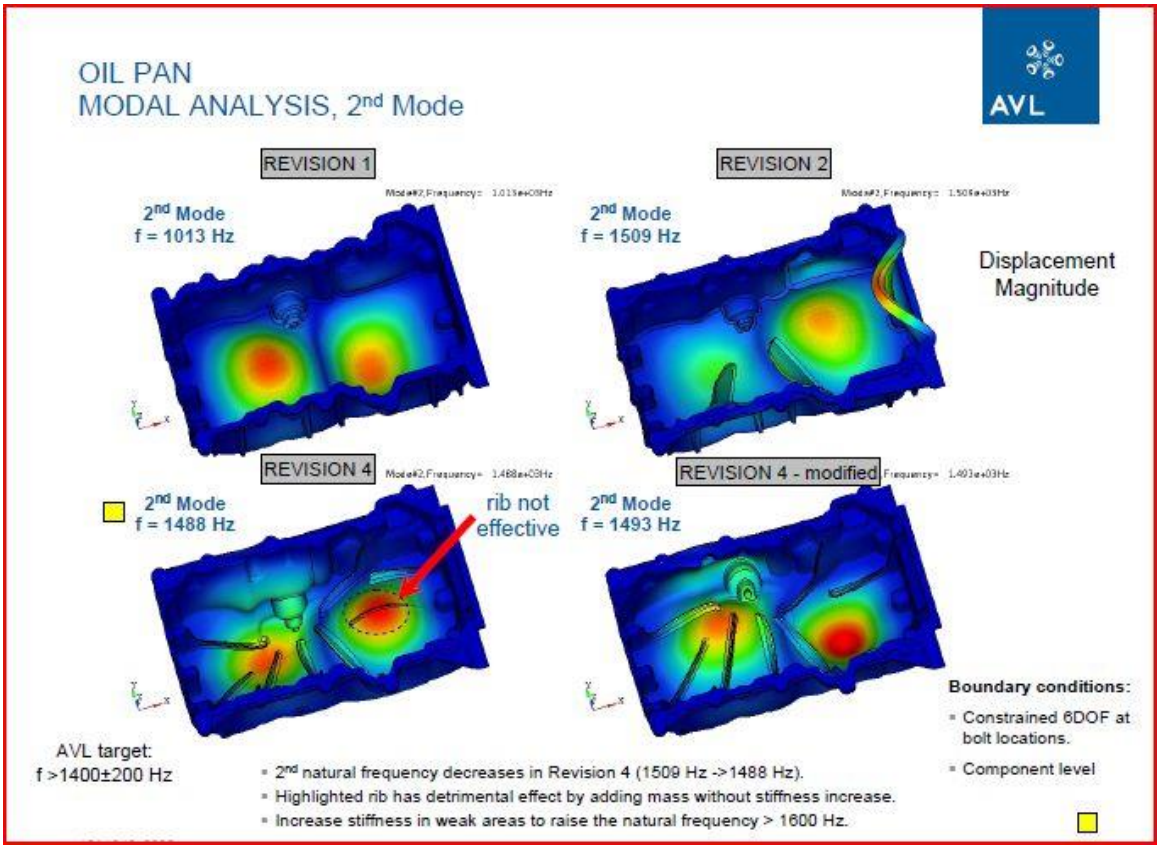


***Figure 130 - Oil pan NVH analysis.***

## Rear Seal Retainer

The rear seal retainer is shown in Figure 131. Because the rear seal retainer is not highly loaded, the design was based on previous rear sealing housing designs, but incorporated the following features:

- The part was made out of billet 356 aluminum.
- A new MicroTorq seal (Figure 126) was used for crankshaft sealing.

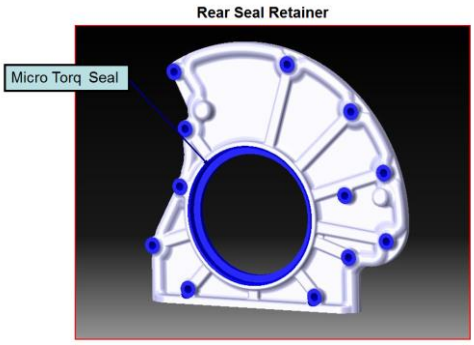


***Figure 131 - Rear seal retainer.***

# Low Pressure EGR System

## Design Objectives

- Support 15% low pressure (LP) EGR schedule up to 13 bar BMEP based on value optimization from previous LP EGR project.
- Include margin in subsystem to assess EGR rates up to 20% and extension of EGR map to higher BMEP levels.
- Select components and design package to be production representative.
- Assess key functional attributes such as cooling effectiveness, flow capability, flow distribution, and mixing.
- Assess key robustness attributes including coolant flow requirement, modal analysis, and thermo-mechanical stress analysis.

## Design Assumptions

- System to support 15% EGR at 4000rpm, 15 bar BMEP and 20% EGR at 4000 rpm, 13 bar BMEP while not exceeding 160 ºC compressor outlet temperature at hot ambient (38ºC) conditions.
- LP EGR system with turbine integrated take-off (pre-catalyst).
- “Shell-and-tube” EGR cooler cooled with engine coolant.
- “Cold-side” DC motor linear, single poppet EGR valve. EGR valve to provide dynamic range capability for 5% EGR at 1000rpm, 1 bar BMEP up to 15% EGR at 4000rpm, 15bar BMEP.
- Separate, normally open “low pressure” AIS throttle for EGR flow enhancement and control to provide 8 kPa over LP EGR valve when not available naturally. Throttle pressure drop to be less than 1 kPa when WOT at peak air flow.
- Pre-compressor introduction of EGR with appropriate mixing length.
- EGR tubes to include de-coupling bellows and heat protection as required.
- Added sensor set: EGR cooler outlet temperature, LP AIS temperature, pressure and humidity, pre-CAC intake oxygen sensors. Optional EGR cooler pressure sensor.

## System / Component Summary

A description of LP EGR components with part numbers is shown in position relative to the turbocharger in Figure 132. Both the LP EGR valve and LP AIS throttle were controlled via separate control boxes which simplified control from the PCM to a simple analog output control signal. All valve-specific control algorithms including the PID control settings, soft-landing, closed position learning, dithering, and other key control algorithms were contained within the control boxes.

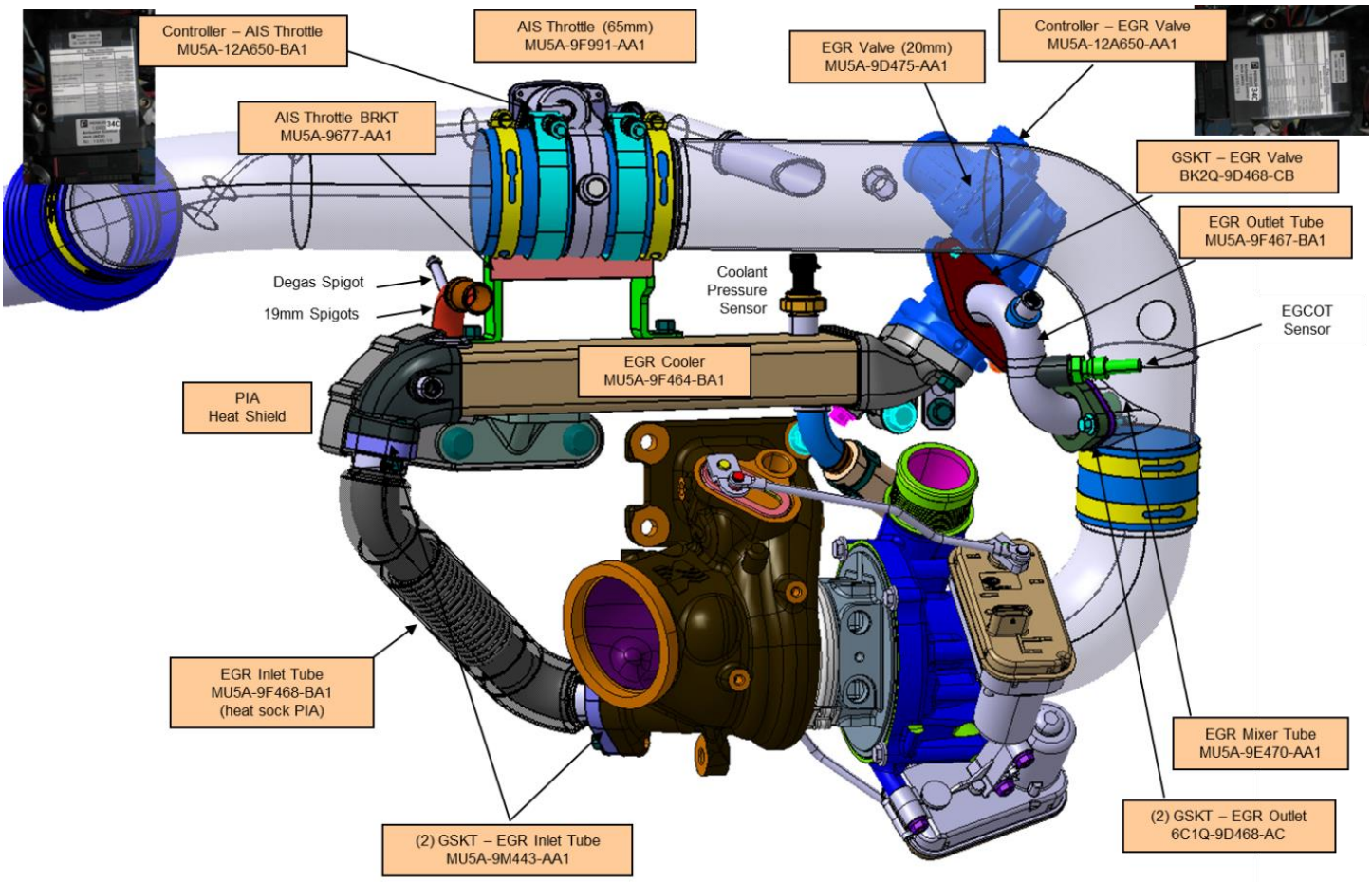


***Figure 132 - 2.3L GTDI engine low pressure EGR system.***

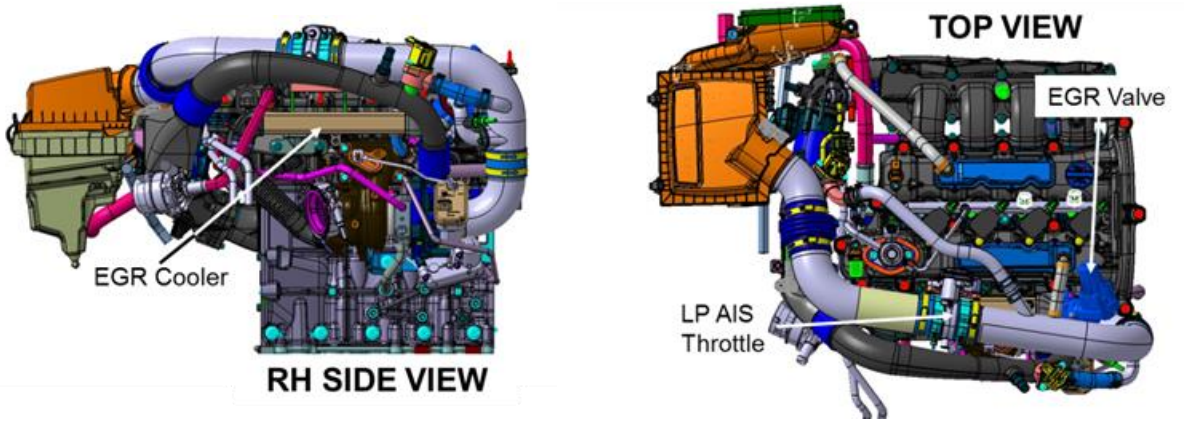


Figure 133 shows the LP EGR system along with the other engine components packaged above the down-swept turbocharger alongside the cylinder head. This is a good location for the EGR cooler, providing rigid mounting to the cylinder head, avoiding low spots to avoid condensation collection while not packaging the system above the cylinder head where coolant de-gassing can be an issue. Note that a degas spigot is provided on the EGR cooler outlet spigot to avoid air pockets in the EGR cooler coolant cavity.

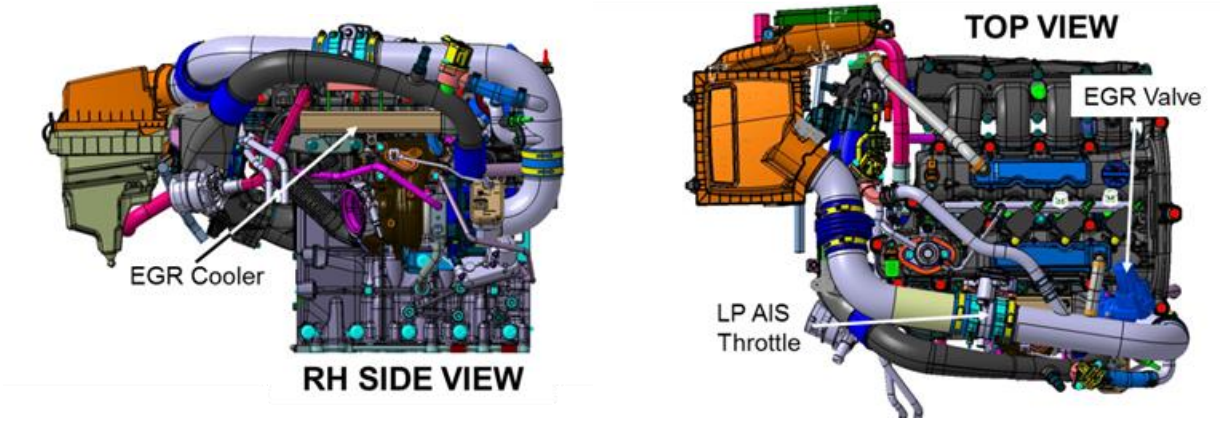


***Figure 133 - Low pressure EGR System with 2.3L GTDI engine.***

A study was performed to understand the extent of the EGR schedule required to maximize the M-H cycle fuel economy benefit as well as provide a fuel economy benefit in more heavily loaded cycles such as US06. For the 2.3L engine in the vehicle producing an engine displacement (liters) to vehicle mass (metric tons) ratio of 1.2, an EGR schedule extending to 11 bar BMEP fully covers the M-H cycle and an EGR schedule extending to 15 bar BMEP covers the US06 cycle. This was based on CVSP inputs for the DOE project and LP EGR benefits from the 91RON 3.5L iVCT GTDI data set adjusted for 98 RON and TiVCT. The fuel economy improvement trends relative to EGR schedule BMEP limit are shown in Figure 134. The fuel economy benefits are modeling results based on steady state testing and are for relative comparison purposes only.

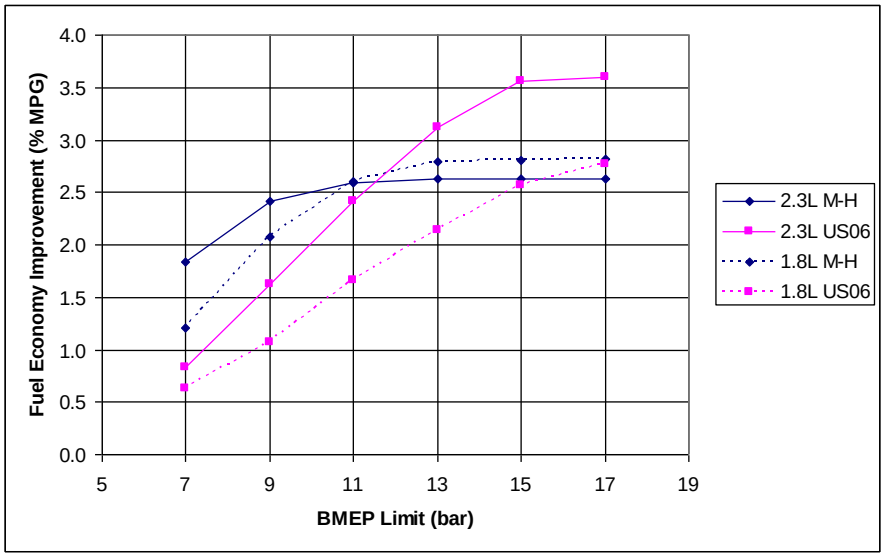


***Figure 134 - EGR schedule extent sensitivity study.***

GT POWER modeling was performed to confirm the EGR cooler sizing and compressor outlet temperature limits were met (Figure 135).

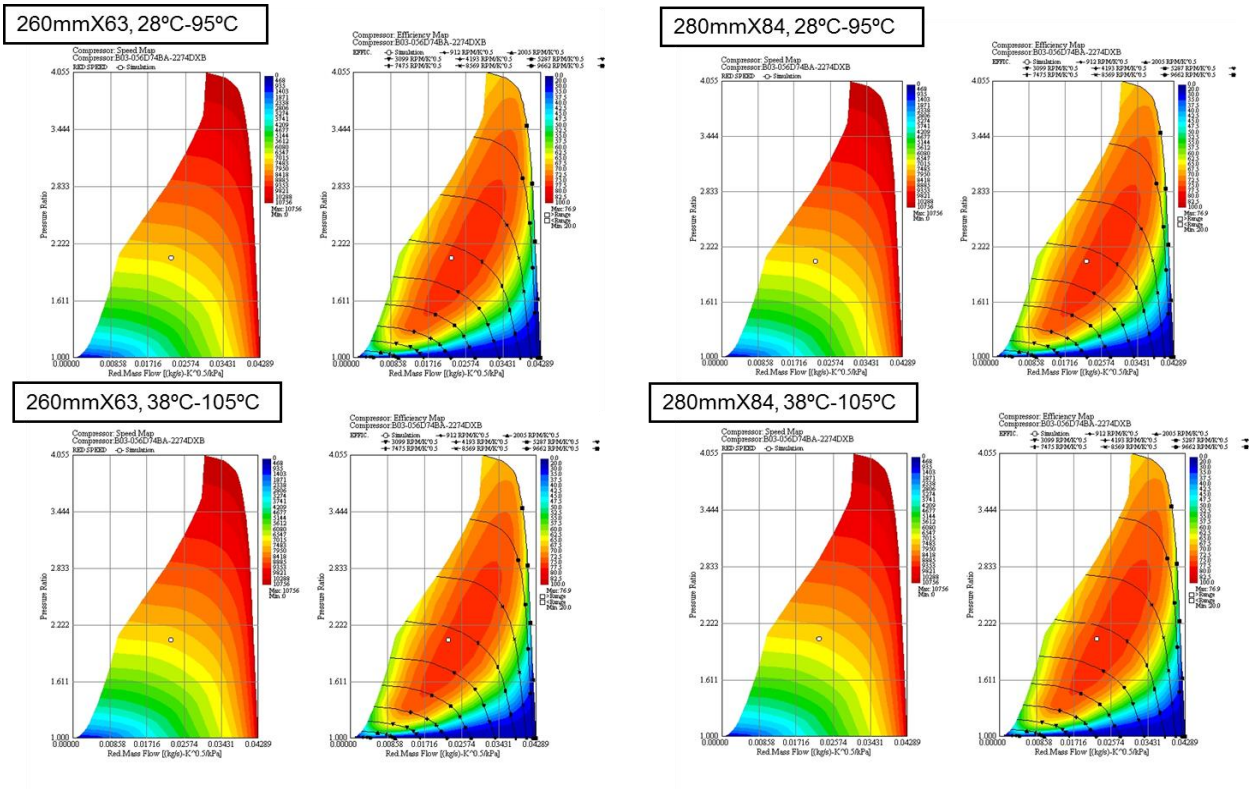


***Figure 135 - Compressor outlet temperature study for two different EGR cooler sizes.***

It was determined that at hot ambient conditions (ambient temperature = 38 ºC and coolant temperature = 105 ºC), the 260 mm long EGR cooler with 63XØ5 mm spiral tubes produced a compressor outlet temperature of 151 ºC which is below the 160 ºC limit at 4000 rpm, 15 bar BMEP and 15 % EGR.

A system pressure drop analysis was performed and components were found to meet their respective pressure drop targets. Note in Figure 136 that the 3D CFD methodology showed higher pressure drop in the EGR inlet tube than the 0D method as the tube corrugations were included in the 3D study. Otherwise, the 3D calculations matched the earlier 0D predictions fairly well. This study also confirmed that the EGR valve was appropriately sized and that the LP AIS throttle can provide the necessary ΔP over the EGR valve over the range of EGR schedule. A GT power study also confirmed that the boost requirements can be met with the LP AIS throttle usage planned.

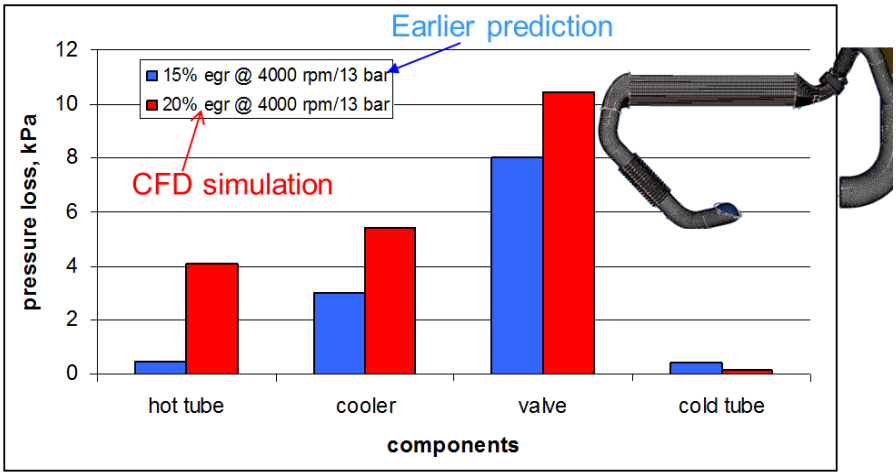


***Figure 136 - LP EGR system pressure drop analysis.***

The CFD study also checked flow distribution over the inlet of the EGR cooler, which met a demanding +/-10% flow uniformity target (Figure 137).

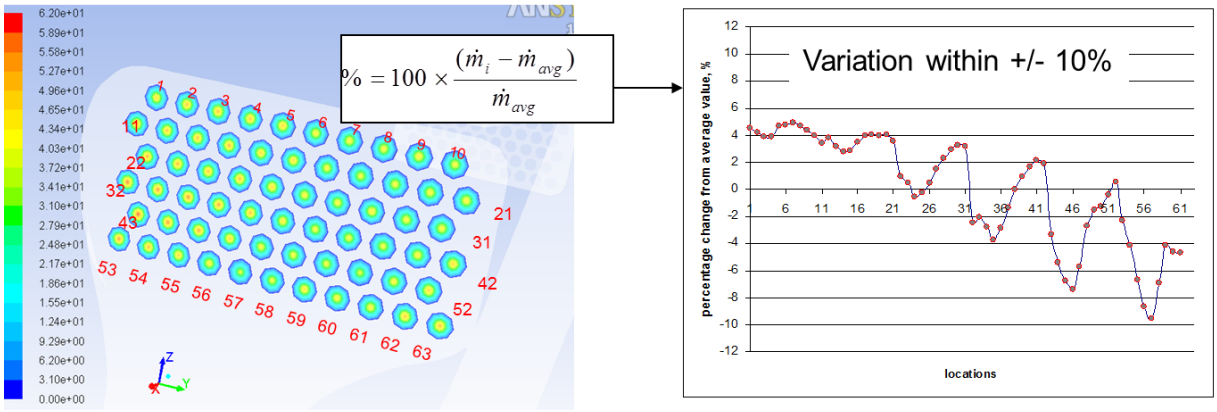


***Figure 137 - EGR cooler flow distribution study.***

Finally, 3D CFD was used to evaluate LP EGR mixing and temperature uniformity entering the compressor wheel. A study was performed at 4000 rpm / 13 bar BMEP / 20 % EGR with an EGR cooler outlet temperature of 143 ºC and an ambient air inlet temperature of 27 ºC. As shown in Figure 138, the maximum temperature deviation entering the compressor was reduced from 45 ºC to 15 ºC by migrating from an angled introduction of LP EGR to a 90-degree introduction with a slight protrusion.

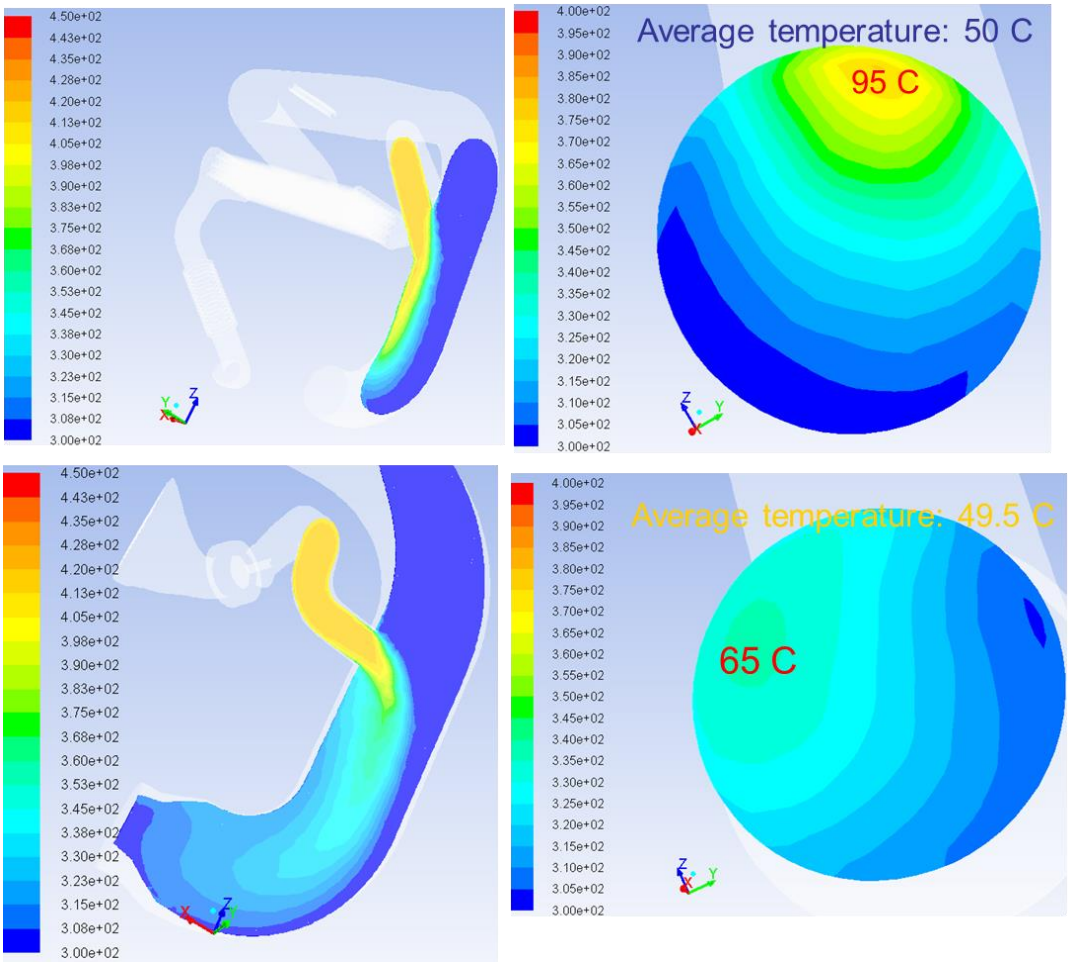


***Figure 138 - LP EGR pre-compressor mixing study.***

## Design Verification

Production level CAE methods were employed to ensure the robustness of the 2.3L engine LP EGR system. A standard coolant flow calculation methodology was used to determine required coolant flow in the EGR cooler to avoid coolant boiling including appropriate noise factors such as hot ambient/coolant temperatures, glycol/water mix, cooling system pressure and coolant flow maldistribution at the "hot end" of the EGR cooler (captured in the "e-ratio"). The coolant pump curve includes an assist from an electric water pump on the main engine coolant circuit to increase low rpm coolant flow. Only in the case of hot ambient temperatures with a complete loss of water pump suction pressure (i.e., zero pressure in the degas bottle) does the model predict coolant boiling (Figure 139).

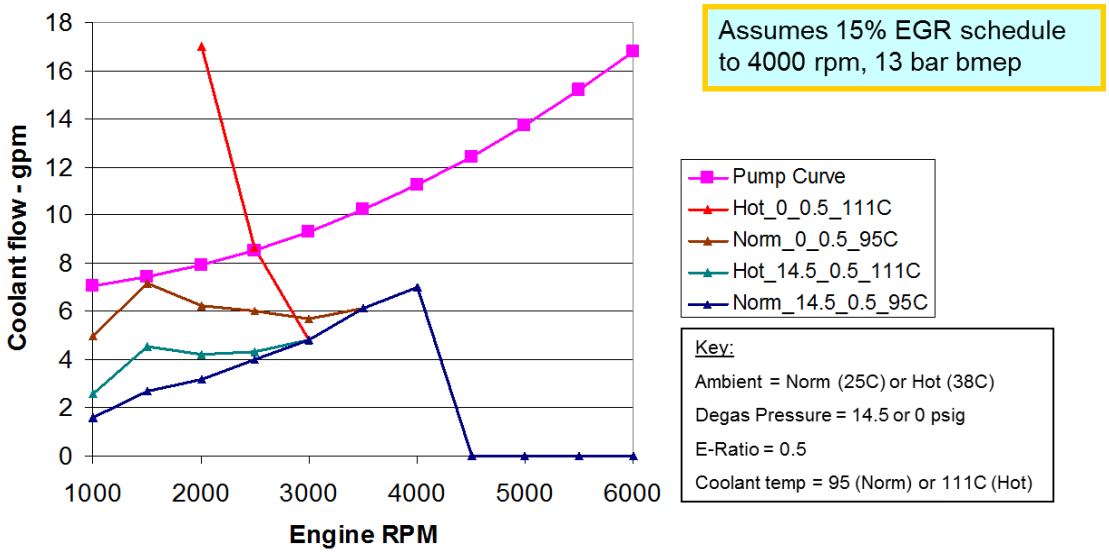


***Figure 139 - EGR cooler coolant flow requirement analysis.***

Extensive 3D CFD analyses were performed on the EGR cooler coolant cavity to ensure appropriate coolant flow distribution over the "hot end" of the EGR cooler, including the optimization of the internal baffling to balance coolant flow distribution with pressure drop. Five different baffle configurations were analyzed, with coolant temperatures reduced 25 ºC to acceptable levels and pressure drop reduced 14% under hot ambient conditions (Figure 140).

A modal analysis was performed on the entire EGR subsystem and the first mode was found to be 212 Hz (EGR valve rocking) which was below the target of 290 Hz. A strap bracket was added to support the top, cantilevered portion of the EGR valve to resolve this issue.

Lastly, a thermo-mechanical stress analysis was performed on the EGR cooler inlet tube including thermal, vibrational, and turbo-displacement inputs to the EGR "hot side" tube. The analysis was used to verify the correct number of de-coupling corrugations to avoid exceeding peak stress limits (Figure 141).

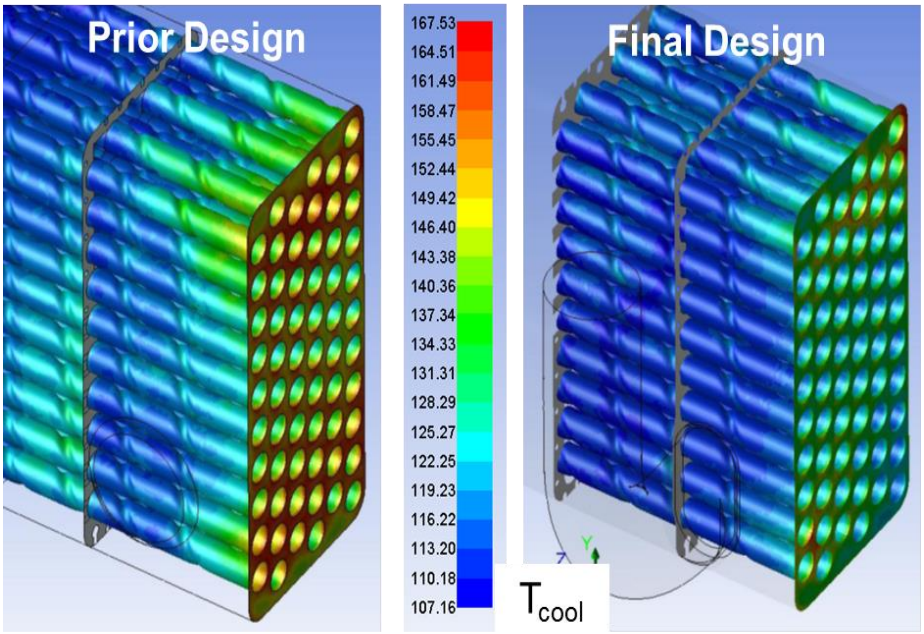


***Figure 140 - EGR cooler internal coolant cavity CFD study.***

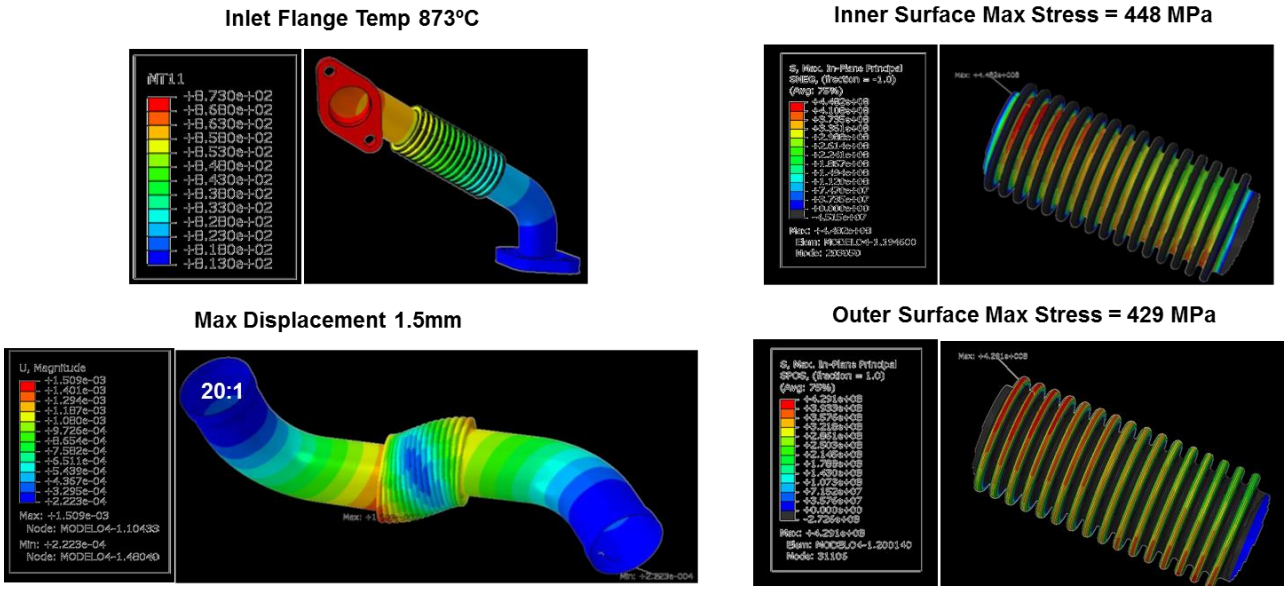


***Figure 141 - EGR inlet tube thermo-mechanical stress analysis from Borg-Warner.***

# Cooling System

## Design Objectives

The main objective of the cooling system is to protect the engine from exceeding critical metal temperature limits by providing adequate coolant flow under different operating conditions. Additional objectives are as follows:

- Achieve faster warm-up through split cooling.
- Minimize parasitic losses of water pump.
- Protect coolant from after-boil during engine shut-down.
- Design the cooling system for a Fusion demonstrator vehicle with the engine.
- Provide sufficient flow for EGR cooling.
- Maintain heater performance during start-stop condition.

## Design Assumptions

Design assumptions for the cooling system were as follows:

- Split-parallel flow cooling strategy.
- FEAD driven mechanical clutched coolant pump.
- Two thermostats (main thermostat and block thermostat).
- Auxiliary after-run electric coolant pump.
- Oil cooler.
- Two water-to-air charge air coolers (split WACAC).
    - Integrated into intake manifold
    - Remote mounted
- Low temperature coolant loop with electric coolant pump.
- Dual electric fans.

## System / Component Summary: Function, CAD Snapshots, Schematics

The cooling system is divided into two cooling loops, the high temperature loop (HTL) and low temperature loop (LTL). The HTL supports the cooling of the base engine, oil cooler, turbocharger, EGR cooler, heater core, and transmission oil cooler, while the LTL supports the integrated and remote mounted charge air coolers and water cooled condenser. General schematics of the two coolant loops are shown in Figure 142. The HTL is driven by a mechanical pump and a supplemental electric pump, and the LTL is driven by an electric pump.

## Design Verification Completed: CAE, Bench Test, Dyno Test

- 1D Simulations of both HTL and LTL completed
- 3D CFD of full vehicle under hood cooling pack sizing completed.
- Water pump FEA analysis completed.
- Water pump CFD analysis completed.
- 3D CHT analysis of cylinder head/block metal temperature prediction completed.
- Flow lab bench test of HTL and LTL completed.
- Dyno test with instrumented engine under peak load conditions completed.

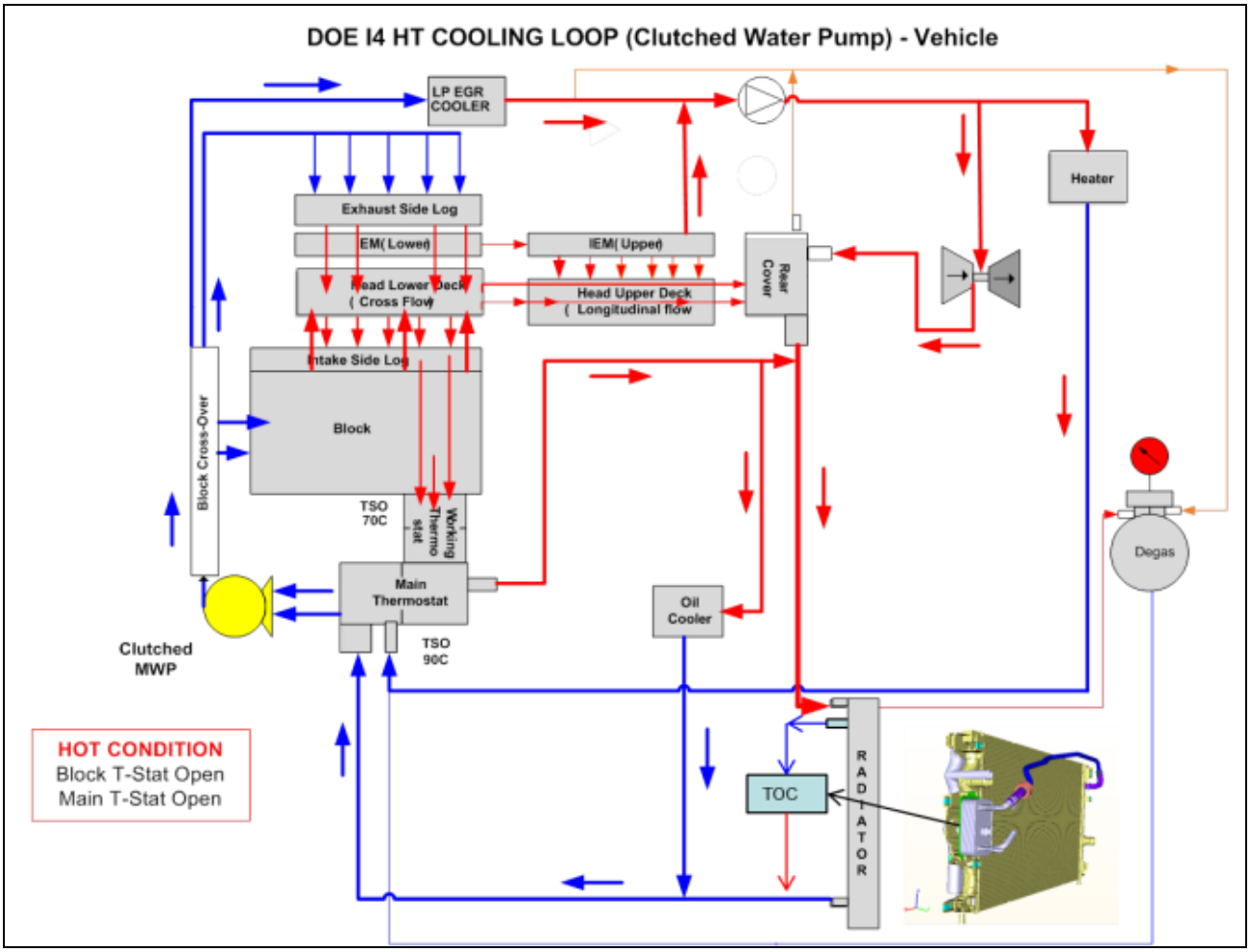


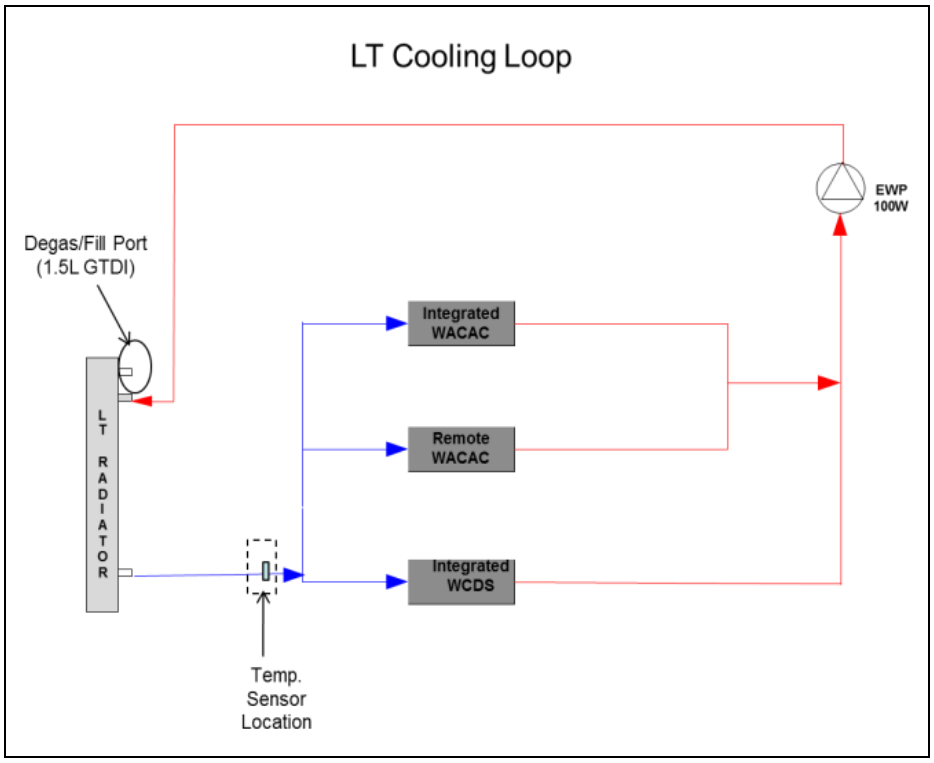


***Figure 142 - Cooling system schematics of high (top) and low (bottom) temperature loops.***

# Multi-Cylinder Engine Development

## Part Load

### Mini-Map BSFC Status vs. Targets

Figure 143 shows the 2.3L DOE engine BSFC status at mini-map points with optimized settings and 15% cooled EGR. The top graph shows the BSFC status compared to the target, while the bottom graph shows the % difference compared to the target. The BSFC targets for the engine were cascaded based on Ford Corporate Vehicle Simulation Program (CVSP) fuel analysis. As shown in Figure 143, the BSFC of the 2.3L GTDI DOE engine at all of the mini-map points is better than the corresponding BSFC target.

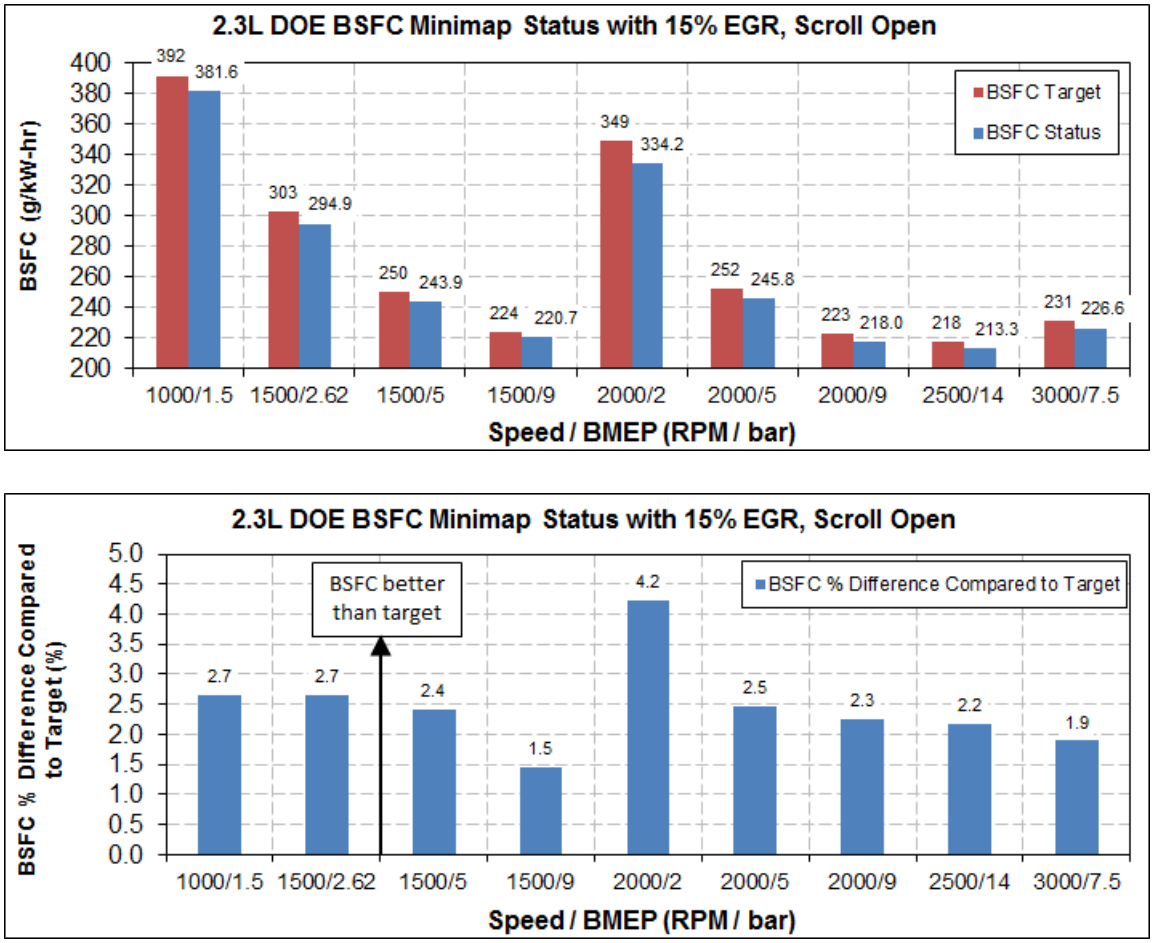


***Figure 143 - 2.3L DOE BSFC status at mini-map points (top graph) and % BSFC difference compared to the targets (bottom graph).***

### Benefit of Adding 15% EGR

Figure 144 shows multiple samples of the % BSFC improvement from adding 15% EGR. Both zero and 15% EGR were set to their respective optimal settings. Each comparison was taken back-to-back to maximize the accuracy of the measured difference.

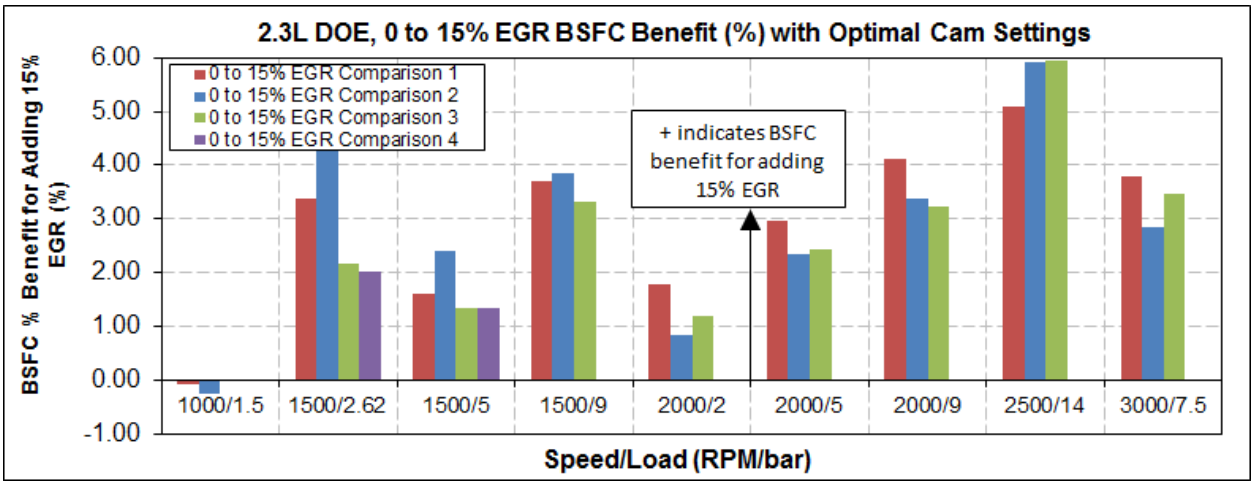


***Figure 144 - 2.3L DOE engine % BSFC improvement from 0 to 15% EGR from multiple samples.***

Adding EGR improves fuel economy at any speed/load where the engine has sufficient combustion stability to tolerate the added EGR, provided the EGR doesn't negatively impact combustion phasing due to knock.

Benefits of Cooled EGR:

**1.** Less heat is lost to the coolant and exhaust.

- Adding EGR lowers burned gas temperatures because the chemical energy released during combustion heats a greater mass of gases. Lower burned gas temperatures lead to less heat being lost to the coolant and the exhaust.

**2.** Pumping work (PMEP) reduction at low-to-medium load.

- For a given speed/load/cam/wastegate position, as more diluent is added, MAP increases because the engine has to flow the fresh charge plus the diluent. The increase in MAP results in less intake stroke pumping work. Adding a diluent at low-to-medium loads increases MAP and reduces pumping work since the engine is capable of flowing the fresh charge plus the diluent without additional help from cam phasing or wastegate position.

**3.** Greater conversion of CO into $CO_2$

- As EGR is increased, more CO is converted to $CO_2$ during combustion. The increase in $CO_2$ leads to more engine work because creating a molecule of $CO_2$ releases significantly more energy than a molecule of CO (consider that the enthalpy of formation for $CO_2$ is approximately -393.5 MJ/kmol compared to -110.5 MJ/kmol for CO). Possible mechanisms behind the reduction in CO are better A/F mixing and reduced dissociation (due to lower burned gas temperatures).

**4.** Combustion phasing improvement (CA50 reduction) at knock limited conditions.

- Adding cooled EGR helps to mitigate knock by making it less likely the critical molecules in the end-gas will collide and lead to the reactions that cause knock.

Drawbacks of Cooled EGR:

**1.** Hydrocarbon (HC) penalty.

- As cooled EGR is added, experimental data shows that HC emissions increase. It is hypothesized that the increase in HC emissions are due to earlier flame quenching from both the dilute mixture and lower burned gas temperatures which result in less oxidation of HC during the expansion stroke.

2. Combustion instability.

- Adding cooled EGR negatively impacts combustion stability because it slows down combustion, making the burn durations longer and more variable. When cooled EGR is added to an air-fuel mixture, the flame front reactions become slower and more variable because the burned gas temperature is lower and the diluent makes it more difficult for the fuel molecules and oxygen to collide.

3. Light load cam phasing penalty and medium-to-high load wastegate/cam phasing penalty.

- At light loads where combustion stability is often poor, adding cooled EGR degrades combustion stability even further for the reasons described in 2) above. In addition, at light loads the engine is able to tolerate more internal EGR (hot) than external cooled EGR. To compensate for the external cooled EGR, the cams need to be phased in such a way to reduce internal residual and generate heat at the time of spark to reliably ignite the charge. The net effect of these actions is typically a reduction in the overall residual fraction and a degradation in fuel economy at light loads.
- At medium-to-high load, there will be a point where the increase in MAP needed to flow the EGR requires enough additional wastegate and/or cam phasing to meet the requested torque that PMEP is worse than the base case without EGR. The net result of adding EGR will still be a fuel economy improvement, but it will be less than if the engine had the capability to flow the fresh charge and the EGR without the additional wastegate and/or cam advance.

## Scroll Closed vs. Scroll Open Fuel Benefits with 15% EGR

The turbocharger on the 2.3L DOE engine has an electric wastegate and a turbine scroll control valve. The strategy for the electric wastegate is to run open, unless more boost is needed to meet the torque request. An assessment of the fuel impact of closed vs. open scroll is covered in this section.

The entrance to the turbine has two “ports” as shown in Figure 145 and Figure 146. The turbo scroll control valve is able to open or close one of the ports into the turbine, which has some advantages/disadvantages. With the turbo scroll control valve closed, one port is blocked to the turbine, which has the following impacts:

- The exhaust velocity into the turbine is increased because the area into the turbine is reduced. The increased velocity improves transient response and provides good low speed torque.

- The pressure in the exhaust increases because the orifice flow coefficient and area are reduced. The increase in exhaust pressure causes exhaust stroke pumping work to rise and also increases in-cylinder residual which negatively impacts combustion phasing at knock-limited conditions. A cylinder pressure pumping loop showing the increased exhaust pressure from closing the scroll at 2500/14 bar is shown in Figure 147.

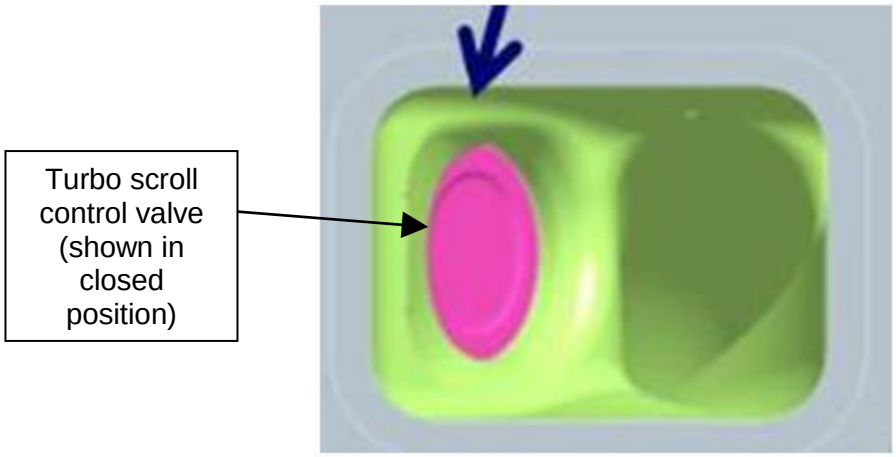


***Figure 145 - Flange view of exhaust entrance into turbine.***

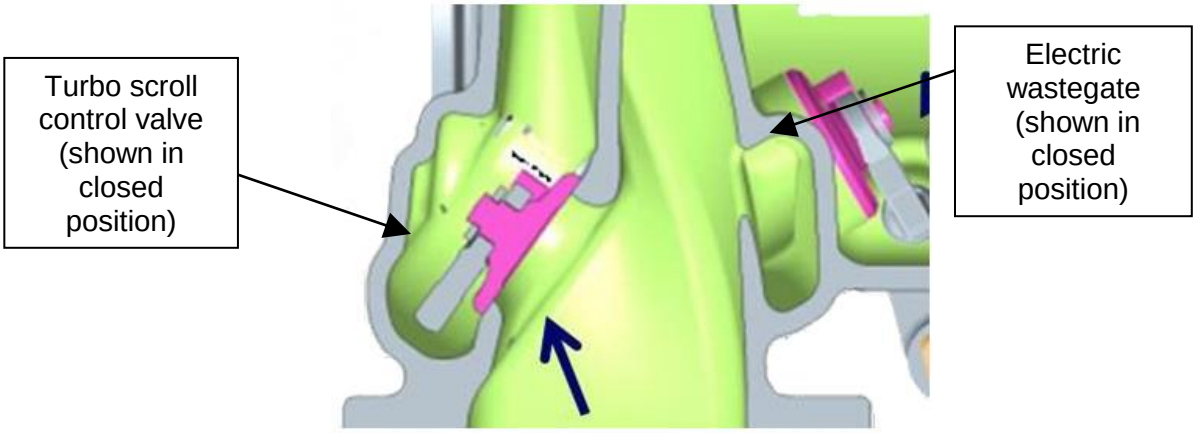


***Figure 146 - Top view of exhaust entrance into turbine.***

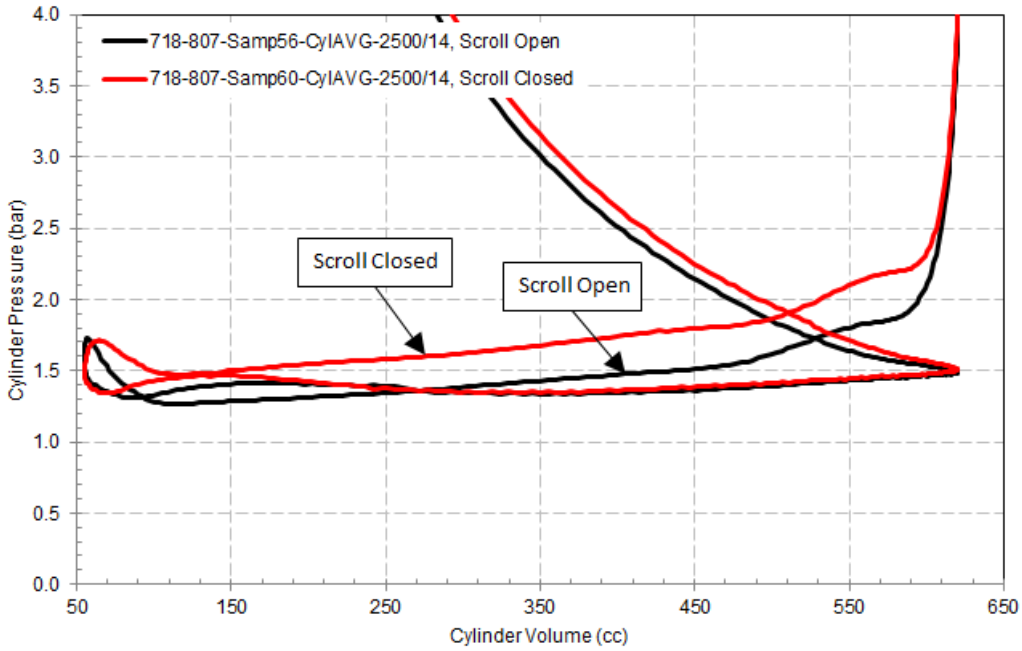


***Figure 147 - Pumping loops at 2500 rpm/ 14 bar BMEP with the turbo scroll control valve open (black line) and closed (red line).***

Figure 148 through Figure 150 show the scroll closed to scroll open fuel economy benefits at mini-map points with all points utilizing 15% EGR. Figure 148 shows the reduction in turbine inlet pressure from closed to open scroll (top graph) and the corresponding fuel benefit (bottom graph) that results from the reducing the exhaust pressure and pumping work with the scroll open.

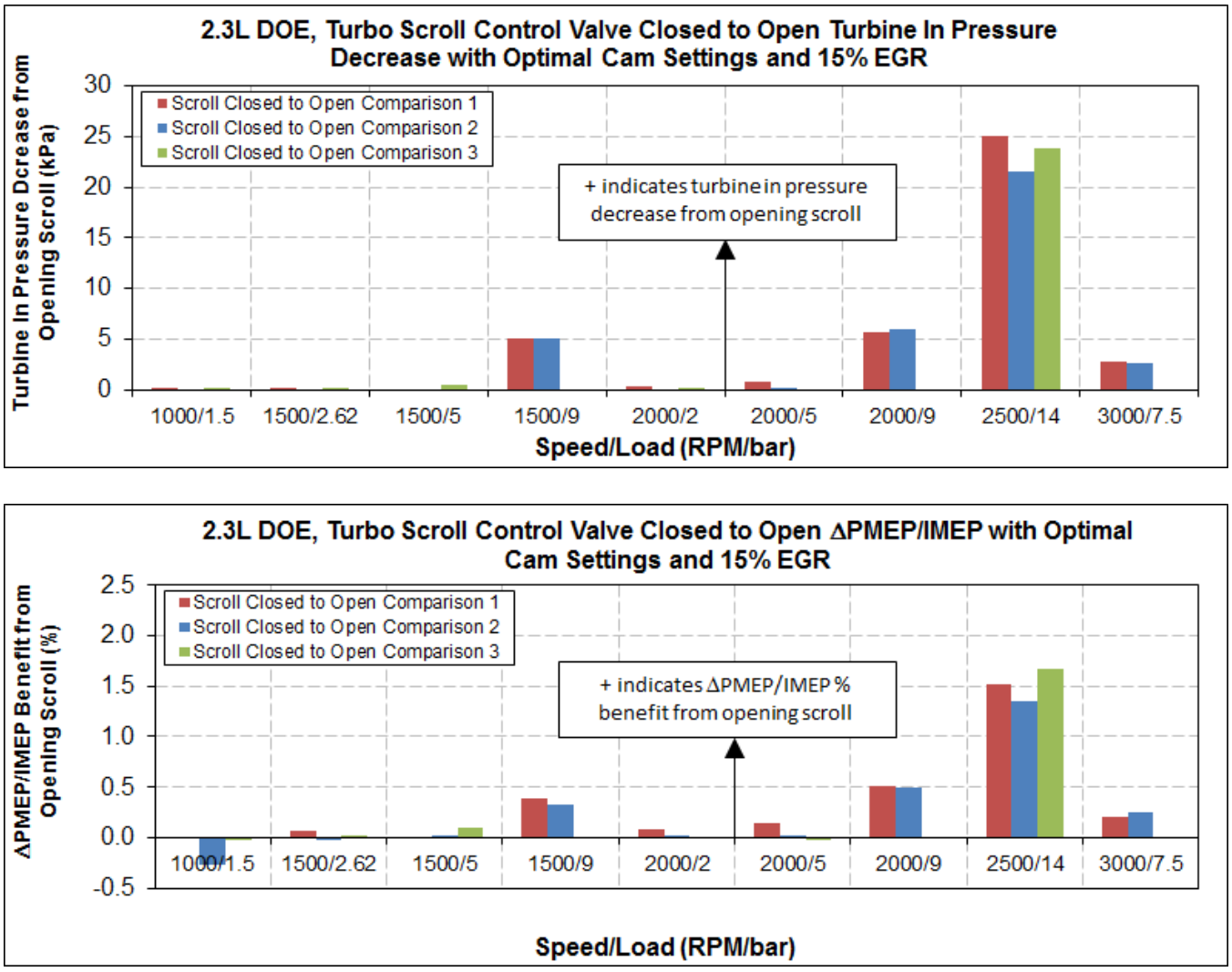


***Figure 148 - Turbo scroll control valve closed to open turbine in pressure decrease (top graph) and the corresponding pumping work (ΔPMEP/IMEP) fuel benefit (bottom graph) at mini-map points.***

Figure 149 shows the CA50 improvement (top graph) and the corresponding % ISFC fuel benefit from the CA50 improvement (bottom graph) with the scroll open. Figure 150 shows the sum of the pumping work and CA50 improvements. Each comparison was taken two to three times, and was run back-to-back for maximum accuracy of the measured difference.

The measured BSFC benefit for many of the mini-map points was within +/- 0.5% (close to the accuracy of the fuel meter), and therefore it was deemed more accurate to use the PMEP fuel benefit (ΔPMEP/IMEP) and an empirical CA50 vs. % ISFC correlation to determine the fuel benefits from opening the turbo scroll control valve.

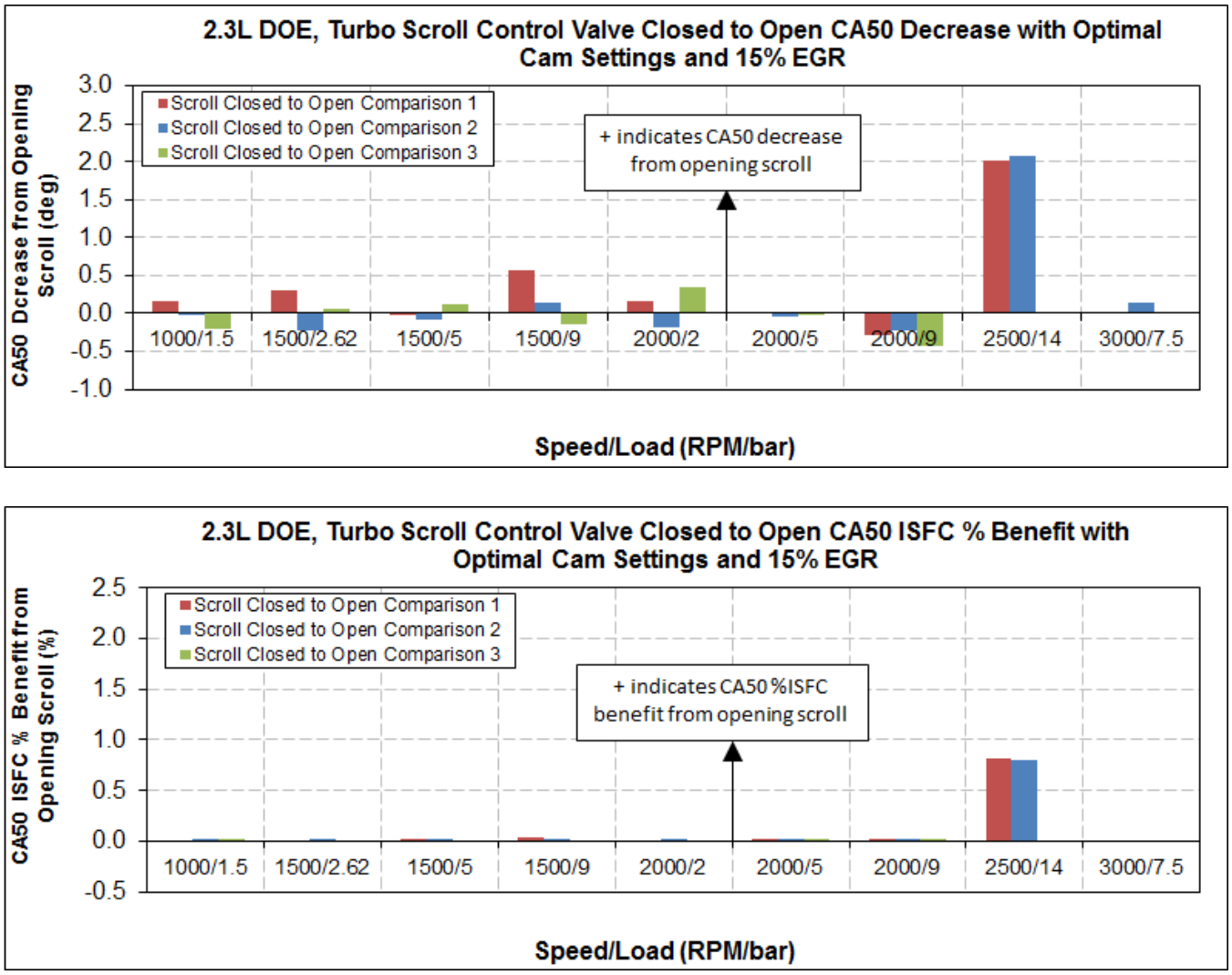


***Figure 149 - Turbo scroll control valve closed to open CA50 improvement (top graph) and the corresponding %ISFC fuel benefit (bottom graph) at mini-map points.***

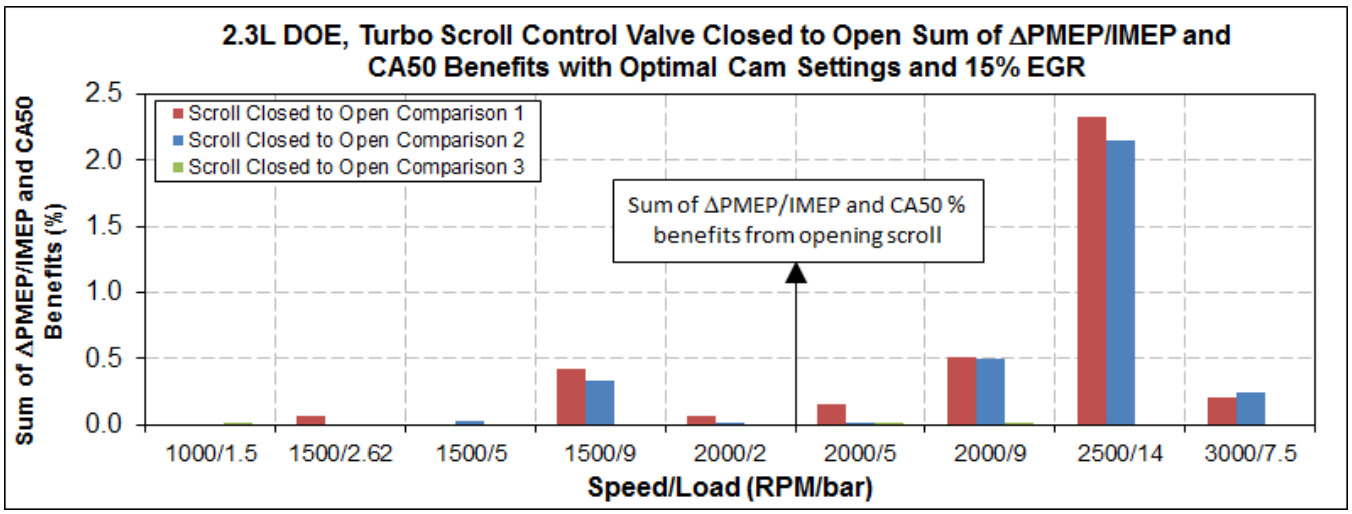


***Figure 150 - Turbo scroll control valve closed to open sum of ΔPMEP/IMEP and CA50 % fuel consumption benefits.***

## Variable Displacement Oil Pump and Oil Squirter Effects on Fuel Consumption

Variable Displacement Oil Pump

A cut-away view of the variable displacement oil pump (VDOP) is shown in Figure 151. When the VDOP solenoid valve is actuated, an oil pressure chamber behind the blue ring 'slide' pushes the blue ring 'slide' down to be more concentric with the rotor. The reduced eccentricity between the outer ring and rotor reduces output flow and oil pressure.

The blue ring 'slide' can only be pushed down if oil pressure is greater than about 280 kPa (40 psi). This amount of pressure is needed to overcome the priming spring which provides force to keep the VDOP in the high pressure (high eccentricity) mode.

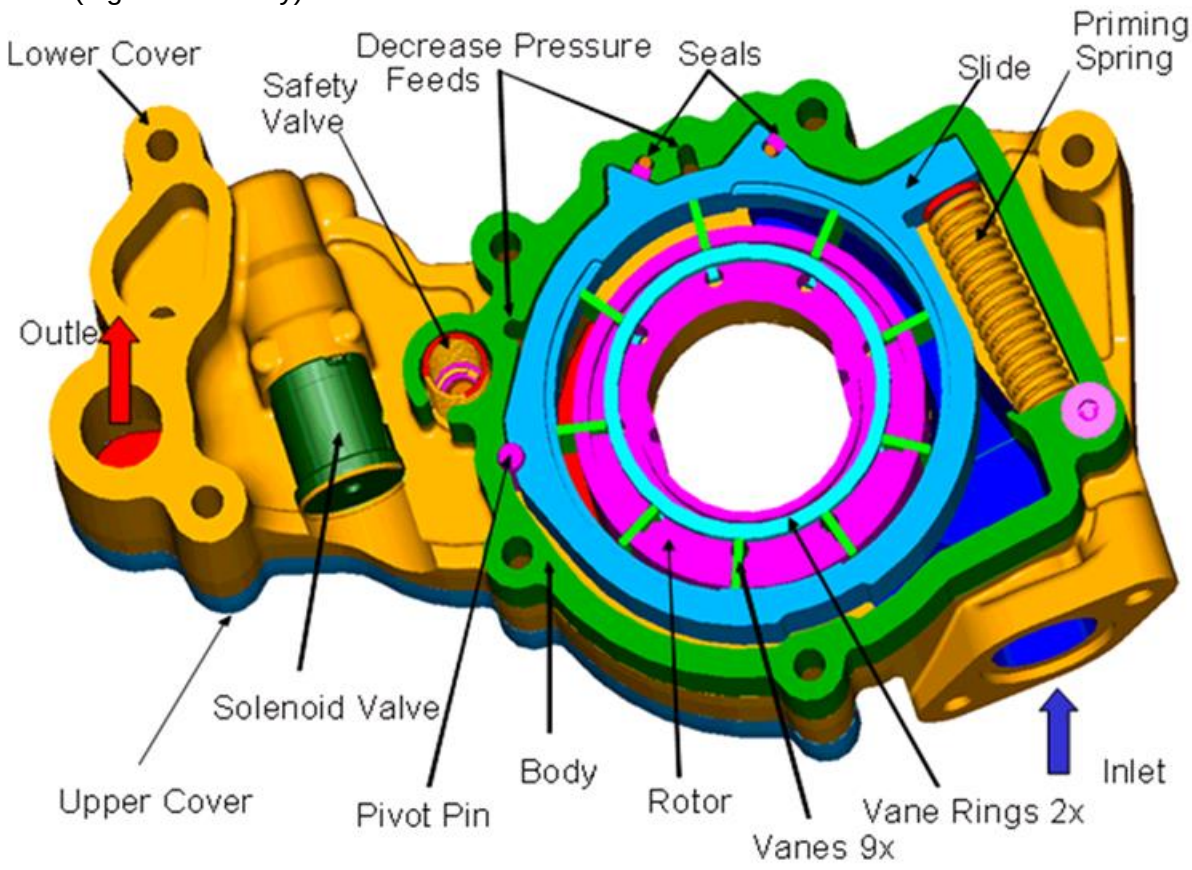


***Figure 151 - Cut-away view of variable displacement oil pump (VDOP).***

The fuel benefit of the VDOP scales based on the oil pressure reduction from high pressure (HP) to low pressure (LP) mode. The greater the oil pressure change, the bigger the friction reduction, and the greater the BSFC benefit.

The fuel impact of the VDOP is coupled to the oil squirters because the oil squirters have a direct impact on oil pressure. When the oil squirters are on, part of the oil flow is diverted to spraying oil on the underside of the pistons, which lowers oil pressure. Conversely, when the oil squirters are off, the oil pressure is higher. Therefore, it would be expected that the BSFC impact of the VDOP to be smaller when the oil squirters are on and larger when the oil squirters are off because when the oil squirters are off, greater pressure reductions can be achieved by switching the VDOP from HP to LP mode. A graph showing the oil pressure with all of the permutations of VDOP in HP/LP mode and the oil squirters on and off is shown in Figure 152.

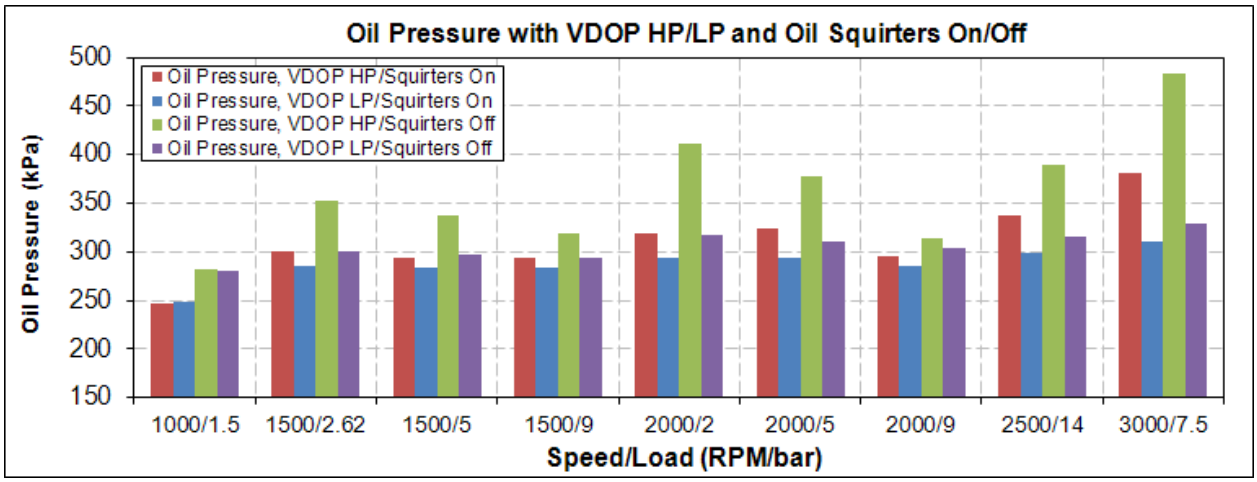


***Figure 152 - Oil pressure at mini-map points with all permutations of VDOP in HP/LP mode and oil squirters on and off.***

Figure 153 shows the % BSFC improvement (red bars) and oil pressure reduction (blue bars) of the variable displacement oil pump shifting from high pressure to low pressure mode at selected mini-map points with the oil squirters on (top graph) and oil squirters off (bottom graph). The data in Figure 153 was run back-to-back on the same day to increase the accuracy of the data. Differences within ± 0.2 (± 0.2% or ± 20 kPa) can be considered negligible. A few observations from Figure 153 are the following:

- The BSFC benefit of the VDOP is significant at more speed/load points and larger when the oil squirters are off.

- It takes a larger pressure reduction at higher loads to get the same BSFC benefit as a lower load point. For example, in the bottom graph of Figure 153, the pressure reduction between the VDOP shifting from HP to LP mode between 2000/5 and 2500/14 was similar at about 70 kPa, but the BSFC improvement at 2000/5 bar was 0.5%, and only about 0.3% at 2500/14. This occurs because the fuel consumption benefit due to a reduction in FMEP is equal to the change in FMEP divided by the IMEP (at constant indicated thermal efficiency). Therefore a larger improvement in FMEP is needed at higher loads to get the same fuel benefit as a lower load point.

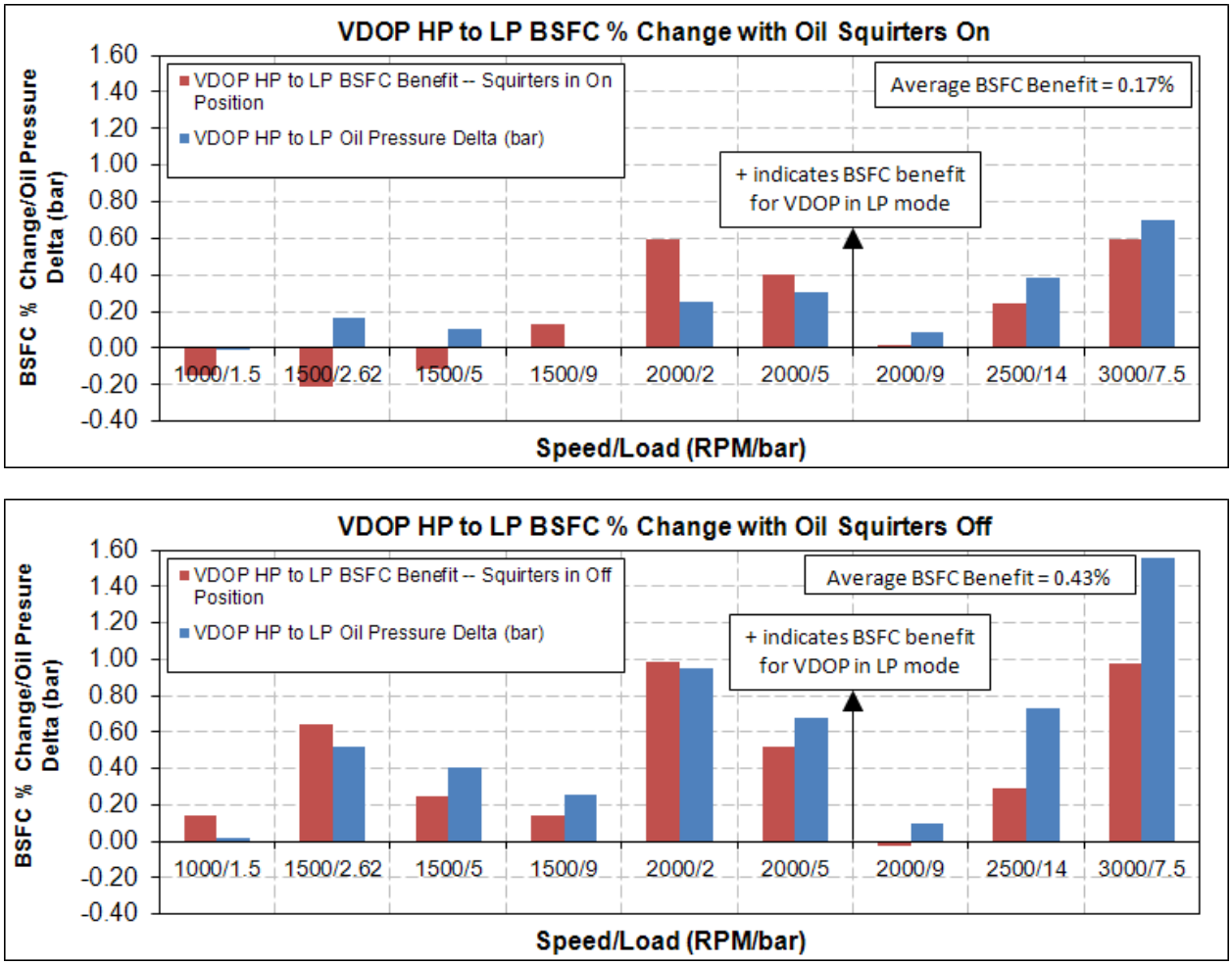


***Figure 153 - VDOP HP to LP mode BSFC % improvement (red bars) and oil pressure reduction (blue bars) at selected mini-map points with the oil squirters on (top graph) and off (bottom graph).***

Oil Squirters

Similar to the VDOP, the fuel benefit of switching the oil squirters on to off is coupled to the VDOP mode. When the oil squirters are switched from on to off, competing factors determine whether or not there is a BSFC benefit. These factors are:

- Switching the oil squirters off results in an increase in the oil pressure and a decrease in the oil temperature. Both the increase in the oil pressure and decrease in oil temperature result in greater amounts of engine friction (FMEP), which in turn causes a corresponding loss in fuel efficiency.
  - A graph showing the oil pressure with all the permutations of VDOP in HP/LP mode and the oil squirters on and off is shown in Figure 152.
  - A graph showing the oil temperature with all the permutations of VDOP in HP/LP mode and the oil squirters on and off is shown in Figure 154.

- Switching the oil squirters off also causes there to be no oil spraying on the underside of the pistons, which increases the piston temperature. An increase in piston temperature translates to less combustion heat lost to the piston, which improves indicated efficiency.

As shown in Figure 152, when the VDOP is in HP mode, there is a bigger increase in oil pressure when the oil squirters are shut off compared to when the VDOP is in LP mode. Because the increase in oil pressure results

in a fuel efficiency loss, it would be expected that there is a bigger fuel efficiency benefit from turning the oil squirters off when the VDOP is in LP mode.

Figure 155 shows the oil squirter on to off BSFC % improvement (red bars) and oil pressure reduction (blue bars) at mini-map points with the VDOP in HP mode (top graph) and LP mode (bottom graph). The data in Figure 155 was run back-to-back on the same day to increase the accuracy of the data. Differences in the range ± 0.2 (± 0.2% or ± 20 kPa) are probably negligible. A couple things to note from Figure 155:

- The negative oil pressure delta in Figure 155 (blue bars) shows how much the oil pressure increases when the oil squirters are turned off. Notice when the oil squirters are turned off with the VDOP in LP mode, the oil pressure increases much less.

- The BSFC benefit of the oil squirters is basically negligible with the VDOP in HP mode, but is significant at more speed/load points and larger when the VDOP is in LP mode.

- Although the trends are not completely clear, if you look at the bottom graph of Figure 155 (VDOP in LP mode) it appears that there is a greater benefit for turning the oil squirters off at lower loads. This trend may be linked to the fact that at lower loads a greater percentage of the total mass of combustion gases comes into close proximity of the piston.

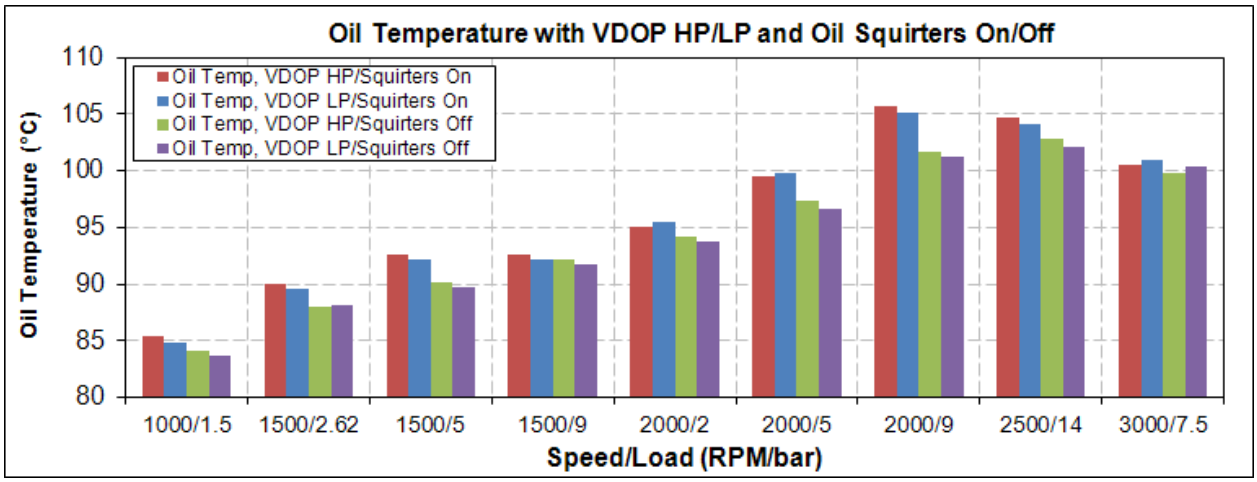


***Figure 154 - Oil temperature at mini-map points with all permutations of VDOP in HP/LP mode and oil squirters on and off.***

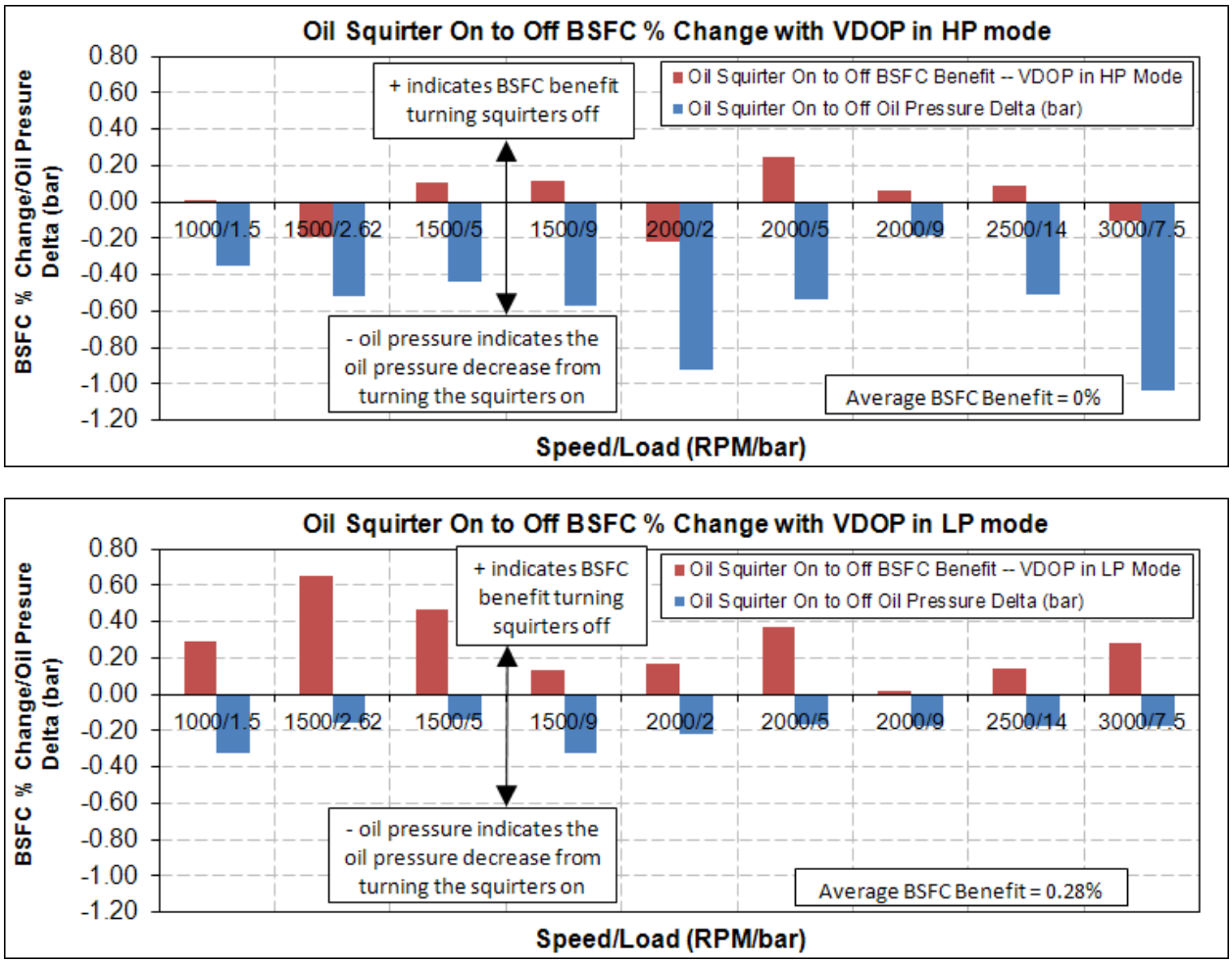


***Figure 155 - Oil squirter on to off BSFC % improvement (red bars) and oil pressure reduction (blue bars) at mini-map points with the VDOP in HP mode (top graph) and LP mode (bottom graph).***

VDOP/Oil Squirter Map

Figure 156 shows a proposed operating map for the VDOP and oil squirters based on the data in this section.

- Low speed/part load – VDOP in LP mode and oil squirters off for best fuel economy.
- Low speed/high load – VDOP in LP mode for fuel economy, and oil squirters on for CA50 (knock) reduction (cooler piston).
- High speed/all loads – VDOP in HP mode for engine protection (higher oil pressures), and oil squirters on for piston cooling (durability) and CA50 (knock) reduction.

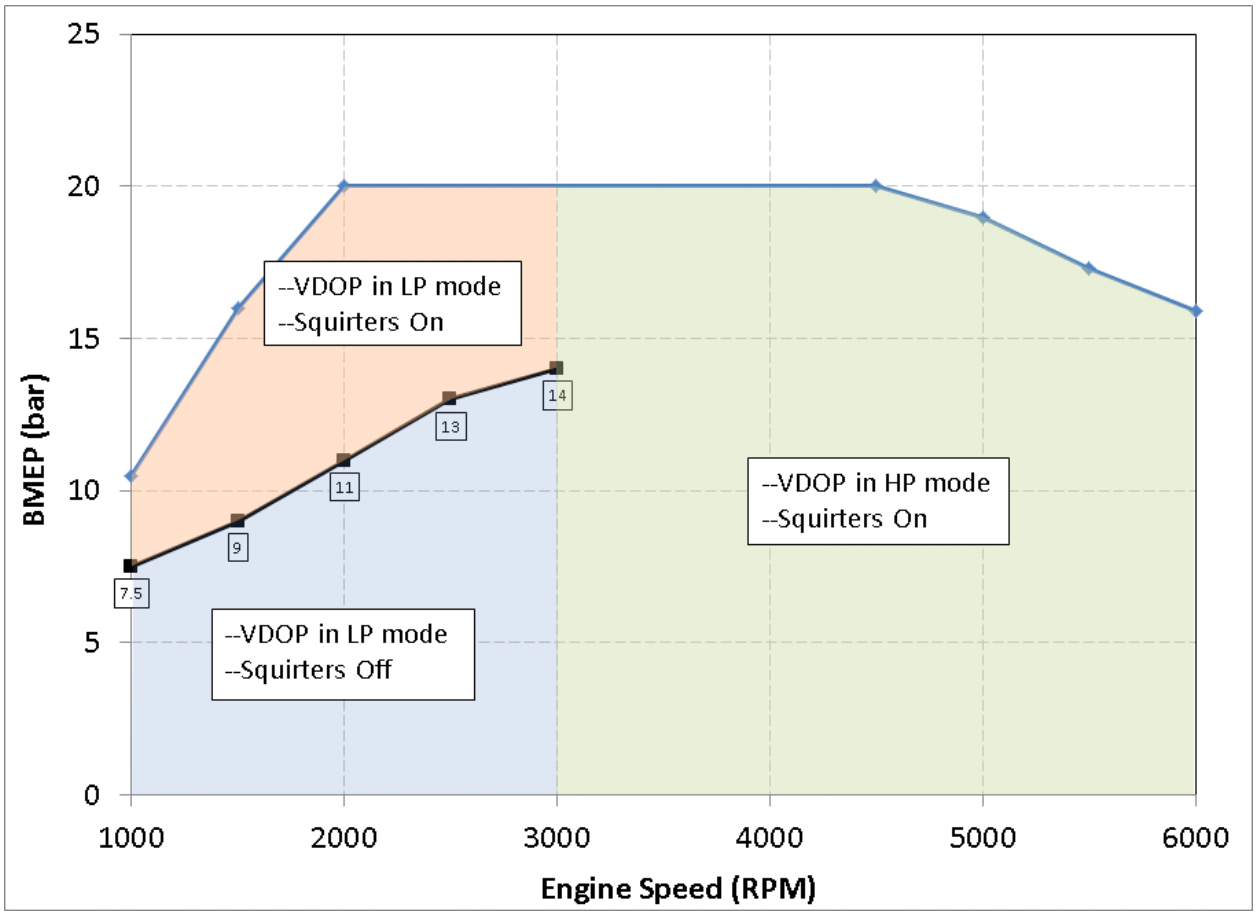


***Figure 156 - Proposed VDOP/oil squirter map.***

## Micro-Stratification Results at 1500/5 bar

Micro-stratification improves BSFC by enabling leaner operation with two injections. The first injection early in the intake stroke provides a homogeneous lean air-fuel mixture; this is where most of fuel is injected. The second injection is a stratified injection late in the compression stroke near spark timing. The second small injection is made near spark timing to get a locally richer mixture and extra turbulence near the spark plug to get more repeatable combustion events, which enables the engine to have stable combustion at leaner overall air-fuel ratios.

The goal of the micro-stratification testing was to obtain the best tradeoff of minimum BSFC and NOx emissions. BSFC and fuel efficiency improve as the air-fuel ratio (A/F) ratio gets leaner as long as the engine combustion is stable due to 3 main factors:

1. Greater conversion of CO to $CO_2$ up to about 16:1 A/F. The increase in $CO_2$ leads to more engine work because creating a molecule of $CO_2$ releases significantly more energy than creating a molecule of CO (the enthalpy of formation for $CO_2$ is approximately -393.5 MJ/kmol compared to -110.5 MJ/kmol for CO).

2. Less pumping work because MAP increases to flow the excess air.

3. Lean of stoichiometry, excess air is a diluent that lowers the burned gas temperatures (combustion products heat a greater mass of gases). Lower burned gas temperatures reduce heat transfer to the walls and improve indicated thermal efficiency (ITE).

NOx emissions are mainly a function of peak burned gas temperature and burned gas oxygen concentration, and thus are affected by A/F ratio, dilution concentration, CA50 (spark timing), and load.
In order to determine the best tradeoff of minimum BSFC and NOx, the following variables were fine-tuned at 1500/5 bar with 0% EGR and 15% EGR (bold text indicates a critical variable).

- **A/F**
  - Strategy for A/F was to run as lean as possible while maintaining acceptable combustion stability.
    - BSFC improves as the A/F gets leaner as long as the engine is stable.
    - NOx emissions improve past a lambda of ~1.1.

- **DIMINPW2** (minimum pulse width on injection 2)
  - Strategy for DIMINPW2 was to run with the smallest pulse width possible on injection 2 (limited by either combustion stability or injector capability).
    - Smaller pulse width on injection 2 improved both BSFC and NOx up to the combustion stability limit. The combustion stability limit appears to be burn rate related; experimental data showed that a 0 to 10% burn time greater than ~35° resulted in unstable combustion.
- **CA50**
  - Strategy with CA50 was to sweep this variable to get the optimal tradeoff of BSFC/NOx/combustion stability.
    - CA50 traded off significant amounts of BSFC, stability, and NOx. The optimal CA50 with micro-stratification at 1500/5 bar with both 0 and 15% EGR occurred between a CA50 of about 1-3° aTDC.

- End of second injection relative to spark (EOI2 relative to spark) [+ value indicates that EOI is before spark]
  - Strategy with end of second injection relative to spark was to stay in the range +5° to -10°.
    - Experimental data showed that as long as EOI2 relative to spark was in range of +5 to -10 the variable was not very important; it traded off a slight amount of NOx and stability.
    - Earlier than ~+10 resulted in stability issues.

- Fuel rail pressure (FRP)
  - FRP needed to be 1450 psi or above to avoid smoke. A value between 2000-2100 psi was chosen to minimize fuel rail pressure dynamics.
    - Fuel rail pressure dynamics were significant with lean air/fuel ratios at 1500/5 bar with the 2.3L GTDI DOE hardware. In order to compensate for the fuel rail dynamics, the fuel to each cylinder was trimmed to bring CA50 within about a degree between all the cylinders.
    - Other than needing to be at 1450 psi and above, FRP was surprisingly not an important variable. At each FRP tested, a DIMINPW2 sweep was done. It was found that the same optimal BSFC, NOx, and stability were attainable at the most favorable DIMINPW2 for every FRP tested.

All the 1500 rpm / 5 bar micro-stratification data sweeps were performed with optimal stability cam timing (-30/10). These cam timings were chosen because they provided the best combination of stability, compression heating, and the lowest amount of internal residual; which allowed the leanest A/F possible. The drawbacks of running optimum stability timing are it negatively impacts fuel by about ~4% compared to optimum conditions for BSFC at stoichiometry at this speed/load, and it is the cam position with the greatest NOx.

When the optimal micro-stratification settings were determined at 1500/5 bar for both 0 and 15% EGR, 3 back-to-back comparison runs were taken, assessing the BSFC/NOx/stability between the following four optimized conditions. All points were taken 3 times each run to get a reliable average for the data.

- 1500/5, 0% EGR, 14.6:1 A/F, baseline with 0% EGR
- 1500/5, 15% EGR, 14.6:1 A/F, baseline with 15% EGR
- 1500/5, 15% EGR, 22:1 A/F, micro-stratification (this was the optimal A/F with 15% EGR)
- 1500/5, 0% EGR, 26:1 A/F, micro-stratification (this was the optimal A/F with 0% EGR)

The blue bars in Figure 157 are the averaged data from comparison run 1, the red bars are the averaged data from comparison run 2, and the green bars are the averaged data from comparison run 3. BSFC is the graph in the upper left, feedgas NOx is the graph in the upper right, ERMSIMEP_COV is the graph in the lower left (engine root mean squared COV of IMEP, a measure of the combustion stability, <2% is acceptable combustion stability), ELSIMEP_LNV is the graph in the lower right (the lowest normalized value of IMEP, >70% is acceptable combustion).

Figure 158 shows the percent BSFC benefits from the BSFC data in Figure 157. The top graph of Figure 158 shows the percent BSFC benefits relative to 14.6:1 A/F, 0% EGR, and the bottom graph of Figure 158 shows the % BSFC benefits relative to 14.6:1 A/F, 15% EGR.

Note the following from Figure 157 and Figure 158 at 1500 rpm/5 bar:

- Micro-stratification has significant % BSFC benefit relative to both 14.6:1 with 0% EGR (about 7.3%) and 14.6:1 with 15% EGR (about 5.6%).
- The optimized micro-stratification results with either 0% EGR or 15% EGR achieve approximately the same BSFC (about 230 g/kW-hr), NOx (about 260 ppm), and stability.

Some other observations from the micro-stratification testing are as follows:

- At 1500 rpm with optimum stability cam timing, 5 bar is close to the maximum load attainable with micro-stratification on this engine (MAP is approximately 91 kPa).
- Micro-stratification testing was attempted at 1500/5 bar with -3/3 cam timing, since -3/3 looked promising with low internal residual and significantly improved pumping work compared to optimum stability cam timing, but there was not enough torque reserve to get the A/F lean enough to get good results.

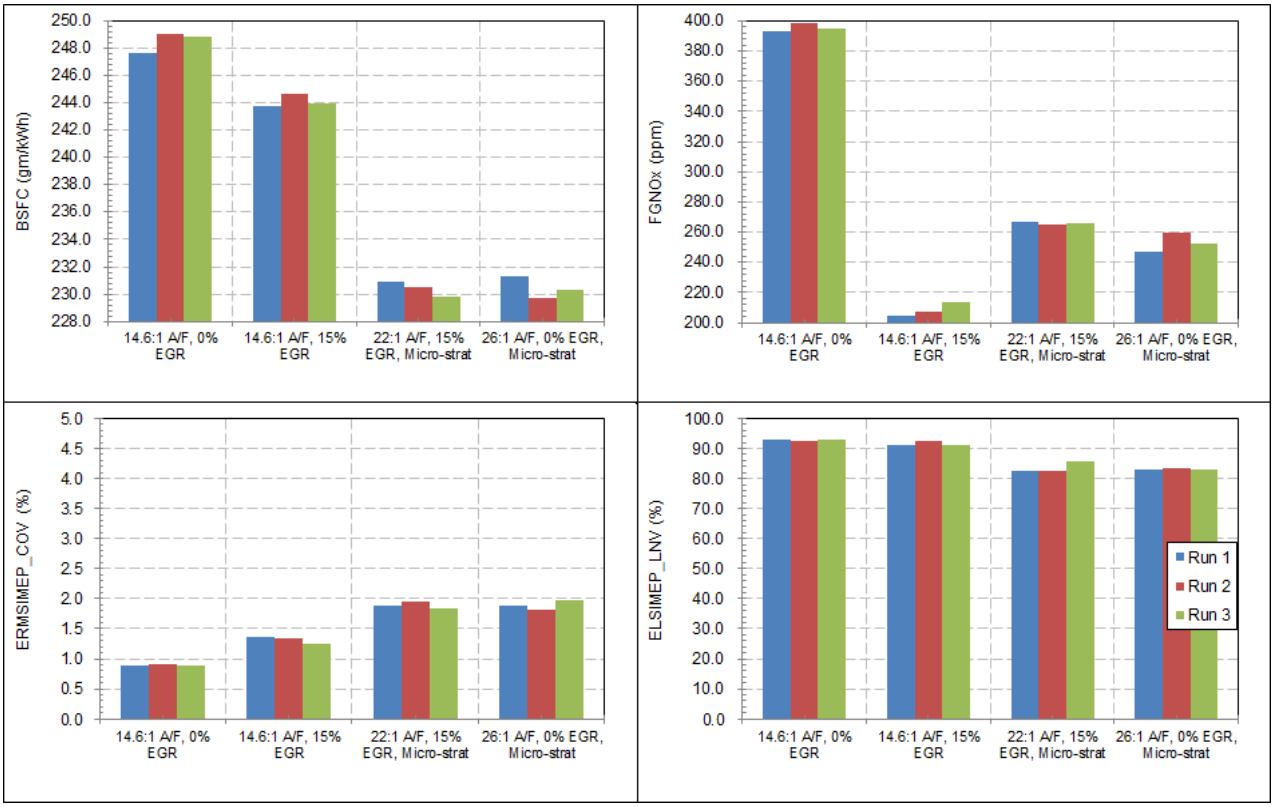


***Figure 157 - Optimized results at 1500/5 bar with four combinations: [14.6:1 A/F and 0% EGR], [14.6:1 A/F and 15% EGR], [22:1 A/F, 15% EGR, micro-strat], and [26:1 A/F, 0% EGR, micro-strat].***

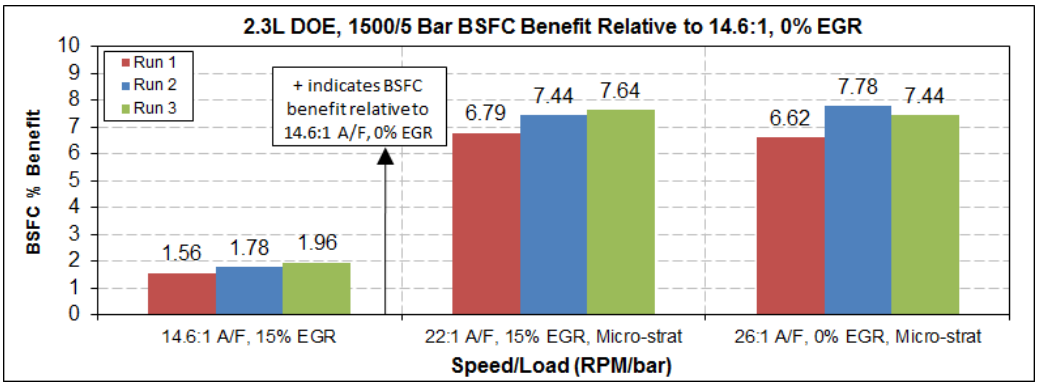


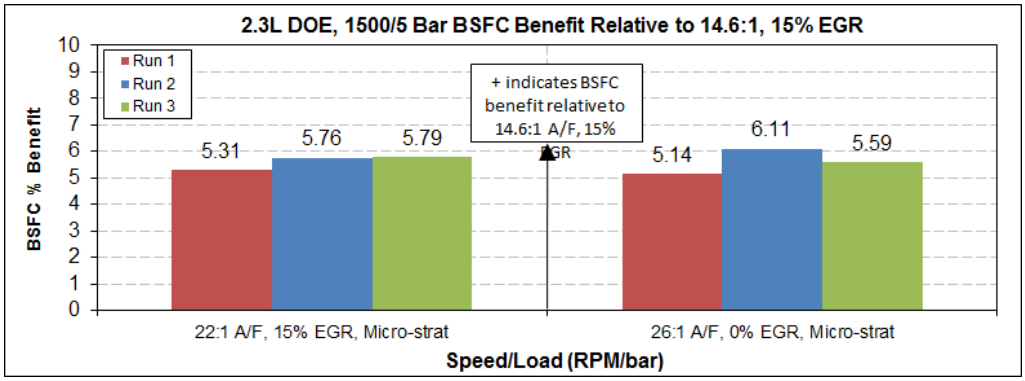


***Figure 158 - % BSFC benefit relative to 14.6:1 A/F, 0% EGR (top graph) and 14.6:1 A/F, 15% EGR (bottom graph).***

## Low Load Combustion Stability

The objective of the low load combustion stability testing was to determine how much EGR the engine could tolerate at its limiting conditions and to ensure the engine is robust to spark retard at idle. The testing consisted of the following three sweeps outlined below, and the combustion stability was evaluated vs. the criteria for each of these conditions.

- 1500 RPM, 0.7 bar BMEP, EGR sweep
  - Viewed this speed/load as a realistic minimum load you could maintain in a vehicle for an extended period (not a fast transient). For example, coming down a long shallow grade or driving with a high tailwind.
  - Combustion criteria:
    - ERMSIMEP_SD < 7 kPa
    - ELSIMEP_LNV > 70%

- 1000 RPM, 0.12 EECLOAD, 0 torque, EGR sweep
  - Simulates the case just before entering deceleration fuel shut-off.
  - Combustion criteria:
    - No misfire (ELSIMEP_LNV > 0)
    - Hydrocarbons < 15,000 PPM C1 (FGHC < 15000)

- 600 RPM, 0.7 bar BMEP, universal idle with 0% EGR, spark sweep
  - Universal idle point - not planning to run EGR at idle
  - Combustion criteria:
    - Robust to 15° of spark retard from MBT for torque reserve
    - ELSIMEP_SD < 14 kPa
    - ELSIMEP_LNV > 70%

Determining Optimum Stability Cam Position

The three sweeps above need to be run with optimal stability cam timing. In order to find the optimum stability position, intake VCT sweeps were evaluated at 1500 RPM / 0.7 bar BMEP. The optimum stability position was chosen as the point with the best combustion stability (lowest ERMSIMEP_SD and highest ELSIMEP_LNV), and also the greatest amount of compression heating (indicated by highest FGNOx and shortest 0-10% burn time). Figure 159 shows the intake VCT sweeps used to determine the optimum stability cam positions. The initial intake sweeps were taken with 0, 10, and 20° of exhaust retard (black, red and blue lines, respectively) and 0% EGR. In Figure 159, the upper left graph is ERMSIMEP_SD (engine RMS standard deviation of IMEP, <7 kPa indicates good combustion stability), the upper right graph is ELSIMEP_LNV (lowest normalized value of IMEP as a percentage of the mean IMEP, >70% indicates good combustion). The lower left graph is feedgas NOx, and the lower right graph is average 0-10% burn time. Based on the initial results, optimum stability cam timing appeared to be either -40/10 or -30/10. One more intake VCT sweep was taken with 15% EGR (pink line), and the optimum stability cam position was determined to be -30/10, because it was the point with the best combustion stability and highest compression heating.

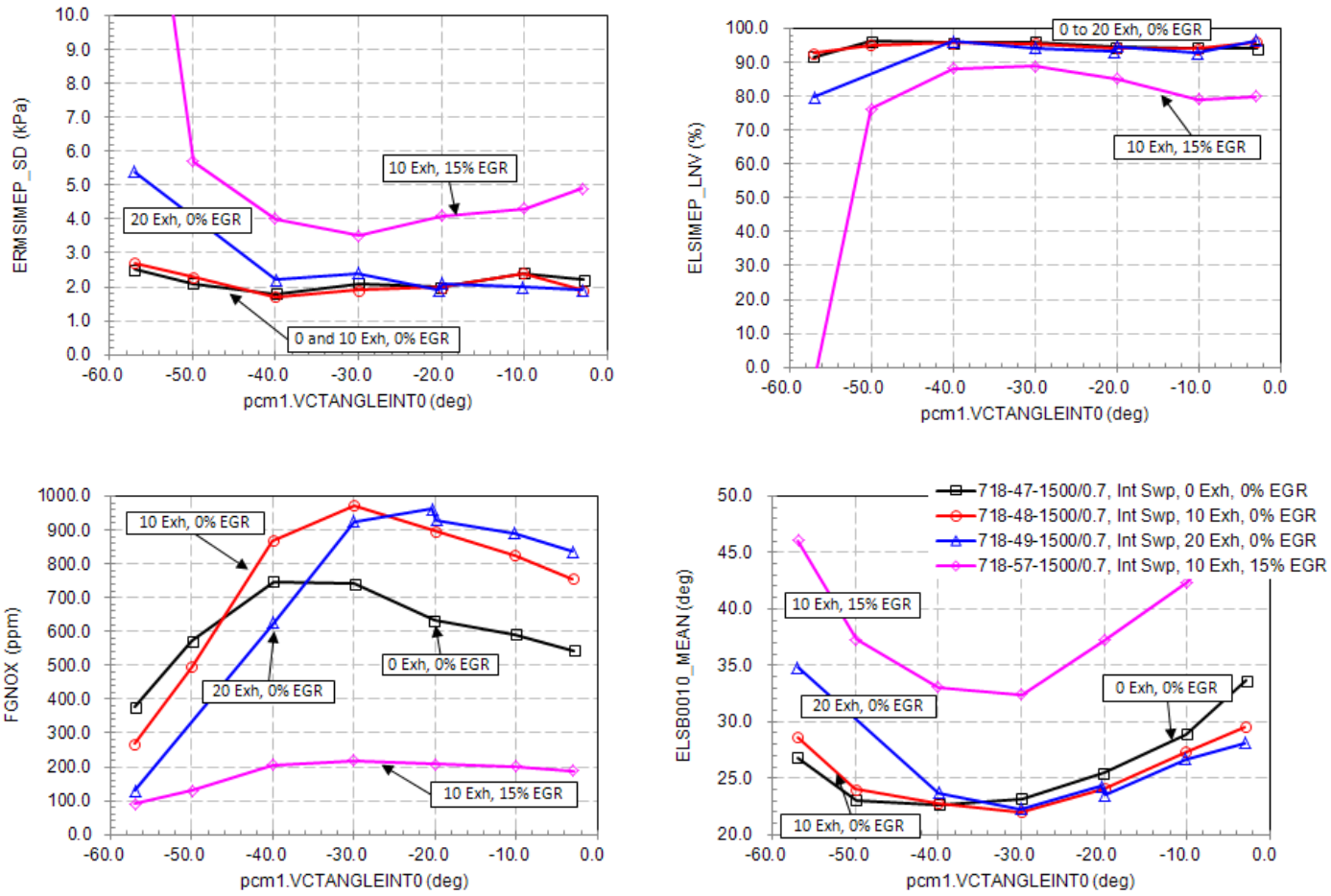


***Figure 159 - Intake VCT sweeps at various levels of exhaust VCT and EGR to determine optimum stability cam timing.***

1500 RPM, 0.7 bar BMEP, EGR sweep

1500 RPM 0.7 bar BMEP is viewed as a realistic minimum load you could maintain in a vehicle for an extended period (not a fast transient). For example, coming down a long shallow grade or driving with a high tailwind. The combustion criteria for this point are:

- ERMSIMEP_SD < 7 kPa
- ELSIMEP_LNV > 70%

Figure 160 shows the 1500/0.7 EGR sweep, which was run with the optimal stability cam position (-30/10). The upper left graph in Figure 160 is ERMSIMEP_SD (RMS standard deviation of IMEP, <7 kPa indicates good combustion stability), and the upper right graph is ELSIMEP_LNV (lowest normalized value of IMEP expressed as a percentage of the mean IMEP, >70% indicates good combustion). The lower left graph is average 0-10% burn time, and the lower right graph is individual cylinder standard deviation of IMEP. Based on the data in Figure 160 and the combustion criteria shown above (indicated with red dotted lines in the graphs), the 2.3L DOE engine appears to have ~20% cooled EGR tolerance at this speed/load.

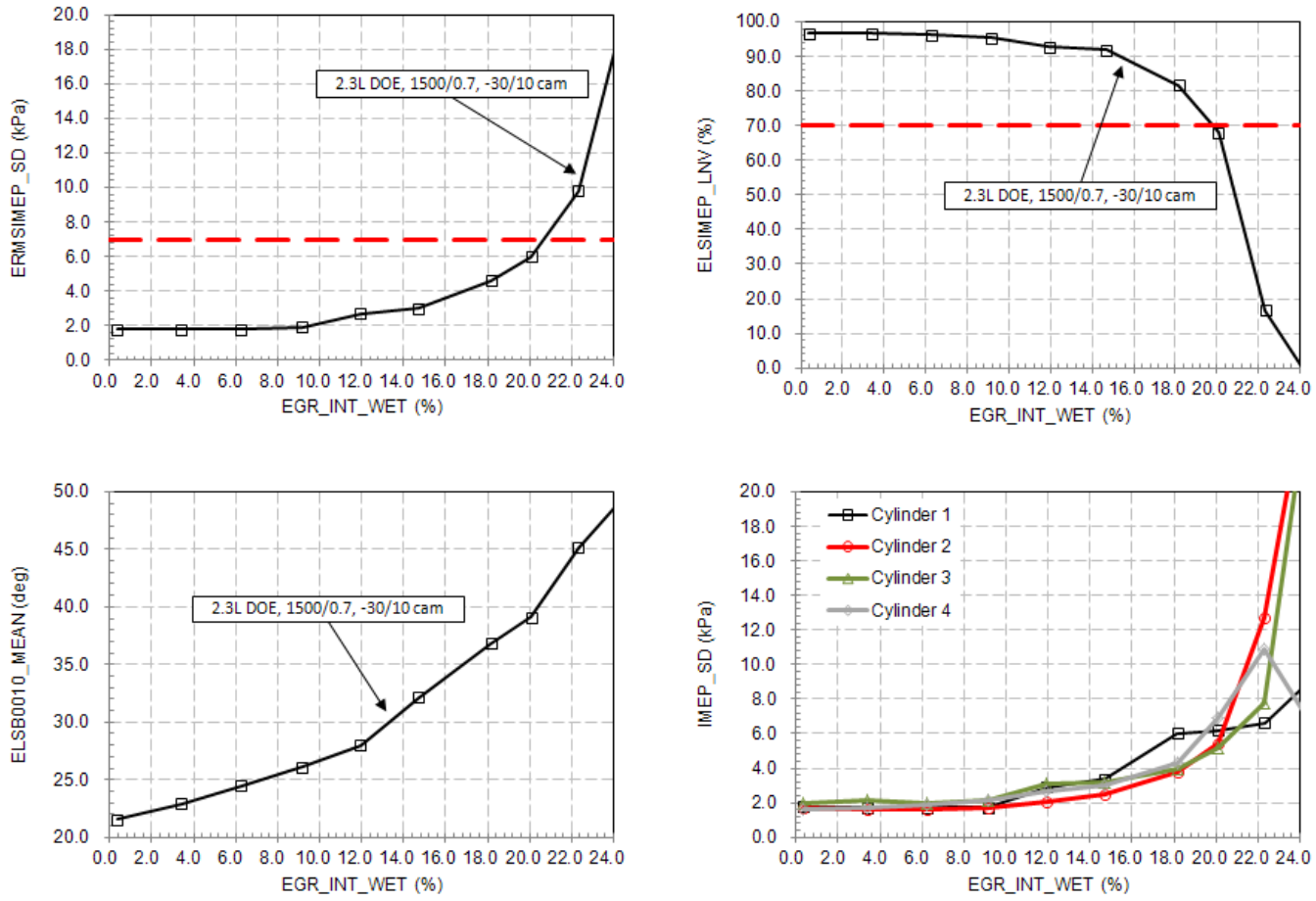


***Figure 160 - EGR sweep at 1500 RPM, 0.7 bar BMEP.***

1000 RPM, 0.12 EECLOAD, 0 torque, EGR sweep

The 1000 RPM, 0.12 EEC Load, 0 torque EGR sweep simulates the limiting case just before entering ADFSO (advanced deceleration fuel shut off). The combustion criteria for this point are:

- No misfire (ELSIMEP_LNV > 0)
- Hydrocarbons < 15,000 PPM C1 (FGHC < 15000)

Figure 161 shows the 1000 RPM, 0.12 EECLOAD, 0 torque, EGR sweep which was run at the optimum stability cam position (-30/10). The upper left graph is ELSIMEP_LNV (lowest normalized IMEP percentage, >0% indicates no misfires, the upper right graph is FGHC (feedgas hydrocarbons), the lower left graph is average 0-10% burn time, and the lower right graph is individual cylinder standard deviation of IMEP. Based on the data in Figure 161, the 2.3L DOE is robust to misfire at this speed/load, but FGHC do hit the 15,000 C1 ppm limit at about 15% EGR. To lower the FGHC, a slightly higher minimum EECLOAD may be required if the EGR schedule is greater than 15% EGR.

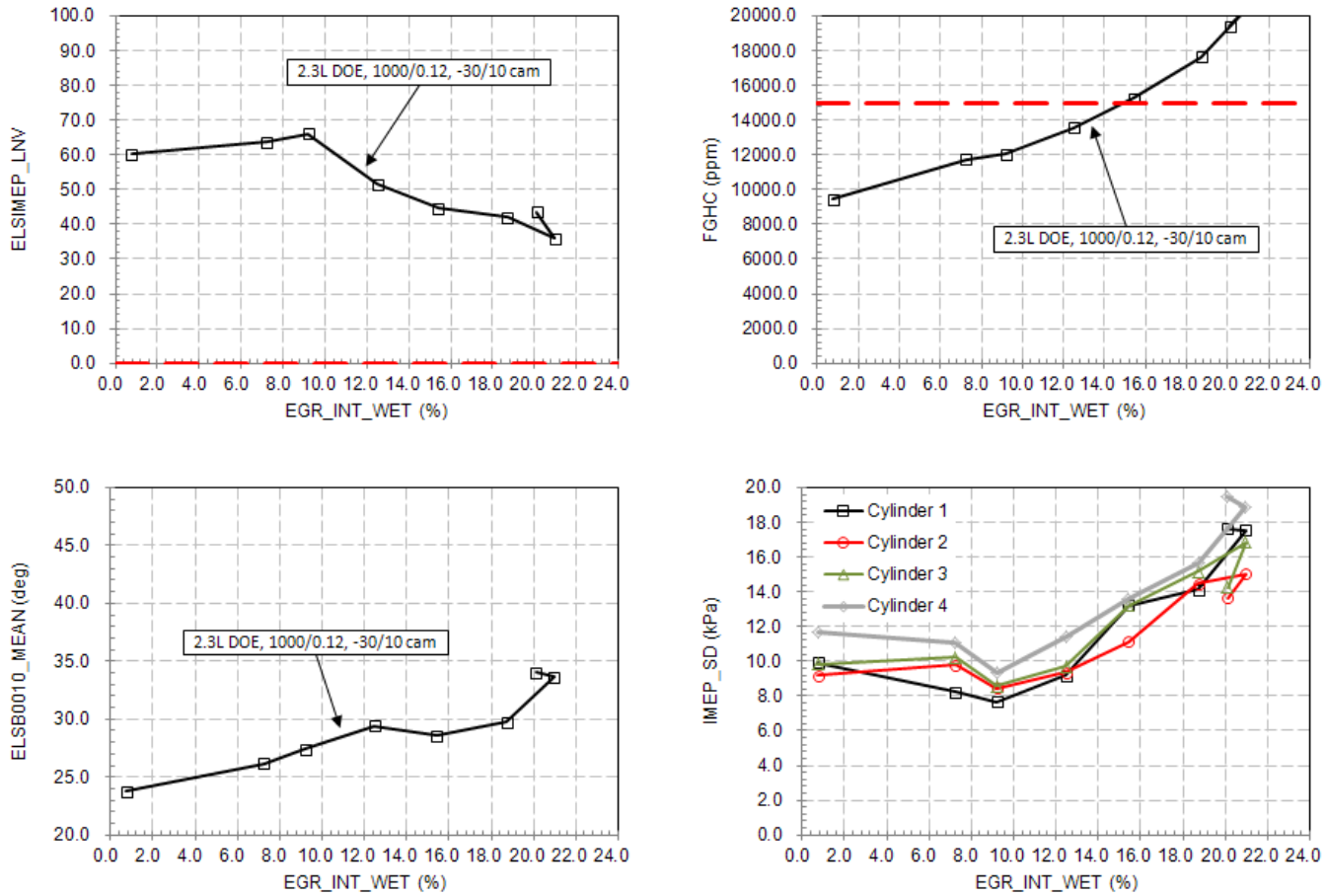


***Figure 161 - EGR sweep at 1000 RPM, 0.12 EECLOAD, 0 torque.***

600 RPM, 0.7 bar BMEP, universal idle with 0% EGR, spark sweeps

For the universal idle point at 600 RPM, 0.7 bar BMEP, 0% EGR, the combustion criteria are:

- Be robust to 15° of spark retard from MBT for torque reserve
- ELSIMEP_SD < 14 kPa
- ELSIMEP_LNV > 70%

Since the 2.3L DOE engine was so stable at this condition, the intake cam was able to be set to 0° for improved fuel economy, and the exhaust cam was swept from 0 to 50° to see how much internal residual the engine could tolerate, and how low of a fuel flow per liter could be attained. Figure 162 shows the results of the spark sweeps from the 2.3L DOE engine at various levels of exhaust retard. In Figure 162, the upper left graph is ELSIMEP_SD (standard deviation of IMEP, < 14 kPa indicates good combustion). The upper right graph is ELSIMEP_LNV (lowest normalized value of IMEP expressed as a percentage of the mean IMEP, >70% indicates good combustion.) The lower left graph is CA50 location, and the lower right graph is fuel flow per liter. It can be seen in Figure 162 that the 0/30 cam setting (blue line) is the optimal cam setting for the 2.3L DOE engine at this point, as it has excellent combustion stability (all points easily meet the combustion criteria), and is robust to 15° of spark retard.

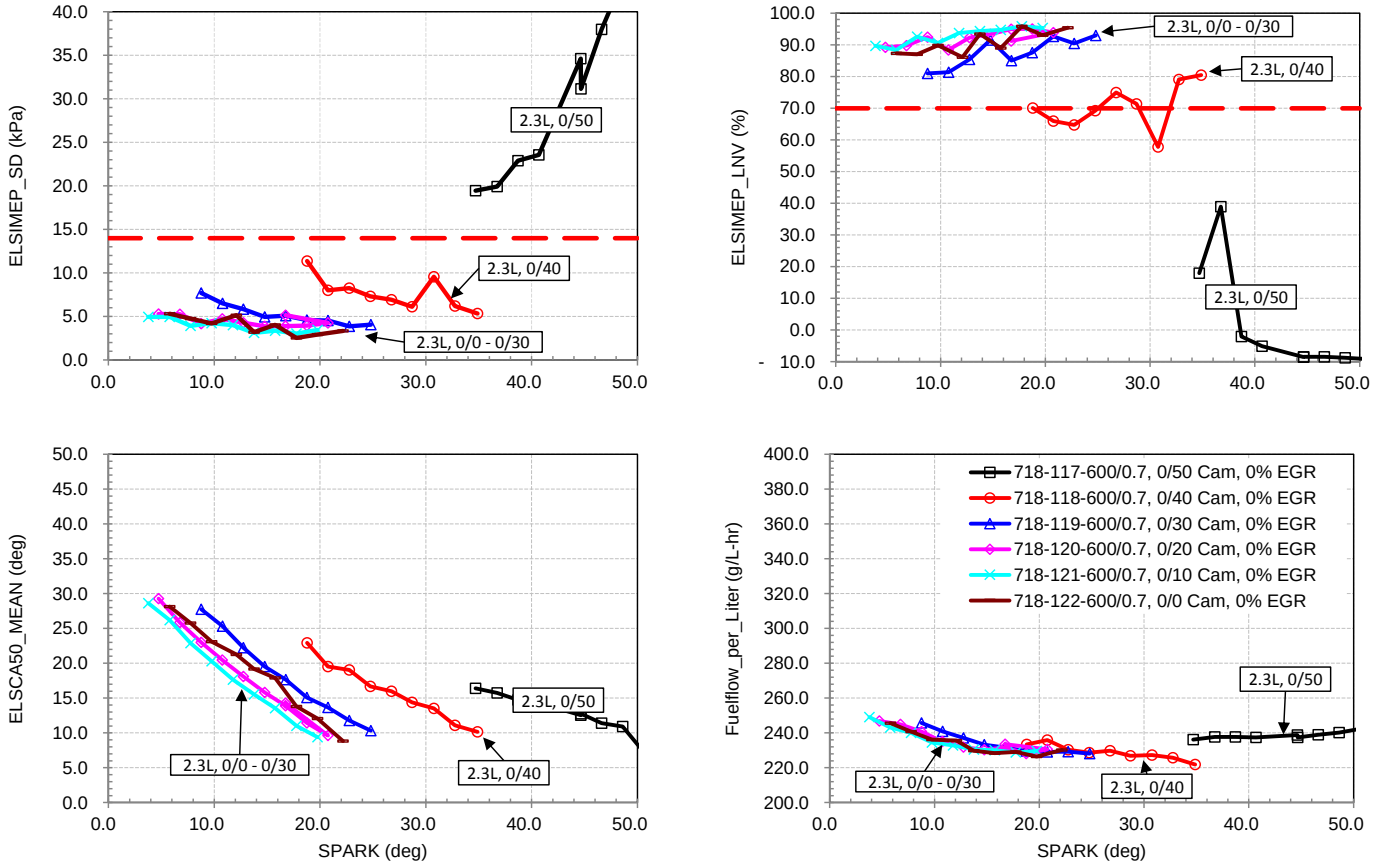


***Figure 162 - 600 RPM, 0.7 bar BMEP with 0% EGR, spark sweeps with 0° intake and various exhaust cam retards.***

## Cam Timing Optimization

Cam timing ranges with TiVCT for the 2.3L DOE engine are shown in Figure 163.

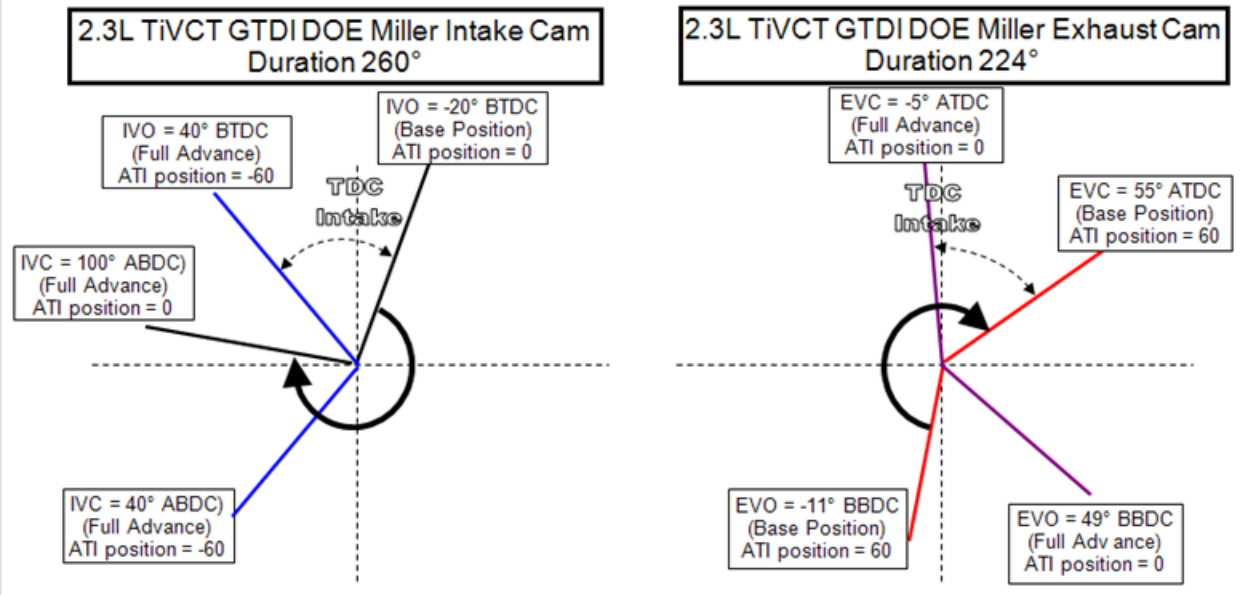


***Figure 163 - Cam timing diagrams for 2.3L DOE engine.***

In the figures which follow in this section, cam timings are given as relative to the base positions, for example, minus 60 intake timing is 60° advanced from the base position, and plus 60 exhaust timing is 60° retarded from the base position.

In order to optimize cam timings for the 2.3L DOE engine, full factorial intake and exhaust sweeps were performed at various loads at 1500 and 2000 RPM (these engine speeds encompass nearly all the fuel on the EPA City, EPA Highway, and US06 cycles, as shown in Figure 164, Figure 165, and Figure 166, respectively.)

The operating assumptions used for the full factorial sweeps are shown below:

- Minimum throttle plate ΔP (TPDP) = 7 kPa
- 0 and 15% EGR
- EGR valve ΔP = 4 kPa when EGR is on
- 38°C remote and integrated CAC inlet water temps
- Lambda = Stoich
- MBT/BL spark timing
- 38°C/56 grains humidity inlet air
- Exhaust valve 100% open/reflective orifice plate exhaust

Throughout the rest of this section, four examples of the full factorial cam sweeps will be presented to show how the optimal cam positions were determined.

Fuel Weighting Contour Plots from e-CVSP

Figure 164, Figure 165, and Figure 166 show the 2.3L GTDI DOE Miller e-CVSP fuel weightings for the EPA city, EPA highway, and US06 cycles, respectively.

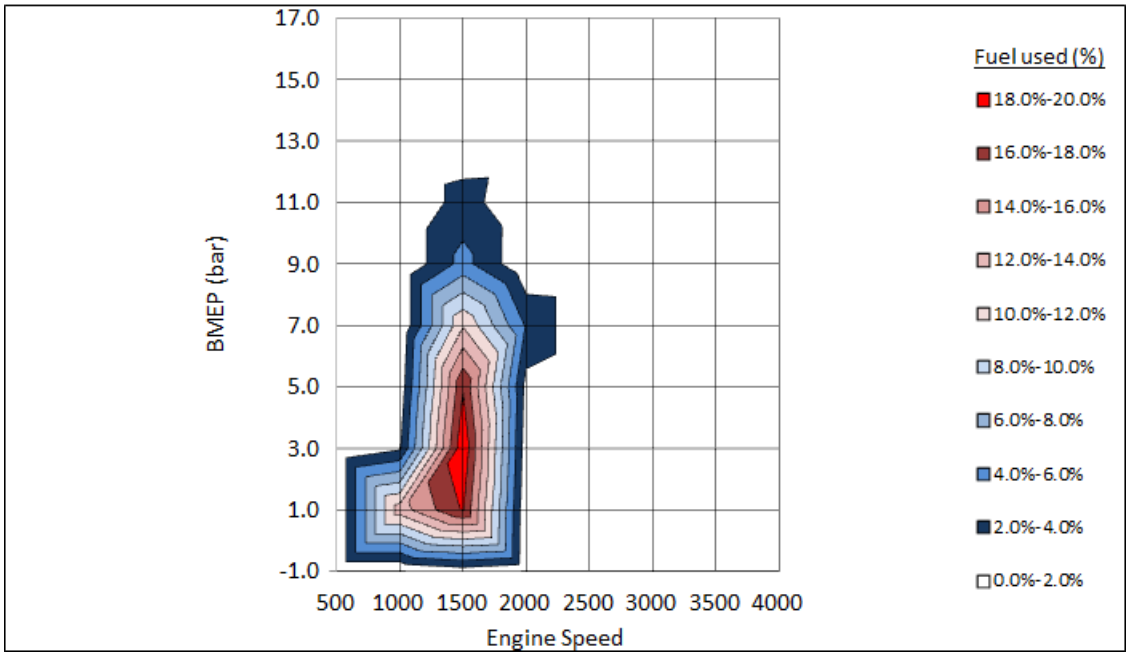


***Figure 164 - EPA city cycle fuel usage contour plot from e-CVSP.***

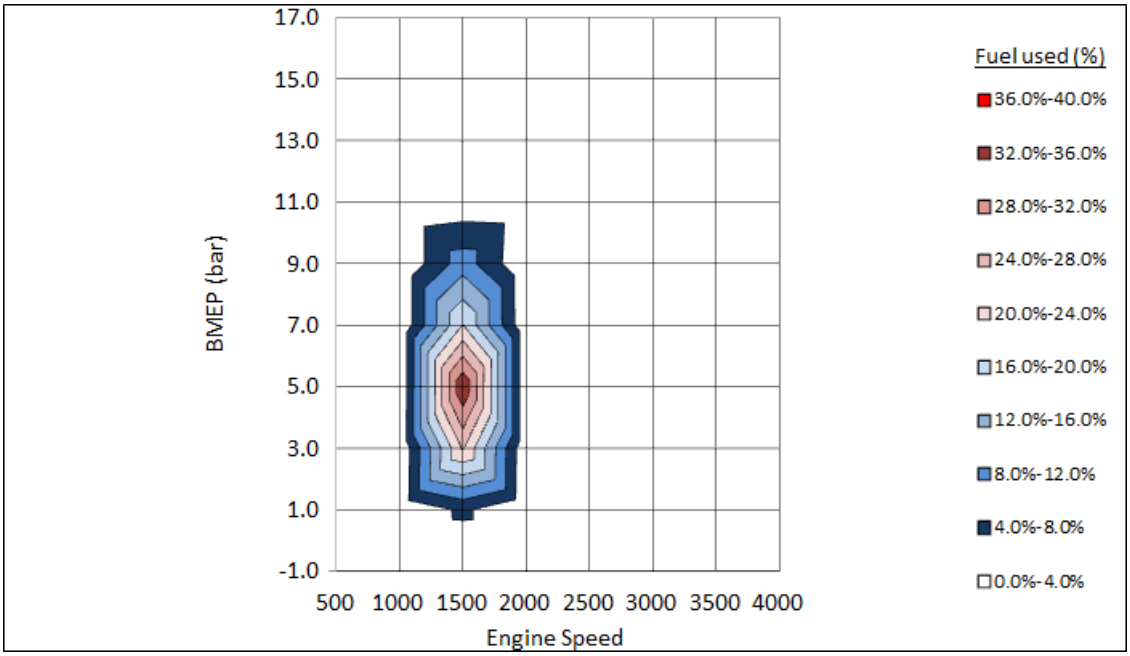


***Figure 165 - EPA highway cycle fuel usage contour plot from e-CVSP.***

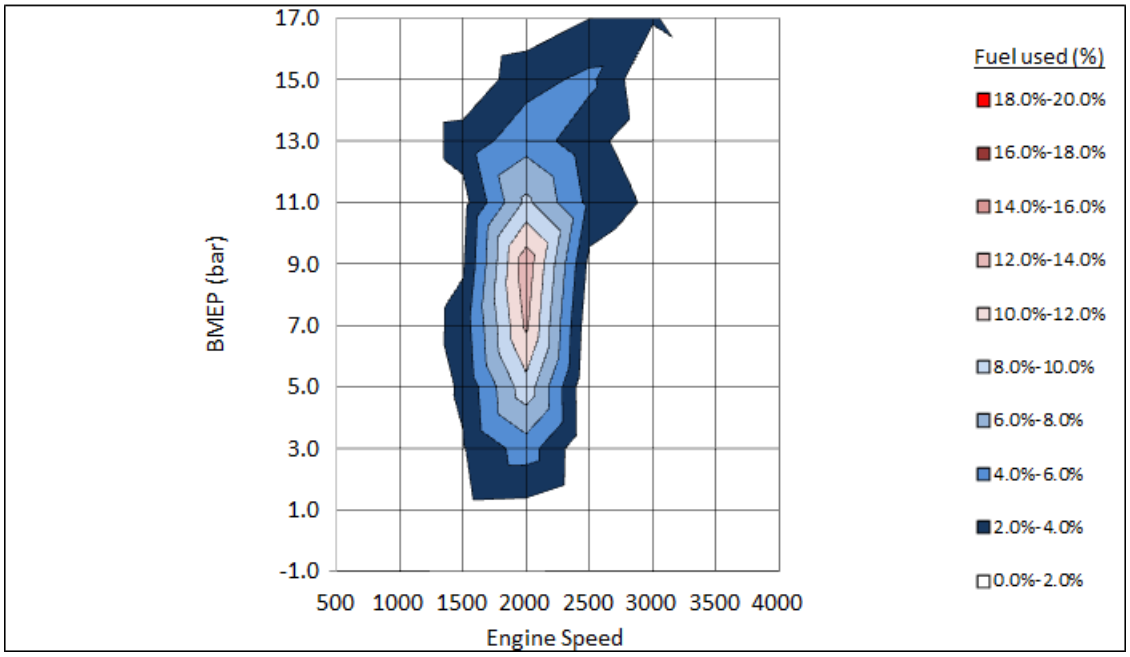


***Figure 166 - US06 cycle fuel usage contour plot from e-CVSP.***

Lower Loads (~2.62 bar and under)

For the lower load points, the general strategy is to get as much internal residual into the cylinder as the engine can tolerate while still meeting the combustion stability criteria.

The data shown in Figure 167 are from full factorial intake and exhaust cam sweeps at 1500/2.62 bar, 15% EGR. The upper left graph is BSFC (hot colors are lower BSFC), the upper right graph is adjusted PMEP (cold colors are lower pumping work), the lower left graph is feedgas NOx (cold colors indicate more dilution) and the lower right graph shows combustion stability via ERMISMEP_COV (cold colors indicate better combustion stability). Looking at the BSFC graph (upper left graph in Figure 167), where hot colors are better BSFC, it can

be seen that -3/50 is the optimal cam position. -3/50 was the optimal cam position because it was the point with the best compromise of maximum dilution (see feedgas NOx graph) and minimum pumping work (see adjusted PMEP graph) while still meeting the combustion criterion (see ERMSIMEP_COV graph).

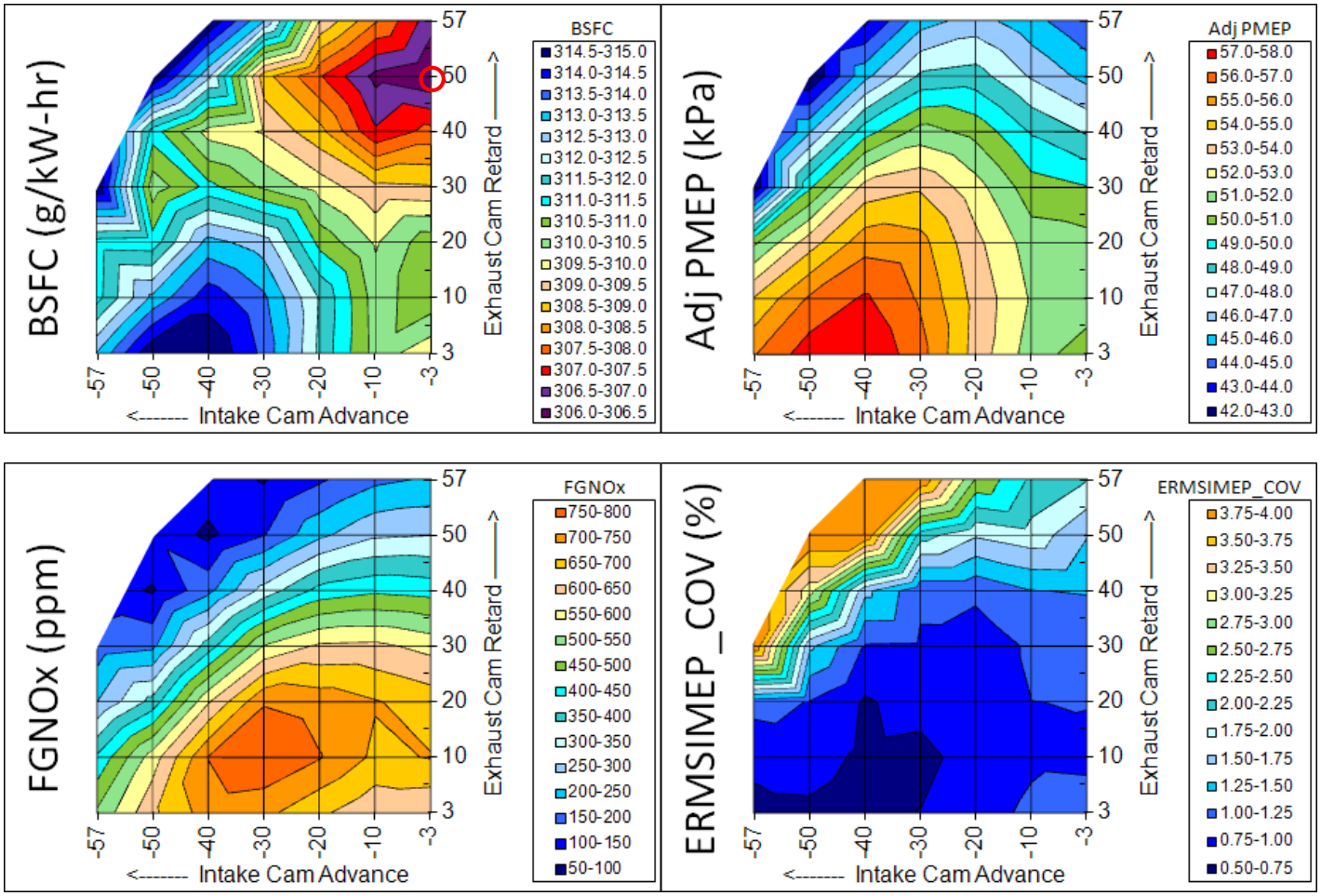


***Figure 167 - 1500/2.62 bar, 15% EGR, scroll closed full factorial intake and exhaust sweeps.***

Light-to-Medium Loads (~5-7 bar)

For the light-to-medium load points, combustion is stable across the full cam space, so the general strategy is to find the point with the best compromise of minimum pumping work and maximum residual.

The data shown in Figure 168 are from full factorial intake and exhaust cam sweeps at 2000/5 bar, 15% EGR. The upper left graph is the sum of % NSFC benefit (hot colors are lower fuel consumption), upper right graph is adjusted PMEP (cold colors are lower pumping work), lower left graph is feedgas NOx (cold colors indicate more dilution) and the lower right graph shows pumping loop comparisons from selected points in the adjusted PMEP graph. Looking at the sum of % NSFC benefit (upper left graph in Figure 168), it can be seen that both -57/30 and -10/3 are optimal cam positions. In Figure 168, the sum of % NSFC benefit was used in place of BSFC because the BSFC data was erroneous.

-57/30 is one of the optimal positions because it is a compromise of somewhat low pumping work (see adjusted PMEP graph) and somewhat high dilution (see feedgas NOx graph). -10/3 is one of the optimal points because relative to the other cam positions the pumping work is significantly lower.

The colors of the pumping loops shown on the lower right graph of Figure 28 correspond to the stars from the adjusted pumping work graph. For instance, the black pumping loop is at a cam position of -57/57. It can be seen in the black pumping loop (-57/57) that EVO pumping loss is very high from the late opening of the

exhaust valve (EVO is -8° BBDC). Moving from the black pumping loop (-57/57) to the red pumping loop (-57/30) to the blue pumping loop (-57/3), the improvement in pumping work comes mainly from the reduction in EVO loss. Moving from the blue pumping loop (-57/3) to the grey pumping loop (-10/3), the exhaust pumping work is more or less the same, but the grey pumping loop has a large advantage during the intake stroke because -10/3 cam timing requires a higher MAP to make the same torque due to late IVC.

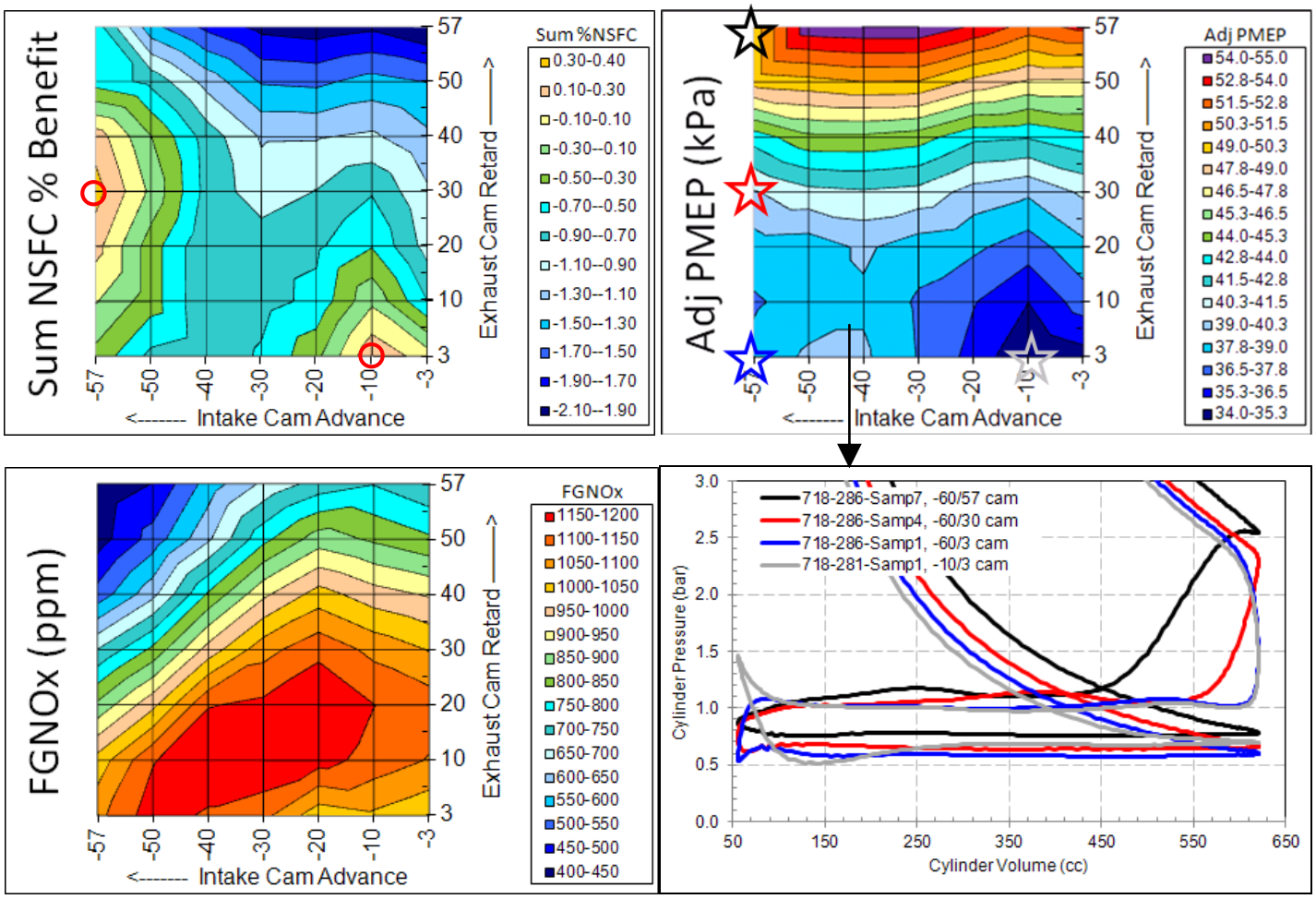


***Figure 168 - 2000/5 bar, 15% EGR, scroll closed full factorial intake and exhaust sweeps.***

Medium-to-high loads (~7-9 bar)

For the medium-to-high load points, the amount of internal residual that can be obtained across the cam space is minimal, because the MAP is high enough at these speed/load points that not much flow from the cylinder to the intake manifold can occur. Therefore, the general strategy is to find the point with the lowest pumping work and best air/fuel mixing.

The data shown in Figure 169 are from full factorial intake and exhaust cam sweeps at 2000/9 bar, 15% EGR, turbo scroll control valve open. The upper left graph is BSFC (hot colors are lower BSFC), the upper right graph is adjusted PMEP (cold colors are lower pumping work), the lower left graph is feedgas CO (cold colors indicate better mixing) and the lower right graph shows pumping work comparisons from selected points in the adjusted PMEP graph. The white areas in the graphs of Figure 169 below an intake advance of 20° indicate areas in the cam space where the TPDP requirement of 7 kPa could not be met. The white areas above an exhaust retard of 50 are cam positions that were not run because the EVO loss is so high at those conditions that they will not have good BSFC.

Looking at the BSFC graph (upper left graph in Figure 169), it can be seen that -57/3 is the optimal cam position. -57/3 is the optimal position because it is one of the points with the lowest pumping work (see adjusted PMEP graph) and has good air/fuel mixing (see feedgas CO graph).

The colors of the pumping loops shown on the lower right graph of Figure 169 correspond to the stars from the adjusted pumping work graph. For instance, the black pumping loop is at a cam position of -57/50. Moving from the black pumping loop (-57/50) to the red pumping loop (-57/3), the improvement in pumping work comes mainly from reduction in EVO loss. Moving from the red pumping loop (-57/3) to the grey pumping loop (-10/3), the overall pumping work is approximately the same. The late IVC at -10/3 (grey) improves the intake stroke pumping work compared to -57/3 (red), but the load is high enough at this point that the grey pumping loop (-10/3) requires wastegate to meet the torque, which causes it to have higher losses in the exhaust stroke, and the overall both pumping work is about the same.

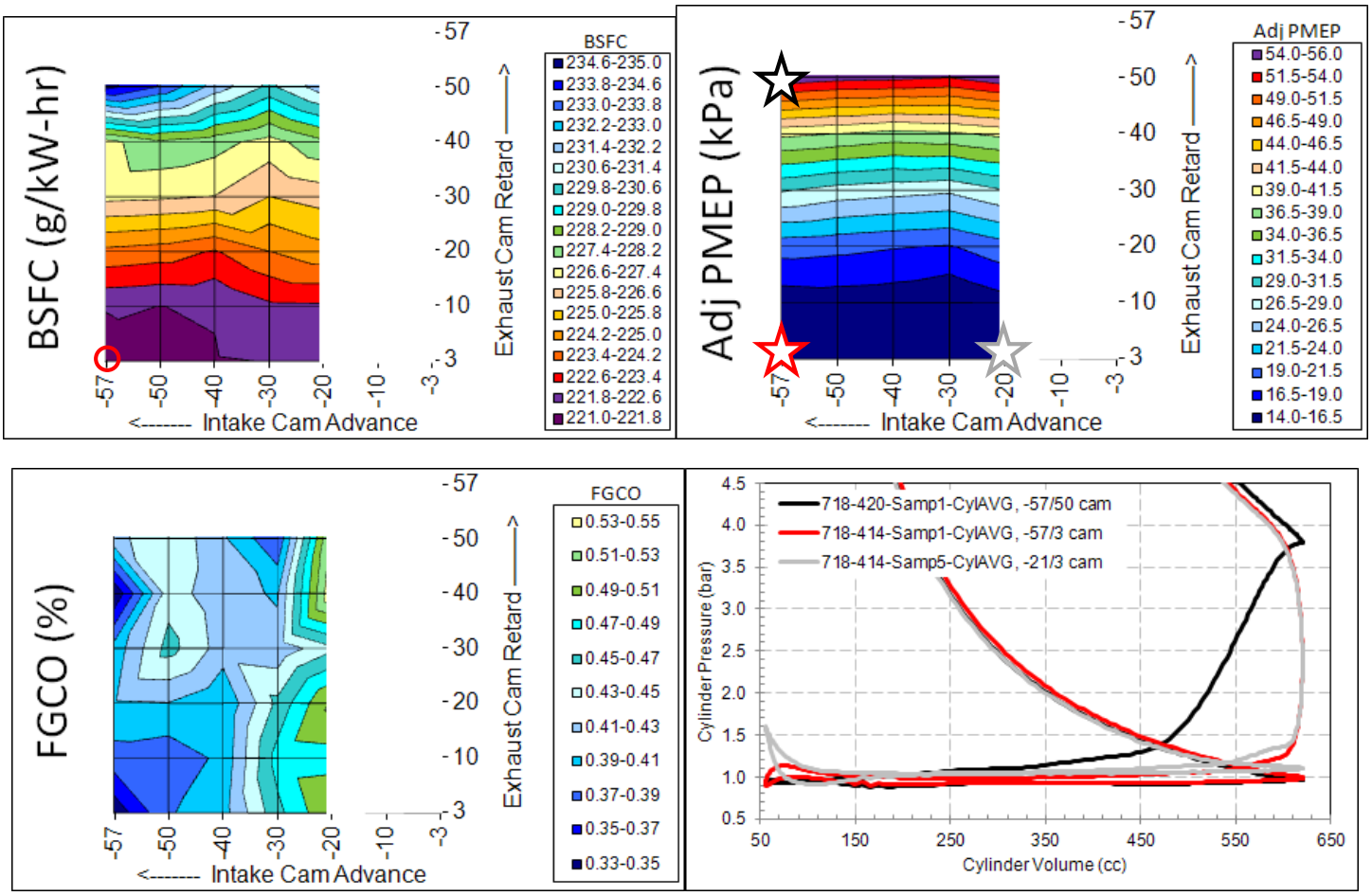


***Figure 169 - 2000/9 bar, 15% EGR, scroll open full factorial intake and exhaust sweeps.***

High Loads

For high load points where knock occurs, the general strategy is to find the point with the lowest pumping work and best combustion phasing (minimum CA50).

The data shown in Figure 170 are from full factorial intake and exhaust cam sweeps at 2500/14 bar, 15% EGR, turbo scroll control valve open. The upper left graph is BSFC (hot colors are lower BSFC), the upper right graph is adjusted PMEP (cold colors are lower pumping work), the lower left graph is CA50 (cold colors indicate better combustion phasing), and the lower right graph shows pumping work comparisons from selected points in the adjusted PMEP graph. The white areas in the graphs of Figure 170 at and below an exhaust retard of 30 indicate areas in the cam space where the TPDP requirement of 7 kPa could not be met.

The white areas above an exhaust retard of 30 are cam positions that were not run because the EVO loss is so high at those conditions that they will not have good BSFC. Looking at the BSFC graph (upper left graph in Figure 170), it can be seen that either -30/10 or -33/3 are the optimal cam positions.

-30/10 is one of the optimal positions because it has relatively low pumping work (see adjusted PMEP graph) and has one of the lowest CA50 values (see CA50 graph). -33/3 is one of the optimal positions because it has one of the lowest values for pumping work, with a relatively low CA50.

The colors of the pumping loops shown on the lower right graph of Figure 170 correspond to the stars from the adjusted pumping work graph. For instance, the black pumping loop is at a cam position of -57/30. Moving from the black pumping loop (-57/30) to the red pumping loop (-57/3), the improvement in pumping work comes mainly from reduction in EVO loss. Moving from the red pumping loop (-57/3) to the grey pumping loop (-33/3), the overall pumping work is similar. The late IVC at -33/3 (grey) improves the intake stroke pumping work compared to -57/3 (red), but the load is high enough at this point that the grey pumping loop (-10/3) requires additional wastegate to meet the torque, which causes it to have higher losses in the exhaust stroke, and the overall both pumping work is about the same.

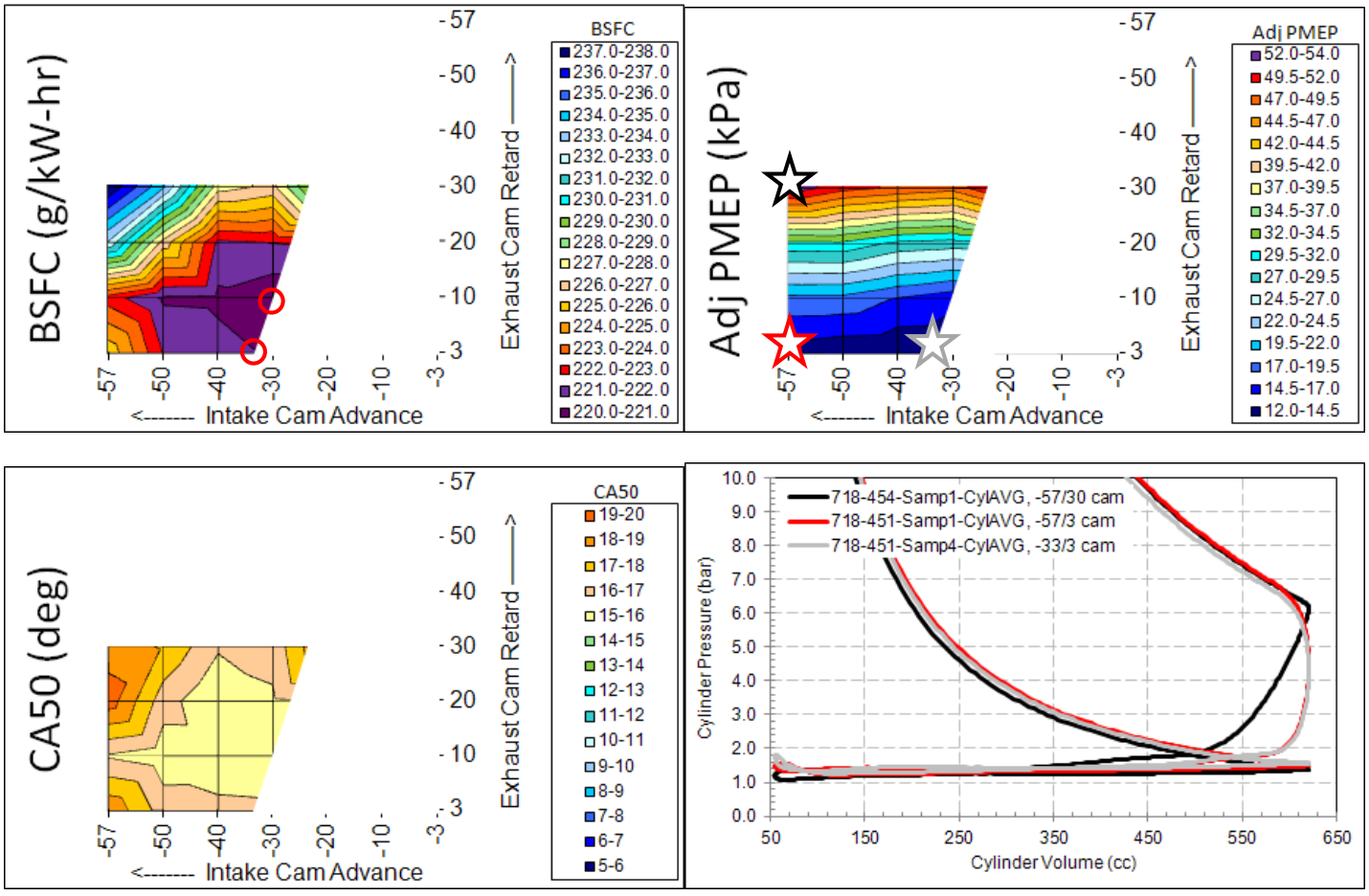


***Figure 170 - 2500/14 bar, 15% EGR, scroll open full factorial intake and exhaust sweeps.***

## SOI/FRP Maps

The combustion system of the 2.3L DOE GTDI engine utilizes the following elements:

- Transverse central direct injection (shown in Figure 6).
- High pressure fuel system capable of 200 bar fuel pressure.
- Compression ratio = 11.5:1.
- Tumble ratio ~1.7.

It was desired to investigate BSFC and smoke for this combustion system with start of injection/fuel rail pressure (SOI/FRP) maps at 1500/5, 2000/9 and 2500/14 bar BMEP. In the SOI/FRP plots, SOI is referenced in degrees from top dead center (TDC) firing. An SOI of 360 means that the start of injection occurs at TDC in the intake stroke, an SOI of 340 means that start of injection occurs 20° after TDC in the intake stroke, and so on. For FRP, the pressure shown in the plots is expressed in units of PSI; therefore a FRP of 1450 corresponds to 100 bar and a FRP of 2900 corresponds to 200 bar.

- The selected plots from the SOI/FRP map at 1500 rpm/5 bar are shown in Figure 171 and Figure 172. The optimal tradeoff of BSFC/smoke at 1500/5 was a SOI of 330 and a FRP of 2900.

- The selected plots from the SOI/FRP map at 2000 rpm/9 bar are shown in Figure 173 and Figure 174. The optimal tradeoff of BSFC/smoke at 2000/9 was a SOI of 310-320 and a FRP of 2900.

- The selected plots from the SOI/FRP map at 2500/14 bar are shown in Figure 175 and Figure 176. The optimal tradeoff of BSFC/smoke at 2500/14 was a SOI of 330 and a FRP of 2900.

At all three speed/loads tested, BSFC improves with SOI timing closer to TDC on the intake stroke (towards 360) and with higher FRP. The factors that affect BSFC in the SOI/FRP sweeps are PMEP, BSCO, BSHC, CA50 (CA50 is only a factor at 2500/14), and the friction/pumping work associated with pressurizing the fuel.

- PMEP appears to be affected by only SOI. As SOI timing gets farther away from TDC on the intake stroke (towards 290), less of the fuel is evaporated by the piston, and more by the intake charge. Vaporization of the liquid fuel causes the temperature of the intake charge to decrease. Cooler intake charge temperatures lower MAP and increase PMEP.

- BSCO improves with SOI timing closer to TDC on the intake stroke (towards 360) and with higher FRP. The main mechanism for lower CO emissions is improved air-fuel mixing in the cylinder. As SOI timing gets closer to TDC on the intake stroke (towards 360), mixing improves because earlier SOI timing gives more time for the fuel and air to mix before spark occurs.

- It is hypothesized that higher FRP improves BSCO because higher pressure typically produces smaller fuel droplets which are easier to evaporate, and this may give additional time for the fuel and air to mix.

- BSHC tends to improve with SOI timing closer to TDC on the intake stroke (towards 360) and with higher FRP. The main mechanism for BSHC improvement is assumed to be that less fuel ends up in the crevice volumes. Without visualization of the fuel spray, it is not possible to know exactly what is occurring with the spray that affects the amount of fuel ending up in crevice volumes and resulting in the trends shown in the SOI/FRP maps.

- CA50 was only knock limited in the 2500/14 SOI/FRP map. In this map, CA50 was mainly improved by higher FRP, but why FRP affects CA50 so significantly is not understood.

In general, smoke improves with higher FRP and SOI timing closer to TDC on the intake stroke (towards 360) up to the “smoke knee”. Smoke consists of long hydrocarbon chains that are formed from incomplete combustion. Poor mixing and wall/piston impingement are the typical factors that increase smoke. Piston impingement is the major contributor to the “smoke knee” in this engine. Piston impingement causes smoke

because poor fuel vaporization results in locally very rich combustion. A general rule of thumb is to stay 20° away from the observed “smoke knee”.

Higher FRP and SOI timing closer to TDC on the intake stroke (towards 360) up to the “smoke knee” improve smoke because mixing is improved and combustion is more complete. Earlier SOI timing gives the fuel/air mixture more time to mix, and it is hypothesized that higher FRP produces smaller fuel droplets which are easier to evaporate and again may give the fuel/air mixture more time to mix.

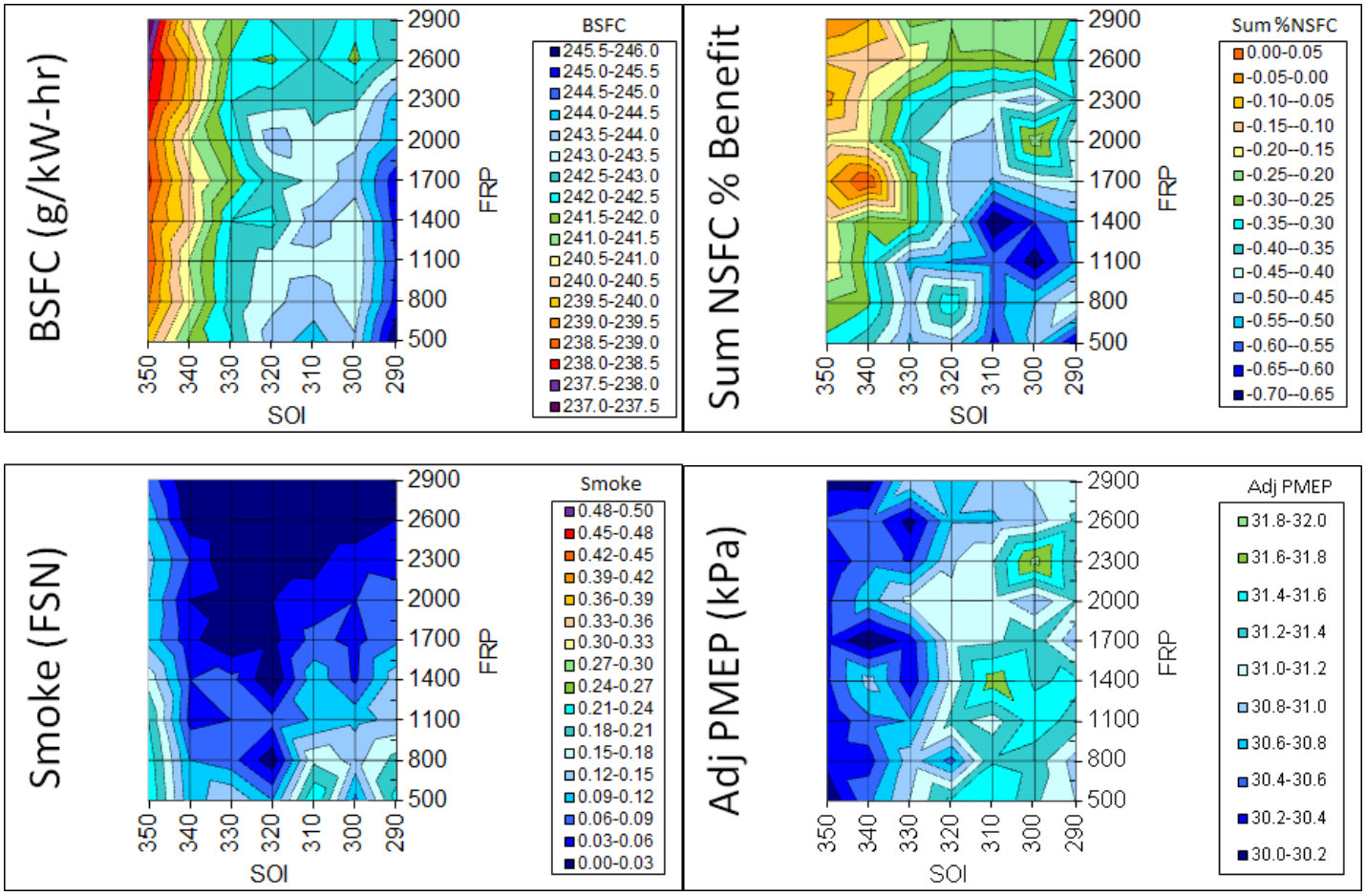


***Figure 171 - 1500/5 bar, 15% EGR, scroll open full factorial SOI and FRP sweeps.***

Upper left graph is BSFC (hot colors are lower BSFC), upper right graph is the sum of NSFC% benefit (hot colors indicate better FE), lower left graph is smoke (cold colors are lower smoke), and the lower right graph is adjusted PMEP (cold colors are lower pumping work).

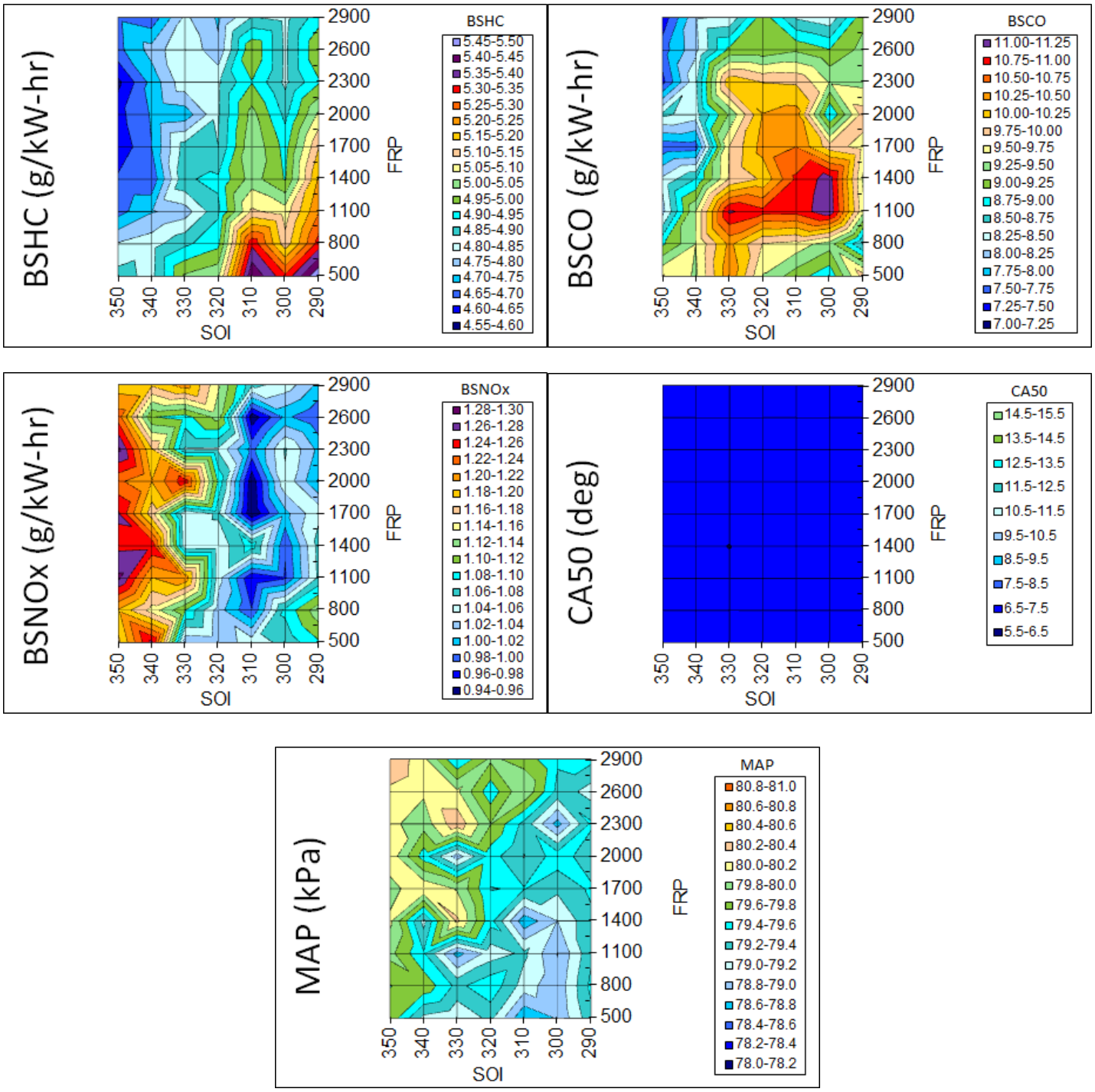


***Figure 172 - 1500/5 bar, 15% EGR, scroll open full factorial SOI and FRP sweeps.***

Upper left graph is BSHC (cold colors indicate lower HC emissions), upper right graph is BSCO (cold colors indicate lower CO emissions), middle left graph is BSNOx (cold colors indicate lower NOx emissions), middle right graph is CA50 (cold colors indicate lower CA50) and the lower left graph is MAP (hot colors indicate higher MAP).

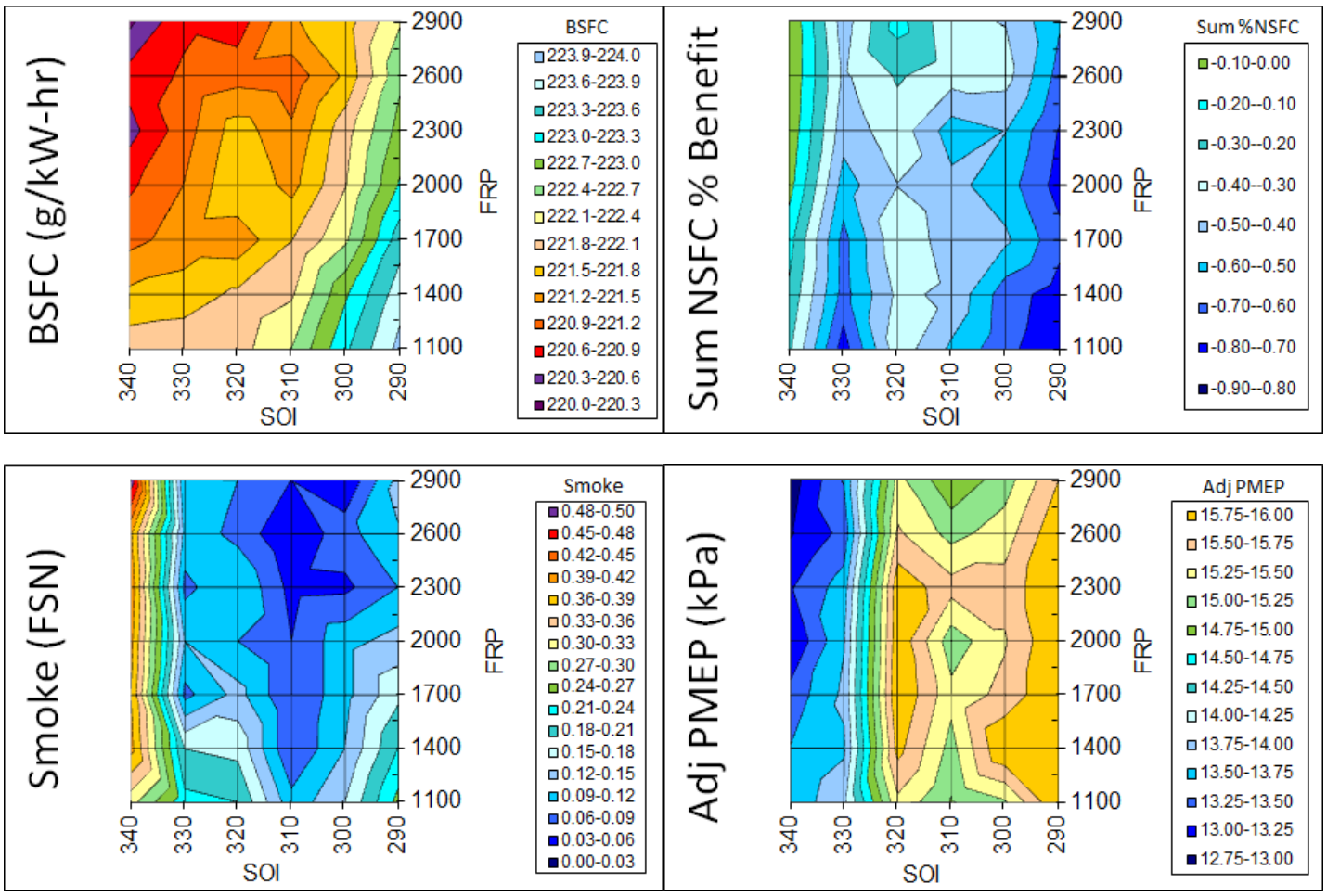


***Figure 173 - 2000/9 bar, 15% EGR, scroll open full factorial SOI and FRP sweeps.***

Upper left graph is BSFC (hot colors are lower BSFC), upper right graph is the sum of NSFC% benefit (hot colors indicate better FE), lower left graph is smoke (cold colors are lower smoke), and the lower right graph is adjusted PMEP (cold colors are lower pumping work).

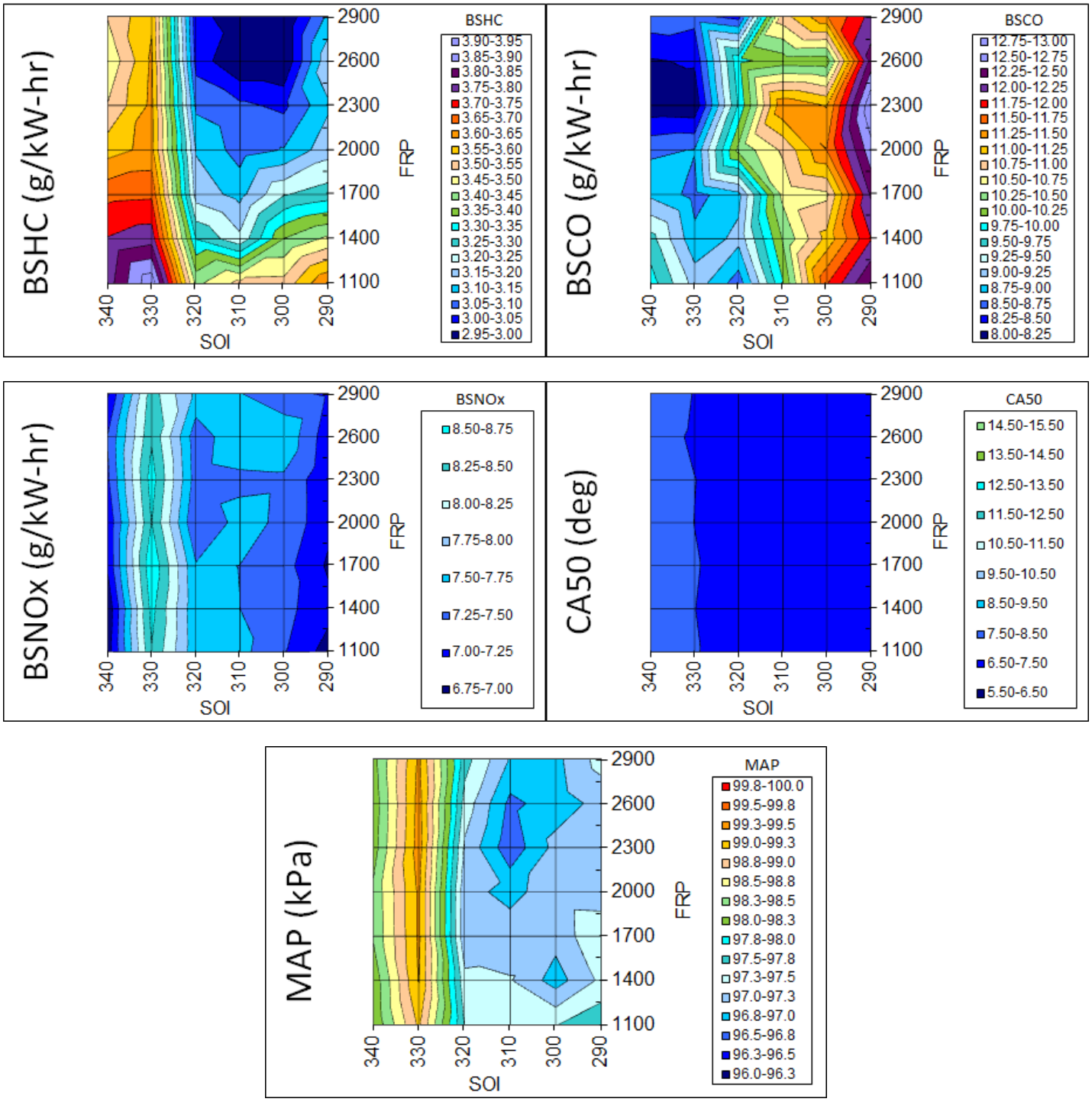


***Figure 174 - 2000/9 bar, 15% EGR, scroll open full factorial SOI and FRP sweeps.***

Upper left graph is BSHC (cold colors indicate lower HC emissions), upper right graph is BSCO (cold colors indicate lower CO emissions), middle left graph is BSNOx (cold colors indicate lower NOx emissions), middle right graph is CA50 (cold colors indicate lower CA50) and the lower left graph is MAP (hot colors indicate higher MAP).

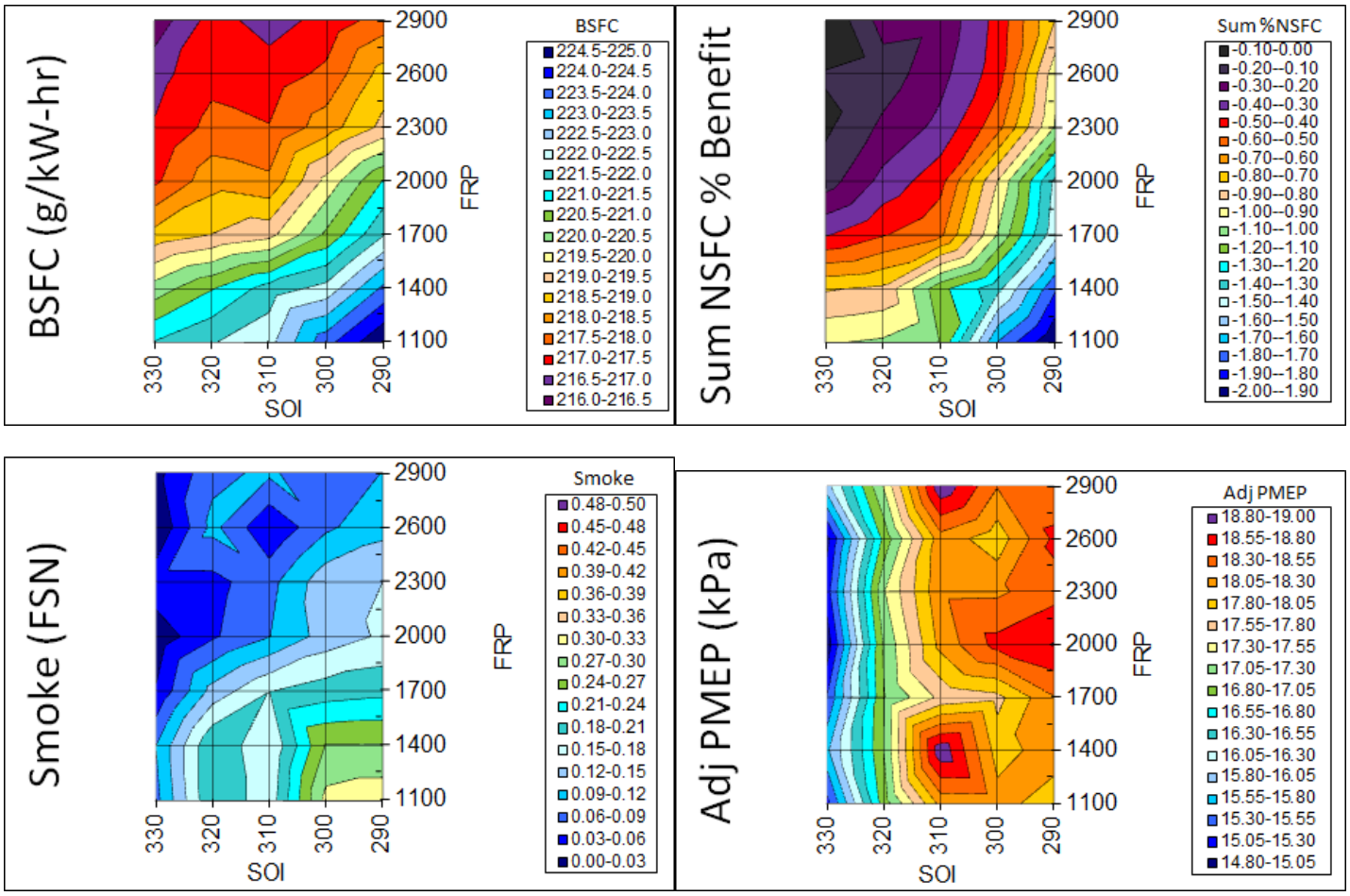


***Figure 175 - 2500/14 bar, 15% EGR, scroll open full factorial SOI and FRP sweeps.***

Upper left graph is BSFC (hot colors are lower BSFC), upper right graph is the sum of NSFC% benefit (hot colors indicate better FE), lower left graph is smoke (cold colors are lower smoke), and the lower right graph is adjusted PMEP (cold colors are lower pumping work).

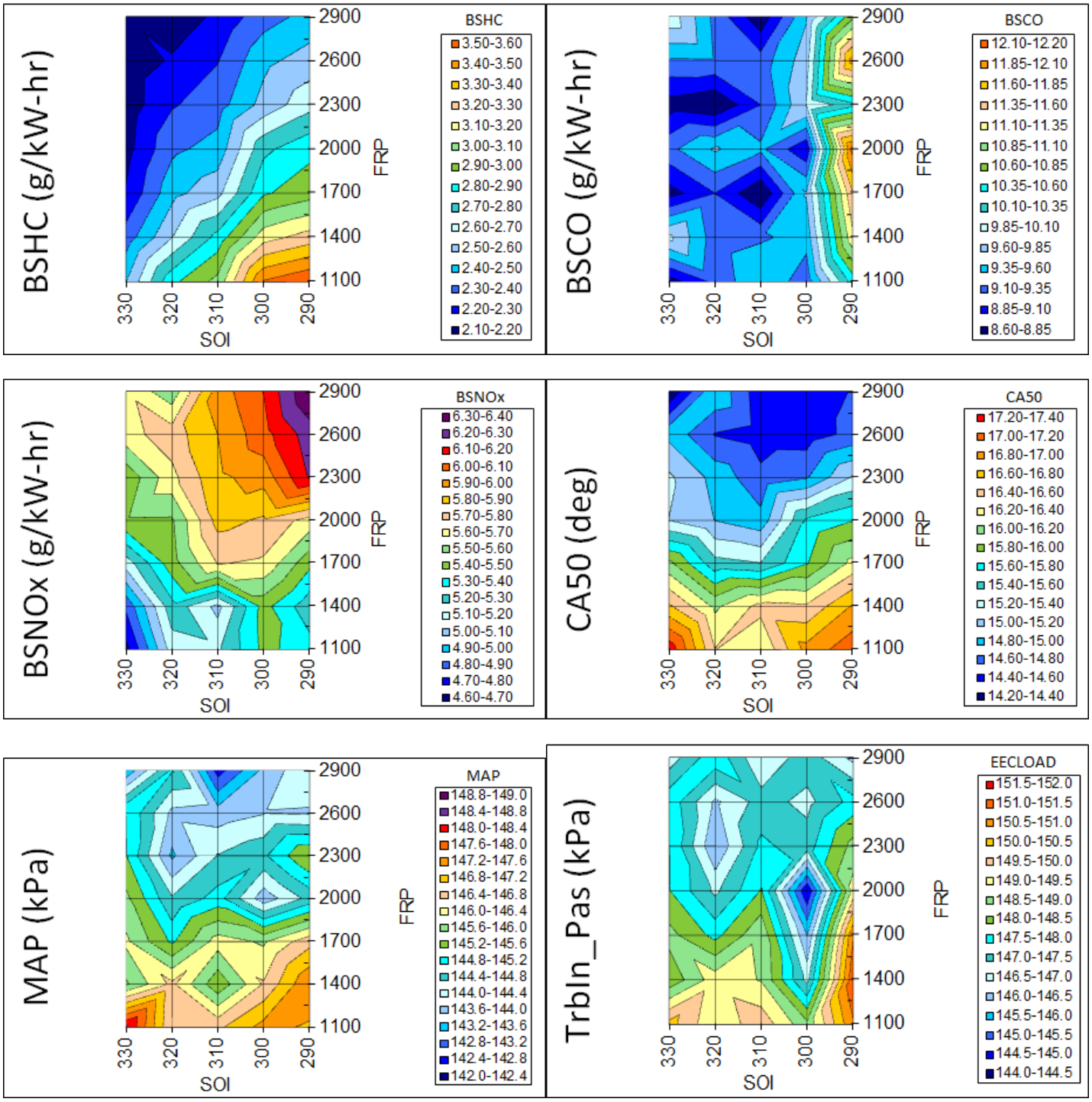


***Figure 176 - 2500/14 bar, 15% EGR, scroll open full factorial SOI and FRP sweeps.***

Upper left graph is BSHC (cold colors indicate lower HC emissions), upper right graph is BSCO (cold colors indicate lower CO emissions), middle left graph is BSNOx (cold colors indicate lower NOx emissions), middle right graph is CA50 (cold colors indicate lower CA50), lower left graph is MAP (hot colors indicate higher MAP) and the lower right graph is turbine in pressure (hot colors indicate higher turbine in pressure).

## Full Load

The full load targets for the 2.3L DOE engine were defined using a Ford analytical toolset to match the performance metrics of the baseline 2010 3.5L Taurus / Fusion. The analytical toolset captures the effects of the naturally-aspirated torque before boost is generated, the transient time-to-torque, and the boosted full load torque, and was developed specifically for EcoBoost powertrain matching.

### Steady State Performance

Final full load performance parameters for the 2.3L DOE engine are shown across the speed range from 1000 rpm to 5500 rpm in Figure 177 through Figure 181. On each figure, two runs are shown as the green and black solid lines. In Figure 177, the target BMEP curve and peak power level are shown as red dashed lines. As shown, the engine meets the full load target of 20 bar BMEP between 2000 rpm and 4500 rpm, and the peak power target of 80 kW/L.

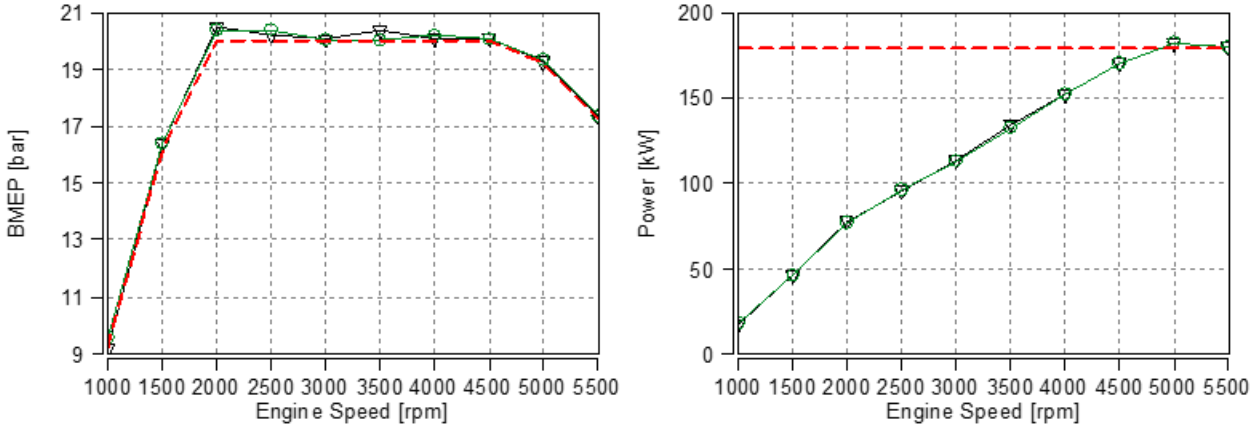


***Figure 177 - Full load BMEP and brake power vs. engine speed.***

Full load performance was assessed subject to the following constraints and limits, shown as red dashed lines in Figure 178 through Figure 181: CA50 < 32°ATDC, compressor outlet temperature < 180°C, peak cylinder pressure (mean + 3 sigma) ≤100 bar, feedgas $O_2$ blowthrough ≤ 1.5%, turbine inlet temperature ≤ 960°C, air-fuel ratio at peak power > 10:1, and turbocharger speed < 200,000 rpm. Meeting the full load targets was challenging at 11.5:1 compression ratio and required detailed parameter optimization to balance these constraints.

Combustion phasing (as measured by the crank angle location of 50% mass fraction burned), air-fuel ratio, turbine inlet temperature, and smoke number are shown in Figure 178. Combustion phasing is well within the guideline of 32° aTDC, indicating a good balance of attributes that affect engine knock. The engine reaches the turbine inlet temperature limit of 960 °C at 3500 rpm, requiring enrichment to control exhaust temperature to the turbine inlet temperature limit at higher speeds. The stoichiometric air-fuel ratio up to 3000 rpm forecasts good on-road fuel consumption. At peak power, the engine is running 11.5:1 A/F, significantly leaner than the 10:1 A/F enrichment limit. Smoke emissions are extremely low while the engine is running at stoichiometry, and increase only moderately to 0.2 FSN at peak power, still far below the full load limit of 1.0 FSN.

Combustion stability (as measured by the RMS of the COV of IMEP values for the four cylinders), IVO, EVC, and feedgas $O_2$ are shown in Figure 179. Combustion stability is very good, varying between 1 and 2%, consistent with the CA50 values shown in Figure 178. Overlap (IVO plus EVC) is set at to 68° at low engine speeds to provide scavenging of residual gas from the clearance volume, as evidenced by the exhaust $O_2$ concentration, which also indicates some blowthrough of fresh air. The exhaust $O_2$ is slightly above the 1.5% guideline at 1500 rpm.

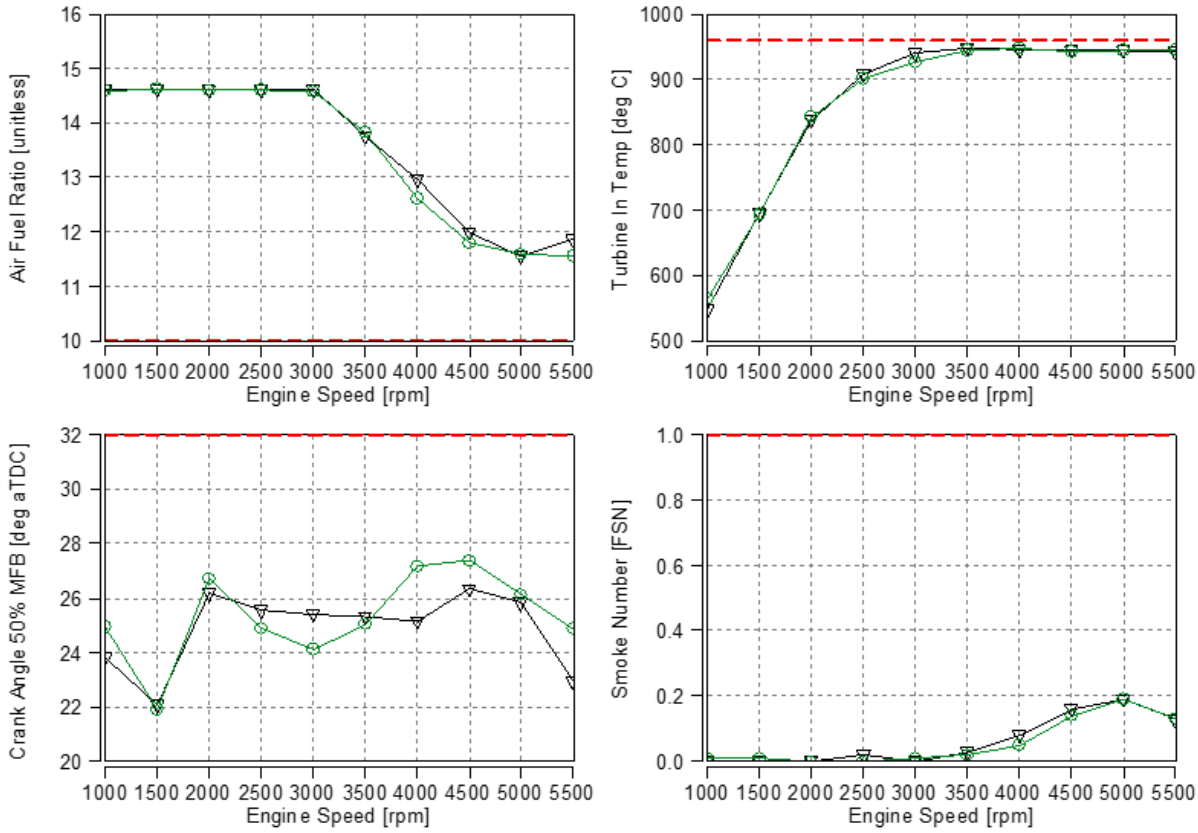


***Figure 178 - Air-fuel ratio, turbine inlet temperature, combustion phasing, and smoke number vs. engine speed at full load.***

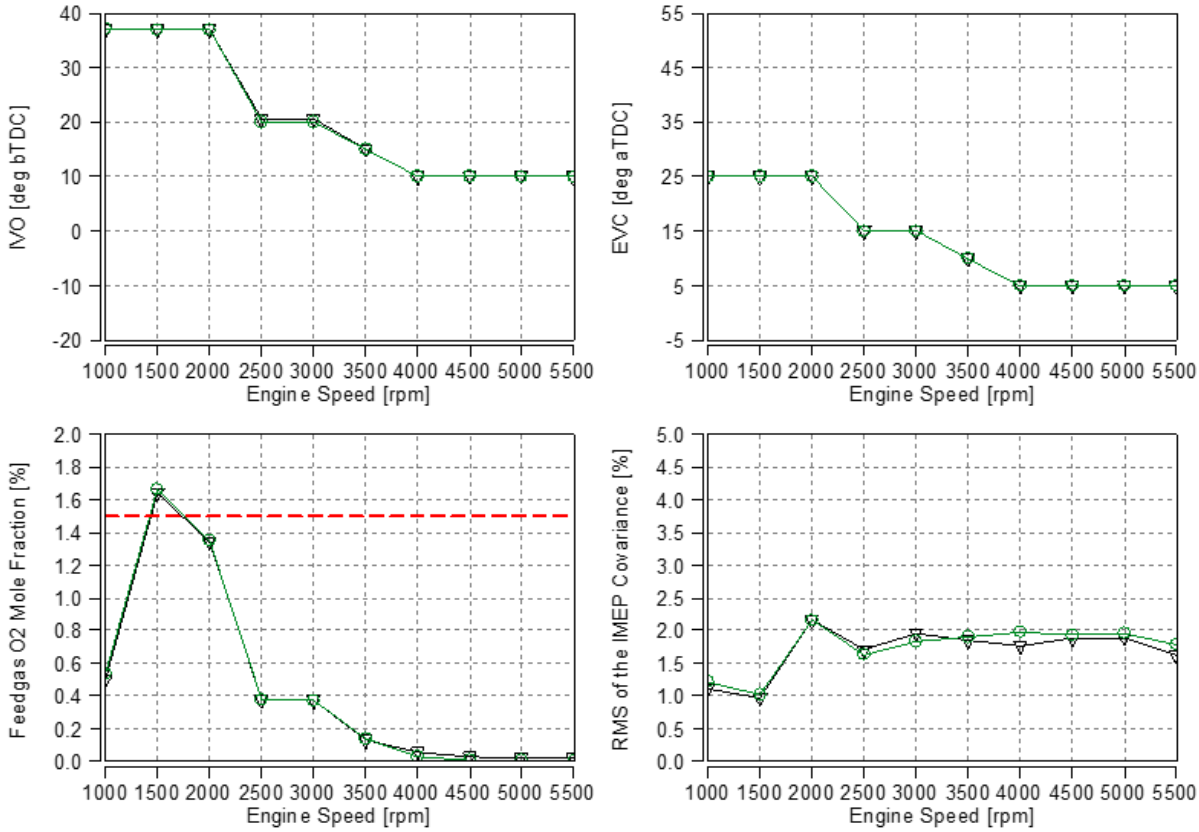


***Figure 179 - Valve timings, feedgas $O_2$, and combustion stability vs. engine speed at full load.***

IMEP, manifold absolute pressure (MAP), wastegate duty cycle, and peak cylinder pressure are shown in Figure 180. IMEP increases as the MAP increases. The wastegate duty cycle is used to control the boost level and MAP to achieve the BMEP targets. The peak cylinder pressure (mean + 3 sigma for all cylinders) is at the 100 bar limit from 2000 rpm to 5500 rpm. The peak cylinder pressure limit is a structural HCF limit of the engine. Further increase of torque would require retarding spark timing to reduce peak cylinder pressure and adding boost, increasing peak cylinder pressure back up to the 100 bar limit. At engine speeds above 3500 rpm, where the engine is at the turbine inlet temperature limit, this would also require additional enrichment, since retarding spark timing will increase exhaust temperature. Further enrichment would degrade full load fuel consumption and would also tend to increase smoke (PM) emissions.

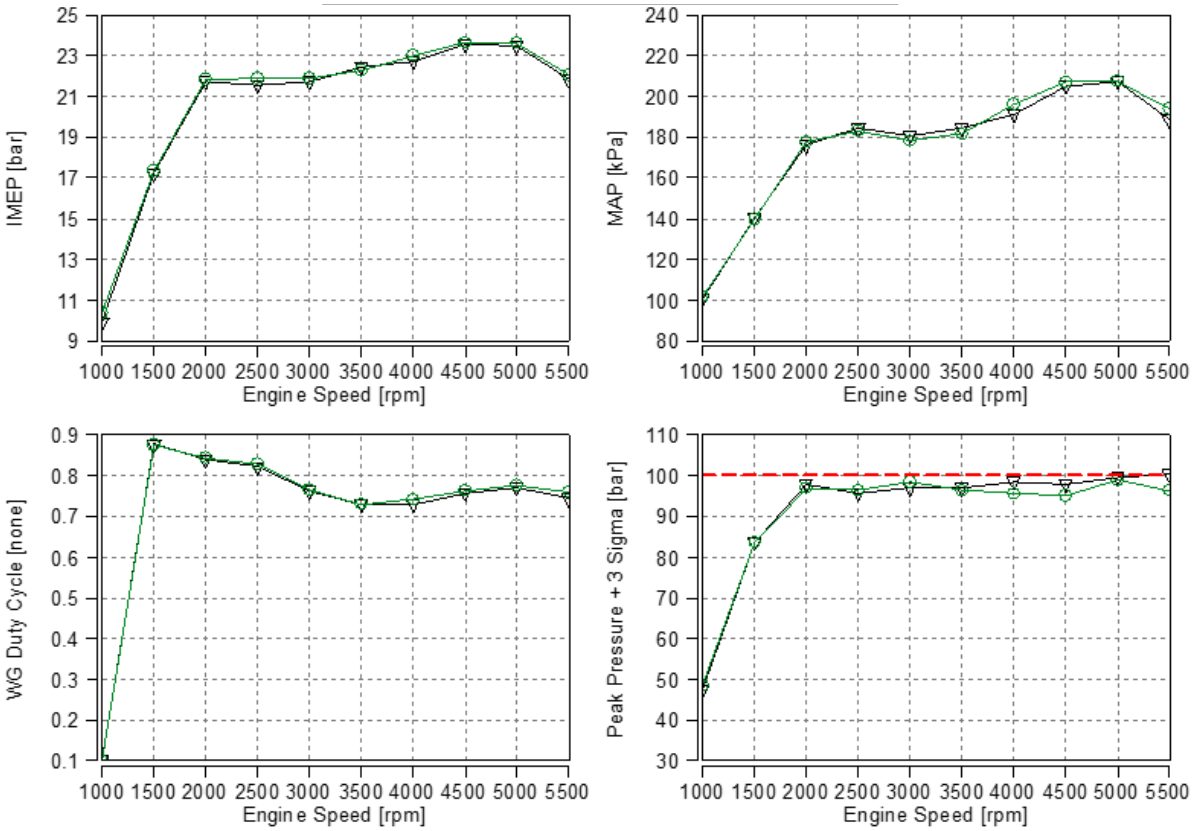


***Figure 180 - IMEP, MAP, wastegate duty cycle, and peak pressure vs. engine speed at full load.***

Compressor outlet temperature and turbocharger speed are shown in Figure 181. Both of these parameters have a substantial margin relative to their respective limits. PMEP and turbine inlet pressure are also shown in Figure 181. The PMEP (pumping work normalized by engine displacement) increases with engine speed as the exhaust restriction including the restriction of the turbine and wastegate increases, as shown by the turbine inlet pressure which increases to 3.2 bar at 5000 rpm. Pumping work is illustrated by the cylinder pressure pumping loops for 1500 rpm, 3000 rpm, and 5000 rpm in Figure 183, Figure 184, and Figure 185, respectively. As shown in Figure 184 and Figure 185, it is evident that improved performance could be attained at mid and high engine speeds by using a longer duration exhaust event, but using a longer exhaust duration would have precluded achieving the BMEP targets at low engine speeds due to the effects of exhaust blowdown interference.

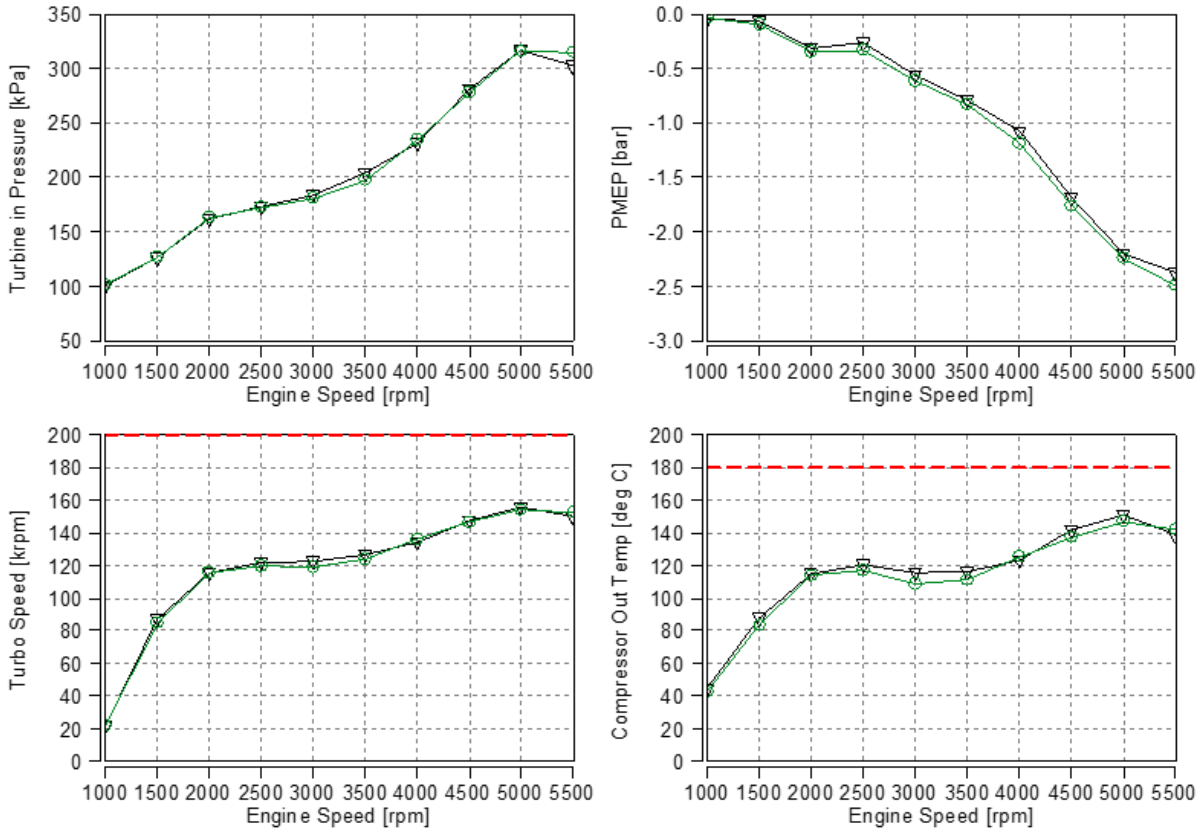


***Figure 181 - Turbine inlet pressure, PMEP, turbocharger speed, and compressor outlet temperature vs. engine speed at full load.***

VCT settings were optimized at each engine speed. An example of the contour plots generated for each speed are shown in Figure 182 for 3000 rpm, where cam timings for optimum efficiency were determined to be 20° bTDC IVO and 15° aTDC IVC.

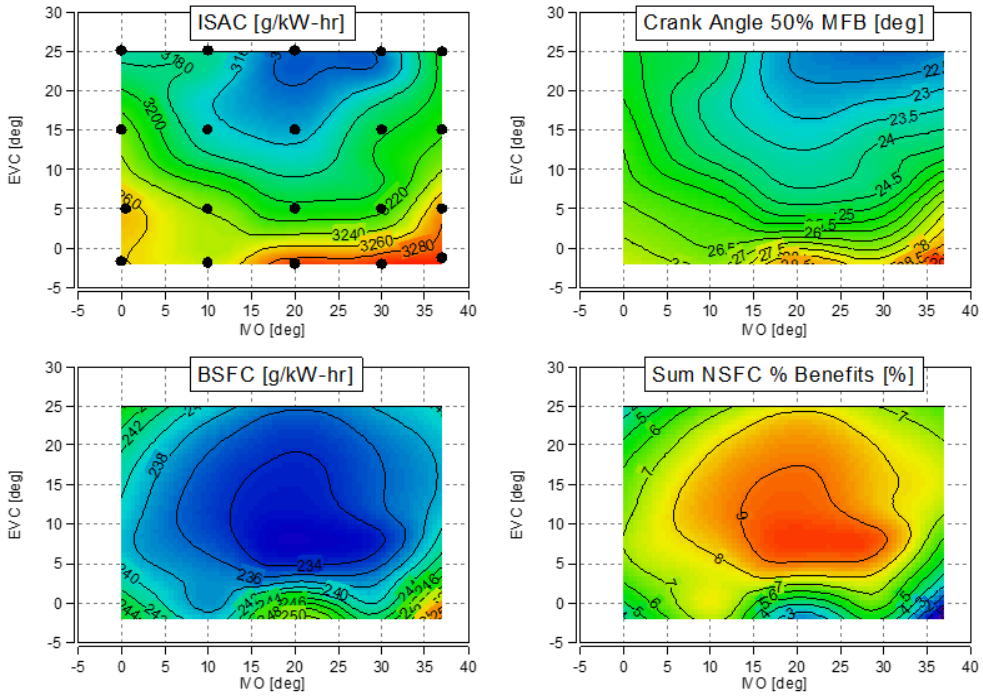


***Figure 182 - Optimization of VCT settings at 3000 rpm for best efficiency.***

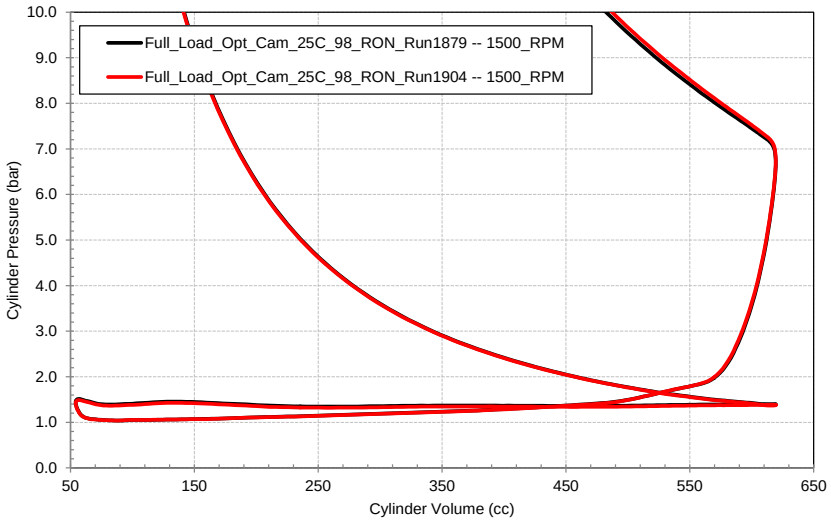


***Figure 183 - Cylinder pressure pumping loop at 1500 rpm.***

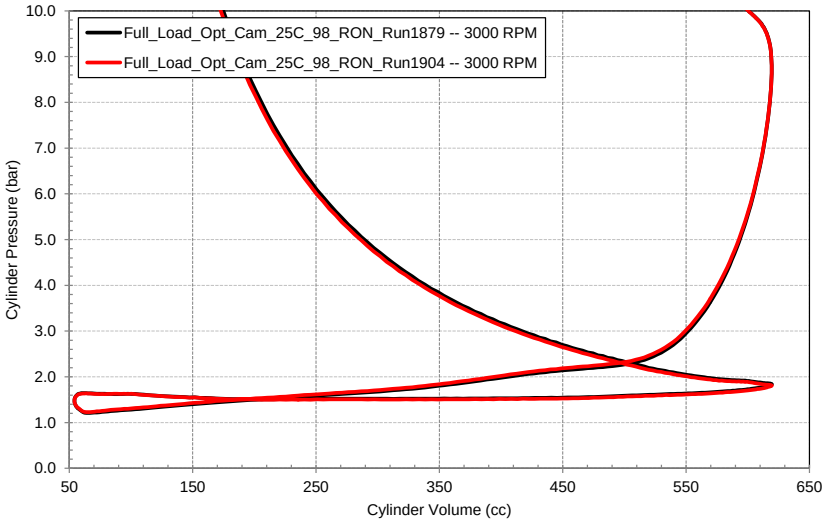


***Figure 184 - Cylinder pressure pumping loop at 3000 rpm.***

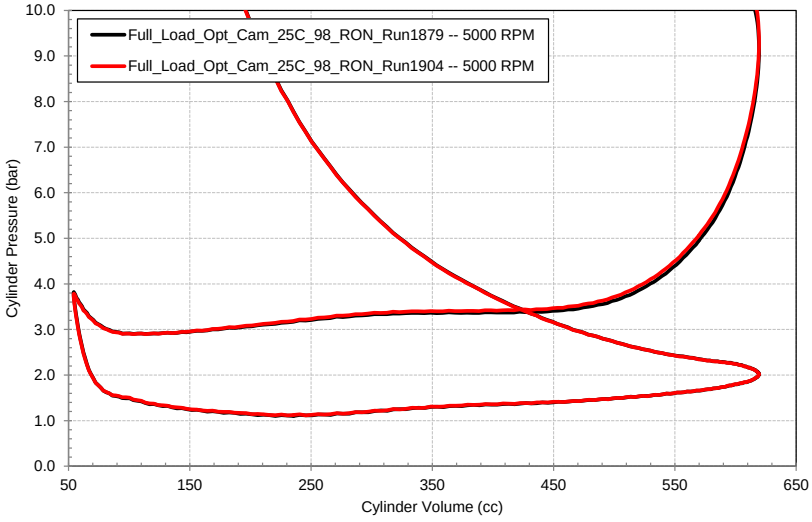


***Figure 185 - Cylinder pressure pumping loop at 5000 rpm.***

## Transient Time-to-Torque

Transient time-to-torque (TTT) was determined as a function of engine speed. This test is conducted on engine dynamometer by performing a throttle tip-in from 1 bar BMEP to full load at constant engine speed. Cylinder pressure vs. crank angle is measured on all cylinders, and the NMEP is calculated during the transient to full torque. (NMEP is the integral of PdV over the full engine cycle normalized for the engine displacement.) The metric used to quantify the TTT is the time required for the NMEP to increase from 5 bar to the full load value.

Results are shown in Figure 186 for the turbine scroll control valve open and closed. The TTT target for vehicle performance is 1.5 sec at 1500 rpm. As shown in Figure 186, the engine achieves the target with the turbine scroll control valve closed.

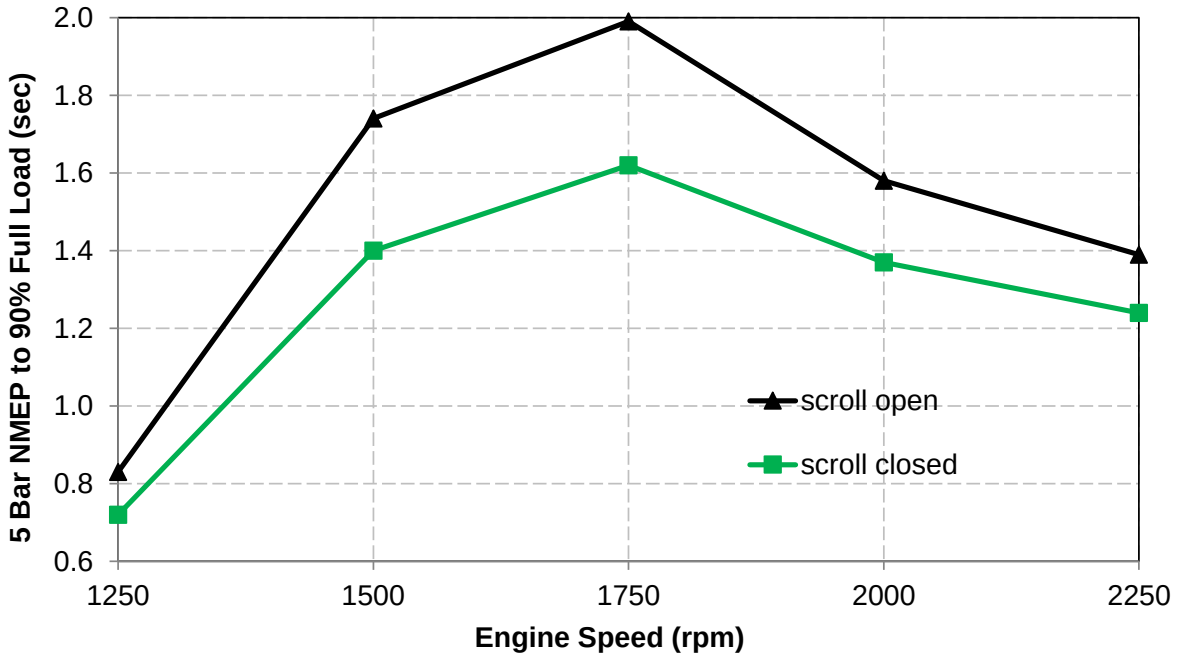


***Figure 186 - Transient time-to-torque vs. engine speed.***

## Summary

The 2.3L DOE engine achieves the steady state full load BMEP and transient TTT targets, ensuring that the performance metrics of the baseline vehicle with the 2.3L DOE powertrain would match those of the baseline vehicle with the baseline powertrain.

## Engine Mapping

Engine Mapping is performed to fill critical calibration tables for the powertrain control module (PCM) software. Steady state engine mapping was completed at Ford's Engine Laboratory Dynamometer facility (Figure 187). Indolene clear fuel nominally rated at 97 RON was used for testing and validation.

Engines used for mapping were as follows:
Engine #3: CT-998-AAX0-KST-XBD-31586 Test Request: AC7462
Engine #7: CT-998-AAX0-KST-XBD-31588 Test Request: AE8299

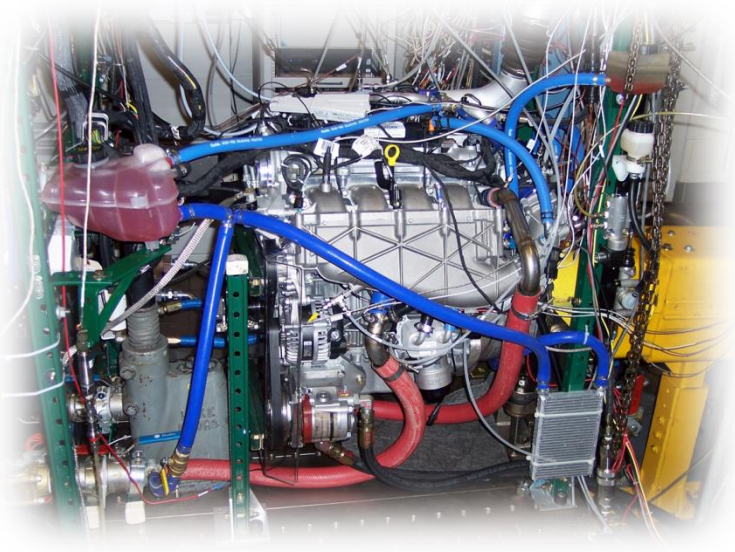

***Figure 187 - Mapping engine installed in dynamometer test cell.***

Mapping is performed in several key work streams: Cam Optimization, Start of Injection (SOI) / Fuel Rail Pressure (FRP), Air Charge, Turbocharger Controls, Torque/MBT/Exhaust Temperatures, Borderline Spark, and EGR. When those phases are complete, validation is performed by running all actuators in automatic mode and performing load sweeps over a range of speeds. The calibration values are compared against instrumentation values. Mapping and validation was completed using Autotest for autonomous engine mapping.

Key calibration parameters are included in each section below.

Electric TiVCT Cam Timing Optimization:
In this section, the track that the cam phasing follows is determined, as well as where along that track the cams will be scheduled, based on the operating conditions of the engine. The cams are generally scheduled to provide the best fuel economy, while avoiding combustion instability or high emissions. The proposed cam schedule is compared to the development mini-map data for consistency.

In the validation phase, the cam scheduling had to be adjusted. For best fuel economy, the intake cam was either fully advanced or fully retarded. The transition from full retard to full advance was too aggressive and had to be smoothed over a larger load range. The original and updated intake path for 1500 rpm is shown in the graph below.

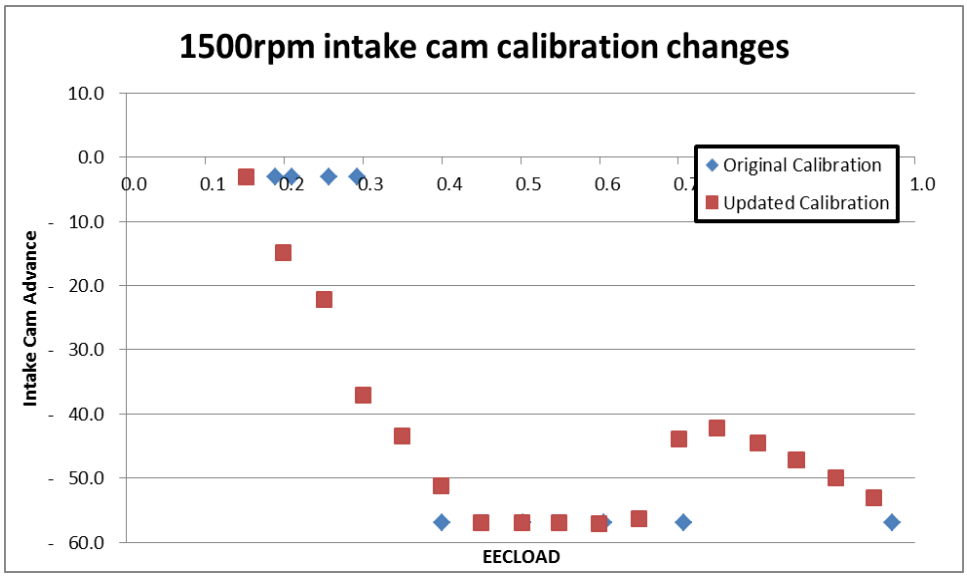


***Figure 188 - Initial and updated calibrations for intake cam advance vs. EEC Load.***

Direct Injection SOI and FRP Optimization:
SOI and FRP tables are developed by sweeping SOI and FRP at a range of speeds and loads. The corresponding tables are calibrated for best fuel efficiency while avoiding any steep increases in particulate emissions. Due to minimum pulse width concerns at light load, fuel rail pressure was reduced to 1100 psi for low speeds and low flows.

Air Charge:
Air charge is calibrated by running throttle sweeps at many speeds and cam positions. This is the most time-consuming and critical section of the process. Air blowthrough tables are calibrated in this section as well.

Turbo Controls:
Wastegate duty-cycle sweeps are performed at various speeds and loads in this section. The data can be mined to calibrate exhaust manifold pressure, exhaust backpressure, turbocharger performance, induction loss, and turbine protection tables.

Torque/MBT/Exhaust Temps:
Spark sweeps are performed at a range of speed and load conditions. This data is used to determine MBT spark. When MBT is determined, indicated torque, brake torque, and exhaust temperature tables can then be calibrated with the appropriate corresponding data.

Borderline Spark:
Borderline spark is calibrated via spark sweeps at a range of speeds and loads. Additionally, tables accounting for the effects of retarded spark on air charge temperature and engine coolant temperature are calibrated.

In this case, an automated testing program was used to perform the spark retard sweeps. An FKI4 limit was used to protect the engine from harsh knock. (FKI4 is Ford's knock algorithm based on cylinder pressure data.)

EGR:
Some of the calibration tables in the engine's control software have versions for EGR which also need to be calibrated. Cam optimization was also completed at 15% EGR to determine where along the cam track cam-timing would be optimal with cooled EGR. Both borderline and MBT spark are affected by EGR, so EGR spark modifier tables also have to be calibrated. They are calibrated by comparing 0% EGR spark-timing and 15% EGR spark-timing.

Advanced Technologies:
Scroll Control: Not used during steady-state mapping. The scroll control valve is only operated during a transient maneuver and was held open for the engine map.
VDOP/Oil squirters: Auto strategy was unavailable at the time of mapping. High pressure VDOP and oil squirters were engaged at 3000 rpm and above.

Cooled EGR:
EGR valve and low pressure air induction system throttle were manually controlled during mapping. A pressure difference of 4 kPa across the EGR valve and 15% EGR were the program targets.

## Validation

Validation was primarily completed by running pedal sweeps at different speeds with an auto calibration, controlled by Autotest. Measures of success are as follows:

- Air charge is +/- 5%.
- Inferred torque is +/-5 Nm or +/- 5%, whichever is larger.
- EXHMAP is +/- 2 inHg.
- EXHBP is +/- 2 inHg.
- Combustion stability is COV_IMEP <2 % for IMEP > 3.5 bar or SD_IMEP<7Kpa for IMEP < 3.5 bar.
- B/L spark should show FKI4 value ~ 0.3.
- MBT is checked via CA50.

## Challenges

Autotest is the standard tool used by the mapping group to quickly collect a large amount of data. Autotest was upgraded to meet the specific requirements of the 2.3L DOE engine mapping.

Maintaining 4 kPa across the EGR valve provided a challenge. While a low pressure difference is best for fuel economy, it is problematic for control. The traditional measure of success for the exhaust map model accuracy is greater than the desired pressure across the EGR valve.

Due to early mechanical non-conformance in other test cells, much of the initial mapping data was limited to 1.0 and later 1.3 EEC Load. Speed was also limited to 3000 rpm for a period of time. Some of the air charge tables were modeled where data was unavailable. Other tables, like the exhaust manifold pressure model, needed to be recalibrated once the speed and load limitations were lifted. The self-imposed limitations caused significant mapping rework, but kept the two engines from failing. The second engine had well over 1,000 test hours when it was finally removed from the test cell. (Note: Instead of installing new parts into the original engine in the cell, a backup engine was installed in the test room.)

Manifold charge temperature (MCT) sensors proved ineffective, so MCT had to be inferred based on CAC coolant inlet temperatures and TCT.

After mapping was completed, follow-up work was completed to better examine high load operation and address instabilities seen in-vehicle.

## Select Results

A final validation test was run. Measured vs. PCM load results mostly fell within the 5% measure of success. There were some errors at lower speeds and lower loads, but they were deemed acceptable.

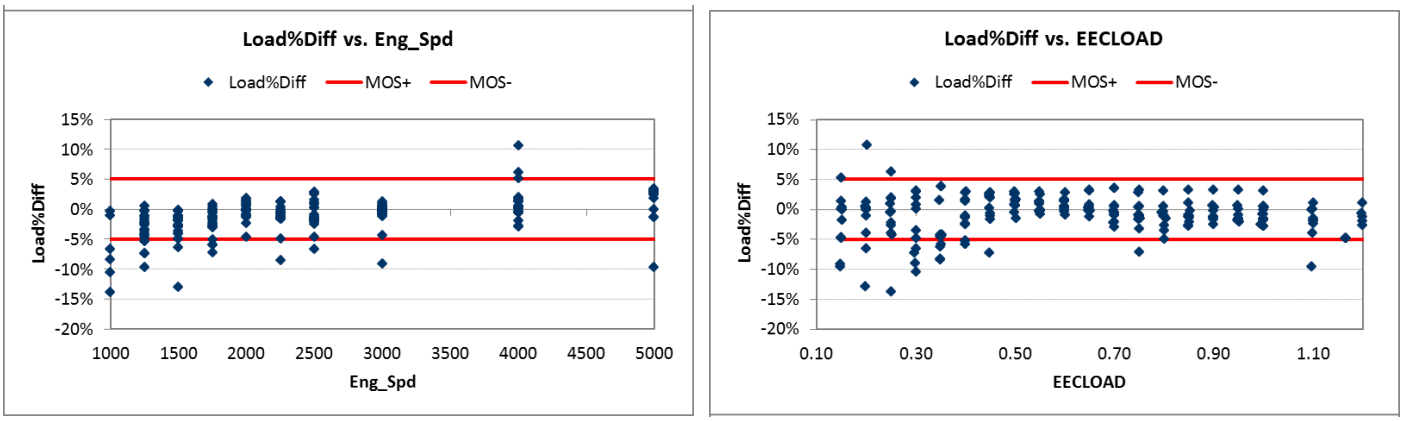


***Figure 189 - Difference in percent load between engine data and map vs. engine speed (left) and EEC Load (right).***

Measured and PCM brake torque also mostly fell within the measures of success. There is a slight calibration error at 5000 rpm, but for fuel economy demonstration purposes, it was decided that the issue does not warrant correction. The calibration was verified not to exceed component design limits even at operating conditions with the torque error.

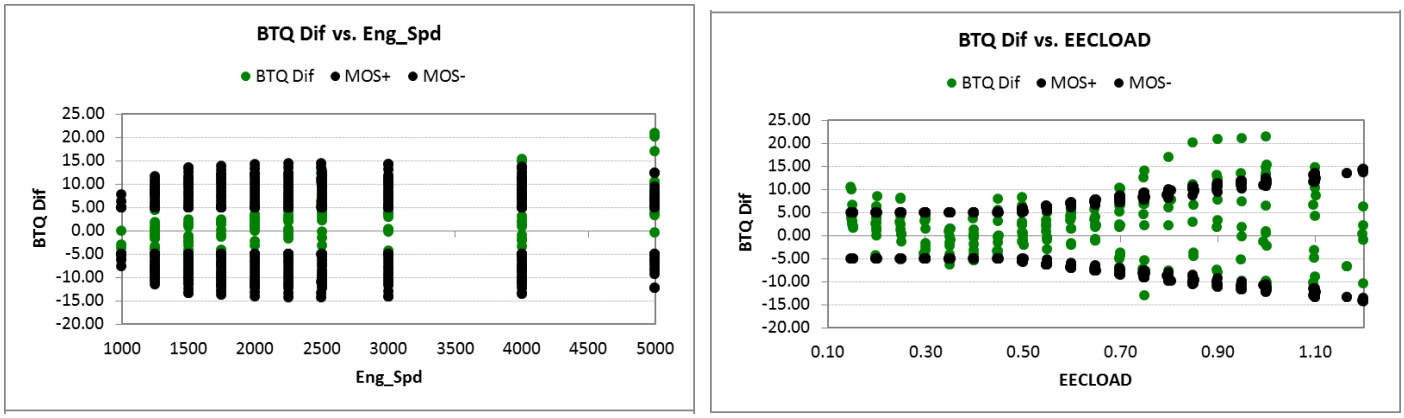


***Figure 190 - Difference in brake torque between engine data and map vs. engine speed (left) and EEC Load (right).***

Exhaust backpressure and exhaust manifold pressure were both well within the 2 inhg pressure measure of success for the speed and load range tested, as shown in Figure 191.

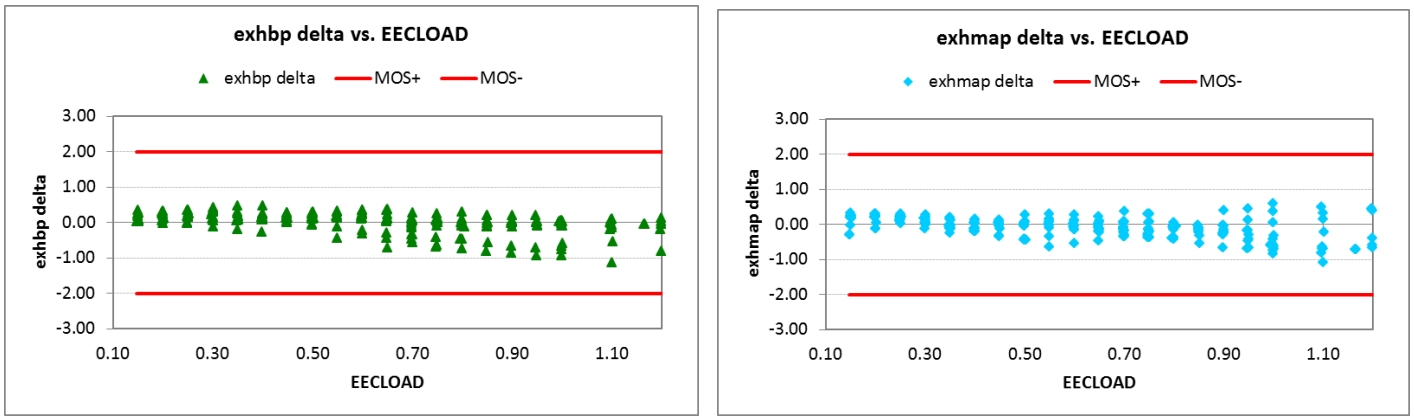


***Figure 191 - Difference in exhaust backpressure and manifold pressure between engine data and regressed engine map.***

CA50 for the non-EGR and EGR points are shown in Figure 192. The EGR points ranged from 5-15% EGR.

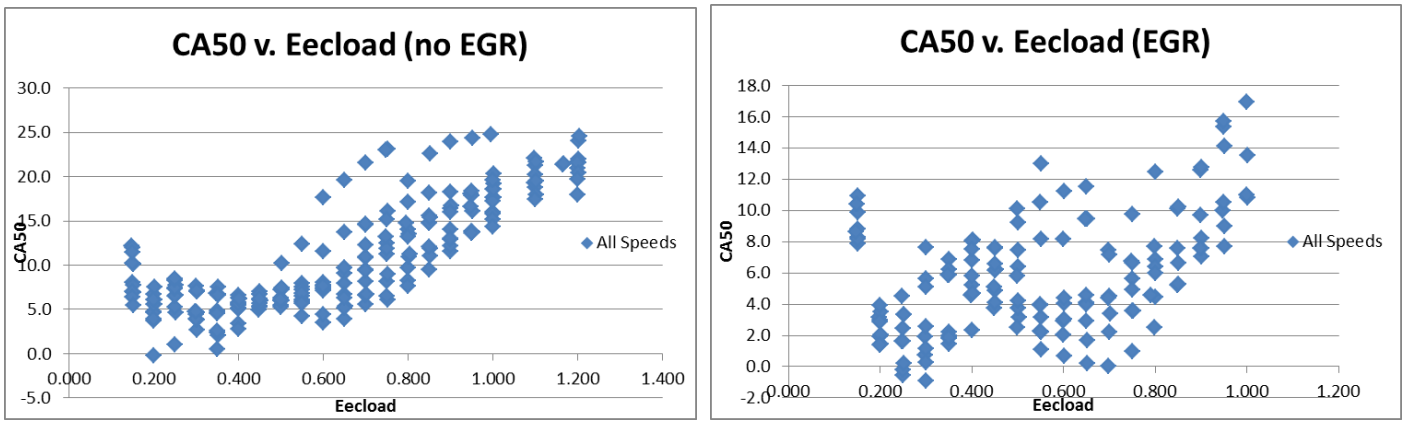


***Figure 192 - CA50 vs. EEC Load (air flow) for mapping data.***

## Steady State Emissions with Cold Fluids

The transient emissions development process at Ford was used to optimize and evaluate cold start and warm-up emissions. This process includes two key work streams:

1. Steady state cold fluids mapping to determine calibration settings for the DI control factors and cam timing.
2. Starter motor cranked cold starts to measure cumulative emissions, combustion stability, and catalyst light-off performance.

The focus of this section is the first phase of the process, in which the engine is run at steady state with cold fluids. The objective of steady state cold fluids mapping is to identify preliminary calibration settings to be used in transient cold start development, including:

- Direct Injection settings
- Injection timing, including up to 2 injections per event
- Split ratio for two fuel injections
- Fuel injection pressure
- Air-fuel ratio target
- Cam Timing settings
- Intake timing (shown as degrees retard from the base position shown in Figure 193 )
- Exhaust timing (shown as degrees retard from the base position shown in Figure 193)
- Spark retard settings
- Turbo actuator settings
- Electric wastegate
- Electric scroll control valve

This testing used Magneti Marelli 6 hole 34A 15 cc/sec fuel injectors, as determined during the SCE testing. The timing range of the twin independent electric VCT is shown in Figure 193, where the intake camshaft is shown in blue at full retard, and the exhaust camshaft is shown in red at full advance.

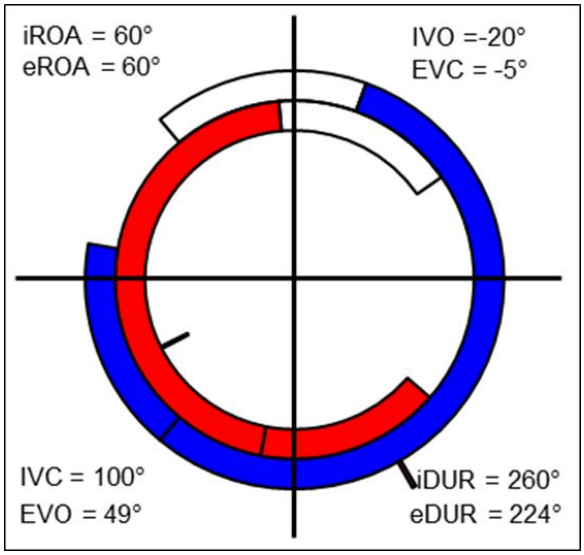


***Figure 193 - 2.3L I4 DOE cam timing.***

There are three unique phases of the engine start calibration which can be optimized via the steady state cold fluids mapping: 1) neutral idle, 2) drive idle, and 3) drive away. During each of these phases, injection timing, injection split ratio, injection pressure, air-fuel ratio target, cam timing, wastegate, and scroll control valve settings can all be varied. Neutral idle results, acquired first, were used as a starting point for both the drive idle and the drive away to reduce test time. For each of the phases, levels were swept for multiple control factors and the results analyzed to identify balanced attribute settings.

## Phase 1, Cold Neutral Idle

The first phase of testing is to emulate the cold neutral idle of a cold start. During an emissions cycle test, this phase is between the cold cranking and run up and the drive engagement, roughly from 2 seconds to 15 seconds of the test. For a typical driver, this can take longer or shorter in time, so it is important to find a robust solution that will satisfy regulatory and driver requirements. In each of the figures, factors which were held constant are shown below the graphs.

The first test of the engine was to run the cold idle with a single injection during the intake stroke, and sweep the injection timing, and run two injection pressures. The intent was to establish the cold idle capability of the engine when operating with what is assumed to be a “homogeneous” air-fuel mixture, although it is likely that the air-fuel mixture at the time of ignition is not completely uniform.

The data in Figure 194 shows trends similar to other DI engines, where earlier injection timing resulted in better mixing, thus lowering the HC emissions. It also showed the trend of lowering the PM emissions until it appears that the injection is early enough to have piston impingement influence the PM emissions. The data also shows that the engine is not very sensitive to fuel pressure during the cold idle phase. NOx, PM, CO, and stability do not change much, but there is an improvement in HC with higher fuel pressure for some of the injection timings.

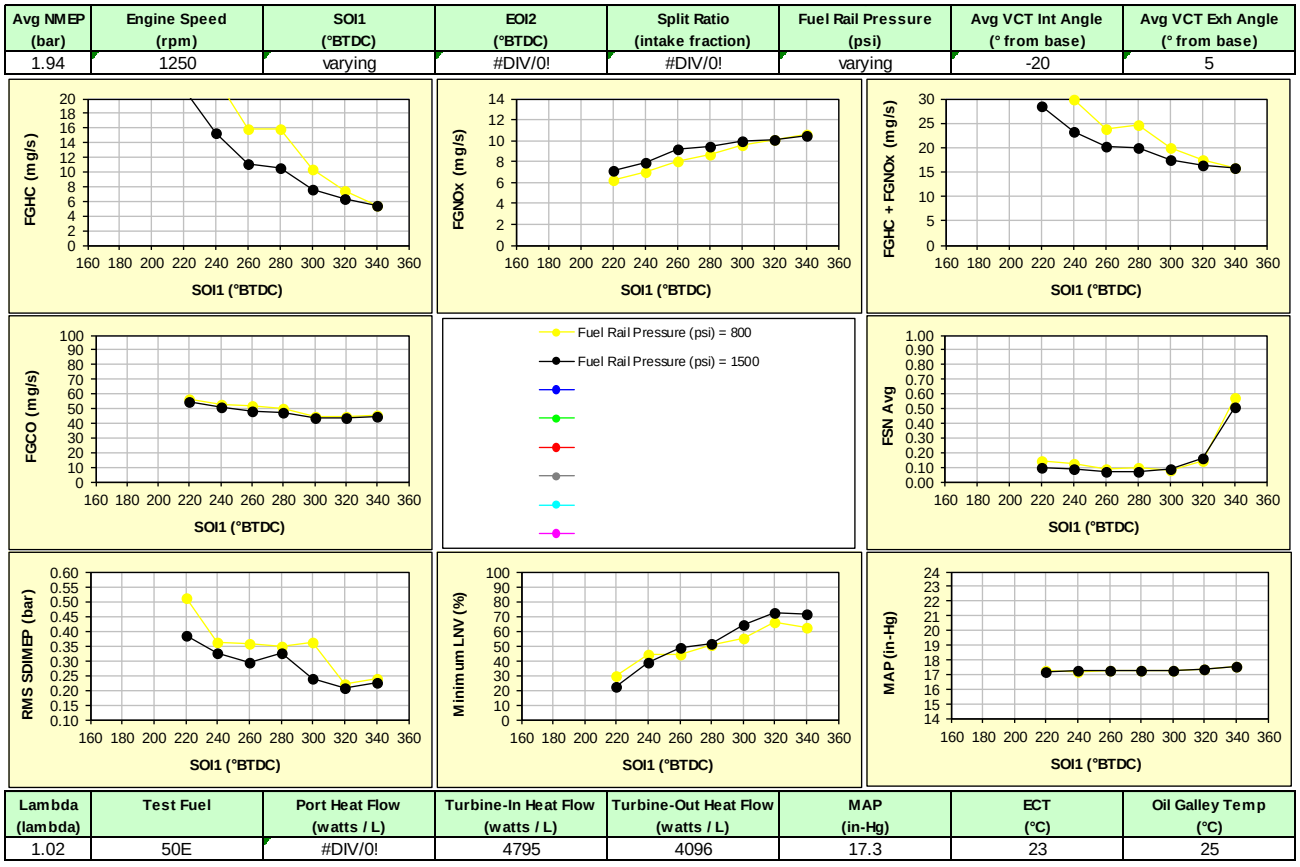


***Figure 194 - SOI1 and fuel rail pressure sweep with single intake injection.***

Next, two split ratios were run where the SCE development indicated the targets for gaseous and PM emissions as well as combustion stability could be met - 50/50 and 90/10 split ratios. For both split ratios, both the SOI of the intake injection and the EOI of the compression injection were swept, the throttle was fixed to keep the air flow constant, cams were set at -20IVCT/5EVCT, which is similar to the base position of other engines, and the spark was adjusted to maintain an IMEP of 1.9 bar. The results are shown in Figure 195 for the 50/50 split ratio and Figure 196 for the 90/10 split ratio.

| Avg NMEP (bar) | Engine Speed (rpm) | SOI1 (°BTDC) | EOI2 (°BTDC) | Split Ratio (intake fraction) | Fuel Rail Pressure (psi) | Avg VCT Int Angle (° from base) | Avg VCT Exh Angle (° from base) |
|---|---|---|---|---|---|---|---|
| 1.90 | 1250 | varying | varying | 0.50 | 801 | -20 | 5 |

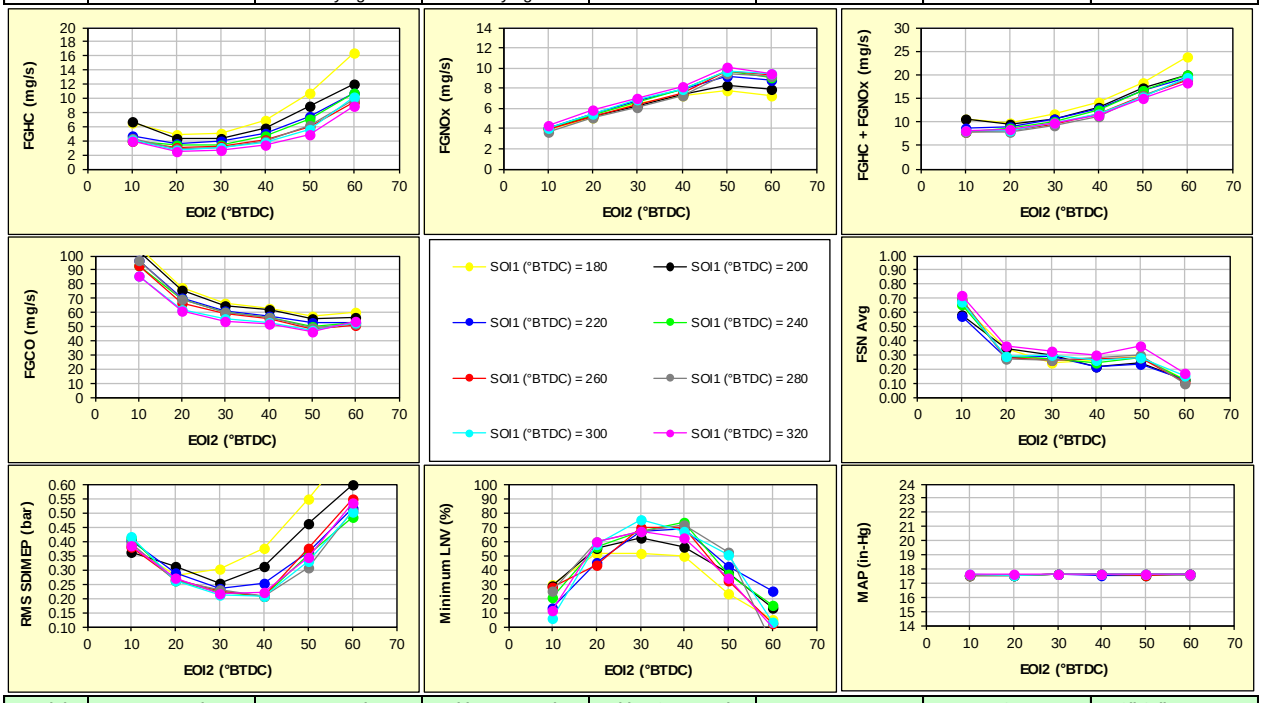


| Lambda (lambda) | Test Fuel | Port Heat Flow (watts / L) | Turbine-In Heat Flow (watts / L) | Turbine-Out Heat Flow (watts / L) | MAP (in-Hg) | ECT (°C) | Oil Galley Temp (°C) |
|---|---|---|---|---|---|---|---|
| 1.02 | 50E | #DIV/0! | 5215 | 4279 | 17.6 | 23 | 24 |

***Figure 195 - EOI2 and SOI1 sweep with 50/50 split ratio.***

| Avg NMEP (bar) | Engine Speed (rpm) | SOI1 (°BTDC) | EOI2 (°BTDC) | Split Ratio (intake fraction) | Fuel Rail Pressure (psi) | Avg VCT Int Angle (° from base) | Avg VCT Exh Angle (° from base) |
|---|---|---|---|---|---|---|---|
| 1.90 | 1250 | varying | varying | 0.90 | 801 | -20 | 5 |

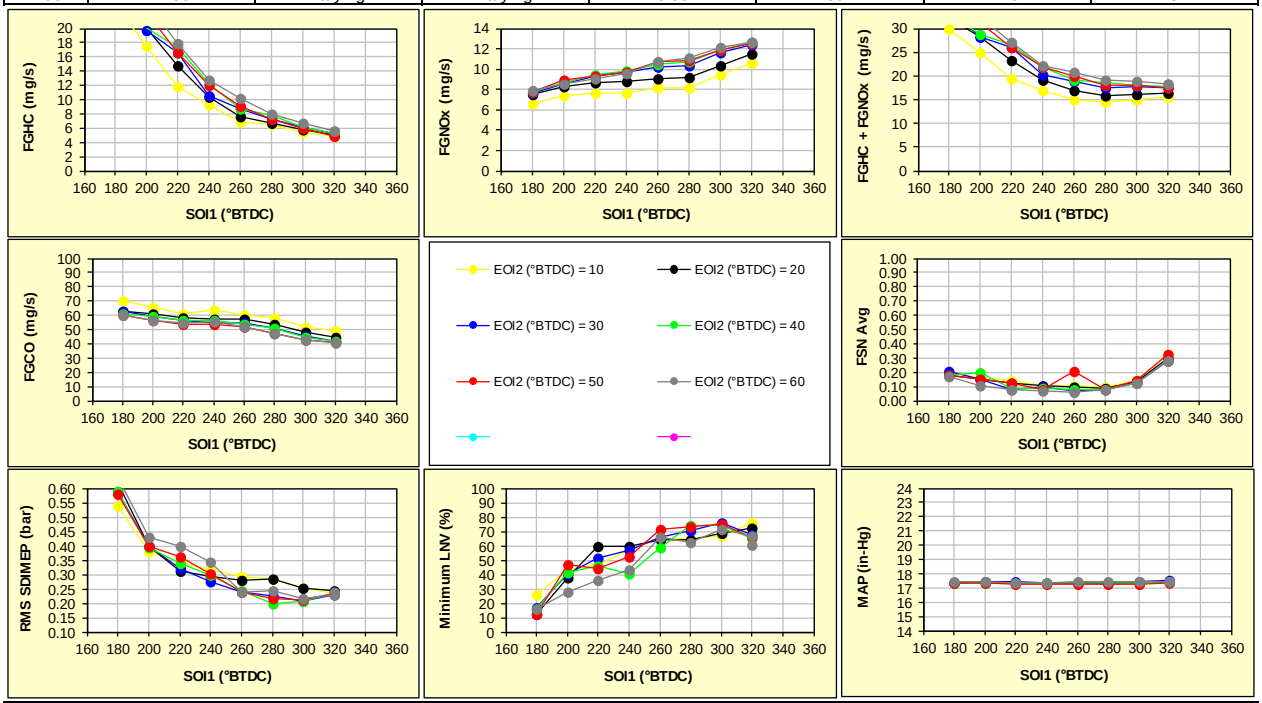


| Lambda (lambda) | Test Fuel | Port Heat Flow (watts / L) | Turbine-In Heat Flow (watts / L) | Turbine-Out Heat Flow (watts / L) | MAP (in-Hg) | ECT (°C) | Oil Galley Temp (°C) |
|---|---|---|---|---|---|---|---|
| 1.02 | 50E | #DIV/0! | 5020 | 3998 | 17.4 | 23 | 25 |

***Figure 196 - EOI2 and SOI1 sweep with 90/10 split ratio.***

The 50/50 split ratio data in Figure 195 showed good gaseous emissions, but the PM emissions were high. The data is shown sweeping the EOI of the second injection, with different SOI timings of the first injection on different lines. The data shows that the results are very dependent on the second injection timing but not on the first injection timing.

The 90/10 split ratio showed the opposite trend of the 50/50 data - elevated gaseous emissions but low PM emissions. Unlike the 50/50 graph, the 90/10 data is plotted sweeping the SOI of the first injection with different lines of the EOI of the second injection. This time, the data shows the results being very dependent on the timing of the first injection, and not on the second injection.

Based on these results, split ratio was swept to see if other ratios would provide a better compromise - 80/20, 70/30, 60/40, and even 30/70. The result was the 70/30 split ratio data of Figure 197. It exhibited the best compromise of combustion stability, gaseous emissions, and PM emissions. Of the 70/30 split ratio data, the results with the first injection at 300° bTDC and the second injection at 30° bTDC showed the best combination of HC, NOx, CO, PM, and combustion stability. In addition, the 70/30 split ratio showed a reasonable range of robustness for gaseous and particulate emissions, with SOI1/EOI2 extremes of 320/20 and 280/40 (inclusive) showing reasonable results as well.

| Avg NMEP (bar) | Engine Speed (rpm) | SOI1 (°BTDC) | EOI2 (°BTDC) | Split Ratio (intake fraction) | Fuel Rail Pressure (psi) | Avg VCT Int Angle (° from base) | Avg VCT Exh Angle (° from base) |
|---|---|---|---|---|---|---|---|
| 1.88 | 1250 | varying | varying | 0.70 | 801 | -20 | 5 |

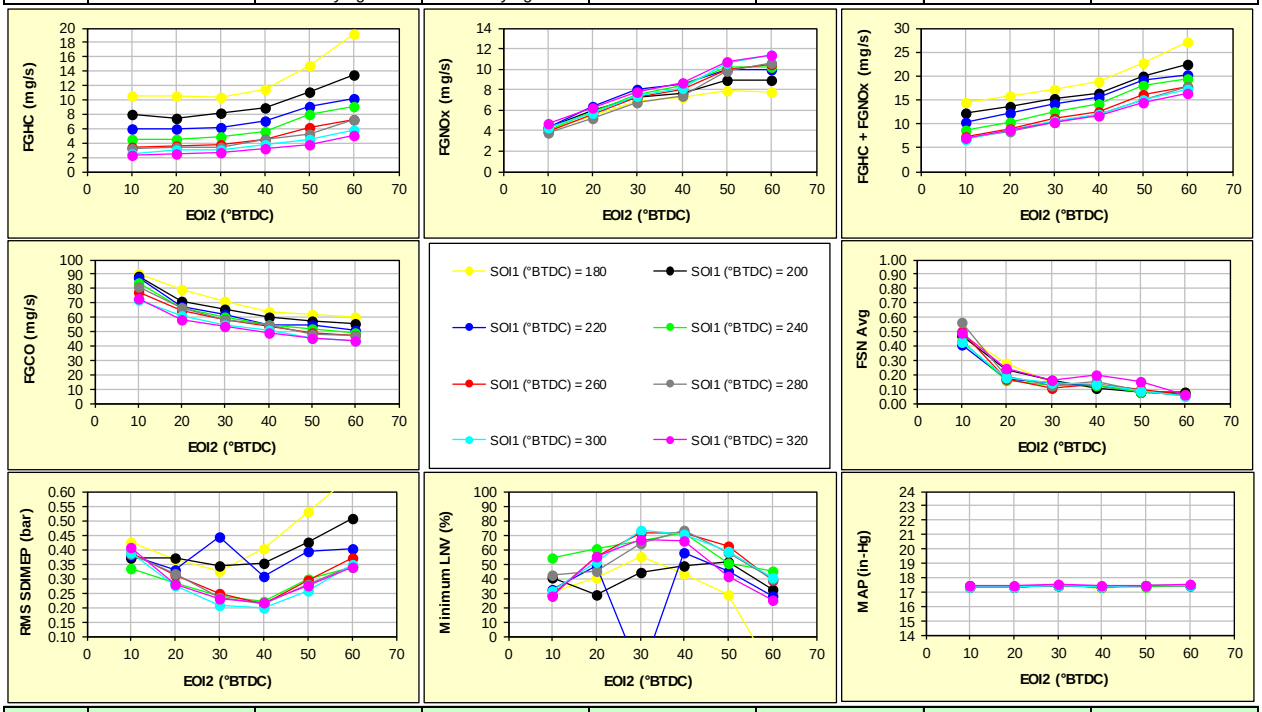


| Lambda (lambda) | Test Fuel | Port Heat Flow (watts / L) | Turbine-In Heat Flow (watts / L) | Turbine-Out Heat Flow (watts / L) | MAP (in-Hg) | ECT (°C) | Oil Galley Temp (°C) |
|---|---|---|---|---|---|---|---|
| 1.02 | 50E | #DIV/0! | 5151 | 4329 | 17.4 | 24 | 24 |

***Figure 197 - EOI2 and SOI1 sweep with 70/30 split ratio.***

Having determined the best settings for injection timing, split ratio, and FRP, the next procedure was to sweep the cam timing. The electric VCT mechanism has a range of 60° on both the intake and exhaust cams. A unique feature of electric VCT compared to hydraulically actuated VCT is the ability to phase to the best setting immediately without having to wait for sufficient oil pressure. For this development, 70/30 split ratio with 280/40 SOI1/EOI2 timing was held constant, the throttle was varied to keep the airflow constant across all of the tests, and the spark was varied to keep the NMEP at 1.9 bar.

Examining Figure 198, choosing the cam timing required evaluating the best compromise of gaseous emissions, PM emissions, and combustion stability. Based on that, the engine seems to run well at -30 IVCT/

30 EVCT. Much like the injection split ratio/timing study, the cam timing settings appear to be reasonably robust for gaseous and PM emissions, with -40/20 and -20/40 showing reasonable results. But the overall improvement in combustion stability as well as slightly better HC emissions appears to be worth the tradeoff of slightly higher NOx when comparing -30/30 to both -40/20 and -20/40.

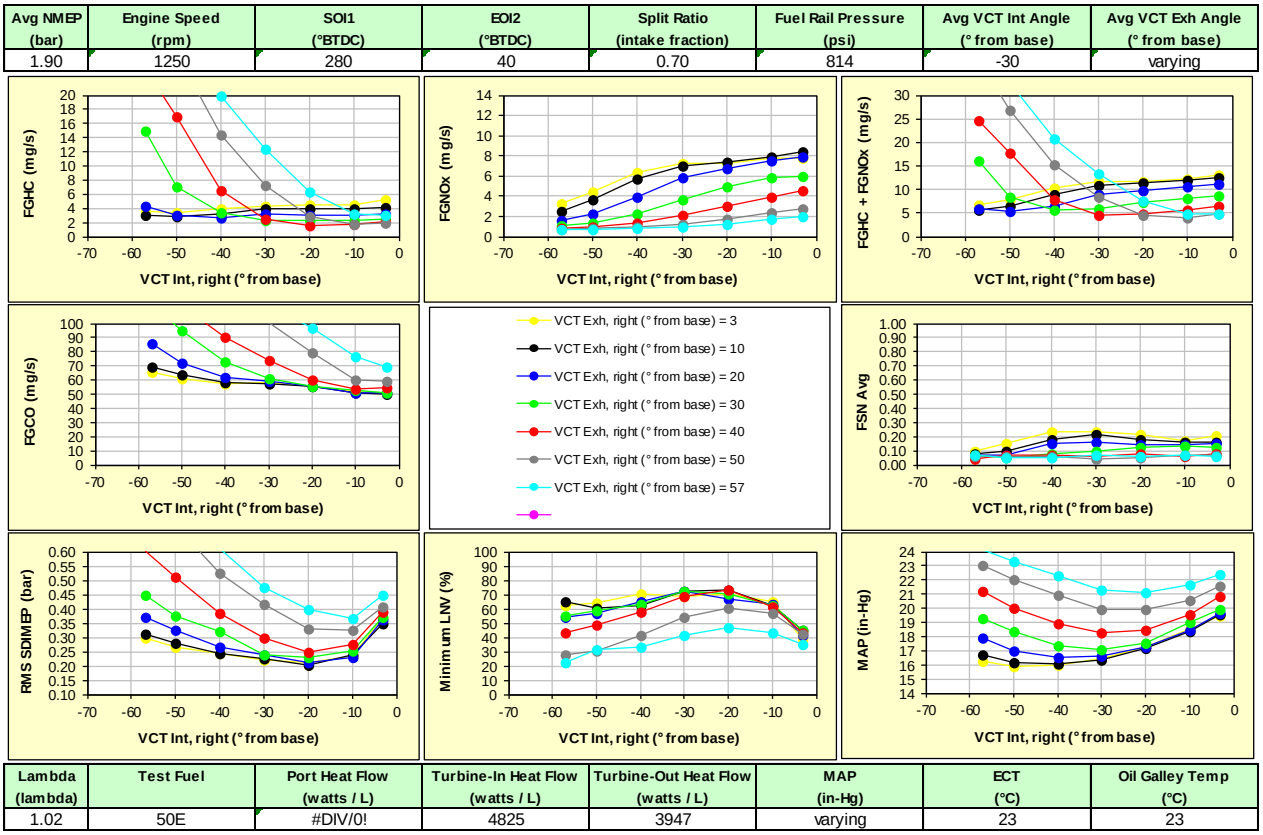


***Figure 198 - Intake and exhaust cam sweep with 70/30 split ratio.***

Next, the engine was tested varying the spark timing (heat sweep), air-fuel ratio target, and injection pressure. All were run to maintain a NMEP of 1.9 bar, and some with other changes as well, which will be discussed.

The spark timing sweep (shown as heat flow) in Figure 199 shows a very wide range of spark timing that will meet combustion stability targets. If more heat is needed for catalyst light-off, the engine will be able to retard spark more without a major penalty to combustion stability. There will be a slight improvement to HC and an increase of NOx flow (higher flow rate). Note, thermal conditions in the combustion chamber differ from actual cold starts. This effect will be investigated again during the cold start phase of TED. This testing also identified a PM concern that turned out to be a drift problem due to a deposit issue with the Magneti Marelli injectors when running non-detergent indolene clear fuel. This was demonstrated by cleaning the injectors on this engine and retesting, as well as testing of detergent fuel on a different engine.

| Avg NMEP (bar) | Engine Speed (rpm) | SOI1 (°BTDC) | EOI2 (°BTDC) | Split Ratio (intake fraction) | Fuel Rail Pressure (psi) | Avg VCT Int Angle (° from base) | Avg VCT Exh Angle (° from base) |
|---|---|---|---|---|---|---|---|
| 1.90 | 1250 | varying | 40 | 0.70 | 817 | -30 | 30 |

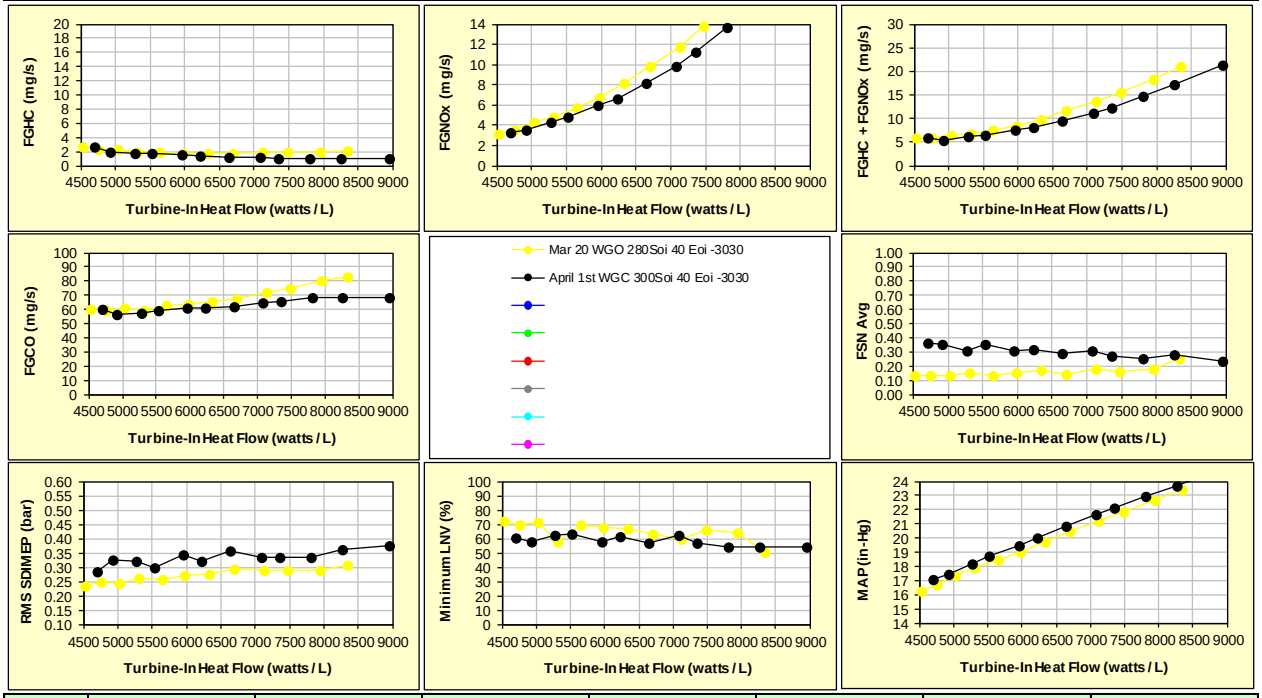


| Lambda (lambda) | Test Fuel | Port Heat Flow (watts / L) | Turbine-In Heat Flow (watts / L) | Turbine-Out Heat Flow (watts / L) | MAP (in-Hg) | ECT (°C) | Oil Galley Temp (°C) |
|---|---|---|---|---|---|---|---|
| 1.02 | 50E | #DIV/0! | varying | varying | varying | 25 | 25 |

***Figure 199 - Heat flow (spark timing) sweep with 70/30 split ratio.***

The air fuel ratio sweep shown in Figure 200 demonstrated that the best emissions were at 1.02 lambda, but the HC emissions are robust to just rich of 1.0 lambda. With this ability, the engine can run at 1.0 or 1.01 lambda during the time the catalysts are warming up to a working temperature, and not be oversaturated with oxygen and reduce the risk of NOx breakthroughs during the first hill.

The fuel rail pressure sweep shown in Figure 201 demonstrated that emissions and combustion with this engine are relatively insensitive to injection pressure changes. This is unlike many other direct injection engines which show a strong trend of better PM and gaseous emissions with higher pressure. This was also seen during single injection testing in Figure 194. Along with the pressure sweep, split ratio was swept at the same time, confirming the 70/30 as the most reasonable compromise of emissions and stability.

| Avg NMEP (bar) | Engine Speed (rpm) | SOI1 (°BTDC) | EOI2 (°BTDC) | Split Ratio (intake fraction) | Fuel Rail Pressure (psi) | Avg VCT Int Angle (° from base) | Avg VCT Exh Angle (° from base) |
|---|---|---|---|---|---|---|---|
| 1.90 | 1250 | varying | 40 | 0.70 | 815 | -30 | 30 |

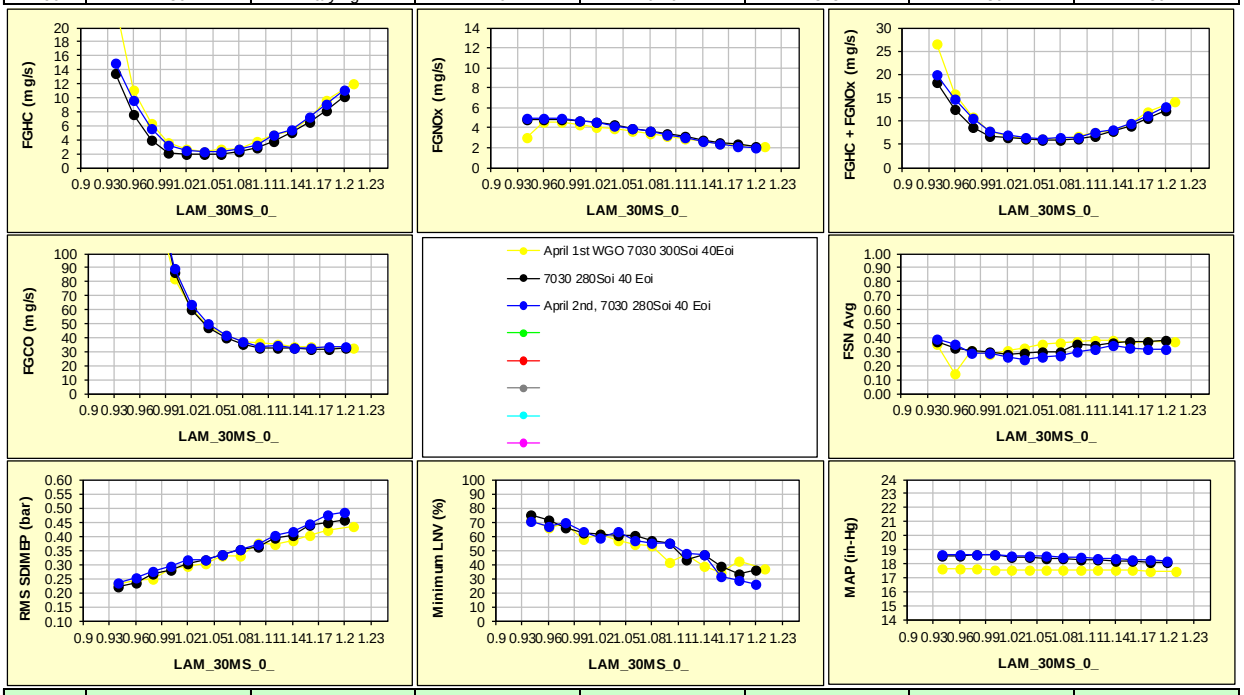


| Lambda (lambda) | Test Fuel | Port Heat Flow (watts / L) | Turbine-In Heat Flow (watts / L) | Turbine-Out Heat Flow (watts / L) | MAP (in-Hg) | ECT (°C) | Oil Galley Temp (°C) |
|---|---|---|---|---|---|---|---|
| 1.07 | 50E | #DIV/0! | 5078 | 4302 | 18.1 | 24 | 25 |

***Figure 200 - Air-fuel ratio sweep with 70/30 split ratio.***

| Avg NMEP (bar) | Engine Speed (rpm) | SOI1 (°BTDC) | EOI2 (°BTDC) | Split Ratio (intake fraction) | Fuel Rail Pressure (psi) | Avg VCT Int Angle (° from base) | Avg VCT Exh Angle (° from base) |
|---|---|---|---|---|---|---|---|
| 1.92 | 1250 | varying | 40 | varying | varying | -29 | varying |

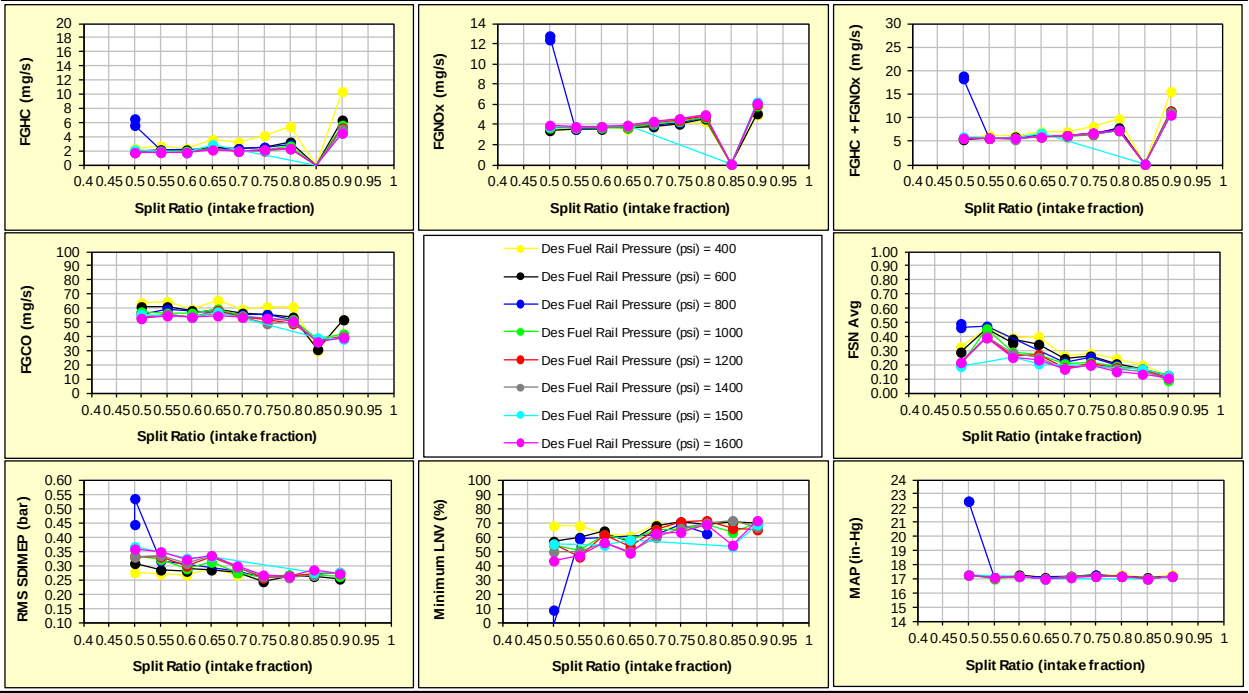


| Lambda (lambda) | Test Fuel | Port Heat Flow (watts / L) | Turbine-In Heat Flow (watts / L) | Turbine-Out Heat Flow (watts / L) | MAP (in-Hg) | ECT (°C) | Oil Galley Temp (°C) |
|---|---|---|---|---|---|---|---|
| 1.02 | 50E | #DIV/0! | 5057 | 4167 | 17.3 | 25 | 24 |

***Figure 201 - Split ratio and fuel ratio pressure sweep at 290/40 injection timing, -30/30 cam timing.***

The final part that was run during the neutral idle portion was the wastegate position and the scroll control valve position. Since it is hypothesized that they will affect the heat flow significantly, spark was swept to achieve the heat flux sweep.

The data is mixed in Figure 202, but due to the nature of the cold fluids testing, where the engine is run for an extended time at steady state, any transient heat flow advantages could have been masked. Lacking direction from the cold fluids testing, the cold start testing will be run with the wastegate open and the scroll control valve closed- which in theory should minimize the amount of exposed materials that the exhaust gases will have to warm in addition to the catalysts.

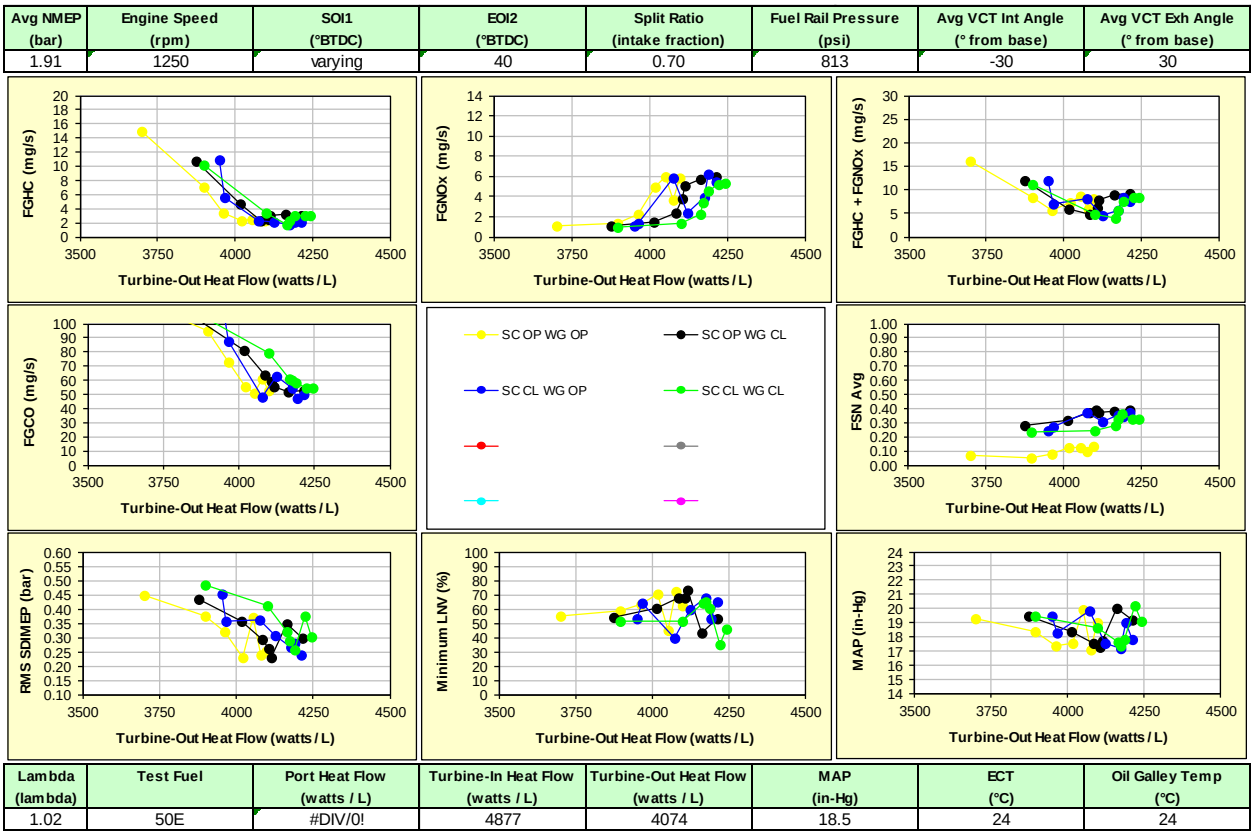


***Figure 202 - Heat flow, scroll control valve and wastegate sweep.***

## Phase 2, Cold Drive Idle

The next phase of testing emulates the time after the transmission is changed from park to drive on a cold engine and lasts through when the driver accelerates from stop. During an emissions test, the drive engagement occurs at 15 seconds, and the drive away occurs at 20 seconds. This portion of the test is also where the closed loop fuel typically begins to operate, and ideally the catalyst is warm enough to start catalysis, and is transitioning to a fully operating temperature range.

The initial development assumes the calibration for drive idle is the same as that for neutral idle, as the approach is straightforward if the calibration remains the same. To see if the settings for the neutral idle would apply, the testing was limited to injection timing sweeps at three split ratios, as well as limited cam timing sweeps.

As expected, the higher load of the drive idle resulted in much higher hydrocarbon emissions, as well as elevated NOx emissions. This can be seen in the following injection timing sweep data with 70/30 split ratio, and followed in the 80/20 testing as well as the 50/50 testing.

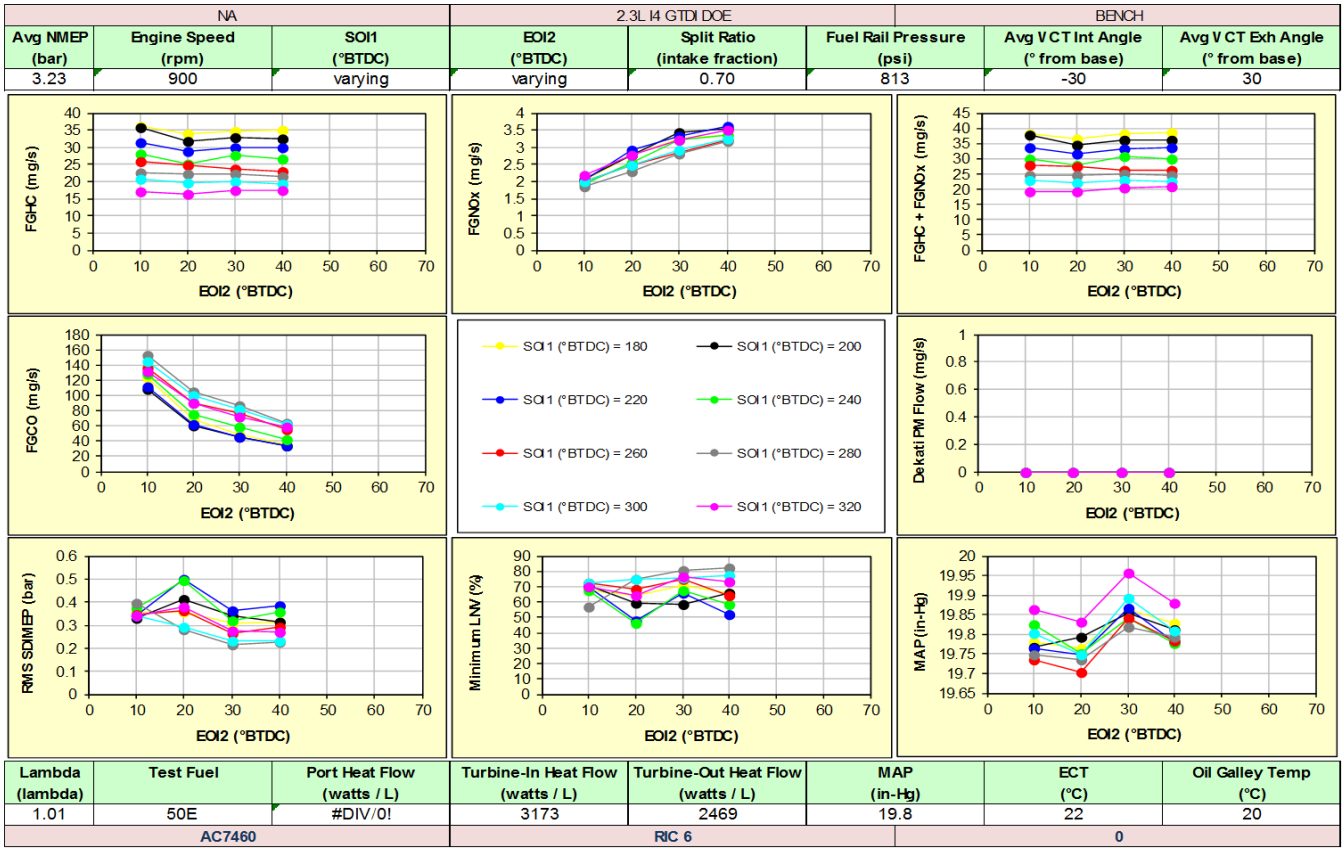


***Figure 203 - SOI1 and EOI2 sweep with 70/30 split ratio.***

The drive idle data, shown in Figure 203, does indicate that the neutral idle settings will work well - the FGHC+NOx was low at 300° bTDC timing, and the earlier second injection resulted in lower smoke.

Next a cam sweep test was performed. During the testing, the smoke and stability measurement instrumentation was not working correctly, so some data is missing. The cam sweep data, Figure 204, showed that the neutral idle setting of -30 intake, +30 exhaust will work, but a small adjustment could result in better emissions - both -20/40 and -20/20 are slight improvements. Depending on the cam tracks available for mapping, the movement will be decided based on track availability.

| Avg NMEP (bar) | Engine Speed (rpm) | SOI1 (°BTDC) | EOI2 (°BTDC) | Split Ratio (intake fraction) | Fuel Rail Pressure (psi) | Avg VCT Int Angle (° from base) | Avg VCT Exh Angle (° from base) |
|---|---|---|---|---|---|---|---|
| -1.49 | 900 | 300 | 30 | 0.70 | 797 | -29 | varying |

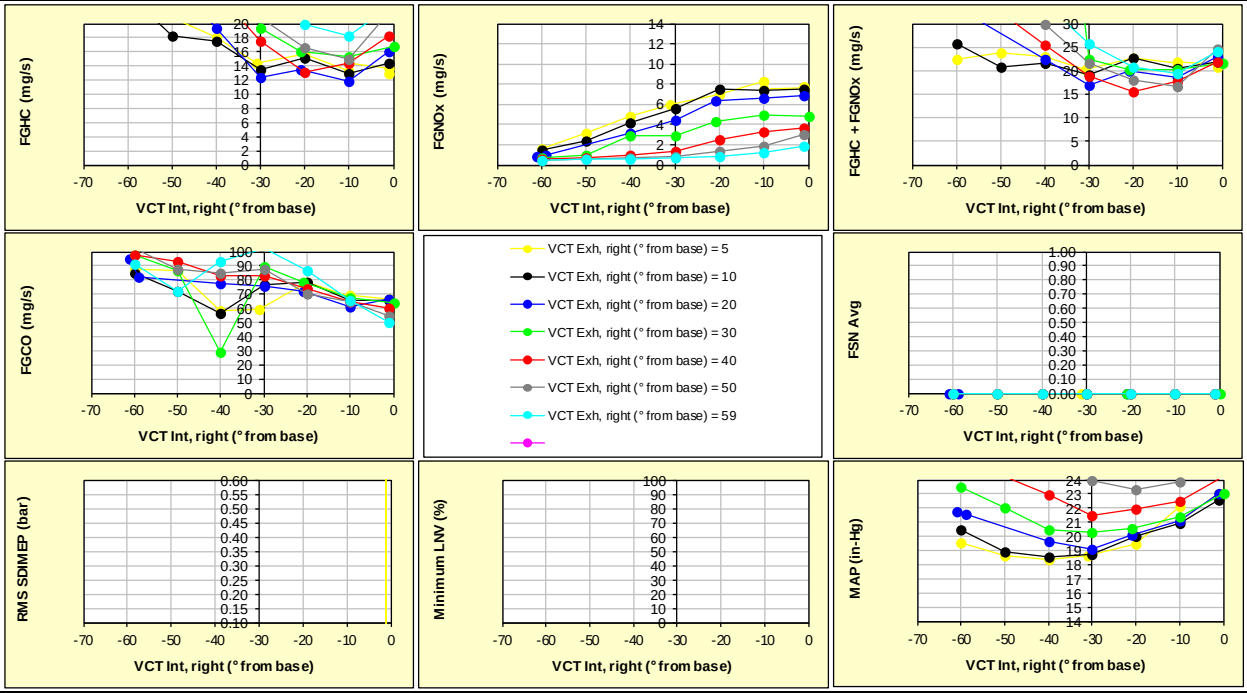


| Lambda (lambda) | Test Fuel | Port Heat Flow (watts / L) | Turbine-In Heat Flow (watts / L) | Turbine-Out Heat Flow (watts / L) | MAP (in-Hg) | ECT (°C) | Oil Galley Temp (°C) |
|---|---|---|---|---|---|---|---|
| 1.03 | 50E | #DIV/0! | 3406 | 2860 | varying | 22 | 18 |

***Figure 204 - Intake and exhaust cam sweep with 70/30 split ratio.***

## Phase 3, Simulated Drive Away

The final part of the cold fluids testing portion of the transient emissions development work focused on the drive away portion of the cold start. On an emissions test, this occurs at roughly 20 seconds. This can be a sensitive portion of the test where the catalyst is not always up to temperature, and combustion stability issues may be more apparent to the driver.

The testing in this phase assumes that single injection is a more likely setting, as intake/compression injection tends to elevate PM during this transient. This results in limited testing - sweeping the single injection timing, cam timing, and spark timing. All the tests were run at 1600 rpm and a load of 6.5 bar NMEP, which is representative of the average torque during the drive away.

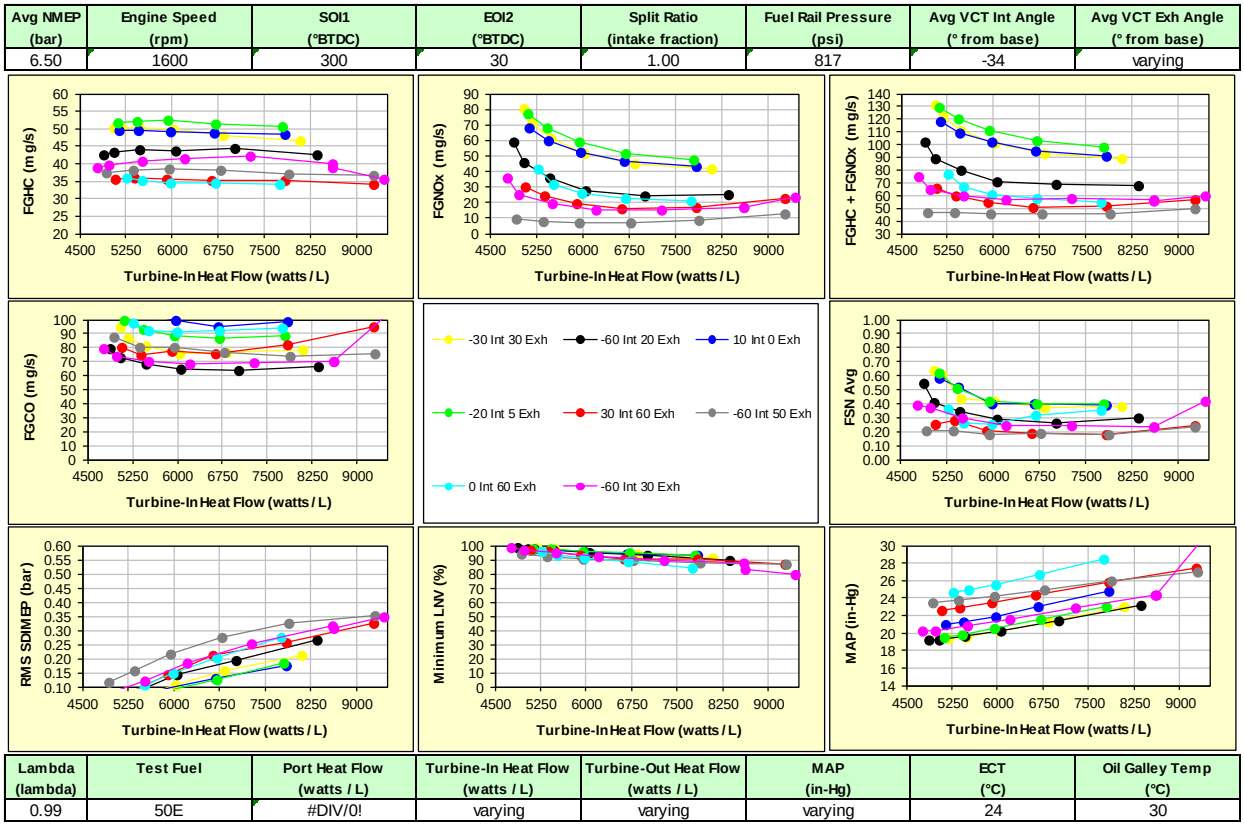


***Figure 205 - Heat flow and cam timing sweep with intake only injection.***

Not surprisingly, the spark sweep (as seen as heat flow, Figure 205) showed a moderate influence on gaseous and PM emissions as well as stability which allows the engine to run various spark settings - if the catalysts require a little more heat, or running at MBT for best fuel economy. The data shows that the -30/30 cam settings determined for the neutral idle are not the ideal settings for the drive away; the -30/30 cam timing resulted in high HC and NOx emissions, whereas several other cam settings with later exhaust and/or earlier intake timing (more exhaust expansion and/or more overlap) were better for gaseous emissions, with only a moderate compromise on stability.

## Summary of Results

The steady state cold fluids testing successfully characterized fuel injection, cam, and spark settings against the key attributes, allowing preliminary settings to be selected for the transient cold start and warm up testing. Based on the cold fluids results, the transient cold start testing initially focused on the following settings:

Cold Neutral and Drive Idle:

- 70/30 intake/compression injection split ratio
- 300 SOI bTDC/ 30 EOI bTDC injection timing for the above split injection
- -30 IVCT / + 30 EVCT cam timing for the neutral idle
- -20 IVCT /+20 EVCT cam timing for the drive idle

Drive away:

- Cam timings of 0/60, -30/60, -60/30 are all better than the cold idle cam timing
- Single injection of 300° bTDC

Fuel rail pressure was found to have only a minor impact on the cold emissions. As shown above, best emissions settings during the drive away differed from the cold idle for fuel injection scheduling as well as cam timing. The selection of the final cam timing for drive away was based on the engine mapping and transient cold start and warm-up test results.

## Transient Cold Start Emissions Development

The transient emissions development process at Ford was used to optimize and evaluate cold start and warm-up emissions. This process includes two key work streams:

1. Steady state cold fluids mapping to determine calibration settings for the DI control factors and cam timings.
2. Starter motor cranked cold starts to measure cumulative emissions, combustion stability, and catalyst light-off performance.

The preceding section described the cold fluids mapping process. The focus of this section is the second phase of the process, in which the engine is started at ~ 70°F with a starter motor, and undergoes a transient warm-up simulating the first portion of the FTP on an engine only dynamometer. The objective of the transient cold start testing is to validate the settings found in the cold fluids mapping process by measuring cumulative emissions, combustion stability, and catalyst light-off performance. The settings include:

- Direct injection settings
  - Injection timing
  - Split ratio
  - Injection pressure
  - Air-fuel ratio target
- Cam timing settings
  - Intake timing
  - Exhaust timing
- Heat flux settings (i.e., mass flow and spark retard)
- Turbocharger actuator settings
  - Electric wastegate
  - Electric scroll control valve

The targets for the transient cold start testing for cumulative emissions and catalyst light-off performance are shown in Table 12. The 0-20 second values shown are consistent with a vehicle that demonstrates SULEV30 tailpipe emissions and, if met during the transient emission development process, provide high confidence that full FTP cycle tailpipe emission goals can be achieved.

***Table 12 - Transient cold start targets.***

| ***21° C. Cold Start Emissions*** | | | |
|---|---|---|---|
| | **method** | **units** | **target** |
| **Heat Fluxes and Temperatures** | | | |
| catalyst inlet gas temperature @ 15s on FTP75 | cold start, 1/16" t/c | °C | 425 |
| catalyst midbed temperature @ 20s on FTP75 | cold start, 1/16" t/c | °C | 345 |
| **Attributes (bold = tracked in comb. workbook)** | | | |
| **0-20s Cumulative** | | | |
| **0-20s FGHC** | bench FID | mg | 100 |
| **0-20s FGNOx** | bench | mg | 127 |
| **0-20s FGCO** | bench | mg | |
| 0-20s FGHC + FGNOx | bench + bench | mg | 227 |
| **0-20s Particulate Mass, PM** | integrated modal | mg | **3.0** |
| 0-20s Particulate Number, PN | integrated modal | # | |

The hardware used for this testing is listed below:

Catalysts: Full useful life (FUL)
Fuel injector: Magneti Marelli 6 Hole 34A 15 cc/sec
Fuel injector driver: Bosch HDEV5.1
Spark plug: 4.5 mm reach, 0.034” gap
Ignition: Diamond coil 120 mJ
VCT: Twin independent electric

Cam timings and the range of the electric VCT units were previously shown in Figure 193.

## Test Procedure

The engine dynamometer cold start and drive away transient procedure simulates a vehicle cold start at 70°F, to replicate the first 30 seconds of a FTP 75 test. The first 30 seconds of the FTP are as follows: engine start via the starter (not the dynamometer), an idle simulating a neutral idle, an idle simulating a drive engagement, and then a drive away transient (DAT) tip-in, as shown in Figure 206.

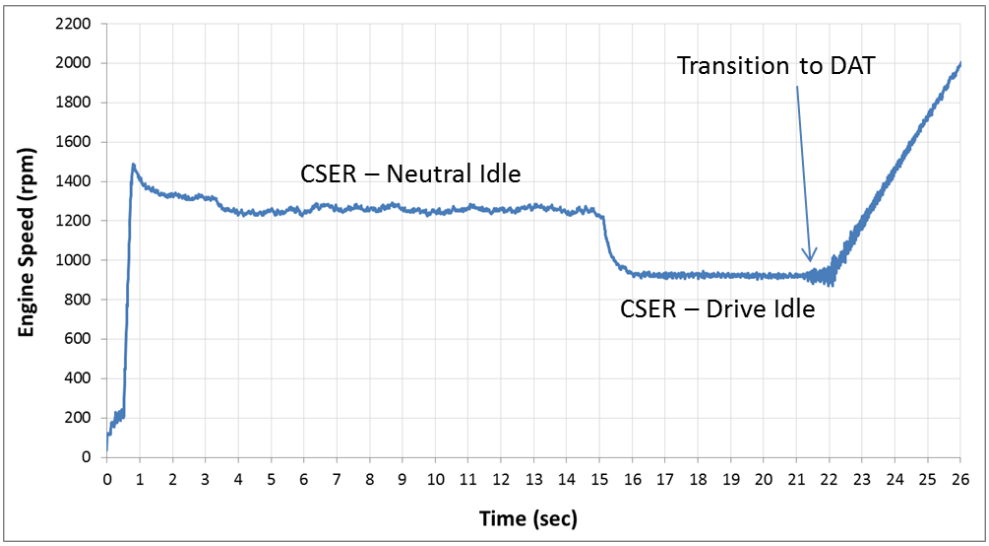


***Figure 206 - Engine dynamometer transient cold start, neutral idle, drive idle, and drive away.***

Gaseous emissions are measured with modal emissions benches, unburned HC are also measured with a fast flame ionization detector (fast FID) as well, and particulates are measured using a micro-soot sensor. Mass flow data is used to calculate the mass of emissions that are produced by the engine. Exhaust temperatures are measured at the turbocharger inlet, turbocharger outlet, catalyst inlet, and catalyst midbed (1” down from the front face of the brick).

During this testing, the procedure was defined and the controller was tuned to follow the trace. After the engine ran in a satisfactory manner for the entire test, fresh catalysts were installed and the settings from the cold fluids testing described in the previous section were used. These settings were:

Part 1, neutral idle:
- Split ratio of 70% intake/ 30% compression injection by mass
- SOI of 300° bTDC/30° bTDC for the above split injection.
- VCT settings at -30° IVCT, +30° EVCT retard from base

Part 2, drive idle:
- Split ratio of 70 intake/ 30 compression injection by mass
- SOI of 300° bTDC/30° bTDC for the above split injection.
- VCT setting at -30° intake, +20° exhaust, changed to -20°/+20° for smoother cam calibration.

Part 3, drive away:
- Split with a separation of 2.0 msec, but single injection should be similar.
- Injection timing 300° bTDC.

The cold fluids testing also showed a wide range of acceptable cam timings for the drive away. Each of these cam timings require an accompanying air charge and torque calibration to maintain adequate air/fuel control during the drive away maneuver. Unfortunately, the lack of this calibration data resulted in unsatisfactory combustion. The testing also illustrated that cam control during the shutdown/start up is required. This functionality was added to the controller.

When the testing resulted in stable combustion and repeatable testing, a fully aged catalyst system was installed for testing of the cold start and drive away.

## Results and Conclusions

The first test was a heat flow study, where the mass flow through engine was swept and the spark timing varied from 15° to 24° aTDC to maintain constant NMEP. All other settings were held constant (Figure 207).

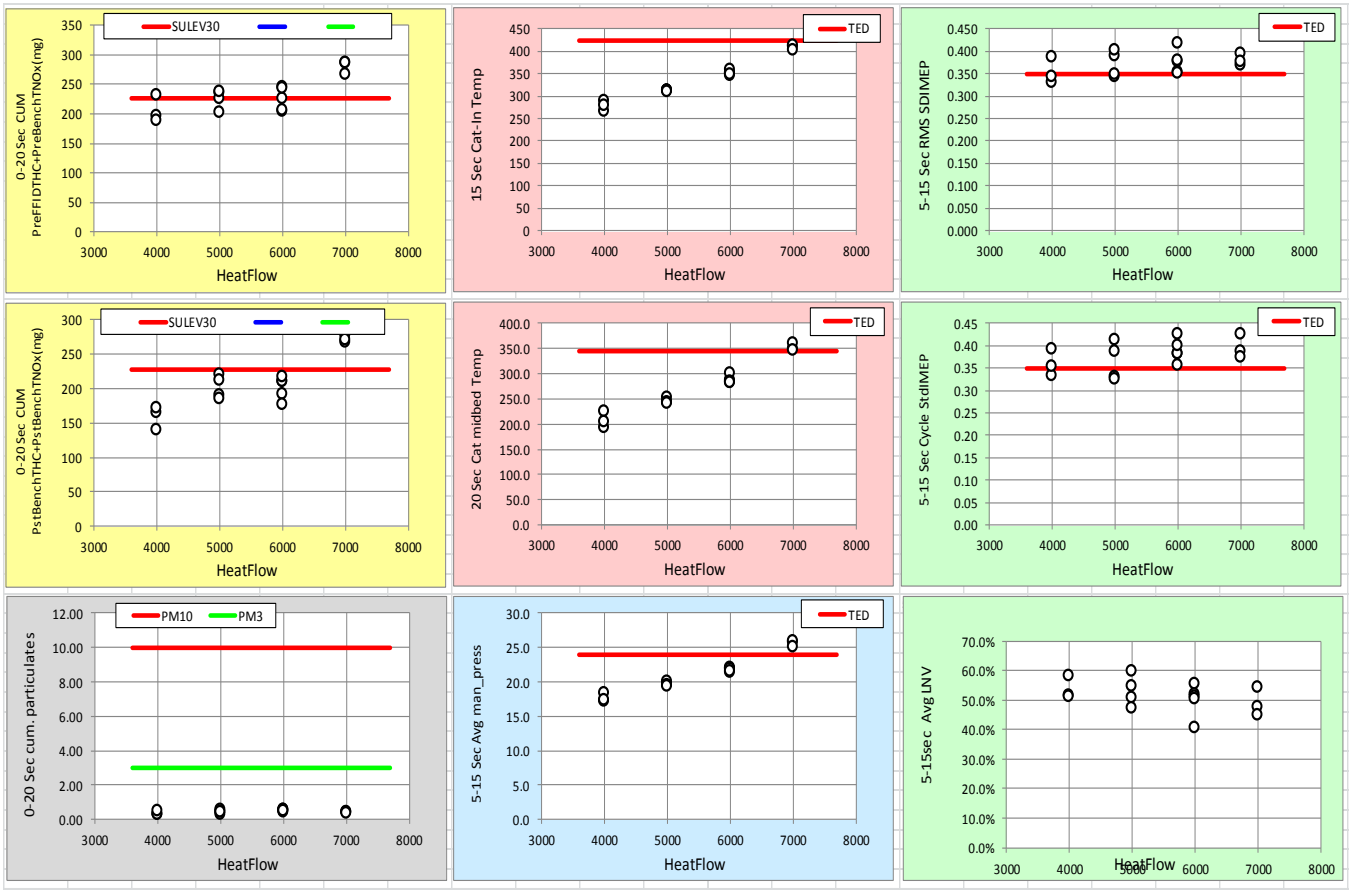


***Figure 207 - Heat flow study with mass flow and spark timing swept between 15° to 24° aTDC. Heat flow units are in Watts/liter of engine displacement.***

The data showed the feedgas emissions were meeting the target, the post catalyst emissions were meeting the target, the particulate emissions were below the target, the catalyst inlet and catalyst midbed temperatures were not meeting the target, the engine vacuum was meeting the target, and the combustion stability was slightly above the target.

It was shown that during the drive away part of the test, which is included in the data in Figure 207, the lack of firm mapping data at the time the testing was conducted caused some instability as well as increased emissions. So while the feedgas emission results were borderline, with proper mapping data as well as calibrated transient fuel, the engine should meet the target. Also, while the engine was converted for later testing, it was found that the midbed thermocouple was installed at 42 mm downstream of the brick face rather than the desired 25.4 mm. This explains the lower than expected midbed temperatures shown in Figure 207.

The next test was an air-fuel sweep during the idle portion. The target air-fuel ratio was swept corresponding to a lambda range of 1.00 to 1.06. The results are shown in Figure 208.

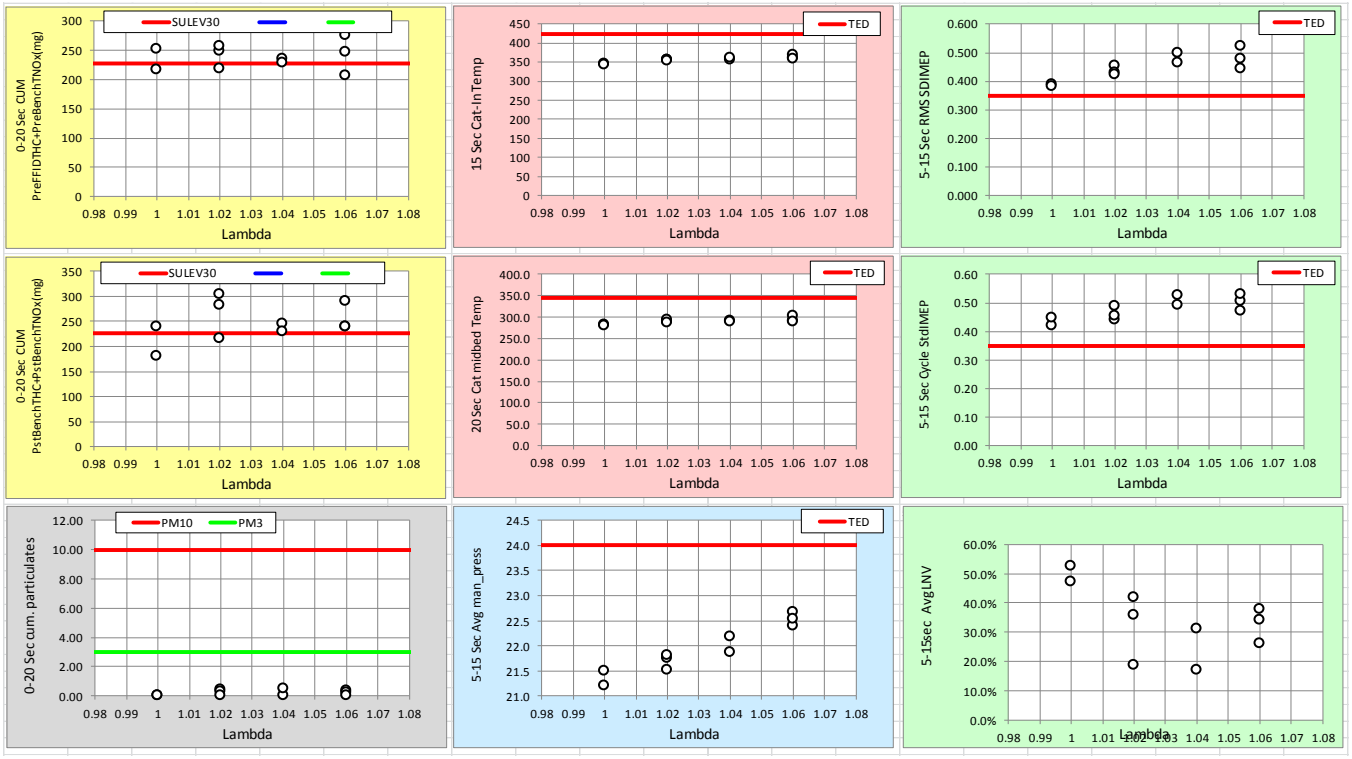


***Figure 208 - Lambda sweep during the cold idle portion of the test.***

During this testing, the crank control of the cams as well as the transient during the tip-in appeared to confound the resulting data. Evaluating only the 5-15 second range for both HC and NOx in Figure 209, the results indicate that the sum of HC+NOx is lowest at 1.02 lambda, which is consistent with other engines.

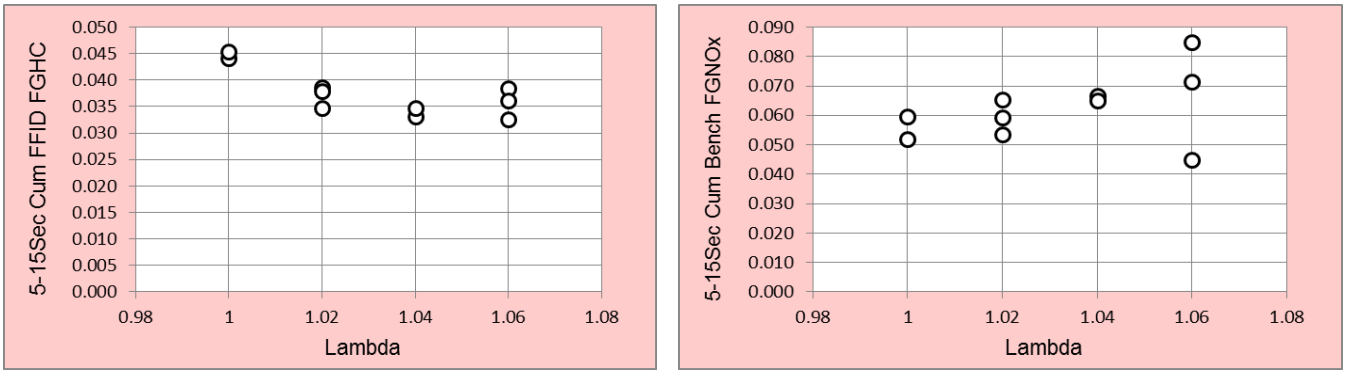


***Figure 209 - Cumulative feedgas HC and NOx vs. lambda during the 5 -15 sec period.***

The next investigation was wastegate and turbocharger scroll control positions. The intent is to minimize the heat losses through the turbocharger hardware. Both the wastegate and scroll valve have the potential to change how the exhaust gases pass through the turbocharger and thus heat losses. Figure 210 shows the four possible combinations of wastegate and scroll valve position as a function of catalyst warming heat flux. Similar to the data showin in Figure 207, heat flux is varied by sweeping mass flow and adjusting spark to maintain constant NMEP.

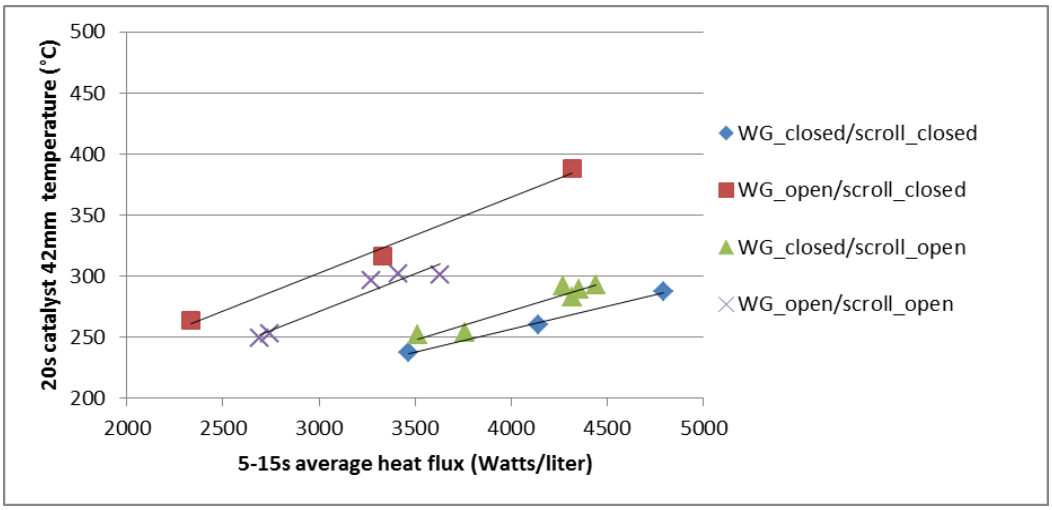


***Figure 210 - Effect of wastegate and scroll control valve positions on catalyst midbed temperature at 20 seconds.***

As expected, an open wastegate improves the catalyst temperatures over a closed wastegate. The scroll valve position had less of an impact overall but did show a small interaction with wastegate position. When the wastegate is closed, an open scroll valve is slightly better. When the wastegate is open, a closed scroll valve provides better catalyst temperatures. Turbocharger response should also be considered. A closed wastegate and closed scroll valve provide better boost characteristics. Vehicle testing will determine if both attributes can be met.

1/8" thermocouples, due to their long response times, make it difficult to interpret transient data so 1/16" thermocouples were installed, and the heat (spark timing) sweeps were repeated. At the same time, the engine starting issue was resolved so the emissions data as well as the exhaust temperatures can be used. These final results are shown in Figure 211.

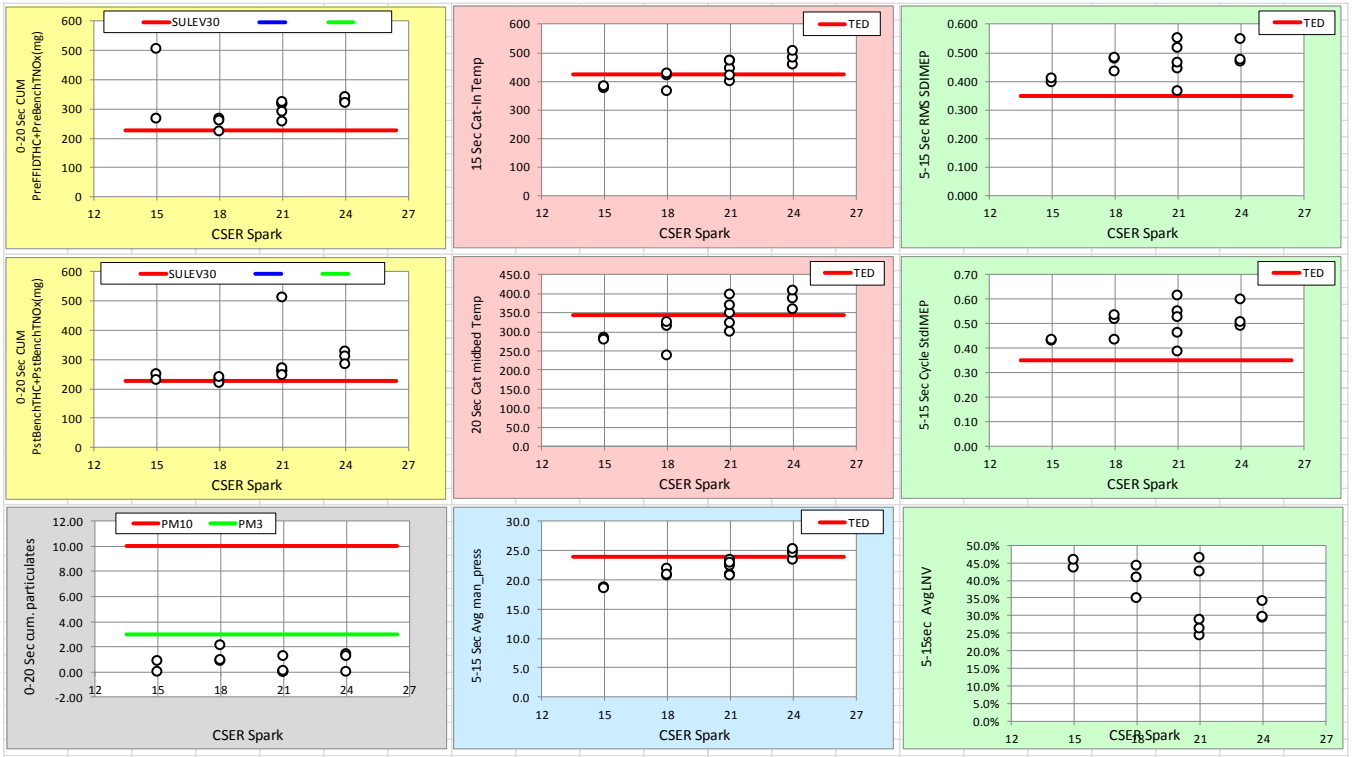


***Figure 211 - Repeat of heat flow study with mass flow and spark timing swept between 15° to 24° aTDC.***

Using the mapping data available when this data set was run, the results shows that the engine is making gaseous emissions and catalyst temperature targets at 18°aTDC of spark timing (the yellow and red graphs). PM and manifold vacuum are better than the program targets (gray and blue graphs). Stability is slightly above the program target and was assessed in the vehicle. With the gaseous emissions levels right at the targets, some additional calibration work in the vehicle was needed to comfortably meet the program SULEV30 targets.

## Summary

Using settings generated in the cold fluids testing, transient emissions development demonstrates the 2.3L DOE engine appears capable of meeting the SULEV30 standards for gaseous and particulate emissions, as shown in Table 13.

***Table 13 - Emission targets and transient cold start attribute results.***

| **Tailpipe Standards** | **Tier 2 Bin 2** | **Tier 3 SULEV30** |
|---|---|---|
| NMOG | 10 mg / mi | -- |
| NOx | 20 mg / mi | -- |
| NMOG + NOx | -- | 30 mg / mi |
| PM | 10 mg / mi | 3 mg / mi |

| **Cold Start Attribute** | **Units** | **Target[1]** | **Status** |
|---|---|---|---|
| 0-20s Cumulative FGHC + FGNOx | mg | 227 | 224 |
| 0-20s Cumulative Particulate Mass (PM) | mg | 3.0 | 1.3 |
| 5-15s CSER stability (RMS_SDIMEP) | bar | 0.35 | 0.48 |

[1] Evaluated at a cold idle heat flux that achieves ~350°C catalyst mid-bed @ 20 seconds after engine start.

Vehicle development explored opportunities using more complete engine mapping data, optimized cam timings during the drive away, and shut down control of cam timing for open loop fuel control during crank and run up to improve the emission margins relative to the standards.

# Vehicle Build and Calibration

Four 2013MY Fusion vehicles were procured for the vehicle calibration phase of the project. Powertrain-vehicle integration tasks were completed on these four vehicles, including removal of the existing powertrain, preparation for the new powertrain, preparation for new advanced integrated and supporting powertrain systems, and installation of the new powertrain. Installation of the new 2.3L powertrain with measurement instrumentation in the engine compartment is shown in Figure 212.


***Figure 212 - 2.3L engine with measurement instrumentation installed in a Fusion vehicle.***

Features of the Fusion vehicles included:

- Assisted direct start (ADS) technology.
- 6F35 automatic transmission.
- Dual, water cooled charge air coolers.
- Aftertreatment system aged to 150,000 miles using certification methodologies.

Vehicle development utilized input for the initial calibration from various strategy development programs and from the multi-cylinder engine dynamometer development, mapping, cold fluids, and transient cold start programs. In-vehicle development was performed either on the test track/on road or using a chassis dynamometer test cycle.

Initial vehicle calibration tasks included basic startability (crank, run-up, cold / warm idle stability) and basic driveability (tip-in / tip-out stability, acceleration / deceleration stability, transmission scheduling). Vehicle calibration then focused on achieving the fuel economy and emissions project objectives. Much of the development was performed using defined procedures, however, the new technologies incorporated in the project required new procedures for development. These included:

- Cooled EGR
- Electric TiVCT
- Variable displacement oil pump
- Actively controlled piston oil squirters
- Turbocharger scroll control valve
- Turbocharger active (electronically controlled) wastegate

Main vehicle calibration features are listed in Table 14. Controls and calibration releases supporting the calibration tasks were ongoing throughout the vehicle phase of the project.

***Table 14 - Vehicle calibration features.***

| Feature | Status |
|---|---|
| Air Charge | ● |
| Fuel Control | ● |
| Spark & Knock Control | ● |
| Torque Model & Control | ● |
| Boost – Scroll / Wastegate / CBV | ● |
| Cold Start & Warm Up | ● |
| Stop / Start | ● |
| Electric tiVCT | ● |
| Cooling & Lubrication | ● |
| Torque Converter Schedule & Control | ● |
| Shift Schedule & Control | ● |
| Low Pressure Cooled EGR | ● |

◐ Functional h/w & s/w verification complete. 'Safe' vehicle calibration.

◔ Development calibration with full transient control.

● Mature transient calibration. Refinement only as necessary for attribute balancing.

Fuel Economy and Emissions Objectives

The project objectives included vehicle demonstration of a 25% fuel economy improvement relative to the 2010 3.5L V6 FWD Taurus/Fusion on the FTP75/Highway Combo test. The 2010 V6 FWD Taurus/Fusion was certified at 27.78 mpg M-H, resulting in a project fuel economy target of 34.73 mpg M-H. There was also an emissions target of SULEV30 to be demonstrated with a 150,000 mile full useful life (FUL) aged aftertreatment system on the FTP75 and Highway cycles.

Procedure

The fuel economy and emissions testing procedure for the 2.3L Fusion vehicles matched the 2010 3.5L Taurus/Fusion certification methodology and procedure as closely as possible, and included the same chassis dynamometer settings:

- 4250 ETW
- HP@50 12.9
- 55-45 CTD 20.34 sec
- F0-29.19, F1-.2296, F2- 0.0225
- Dyno loads- A- 1.075, B-6.838, C-1.483

The tests that were analyzed were the FTP and the Highway tests, which start from a 75°F cold start following at least an 8 hour soak at 75°F nominal ambient. The FTP cycle is a 3 bag cycle which includes a 10 min soak between bags 2 and 3. The highway portion was run immediately following the FTP test, and was run twice - where the second portion was used for gaseous emissions and fuel economy analysis. This reflected exactly how the 2010 3.5L Taurus was certified.

Emissions development and testing was performed with an E10 certification fuel. This was done as it is the specified fuel for the SULEV30 LEVIII standards that were the program gaseous and particulate emissions targets.

Fuel economy and emissions testing was run at the RIC VERL emissions labs and at the APTL emissions labs. Pictures of a test vehicle on the chassis rolls at the RIC VERL emissions lab are shown in Figure 213.

***Figure 213 - Fusion vehicle on chassis rolls.***

Emissions Results

Particulate testing was performed early in the development, and over four tests the average PM was about 1 mg/mi, well under the 3.0 mg/mi SULEV30 standard. For gaseous emissions, four tests were performed after development of the calibration to optimize fuel economy and gaseous emissions. Using FUL catalysts, the measured emissions met the SULEV30 emissions standards, as shown in Table 15. The results include bags 1, 2, 3, and highway as well as all assisted direct start (ADS) stop-start events.

***Table 15 - Vehicle emission results with catalysts aged to FUL vs. the SULEV30 standard.***

| | SULEV30 Standard | DOE Results |
|---|---|---|
| THC | N/A | 21.4 mg/mi |
| NMHC | N/A | 13.1 mg/mi |
| NMOG | N/A | 14.4 mg/mi<br>(10% correction to the NMHC w/ E10 fuel) |
| NOx | N/A | 10.8 mg/mi |
| NMOG+NOx | 30 mg/mi | 25.2 mg/mi |
| CO | 1.0 mg/mi | 0.24 g/mi |
| PM | 3 mg/mi | 1 mg/mi |

Fuel Economy Results

After the gaseous emissions final development and testing, the fuel for the 2.3L DOE vehicles was changed to an E0 certification fuel to eliminate potential calculation mismatch relative to the baseline 3.5L fuel economy that was measured using E0 fuel. The measured fuel economy for the 2.3L DOE vehicles was:

Bag 1 FE: 27.47 mpg
Bag 2 FE: 27.49 mpg
Bag 3 FE: 32.71 mpg
Hwy FE: 44.93 mpg

Combined M-H FE:  34.30 mpg

The combined M-H fuel economy required two adjustments as described below.

The engine was designed with an integrated balance shaft-oil pump module.  Because the vehicles were equipped with active engine mounts, the balance shafts were not needed for acceptable NVH.  Hence the counterweights were machined from the balance shafts for the vehicle engines.  The shafts remained due to the oil pump design constraint of the integrated balance shaft-oil pump module.  The residual balance shaft friction was measured on component dynamometer and converted to a vehicle level fuel economy effect of 1% M-H fuel economy or 0.34 mpg.

Additionally, downsizing from a 3.5L V6 to a 2.3L I4 GTDI engine yields a 75 pound powertrain weight save. The 2010 Taurus / Fusion was certified at 4250lb ETW.  The next lower weight class is 4000lb ETW, and coast-down coefficients exist only for discrete weight classes.  Thus, the vehicle level fuel economy improvement for decreasing from 4250 to 4000lb ETW was measured on chassis rolls and pro-rated for a 75 pound powertrain weight save, resulting in a net effect of 0.13 mpg.

The final fuel economy improvement was 25.2% relative to the 3.5L V6 baseline, as shown in Table 16, achieving the project objective of 25% improvement.

***Table 16 - Unadjusted M-H vehicle fuel economy results.***

| | **Fuel Economy (mpg)** | **Improvement (%)** |
|---|---|---|
| 2010 3.5L V6 Taurus / Fusion | 27.78 | Baseline |
| | | |
| DOE Adv GTDI 2.3L I4 Fusion – Measured on chassis rolls | 34.30 | 23.5% |
| Measured residual balance shaft friction correction | 0.34 | - |
| Measured powertrain weight save | 0.13 | - |
| | | |
| **DOE Adv GTDI 2.3L I4 – Measured Total** | **34.77** | **25.2%** |

# Aftertreatment Development

The initial intent of the project was to utilize lean burn to improve fuel economy at light-medium load operating conditions. It is well known that a three-way catalyst (TWC) cannot reduce $NO_x$ under lean conditions. While urea injection is a recognized enabler for $NO_x$ emissions compliance during lean operation, such an approach places a burden on the consumer to maintain the urea system. In contrast, the work conducted during this project considered two passive approaches for lean $NO_x$ control which do not require customer maintenance: a lean $NO_x$ trap + selective catalytic reduction (LNT/SCR) system and a passive SCR system in which the $NH_3$ for the SCR catalyst is generated from reduction of the feedgas $NO_x$ on the upstream TWC during rich operation. After a detailed investigation, the TWC+LNT/SCR approach was dismissed due to the inability to desulfate the LNT in the underbody location as required to maintain effectiveness at high mileage. Thus, efforts were focused towards the passive TWC+SCR system, which was less sensitive to the effects of sulfur poisoning. After system design was completed, projections based on detailed accounting indicated that the M-H fuel economy benefit of the passive TWC+SCR system was only 0.8%. This was due to limited opportunities for lean operation due to competing technologies, penalties for enrichment to generate the $NH_3$, and penalties due to the weight of the additional SCR converter. The resulting saving and corresponding fuel economy value was low relative to other technologies under consideration. As a result, lean burn was excluded from the vehicle phase of the DOE engine project. Work conducted during the course of this project on these passive lean burn aftertreatment systems is discussed in detail in SAE papers 2015-01-1004 and 2015-01-1006, which are included below.

Vehicle level testing was conducted with a conventional TWC aftertreatment system. Specifications for the system are shown in Figure 214. 3D CFD was conducted to ensure uniform exhaust gas flow distribution across the catalysts and to determine sensor placement locations.

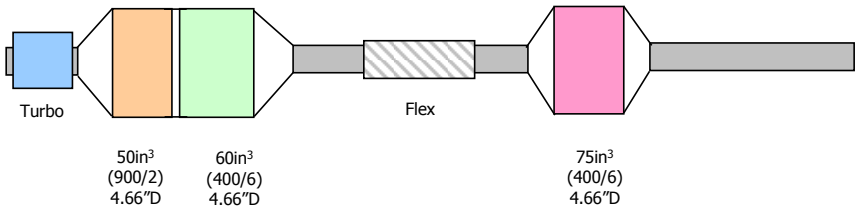


| COMPONENT | SUBSTRATE (D" x L") | CPSI/MIL | VOLUME (L) | VOLUME ($in^3$) | CATALYST FORMULATION | PGM |
|---|---|---|---|---|---|---|
| SS1 - C1 | 4.66" x 2.93" | 900/2 | 0.82 | 50 | REX-1244 | 150g/$ft^3$ (0/146/4) |
| SS2 - C1 | 4.66" x 3.50" | 400/6 | 0.98 | 60 | REX-1244 | 30g/$ft^3$ (0/26/4) |
| SS1 - C2 | 4.66" x 4.40" | 400/6 | 1.23 | 75 | REX-1244 | 12g/$ft^3$ (0/10/2) |

***Figure 214 - TWC system specifications.***

2015-01-1004

# Passive TWC+SCR Systems for Satisfying Tier 2, Bin 2 Emission Standards on Lean-Burn Gasoline Engines

**Joseph Theis, Jeong Kim, and Giovanni Cavataio**
Ford Motor Company

## Abstract

A laboratory study was performed to assess the potential capability of passive TWC+SCR systems to satisfy the Tier 2, Bin 2 emission standards for lean-burn gasoline applications. In this system, the TWC generates the $NH_3$ for the SCR catalyst from the feedgas $NO_x$ during rich operation. Therefore, this approach benefits from high feedgas $NO_x$ during rich operation to generate high levels of $NH_3$ quickly and low feedgas $NO_x$ during lean operation for a low rate of $NH_3$ consumption. It was assumed that the exhaust system needed to include a close-coupled (CC) TWC, an underbody (U/B) TWC, and an U/B SCR converter to satisfy the emission standards during the FTP and US06 tests while allowing lean operation for improved fuel economy during select driving conditions. Target levels for HC, CO, and $NO_x$ during lean/rich cycling were established. With a 30 s lean/10 s rich cycle and 200 ppm NO lean, 1500 ppm NO rich and the equivalent of 3.3 L of SCR volume were required to satisfy the $NO_x$ target. The ability of the CC TWC and U/B TWC to promote steam reforming of the HC during the rich periods was crucial for maintaining the HC slip below the target level. A study on the effects of the A/F ratio and temperature on the $NH_3$ production from the CC TWC revealed that a temperature of 600°C generated high $NH_3$ yields while providing good steam reforming activity. A two-step purge strategy generated high $NH_3$ yields while minimizing the CO slip. The two-step purge and a CC TWC + U/B TWC + SCR catalyst system satisfied the HC, CO, and $NO_x$ slip targets. Sulfur poisoning decreased the steam reforming activity of the TWC as well as its $NH_3$ yield, although the $NO_x$ conversion of the SCR catalyst was not significantly affected by the sulfur. It was assumed that the CC TWC would remain naturally desulfated with routine exposure to hot rich conditions during cold starts, accelerations, and high load operation, thus eliminating the need for an active desulfation strategy.

## Introduction

Automakers are working diligently to improve the fuel economy of their gasoline-powered vehicles in order to improve customer satisfaction and to satisfy future governmental regulations. Simultaneously, the California LEV III regulations and the Federal Tier 2 and Tier 3 regulations are requiring carmakers to lower the emissions of hydrocarbons (HC), carbon monoxide (CO), nitrogen oxides ($NO_x$), and particulate matter (PM) from their vehicles. One strategy that can improve fuel economy is the use of lean operation during select driving modes such as cruises, as lean operation lowers the pumping losses and improves the thermodynamics of combustion. Depending on the engine and combustion strategy, lean operation can improve the fuel economy by as much as 5 to 15% relative to stoichiometric operation. However, it is well known that the current three-way catalyst (TWC) cannot reduce $NO_x$ under lean conditions. Therefore, to allow lean operation while satisfying strict emission regulations, the TWC converter(s) must be supplemented with catalysts that can reduce $NO_x$ during lean operation or during lean/rich cycling. Selective catalytic reduction (SCR) catalysts [1] with urea injection systems are currently being used to reduce the $NO_x$ from diesel engines. Here an aqueous solution of urea is pumped from a storage tank into the exhaust, where the urea decomposes into $NH_3$. The $NH_3$ and $NO_x$ react over the SCR catalyst under lean conditions to produce nitrogen ($N_2$) and water ($H_2O$). A popular SCR formulation used on production diesel trucks contains copper in a chabazite zeolite which provides high $NO_x$ conversion and good thermal durability. One issue is that this system requires the customer to maintain a sufficient supply of the urea solution in the storage tank. Typically, the urea tank is refilled during vehicle service appointments.

To avoid the need for the urea tank, urea injection system, and the customer intervention required to keep the urea tank filled, a lean $NO_x$ trap (LNT) can be used for lean $NO_x$ control [2]. The LNT contains platinum group metal (PGM) such as platinum (Pt), palladium (Pd), and rhodium (Rh) along with $NO_x$ storage materials such as barium (Ba) and cerium (Ce). The LNT adsorbs $NO_x$ during lean operation and reduces the stored $NO_x$ and feedgas $NO_x$ to $N_2$ during periodic rich periods. Another system that does not require customer interaction is referred to as the passive TWC+SCR approach [3]. Here the TWC generates $NH_3$ from the feedgas $NO_x$ during periodic rich periods, and the $NH_3$ is stored on the downstream SCR catalyst. The SCR catalyst then uses the stored $NH_3$ to reduce $NO_x$ during lean operation. A third approach referred to as a TWC+LNT/SCR system combines a LNT with a SCR catalyst for lean $NO_x$ control [4-16]. This LNT/SCR system was shown to demonstrate equivalent $NO_x$ conversion, lower $NH_3$ emissions, and lower PGM costs compared to a LNT of the same total volume [15]. One issue with the LNT, SCR, or LNT/SCR approach is that the rich periods used to purge the LNT and/or to create $NH_3$ for the SCR catalyst reduce the fuel economy by 1 to 2%. Nevertheless, the overall fuel economy improvement from lean/rich cycling is significantly positive.

In 2011, Ford began a 4.5-year demonstration project under joint funding with the DOE to achieve a 25% improvement in fuel economy while achieving Tier 2, Bin 2 emission levels (later modified to Tier 3, Bin 30 emission levels) on a 2.3 L gasoline turbocharged direct-injection (GTDI) engine in a Ford Taurus [17]. For assessing the fuel economy improvement, the baseline vehicle was a Ford Taurus powered by a 3.5 L port-fuel-injected (PFI) naturally-aspirated (NA) engine with independent variable cam timing (iVCT). Several engine technologies were investigated to achieve the 25% improvement in fuel economy, including

turbocharging, downsizing the engine displacement, the use of direct-injection, cooled EGR, and stop-start technology. As an optional action, lean operation during cruises was investigated. To provide $NO_x$ control during the lean periods, two approaches were investigated that did not require customer maintenance: the TWC+LNT/SCR system and the passive TWC+SCR system. This paper summarizes the work on the passive TWC+SCR system. A companion paper describes the work on the TWC+LNT/SCR approach [16]. For both systems, high emphasis was placed on achieving the HC targets as well as the $NO_x$ targets due to the low emission levels allowed for the Tier 2, Bin 2 standards.

## Experimental

### *Catalysts*

The TWC and SCR catalyst samples used in this work were core samples with a length and diameter of 2.54 cm that were extracted from full-size cordierite bricks. It was assumed that the washcoat loadings and platinum group metal (PGM) distributions within the catalyst bricks were uniform. Therefore, the brick locations from where the cores were collected were not recorded.

### *TWC Samples*

The TWC samples contained various levels of oxygen storage capacity (OSC) and PGM loadings that are listed in Table 1. Samples of a production catalyst with a moderate level of OSC on 400 cell per square inch (CPSI) substrates with 4 mil walls (i.e., 400/4) were used with two PGM loadings. One contained 38 gpcf Pd and 2 gpcf Rh (0.62 g/L Pd and 0.033 Rh), and the other contained 196 gpcf Pd and 4 gpcf Rh (i.e., 3.21 g/L Pd and 0.066 g/L Rh). These will be referred to "mod-OSC-40" and "mod-OSC-200" in this paper, respectively. Samples of two non-OSC formulations were used containing either 116 gpcf (1.90 g/L) Pd or 200 gpcf (3.28 g/L) Pd on 400/4 substrates. These will be referred to as "no-OSC-116" and "no-OSC-200" in this paper, respectively. For tests performed with an U/B TWC, the U/B catalyst was a model formulation with either 26 gpcf (i.e., 0.43 g/L) Pd or Pt on a washcoat of ceria/zirconia. These will be referred to as "PdCeZr" and "PtCeZr" in this paper.

### *TWC Aging*

Table 1 also lists the durability schedules used to age the TWC samples prior to testing. The rich/stoich/lean schedule was a proprietary schedule that cycled between rich, stoichiometric, and lean conditions every 60 seconds. The inlet temperature was 800°C, and the maximum bed temperature was 960°C. A full-size brick with the mod-OSC-40 formulation was aged for 120 hours on an engine/dynamometer using the rich/stoich/lean schedule, and a 1" diameter x 1" long core sample was extracted from the brick for laboratory testing. 1" long core samples of the mod-OSC-200 and no-OSC-200 formulations were aged on a pulse-flame combustion reactor (a.k.a. pulsator) [18] with the same rich/stoich/lean schedule for 50 hours. The no-OSC-116 catalyst was degreened on the flow reactor for 2 hours at 800°C with 10% $O_2$, 5% $H_2O$, 5% $CO_2$, and the balance $N_2$. The U/B TWC samples were oven-aged 175 hours at 800°C with stoichiometric exhaust from a pulsator.

### *SCR Samples*

The SCR catalyst used in this project was a copper/chabazite formulation on a 400/4 substrate. This SCR formulation is used in production on the Ford medium duty diesel truck. No further details about the SCR formulation will be provided out of respect for the supplier.

### *SCR Aging*

Some of the early work for this TWC+SCR project was performed with SCR samples that had been aged behind LNTs on the flow reactor for another project [15]. There a 1" long LNT core sample was placed ahead of a 1" long SCR core sample in the flow reactor. One set was aged for 25 hours at an inlet temperature of 800°C with continuously lean exhaust (10% $O_2$, 5% $CO_2$, 5% $H_2O$, balance $N_2$), while a second set was aged for 20 hours under the same conditions. After aging, both 1" SCR catalysts were cut into four 0.25" (0.64 cm) long pieces. That allowed various volumes of SCR catalyst to be investigated for this TWC+SCR project. To allow the evaluation of a 3" long SCR catalyst system, another 1" long sample with the same formulation was obtained that had been hydrothermally aged at 800°C for 80 hours. The aging temperature of 800°C was intended to expose the SCR catalyst to the maximum temperature that could be expected in the U/B location and was not intended to represent a certain mileage or full-useful-life (FUL) conditions. Later experiments were performed with SCR catalysts that were aged downstream of the TWC while the TWC samples were aging on the pulsator for 50 hours with the rich/stoich/lean cycle described above. Here the SCR catalysts were aged with inlet temperatures of 600, 700, or 800°C. This was to determine if the SCR performance could be improved with a reduced aging temperature. For all of the SCR samples, small holes were drilled axially through the pieces so that a 1.6 mm thermocouple could be inserted through the samples for measuring the inlet temperature or the catalyst bed temperature during the aging and performance evaluations.

**Table 1. TWC Catalyst Formulations, PGM Loadings, Aging Schedules**

| Catalyst Designation | OSC Level | PGM loading (gpcf Pt/Pd/Rh) | Aging Protocol |
|---|---|---|---|
| Mod-OSC-40 | Moderate | 0/38/2 | Engine – rich/stoich/lean 800°C inlet 120 hours |
| Mod-OSC-200 | Moderate | 0/196/4 | Pulsator– rich/stoich/lean 800°C inlet 50 hours |
| No-OSC-200 | None | 0/200/0 | Pulsator – rich/stoich/lean 800°C inlet 50 hours |
| No-OSC-116 | None | 0/116/0 | Flow reactor - lean 800°C inlet 2 hours |
| PdCeZr | High | 0/26/0 | Oven – stoichiometry 800°C 175 hours |
| PtCeZr | High | 26/0/0 | Oven – stoichiometry 800°C 175 hours |

### *Performance Evaluations*

The flow reactor used for the performance evaluations contained 2 ovens. Some tests were performed with only a CC TWC and a SCR catalyst (i.e., without the U/B TWC). For these evaluations, the TWC was placed toward the rear of the first oven, and the SCR catalyst was placed toward the rear of the second oven. The 2 ovens were operated at different temperatures to represent the close-coupled position and the underbody position. For evaluations of the CC TWC + U/B TWC + SCR system, the second TWC was placed toward the rear of the second oven, and the SCR catalyst was placed further downstream, as shown in Figure 1. The total length of the CC TWC was usually 1", and it consisted of either one catalyst formulation or two 0.5" pieces with different catalyst formulations butted together. When one TWC washcoat formulation was used, the PGM loading was uniform; when two different washcoat formulations were used,

the total PGM loading was either uniform (e.g., 200 gpcf/200 gpcf) or zoned (e.g., 200 gpcf/40 gpcf). The length of the U/B TWC was 1". The total length of the SCR catalyst was varied during the different experiments. The total flow rate was maintained at 6.4 L/min for all experiments, producing a space velocity of 30,000 $hr^{-1}$ for a 1" long catalyst.

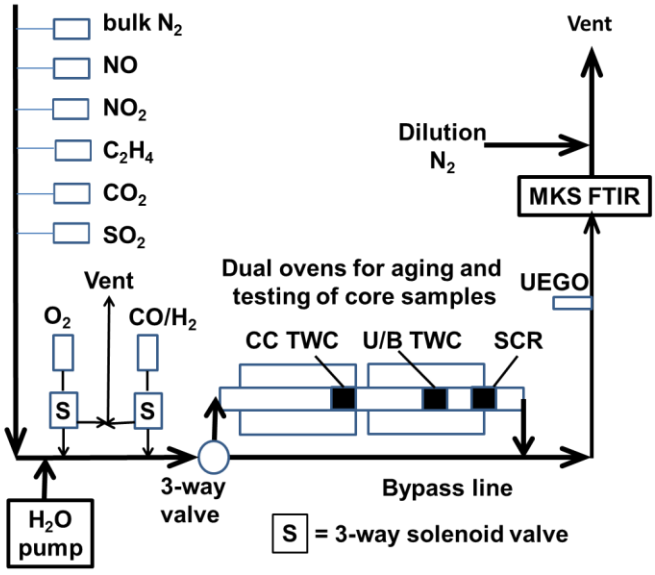


**Figure 1**. Experimental apparatus

Most tests consisted of alternating lean and rich periods (e.g., 30 seconds lean and 5 seconds rich, referred to as a "30/5" cycle). Tests where the lean duration was held constant and the rich purge time was varied are referred to as "purge tests" in this paper. Mass flow controllers were used to control the flow rates of the different gases, and two electronically-controlled three-way solenoid valves were used to switch between the lean (i.e., $O_2$) and rich conditions (i.e., $CO/H_2$). The oxygen ($O_2$) level was always 10% during the lean periods ($\lambda$=A/F ratio/14.6=2.0) and 0% during the rich periods. The $H_2O$ and $CO_2$ concentrations were always 5% during the lean and rich periods. Many of the experiments were performed with 2500 ppm $C_2H_4$ (i.e., 5000 ppm on a C1 basis) during the lean and rich periods. Different NO levels were used during the lean and rich periods. While these NO levels were varied depending on the type of test, the $NO_x$ concentration during the lean periods was usually 200 ppm NO. During the rich periods, the NO level was increased to either 500, 1000, 1500, or 2000 ppm to more accurately simulate actual engine operation and to generate more $NH_3$ for the SCR catalyst. Table 2 shows the CO and $H_2$ concentrations (always in a 3:1 ratio) used during the rich periods to provide rich lambdas of 0.81, 0.86, 0.91, 0.95, or 0.99; these rich lambdas assume a rich NO level of 2000 ppm, and the $C_2H_4$ concentration was 2500 ppm except at 0.99 rich lambda, where it was reduced to 800 ppm. Due to the many different catalyst configurations and test conditions used during this project, the specific details of each experiment will be provided in the section where the results of that experiment are discussed.

**Table 2. CO, $H_2$, NO, and $C_2H_4$ Concentrations for Different Rich Lambdas**

| Rich Lambda | NO ppm | CO % | $H_2$ % | $C_2H_4$ ppm |
|---|---|---|---|---|
| 0.81 | 2000 | 4.0 | 1.30 | 2500 |
| 0.86 | 2000 | 2.5 | 0.83 | 2500 |
| 0.91 | 2000 | 1.5 | 0.50 | 2500 |
| 0.95 | 2000 | 0.5 | 0.17 | 2500 |
| 0.99 | 2000 | 0.5 | 0.17 | 800 |

For all tests, the average concentrations of the feedgas $NO_x$, HC, and CO were determined over several lean/rich cycles while the exhaust was bypassed around the reactor. With the exhaust flowing through the catalyst bed, testing was continued until the performance of the catalyst stabilized. The concentrations of the $NO_x$, HC, and CO at the reactor exit were then averaged over several lean/rich cycles. The average HC, CO, and $NO_x$ conversions were calculated from the average feedgas concentrations and the average concentrations in the reactor exit according to:

Ave % conversion = 100*[1-(ave exit level)/(ave FG level)] (1)

The average yield of $NH_3$ was calculated as a percentage of the feedgas NO level according to:

Ave % $NH_3$ yield = 100*[(ave $NH_3$ level)/ave FG NO level] (2)

The average yield of $N_2O$ was calculated as a percentage of the feedgas NO level from:

Ave % $N_2O$ yield = 100*[2*(ave $N_2O$ level)/ave FG NO level] (3)

where the factor of 2 accounts for the fact that two molecules of NO are required to produce one molecule of $N_2O$.

The feedgas and the exhaust from the reactor were analyzed with a 1 Hz MKS Fourier transform infrared (FTIR) analyzer equipped with a sample line heated to 191°C.

## Results and Discussion

### *Emission Budgeting*

Emission budgeting was performed to determine the maximum allowable levels of HC, CO, and $NO_x$ during lean/rich cycling on cruises that still allowed the Tier 2, Bin 2 standards to be met. The limits for HC, CO, and $NO_x$ on the FTP after 120,000 miles of driving are 10 mg/mile, 2.1 g/mile, and 20 mg/mile, respectively. Estimates were made for the emissions during the cold-start portion of the FTP and during warmed-up operation at stoichiometry. When possible, data from other vehicles were used to approximate these levels. Table 3 shows these estimates along with the desired engineering tolerances for HC, CO, and $NO_x$ during the FTP. This left target emission levels during lean/rich cycling of 1 mg/mile, 1.3 gm/mile, and 5 mg/mile for HC, CO, and $NO_x$, respectively. The PM (particulate matter) standard for Tier 2, Bin 2 is 10 mg/mile; it was assumed that the engine-out level of PM would satisfy this limit, so a gasoline particulate filter (GPF) was not considered for this project.

Table 3. Emission Budgeting to Satisfy Tier 2, Bin 2 Emission Standards

| Tier 2, Bin 2 Standards | HC | NOx | CO |
|---|---|---|---|
| Emission Requirement | 10 mg/mile | 20 mg/mile | 2.1 g/mile |
| Engineering tolerance | 1.7 | 5 | 0.5 |
| Cold-start emissions | ~7 | 7 | 0.3 |
| Stoichiometric emissions (Post-lightoff) | ~0 | 3 | ~0 |
| Lean/rich cycling emissions | 1 | 5 | 1.3 |

### *Effects of SCR Volume & Rich NO Level*

Initial experiments on the passive TWC+SCR system were performed using 1.0", 1.5" and 2.0" of the Cu/zeolite SCR pieces from the previous LNT/SCR study [15]. To allow the evaluation of a 3" long SCR system, a third 1" piece of the SCR catalyst was obtained that had been hydrothermally aged at 800°C for 80 hours. It was assumed that the TWC needed to have a reduced level of oxygen storage capacity (OSC) relative to typical three-way catalysts used on vehicles today in order to promote $NH_3$ formation. However, the TWC still needed some OSC to provide good 3-way activity and diagnostic capabilities during warmed-up stoichiometric operation. Therefore, the front 0.5" of the TWC consisted of the no-OSC-116 formulation aged 2 h under lean conditions, and this was followed by 0.5" of the mod-OSC-40 formulation aged 120 h on an engine/ dynamometer. The TWC and SCR ovens were operated at 550°C and 330°C, respectively; a TWC temperature of 550°C ensured adequate steam reforming activity for HC control during the rich periods, and a SCR temperature of 330°C provided high $NO_x$ conversion activity and reasonable $NH_3$ storage capacity. 30 second lean periods were alternated with 10 second rich periods (i.e., 30/10 cycle) at a rich lambda of 0.86. The total exhaust flow rate was constant at 6.4 L/min. The feedgas level of NO during the lean periods was 220 ppm. 2500 ppm of $C_2H_4$ was injected during both the lean and the rich periods. For all four lengths of SCR catalyst, the feedgas level of NO during the rich periods was varied from 500 to 2000 ppm in order to vary the amount of $NH_3$ produced by the TWC.

It was desired to convert the $NO_x$ concentrations from the reactor (measured in ppm) into the weighted mg/mile $NO_x$ during lean/rich cycling on the intended DOE vehicle to allow easier comparison with the 5.0 mg/mi target from Table 3. Estimates were made for the total weighted exhaust flow on the vehicle during lean operation on the FTP. Using the mileage for Bags 1 and 2 of the FTP (i.e., 7.5 miles) and assuming that all of the $NO_x$ is emitted as $NO_2$ (46 g/mole) per EPA protocol, the ppm $NO_x$ from the reactor and the exhaust flow rate from the vehicle were used to project the weighted mg/mile $NO_x$ on the vehicle during lean/rich cycling.

Figure 2 shows the weighted $NO_x$ slip as a function of the rich NO concentration for SCR lengths of 1.0", 1.5", 2.0", and 3.0". These catalyst lengths on the reactor corresponded to 1.7, 2.5, 3.3, and 5.0 L of SCR catalyst on the intended DOE vehicle, based on the space velocity from the reactor and the estimated exhaust flow rate from the vehicle. For all four volumes, the $NO_x$ slip decreased as the rich NO concentration increased from 500 ppm to 1500 ppm; there was little improvement when the rich NO level was further increased from 1500 ppm to 2000 ppm. The $NO_x$ slip also decreased as the length of SCR catalyst increased from 1" to 3". The $NO_x$ slip was near the target of 5.0 mg/mile with the 2" long SCR when the rich NO level was at least 1500 ppm, while the 3" long SCR satisfied the target level comfortably when the rich NO level was at least 1500 ppm.

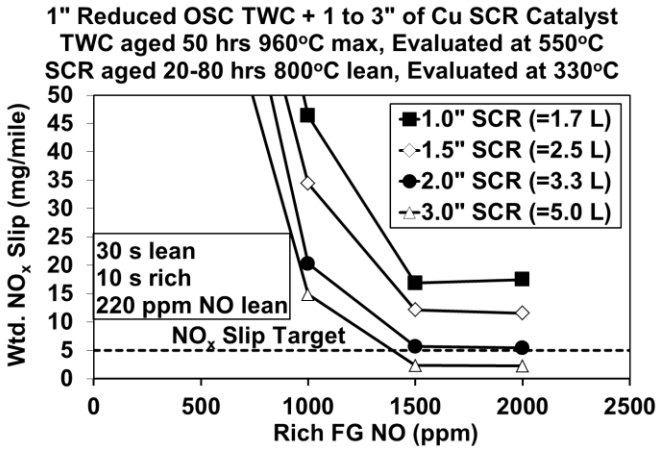


Figure 2. Weighted $NO_x$ slip as a function of rich feedgas NO level for 1" TWC + SCR catalyst with lengths of 1.0", 1.5", 2.0", and 3.0". 30/10 cycle, 0.86 rich λ, 550°C in TWC and 330°C in SCR catalyst.

These results indicated that an aged TWC+SCR system had the potential to satisfy the $NO_x$ slip target of 5.0 mg/mile with a reduced-OSC TWC, sufficient SCR volume, low feedgas $NO_x$ lean, and high feedgas $NO_x$ rich. High feedgas $NO_x$ levels during rich operation increase the $NH_3$ production and thereby improve the $NO_x$ conversion while reducing the rich purge times required.

In the companion paper on the TWC+LNT/SCR system [16], exhaust modeling was used to determine that the LNT/SCR converter needed to be placed approximately 44" downstream of the U/B TWC to maintain the LNT/SCR converter in its optimum temperature range of 300-350°C during the FTP. The SCR converter needs to be placed in a similar location to maintain its temperature near 300 to 320°C during the FTP.

### *Effects of Lean Duration*

Similar tests were performed on the 1" TWC + 3" SCR system where the rich periods were maintained at 10 seconds but the lean durations were extended to 45 and 60 seconds. Figure 3 shows the weighted $NO_x$ slip of the 1" TWC + 3" SCR system for lean durations of 30, 45, and 60 seconds as a function of the rich NO level. While the $NO_x$ slip target was met with a rich NO level of 1500 ppm when the lean duration was 30 seconds, a lean duration of 45 seconds required a rich NO level of approximately 2000 ppm to achieve the $NO_x$ slip target. As expected, a longer lean period required additional $NH_3$ to maintain the same overall $NO_x$ slip. The lean duration of 60 seconds did not achieve the $NO_x$ slip target even with 2000 ppm NO during the rich periods. However, the slope of the line suggests that the target could have been met with a slightly higher rich NO level (e.g., 2100 to 2200 ppm).

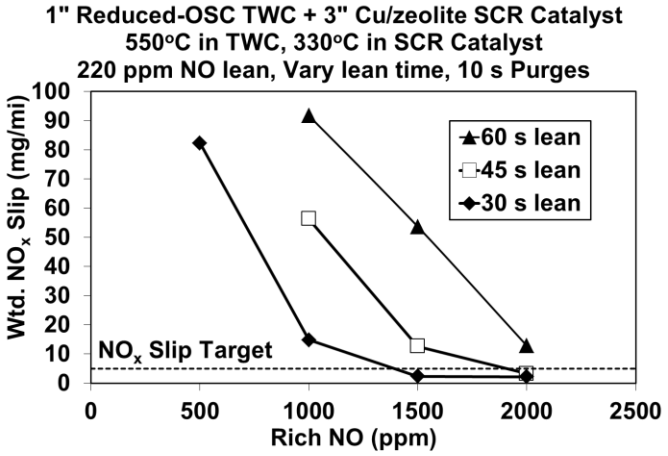


**Figure 3**. Weighted $NO_x$ slip as a function of rich feedgas NO level for 1" TWC + 3" SCR system with 10 s rich periods and lean durations of 30, 45, and 60 s. 220 ppm NO lean and 0.86 rich λ. 550°C in TWC and 330°C in SCR catalyst.

## *Effects of Lean NO Level*

To determine if the system could satisfy the $NO_x$ target with higher feedgas NO levels during lean operation, purge tests were performed on the 1" TWC + 3" SCR system with lean NO levels of 320 and 420 ppm, while the rich NO level was maintained at 2000 ppm. The lean duration was 30 seconds, and the rich duration was varied from 5 to 15 seconds. Figure 4 shows the weighted $NO_x$ slip of the 1" TWC + 3" SCR system as a function of the rich duration for lean NO levels of 220, 320, and 420 ppm. The $NO_x$ slip target was satisfied for all three lean NO levels. The $NO_x$ slip target was met with 10 second rich periods when the lean feedgas NO level was 220 or 320 ppm. When the lean feedgas $NO_x$ level was 420 ppm, the rich duration had to be increased to 12 seconds to produce additional $NH_3$ in order to achieve the $NO_x$ slip target.

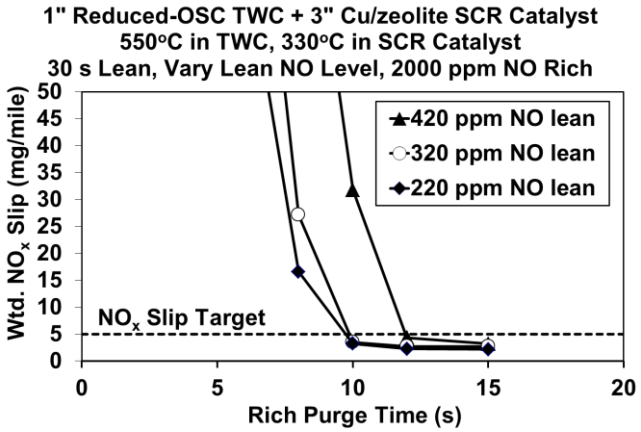


**Figure 4**. Weighted $NO_x$ slip as a function of rich purge time for 1" TWC + 3" SCR system. Lean NO levels of 220, 320, or 420 ppm, rich NO level of 2000 ppm. 30 s lean periods and variable rich purge times. 0.86 rich λ. 550°C in TWC and 330°C in SCR catalyst.

## *Effects of Purge A/F Ratio*

Purge tests were performed on the 1" TWC + 3" SCR system with rich lambdas of 0.91 and 0.95 lambda, achieved by decreasing the rich $CO/H_2$ levels to 1.5/0.5% and 0.5%/0.17%, respectively, while maintaining the 2500 ppm $C_2H_4$ during the lean and rich periods. The lean duration was 30 seconds, and the lean and rich NO levels were 200 and 2000 ppm, respectively. Figure 5 shows that, for a given rich purge time, the weighted $NO_x$ slip of the 1" TWC + 3" SCR system increased as the rich lambda increased from 0.86 to 0.91 to 0.95. As a result, longer purge periods were required to achieve the $NO_x$ slip target (i.e., 10, 13, and 14 seconds for rich lambdas of 0.86, 0.91, and 0.95, respectively).

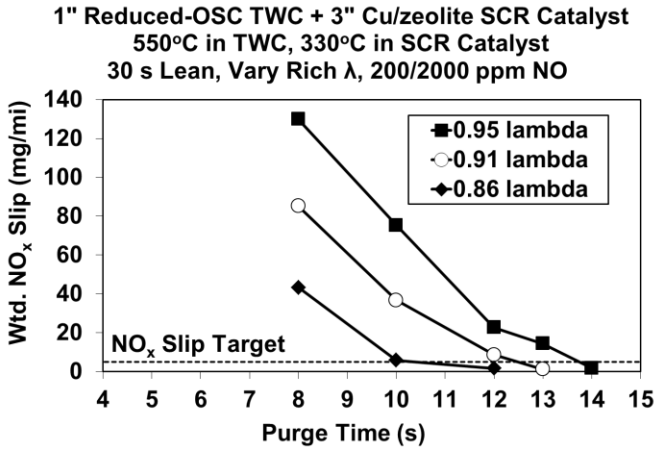


**Figure 5**. Weighted $NO_x$ slip as a function of rich purge time for 1" TWC + 3" SCR system. NO levels of 220 ppm lean and 2000 ppm rich. 30 s lean periods and variable rich purge times. Rich λ of 0.86, 0.91, and 0.95. 550°C in TWC and 330°C in SCR catalyst.

## *HC and CO Emissions*

In the companion paper on the TWC+LNT/SCR system [16], it was shown that the HC slip could satisfy the target level of 1.0 mg/mile as long as the temperature of the TWC was sufficiently high (e.g., 500°C) to provide good steam reforming during rich operation. These requirements also apply to the TWC+SCR system. An additional issue with the TWC+SCR system is the CO slip. To generate $NH_3$ over the TWC, its stored oxygen must be removed. At that point, the TWC will emit high CO levels. Unlike the LNT, the SCR provides very little CO conversion during the rich purges, resulting in high CO slip from the system. Figure 6 shows the weighted CO slip (in grams/mile) from the 1" reduced-OSC TWC at 550°C for rich lambdas of 0.86, 0.91, 0.95, and 0.99 as a function of the rich purge time. For a rich lambda of 0.86, the CO slip exceeded the target level of 1.3 gm/mile with a purge time of only 6 seconds. Yet Figure 5 showed that a purge time of 10 seconds was required with the 1" TWC + 3" SCR system to achieve the $NO_x$ slip target of 5.0 mg/mile with this rich lambda. As a result, the $NO_x$ and CO targets could not be satisfied simultaneously with this rich lambda.

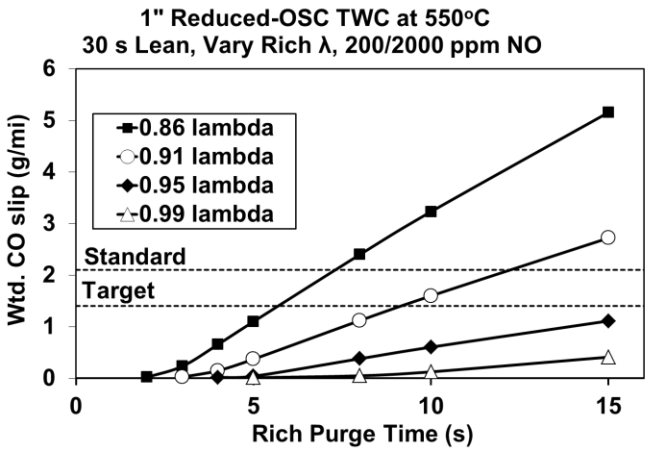


**Figure 6**. Weighted CO slip as a function of rich purge time for 1" TWC. 30 s lean periods and variable rich purge times. Rich λ of 0.86, 0.91, 0.95, and 0.99.

A potential solution to this CO-$NO_x$ tradeoff is a two-step purge, where a fairly rich lambda is used initially to quickly reduce the OSC of the TWC. Then the A/F ratio transitions to a less rich condition for the remainder of the purge. Once the TWC is reduced, it can continue to provide high $NH_3$ yields even with slightly rich lambdas, which will help minimize the CO slip as well as the fuel economy penalty. In addition, the rapid reduction of the OSC will allow the $NO_x$ slip target to be met with relatively short purge periods, which will also minimize the degradation of the fuel economy. The two-step purge will be discussed later in this paper.

These initial tests on the passive TWC+SCR system were encouraging in that the $NO_x$ slip targets could be met with lean durations as long as 60 seconds and lean NO levels as high as 420 ppm when the temperature of the SCR catalyst was around 300-320°C. However, other testing (not shown here) revealed that the $NO_x$ conversion of these particular SCR samples dropped off rapidly at temperatures above 320°C. This unexpected result was attributed to platinum poisoning of the SCR catalysts [19, 20], which resulted from the SCR samples being aged under continuously lean conditions at 800°C for 20 to 25 hours downstream of Pt-containing LNTs and then being evaluated downstream of the LNTs for several months with lean/rich cycling tests. Low concentrations of platinum from the LNT can vaporize and deposit onto the surface of the SCR catalyst, and this platinum can oxidize $NH_3$ to NO or $N_2O$ at higher temperatures. Consequently, it was decided that these particular SCR samples should not be used for further development of the TWC+SCR system. Other SCR samples aged either without a LNT or with a LNT but at milder conditions were used to further develop the TWC+SCR system, as discussed in the next section.

## *Effect of Thermal Aging on SCR Catalyst*

A TWC consisting of 0.5" of no-OSC-200 and 0.5" of mod-OSC-200 was aged with the rich/stoich/lean schedule at an inlet temperature of 800°C (960°C maximum bed temperature). Three 1" pieces of the Cu/zeolite SCR catalyst were aged downstream in a second oven with a maximum bed temperature of 800°C. The aged TWC and the first inch of SCR catalyst were evaluated for TWC+SCR performance on the flow reactor, where a purge test was performed with 30 second lean periods and various rich times with a lambda of 0.86. The feedgas NO level was 200 ppm during the lean periods and 2000 ppm NO during the rich period. Similar tests were performed with 2" and 3" of the SCR catalyst. Figure 7 shows the weighted $NO_x$ slip and the $NH_3$ yield for 1", 2", and 3" of SCR catalyst as a function of the rich purge time.

There was little difference in the $NO_x$ slip and $NH_3$ yield for the 3 lengths of SCR catalyst. Since the first 1" of SCR catalyst emitted significant $NH_3$ for purge times of 7 seconds or more, this suggested that the second and third SCR samples had little $NH_3$ storage capacity. The lowest $NO_x$ slip obtained with 15 second purge periods was 35 mg/mile, which is far above the target level of 5 mg/mile, and the $NH_3$ yield was very high at approximately 45% with this purge time. The average FG level of $NO_x$ was ca. 800 mg/mile with 15 s purges, so the 35 mg/mile $NO_x$ slip corresponded to a respectable $NO_x$ conversion of 96%. However, to achieve the $NO_x$ slip target of 5 mg/mile, the conversion needed to be ca. 99.5%.

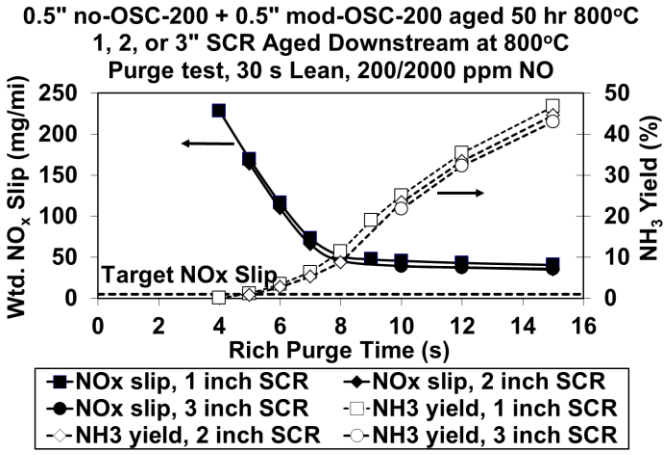


**Figure 7**. Weighted $NO_x$ slip and $NH_3$ yield as a function of rich purge time for 1" TWC + 1", 2", or 3" of SCR catalyst aged at 800°C. NO level 200 ppm lean, 2000 ppm rich. 30 s lean periods, 0.86 rich λ. 530°C in the TWC, 300°C in the SCR catalyst.

It was desired to assess a TWC+SCR system aged on the rich/stoich/lean schedule where the SCR samples had been aged at 700°C instead of 800°C. Rather than aging a new system, a 3" SCR system was put together using SCR samples from LNT/SCR systems that had been previously aged at 700°C on the rich/stoich/lean schedule. Since these LNT/SCR systems had been aged at 700°C on a durability schedule that consisted largely of stoichiometric operation and evaluated on only a few lean/rich cycling tests at temperatures near 300°C, it was felt that any Pt deposition from the LNT onto the SCR samples would be negligible. A purge test was performed on the 1" TWC + 2" of SCR, and another purge test was performed on the 1" TWC + 3" of SCR catalyst. Figure 8 shows the weighted $NO_x$ slip and the $NH_3$ yield for these two tests as a function of the rich purge time. Both lengths of SCR catalyst met the $NO_x$ slip target of 5 mg/mile easily with rich purge times of 7.5 to 8.0 seconds. In addition, the $NH_3$ slip for the 2" SCR catalyst aged at 700°C was lower than that of the 2" catalyst aged at 800°C, while the $NH_3$ slip for the 3" SCR was essentially zero.

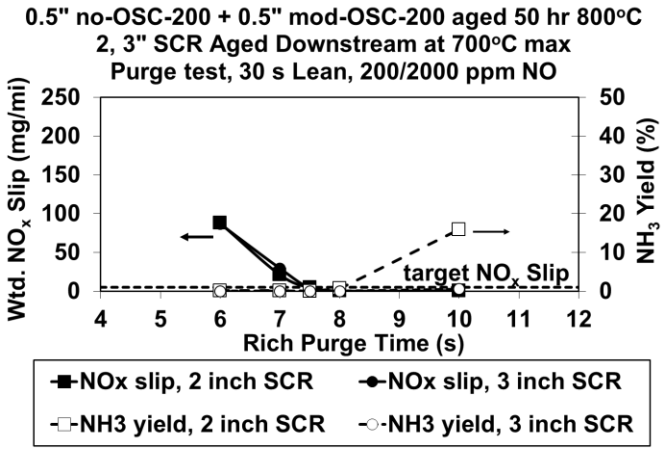


**Figure 8**. Weighted $NO_x$ slip and $NH_3$ yield as a function of rich purge time for 1" TWC + 2" or 3" of SCR catalyst aged at 700°C. NO level 200 ppm lean, 2000 ppm rich. 30 s lean periods, 0.86 rich λ. 530°C in the TWC, 300°C in the SCR catalyst.

The data in Figures 7 and 8 suggest that the SCR samples aged on the rich/stoich/lean cycle at 700°C retained higher $NH_3$ storage capacity than the samples aged at 800°C. Thus, it was concluded that the maximum aging temperature of the SCR catalysts should be limited to 700°C when the aging cycle included stoichiometric and rich operation. This temperature limit was considered feasible on the DOE application due to the large distance of the SCR converter from the exhaust manifold. For the remainder of this report, all tests involving SCR catalysts were performed with SCR samples aged at 700°C on the rich/stoich/lean cycle.

## *$NH_3$ Yield and HC Slip*

Two critical aspects of the passive TWC+SCR system are the generation of $NH_3$ from the CC TWC and U/B TWC and the HC slip during rich operation. Several factors were investigated for their influence on the $NH_3$ yield and HC slip, including the rich lambda, the temperatures of the three-way catalysts, the TWC formulations (e.g., ceria content), and the PGM loadings of the three-way catalysts. Table 2 displays the concentrations of $NO_x$, CO, $H_2$, and $C_2H_4$ used to produce rich lambdas ranging from 0.81 to 0.99 over the course of these experiments. There was no $O_2$ during the rich periods.

## *Effect of Rich Lambda on $NH_3$ Yield from TWC*

A TWC with 0.5" no-OSC-116 and 0.5" mod-OSC-40 was evaluated for $NH_3$ yield at different rich lambdas without the SCR catalyst downstream. Purge tests were performed with rich lambdas of 0.86, 0.91, 0.95, and 0.99, and the $NH_3$ yield averaged over the lean/rich cycle was determined as a function of the rich purge time. Figure 9 shows the average $NH_3$ yield as a function of the purge time for the different rich lambdas. The dashed line in the figure indicates the maximum yield if all the feedgas $NO_x$ was converted into $NH_3$ during the rich periods and no $NO_x$ was stored on the TWC during the lean periods, as stored $NO_x$ could generate additional $NH_3$. For a given purge time, the average $NH_3$ yield from the TWC decreased as the rich lambda increased from 0.86 to 0.99. As a result, longer purge periods would be required with the less rich lambdas to generate enough $NH_3$ to convert the $NO_x$ during the lean periods. This is consistent with the $NO_x$ conversion results shown in Figure 5.

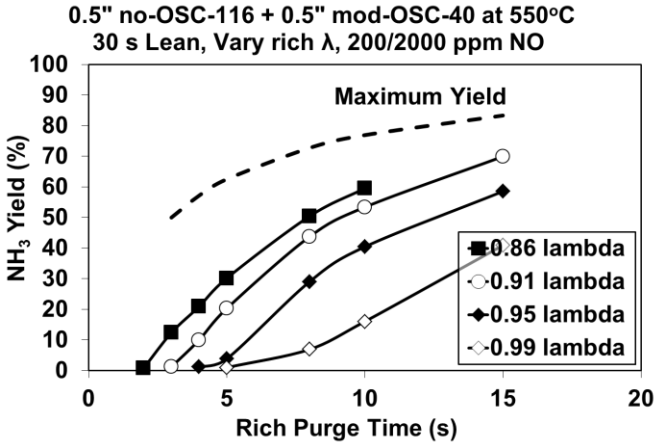


**Figure 9**. Average $NH_3$ yield as a function of rich purge time for 0.5" no-OSC-116 + 0.5" mod-OSC-40 at 550°C. 30 s lean periods and variable rich purge times. Rich λ of 0.86, 0.91, 0.95, and 0.99.

The decrease in $NH_3$ yield as the rich lambda increased from 0.86 to 0.99 is largely due to the increasing delay in the appearance of $NH_3$ following a lean-to-rich transition. Figure 10 shows the $NH_3$ concentration as a function of time for these different rich lambdas (along with a rich lambda of 0.81). As the rich lambda increased from 0.81 to 0.99, the time for the first appearance of $NH_3$ increased from approximately 2 seconds to over 5 seconds, while the time required to achieve nearly 100% conversion of $NO_x$ to $NH_3$ increased from approximately 5 seconds to 14 seconds. This is a result of the increasing time required to overcome the OSC of the TWC with the decreasing level of rich reductants. However, once the catalyst was reduced, the $NH_3$ yield approached 100% even when the A/F ratio was only slightly rich, as in the case with 0.99 lambda.

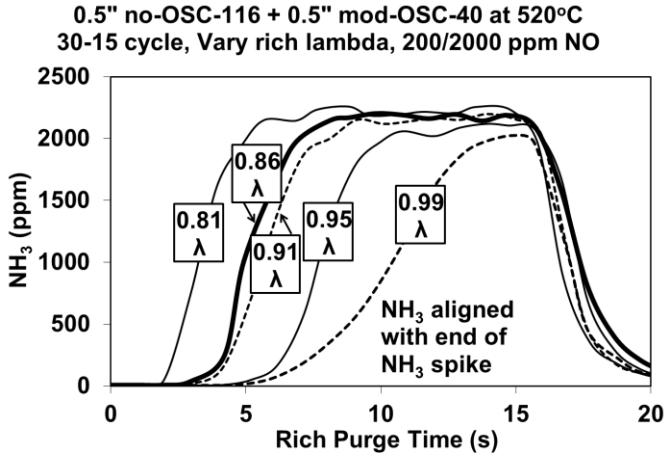


**Figure 10**. $NH_3$ concentration as a function of time for 0.5" no-OSC-116 + 0.5" mod-OSC-40 at 520°C. Rich λ of 0.81, 0.86, 0.91, 0.95, and 0.99. 200 ppm NO lean, 2000 ppm NO rich.

The rich periods consume additional fuel and also take away time that could be spent at lean A/F ratios. Therefore, to generate $NH_3$ quickly and minimize the duration of the rich periods, the data in Figure 10 suggest that the purge A/F ratio needs to be very rich to overcome the OSC of the catalysts as quickly as possible. However, as discussed before, high CO emissions can result if the A/F ratio is held at the very rich A/F ratio for the entire purge period. A two-step purge will be discussed later that reduces the TWC quickly with a very rich A/F ratio and then transitions to a less rich A/F ratio to minimize the CO emissions and fuel consumption of the rich purges. Also, it is intuitive that low-OSC or non-OSC three-way catalysts

would be desirable for generating $NH_3$ quickly. While this is true, it must be balanced against the need for some OSC in the TWC for $NO_x$ lightoff, good 3-way activity at stoichiometry, good steam-reforming of the HC during the rich periods, and for diagnostic capabilities.

### *Effect of PGM in TWC on $NH_3$ Yield & HC Slip*

The PGM loading of the TWC affects its OSC and therefore its $NH_3$ production. This is particularly true for highly loaded Pd-based formulations, since the Pd itself can store and release oxygen in addition to catalyzing the OSC of the ceria in the washcoat. Therefore, the effect of the PGM loading in the TWC was investigated for the effect on the $NH_3$ generation. The catalyst used for Figures 9 and 10 was the 0.5" no-OSC-116 with the 0.5" mod-OSC-40. It was compared to a pulsator-aged TWC system with 0.5" of the no-OSC-200 catalyst and 0.5" of the mod-OSC-200 catalyst. Figure 11 compares the $NH_3$ yields of these two catalysts systems for rich lambdas of 0.81, 0.91, 0.95, and 0.99.

The system with the higher PGM loading required 1 to 2 seconds longer to achieve 500 ppm $NH_3$ for all rich lambdas, attributable to the higher OSC resulting from the higher PGM content. Nevertheless, the $NH_3$ yield for both catalyst systems approached 100% toward the end of the purge periods for all four A/F ratios.

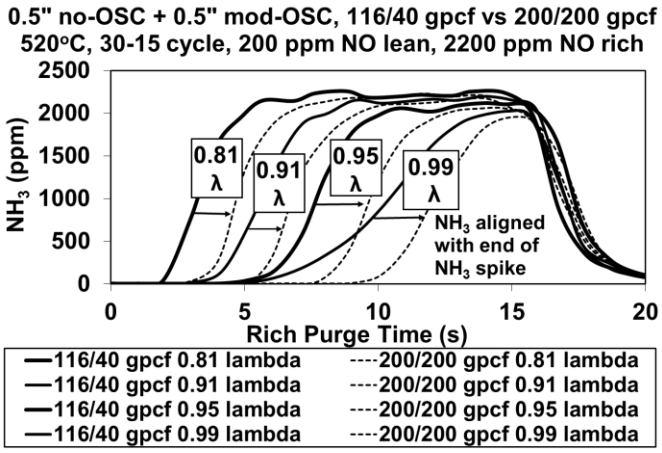


**Figure 11**. $NH_3$ concentration as a function of time for TWCs with 116/40 gpcf and 200/200 gpcf at 520°C. Rich λ of 0.81, 0.91, 0.95, and 0.99.

Regarding the HC slip, it is known that ceria promotes the steam reforming of hydrocarbons during rich operation [21]. Figure 12 compares the $C_2H_4$ slip for the 0.5" no-OSC-200 catalyst alone and the 0.5" no-OSC-200 catalyst + 0.5" mod-OSC-200 when evaluated at the different rich lambdas at 520°C. The 0.5" non-OSC front catalyst allowed high concentrations of $C_2H_4$ to slip at all rich lambdas except for 0.99 lambda. However, the HC slip from the 2x0.5" system was very low at all rich lambdas. This suggested that the rear OSC-containing catalyst was very effective at steam reforming the $C_2H_4$ that slipped past the front non-OSC catalyst during the rich periods. While a non-OSC TWC would be desirable for generating high levels of $NH_3$ in the shortest time, Figure 12 confirms that some OSC is required in the TWC for effective steam reforming of the HC during the rich periods.

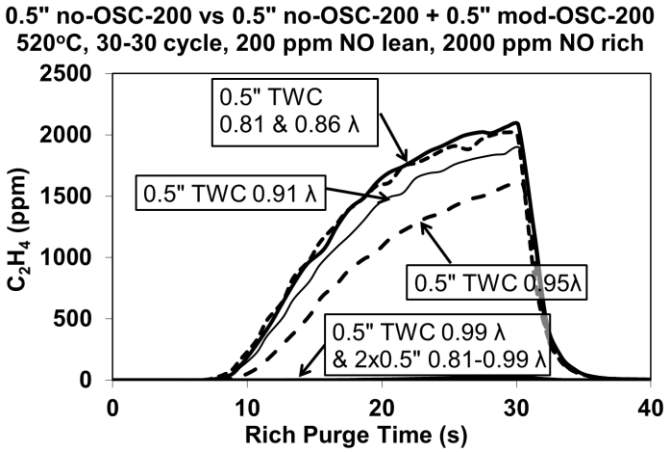


**Figure 12**. HC slip as a function of time for 0.5" no-OSC-200 catalyst and 0.5" no-OSC-200 + 0.5" mod-OSC-200) at 520°C. Rich λ of 0.81, 0.86, 0.91, 0.95, and 0.99.

A PGM loading of 200 gpcf in both zones of the CC TWC is a relatively high loading. Thus, it would be desirable to reduce the PGM loading in the CC TWC to lower the cost and improve the value of the lean aftertreatment system. Thus, a comparably-aged TWC with the same loading of 200 gpcf Pd in the front non-OSC zone but with the reduced loading of 40 gpcf Pd/Rh in the rear OSC-containing zone was evaluated at 520°C on the 30/30 cycle with the different rich lambdas.

Figure 13 compares the $C_2H_4$ slip from the 2x0.5" system with 200/200 gpcf and the 2x0.5" system with 200/40 gpcf at the five rich lambdas. The $C_2H_4$ slip from the 2x0.5" 200/40 gpcf system was much higher than that of the 2x0.5" 200/200 gpcf system except at 0.99 lambda. This suggested that the 200 gpcf PGM loading in the rear zone of the 200/200 gpcf system was more effective for steam reforming than the 40 gpcf loading. If there were no U/B TWC downstream of the CC TWC, the PGM loadings of both bricks of the CC TWC would need to be high to ensure good HC conversion during the rich periods. Fortunately, as will be shown later, the U/B TWC does provide some steam reforming of the HC during rich operation, which allows the PGM loading in the rear brick of the CC TWC to be lowered for improved cost effectiveness.

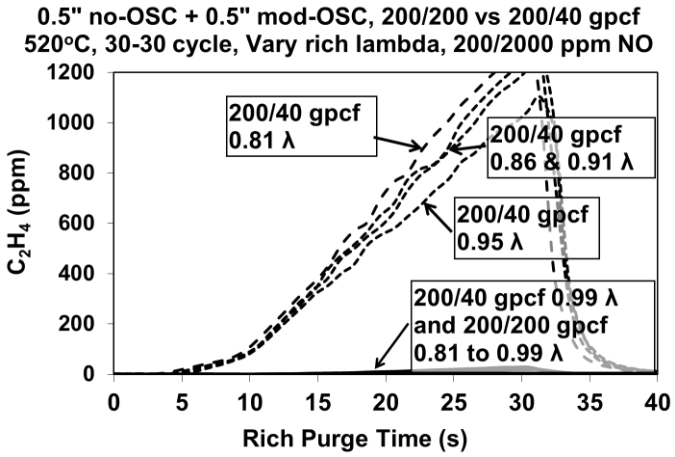


**Figure 13**. HC slip as a function of time for 0.5" no-OSC-200 + 0.5" mod-OSC-40 catalyst and 0.5" no-OSC-200 + 0.5" mod-OSC-200 catalyst at 520°C. Rich λ of 0.81, 0.86, 0.91, 0.95, and 0.99.

## *Effect of TWC Temperature on $NH_3$ Yield*

The high-loaded TWC (i.e., 0.5" no-OSC-200 + 0.5" mod-OSC-200) was evaluated on 30 s lean/30 s rich tests with a rich lambda of 0.99 and catalyst bed temperatures ranging from 325°C to 734°C. Figure 14 shows the $NH_3$ generation as a function of time at the different temperatures. As the temperature increased from 325°C to 525°C, the delay in the onset of $NH_3$ production increased, attributable to the increasing OSC of the catalyst. Above 550°C, the delay in $NH_3$ production decreased. This was attributed to the increasing kinetics of OSC reduction and $NH_3$ generation, which apparently overcame any further increase in OSC as the temperature increased. Also, as the temperature increased from 325°C to 525°C, the peak $NH_3$ yield increased to near 100%. Between 525°C and 608°C, the peak $NH_3$ yield remained near 100%. But as the temperature increased from 608°C to 734°C, the peak $NH_3$ yield dropped. Thus, to minimize the delay in $NH_3$ generation and maximize the peak $NH_3$ yield, the TWC needed to operate at temperatures near 600°C. While not shown here, this temperature also resulted in low $C_2H_4$ slip due to good steam reforming activity.

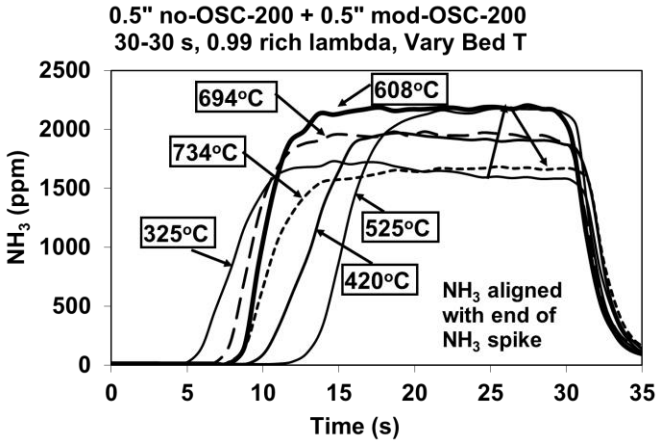


**Figure 14**. $NH_3$ concentration as a function of time for 0.5" no-OSC-200 + 0.5" mod-OSC-200 at different temperatures and a rich λ of 0.99.

## *$NH_3$ Yield & HC Slip from CC TWC + U/B TWC*

Up to this point, the systems evaluated contained only a CC TWC and no U/B TWC. However, it is anticipated that the DOE aftertreatment system will require both TWCs in addition to a third U/B SCR converter to satisfy the emission standards during the FTP and US06 tests while allowing lean operation for improved fuel economy. Therefore, tests were performed on a CC TWC + U/B TWC system to assess the effect of the U/B TWC on the $NH_3$ yield and HC slip.

The CC TWC consisted of a 0.5" no-OSC-200 catalyst and a 0.5" mod-OSC-40 catalyst. The 1" long U/B TWC was a model catalyst containing either 26 gpcf Pd or Pt on ceria/zirconia. Prior to testing, these U/B TWCs were aged for 175 hours at 800°C in an oven with stoichiometric exhaust from a pulsator. 30 second lean/30 second rich cycles were performed with a rich lambda of 0.81, and the CC TWC and U/B TWC were operated at ca. 500°C and 400°C, respectively. Figure 15 shows the $NH_3$ and $C_2H_4$ slip during the rich periods for the front 0.5" no-OSC-200 piece, the 2x0.5" CC TWC, and the 2x0.5" CC TWC + U/B TWC with either the Pd or Pt model catalysts.

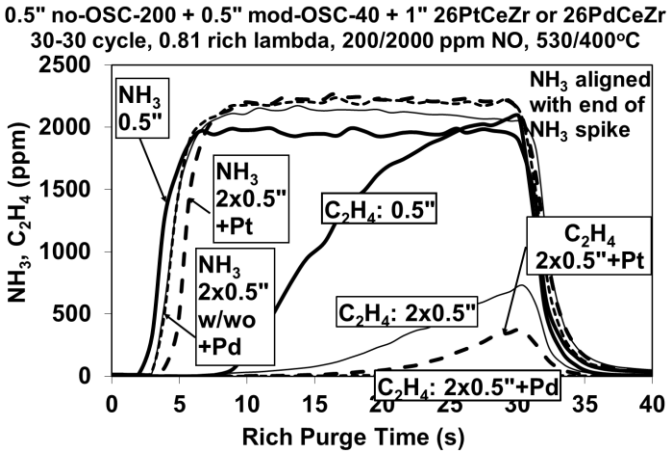


**Figure 15**. $NH_3$ & $C_2H_4$ slip during 30 second rich periods for 0.5" no-OSC-200, 2x0.5" CC TWC, 2x0.5" CC TWC + 1" PdCeZr, and 2x0.5" CC TWC + 1" PtCeZr. 0.81 rich λ. CC TWC at 500°C, U/B TWC at 400°C.

The front 0.5" no-OSC-200 catalyst began to emit $NH_3$ after only 2-3 seconds of rich operation and achieved a $NH_3$ yield near 90% at steady-state. The rear 0.5" OSC-containing catalyst in the CC TWC consumed some of that $NH_3$ and delayed the $NH_3$ appearance by about 1 second. However, the rear TWC zone increased the $NH_3$ yield to ca. 98% at steady-state. The Pd-containing U/B TWC did not cause any further delay in the appearance of $NH_3$, but the Pt-containing U/B TWC delayed the appearance of $NH_3$ for another 1 to 2 seconds. However, both U/B TWCs increased the steady-state $NH_3$ generation to near 100%. While not shown here, it should be mentioned that the U/B TWC caused significantly longer delays in the appearance of $NH_3$ with rich lambdas of 0.91, 0.95, and 0.99. Thus, it is important to reduce the OSC of both catalysts quickly with a deeper rich purge before transitioning to a slightly rich condition.

Figure 15 also shows the $C_2H_4$ slip for the same catalyst pieces. The $C_2H_4$ slip from the front 0.5" no-OSC-200 catalyst was high due to poor steam reforming capability without ceria. The rear 0.5" OSC-containing zone of the CC TWC provided much better steam reforming capability, but the $C_2H_4$ slip increased to unacceptable levels near the end of the 30 second rich purge period. The PtCeZr U/B catalyst provided more steam reforming and reduced the $C_2H_4$ slip from the CC TWC. The PdCeZr U/B catalyst provided even better steam reforming than the PtCeZr U/B catalyst and reduced the $C_2H_4$ slip to very low levels even after 30 seconds of rich operation.

## *Tests on CC TWC + U/B TWC + U/B SCR System*

Reactor evaluations of the complete CC TWC + U/B TWC + U/B SCR system were performed. The PdCeZr U/B catalyst was used for this testing due to its superior steam reforming capability. A 1" long SCR catalyst was placed downstream of the second oven so that it operated at ca. 330-340°C, and a purge test with 30 second lean periods and a rich lambda of 0.86 was performed. The NO levels were 200 ppm lean and 2000 ppm rich. Similar tests were performed with 2" and 3" of SCR catalyst. Figure 16 is a semilog plot of the weighted $NO_x$ slip versus the rich purge time for the 3 SCR lengths. The 1" SCR length achieved a $NO_x$ slip very near the target of 5.0 mg/mile with 7 second purges. The 2" and 3" SCR lengths achieved much lower $NO_x$ slip and easily satisfied the target level of $NO_x$ with similar purge times.

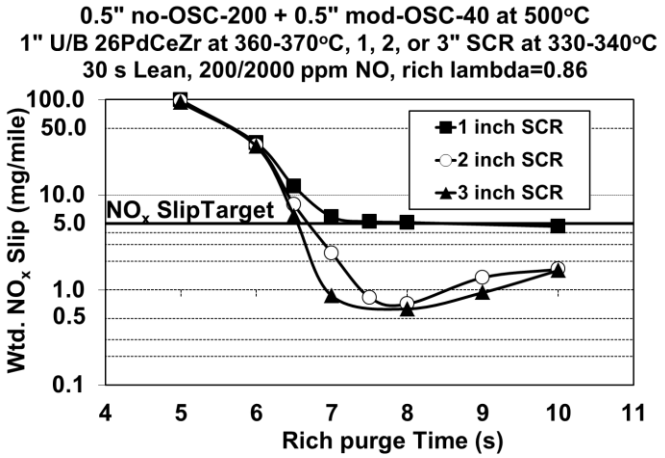


**Figure 16**. Weighted $NO_x$ slip during purge tests with 2x0.5" CC TWC + 1" PdCeZr U/B TWC + SCR catalysts with lengths of 1", 2", and 3". 30 second lean periods. 200 ppm NO lean, 2000 ppm NO rich. 0.86 rich λ. CC TWC, U/B TWC, and U/B SCR catalyst at 500°C, 360°C, & 330°C, respectively.

Figure 17 shows the corresponding $NH_3$ and $N_2O$ yields for the data in Figure 16. The $N_2O$ yields (solid lines) were on the order of a few percent and increased only modestly as the rich purge time increased. The $NH_3$ yields increased as the purge time increased and also increased as the volume of SCR decreased. For the 7 s purge time that satisfied the $NO_x$ slip target with 2" and 3" SCR lengths in Figure 16, the $NH_3$ slip was very low. These results demonstrate the feasibility of meeting the target $NO_x$ levels with low $NH_3$ slip and relatively low $N_2O$ slip with the passive TWC+SCR system.

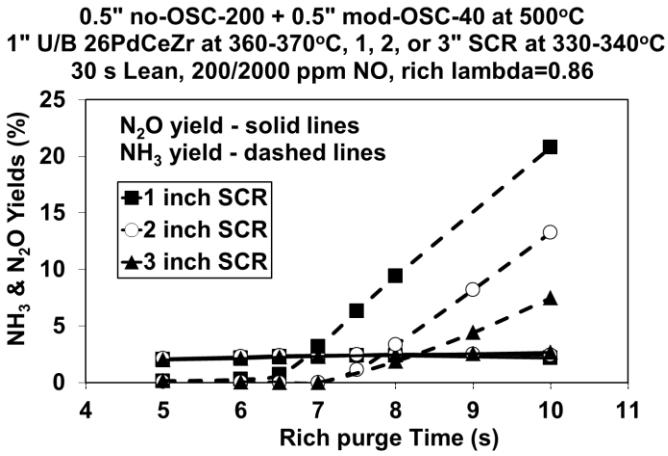


**Figure 17**. $NH_3$ & $N_2O$ yields during purge tests with 2x0.5" CC TWC + 1" PdCeZr U/B TWC + SCR catalysts with lengths of 1", 2", and 3". 30 second lean periods. 200 ppm NO lean, 2000 ppm NO rich. 0.86 rich λ. CC TWC, U/B TWC, and U/B SCR catalyst at 500°C, 360°C, & 330°C, respectively.

Similar tests were performed with the 3" long SCR catalyst with 45 and 60 second lean periods (data not shown). For lean durations of 30, 45, and 60 s, the $NO_x$ slip target was satisfied with 6.5, 8.5, and 10 seconds, respectively. The effect of the lean NO concentration was also evaluated with 400 and 600 ppm NO lean, while the lean duration was maintained at 30 seconds and the rich NO concentration was maintained at 2000 ppm. For lean NO levels of 200, 400, and 600 ppm, the $NO_x$ slip target was met with rich purge times of 6.5, 9.5, and 11.5 seconds, respectively. Thus, the CC TWC + U/B TWC + U/B SCR system was able to satisfy the $NO_x$ slip target with lean periods as long as 60 seconds and lean NO levels as high as 600 ppm.

## *2-Step Purge*

As mentioned earlier, the 2-step purge uses several seconds of a relatively rich lambda to remove the oxygen stored on the TWC. Then the AFR transitions to a less rich lambda to continue the $NH_3$ generation while minimizing the CO slip and the impact on FE. To demonstrate, a 2x0.5" CC TWC with 0.5" no-OSC-200 + 0.5" mod-200-40 was evaluated at 500°C with a 30 s lean/15 s rich cycle. The rich lambda was 0.88 for the first part of the purge and 0.99 for the remainder of the purge. The NO levels were 200 ppm lean and 2000 ppm rich, and the $C_2H_4$ concentration remained at 800 ppm during both rich and lean operation. Figure 18 shows the $NH_3$ production during the purge period where the 0.88 lambda was used for 0, 1, 2, 3, 4, and 15 seconds; the 0 and 15 second cases correspond to the limiting cases of 0.99 lambda for the entire purge and 0.88 lambda for the entire purge, respectively. With 0 and 1 seconds of 0.88 lambda, $NH_3$ was not observed until ca. 8 seconds. With 2, 3, 4, and 15 seconds of 0.88 lambda, $NH_3$ was observed after ca. 4 seconds, or approximately half of the time required when 0.99 lambda was used for the entire purge period. This suggested that 2 seconds of extra rich operation was sufficient to reduce the OSC of this CC TWC.

The U/B TWC will require additional time at the richer A/F to overcome its OSC. To demonstrate, the PdCeZr catalyst was placed in the second oven, and similar tests were performed on the CC TWC + U/B TWC system except that the total rich time was increased to 30 seconds (data not shown). The CC and U/B TWCs were operated at ca. 500°C and 360°C, respectively. 4 and 5 seconds at 0.88 lambda generated nearly as much $NH_3$ as when 0.88 lambda was used for the entire purge. So 4 seconds at 0.88 lambda was sufficient to reduce the OSC of both the CC TWC and U/B TWC. An initial 3 seconds at 0.81 lambda produced similar amounts of $NH_3$ as an initial 4 seconds at 0.88 lambda.

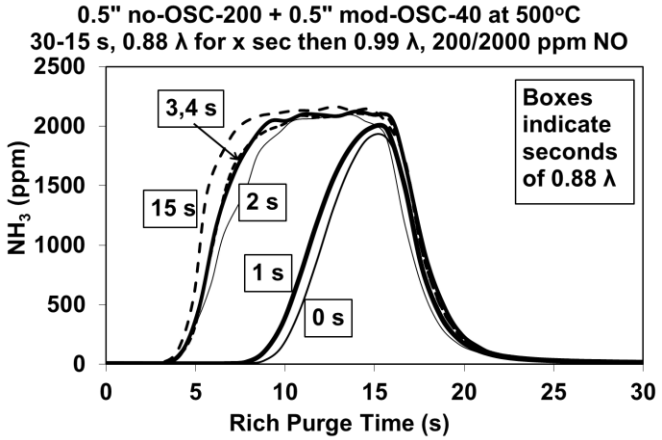


**Figure 18**. $NH_3$ generation during 30/15 cycle with 2x0.5" CC TWC at 500°C. 200 ppm NO lean, 2000 ppm NO rich, 800 ppm $C_2H_4$ lean and rich. 0.88 rich λ for x seconds, 0.99 rich λ for remainder of purge period.

## *CC TWC + U/B TWC + U/B SCR System with 2-Step Purge*

Finally, 2" of the SCR catalyst was placed downstream of the second oven, and purge tests with 30 second lean periods were performed on the complete 2x0.5" CC TWC + 1" PdCeZr U/B TWC + 2" SCR system with the 2-step purges. The initial rich lambda was either 0.82 or 0.88, and this was maintained for 3 or 4 seconds before transitioning to 0.99 lambda for the remainder of the purge. As limiting cases, tests were also performed with constant lambdas of 0.82, 0.86, and 0.99 for the entire purge period. Figure 19 is a

semilog plot that shows the $NO_x$ slip as a function of rich purge time for the tests with 2-step purges and the 3 tests with constant lambda. With a constant lambda of 0.99, a rich period of 23 seconds was required to satisfy the 5.0 mg/mile target. With constant lambdas of 0.82 or 0.86, the $NO_x$ target was met with only 7 second purges. 3 and 4 seconds with 0.88 lambda reduced the total purge times to 14 and 10 seconds, respectively. However, 3 and 4 seconds with 0.82 lambda reduced the total purge times to more acceptable durations of 8 and 7 seconds, respectively.

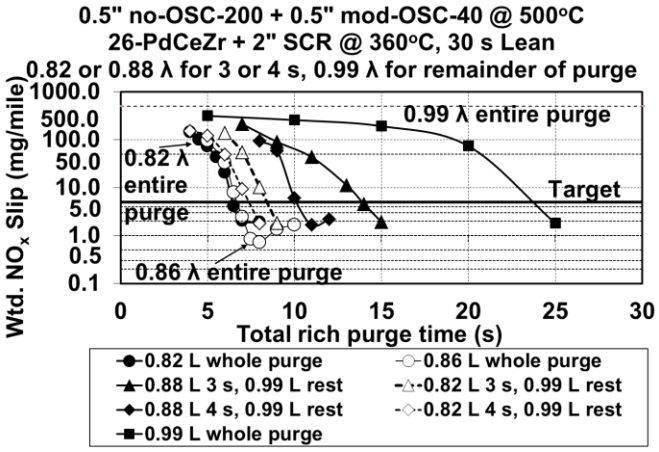


**Figure 19**. Weighted $NO_x$ slip on purge tests with 2x0.5" CC TWC + 1" PdCeZr U/B TWC + 2" SCR. CC TWC, U/B TWC, & U/B SCR catalyst at 500°C, 360°C, & 330°C, respectively. 200 ppm NO lean, 2000 ppm NO rich, 800 ppm $C_2H_4$ lean and rich. 30 second lean periods, 1 or 2-step purges.

As stated before, a principal advantage of the 2-step purge is reduced CO emissions. With constant lambdas of 0.82 or 0.86, the CO slip exceeded the target level of 1.3 g/mile with longer purge times. But with the 2-step purges, the CO levels were comfortably below the target level (data not shown). For example, with 0.82 lambda for 3 or 4 seconds, the CO slip was ca. 0.30 or 0.60 g/mile, respectively. While not shown, the HC slip also met the target level with the 2x0.5" CC TWC + 1" PdCeZr U/B TWC + 2" SCR system and the 2-step purges. Thus, with optimized catalyst formulations, catalyst temperatures, lean and rich NO concentrations, and the 2-step purge, the passive TWC+SCR system was capable of satisfying the HC, CO, and $NO_x$ target levels during lean/rich cycling.

## *Sulfur Poisoning of TWC+SCR System*

In addition to its high cost, a primary reason that the TWC+LNT/SCR system development was terminated was its strong sensitivity to sulfur poisoning. It was determined that the LNT could not be desulfated in the U/B location that was needed for optimum emissions performance without the addition of other costly hardware such as an air pump or an exhaust fuel injector. Therefore, the effects of sulfur poisoning on the passive TWC+SCR system were also examined.

A CC TWC was poisoned with $SO_2$ to assess the effects of sulfur on the $NH_3$ generation and steam reforming capability of the catalyst. The 0.5" no-OSC-200 catalyst and the 0.5" mod-OSC-200 catalyst were placed in the oven and exposed to a 30/8 cycle at 500°C for ca. 3 hours with 10 ppm $SO_2$ in the feedgas. The rich lambda was at 0.86 for the entire purge period. Figure 20 shows the maximum HC, CO, and $NH_3$ concentrations during the rich periods as a function of time. The TWC was very effective for promoting the steam reforming of the $C_2H_4$ at the beginning of the test, but $C_2H_4$ began to slip through the TWC after 40 minutes of poisoning. After ca. 2.5 hours, the maximum $C_2H_4$ concentration was near the feedgas level of 2500 ppm, indicating that the steam reforming capability was severely degraded by the sulfur. Since the rich lambda was at 0.86 for the entire purge, the CO emissions were high even at the beginning of the test. The CO emissions also increased during the poisoning test. The figure also shows that the maximum $NH_3$ concentration decreased significantly during the sulfur poisoning, dropping from approximately 2000 ppm at the beginning of the test to 300 ppm at the end of the 3 hours of poisoning.

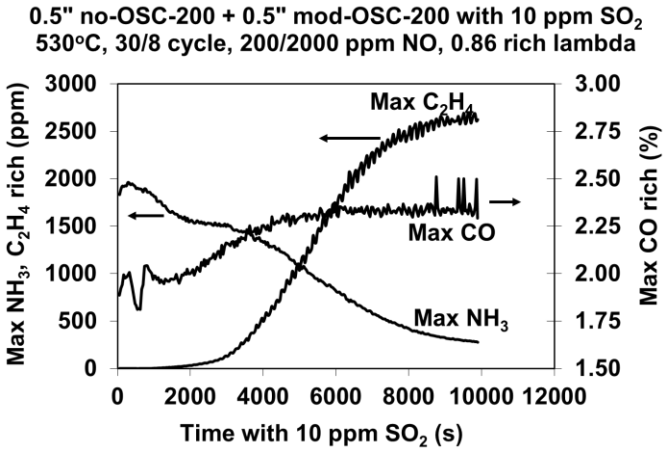


**Figure 20**. Maximum concentrations of $NH_3$, $C_2H_4$, and CO from 0.5" no-OSC-200 + 0.5" mod-OSC-200 catalyst on 30/8 cycle at 500°C as a function of time with 10 ppm $SO_2$. 200 ppm NO lean, 2000 ppm NO rich, 2500 ppm $C_2H_4$ lean & rich. 0.86 rich λ.

The poisoned TWC was evaluated on the same 30/8 cycle at several steady-state temperatures between 450 and 530°C. The TWC was then desulfated with rich exhaust at 700°C to remove the sulfur. Then the desulfated TWC was evaluated on the 30/8 cycle as the temperature was ramped down from ca. 650°C to 300°C. Figure 21 shows that the $NH_3$ production from the poisoned TWC was very sensitive to the temperature, decreasing from a maximum value of 2000 ppm near 450°C to a maximum value of 300 ppm at ca. 520°C. However, after the desulfation, the maximum $NH_3$ concentration was near 2000 ppm from 630°C to 370°C.

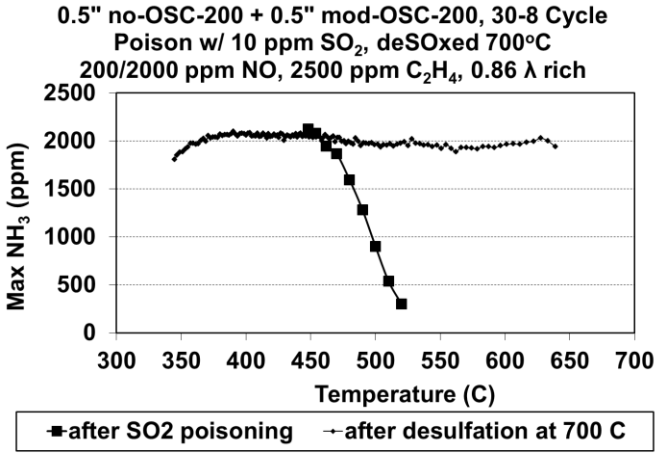


**Figure 21**. Maximum $NH_3$ from 0.5" no-OSC-200 TWC + 0.5" mod-OSC-200 TWC on 30/8 cycle as a function of temperature after poisoning with 10 ppm $SO_2$ and after a rich desulfation at 700°C. 200 ppm NO lean, 2000 ppm NO rich, 2500 ppm $C_2H_4$ lean and rich. 0.86 rich λ.

A 3" long SCR catalyst aged at 700°C was placed downstream of the desulfated 2x0.5" CC TWC, and the system was evaluated as a

function of time on the 30/8 cycle with 5 ppm $SO_2$. There was no U/B TWC during this testing, and the rich lambda was 0.86. Figure 22 shows that both the weighted $C_2H_4$ and $NO_x$ emissions exceeded their respective targets after a relatively short time. However, when the HC was turned off and the $CO/H_2$ was increased to 3.5/1.2% to maintain the same rich lambda, the $NO_x$ slip fell to a value far below the target value of 5 mg/mile. When the $CO/H_2$ was returned to 2.5/0.8% and the HC restored, the $NO_x$ slip increased to over 100 mg/mile. These results suggested that the SCR catalyst itself was not significantly affected by the sulfur poisoning, as it was possible to obtain very high $NO_x$ conversions from the poisoned system with the proper feedgas composition. The primary reason for the increase in $NO_x$ slip during the poisoning was a decrease in $NH_3$ production from the TWC. As shown earlier, the increase in HC slip during the poisoning could be attributed to the severe effect of $SO_2$ poisoning on the steam reforming reaction.

Further testing on the poisoned TWC alone revealed that the increase in $NH_3$ production when the HC was turned off was due to a drop in catalyst temperature rather than a chemical effect. This is because the HC flows during both lean and rich operation, and the oxidation of 2500 ppm $C_2H_4$ during the lean periods produced an exotherm on the order of 100°C. Therefore, when the HC was shut off, the catalyst bed temperature dropped from ca. 520°C to 440°C. As shown in Figure 21, the $NH_3$ production from the poisoned TWC was significantly higher at 440°C than at 520°C, and this resulted in the much lower $NO_x$ slip. To confirm that the increase in $NH_3$ production was due to thermal effects and not a chemical effect, the $NH_3$ production from the TWC remained low when the rich HC was turned off and the $CO/H_2$ increased to maintain the rich lambda but the lean HC remained on in order to maintain the bed temperature near 520°C. But when the lean HC was also turned off, the bed temperature dropped and the $NH_3$ yield rose to high levels.

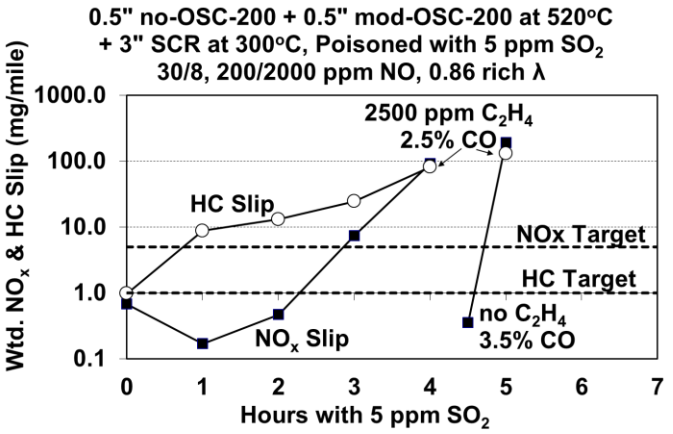


**Figure 22**. Weighted $C_2H_4$ & $NO_x$ slip from 0.5" no-OSC-200 + 0.5" mod-OSC-200 TWC + 3" SCR on 30/8 cycle versus time with 5 ppm $SO_2$. 200 ppm NO lean, 2000 ppm NO rich, 2500 ppm $C_2H_4$ lean and rich. 0.86 rich λ.

Thus, it was concluded that the SCR catalyst was not significantly affected by sulfur poisoning, but the $NH_3$ production and steam reforming capability of the TWC were degraded significantly by the sulfur during continuous operation at temperatures near 500°C. It was shown in the companion paper on the TWC+LNT/SCR system [16] that the poisoned TWC could be desulfated with rich exhaust at 700°C. Such conditions are expected to be encountered routinely by close-coupled TWCs during cold-starts (from rapid heating strategies), accelerations, and high load operation. As an example, reference [16] displays the projected temperatures of the CC TWC, U/B TWC, and the U/B LNT/SCR catalyst during the FTP based on computer modeling. The projected temperatures of the CC TWC during phases 1 and 3 of the test exceeded 700°C due to rapid catalyst heating strategies. US06 testing of other vehicles indicated that the temperatures of the CC TWC achieved 750°C and even 850°C with occasional rich operation during heavy accelerations. As a result, it is assumed that the TWC would remain naturally desulfated and maintain good HC control and $NH_3$ generation capability. In addition, the lower fuel sulfur levels that will be required with the Tier 3 regulations will reduce the rate of sulfur poisoning and further improve the likelihood that natural desulfations will occur before the steam reforming and $NH_3$ generation capabilities of the CC TWC are significantly affected by sulfur. Therefore, it was concluded that the passive TWC+SCR system would not need an active desulfation strategy. This is a significant advantage of the TWC+SCR system relative to the TWC+LNT/SCR system because it avoids the fuel penalties and emission penalties associated with the desulfations. However, it is recommended that a desulfation strategy be available on the vehicle in the event of extended low load operation.

### *Impact of Future Emission Standards on Passive TWC+SCR Approach*

One of the great emission challenges during lean/rich cycling is the control of hydrocarbons during the rich periods, as nearly 100% HC conversion is required through steam reforming to satisfy the very low HC limits for the Tier 2, Bin 2 and LEV 2 emission standards. It is noted that the new Tier 3 and LEV III emission standards specify limits for NMOG+$NO_x$ rather than separate emission levels for NMOG and $NO_x$. This potentially could offer some relief in the rich HC conversion requirements, as slightly higher NMOG emissions could be tolerated provided the $NO_x$ emissions remained low. However, assuming that the sum of the cold-start emissions, stoichiometric emissions, and the engineering tolerances for HC and $NO_x$ in Table 3 remain approximately the same, the sum of the HC and $NO_x$ during lean/rich cycling would still need to be maintained at or below 6 mg/mile in order to satisfy a Tier 3, Bin 30 standard. Under the conditions of these experiments, a feedgas level of 2500 ppm $C_2H_4$ corresponds to approximately 1800 mg/mile. Assuming a 30 s lean/10 s rich cycle and the best-case scenario of 100% $NO_x$ conversion during lean/rich cycling and 100% HC conversion during the lean periods, the rich HC conversion through steam reforming would still need to be over 98.5%. Since 100% $NO_x$ conversion is not a realistic assumption during lean/rich cycling, the combined NMOG+$NO_x$ limits of the Tier 3 and LEV III regulations offer only a minimal relief in the rich HC conversion requirements.

## Summary/Conclusions

This paper summarizes the laboratory investigation of a close-coupled TWC + underbody TWC + underbody SCR catalyst system that could potentially allow lean operation during cruises for improved fuel economy on gasoline-powered vehicles while meeting the Tier 2, Bin 2 emission standards. Essentially all of the $NH_3$ for the SCR catalyst is generated from the feedgas $NO_x$ during rich operation. Therefore, this approach benefits from a high feedgas $NO_x$ concentration during rich operation to generate high levels of $NH_3$ quickly and a low feedgas $NO_x$ concentration during lean operation to reduce the rate of $NH_3$ consumption. Maximum HC, CO, and $NO_x$ levels during lean/rich cycling were established. With a reduced-OSC TWC and 200 ppm NO lean, it was shown that the $NO_x$ slip target could be satisfied with 1500 ppm NO during the rich periods and the equivalent of 3.3 L of SCR catalyst on the intended vehicle. SCR catalysts aged on a rich/stoich/lean durability schedule at 800°C had low $NH_3$ storage capacities, but samples aged at 700°C on the same schedule had significantly higher $NH_3$ capacity. Temperature studies revealed that the CC TWC needed to operate at 600°C to

provide high $NH_3$ levels and good steam reforming capability. It was shown that a 1" CC TWC + 1" U/B TWC + 2" Cu/zeolite SCR catalyst was able to satisfy the HC, CO, and $NO_x$ target levels on the reactor when evaluated with 30 second lean periods and a 2-step purge strategy. Sulfur poisoning increased the HC slip by decreasing the steam reforming capability of the TWC. The $NO_x$ slip also increased during the poisoning, but this was due primarily to reduced $NH_3$ production by the TWC. The TWC can be desulfated with rich operation at temperatures near 700°C. These temperatures are expected to be generated easily in the close-coupled location during cold-starts, accelerations, and high load operation. Therefore, it was concluded that the passive TWC+SCR system did not need an active desulfation strategy that would be required for a TWC+LNT/SCR system. However, it is recommended that a desulfation strategy be available on the vehicle in the event of extended low load operation.

## References


1. H. Bosch and F. Janssen, "Catalytic Reduction of Nitrogen Oxides", Catalysis Today, 2 (1988), p 369.
2. Naoto Miyoshi, S. Matsumoto, K. Katoh, T. Tanaka, J. Harada, N. Takahashi, K. Yokota, M. Sgiura, and K. Kasahara, "Development of New Concept Three-Way Catalyst for Automotive Lean-Burn Engines", SAE Paper no. 950809.
3. C.H. Kim, K. Perry, M. Viola, W. Li, and K. Narayanaswamy, "Three-Way Catalyst Design for Urealess Passive Ammonia SCR: Lean-Burn SIDI Aftertreatment System", SAE Paper no. 2011-01-0306.
4. C. Lambert, "Urea SCR and DPF System for Diesel Sport Utility Vehicle Meeting Tier 2 Bin 5", presented at U.S. Department of Energy Diesel Engine Emissions Reduction (DEER) conference, Chicago, August 2005.
5. J. Schommers and H. Breitbach, "A Global Emission Strategy - Bluetec for Diesel Engines", Auto Technology, Pages 48-51, Mar. 2007.
6. H. Hu, J. Reuter, J. Yan, and J. McCarthy, Jr., "Advanced NOx aftertreatment System and Controls for On-Highway Heavy Duty Diesel Engines:", SAE paper no. 2006-01-3552.
7. R. Roecker, R. Zhan, and R. Stanglmaier, "Feasibility Investigation of a High-Efficiency NOx Aftertreatment System for Diesel Engines", SAE paper no. 2007-01-3983.
8. R. Snow, G. Cavataio, D. Dobson, C. Montreuil, and R. Hammerle, "Calibration of a LNT-SCR Diesel Aftertreatment System", SAE paper no. 2007-01-1244.
9. R. Snow, D. Dobson, R. Hammerle, and S. Katare, "Robustness of a LNT-SCR System to Aging Protocol", SAE paper no. 2007-01-0469.
10. J. McCarthy, Jr. and J. Holtgreven, "Advanced NOx Aftertreatment System Performance Following 150 LNT Desulfation Events", SAE paper no. 2008-01-1541.
11. C. Enderele, G. Vent, and M. Paule, "BLUETEC Diesel Technology - Clean, Efficient and Powerful", SAE paper no. 2008-01-1182.
12. L. Xu, R. McCabe, W. Ruona, and G. Cavataio, "Impact of a Cu-zeolite SCR Catalyst on the Performance of a Diesel LNT+SCR System", SAE paper no. 2009-01-0285.
13. J. Parks and V. Prikhodko, "Ammonia Production and Utilization in a Hybrid LNT+SCR System", SAE paper no. 2009-01-2739.
14. J. Theis, J. Ura, and R. McCabe, "The Effects of Sulfur Poisoning and Desulfation Temperature on the $NO_x$ Conversion of LNT+SCR Systems for Diesel Applications", SAE paper no. 2010-01-0300.
15. J. Theis, M. Dearth, and R. McCabe, "TWC+LNT/SCR Catalyst Systems for $NO_x$ Conversion on Diesel Applications", SAE paper no. 2011-01-0305.
16. J. Theis, J. Kim, and G. Cavataio, "TWC+LNT/SCR Systems for Satisfying Tier 2, Bin 2 Emission Standards on Lean-Burn Gasoline Engines", SAE paper no. 2015-01-1006.
17. Department of Energy Award Number DE-EE0003332.
18. J. Hepburn, D. Dobson, C. Hubbard, and K. Otto, "The Pulse Flame Combustor Revisited", SAE Paper no. 962118.
19. H. Jen, J. Girard, G. Cavataio, and M. Jagner, "Detection, Origin and Effect of Ultra-Low Platinum Contamination on Diesel-SCR Catalysts", SCR paper no. 2008-01-2488.
20. G. Cavataio, H. Jen, J. Girard, D. Dobson, J. Warner, and C. Lambert, "Impact and Prevention of Ultra-Low Contamination of Platinum Group Metals on SCR Catalysts Due to DOC Design", SAE paper no. 2009-01-0627.
21. X. Wang, R. Gorte, "A study of steam reforming of hydrocarbon fuels on Pd/ceria", Appl. Cat. A: General **224** (2002) 209-218.


## Contact Information


Please contact J. Theis (jtheis@ford.com) for further information.


## Acknowledgments


This material is based upon work supported by the Department of Energy under Award Number DE-EE0003332. This report was prepared as an account of work sponsored by an agency of the United States Government. Neither the United States Government nor any agency thereof, nor any of their employees, makes any warranty, express or implied, or assumes any legal liability or responsibility for the accuracy, completeness, or usefulness of any information, apparatus, product, or process disclosed, or represents that its use would not infringe privately owned rights. Reference herein to any specific commercial product, process, or service by trade name, trademark, manufacturer, or otherwise does not necessarily constitute or imply its endorsement, recommendation, or favoring by the United States Government or any agency thereof. The views and opinions of authors expressed herein do not necessarily state or reflect those of the United States Government or any agency thereof.


## Definitions/Abbreviations

| | |
|---|---|
| $C_2H_4$ | Ethylene |
| Ce | Cerium |
| CO | Carbon monoxide |
| $CO_2$ | Carbon dioxide |
| FTP | Federal Test Procedure |
| $H_2$ | Hydrogen |
| $H_2O$ | Water |
| $H_2S$ | Hydrogen sulfide |
| HC | Hydrocarbon |
| LNT | Lean $NO_x$ Trap |
| λ | Lambda = A/F ratio/14.6 |
| $N_2$ | Nitrogen |
| $N_2O$ | Nitrous oxide |
| NO | Nitric oxide |
| $NO_x$ | Oxides of nitrogen = $NO+NO_2$ |
| $NO_2$ | Nitrogen dioxide |

| | | | |
|---|---|---|---|
| $O_2$ | Oxygen | Rh | Rhodium |
| OSC | Oxygen Storage Capacity | SCR | Selective Catalytic Reduction |
| Pt | Platinum | $SO_2$ | Sulfur dioxide |
| Pd | Palladium | TWC | Three-way catalyst |
| PGM | Platinum Group Metal | US06 | Supplemental FTP test |

2015-01-1006

# TWC+LNT/SCR Systems for Satisfying Tier 2, Bin 2 Emission Standards on Lean-Burn Gasoline Engines

**Joseph Theis, Jeong Kim, and Giovanni Cavataio**
Ford Motor Company

## Abstract

A laboratory study was performed to assess the potential capability of TWC+LNT/SCR systems to satisfy the Tier 2, Bin 2 emission standards for lean-burn gasoline applications. It was assumed that the exhaust system would need a close-coupled (CC) TWC, an underbody (U/B) TWC, and a third U/B LNT/SCR converter to satisfy the emission standards on the FTP and US06 tests while allowing lean operation for improved fuel economy during select driving conditions. Target levels for HC, CO, and $NO_x$ during lean/rich cycling were established. Sizing studies were performed to determine the minimum LNT/SCR volume needed to satisfy the $NO_x$ target. The ability of the TWC to oxidize the HC during rich operation through steam reforming was crucial for satisfying the HC target. Temperature studies indicated that the CC TWC needed to operate at a minimum of 500°C to provide good steam reforming activity, while the LNT/SCR needed to operate between 300 and 350°C to satisfy the $NO_x$ slip target while minimizing the slip of $NH_3$, $N_2O$, and HC during the purges. Sulfur poisoning increased the HC slip by degrading the steam reforming reaction, and the sulfur increased the $NO_x$ slip by decreasing the $NO_x$ storage capacity of the LNT. Both the TWC and LNT/SCR could be desulfated with rich exhaust at 700°C. However, it was projected that the ability to obtain 700°C at the underbody LNT/SCR location would be difficult without additional exhaust hardware, such as fuel injectors or air pumps. Consequently, development of the LNT/SCR system was terminated in favor of a passive TWC+SCR approach because of its superior sulfur tolerance. Investigations into the passive TWC+SCR approach are discussed in a companion SAE paper.

## Introduction

Automakers are working diligently to improve the fuel economy of their gasoline-powered vehicles to improve customer satisfaction and to satisfy future governmental regulations. Simultaneously, the California LEV III regulations and the Federal Tier 2 and Tier 3 regulations are requiring carmakers to lower the emissions of hydrocarbons (HC), carbon monoxide (CO), nitrogen oxides ($NO_x$), and particulate matter (PM) from their vehicles. One strategy that can provide better fuel economy is the use of lean operation during select driving modes such as cruises, as lean operation lowers the pumping losses and improves the thermodynamics of combustion. Depending on the engine and combustion strategy, lean operation can improve the fuel economy by as much as 5 to 15% relative to stoichiometric operation. However, it is well known that the three-way catalyst (TWC) cannot reduce $NO_x$ under lean conditions. Therefore, to allow lean operation while satisfying strict emission regulations, the TWC converter(s) must be supplemented with catalysts that can reduce $NO_x$ during lean operation or during lean/rich cycling. Selective catalytic reduction (SCR) catalysts [1] with urea injection systems are currently being used to reduce the $NO_x$ emissions from diesel engines. Here an aqueous solution of urea is pumped from a storage tank into the exhaust, where the urea decomposes into $NH_3$. The $NH_3$ and $NO_x$ react over the SCR catalyst under lean conditions to produce nitrogen ($N_2$) and water ($H_2O$). A popular SCR formulation used on production diesel trucks contains copper in a chabazite zeolite which provides high $NO_x$ conversion and good thermal durability. One issue is that this system requires the customer to maintain a sufficient supply of the urea solution in the storage tank. Typically, the urea tank is refilled during vehicle service appointments.

An alternative catalyst for treating $NO_x$ under lean conditions which does not require the urea injection system is the lean $NO_x$ trap (LNT). The LNT contains platinum group metals (PGM) such as platinum (Pt), palladium (Pd), and rhodium (Rh) along with $NO_x$ storage materials such as barium (Ba) and cerium (Ce). During lean operation, the platinum oxidizes the NO in the exhaust to $NO_2$, and the $NO_2$ reacts with the $NO_x$ storage materials to form nitrates [2]. Periodically, the A/F ratio is driven to a rich condition, and the nitrates decompose, releasing the $NO_x$ which reacts with the reductants in the rich exhaust [e.g., HC, CO, and hydrogen ($H_2$)] to produce $N_2$ and carbon dioxide ($CO_2$) and/or $H_2O$. Another promising aftertreatment system for lean $NO_x$ control combines the LNT and SCR technologies, where $NH_3$ produced by the LNT during the rich periods is stored on the downstream SCR catalyst and used to reduce $NO_x$ that slips past the LNT during the lean periods [3-14]. Theis et al. [14] showed that a 4-zoned or 8-zoned catalyst system with alternating segments of LNT and SCR catalyst provided similar $NO_x$ conversion and reduced $NH_3$ slip during lean/rich cycling relative to a conventional 2-zone LNT/SCR configuration, where a single LNT catalyst is placed upstream of a single SCR catalyst. The lower $NH_3$ slip was attributed to an improved balance of $NO_x$ and $NH_3$ in the SCR zones of the multi-zone configurations. The multi-zoned approach also reduced the $N_2O$ formation and HC slip.

A fourth lean $NO_x$ aftertreatment system is the passive TWC+SCR approach [15]. Here the TWC generates $NH_3$ from the feedgas $NO_x$ during rich periods, and the $NH_3$ is stored on the downstream SCR catalyst. The SCR catalyst then uses the stored $NH_3$ to reduce $NO_x$ during lean operation.
One issue with the LNT, passive SCR, or LNT/SCR approach is that the rich periods used to purge the LNT and/or to create $NH_3$ for the SCR catalyst reduce the fuel economy by 1 to 2%. Nevertheless, the overall fuel economy improvement from lean/rich cycling is significantly positive.

In 2011, Ford began a 4.5-year demonstration project under joint funding with the DOE to achieve a 25% improvement in fuel economy while achieving Tier 2, Bin 2 emission levels (later modified to Tier 3, Bin 30 emission levels) on a 2.3 L gasoline turbocharged direct-injection (GTDI) engine in a Ford Taurus [16]. For assessing the fuel economy improvement, the baseline vehicle was a Ford Taurus powered by a 3.5 L port-fuel-injected (PFI) naturally-aspirated (NA) engine with independent variable cam timing (iVCT). Several engine technologies were investigated to achieve the 25% improvement in fuel economy, including turbocharging, downsizing the engine displacement, the use of direct-injection, cooled EGR, and stop-start technology. As an optional action, lean operation during cruises was investigated. To provide $NO_x$ control during the lean periods, two passive approaches were investigated that did not require customer maintenance: the TWC+LNT/SCR system and the TWC+SCR system. This paper summarizes the work on the TWC+LNT/SCR system. A companion paper describes the work on the TWC+SCR approach [17]. For both systems, high emphasis was placed on achieving the HC targets as well as the $NO_x$ targets due to the very low emissions levels allowed for the Tier 2, Bin 2 standards.

## Experimental

### *Catalysts*

The TWC, LNT, and SCR catalyst samples used in this work were core samples with a length and diameter of 2.54 cm that were extracted from full-size cordierite bricks. It was assumed that the washcoat loadings and PGM distributions within the catalyst bricks were uniform. Therefore, the brick locations from where the cores were collected were not recorded.

### *TWC Samples*

Several TWC technologies were used containing various levels of oxygen storage capacity (OSC) and platinum group metal (PGM) loadings that are listed in Table 1. The high OSC catalyst was a production formulation containing 96 grams per cubic foot (gpcf) Pd and 4 gpcf Rh (i.e., 1.57 g/L Pd and 0.066 g/L Rh) on a 900 cell per square inch (CPSI) substrate with 2 mil walls (i.e., 900/2). This formulation will be referred to as "hi-OSC-100" in this paper. Samples of another production catalyst with a moderate level of OSC on 400/4 substrates were used with two PGM loadings. One contained 38 gpcf Pd and 2 gpcf Rh (0.62 g/L Pd and 0.033 Rh), while the other contained 196 gpcf Pd and 4 gpcf Rh (i.e., 3.21 g/L Pd and 0.066 g/L Rh). These catalysts will be referred to "mod-OSC-40" and "mod-OSC-200", respectively. Finally, samples of two non-OSC formulations were used containing either 116 gpcf (1.90 g/L) Pd or 200 gpcf (3.28 g/L) Pd on 400/4 substrates. These will be referred to as "no-OSC-116" and "no-OSC-200", respectively.

### *TWC Aging*

Table 1 also lists the durability schedules used to age the TWC samples prior to testing. The rich/stoich/lean schedule was a proprietary schedule that cycled between rich, stoichiometric, and lean conditions every 60 seconds. The inlet temperature was 800°C, and the maximum bed temperature was 960°C. A full size converter with the hi-OSC-100 formulation was aged on the schedule to the equivalent of 120K miles on an engine/dynamometer, and a 1" by 1" core sample was extracted from the brick for laboratory testing. For the samples aged on the pulse-flame combustion reactor (a.k.a. pulsator) [18], core samples of 1" diameter were aged with the same rich/stoich/lean schedule at an inlet temperature of 800°C for 50 hours. The no-OSC-116 catalyst was degreened on the flow reactor for 2 hours at 800°C under lean conditions with 10% $O_2$, 5% $H_2O$, 5% $CO_2$, and the balance $N_2$.

**Table 1. TWC Catalyst Formulations, PGM Loadings, Aging Schedules**

| Catalyst Designation | OSC Level | PGM loading (gpcf Pt/Pd/Rh) | Aging Protocol |
|---|---|---|---|
| Hi-OSC-100 | High | 0/96/4 | Engine - rich/stoich/lean 120K miles equiv |
| Mod-OSC-40 | Moderate | 0/38/2 | Pulsator – rich/stoich/lean 800°C inlet 50 hours |
| Mod-OSC-200 | Moderate | 0/196/4 | Pulsator– rich/stoich/lean 800°C inlet 50 hours |
| No-OSC-200 | None | 0/200/0 | Pulsator – rich/stoich/lean 800°C inlet 50 hours |
| No-OSC-116 | None | 0/116/0 | Flow reactor - lean 800°C inlet 2 hours |

### *LNT & SCR Samples*

The LNT used in this work was a formulation containing barium and cerium and catalyzed with 85 gpcf of PGM (73/7.5/4.5 gpcf Pt/Pd/Rh) on 400/6 substrates. The SCR catalyst was a copper/chabazite formulation on 400/4 substrates. This SCR formulation is used in production on the Ford medium duty diesel truck. No further details about the LNT or SCR formulations will be provided out of respect for the supplier.

### *LNT & SCR Aging*

Some of the early work for this project was performed with LNT and SCR samples that had been previously aged on the flow reactor for another project [14], where a 1" long LNT core sample was placed ahead of a 1" long SCR core sample in the flow reactor. One set was aged for 25 hours at an inlet temperature of 800°C with continuously lean exhaust (10% $O_2$, 5% $CO_2$, 5% $H_2O$, balance $N_2$), while a second set was aged for 20 hours under the same conditions. The aging temperature of 800°C was intended to expose the LNTs and SCR catalysts to the maximum temperature that could be expected in the U/B location and was not intended to represent a certain mileage or full-useful-life (FUL) conditions. After aging, both LNT samples and the SCR catalyst from set 2 were cut into four 0.25" (0.64 cm) long pieces so various configurations of LNT and SCR catalyst could be investigated during the performance evaluations. Later experiments for this project were performed with multi-zone LNT/SCR catalyst systems that were aged downstream of a TWC while the TWC samples were aging on the pulsator with the rich/stoich/lean cycle as described above. Here six 0.5" core samples with alternating LNT and SCR zones were aged with inlet temperatures of 600, 700, or 800°C to determine if the LNT/SCR performance could be improved with a reduced aging temperature. For all of the LNT and SCR samples, small holes were drilled axially through the pieces so that a 1.6 mm thermocouple could be inserted through the samples for measuring the inlet temperature or the catalyst bed temperature during the aging and performance evaluations.

### *Performance Evaluations*

The flow reactor used for the performance evaluations contained 2 ovens, as shown in Figure 1. The TWC was placed toward the rear of the first oven, and the LNT or LNT/SCR system was placed toward the rear of the second oven. The 2 ovens were operated at different temperatures to represent the close-coupled position and the underbody position. The total length of the TWC was usually 1", and

it consisted of either one catalyst formulation or two 0.5" pieces with different catalyst formulations butted together. When one TWC washcoat formulation was used, the PGM loading was uniform; when two different washcoat formulations were used, the total PGM loading was either uniform (e.g., 200 gpcf/200 gpcf) or zoned (e.g., 200 gpcf/40 gpcf). The total length of the LNT or LNT/SCR system was varied during the different experiments. The total flow rate was maintained at 6.4 L/min for all experiments, resulting in a space velocity of 30,000 $hr^{-1}$ for a 1" long catalyst. While it is recognized that an U/B TWC would be needed on the vehicle to supplement the CC TWC and satisfy the Tier 2, Bin 2 emission standards during the FTP and US06 test cycles, the laboratory testing neglected the U/B TWC and involved samples representing only the CC TWC and U/B LNT/SCR catalyst.

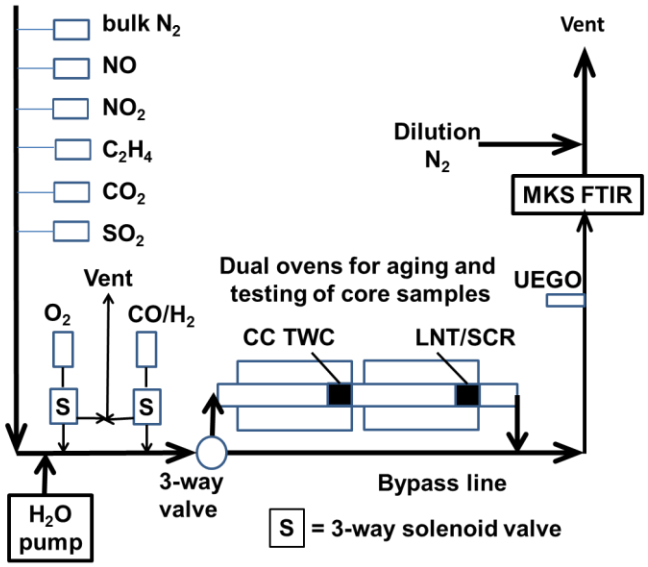


Figure. 1. Experimental apparatus

Most tests consisted of alternating lean and rich periods (e.g., 60 seconds lean and 5 seconds rich, referred to as a "60/5" cycle). Tests where the lean duration was held constant and the rich purge time was varied are referred to as "purge tests" in this paper. Mass flow controllers were used to control the flow rates of the different gases, and two electronically-controlled three-way solenoid valves were used to switch between the lean condition (i.e., $O_2$) and the rich condition (i.e., $CO/H_2$). The oxygen level was always 10% during the lean periods ($\lambda$=A/F ratio/14.6=2.0) and 0% during the rich periods. The $H_2O$ and $CO_2$ concentrations were always 5% during the lean and rich periods. Many of the experiments were performed with 2500 ppm $C_2H_4$ (i.e., 5000 ppm on a C1 basis) during both the lean and rich periods, although some early tests included the $C_2H_4$ only during the rich periods. For most tests, different NO levels were used during the lean and rich periods. While these NO levels were varied throughout the project depending on the type of test, the NO concentration during the lean periods was usually 200 ppm NO. During the rich periods, the NO level was increased to either 500 or 1000 ppm to more accurately simulate engine operation. The CO concentration during the rich periods was set at 4.0, 2.5, 1.5, or 0.5% to provide rich lambdas of 0.81, 0.86, 0.91, or 0.95 when 2500 ppm $C_2H_4$ was used; the $H_2$ level was always 1/3 the CO level. To provide a rich lambda of 0.99, the CO and $H_2$ levels were maintained at 0.5% and 0.17% while the $C_2H_4$ concentration was lowered to 800 ppm. Due to the many different catalyst configurations and test conditions used during this project, the specific details of each experiment will be provided in the section where the results of that experiment are discussed.

For all tests, the average concentrations of the feedgas $NO_x$, HC, and CO were determined over several lean/rich cycles while the exhaust was bypassed around the reactor. With the exhaust flowing through the catalyst bed, testing was continued until the performance of the catalyst stabilized. The concentrations of the $NO_x$, HC, and CO at the reactor exit were then averaged over several lean/rich cycles. The average HC, CO, and $NO_x$ conversions were calculated from the average feedgas concentrations and the average concentrations in the reactor exit according to:

$$\text{Ave \% conversion} = 100*[1-(\text{ave exit level})/(\text{ave FG level})] \quad (1)$$

The average yield of $NH_3$ was calculated as a percentage of the feedgas NO level according to:

$$\text{Ave \% } NH_3 \text{ yield} = 100*[(\text{ave } NH_3 \text{ level})/\text{ave FG NO level}] \quad (2)$$

The average yield of $N_2O$ was calculated as a percentage of the feedgas NO level from:

$$\text{Ave \% } N_2O \text{ yield} = 100*[2*(\text{ave } N_2O \text{ level})/\text{ave FG NO level}] \quad (3)$$

where the factor of 2 accounts for the fact that two molecules of NO are required to produce one molecule of $N_2O$.

The feedgas and the exhaust from the reactor were analyzed with a 1 Hz MKS Fourier transform infrared (FTIR) analyzer equipped with a sample line heated to 191°C.

## Results and Discussion

### *Emission Budgeting*

Emission budgeting was performed to determine the maximum allowable levels of HC, CO, and $NO_x$ during lean/rich cycling on cruises that still allowed the Tier 2, Bin 2 standards to be met. The limits for HC, CO, and $NO_x$ on the FTP are 10 mg/mile, 2.1 g/mile, and 20 mg/mile, respectively, after 120,000 miles of driving. Estimates were made for the emissions during the cold-start portion of the FTP and during warmed-up operation at stoichiometry. When possible, data from other vehicles were used to approximate these levels. Table 2 shows these estimates along with the desired engineering tolerances for HC, CO, and $NO_x$ during the FTP. This left target emission levels during lean/rich cycling of 1 mg/mile, 1.3 gm/mile, and 5 mg/mile for HC, CO, and $NO_x$, respectively. The particulate matter standard for Tier 2, Bin 2 is 10 mg/mile; it was assumed that the engine-out level of PM would satisfy this limit, so a gasoline particulate filter (GPF) was not considered for this project.

Table 2. Emission Budgeting to Satisfy Tier 2, Bin 2 Emission Standards

| Tier 2, Bin 2 Standards | HC | NOx | CO |
|---|---|---|---|
| Emission Requirement | 10 mg/mile | 20 mg/mile | 2.1 g/mile |
| Engineering tolerance | 1.7 | 5 | 0.5 |
| Cold-start emissions | ~7 | 7 | 0.3 |
| Stoichiometric emissions (Post-lightoff) | ~0 | 3 | ~0 |
| Lean/rich cycling emissions | 1 | 5 | 1.3 |

### *Multi-Zone LNT/SCR Design*

Previously, it was shown that a LNT/SCR system provided similar $NO_x$ conversion during lean/rich cycling as an all-LNT with the same total volume [14]. Since there is no PGM in the SCR catalyst, the LNT/SCR system uses 50% less PGM than the all-LNT approach and is therefore significantly lower in cost. In addition, it was shown that 4 or 8 alternating zones of LNT and SCR catalyst provided similar $NO_x$ conversion and lower $NH_3$ slip relative to a sequential or 2-zone LNT/SCR design, where a single LNT is followed by a single SCR catalyst. This was attributed to a better balance of $NO_x$ and $NH_3$ within the SCR zones of the multi-zone systems, resulting in better consumption of the stored $NH_3$. Also, the multi-zone configurations produced less $N_2O$ than the all-LNT or 2-zone LNT/SCR designs. This was attributed to the fact that a significant portion of the $NO_x$ conversion occurred in the SCR zones of the multi-zone designs, and the copper/zeolite SCR catalyst is less prone for generating $N_2O$ than the platinum-containing LNT. The 4-zone and 8-zone LNT/SCR designs produced similar $NH_3$ yields, so the 4-zone design was initially selected for the DOE project because it would be easier to manufacture in production.

### *LNT/SCR Volume Optimization*

An experiment was performed to determine the minimum volume of LNT/SCR required to satisfy the $NO_x$ slip target of 5 mg/mile. The hi-OSC-100 TWC sample aged on an engine/dynamometer was placed in the first oven, heated to 500°C to represent the close-coupled location, and tested alone using a 60 s lean/10 s rich cycle (i.e., 60/10 test). The rich lambda was 0.86, the $C_2H_4$ level was 2500 ppm during lean and rich operation, and the NO levels were 200 ppm lean and 500 ppm rich. A LNT/SCR catalyst was installed in a second oven downstream and operated at 300°C to simulate the underbody location, and similar 60/10 tests were performed. To vary the volume of the LNT/SCR catalyst, the LNT/SCR contained from one up to six 0.50" long zones with alternating LNT and SCR catalysts. The exhaust flow rate was held at 6.4 L/min for these tests, so the space velocity (accounting for both the TWC and the LNT/SCR volumes) ranged from 30K $hr^{-1}$ for the 1" TWC by itself down to 7.5K $hr^{-1}$ for the 1" TWC + 3" LNT/SCR system.

It was desired to convert the $NO_x$ concentrations from the reactor (measured in ppm) into the weighted mg/mile $NO_x$ during lean/rich cycling on the intended DOE vehicle in order to allow easier comparison with the 5.0 mg/mi target from Table 2. Estimates were made for the total weighted exhaust flow on the vehicle during lean operation on the FTP. Using the mileage for Bags 1 and 2 of the FTP (i.e., 7.5 miles) and assuming that all of the $NO_x$ is emitted as $NO_2$ (46 g/mole) per EPA protocol, the ppm $NO_x$ from the reactor and the lean exhaust flow from the vehicle were used to project the weighted mg/mile $NO_x$ during lean/rich cycling on the vehicle. Figure 2 is a semi-log plot showing the weighted mg/mile $NO_x$ as a function of the total catalyst length, accounting for the TWC and LNT/SCR system. The TWC alone reduced the feedgas $NO_x$ of 230 mg/mile to 194 mg/mile, thereby providing approximately 16% $NO_x$ conversion during the 60/10 cycle. This was attributed to nearly 100% $NO_x$ conversion during the rich periods and essentially no $NO_x$ conversion during the lean periods. After the first LNT/SCR zone, the $NO_x$ slip was reduced to 26.0 mg/mile, corresponding to an overall $NO_x$ conversion of 88.7%. The second LNT/SCR zone further reduced the $NO_x$ to 17.4 mg/mile with an overall $NO_x$ conversion of 92.4%, and the third LNT/SCR zone reduced the $NO_x$ slip to 4.4 mg/mile, corresponding to an overall $NO_x$ conversion of 98.1%. Thus, the $NO_x$ slip target of 5 mg/mile was successfully met on the lab reactor. However, a relatively large volume of LNT/SCR was required, resulting in the relatively low space velocity of 7.5K $hr^{-1}$. Using the average flow rate during lean operation on the vehicle, this translated into a total catalyst volume of 6.8 L on the intended application. Assuming a 1.8 L TWC, this suggested a 5.0 L LNT/SCR would be needed to meet the target $NO_x$ level. This testing was performed without an U/B TWC; however, since an U/B TWC would provide little or no $NO_x$ conversion during lean operation, it was assumed that the LNT/SCR volume would still need to be 5.0 L.

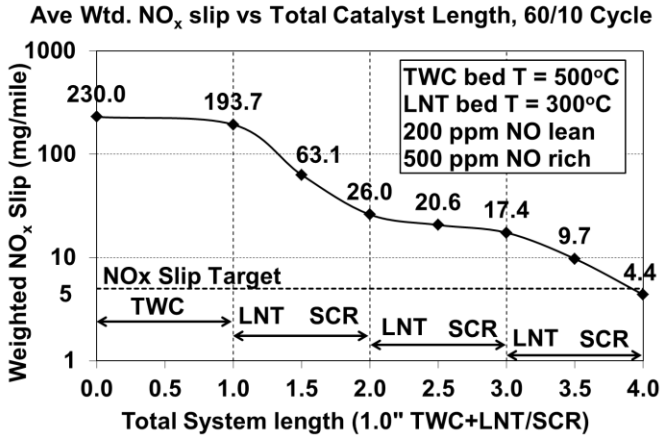


**Figure 2**. Semilog plot of weighted $NO_x$ slip vs total catalyst length for 1" hi-OSC-100 TWC + (1 to 6)x0.5" LNT/SCR system. 60/10 cycle, 200 ppm NO lean, 500 ppm NO rich, 500°C in TWC, 300°C in LNT/SCR, 0.86 rich λ.

### *TWC and LNT/SCR Temperature Optimization*

The temperatures of the TWC and LNT/SCR catalysts during lean/rich cycling are critical for achieving the emission targets. Therefore, tests were performed to determine the optimum temperature ranges for these catalysts. The effect of the TWC temperature on the performance of the TWC+LNT/SCR system was assessed by varying the inlet temperature of the 1" hi-OSC-100 TWC from 400°C to 525°C while holding the bed temperature of the 6x0.5" LNT/SCR system constant at 300°C. The rich lambda again was 0.86, and the feedgas $NO_x$ concentrations were 200 ppm lean and 500 ppm rich. 60 second lean periods were alternated with rich periods of different duration ranging from 6 or 7 seconds up to 15 seconds. Figure 3 shows the weighted mg/mile HC as a function of the weighted mg/mile $NO_x$ for TWC inlet temperatures of 400, 425, 450, 475, 500, and 525°C. Both the HC and $NO_x$ targets could be satisfied when the TWC inlet temperature was 450°C and above. With TWC temperatures of 425°C and 400°C, the HC emissions exceeded the target. This was primarily due to insufficient steam reforming activity [i.e., $CH_2 + H_2O = CO + 2H_2$] during the rich purges at these temperatures. Figure 3 suggests that temperatures of 450°C and above are required to achieve sufficient steam reforming activity for controlling the HC emissions during rich operation.

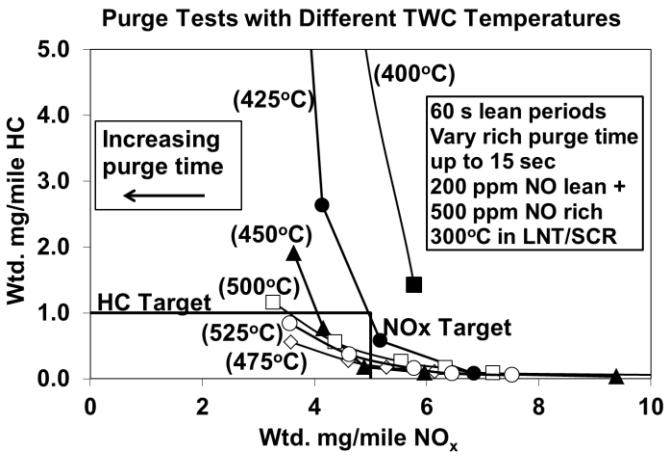


**Figure 3**. Weighted HC slip versus weighted $NO_x$ slip for 1" hi-OSC-100 TWC + 6x0.5" LNT/SCR system with various TWC inlet temperatures (in parentheses). 60 s lean and various rich times, 200 ppm NO lean, 500 ppm NO rich, 300°C in LNT/SCR system, 0.86 rich λ.

Similarly, the effect of the LNT/SCR temperature on the emission performance of the catalyst system was assessed. The inlet temperature of the TWC was maintained at 500°C, while purge tests were performed with LNT/SCR bed temperatures of 200, 225, 250, 275, 300, 325, and 350°C. Figure 4 shows that both the $NO_x$ and HC targets could be satisfied when the LNT/SCR was between 225°C and 350°C. The system was further evaluated over a broad range of TWC and LNT/SCR temperatures. Figure 5 displays the TWC inlet temperatures and LNT/SCR bed temperatures where both the HC and $NO_x$ satisfied the target values from Table 2. Figure 5 shows that the TWC needs to be at a minimum of 450°C to provide adequate steam reforming of the HC during rich operation, while the LNT/SCR generally needs to be between 250°C and 350°C to provide the required $NO_x$ conversion activity during lean/rich cycling.

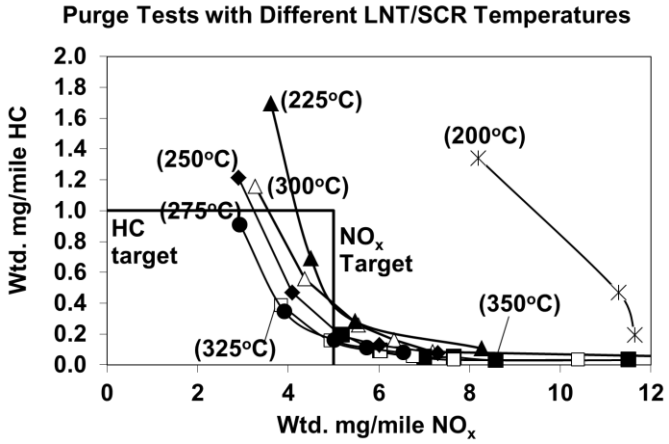


**Figure 4**. Weighted HC slip versus weighted $NO_x$ slip for 1" hi-OSC-100 TWC + 6x0.5" LNT/SCR system with various LNT/SCR temperatures (in parentheses). 60 s lean and various rich times, 200 ppm NO lean, 500 ppm NO rich, TWC inlet temperature of 500°C, 0.86 rich λ.

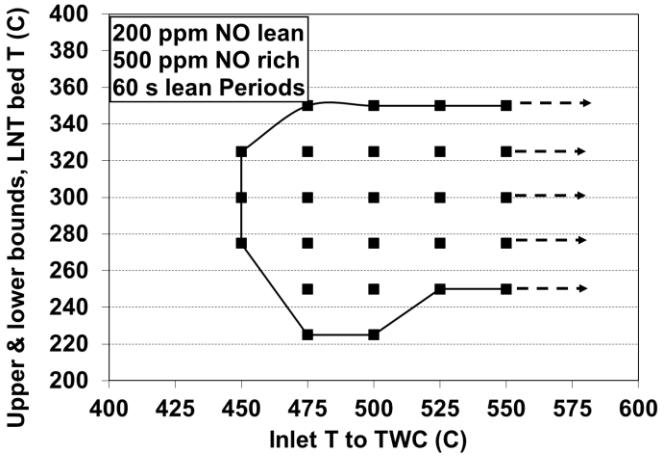


**Figure 5**. Inlet temperatures for 1" hi-OSC-100 TWC and bed temperatures for 6x0.5" LNT/SCR system where both the projected HC and $NO_x$ slips satisfied the target levels of 1.0 mg/mile and 5.0 mg/mile.

## *Catalyst Formulation Tradeoffs*

It is well known that modern three-way catalysts typically contain high levels of ceria or a mixture of ceria and zirconia to promote oxygen storage and release when the A/F ratio of the engine is oscillating between lean and rich conditions during normal closed-loop control about stoichiometry. The amount of oxygen that the catalyst can store is referred to as its oxygen storage capacity (OSC). High OSC in the TWC is particularly beneficial during stoichiometric operation at high loads, where the exhaust flow rates are high. The ceria also promotes $NO_x$ light-off during a cold start, and it can promote catalyst durability by maintaining the dispersion of the PGM [19]. This is particularly true for Pt and Pd. In addition, the ceria is critical for the steam reforming reaction, which minimizes the HC slip during the rich purges [20]. Finally, the OSC of the TWC is important for satisfying the catalyst monitoring requirements for OBD II. However, a high level of ceria in the TWC requires longer purges during lean/rich cycling, which increases the fuel economy penalty associated with the rich purges. Thus, the OSC level of the TWC needs to be optimized for lean-burn applications.

Tests were performed to examine the effects of the OSC in the TWC on the $NO_x$ slip during lean/rich cycling. Three 1" long three-way catalysts with different levels of OSC (i.e., hi-OSC-100, mod-OSC-40, and no-OSC-116) were tested upstream of a 7x0.5" zoned SCR/LNT/SCR system, where an additional 0.5" SCR zone was placed in front of the 6x0.5" LNT/SCR system (the reasons for this will be discussed later). During these purge tests, 60 second lean periods were alternated with rich periods of various duration. The TWC and SCR/LNT/SCR system were operated at 500°C and 300°C, respectively, and the feedgas NO level was 200 ppm lean and 500 ppm rich. Figure 6 shows the weighted $NO_x$ slip as a function of the rich purge time for the 3 levels of OSC in the TWC. For a given purge time, the $NO_x$ slip decreased as the OSC of the TWC decreased, attributable to improved utilization of the rich reductants for purging the LNT. Thus, a lower OSC in the TWC reduced the purge times required during lean/rich cycling. However, this must be balanced against the need for OSC in the TWC for $NO_x$ light-off, good 3-way conversion during stoichiometric operation at high loads, good steam reforming activity during rich operation, catalyst durability, and diagnostic capabilities.

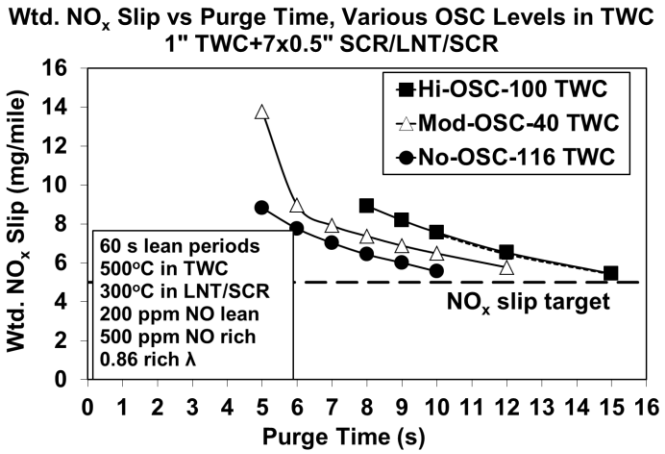


**Figure 6**. Weighted $NO_x$ slip vs rich purge time for 1" TWC + 7x0.5" SCR/LNT/SCR. Vary OSC in TWC. 500°C in TWC, 300°C in LNT/SCR.

Similar to the TWC, LNT formulations typically contain high levels of ceria. The ceria increases the $NO_x$ storage capacity of the LNT at low temperatures, improves catalyst durability by maintaining the Pt dispersion, and improves the tolerance to sulfur poisoning [21]. Finally, the ceria promotes the water-gas-shift reaction [i.e., $CO+H_2O=CO_2+H_2$] during rich desulfations, and the additional $H_2$ improves the effectiveness of the desulfations. However, the higher OSC in the LNT requires longer purges, which again increases the fuel economy penalty associated with the rich purge periods.

To assess the effects of a lower OSC in the LNT, samples with a 50% reduction in cerium content were received from the supplier. Core samples of this LNT were degreened for 32 hours with an inlet temperature of 600°C (approximately 680°C maximum bed temperature). Figure 7 displays the weighted $NO_x$ slip of the baseline 1" TWC + 7x0.5" SCR/LNT/SCR system, which included the hi-OSC-100 TWC and the 7x0.5" SCR/LNT/SCR system with high OSC in the LNT. The 1" TWC and the 7x0.5" SCR/LNT/SCR system were operated at 500°C and 350°C, respectively, during the purge test. A purge time of 15 s was required for the $NO_x$ slip of this system to approach the target level of 5 mg/mile. It is noted that most of these LNT & SCR catalyst samples had been evaluated under lean/rich cycling conditions for several months following their initial 20 to 25 hours of lean aging at 800°C, and as such this system was considered to represent medium to high mileage conditions. The 7x0.5" multi-zone SCR/LNT/SCR system was then replaced with the mildly-aged 1" LNT with 50% less cerium (i.e., without the SCR catalyst) and evaluated on the purge test. This system satisfied the $NO_x$ slip target with only 7 second purges compared to 15 seconds with the baseline system, reducing the purge fuel requirements by over 50%. Some of this improvement could be attributed to the reduced degree of aging as well as the reduced volume of LNT (i.e., 1.0" vs 1.5" length), but some of the reduction in purge time was attributed to the lower OSC level in the LNT. The hi-OSC-100 TWC was then replaced with the 1" no-OSC-116 TWC and evaluated with the 1" reduced-OSC LNT. The purge time required to satisfy the target was reduced further from 7 s to 6 s.

While the purge times were reduced with the lower OSC level in the LNT, Figure 7 also shows that the $NH_3$ yields from the reduced-OSC LNT were quite high because there was no downstream SCR to adsorb the $NH_3$, resulting in 25 to 40% $NH_3$ yields with the purge times required to achieve the target $NO_x$ level. Therefore, the 1" reduced-OSC LNT was cut into two pieces and combined with two 0.5" SCR zones to produce a 4x0.5" LNT/SCR system with reduced OSC. This reduced-OSC LNT/SCR system was evaluated with the 1" no-OSC-116 TWC. While not shown here, the $NO_x$ slip target was met with 5.5 s purges, nearly 1/3 of the 15 s purge time required for the baseline system. Also, the $NH_3$ yield for this 1" non-OSC TWC + reduced-OSC 4x0.5" LNT/SCR system was reduced to only a few percent.

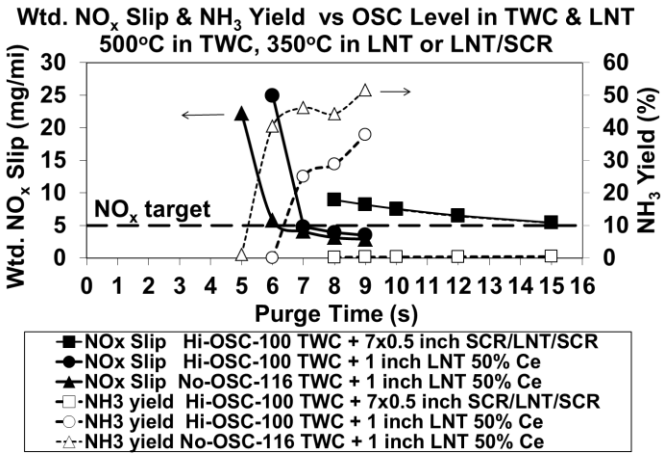


**Figure 7**. Weighted $NO_x$ slip and $NH_3$ yield vs rich purge time for 1" hi-OSC-100 TWC + 7x0.5" SCR/LNT/SCR, 1" hi-OSC-100 TWC + 1" LNT w/ 50% Ce, and 1" no-OSC-116 TWC + 1" LNT w/ 50% Ce. 500°C in TWC, 350°C in LNT or LNT/SCR, 0.86 rich λ.

## *$N_2O$ Slip*

$N_2O$ emissions have emerged as an important consideration for aftertreatment systems because of the new greenhouse gas regulations being implemented. Therefore, efforts were made to minimize the production of $N_2O$ from the proposed aftertreatment system. Three factors were identified as having large influence on the $N_2O$ generation: the LNT/SCR catalyst configuration, the purge strategy, and the LNT/SCR temperature. In Figure 6, it was mentioned that an extra 0.5" SCR zone was placed in front of the 6x0.5" multi-zone LNT/SCR system. This front SCR zone was intended to capture $NH_3$ that was produced by the TWC during the early stages of a purge and prevent that $NH_3$ from being oxidized to NO or $N_2O$ over the first LNT zone, which could still be in an oxidized state at that point in time. The front SCR zone could also use the stored $NH_3$ to reduce $NO_x$ during subsequent lean periods. Therefore, the first zone of the multi-zone LNT/SCR system should always be an SCR catalyst.

The purge strategy can also affect the generation of $N_2O$, particularly with the multi-zone LNT/SCR designs. If the purges are excessively long, the SCR zones can become saturated with $NH_3$. During a lean period, some of the $NH_3$ can desorb from the SCR catalyst if the temperature increases, and a downstream LNT zone can oxidize that $NH_3$ to $N_2O$. Thus, it is important to optimize the duration of the rich purges to avoid saturating the SCR zones with $NH_3$. This also would be beneficial for the fuel consumption, as excessively long purges waste fuel and degrade the fuel economy.

Finally, the temperature of the LNT/SCR has a strong influence on the $N_2O$ generation. To demonstrate, three catalyst systems were evaluated during lean/rich cycling tests where the TWC was operated at 500°C and the temperature of the LNT/SCR was varied. The first two systems consisted of the 1" hi-OSC-100 TWC or the 1" no-OSC-116 TWC with the 1" LNT with reduced OSC; the third system consisted of the 1" no-OSC-116 TWC with the 4x0.5" LNT/SCR system with reduced OSC. Figure 8 shows the $N_2O$ yield [i.e., 2x100%*(average $N_2O$)/(FG NO)] as a function of the LNT temperature. The $N_2O$ yield decreased significantly as the LNT

temperature increased, and the yield was less than 2% at temperatures above 375°C for all three systems. However, Figure 5 showed that the LNT/SCR needed to operate between 250 and 350°C to achieve the $NO_x$ slip targets. Figures 5 and 8 together suggest that the LNT/SCR needs to operate between 300°C and 350°C in order to meet the $NO_x$ slip targets while simultaneously minimizing the $N_2O$ yield. While not shown here, these higher temperatures also minimized the slip of $NH_3$.

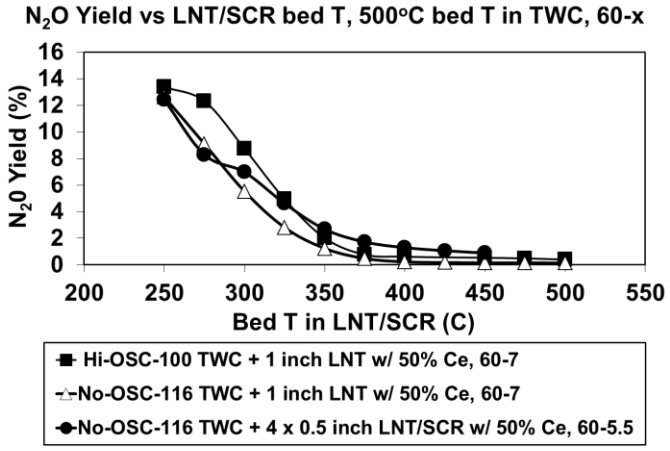


**Figure 8**. $N_2O$ yield for 3 catalysts systems as a function of LNT/SCR bed temperature during purge tests. Inlet temperature of 500°C for 1" TWC, 0.86 rich λ.

## *HC Slip*

One of the greatest challenges for the LNT/SCR system is the minimization of the HC slip due to the very low levels allowed (i.e., target level of 1.0 mg/mile HC vs 5.0 mg/mile $NO_x$ during lean/rich cycling) and the fact that rich operation is required to purge the LNT and generate $NH_3$ for the SCR catalyst. Thus, it is critical that the TWC has effective steam reforming capability during the rich purges. Figure 5 suggested that the TWC needed to operate at a minimum temperature of 450°C for effective steam reforming. Additional testing was performed to further explore the effect of temperature on the steam reforming capability of the TWC.

Purge tests were performed on the 1" hi-OSC-100 TWC coupled with the high-OSC 6x0.5" multi-zone LNT/SCR system, where the lean periods were 60 seconds in duration. The inlet temperature of the TWC was varied from 450°C to 550°C, while the bed temperature of the LNT/SCR was maintained at 275°C. The NO level was 200 ppm lean and 500 ppm rich. For these early tests, 2500 ppm of $C_2H_4$ was injected only during the rich periods. Figure 9 displays the weighted HC slip as a function of the rich purge time for these tests. The HC slip was quite sensitive to the purge time when the TWC was operating at 450°C and exceeded the HC slip target with purges of 8 seconds or more. However, the HC slip was much more robust to the purge time when the TWC operated at 475°C, and the lowest HC slip was obtained with a TWC temperature between 500°C and 525°C. Therefore, it was concluded that the minimum temperature of the TWC needed to be at least 500°C to maximize its steam reforming capability.

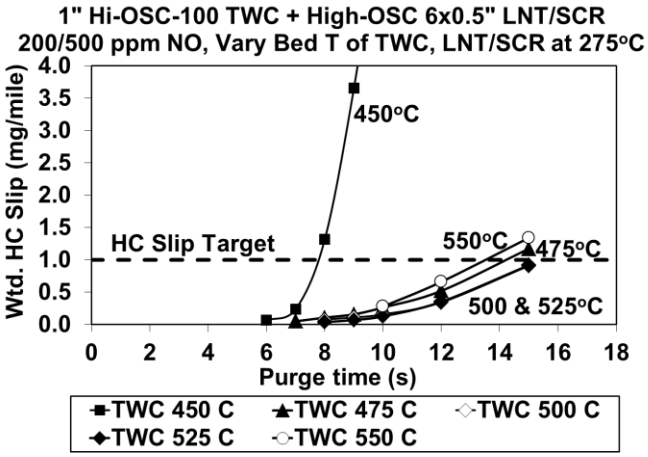


**Figure 9**. Weighted HC slip on purge tests with 1" hi-OSC-100 TWC + 6x0.5" LNT/SCR system. 200 ppm NO lean, 500 ppm NO rich, 2500 ppm $C_2H_4$ injected during rich periods. Vary bed T in TWC, 275°C in LNT/SCR.

The majority of the HC conversion is expected to occur within the CC TWC (and U/B TWC) due to the higher temperatures in these catalysts. However, it was found that the LNT/SCR converter can provide a small contribution to the overall HC conversion. Purge tests were performed where the inlet temperature to the CC TWC was maintained at 500°C and the bed temperature of the LNT/SCR was varied from 225°C to 350°C. Figure 10 shows the weighted HC slip as a function of the rich purge time for the different LNT/SCR temperatures. When the LNT/SCR was at 250°C or below, the HC slip was above the target of 1.0 mg/mile with 15 s purges. However, when the LNT/SCR was operated at 275°C or 300°C, the HC slip was very near the target of 1.0 mg/mile with 15 s purges. When the LNT/SCR was operated at 325°C or 350°C, the HC slip with 15 second purges was under 0.50 mg/mile, which is comfortably below the HC slip target. So in addition to lowering the $N_2O$ and $NH_3$ emissions, operating the LNT/SCR at a bed temperature of 325 to 350°C helps minimize the HC slip during the rich purges.

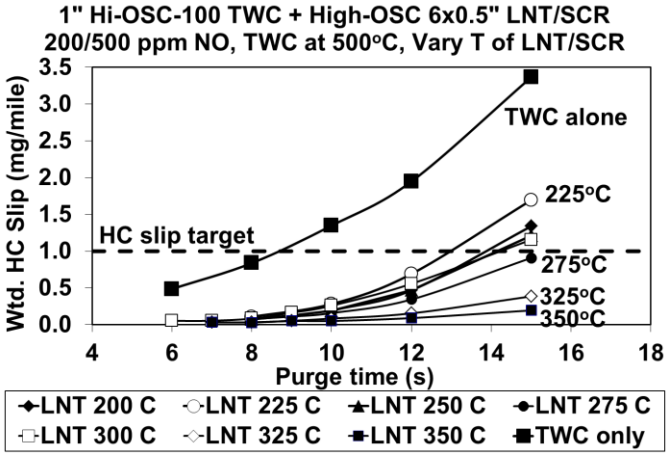


**Figure 10.** Weighted HC slip on purge tests for 1" hi-OSC-100 TWC + 6x0.5" LNT/SCR system. 200 ppm NO lean, 500 ppm NO rich. 2500 ppm $C_2H_4$ injected during rich periods. 500°C in TWC, vary bed T in LNT/SCR.

## *Exhaust System Modeling*

It has been shown that the LNT/SCR needs to operate between 300°C and 350°C to satisfy the $NO_x$ slip target while minimizing the slip of $N_2O$, $NH_3$, and HC. Computer modeling was used to estimate the required distance between the U/B TWC and U/B LNT/SCR

converter to maintain the temperature of the LNT/SCR in this range during the FTP. Surrogate vehicle data and engine-dynamometer data were used to estimate the inlet temperature to the CC TWC during an FTP test. For this modeling exercise, the engine operated at a lean A/F ratio when possible and at stoichiometry the rest of the time. A pipe model was used to estimate the temperature drops between the CC TWC and U/B TWC and between the U/B TWC and LNT/SCR converter. The model indicated that a flex coupling and 44" of pipe between the U/B TWC and LNT/SCR converter were needed to keep the temperature of the LNT/SCR catalysts between 300 and 350°C for the majority of the test. Figure 11 shows the estimated temperatures of the CC TWC, U/B TWC, and U/B LNT/SCR catalysts over the FTP cycle with the 44" of pipe.

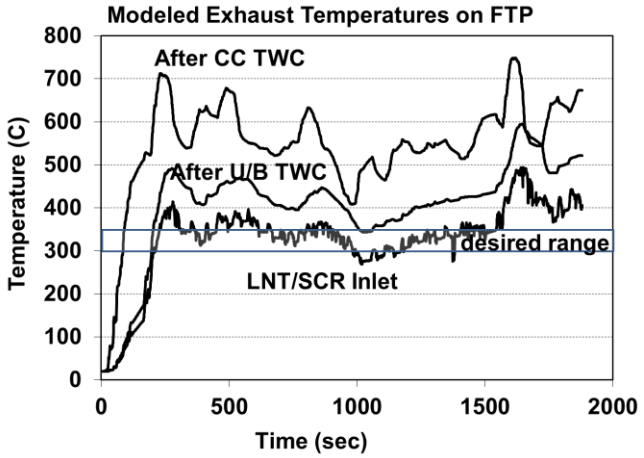


**Figure 11**. Projected temperatures for the CC TWC, U/B TWC, and U/B LNT/SCR catalysts during the FTP for intended DOE application.

## *Thermal Aging Studies*

A significant challenge with the LNT/SCR approach is the high cost of the LNT, due primarily to the high loadings of platinum that are typically used. To lower the cost of the aftertreatment system, it was desired to reduce the volume of the LNT. However, Figure 2 indicated that the $NO_x$ slip target was met only with the 6x0.5" LNT/SCR system, where half of the catalyst volume was LNT. Those specific catalyst pieces were originally aged for 20-25 hours at 800°C under lean conditions and then evaluated on lean/rich cycling tests over a period of several months. To maintain higher $NO_x$ storage capacity and allow a reduction in the volume of the LNT, the aging temperature of the LNT/SCR needed to be decreased.

Three systems consisting of a reduced-OSC 1" TWC + high-OSC 6x0.5" LNT/SCR were aged for 50 hours on a pulse-flame combustion reactor. For each system, the three-way catalyst was aged on the rich/stoich/lean schedule at 800°C inlet (960°C max bed temperature), while the 6x0.5" LNT/SCR system was aged downstream in a second oven at bed temperatures of 600, 700, or 800°C. Purge tests with 60 second lean periods were performed on a TWC consisting of 0.5" of no-OSC-200 combined with 0.5" of mod-OSC-200. Then the same reduced-OSC TWC was tested with the three 6x0.5" LNT/SCR systems. Figure 12 shows the feedgas level of $NO_x$ along with the weighted results for the TWC alone and the three TWC+6x0.5" LNT/SCR systems. The data are displayed in a semilog format so that the feedgas level of 230 mg/mile $NO_x$ and tailpipe levels as low as 0.10 mg/mile $NO_x$ can be easily observed on the same graph. All three TWC+6x0.5" LNT/SCR systems met the $NO_x$ slip target of 5.0 mg/mile easily. The system aged at 800°C met the target with the shortest purge times, attributable to a reduction of the OSC in the LNT as a result of the 800°C aging temperature.

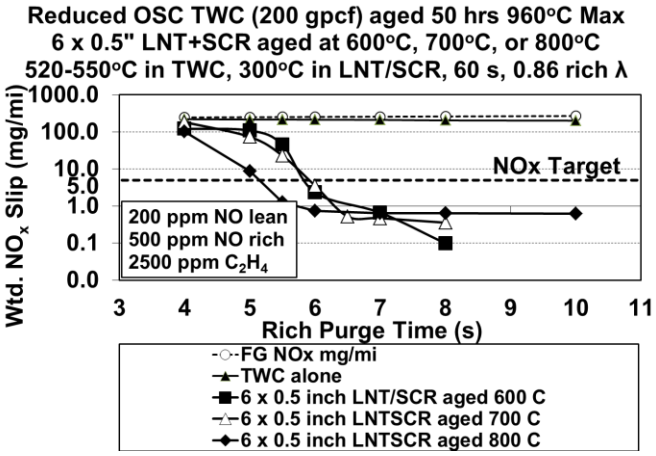


**Figure 12**. Weighted $NO_x$ slip for 0.5" no-OSC-200 TWC + 0.5" mod-OSC-200 TWC + 6x0.5" LNT/SCR systems on purge tests. TWC aged on rich/stoich/lean schedule for 50 hours 960°C max; LNT/SCR aged downstream at 600, 700, or 800°C.

To investigate the potential for decreasing the LNT volume, Figure 13 compares the weighted $NO_x$ slip for the same TWC and the first inch of the three aged LNT/SCR systems (i.e., 1" TWC+2x0.5" LNT/SCR) on purge tests with 60 second lean periods. For the shorter purge times (e.g., 5 seconds), the LNT/SCR system aged at 800°C resulted in slightly lower $NO_x$ slip than the systems aged at 600°C or 700°C. Again, this is attributed to a reduction of the OSC in the LNT as a result of the 800°C aging temperature. For purge times of 6 to 8 seconds, however, the 2x0.5" LNT/SCR aged at 800°C did not satisfy the $NO_x$ slip target, while the LNT/SCR systems aged at 700°C and 600°C met the target comfortably. This is because the LNT/SCR systems aged at 600°C and 700°C retained more $NO_x$ storage capacity than the system aged at 800°C. These data suggest that if the maximum temperature of the LNT/SCR can be limited to 700°C, the volume of LNT can be reduced, resulting in a significant cost reduction for the aftertreatment system. In the location required to maintain the LNT/SCR in its desired temperature range during the FTP (i.e., 44" from U/B TWC), a maximum aging temperature of 700°C was considered feasible.

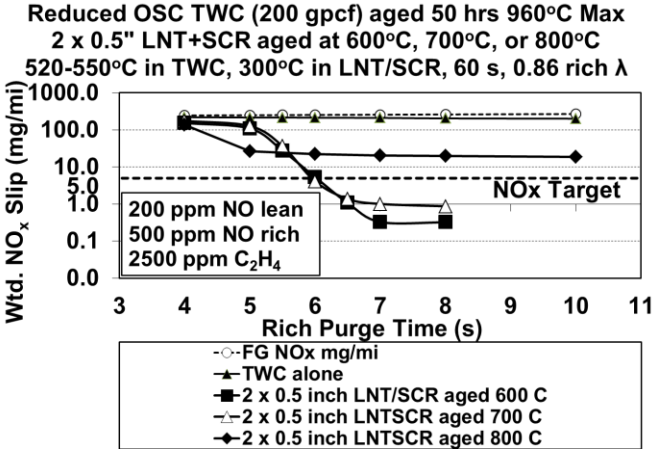


**Figure 13**. Weighted $NO_x$ slip for 0.5" no-OSC-200 TWC + 0.5" mod-OSC-200 TWC + 2x0.5" LNT/SCR systems on purge tests. TWC aged on rich/stoich/lean schedule for 50 hours 960°C max; LNT/SCR aged downstream at 600, 700, or 800°C.

## *Sulfur Poisoning*

One of the primary issues with the LNT is its susceptibility to $SO_2$ poisoning. $SO_2$ is formed from the combustion of sulfur-containing species in the fuel and oil and is therefore always present in the exhaust. The same materials that react with $NO_x$ to form nitrates (e.g., Ba, Cs, Ce) also react with $SO_2$ to form sulfates. These sulfates poison the $NO_x$ storage sites and prevent them from storing $NO_x$ until the sulfur can be removed. The process of removing sulfur from a poisoned LNT is referred to as desulfation. This typically requires several minutes of rich operation at temperatures on the order of 700°C. Under these conditions, the sulfates become unstable and decompose, releasing the sulfur and restoring the ability of the $NO_x$ storage sites to form nitrates again. The required frequency of these desulfations depends on the level of sulfur in the fuel, the emission levels that are desired, and the current $NO_x$ storage capacity of the LNT. A decrease in the $NO_x$ storage capacity due to a decrease in the LNT volume and/or thermal degradation requires more frequent desulfations to ensure compliance with the emission standards.

To demonstrate the effects of $SO_2$ poisoning, a 1" reduced-OSC TWC aged for 50 hours on the rich/stoich/lean schedule and the 6x0.5" high-OSC LNT/SCR system aged at 800°C were evaluated on a 60 second lean/6 second rich cycle as a function of time with 5 ppm $SO_2$ in the exhaust. This sulfur level in the exhaust represents a fuel sulfur level of approximately 150 ppm on a vehicle. This is higher than the typical sulfur levels in gasoline today and is significantly higher than the allowable levels in future fuels. As such, the use of 5 ppm $SO_2$ accelerated the poisoning of the catalyst. The TWC and LNT/SCR were operated at 520°C and 300°C, respectively. The feedgas NO concentration was 200 ppm lean and 1000 ppm rich. 2500 ppm of $C_2H_4$ was injected during both lean and rich periods. Figure 14 shows the projected HC, CO, and $NO_x$ emissions as a function of the poisoning time. The break in the data at approximately 7 hours occurred when the reactor was turned off for the evening and restarted the next day.

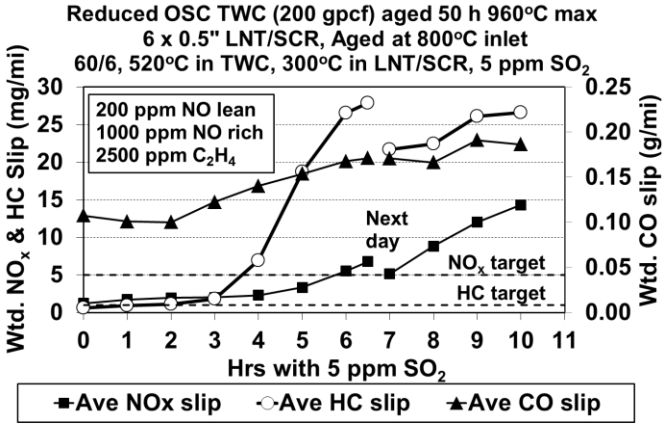


**Figure 14**. Weighted slip of HC, CO, and $NO_x$ for 0.5" no-OSC-200 TWC + 0.5" mod-OSC-200 TWC + 6x0.5" LNT/SCR system on poisoning test with 5 ppm $SO_2$. TWC aged on rich/stoich/lean schedule for 50 hours 960°C max; LNT/SCR aged downstream at 800°C. TWC poisoned at 520°C, 6x0.5" LNT/SCR at 300°C.

On this initial poisoning test, the $NO_x$ slip exceeded the 5.0 mg/mile target after approximately 6 hours. However, the HC slip exceeded the 1.0 mg/mile target after only 2 hours of poisoning. The CO slip increased slightly during the 10 hour poisoning test but was still far below the target limit of 1.3 g/mile.

The 6 hours with 5 ppm $SO_2$ on the reactor was converted into the projected mileage between desulfations on a vehicle. Assuming an average fuel sulfur content of 30 ppm and an A/F ratio of 30:1 during lean operation, the exhaust from the engine would contain about 1 ppm $SO_2$. Therefore, the use of 5 ppm $SO_2$ on the reactor accelerated the rate of sulfur poisoning by a factor of 5 assuming similar space velocities. So 6 hours on the reactor with 5 ppm $SO_2$ corresponded to 30 hours on the vehicle with 1 ppm $SO_2$ in the exhaust. Assuming an average vehicle speed of 25 MPH, these test results suggest that the LNT/SCR converter would need to be desulfated every 750 miles to maintain the $NO_x$ emissions below the 5.0 mg/mile target.

The HC emissions during the lean periods remained quite low over the entire test, but the HC emissions during the rich purges increased substantially. The maximum HC slip during purges at the beginning of the poisoning run was 2.4 ppm $C_2H_4$, but after 6 hours of poisoning the maximum HC slip was over 1200 ppm $C_2H_4$. This increase in HC slip during the purges was attributed to the severe effects of sulfur poisoning on the steam reforming reaction. To recover the steam reforming activity and thereby maintain the HC emissions below the 1.0 mg/mile target, Figure 14 indicates that the TWC would need to be desulfated every 250 miles.

## *Desulfations on the Reactor*

Tests were performed on the reactor to determine the conditions necessary to desulfate the TWC and recover its steam reforming capability. The poisoned TWC was exposed to 5 minutes of neutral operation at 600°C. Then the TWC was cooled to 520°C, and the performance of the TWC+LNT/SCR system was evaluated on 60/6 cycles at the same conditions used during the poisoning; i.e., temperatures of 520°C and 300°C for the TWC and LNT/SCR, 200 ppm NO lean, 1000 ppm NO rich, and 2500 ppm $C_2H_4$ during lean and rich operation. Similarly, the performance was evaluated after the TWC was desulfated rich for 5 minutes at 600°C, 650°C, and 710°C. During these experiments, the LNT/SCR catalyst was not desulfated but remained at 300°C.

The HC slip decreased following each desulfation event. Compared to the overall HC slip of 26.6 mg/mile following the poisoning, the slip dropped to 17.4, 6.2, 1.8, and 1.1 mg/mile after the neutral desulfation at 600°C and the rich desulfations at 600, 650, and 710°C, respectively. The neutral desulfation resulted in only a modest decrease in HC slip, while the rich desulfations at 600°C and 650°C resulted in much larger reductions in HC slip. However, a rich desulfation at 710°C was required to reduce the HC slip to a level that was close to the target of 1.0 mg/mile. Therefore, it was concluded that both the CC TWC and U/B TWC would need to be periodically exposed to several minutes of rich operation at temperatures near 700°C to prevent sulfur accumulation and the consequent degradation of their steam reforming capability.

Previous testing on lean $NO_x$ traps indicated that 10 to 15 minutes of rich operation at 675 to 750°C are required to recover the $NO_x$ storage capacity of a poisoned LNT [22]. Therefore, after the TWC was desulfated, the LNT was desulfated by heating the second oven to achieve a bed temperature of 700°C under rich conditions. The desulfated system was then evaluated on a second poisoning test with 5 ppm $SO_2$. Following this second poisoning, the TWC and LNT/SCR were both desulfated at 750°C, and then a third poisoning test was performed. Figure 15 shows the $NO_x$ slip during all 3 tests as a function of the poisoning time. During the first poisoning, the system was able to tolerate 6 hours with 5 ppm $SO_2$ before the $NO_x$ slip exceeded the target value of 5 mg/mile. However, the system was only able to tolerate 4 hours before exceeding the $NO_x$ slip target on the 2nd poisoning. Even though the LNT was desulfated at 750°C

following the 2nd poisoning, the $NO_x$ slip again exceeded the target after only 4 hours on the 3rd poisoning. A possible explanation is that some $NO_x$ storage sites remained poisoned with sulfur following the high temperature desulfations. With less "excess" $NO_x$ storage capacity to adsorb some of the $SO_2$, the $NO_x$ slip began to be impacted by the $SO_2$ sooner on second and subsequent poisonings.

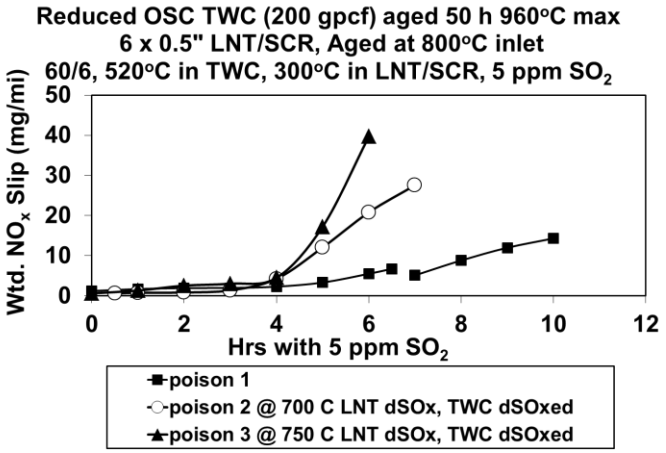


**Figure 15**. Weighted $NO_x$ slip during 3 poisonings of 0.5" no-OSC-200 + 0.5" mod-OSC-200 + 6x0.5" LNT/SCR system during 60/6 cycle with 5 ppm $SO_2$. TWC at 520°C, 6x0.5" LNT/SCR at 300°C.

## *Desulfations on the Vehicle*

The previous section showed that periodic rich conditions at 700°C are needed to recover the steam reforming capability of the TWC. It is expected that such conditions would be generated routinely within the CC TWC, particularly during high load operation (e.g., during the US06 test). However, depending on its location, it could be challenging to generate catalyst temperatures of 700°C in the underbody TWC, and it will definitely be challenging to generate such temperatures in the LNT/SCR due to its large distance from the exhaust manifold. Since the LNT/SCR converter is positioned to operate at 300-350°C during FTP conditions, the bed temperature needs to be increased by 350 to 400°C in order to achieve 700°C and desulfate the LNT.

One technique that can be used to increase the exhaust temperature during a desulfation involves retarding the spark timing so that more of the combustion occurs late in the combustion cycle. As a result, more of the energy in the fuel is released as heat to the exhaust gas instead of being used for mechanical work. On a 6.8 L 3-valve engine, the temperature of the CC TWC was increased by approximately 70°C when the spark timing was retarded from 40 degrees BTDC to 10 degrees BTDC. This is a significant increase in temperature, but obviously other actions would need to be taken to generate the 350-400°C increase in bed temperature required for desulfating the LNT.

A technique that can be used to generate an exotherm in the LNT is referred to as "air/fuel wobbling", where extended lean periods are alternated with extended rich periods [23]. Oxygen is stored in the OSC materials of the LNT during the lean periods, and the stored oxygen reacts with the reductants in the exhaust (i.e., HC, CO, $H_2$) during the rich periods. Even though the reduction of ceria is endothermic, the oxidation of the reductants makes the overall process exothermic [24]. After a transition from rich to lean, both the re-oxidation of the reduced ceria and the oxidation of the hydrocarbons are exothermic and generate more heat. With the proper combination of A/F ratios and durations of the lean and rich periods, reasonably large catalyst exotherms can be produced. However, if the CC TWC and/or U/B TWC contain high levels of OSC, most of the exotherm will occur on those catalysts instead of the LNT. Therefore, in order to minimize the exotherm in the three-way catalysts and generate as much exotherm as possible on the LNT, low or non-OSC three-way catalysts are needed.

A/F wobbling tests were performed on a 1.0" TWC + 3x0.5" LNT system (i.e., without the SCR zones). To minimize the exotherm on the TWC, the no-OSC-200 Pd-only formulation was used. The lean and rich times were either 4 or 5 seconds, and the $O_2$ content during the lean periods was either 2% or 7%. During the rich periods, the CO and $H_2$ levels were 2.5% and 0.8%, respectively, and the HC concentration was 2500 ppm of $C_2H_4$ during both lean and rich operation. Figure 16 shows the average temperatures in the TWC and the LNT for these different conditions. The baseline bed temperatures of the TWC and LNT with only $N_2$ flowing through the reactor were 491 and 483°C, respectively. When the lean periods contained 2% $O_2$, the maximum exotherms on the TWC and LNT were 51°C and 23°C, respectively. When the $O_2$ level during the lean periods was increased to 7%, the maximum exotherms on the TWC and LNT were 84°C and 23°C. Even with a non-OSC TWC, most of the exotherm occurred on the TWC. This was attributed to the oxidation of $C_2H_4$ on the TWC during lean operation and the fact that the Pd in the TWC can store and release oxygen. During the rich periods, the reductants in the exhaust react with the oxygen stored on the Pd to create an exotherm. As a result, the exotherms generated on the downstream LNT were relatively small.

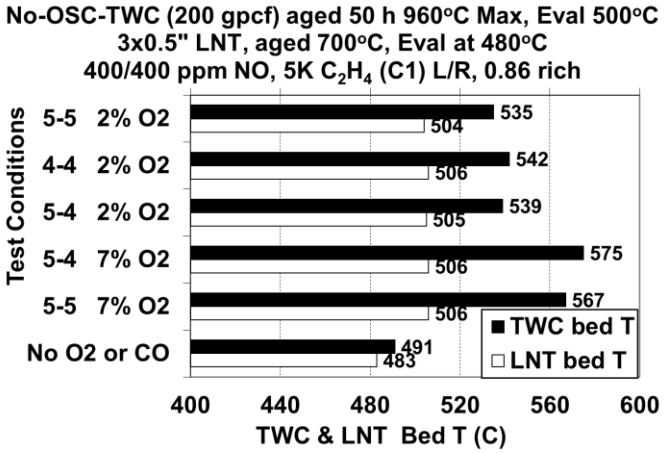


**Figure 16**. Bed temperatures in CC TWC and U/B LNT during A/F wobbling on 1" no-OSC-200 TWC + 3x0.5" LNT system. Base temperature near 490°C for both catalysts.

From this work, it was concluded that it would be very difficult to desulfate the LNT on an I-4 engine using only spark retard and A/F wobbling. Additional hardware would be required to generate a larger exotherm on the LNT. For example, an air pump could be used to inject air into the exhaust before the LNT. By operating the engine at a rich AFR, a large exotherm could be produced in the LNT. Alternatively, the engine could be operated at a lean A/F ratio, and an exhaust fuel injector could be used to inject fuel ahead of the LNT and produce the exotherm. However, the air pump or fuel injector and the accompanying control system would need to be included in the cost of the aftertreatment system, making the system more expensive and complex from a controls aspect. Even if the desulfation temperatures could be generated, the desulfations consume additional fuel and take away some of the fuel economy benefit offered by lean operation. Finally, the rich desulfations are expected to generate additional emissions of $NO_x$, CO, and HC.

These extra emissions would need to be averaged in with the emissions generated during normal FTP testing, requiring even lower emissions during the FTP in order to satisfy the target levels.

## Additional Discussion

The new Tier 3 and LEV III emission standards specify limits for NMOG+$NO_x$ rather than separate emission levels for NMOG and $NO_x$ as specified with the Tier 2 and LEV II standards. For example, Tier 3, Bin 30 specifies 30 mg/mile for NMOG+$NO_x$, compared to the separate Tier 2, Bin 2 limits of 10 mg/mile for NMOG and 20 mg/mile for $NO_x$. As a result, slightly higher $NO_x$ emissions could be tolerated as long as the NMOG emissions are lowered accordingly, and vice-versa. However, assuming that the sum of the cold-start emissions, stoichiometric emissions, and the engineering tolerances for HC and $NO_x$ in Table 2 remained approximately the same, the sum of the HC and $NO_x$ during lean/rich cycling would still need to be maintained at 6 mg/mile or below for the Tier 3, Bin 30 standards. Figure 15 showed that the $NO_x$ slip alone was much higher than 6 mg/mile after several hours of sulfur poisoning, particularly on the second and third poisonings. Therefore, there still would be a need to desulfate the LNT/SCR system periodically.

Starting in 2017, the Tier 3 standards establish an average sulfur content of 10 ppm in the fuel across the U.S. These lower sulfur levels would slow down the rate of sulfur accumulation. However, the sulfur would still accumulate on the LNT and deactivate its $NO_x$ storage capacity. Without the capability of desulfating the LNT, the $NO_x$ emissions would eventually exceed the 6 mg/mile limit during lean/rich cycling.

During the development of the TWC+SCR system [17], it was discovered that the SCR samples used during the testing of the TWC+LNT/SCR systems had been poisoned by low levels of Pt [25, 26], attributable to the SCR samples being aged behind the Pt-containing LNT under lean conditions at 800°C and then being evaluated behind the LNT for several months with lean/rich cycling tests. This Pt poisoning was indicated by the $NO_x$ conversion of the SCR samples dropping off rapidly at temperatures above 320°C when evaluated with $NH_3$ and $NO_x$, which can result from the Pt oxidizing some of the ammonia. However, the high $NO_x$ conversions obtained with the TWC+LNT/SCR systems suggest that this Pt poisoning did not have a significant impact on the results presented in this paper. This could be attributed to the fact that much of the $NO_x$ conversion was provided by the LNT and because many of the tests were performed with LNT/SCR bed temperatures near 300°C, which is below the temperature where $NH_3$ oxidation became a significant issue.

## Summary/Conclusions

This paper summarizes the laboratory investigation of a close-coupled TWC + underbody LNT/SCR system that could potentially allow lean operation during cruises for improved fuel economy while meeting the Tier 2, Bin 2 emission standards. After maximum HC, CO, and $NO_x$ levels during lean/rich cycling were established, it was shown that a 1" CC TWC with reduced OSC and an underbody 6x0.5" multi-zone LNT/SCR system was able to satisfy the $NO_x$ and HC targets when the temperature of the TWC was at least 500°C and the temperature of the LNT/SCR was between 250°C and 350°C. The minimum temperature of 500°C for the TWC was to ensure adequate steam reforming capability to minimize the HC slip during rich operation. Operating the LNT/SCR between 300°C and 350°C allowed the $NO_x$ target to be met while minimizing the HC slip and $NH_3$ and $N_2O$ generation. Exhaust system modeling indicated that the LNT/SCR catalyst would need to be placed 44" downstream of an U/B TWC to achieve the desired temperature range of 300-350°C during the FTP. Limiting the maximum aging temperature of the LNT/SCR to 700°C allowed the volume of LNT to be decreased, decreasing its cost and enhancing the value of the lean aftertreatment system. Sulfur poisoning increased the HC slip by decreasing the steam reforming capability of the TWC during the rich purges; the poisoning also increased the $NO_x$ slip by decreasing the $NO_x$ storage capacity of the LNT. Both the TWC and LNT/SCR could be desulfated with several minutes of rich operation at temperatures near 700°C. While these conditions are expected to be generated easily in the close-coupled location, it was determined that it would be difficult to generate such temperatures in the LNT/SCR location without additional exhaust hardware. Therefore, the decision was made to curtail development of the TWC+LNT/SCR system and focus on the development of a passive TWC+SCR system because of its superior sulfur tolerance and ease of desulfation. The development of the passive TWC+SCR system is discussed in a companion SAE paper [17].

## References


1. H. Bosch and F. Janssen, "Catalytic Reduction of Nitrogen Oxides", Catalysis Today, 2 (1988), p 369.
2. Naoto Miyoshi, S. Matsumoto, K. Katoh, T. Tanaka, J. Harada, N. Takahashi, K. Yokota, M. Sgiura, and K. Kasahara, "Development of New Concept Three-Way Catalyst for Automotive Lean-Burn Engines", SAE Paper no. 950809.
3. C. Lambert, "Urea SCR and DPF System for Diesel Sport Utility Vehicle Meeting Tier 2 Bin 5", presented at U.S. Department of Energy Diesel Engine Emissions Reduction (DEER) conference, Chicago, August 2005.
4. J. Schommers and H. Breitbach, "A Global Emission Strategy - Bluetec for Diesel Engines", Auto Technology, Pages 48-51, Mar. 2007.
5. H. Hu, J. Reuter, J. Yan, and J. McCarthy, Jr., "Advanced NOx aftertreatment System and Controls for On-Highway Heavy Duty Diesel Engines:", SAE paper no. 2006-01-3552.
6. R. Roecker, R. Zhan, and R. Stanglmaier, "Feasibility Investigation of a High-Efficiency NOx Aftertreatment System for Diesel Engines", SAE paper no. 2007-01-3983.
7. R. Snow, G. Cavataio, D. Dobson, C. Montreuil, and R. Hammerle, "Calibration of a LNT-SCR Diesel Aftertreatment System", SAE paper no. 2007-01-1244.
8. R. Snow, D. Dobson, R. Hammerle, and S. Katare, "Robustness of a LNT-SCR System to Aging Protocol", SAE paper no. 2007-01-0469.
9. J. McCarthy, Jr. and J. Holtgreven, "Advanced NOx Aftertreatment System Performance Following 150 LNT Desulfation Events", SAE paper no. 2008-01-1541.
10. C. Enderele, G. Vent, and M. Paule, "BLUETEC Diesel Technology - Clean, Efficient and Powerful", SAE paper no. 2008-01-1182.
11. L. Xu, R. McCabe, W. Ruona, and G. Cavataio, "Impact of a Cu-zeolite SCR Catalyst on the Performance of a Diesel LNT+SCR System", SAE paper no. 2009-01-0285.
12. J. Parks and V. Prikhodko, "Ammonia Production and Utilization in a Hybrid LNT+SCR System", SAE paper no. 2009-01-2739.
13. J. Theis, J. Ura, and R. McCabe, "The Effects of Sulfur Poisoning and Desulfation Temperature on the $NO_x$ Conversion of LNT+SCR Systems for Diesel Applications", SAE paper no. 2010-01-0300.
14. J. Theis, M. Dearth, and R. McCabe, "LNT+SCR Catalyst Systems for $NO_x$ Conversion on Diesel Applications", SAE paper no. 2011-01-0305.

15. C.H. Kim, K. Perry, M. Viola, W. Li, and K. Narayanaswamy, “Three-Way Catalyst Design for Urealess Passive Ammonia SCR: Lean-Burn SIDI Aftertreatment System”, SAE Paper no. 2011-01-0306.
16. Department of Energy Award Number DE-EE0003332.
17. J. Theis, J. Kim, and G. Cavataio, “TWC+SCR Systems for Satisfying Tier 2, Bin 2 Emission Standards on Lean-Burn Gasoline Engines”, SAE Paper no. 2015-01-1004.
18. J. Hepburn, D. Dobson, C. Hubbard, and K. Otto, "The Pulse Flame Combustor Revisited", SAE Paper no. 962118.
19. G. Fisher, J. Theis, M. Casarella, and S. Mahan, "The Role of Ceria in Automotive Exhaust Catalysis and OBD-II Catalyst Monitoring", SAE Paper no. 931034.
20. X. Wang, R. Gorte, “A study of steam reforming of hydrocarbon fuels on Pd/ceria”, Appl. Cat. A: General **224** (2002) 209-218.
21. J. Theis, J. Ura, C. Goralski Jr., H. Jen, E. Thanasiu, Y. Graves, A. Takami, H. Yamada, and S. Miyoshi, “The Effect of Ceria Content on the Performance of a $NO_x$ Trap”, SAE Paper no. 2003-01-1160.
22. J. Theis, J. Li, J. Ura, and R. Hurley, "The Desulfation Characteristics of Lean $NO_x$ Traps", SAE Paper no. 2002-01-0733.
23. J.R. Asik, G.M. Meyer, and D. Dobson, "Lean $NO_x$ Trap Desulfation Through Rapid Air Fuel Modulation", SAE paper no. 2000-01-1200.
24. J. Theis, J. Ura, J. Li, G. Surnilla, J. Roth, and C. Goralski Jr., "$NO_x$ Release Characteristics of Lean $NO_x$ Traps During Rich Purges", SAE paper no. 2003-01-1159.
25. H. Jen, J. Girard, G. Cavataio, and M. Jagner, “Detection, Origin and Effect of Ultra-Low Platinum Contamination on Diesel-SCR Catalysts”, SCR paper no. 2008-01-2488.
26. G. Cavataio, H. Jen, J. Girard, D. Dobson, J. Warner, and C. Lambert, “Impact and Prevention of Ultra-Low Contamination of Platinum Group Metals on SCR Catalysts Due to DOC Design”, SAE paper no. 2009-01-0627.

## Contact Information

Please contact J. Theis at jtheis@ford.com for further information.

## Acknowledgments

This material is based upon work supported by the Department of Energy under Award Number DE-EE0003332. This report was prepared as an account of work sponsored by an agency of the United States Government. Neither the United States Government nor any agency thereof, nor any of their employees, makes any warranty, express or implied, or assumes any legal liability or responsibility for the accuracy, completeness, or usefulness of any information, apparatus, product, or process disclosed, or represents that its use would not infringe privately owned rights. Reference herein to any specific commercial product, process, or service by trade name, trademark, manufacturer, or otherwise does not necessarily constitute or imply its endorsement, recommendation, or favoring by the United States Government or any agency thereof. The views and opinions of authors expressed herein do not necessarily state or reflect those of the United States Government or any agency thereof.

## Definitions/Abbreviations

| | |
|---|---|
| A/F | Air/fuel ratio |
| $C_2H_4$ | Ethylene |
| Ce | Cerium |
| CO | Carbon monoxide |
| $CO_2$ | Carbon dioxide |
| FTP | Federal Test Procedure |
| $H_2$ | Hydrogen |
| $H_2O$ | Water |
| $H_2S$ | Hydrogen sulfide |
| HC | Hydrocarbon |
| LNT | Lean $NO_x$ Trap |
| $N_2$ | Nitrogen |
| $N_2O$ | Nitrous oxide |
| NO | Nitric oxide |
| $NO_x$ | Oxides of nitrogen = NO +$NO_2$ |
| $NO_2$ | Nitrogen dioxide |
| $O_2$ | Oxygen |
| OSC | Oxygen Storage Capacity |
| PM | Particulate Matter |
| Pt | Platinum |
| Pd | Palladium |
| PGM | Platinum Group Metal |
| Rh | Rhodium |
| SCR | Selective Catalytic Reduction |
| $SO_2$ | Sulfur dioxide |
| TWC | Three-way catalyst |
| US06 | Supplemental FTP test |

# Combustion Research (MTU)

MTU provided support to Ford in the research and development of advanced ignition concepts and systems to expand the dilute / lean engine operating limits, as shown in Table 17. The research and corresponding results for each of these areas are summarized below.

***Table 17 - Combustion research areas and deliverables for MTU.***

| Research Area | | Deliverables | Pressure Vessel | Engine Dyno |
|---|---|---|---|---|
| 1 | Advanced Ignition – Ignition and Flame Kernel Development | Gain insight to the fundamental physics of the interaction of combustion system attributes & ignition system design variables relative to both design factors & noise factors; use results to develop an analytical spark discharge model. | ✓ | |
| 2 | Advanced Ignition – Impact on Lean and Dilute | Validate the findings from the pressure vessel & predictions of the resultant model on a mature combustion system, focusing on dilute & lean operating conditions. | | ✓ |
| 3 | Planer Laser Induced Fluorescence | Apply laser-based diagnostics to characterize multi-phase fuel / air mixing under controlled high pressure & temperature conditions; use data for CFD spray model development & spray pattern optimization. | ✓ | |
| 4 | Combustion Sensing and Control | Assess production viable combustion sensing techniques; detect location of 50% mass fraction burned & combustion stability for closed loop combustion control. | | ✓ |
| 5 | Advanced Knock Detection with Coordinated Engine Control | Compare stochastic knock control to various conventional control techniques. | | ✓ |
| 6 | Combustion Surface Temperature | Measure instantaneous temperatures of combustion chamber components under lean, dilute, & boosted operation to improve numerical models and reduce knock tendency. | | ✓ |

Michigan Technological University
Department of Mechanical Engineering-Engineering Mechanics
815 R. L. Smith ME-EM Building
1400 Townsend Drive
Houghton, Michigan 49931-1295
906-487-2551, 2561 • Fax 906-487-2822
www.me.mtu.edu

APS LABS

**Contact Info**

**Dr. Jeffrey D. Naber**
Ronald E. and Elaine Starr Professor of Mechanical Engineering
Director of Advanced Power Systems Research Center
Mechanical Engineering – Engineering Mechanics Department
Michigan Technological University
1400 Townsend Dr.
Houghton, MI 49931
Tel: 906.487.1938
Email: jnaber@mtu.edu

---

# Michigan Tech - Task 8 Combustion DOE Program Report for Ford Program *Advanced Gasoline Turbocharged Direct Injection (GTDI) Engine Development*

*Ford Program Manager*
*Corey E. Weaver*
*Project ID: ACE065*

Ford - Michigan Tech Program Manager

Garlan Huberts
Ford Motor Company
Research and Advanced Powertrain Controls
RIC Rm 1625
313-845-6188
ghuberts@ford.com

## Task 8. Table of Contents

| | | | Year 1 | | | | Year 2 | | | | Year 3 | | | | Year 4 | | | | Year 5 | |
|---|---|---|---|---|---|---|---|---|---|---|---|---|---|---|---|---|---|---|---|---|
| | | | Q1 | Q2 | Q3 | Q4 | Q1 | Q2 | Q3 | Q4 | Q1 | Q2 | Q3 | Q4 | Q1 | Q2 | Q3 | Q4 | Q1 | Q2 |
| | | | Phase 1 0 to 6 | | Phase 2 7 to 18 | | | | | | Phase 3 19 to 27 | | | | Phase 4 27 to 54 | | | | | |
| Area of Research / Development | | | | | | | | | | | | | | | | | | | | |
| # | Engine | Test Bed | V6 | V6 | V6 | V6 | V6 | V6 | I4 | I4 | I4 | I4 | I4 | I4 | X | X | X | X | X | X |
| 1 | Advanced Ignition - Ignition and flame kernal studies | CL | | | R | | | R | | | | | | R | | | | | | |
| 2 | Advanced Ignition - Impact on Combustion | ED | | | | R | | CR | | R | | | | R | | | | | | |
| 3 | GDI Air Fuel Mixing via PLIF for Fuel Injection Optimization | CL | | | | | R | | | R | | | | R | | | | | | |
| 4 | Combustion Sensing and Phasing Control | ED - CL | | | | R | | R | | R | | CR | | R | | | | | | |
| 5 | Advanced Knock Detection & Control | ED | | | | $CR^1$ | | | | R | | $CR^2$ | | R | | | | | | |
| 6 | In-Cylinder Temperatures and Heat Transfer | ED | | | | | | R | | | | | | R | | | | | | |

| | |
|---|---|
| CL | Combustion Laboratory with Press. Vessel |
| ED | Engine Dyno operating V6 then I4 engines |

Primary Development
Application / Tuning / Calibration in support of Implementation Ready

| | |
|---|---|
| R | Report |
| CR | Concept Ready Report |
| $CR^1$ | Advanced knock detection |
| $CR^2$ | Advanced knock control |

The following are summaries of the 8 subtasks. Further details are given in theses, publications, and internal reports.

Task 8.1 – Advanced Ignition – Ignition and Flame Kernel Development: Continuously investigate advanced ignition system concepts and develop an ignition model applicable to lean and dilute spark-ignition engines based upon studies conducted in an optical combustion vessel. The task focuses on further refining flame kernel characteristics. The impact of ignition parameters such as spark energy power and multi-strike on flame kernel development and the dependence of electrode temperature, electrode orientation with respect to the mean flow, and electrode gap over pressures and temperatures characteristics of early and late-cycle injection conditions will be examined. Finally, the effect of turbulent intensity at the location of the spark gap on the lean and dilute mixture limits will be determined.

Summary [Zhang et al. 2013, Zhang 2014]: An operational scheme with fuel-lean and exhaust gas dilution in spark-ignited engines increases thermal efficiency and decreases NOx emission, while these operations inherently induce combustion instability and thus large cycle-to-cycle variation in engine. In order to stabilize combustion variations, the development of an advanced ignition system is becoming critical. To quantify the impact of spark-ignition discharge, ignitability tests were conducted in an optically accessible combustion vessel to characterize the flame kernel development of lean methane-air mixture with $CO_2$ simulating exhaust diluent. A shrouded fan was used to generate turbulence in the vicinity of J-gap spark plug and a Variable Output Ignition System (VOIS) capable of producing a varied set of spark discharge patterns was developed and used as an ignition source. The main feature of the VOIS is to vary the secondary current during glow discharge including naturally decaying and truncated with multiple strikes. These discharge patterns were studied to characterize the interaction of discharge phases and initial flame formation. High-speed Schlieren optical setup was employed for visualization with synchronous measurement of discharge waveforms. The results showed that multi-strike discharge was able to generate multiple flame kernels whose interactions affect flame initiation. With proper timing of each discharge event the individual kernels merge and lead to propagating flame. However, this flame initiation is highly subjected to the flow field in the vicinity of spark plug. Based on these observations, a mathematical description of the discharge timing requirements is formulated to describe the multi-kernel flame initiation under turbulence.

Zhang, A., Cung, K., Lee, S., Naber, J., Huberts, G., Czekala, M., and Qu, Q., "The Impact of Spark Discharge Pattern on Flame Initiation in a Turbulent Lean and Dilute Mixture in a Pressurized Combustion Vessel," SAE Int. J. Engines 6 (1) : 435-446, 2013, doi:10.4271/2013-01-1627.

Zhang, A., Combustion Initiation by Electrical-discharge-induced Plasma in Lean and Dilute Methane-air Mixture: Experimental and Modeling Investigation, MTU PhD Thesis 2014.

Task 8.2 – Advanced Ignition – Impact on Lean and Dilution Combustion: Engine studies will be conducted on the V6 to optimize the ignition parameters to increase combustion rates, reduce combustion variation, and increase the ignition limits for highly dilute and lean mixtures while maintaining a robust ignition subsystem. The advanced ignition systems (Task 8.1) will be evaluated. Improved first principles ignition correlations will be developed to integrate with 1D predictive combustion simulation and CFD codes.

Summary [Chen 2015, Chen et al. 2013] High dilution combustion is a promising technology to continue improving gasoline spark-ignition (SI) engine fuel conversion efficiency and for the reduction of nitrogen oxide emissions. Dilution is principally limited in SI engines by ignition, flame kernel development, successful transition to the turbulent propagating flame during the bulk burn portion of combustion process and the resulting combustion stability. However, the SI gasoline turbocharged directed injection (GTDI) engine ignition requirements, especially at the combustion stability limit, are not well understood and must be better characterized to enable improved designs.

A multi-discharge, electronically control, inductive ignition system was employed on a multi-cylinder GTDI engine to control and quantify the ignition and combustion processes under high dilution operation. The ignition system, developed by Ford Motor Company and integrated on the engine, is a Variable Output Ignition System (VOIS) enabling flexible spark discharge patterns with control of ignition energy, duration, and phasing. In this study two coil discharges were examined under both continuous and discontinuous conditions by delaying the second discharge with respect to the first. Ignition secondary voltage and current were measured with a high speed analog to digital recorder to measure and quantify the breakdown voltages, ignition duration, ignition energy, and other ignition metrics over 300 cycles of continuous engine operation. Simultaneously 300 cycles of crank-angle resolved cylinder pressure and other data was recorded to analyze cycle based work and combustion rates and to correlate ignition with combustion.

Chen, W. Impact of Spark Ignition Duration, Energy and Phasing on combustion and Performance in a Gaosline Turbocharged Direct Injection Engine Near the Dilute Limit, MTU PhD Thesis 2015.

Chen, W., Madison, D., Dice, P., Naber, J. Chen, B., Miers, S., Czekala, M., Glugla, C., Qu, Q, and Huberts, G. "Impact of Ignition Energy Phasing and Spark Gap on Combustion in a Homogenous Direct Injection Gasoline SI Engine Near the EGR Limit," SAE Technical Paper 2013-01-1630, 2013, doi:10.4271/2013-01-1630.

Task 8.3 – GDI Air Fuel Mixing via PLIF for Fuel Injection Optimization: Laser-based diagnostic techniques will be applied to characterize the transient and heterogeneous fuel/air mixing at temperatures and pressures characteristic of a boosted GDI engine. Studies will be conducted in the combustion lab. The data obtained will serve as benchmark data for CFD validation and will allow further air-fuel mixing studies and injector spray pattern optimization. This will enhance the base spray studies and target optimization that is currently underway.

Complete summary report contained herein.

MichiganTech
Michigan Technological University

Department of Mechanical Engineering-Engineering Mechanics

815 R. L. Smith ME-EM Building
1400 Townsend Drive
Houghton, Michigan 49931-1295
906-487-2551, 2561 • Fax 906-487-2822
www.me.mtu.edu


**Michigan Tech - Task 8.3 GDI Air Fuel Mixing via PLIF for Fuel Injection Optimization**

# Measurement of Liquid and Vapor Regions within Spray from a 6-hole GDI injector using Planar Laser-induced Exciplex Fluorescence (PLIEF)

**Seong-Young Lee and Anqi Zhang**
**MTU**

**September 4, 2014**

**Introduction**

An understanding of fuel-air mixture formation within the combustion chamber is important in the development of high efficiency direct injection (DI) internal combustion (IC) engines. The information of liquid and vapor phase fuel spatial and temporal distribution can well explain the mixing process and is of development and research interest. The Exciplex (excited-state complex) technique is an application of laser-based diagnostics that is useful for the above purpose, which provides non-intrusive measurement of the fuel mixing and evaporation phenomena prior to combustion starts. Plainer Laser-induced Exciplex Fluorescence (PLIEF) measurements have been performed to visualizing the mixing/vaporizing process of gasoline surrogate spray from a 6-hole GDI (gasoline direct injection) injector inside a constant volume spray - pressure vessel at conditions representative of in-cylinder conditions in a GDI engine. Theoretical background as well as experiment procedure and results are presented as following.

**Exciplex theory**

LIEF is a special case of tracer LIF. The equations describing the mechanism of exciplex (or monomer) emission fluorescence shown in Figure 1 relate with M, M*, UV, E*, and G [1, 2, 3]. These correspond to; M- monomer species, M*- excited monomer state, UV- ultra violet laser excitation energy, E*- excited state complex (exciplex) relating to the G mixture, and G- ground state reactant of mixture. Upon receiving UV-laser excitation, two different color fluorescence come out. One fluorescence, which is due to the emission from the monomer (M), can track evaporating vapor phase fuel. In the vapor phase, the probability of exciplex formation is very low, and therefore the fluorescence emitted by the monomer can be used to track the vapor.

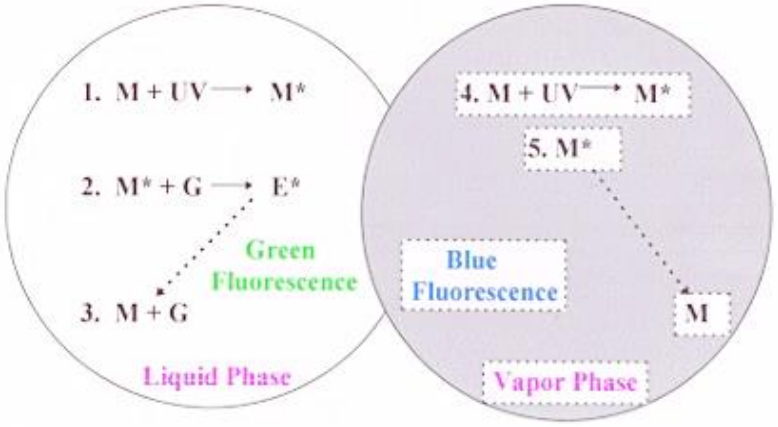


**Figure 1: Mechanism of exciplex (or monomer) emission fluorescence. R1: laser excitation of monomer in liquid, R2: exciplex (excited state complex) formation, liquid phase only, R3: exciplex emission fluorescence occurs in green, R4: laser excitation of monomer in vapor, and R5: monomer emission fluorescence occurs in blue. See also Figure 2.**

On the other hand, some portions of the excited monomers react with the ground state reactant (G), and then produce exciplex emission. An exciplex (short form for the excited-state complex) is a molecular complex that is stable only in the electronically excited state. This exciplex can return dissociatively to the ground state by emitting a fluorescence photon such as $E^* \rightarrow G + M + h\nu$. The exciplex fluorescence is significantly red-shifted (or green fluorescence, i.e., longer wavelength) relative to the monomer fluorescence and can tag the liquid phase fuel. The exciplex-forming reaction (R2) can only take place if the excited monomer M*

encounters a reaction partner G within the lifetime of its excited state. Thus, the probability of exciplex formation is high if both molecules are present in the liquid phase where the density is high and therefore the mean free path of the excited molecules is low. To enhance the exciplex formation rate, the ground state reaction partner G is provided in excess concentration. Therefore, ideally, the LIEF result is spectrally distinct fluorescence from the liquid (exciplex) and vapor (monomer) phases as shown in Figure 2.

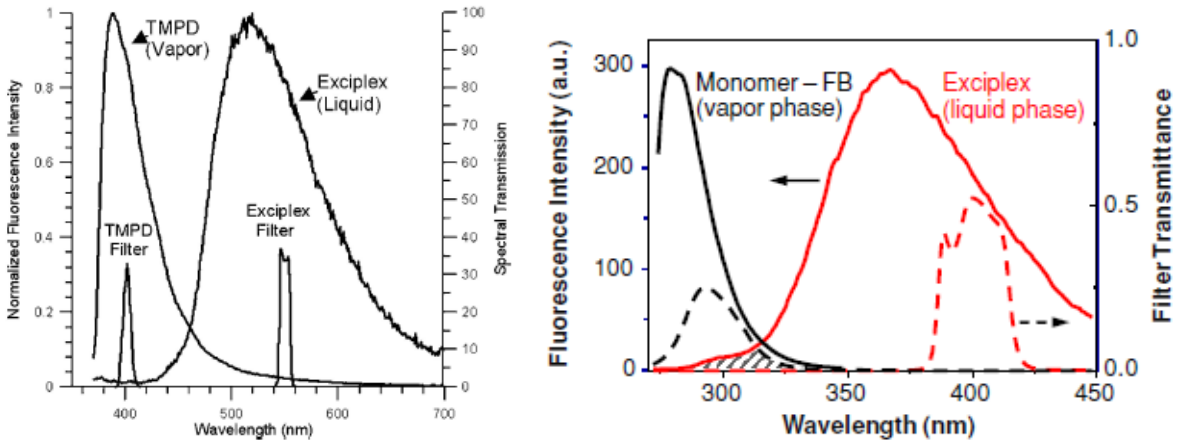


**Figure 2: Spectra of exciplex and monomer fluorescence spectra. Left: excited laser wavelength of 355 nm in the mixture of hexadecae, 1-Me-Np and TMPD and right: excited laser wavelength of 266 nm in the mixture of monomer (FB) and exciplex fluorescence spectra of the FB/DEMA [1,2].**

In practice, the exciplex-based vapor/liquid visualization systems are more complex because both the monomer absorption spectrum and the exciplex-formation process can depend strongly on temperature, co-evaporation of the tracers and base fuel, calibration of the liquid phase signal, liquid-vapor crosstalk (liquid fluorescence that overlaps the vapor fluorescence detection band-pass) and collisional quenching, especially by oxygen.

**Experimental Setup**

Fluorobenzene (FB)/N, N-diethylmethylamine (DEMA) system has been adopted for this study. N-hexane was selected as a single-component gasoline surrogate. The tracer fuel is a mixture of these three components by the fractions listed in Table 1. The fluorescence spectra of this tracer fuel with excitation laser of 266 nm is expected to be same as in Figure 2 (right). A GDI fuel injection system is used to pressurize the tracer fuel to up to 100 bar and deliver it to a 6-hole injector mounted in the constant volume spray-combustion vessel.

**Table 1. Component of FB/DEMA tracer surrogate gasoline fuel**

| Component | Volume fraction |
|---|---|
| n-hexane | 89% |
| DEMA* | 9% |
| FB | 2% |

Optical setup involving the laser, injector, and spray geometry is shown in Figure 3 as a top view apparatus layout. The combustion vessel (CV) at Michigan Technological University is a constant volume combustion visualization device that is capable of withstanding high temperature (up to 2000 K) and high pressure (up to

350 bar). The CV has a cubic inner chamber and the GDI injector is mounted on one side surface of the CV. The rest side surfaces of the cubic CV are equipped with transparent sapphire windows that will allow UV to pass through.

A pulsed Nd:Yag laser system is used to generate UV laser at 266 nm with approximately 7 ns pulse width. Optics such as dichroic mirrors and prisms are used to deflect the laser beam to proper height and position, and the combination of a spherical lens and a cylindrical lens expands the laser beam into a focused thin laser sheet in the near nozzle regions. Note that the spray pattern from this 6-hole GDI injector is not symmetric, as shown in Figure 3 (right). So that the laser sheet and the injector orientation are carefully adjusted to allow the plainer laser shines through the center of Plume 5 as indicated.

Fluorescence signals are captured using an intensified CCD (ICCD, intensified coupled charge device) camera. Two different narrow band-pass filters are used for the two phases of fuels in the spray. The filter for vapor LIF signal has a center wavelength at 280 nm and FWHM (full width at half maximum) of 25 nm (filter model 280FS25). And the liquid LIF filter has a band width of 20 nm at 400 nm center wavelength (filter model 400FS20). The filters' transmittance curve is superposed on spectral response plot of the FB/DEMA tracer system, as shown in Figure 4. There is a "cross talk" wavelength range where the LIF signals of vapor and liquid fuel overlap. By applying the 280FS25 filter, the transmittance in the cross talk region is limited at low level, and the noise from the liquid band is believed to be minimized.

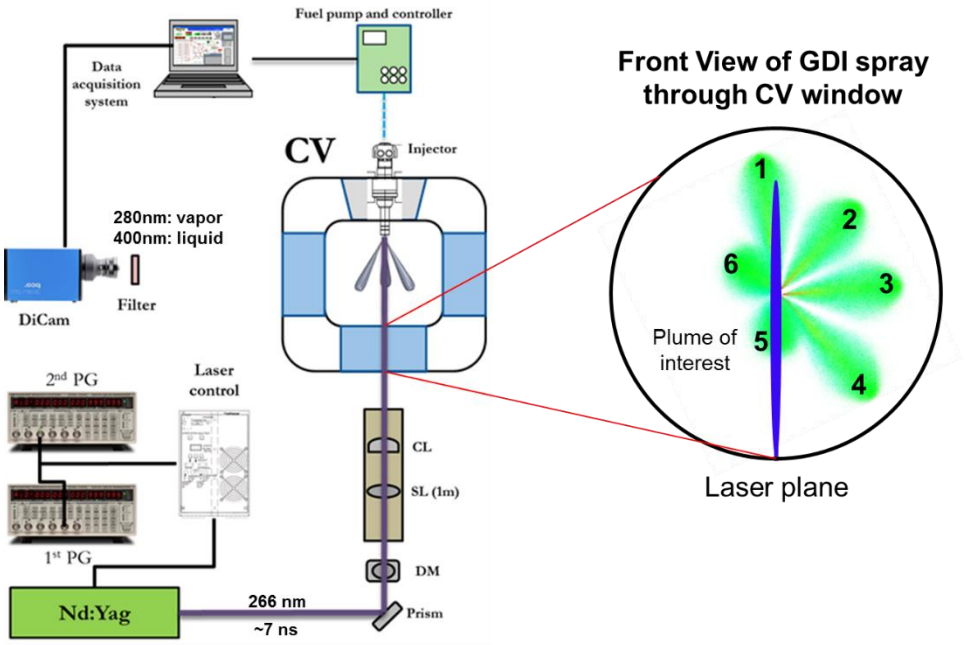


**Figure 3. Apparatus layout for PLIEF tests of GDI spray in the combustion vessel. Left: optical setup, and right: front view of GDI spray through CV window**

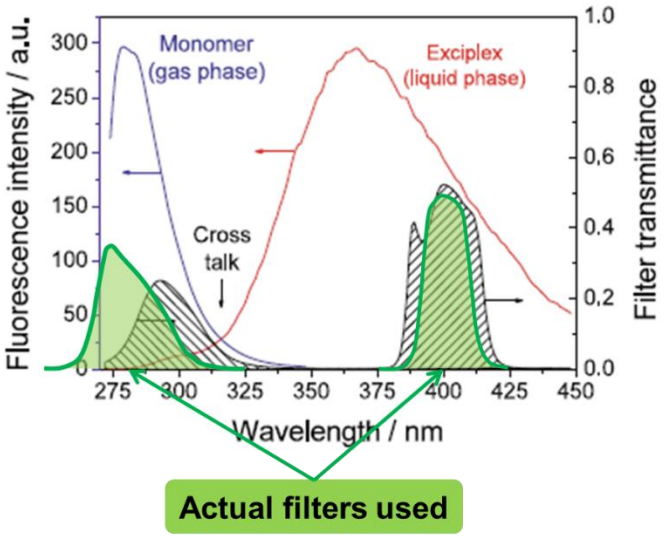


**Figure 4. Liquid and vapor fluorescence filter characteristics for PLIEF imaging**

**Results and discussion**

*Camera timing for LIF signal capturing*

Timing and exposure of the ICCD camera have been tuned prior to the PLIEF tests. It was found in this preliminary test sets that a proper camera delay with respect to the laser pulse is necessary to obtain LIF signals. A comparison case is shown in Figure 5. A zero camera delay case is on the left and the resulting image with 50 ns camera delay is on the right. The two images are captured with the same ambient and injection conditions. The ambient gas is nitrogen at 150 ˚C and 6.9 bar, and the injection pressure is at 50 bar, while the laser timing is at 0.8 ms ASOI (after the start of injection). The filter used was 280 nm, which is for capturing vapor phase fuel. Plume 1 and 5 can be readily recognized from the resulting images. As for the zero camera delay case on the left, high intensity pixels, which are supposed to be vapor signals, are observed in the center part of each plume. Such result is against our intuition since vapor should have higher concentration at the boundary of a liquid spray plume, rather than in the center of it. The spray pattern shown Figure 5 (right) should be more reasonable. High LIF intensity pixels are located at the tip of Plume 5, where liquid fuel is more likely to vaporize and mix with air.

It is suggested that the camera timing has an impact on the LIF image signals. When the camera exposure is overlapped with the laser pulse, scattered laser signal from the liquid fuel will also be captured by the camera. Such scattering intensity could be orders of magnitudes stronger than the LIF and dominant the image. This hypothesis could reasonably explain the resulting image in Figure 5 (left). The streamer-shaped high intensity areas in the center of Plume 1 and 5 can be a good indicator of the liquid core of each plume. So that in order to obtain proper LIF signals, the camera timing has been delayed for approximately 50 ns for all the tested conditions.

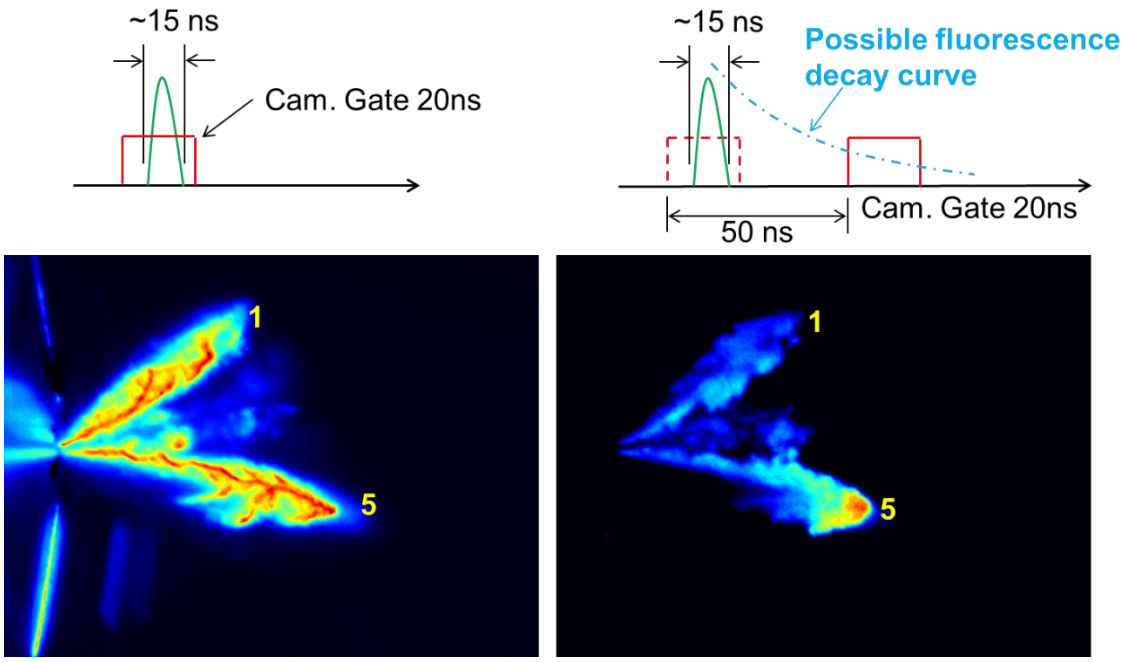


Figure 5. Zero and 50 ns camera delay setups and their corresponding PLIEF images for vapor phase fuel

*Structure of GDI spray*

Measurement of vapor and liquid regions of the GDI spray has been performed following the test matrix in Table 2. Four test conditions are included and for each condition, five test runs are conducted to obtain liquid and vapor region images respectively, resulting in total 40 test runs. Resulting images are averaged for each test condition and image type. Averaged images are shown in Figures 6 and 7. Image intensities are coded with pseudo colors to better represent high intensity regions. Plume 5 is the plume of interest for all these images.

In general for all tested conditions, the liquid fuel distribution is close to the injector tip with high concentration regions in the plume center, while the vapor phase fuel can be observed at the plume front with a different outer profile as the liquid spray. Such observation well explains the liquid/vapor distribution as in the GDI spray. Liquid core reside in the plume center and evaporating occurs around the plume side boundaries as well as the plume front. High vapor concentration is found at the plume front, indicating that fuel vaporization is most intense at the interface between the spray and ambient gases where the momentum difference is high.

**Table 2. Test matrix for PLIEF tests of GDI spray in the Spray/Combustion Vessel**

| $P_{ch}$ (bar) | T (°C) | Injection Duration (ms) | $P_{inj}$ (bar) | PLIF Imagng Timing (ASOI) |
|---|---|---|---|---|
| 6.9 | 150 | 1 ms | 50 | 0.8 & 1.5 ms |
| 6.9 | 150 | 1 ms | 100 | 0.8 & 1.5 ms |

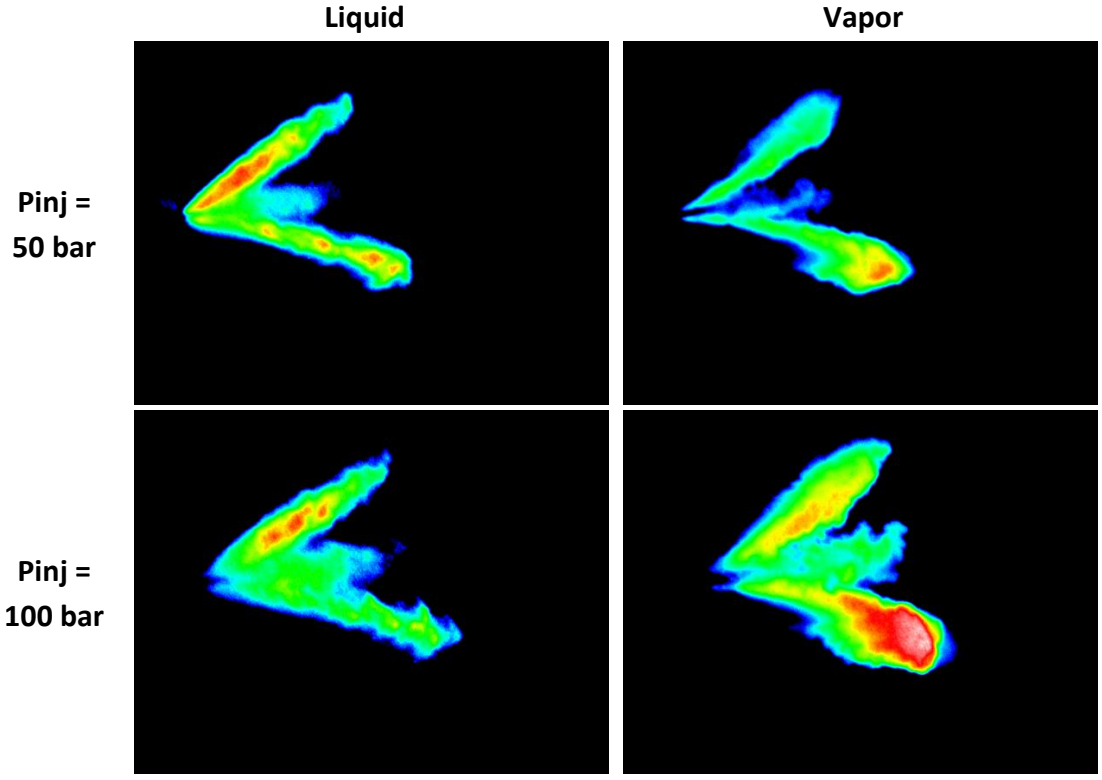


**Figure 6. PLIEF images with pseudo color for liquid and vapor distribution of GDI spray at 0.8 ms ASOI**

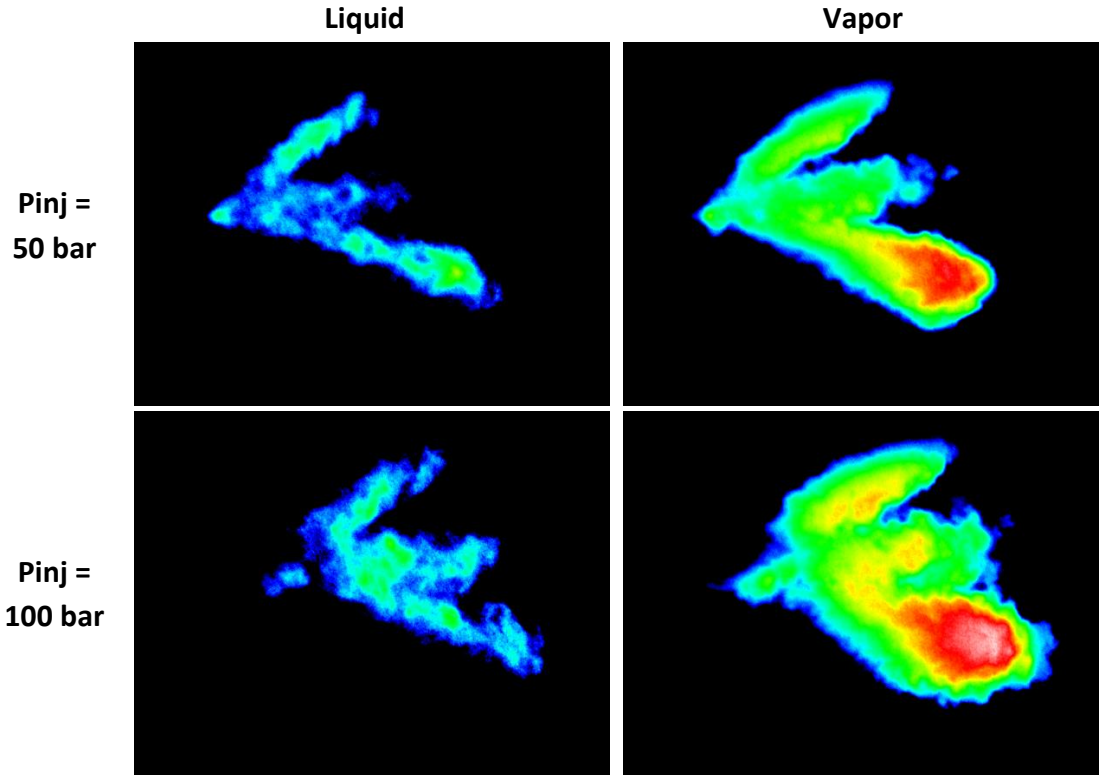


**Figure 7. PLIEF images with pseudo color for liquid and vapor distribution of GDI spray at 1.5 ms ASOI**

Injection pressure plays an important role in determining the distribution pattern. The mixing of GDI spray with ambient air is a momentum driven process and the injection pressure serves as the major source of liquid momentum. As the injection pressure increases, the penetration of liquid fuel does not vary significantly, while a larger vaporized fuel region is formed under 100 bar injection pressure than 50 bar. Images at different instance after the start of injection indicates the time evolution of the GDI spray. At 1.5 ms ASOI, the injection has already ended, so that the liquid region intensity is lower than that of the 0.8 ms ASOI cases. The momentum effect is also more obvious at 1.5 ms ASOI as the whole spray is pushed more downstream relative to the injector once the injection ends.

**Summary and Future Work**

1. Planar laser-induced exciplex fluorescence (PLIEF) has been successfully applied to the 6-hole GDI injector to characterize the vapor and liquid phases of transient surrogate gasoline spray. Vapor and liquid phase measurements of PLIEF have been made independently due to limitation of current visualization system.
2. Spatial and temporal distribution of spray significantly differs in the vapor and liquid phases. High vapor concentration is found at the plume front, indicating that fuel vaporization is most intense at the interface between the spray and ambient gases where the momentum difference is high.
3. The camera timing need to be delayed approximately 50 ns for all the tested conditions in order to measure the proper LIEF signals.
4. As a future work, it is suggested to capture the vapor and liquid phases simultaneously. In addition, quantitative measurement can be possible using the careful calibration of the system.

**References**


1. F. Payri, J. Pastor, J. Pastor, and J. Julia´, 2006, “Diesel Spray Analysis by Means of Planar Laser-Induced Exciplex Fluorescence,” Int. J. Engine Res. 7:77---89.

2. Fansler, Todd D, Michael C Drake, Boguslaw Gajdeczko, Isabell Düwel, Wieland Koban, Frank P Zimmermann, and Christof Schulz. “Quantitative Liquid and Vapor Distribution Measurements in Evaporating Fuel Sprays Using Laser-Induced Exciplex Fluorescence.” Measurement Science and Technology 20, no. 12 (2009): 125401.

3. Düwel, I., W. Koban, F. P. Zimmermann, T. Dreier, and C. Schulz. “Spectroscopic Characterization of the fluorobenzene/DEMA Tracer System for Laser-Induced Exciplex Fluorescence for the Quantitative Study of Evaporating Fuel Sprays.” Applied Physics B 97, no. 4 (December 1, 2009): 909–18. doi:10.1007/s00340-009-3652-3.

Task 8.4 – Combustion Sensing and Control: From combustion pressure signatures for lean and dilute mixtures, determine the critical parameters for rapid detection of combustion phasing and stability. Determine potential value of real-time control of combustion vs. traditional open loop mapping. Investigate production viable sensors (pressure, ion, acceleration, and/or crankshaft speed) in V6 engine. Select most viable technique; determine robustness to noise factors and suitability for real-time control of combustion phasing and stability.

Complete summary report contained herein.

Michigan Technological University
Department of Mechanical Engineering-Engineering Mechanics
815 R. L. Smith ME-EM Building
1400 Townsend Drive
Houghton, Michigan 49931-1295
906-487-2551, 2561 • Fax 906-487-2822
www.me.mtu.edu

APS LABS

**Contact Info**

**Dr. Jeffrey D. Naber**
Ronald E. and Elaine Starr Professor of Mechanical Engineering
Director of Advanced Power Systems Research Center
Mechanical Engineering – Engineering Mechanics Department
Michigan Technological University
1400 Townsend Dr.
Houghton, MI 49931
Tel: 906.487.1938
Email: jnaber@mtu.edu

---

# DOE TASK 4
# Combustion Sensing and Phase Control

Yun Wang, Jeff Naber, & Bo Chen

August 28, 2014

## TABLE OF CONTENTS

**1. CONTROL ARCHITECTURE AND ALGORITHM……... 180**
1.1. TOP LEVEL CONTROL ARCHITECTURE……..180
1.2. SPARK TIMING MANAGEMENT ALGORITHM……..181
*1.2.1. CA50 Control Algorithm……* 182
1.3. FUEL INJECTION MANAGEMENT ALGORITHM…….. 182
**2. CONTROL STRATEGY AND ALGORITHM OFFLINE SIMULATION…… 183**
2.1. FUEL INJECTION MANAGEMENT SIMULATION…… 183
*2.1.1. Simulation methodology……* 183
*2.1.2. Simulation Results and Conclusions……* 184
2.2. SPARK TIMING MANAGEMENT SIMULATION……187
*2.2.1. Simulation methodology……*188
*2.2.2. Simulation Results and Conclusions……* 188

# 1. Control Architecture and Algorithm

## 1.1 Top Level Control Architecture

Figure 1 shows the top level control architecture design. The “TriBox” is a custom controller built around an Infineon TriCore TC1797 Development Board. It is used as a multi-functionality controller which handles both real time spark timing, fuel injection and torque management. Real time combustion metrics estimation, including CA50 and COV IMEP are also conducted by TriBox controller. Control decision is made based on the real time combustion metrics estimation. The major tasks for the TriBox controller are combustion phasing control, combustion stability control, torque modifier and knock limit protection. The inputs to the TriBox controller are from sensors installed on the EcoBoost engine and PCM. Sensor input signals include crank angle, cam position and in-cylinder pressure, intake manifold pressure. The PCM variables, MBT spark timing SPK_MBT, load estimator LOAD_FG, feedback bank lambda LAM_16MS[0]&[1] and feedback throttle angle ETC_TP_ARB, are sent to TriBox controller via CAN communication. For the spark timing control, the TriBox controller will output the spark timing signal to the ignition box based on the real time CA50 estimation. For the fuel injection management, the TriBox controller will send PCM parameters command overall engine lambda MTU_FUL_OVRD_LAM, individual cylinder fuel injection multiplier MTU_FUELMASS_MULT, throttle angle command MTU_ETC_TA_ADDER, fuel injection override switch MTU_FUL_OVRD_SW, fuel injection control mode switch MTU_FUL_CTRL_SW. Then the PCM will control throttle angle and fuel injection according to the command sent by TriBox.

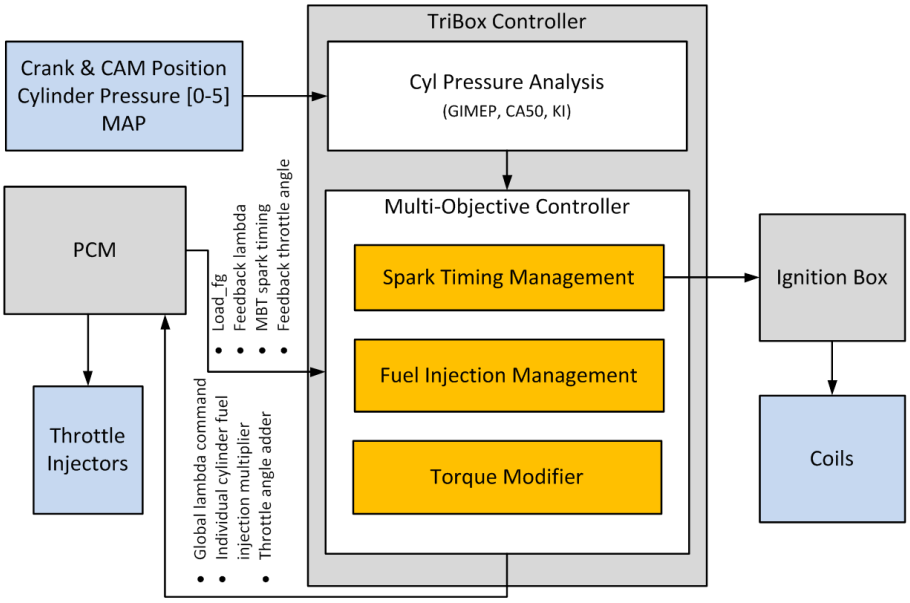


***Figure 1. Top Level Control Architecture***

## 1.2 Spark Timing Management Algorithm

The spark timing management algorithm is shown in the figure 2. It consists of knock limit protection, CA50 PI controller, MBT modifiers based on feedback lambda and adaptive component. The feedback of the PI controller is the difference of the desired CA50 and real-time calculated CA50 in a moving average window. Calibration work has been done on the Ford 3.5L EcoBoost engine to find out that the optimal CA50 is 7° ATDC at 1500 RPM, 2.62Bar in stoichiometric combustion, no EGR case. The MBT modifier is designed for modifying the spark timing in lean combustion case. The adaptive component is designed for compensating optimal CA50 position change in different load position. Knock limit protection will retard the spark timing when the controller detects knock based on the real time knock intensity estimation.

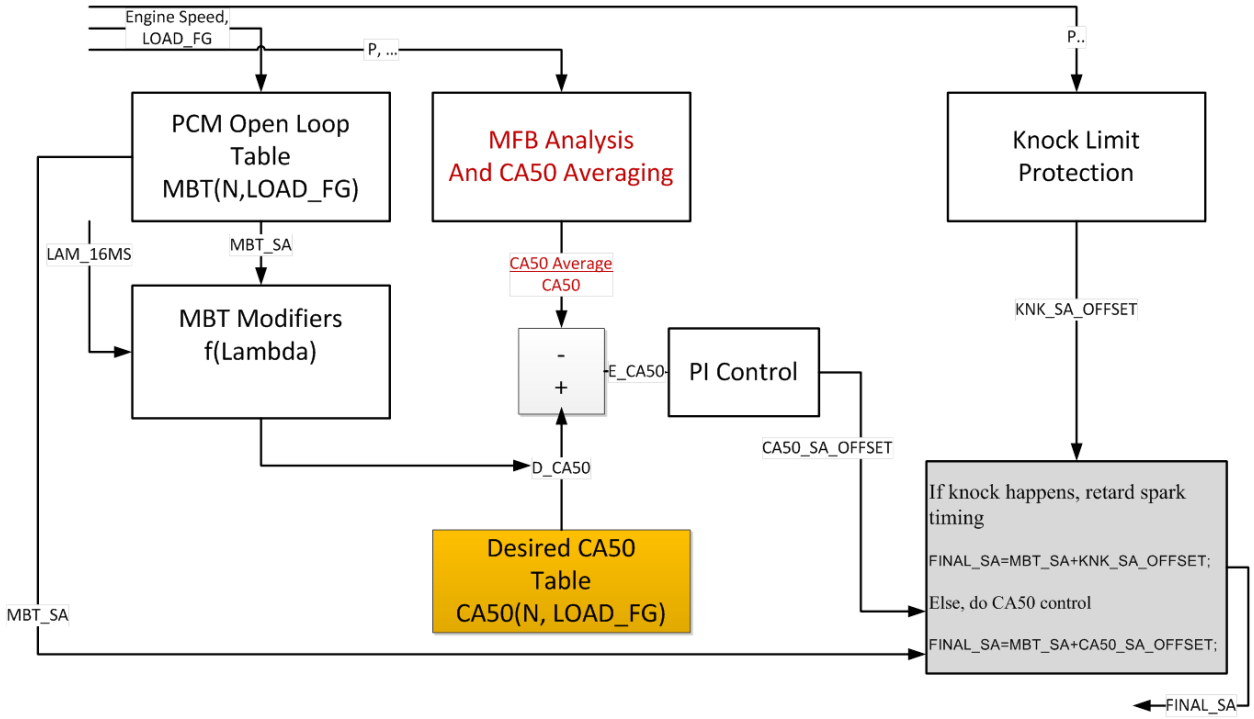


***Figure 2. Spark Timing Management Architecture***

### *1.2.1 CA50 Control Algorithm*

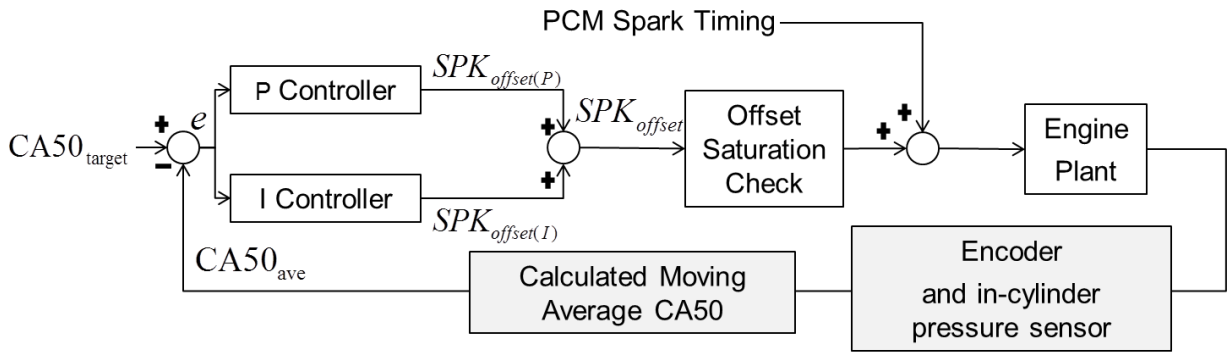


***Figure 3. CA50 controller algorithm***

$$SPK_{offset(P)}(k) = KP \times e(k-1) \quad \text{(Equation 1)}$$

$$SPK_{offset(I)}(k) = SPK_{offset(I)}(k-1) + KI \times e(k-1) \quad \text{(Equation 2)}$$

$$e(k-1) = \mathrm{CA50}_{\mathrm{target}} - \mathrm{CA50}_{\mathrm{ave}}(k-1) \quad \text{(Equation 3)}$$

$$SPK_{offset}(k) = SPK_{offset(P)}(k) + SPK_{offset(I)}(k)_i) = KP \times e(k-1) + SPK_{offset(I)}(k-1) + KI \times e(k-1) \quad \text{(Equation 4)}$$

Figure 3 shows the TriBox CA50 control algorithm. PCM spark timing signal is input to TriBox controller as the baseline. A PI controller is used to schedule the spark timing offset for CA50 control. A moving average CA50 window is used as the feedback of the PI controller. Based on the difference of the target CA50 and calculated average CA50, the PI controller will schedule the spark timing offset for the next cycle. Offset saturation check makes sure that the spark timing offset will not be too advanced to cause knock. Equ. 2 to 5 is the detailed PI controller algorithm for CA50 control.

## 1.3 Fuel Injection Management Algorithm

The fuel injection management architecture is shown in figure 3. The purpose of the fuel injection and torque management architecture is to run the engine as lean as possible while maintaining acceptable combustion stability and torque level. It consists of closed loop whole engine lambda control and adaptive individual cylinder fuel injection trim. For the closed loop whole engine lambda control part, a PI controller is used. The output of the PI controller is the overall engine lambda command. The feedback of the PI controller is the difference between the desired and real time calculated combustion stability indicator value (normalized COV IMEP or burn duration). The adaptive individual cylinder fuel injection trim algorithm is used to trim the individual cylinder's fuel injection to balance the individual cylinder's combustion stability difference.

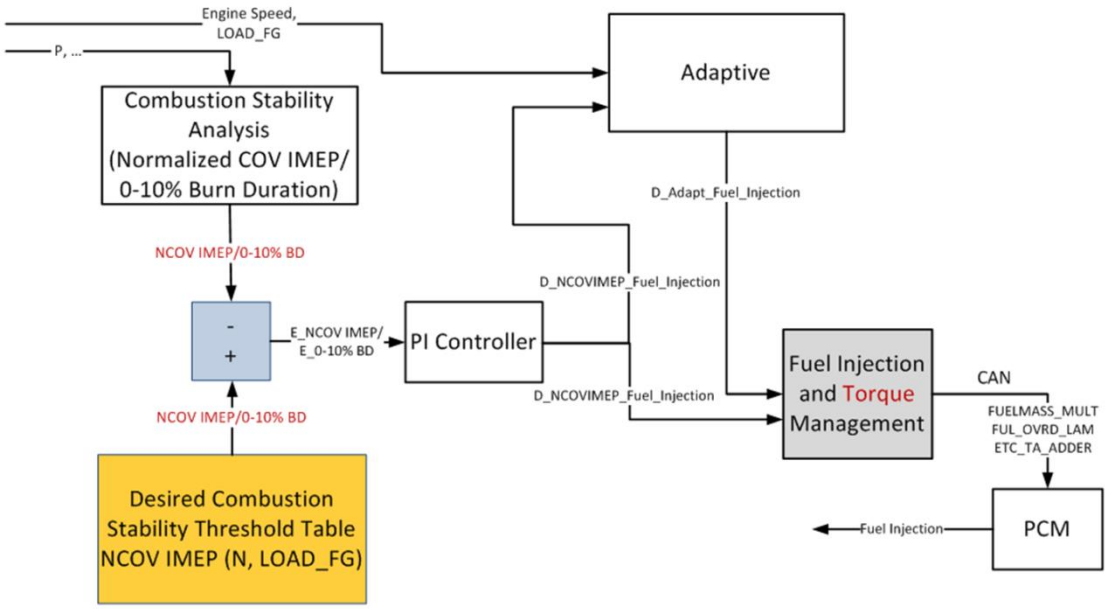


***Figure 4. Fuel Injection Management Architecture***

## 2. Control Strategy and Algorithm Offline Simulation

### 2.1. Fuel Injection Management Simulation

This simulation is used to simulate the fuel injection management algorithm and chose the optimal values for different control parameters. The control parameter to be optimized includes the KP and KI for the whole lambda control and the following parameters for the individual fuel trim algorithm.

**COV_max :** Max COV out of 6 cylinders, the control feedback for whole engine lambda control

**Cycle_Counter :** After max COV reach target, wait for Trim_Start_Cycle to make sure the whole engine lambda control is steady before starting adaptive fuel trim control

**Trim_Start_Cycle Individual_COV[i] :** The COV for cylinder i

**min_COV :** Minimum COV of bank

**Trim_Counter[i] :**To check if the COV of cylinder i is COV_Diff_Threshold larger than the minimum COV of bank, and lasts over M consecutive cycles.

**Fuel_Mass_Multiplier :** Fuel mass multiplier for cylinder i

**FMM_Step_Increase :** The step fuel mass multiplier increase

The flowing performance index are defined to evaluate the controllers performance.

**Response Cycle**: Cycles from control start to COV/BD reaching target;

**Max COV/BD Variation:** the maximum COV/BD variation from target after COV/BD reaching target

**STD COV/BD**: the standard deviation of COV/BD in steady state

#### *2.1.1. Simulation methodology*

The simulation is data based. For each simulation, a set of lambda sweep data collected from the engine dyno is used. The initial lambda is 1. Based on the whole lambda control and individual cylinder lambda trim algorithm, the code will output the lambda for the next combustion. The determination of the IMEP for the each cycle is based on the engine dyno data. The code will generate an random IMEP vale for each cycle at a

specific case. The distribution of the randomly generated IMEP follows the Gaussion distribution of the lambda sweep data. This makes sure the model can reflect the stochastic combustion features of the EcoBoost engine.

### *2.1.2. Simulation Results and Conclusions*

Simulation is run with both COV calculations as feedback :

**$COV_{100C}$**: COV calculated with 100 cycles IMEP and reported at the last cycle;

**Weighted $COV_{25C}$**: COV calculated with 25 cycles weighted IMEP and reported at last cycle;

For comparison purposes, $COV_{100C}$ calculation is used for the STD COV and Max COV Variation evaluation for both COV feedback.

**a) The simulation results for whole engine lambda control**

Impact of KP and KI on STD(max(COV)) in Steady State

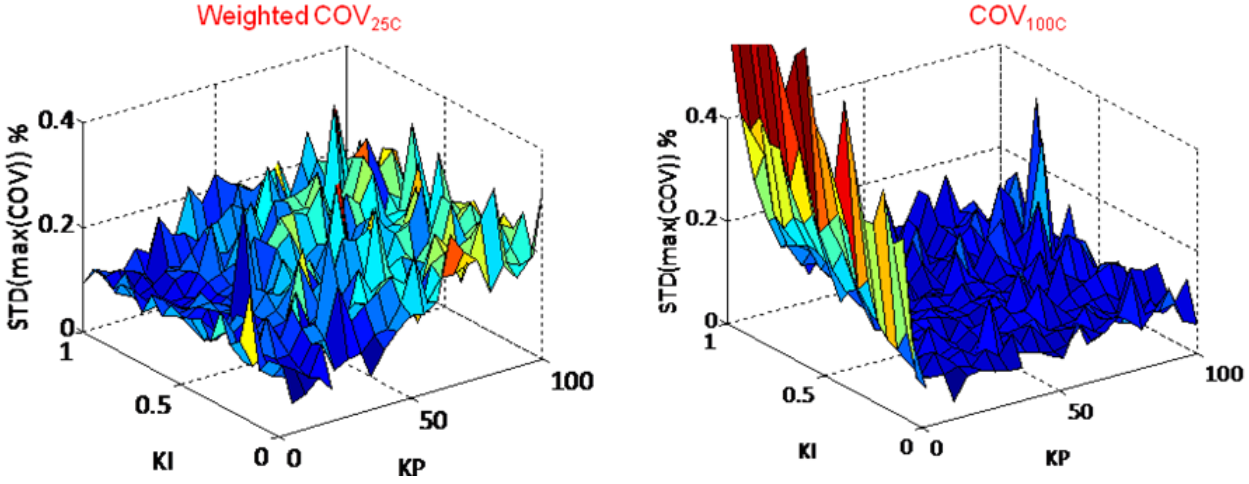


***Figure 5. Impact of KP and KI on STD(max(COV)) in Steady St***

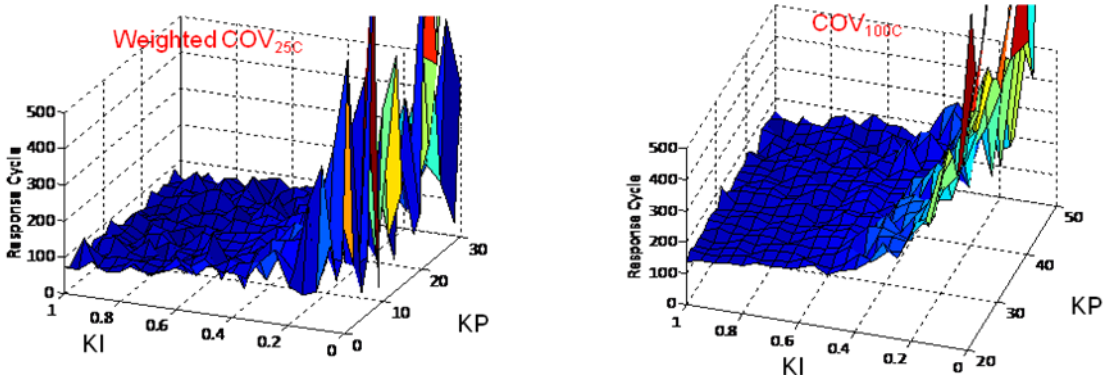


***Figure 6. Impact of KP and KI on Response Cycle***

Compared with 100-cycle $COV_{100C}$, 25-cycle weighted $COV_{25C}$ as feedback has faster response, but the STD(max(COV)) and Max COV Variation are larger.

**Table 1. Fuel Injection Management Optimization Result Based on 25 Cycles COV**

| **Using weighted COV calculation based on 25 cycles** | | | |
|---|---|---|---|
| Optimal Region | STD $COV_{100C}$ | Max $COV_{100C}$ Variation | Response Cycle |
| 0<KP<15, 0.65<KI<1 | 0.05% to 0.15% | 0.05% to 0.30% | 50 to 120 |

**Table 2. Fuel Injection Management Optimization Result Based on 100 Cycles COV**

| **Using COV calculation based on 100 cycles** | | | |
|---|---|---|---|
| Optimal Region | STD $COV_{100C}$ | Max $COV_{100C}$ Variation | Response Cycle |
| 20<KP<35, 0.3<KI<0.4 | 0.05% to 0.1% | 0.03% to 0.20% | 140 200 |

**b) The simulation results for individual fuel trim.**

**Optimization Procedure**: First set a initial point with relatively good performance index (larger mean lambda than only whole engine control) by running some random combinations. With the following initial point, the mean lambda is increased from 1.21 (without fuel trim) to 1.22 for both $COV_{100C}$ and $COV_{25C}$ as feedback; Start from the initial point, conducted a sweep test to optimize each parameter one by one:

The optimization start point is as below.

**Table 3. Optimization Initial Point**

| **Initial Point** | |
|---|---|
| COV_Diff_Threshold=1 | Count_Threshold=10 |
| FMM_Step_Increase=0.01 | Trim_Start_Cycle=50 |

The result of this optimization procedure is converged when different initial points are chosen; And simulation was run 10 times for every test to average the result.

COV_Diff_Threshold and FMM_Step_Increase have the dominant impact on the fuel trim algorithm; For a 2000-cycle simulation, with following parameter configuration, the fuel trim increases the mean lambda to 1.23 ($COV_{100C}$) and 1.22 ($COV_{25C}$ ) respectively from 1.21 (no fuel trim), while not deteriorating whole engine lambda control performance.

The optimization result is shown below.

**Table 4. Offline Fuel Injection Management Optimization Results**

| Parameter | Optimized Value with $COV_{100C}$ Feedback | Optimized Value with $COV_{25C}$ Feedback |
|---|---|---|
| COV_Diff_Threshold | 0.4% to 0.6% | 0.2% to 1% |
| FMM_Step_Increase | 0.01 to 0.02 | 0.01 to 0.03 |
| Count_Threshold | 5 to 50 | 5 to 50 |
| Trim_Start_Cycle | 10 to 100 | 10 to 100 |

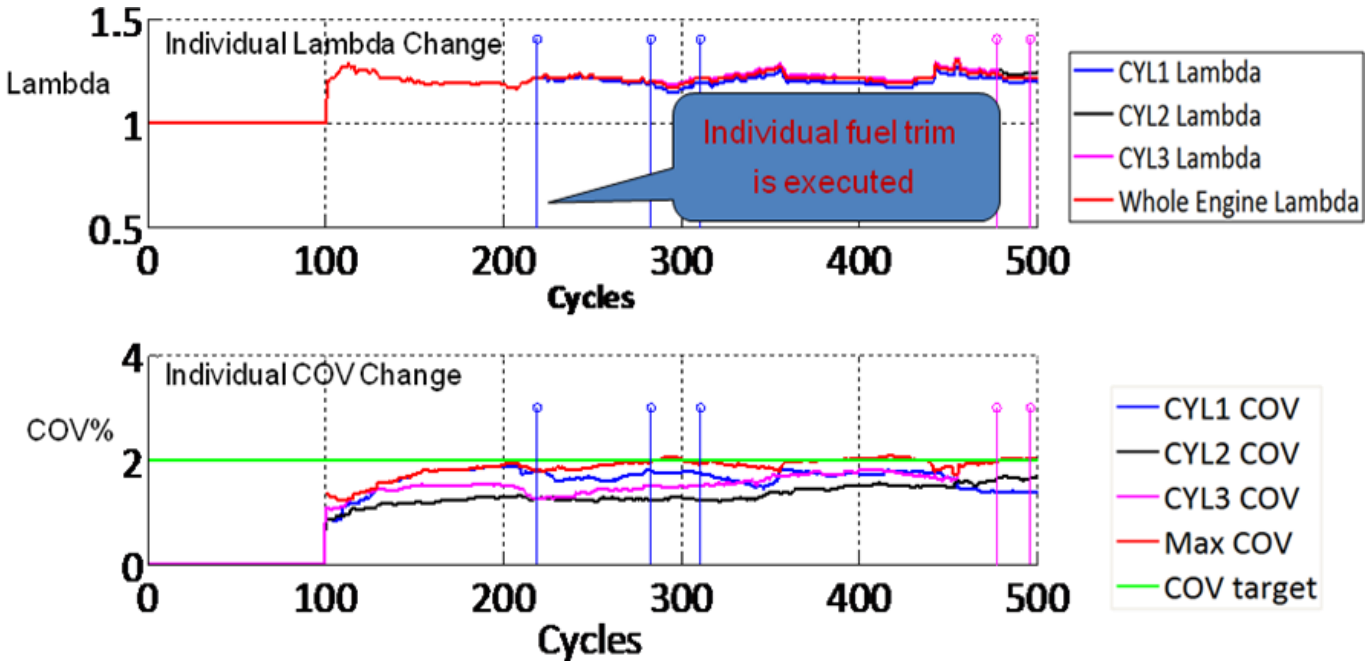


***Figure 7. Simulation results of bank 1with optimized gains and other parameters, using COV100C as feedback, 1500RPM, 2.62Bar.***

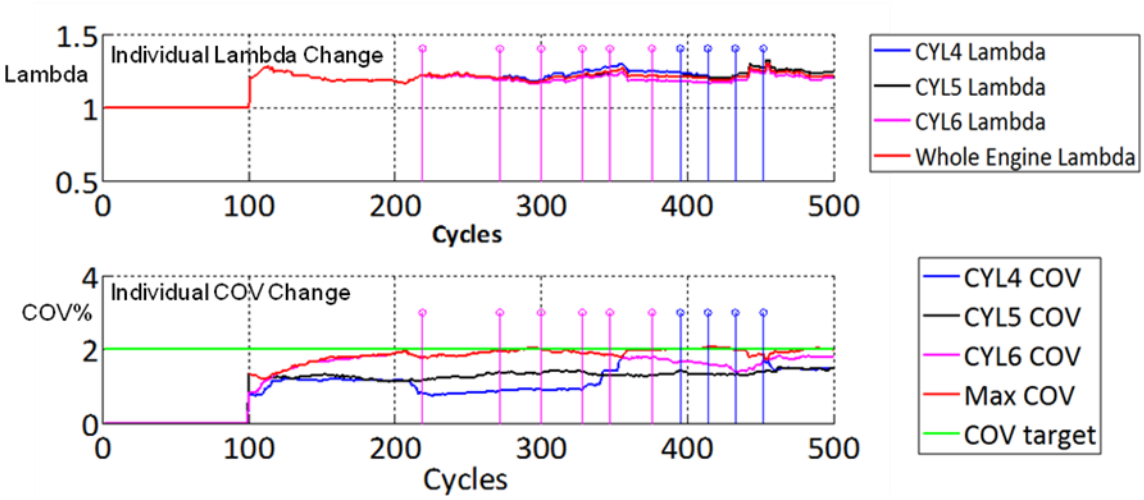


***Figure 8. Simulation results of bank 2 with optimized gains and other parameters, using COV100C as feedback, 1500RPM, 2.62Bar.***

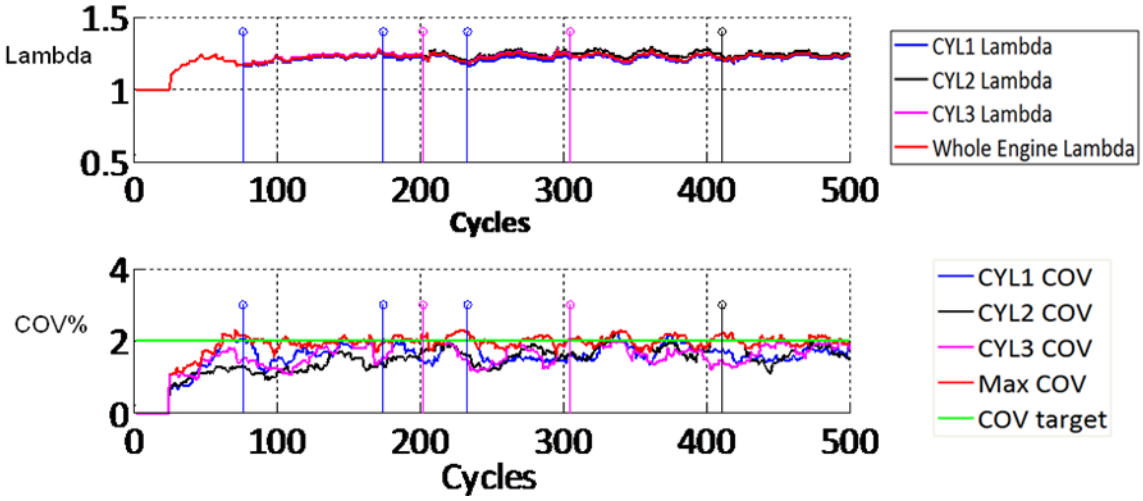


***Figure 9. Simulation results of bank 1 with optimized gains and other parameters, using COV25C as feedback, 1500RPM, 2.62Bar.***

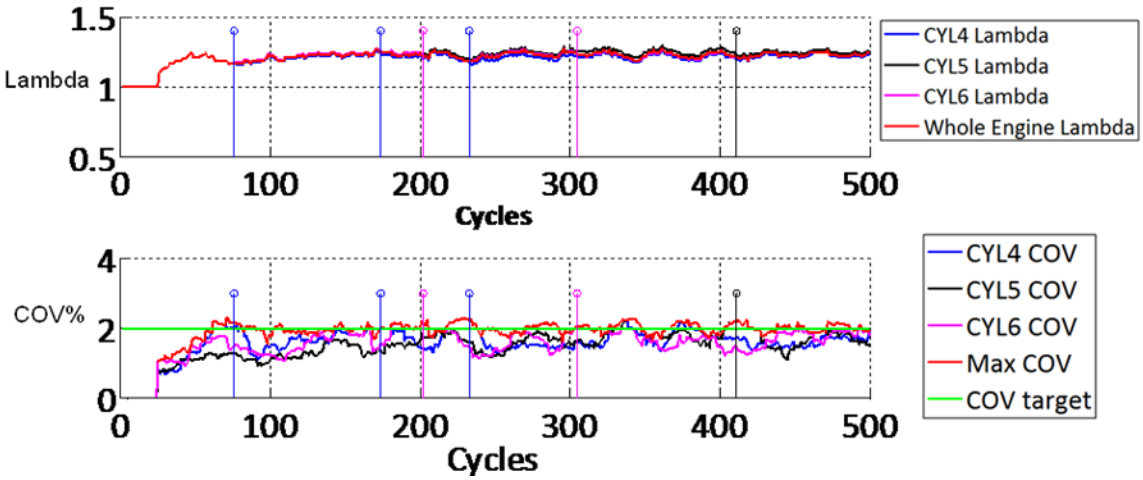


***Figure 10. Simulation results of bank 2 with optimized gains and other parameters, using COV25C as feedback, 1500RPM, 2.62Bar.***

## 2.2. Spark Timing Management Simulation

The spark timing management simulation is used to simulate the CA50 controller's performance offline, in order to choose the optimal gains and average CA50 window size for the CA50 controller. The simulation has been done for the following four test conditions: **Steady state with No EGR, Steady state with 20% EGR, Load transition without EGR and Load transition with 12% EGR.**

Also, some performance index are defined for the CA50 controller.

**Response cycle**: defined as the cycles from the control starts to the first time when average CA50 is within 1 CAD difference from CA50 target.

**Maximum variance for average CA50**: defined as the absolute value of the maximum variance of calculated moving average CA50 from target CA50 value at the steady state.

**Maximum variance for individual CA50**: defined as the absolute value of the maximum variance of the calculated individual CA50 from CA50 target value at the steady state

### *2.2.1. Simulation methodology*

The simulation is data based. For each simulation, a set of spark timing sweep data collected from the engine dyno is used. A CA50 controller logic is written inside code. An initial spark timing need to be set in the code. The CA50 controller will output the spark timing for the next combustion cycle. For the data used for the simulation, each data has 300 cycles.

### *2.2.2. Simulation Results and Conclusions*

**a) The Simulation Result with Steady State**

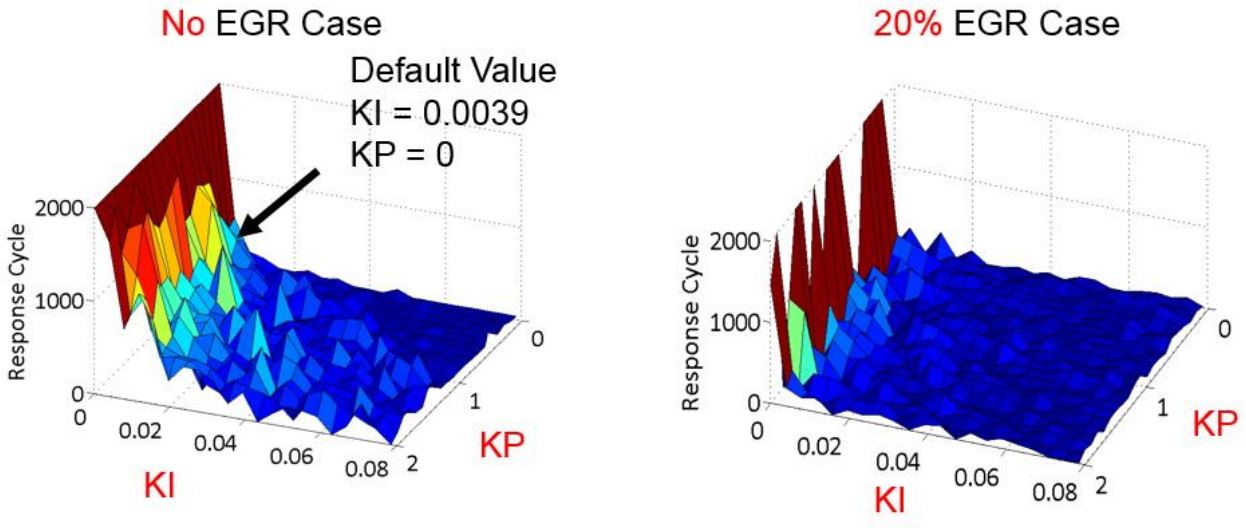


*Figure 11. The Impact of KP and KI to Response Cycle at Steady State Condition*

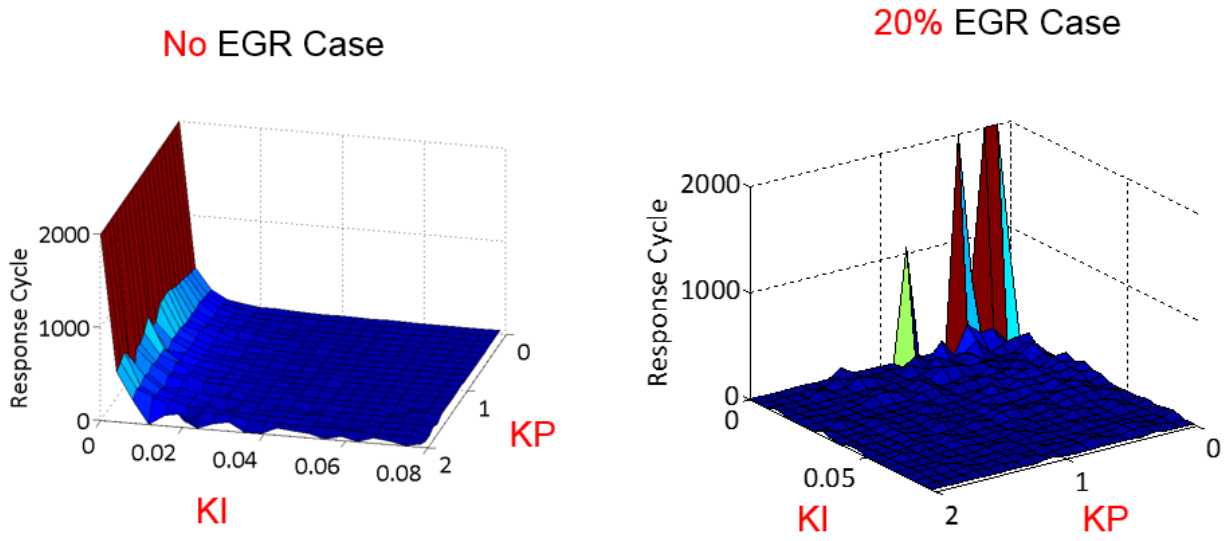


*Figure 12. The Impact of KP and KI to Response Cycle Within 1 Degree at Steady State Condition*

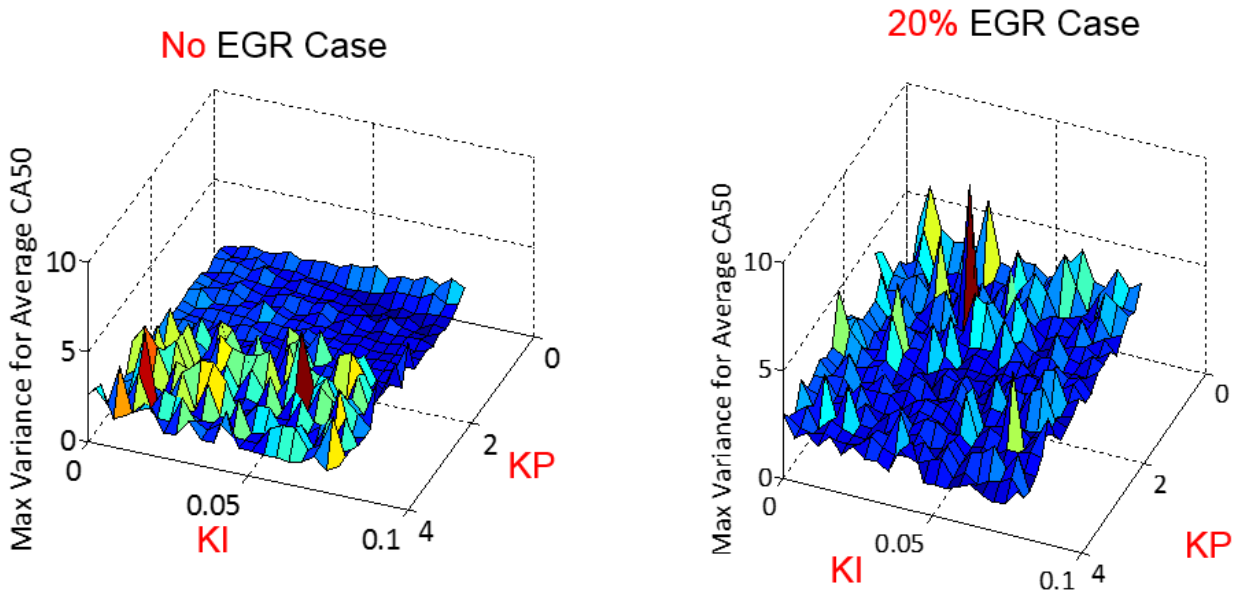


***Figure 13. The Impact of KP and KI Maximum Variance for Average CA50 at Steady State Condition***

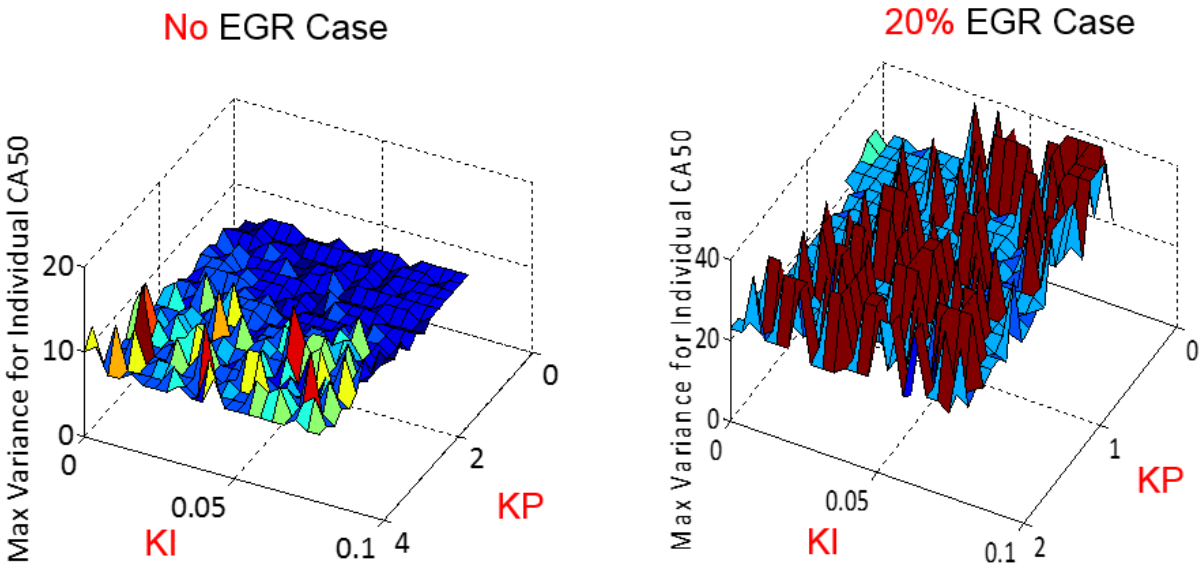


***Figure 14. The Impact of KP and KI to Maximum Variance for Individual CA50 at Steady State Condition***

For No EGR case with 35 point average, KI has the dominant effect on the response cycle while KP has little effect. Increasing KI reduces the response cycle without a negative impact on stability up to KI = 0.08. Increasing KI from default of 0.0039 will improve response. Larger KP will lead to larger maximum variance for the individual and average CA50 from the target CA50 while KI has little effect.

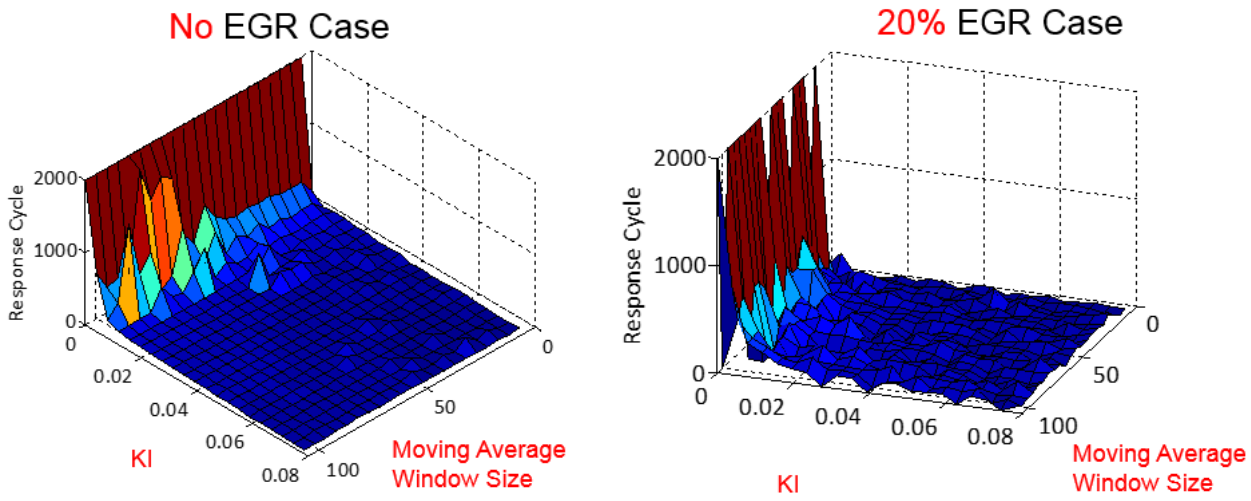


*Figure 15. The Impact of KI and average window size to Response Cycle at Steady State Condition*

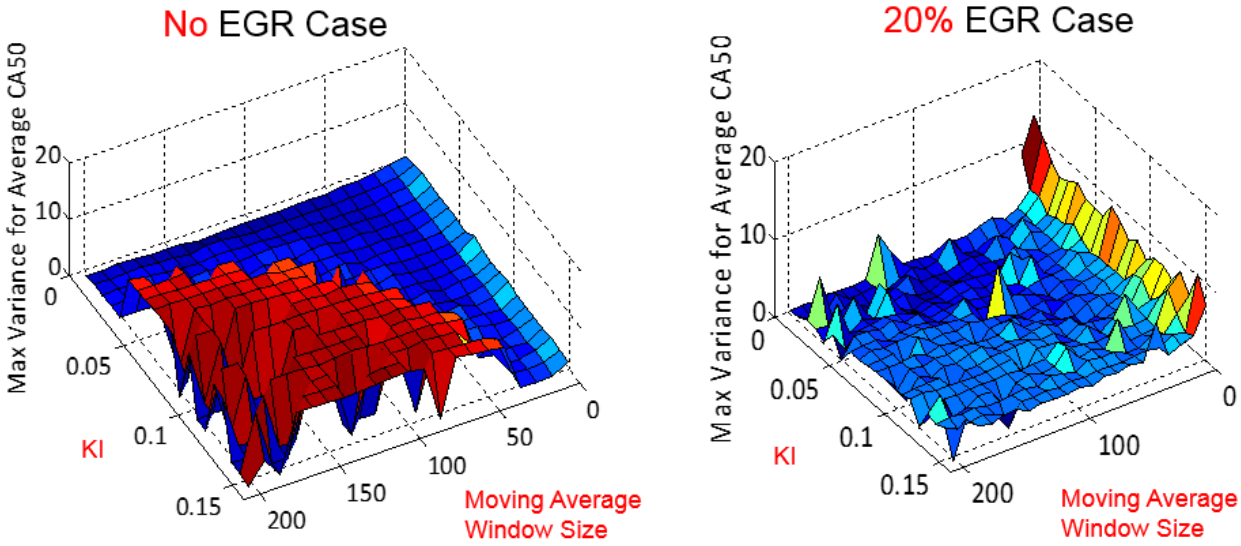


*Figure 16. The Impact of KI and CA50 Average Window Size to Response Cycle Within 1 Degree at Steady State Condition*

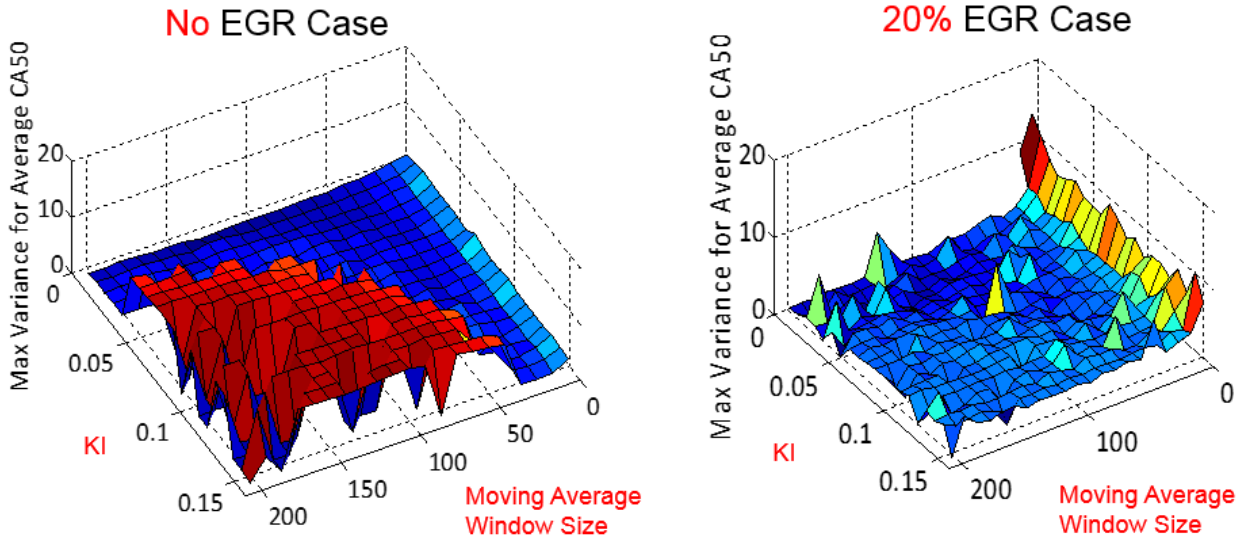


*Figure 17. The Impact of KI and CA50 Average Window Size to Maximum Variance for Average CA50 at Steady State Condition*

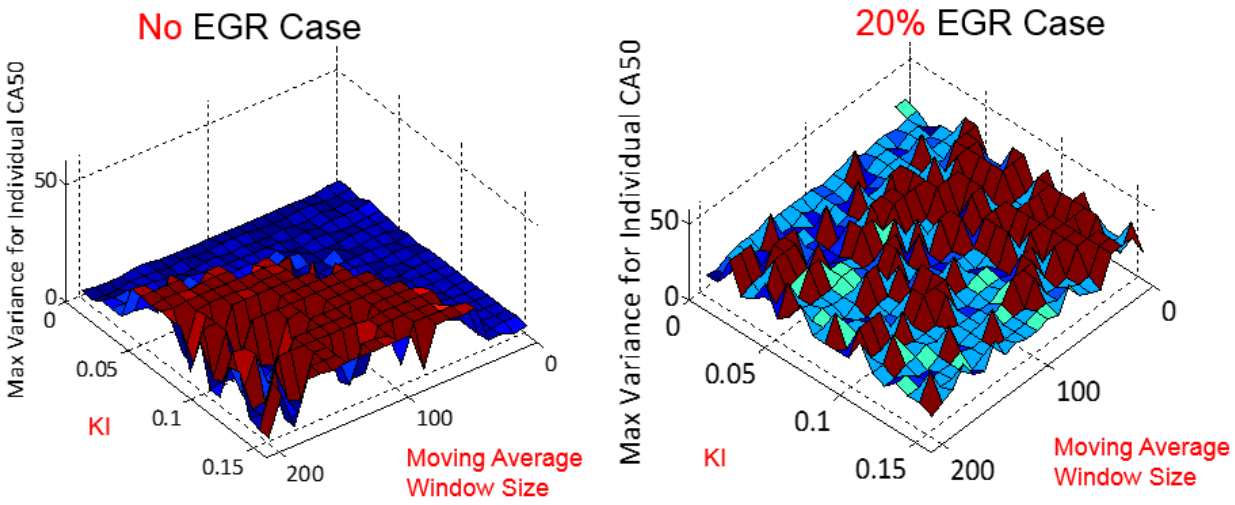


***Figure 18. The Impact of KI and CA50 Average Window Size to Maximum Variance for Individual CA50 at Steady State Condition***

For No EGR Case, when KI< 0.01, increasing the moving average window size will increase the response cycle. When KI>0.01, the moving average window size has little effect on the response cycle. When KI is larger than 0.1, a window size larger than 50 will lead to more than 7 degrees maximum variance increase for average CA50 and more than 10 degrees maximum variance increase for individual CA50. The average moving window size should not be larger than 50 in the case KI is larger than 0.1.

For 20% EGR case, when KI< 0.01, increasing the moving average window size will increase the response cycle. When KI>0.01, the moving average window size has little effect on the response cycle. This is because that when KI>0.01, the response cycle is fast enough to make the calculated CA50 to hit the target before the number of the window size is reached. An moving average window size less than 15 will lead to more than 5 degrees increase of maximum variance for average CA50. The maximum variance for individual CA50 is random. This is due to the high cyclic variability of the combustion process in high EGR case. The difference of the maximum and minimum CA50 is varies from 25 up to 50 degrees even at the same spark timing. The CA50 average moving window size should only varies from 15-50. A minimum window size of 15 cycles should work for the transient condition operation.

**b) The Simulation Result with Load Transition**

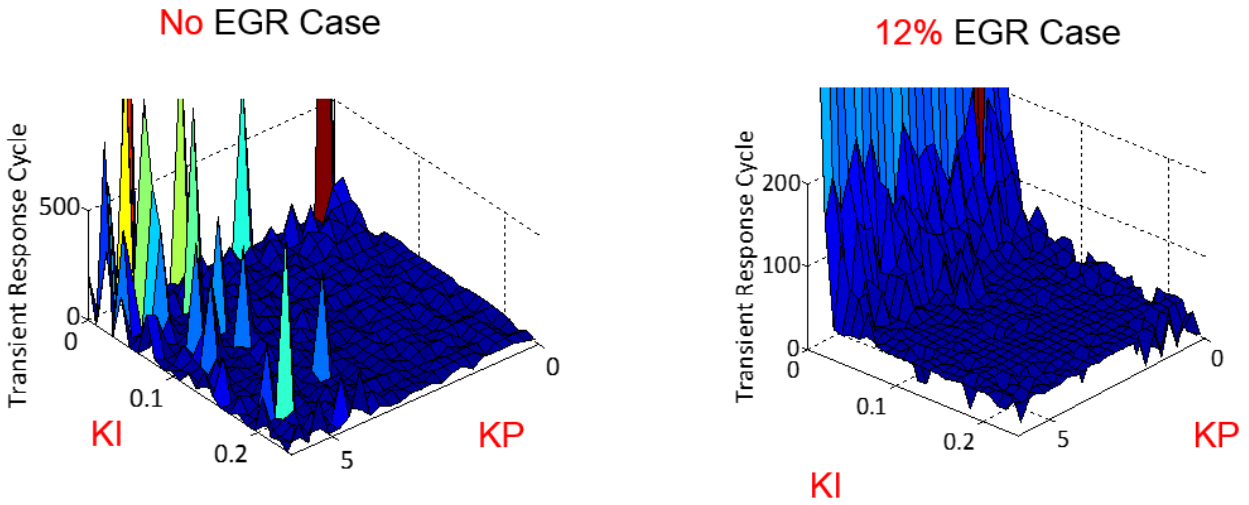


***Figure 19. The Impact of KP and KI to Transient Response Cycle in Load Transition***

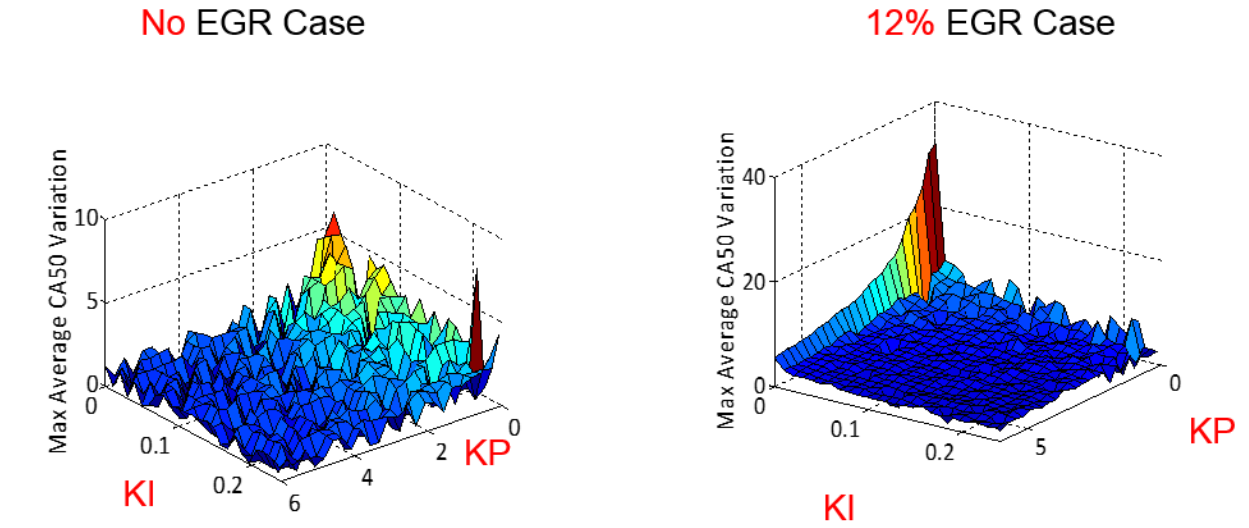


***Figure 20. The Impact of KP and KI to Maximum Average CA50 Variation in Load Transition***

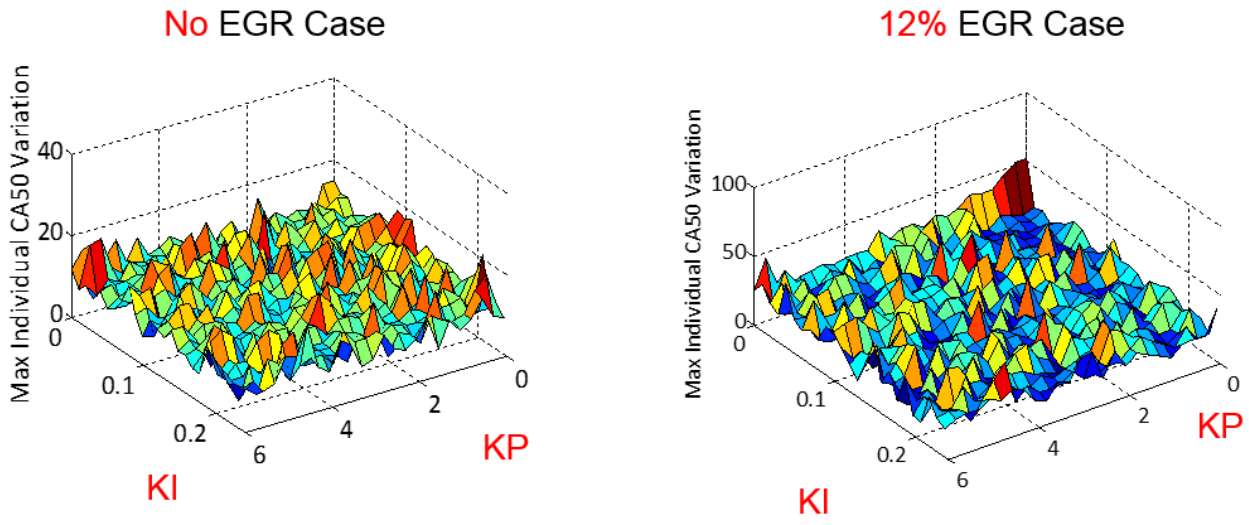


***Figure 21. The Impact of KP and KI to Maximum Individual CA50 Variation in Load Transition***

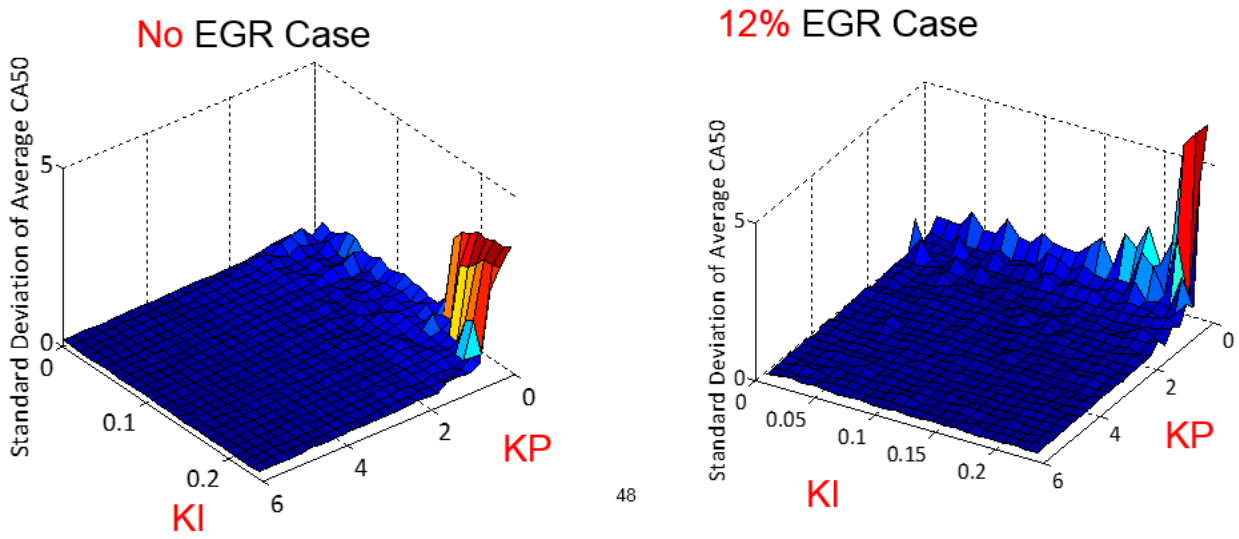


***Figure 22. The Impact of KP and KI to Standard Deviation of Average CA50 in Load Transition***

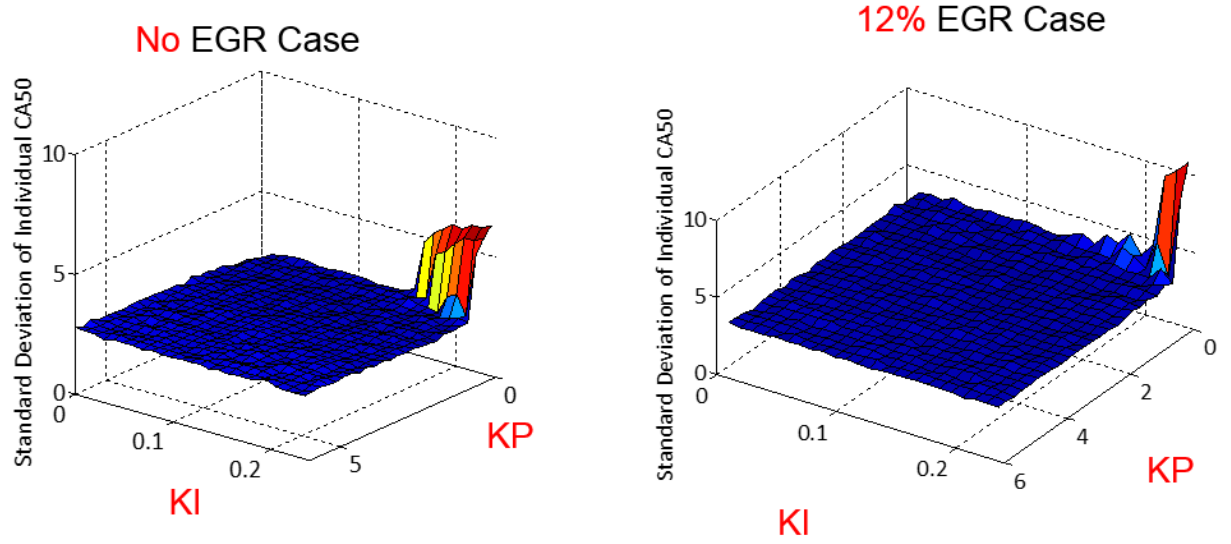


***Figure 23. The Impact of KP and KI to Standard Deviation of Individual CA50 in Load Transition***

Considering performance indexes: 0.05<KI<0.15, 1<KP<3.5 has optimal performance for both no EGR and 12% EGR cases. With the optimal range of KP and KI, the controller performance can achieve below performance.

**Table 5. Performance Index with Optimized KP and KI**

| **Performance Indexes** | **No EGR** | **12% EGR** |
|---|---|---|
| Transient Response Cycle | < 50 Cycles | < 50 Cycles |
| Max Average CA50 Variation during Transition | < 5 CAD | < 10 CAD |
| Max Individual CA50 Variation during Transition | < 20 CAD | < 50 CAD |
| STD of Average CA50 | < 1 CAD | < 1 CAD |
| STD of Average CA50 | < 3 CAD | < 4 CAD |

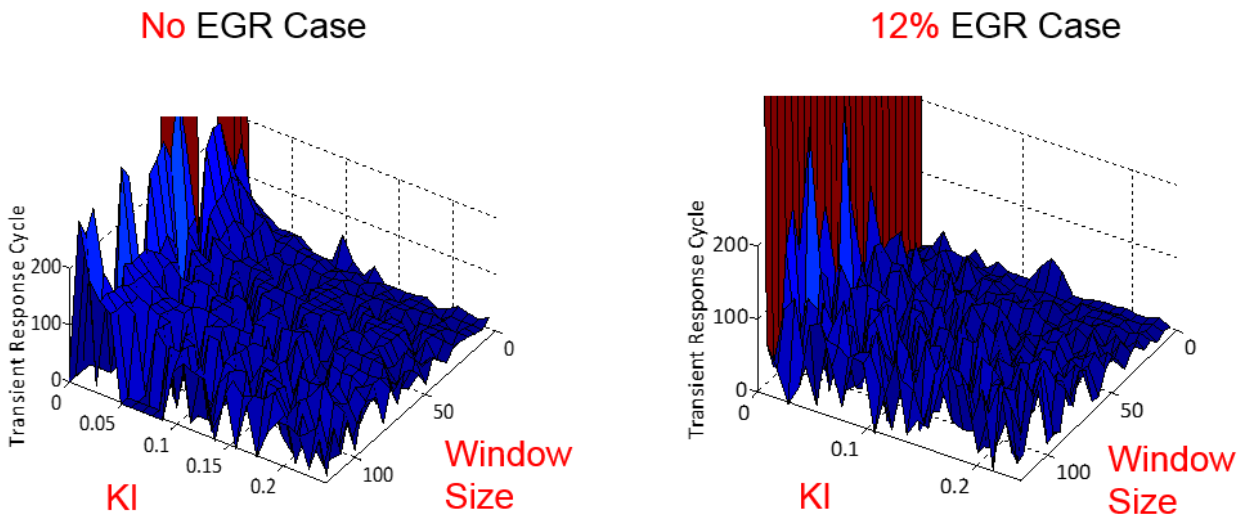


***Figure 24. The Impact of CA50 Average Window Size and KI to the Transient Response Cycle in Load Transition***

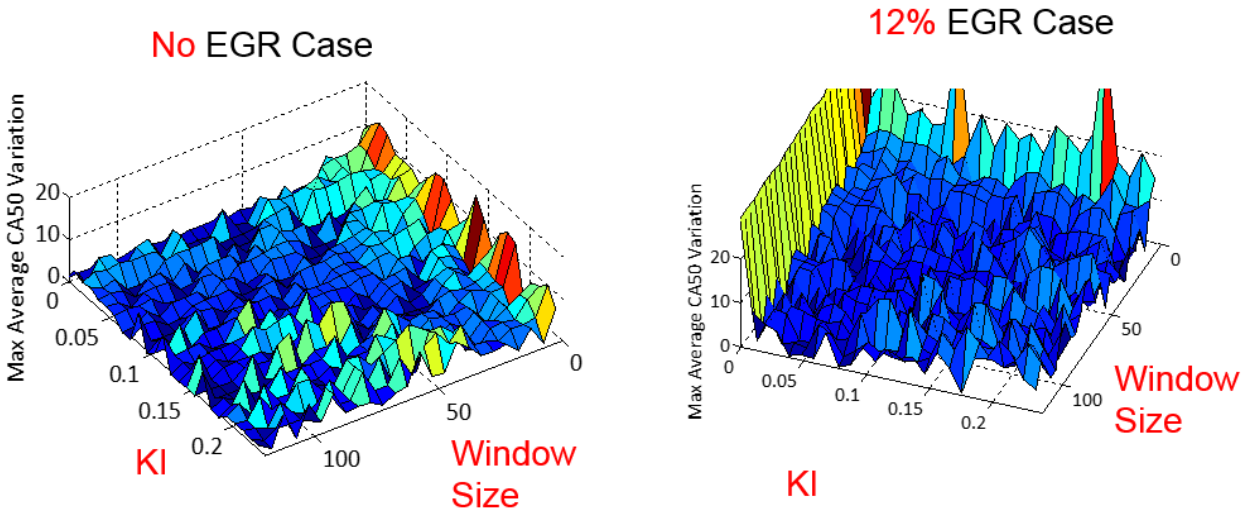


***Figure 25. The Impact of CA50 Average Window Size and KI to the Maximum Average CA50 Variation in Load Transition***

A combination of 0.04<KI<0.1 and 5<window size<35 will have the optimal performance for both no EGR and 12% EGR case. With the optimal range of KP and KI, the controller performance can achieve below performance.

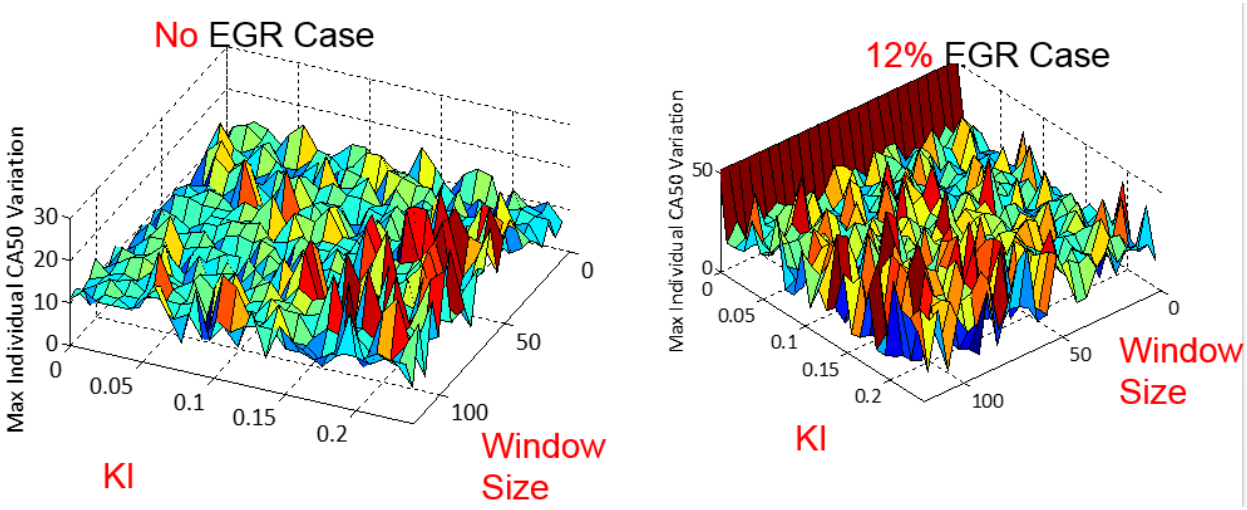


***Figure 26. The Impact of CA50 Average Window Size and KI to the Maximum Individual CA50 Variation in Load Transition***

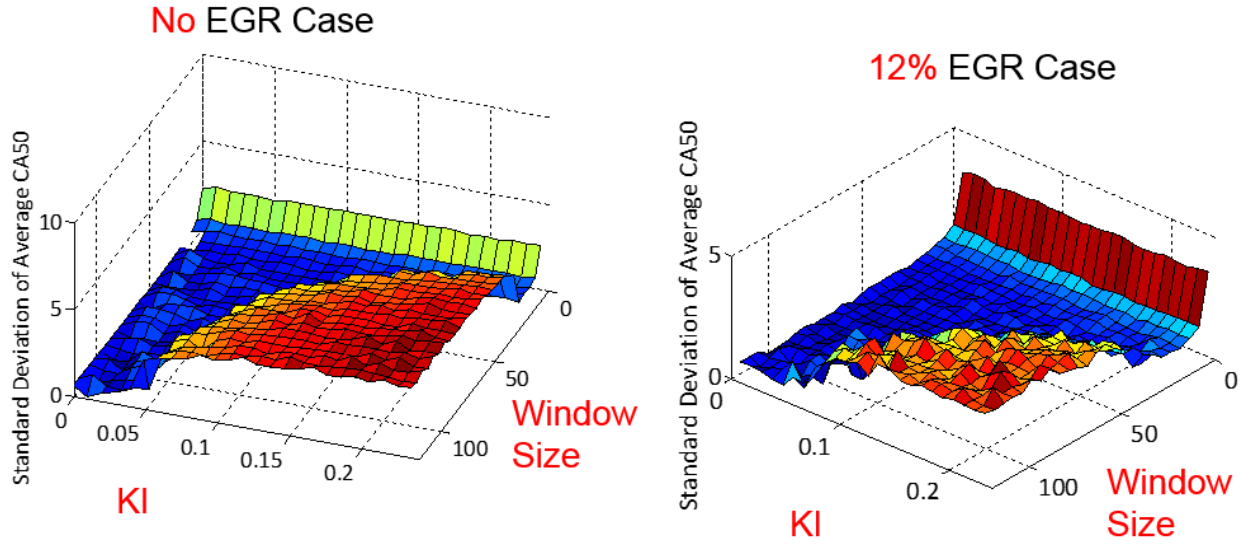


***Figure 27. The Impact of CA50 Average Window Size and KI to the Average CA50 Standard Deviation in Load Transition***

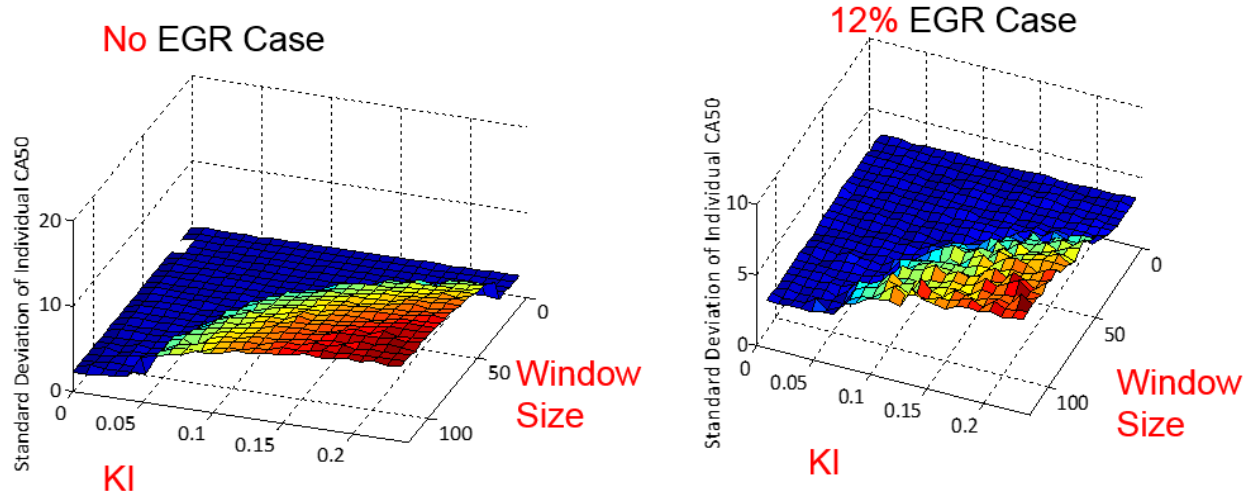


***Figure 28. The Impact of CA50 Average Window Size and KI to the Individual CA50 Standard Deviation in Load Transition***

**Table 6. Performance Indexes with Optimized KI and CA50 Average Window Size**

| **Performance Indexes** | **No EGR** | **EGR** |
|---|---|---|
| Transient Response Cycle | < 50 Cycles | < 50 Cycles |
| Max Average CA50 Variation during Transition | < 6 CAD | < 10 CAD |
| Max Individual CA50 Variation during Transition | < 20 CAD | < 30 CAD |
| STD of Average CA50 | < 1 CAD | < 1 CAD |
| STD of Average CA50 | < 3 CAD | < 4 CAD |

For optimal transient performance with no EGR and 12% EGR at 1500rpm, 2.26bar to 5bar 0.05<KI<0.1, 1<KP<3.5, and 5<window size<30;

Task 8.5 – Advanced Knock Detection and Control: Improved knock detection and control can offer significant reduction in fuel consumption, lower heat transfer, and lower exhaust temperatures. A GDI engine with variable valve timing and external EGR offers additional degrees of freedom to coordinate optimal knock control. Tests will be completed on a V6 engine to validate and compare the stochastic knock detection method to various standard methods. Concept readiness and the advanced knock detection strategy will be assessed.

Summary [Zhang 2014, Zhang et al. 2014,]: The ability to operate a spark-ignition (SI) engine near the knock limit provides a net reduction of engine fuel consumption. This work presents a real-time knock control system based on stochastic knock detection (SKD) algorithm. The real-time stochastic knock control (SKC) system is developed in Matlab Simulink, and the SKC software is integrated with the production engine control strategy through ATI's No-Hooks. The SKC system collects the stochastic knock information and estimates the knock level based on the distribution of knock intensities fit to a log-normal distribution. A desired knock level reference table is created under various engine speeds and loads, which allows the SKC to adapt to changing engine operating conditions. For the steady-state engine operation, a fixed-length weighted discrete FIR filter is used to estimate the knock factor (KF), an indicator of knock intensity level. Both offline simulation and engine dynamometer test result show that stochastic knock control with fixed length FIR filter has slow and excessive retard issue when significant knock event happens. To enhance the knock control response, an integrated feed-forward and feedback knock control strategy is employed. For the heavy knock events, a combination of gain scheduling and a fast retard (FR) is applied based on the detected KF. In addition, a variable length FIR filter is used to reduce the KF estimation time. The performance of the developed knock detection and control system is then evaluated on a V6 3.5L turbocharged engine on a dynamometer test stand.

Luo, W., *Study of Real-Time Stochastic Knock Detection and Control for Spark-Iginition Engines*, MTU PhD Thesis 2014.

Luo, W., Chen, B., Naber, J., and Glugla, C., "Stochastic Knock Detection, Control, Software Integration, and Evaluation on a V6 Spark-Ignition Engine under Steady-State Operation," SAE Technical Paper 2014-01-1358, 2014, doi:10.4271/2014-01-1358.

Task 8.6 – In-Cylinder Temperatures and Heat Transfer: Instrument the V6 engine with fast-response thermocouples heat flux sensors and wireless telemetry to measure piston, exhaust valve, and exhaust valve bridge surface temperatures and cylinder head heat flux. These measurements of temperature and heat flux will be used to understand the thermal environment under highly dilute and boosted engine operation. The data will improve numerical models to reduce surface hot spots and knock tendency under lean/dilute combustion conditions to improve engine thermal efficiency. Complete baseline tests to identify areas of highest temperature and effect of EGR, boost pressure, AFR, fuel injection, and ignition system. Develop first principles heat transfer correlations for improved multi-dimensional numerical models employing conjugate heat transfer analysis. A correlation between in-cylinder temperatures and knock tendency will be developed and validated, complementing Task 8.5.

Summary [Madison, D. 2013, ]: The push for improved fuel economy and reduced emissions has led to great achievementsin engine performance and control. These achievements have increased the efficiency and power density of gasoline engines dramatically in the last two decades. With the added
power density, thermal management of the engine has become increasingly important. Therefore it is critical to have accurate temperature and heat transfer models as well as data to validate them. With the recent adoption of the 2025 Corporate Average Fuel Economy (CAFE) standard, there has been a push to improve the thermal efficiency of internal combustion engines even further. Lean and dilute combustion regimes along with waste heat recovery systems are being explored as options for improving efficiency. In order to understand how these technologies will impact engine performance and each other, this research sought to analyze the engine from both a 1st law energy balance perspective, as well as from a 2nd law exergy analysis. This research also provided insights into the effects of various parameters on in-cylinder temperatures and heat transfer as well as provides data for validation of other models.

It was found that the engine load was the dominant factor for the energy distribution, with higher loads resulting in lower coolant heat transfer and higher brake work and exhaust energy. From an exergy perspective, the exhaust system provided the best waste heat recovery potential due to its significantly higher temperatures compared to the cooling circuit. EGR and lean combustion both resulted in lower combustion chamber and exhaust temperatures; however, in most cases the increased flow rates resulted in a net increase in the energy in the exhaust. The exhaust exergy, on the other hand, was either increased or decreased depending on the location in the exhaust system and the other operating conditions. The effects of dilution from lean operation and EGR were compared using a dilution ratio, and the results showed that lean operation resulted in a larger increase in efficiency than the same amount of dilution with EGR. Finally, a method for identifying fuel spray impingement from piston surface temperature measurements was found.

Madison, D., *Thermal Characterization of a Gasoline Turbocharged Direct Injection (GTDI) Engine Utilizing Lean Operation and Exhaust Gas Recirculation (EGR)*, MTU, PhD Thesis, 2013.

# References


1. Amsden, A.A., "KIVA-3V: A Block-Structured KIVA Program for Engines with Vertical or Canted Valves", Los Alamos National Laboratory Report LA-13313-MS, 1997.
2. Amsden, A.A., "KIVA-3V, Release 2: Improvements to KIVA-3V", Los Alamos National Laboratory Report LA-13608-MS, 1999.
3. Bandel, W., Fraidl, G.K., Kapis, P.E., Sikinger, H., and Cowland, C.N., "The turbocharged GDI Engine: Boosted Synergies for High Fuel Economy Plus Ultra-Low Emission", SAE 2006-01-1266, 2006.
4. Dai, W., "Methodology of CFD Based Engine Cycle Simulation for Applications in Engine Design and Mapping in GPDS", SRR-2005-0116, 2005.
5. Han, Z and Reitz, R.D., "Turbulence Modeling of Internal Combustion Engines Using RNG k-$\varepsilon$ models", Combust. Sci. Tech., 106, 4-6, 267, 1995.
6. Han, Z., Yi, J. and Trigui, N., "Stratified Mixture Formation and Piston Surface Wetting in a DISI Engine", SAE 2002-01-2655, 2002.
7. Han, Z. and Xu, Z., "Wall Film Dynamics Modeling for Impinging Sprays in Engines", SAE 2004-01-0099, 2004.
8. Hancock, D., Fraser, N., Jeremy, M., Sykes, and R., Blaxill, H., “New 3 Cylinder 1.2L Advanced Downsizing Technology Demonstrator Engine”, SAE 2008-01-0611, 2008.
9. Iyer, C.O., Han, Z., and Yi, J., "CFD Modeling of a Vortex-Induced Stratification Combustion (VISC) System", SAE 2004-01-0550, 2004.
10. Iyer, C.O. and Yi, J., "3D CFD Upfront Optimization of the In-Cylinder Flow of the 3.5L V6 EcoBoost Engine", presented at SAE World Congress, SAE 2009-01-1492, 2009.
11. Iyer, C.O. and Yi, J., "Spray Pattern Optimization for the Duratec 3.5L EcoBoost Engine", SAE Powertrains, Fuels and Lubr. Mtg, Florence , Italy, SAE 2009-01-1916, 2009.
12. Kapp, D., Schamel, A., Hinds, B., and Weaver, C., "3.5L V6 EcoBoost – Democratization of Sustainable Engine Technology", Aachen Colloquium, 2008.
13. Lang, O., Habermann, K., Krebber-Hortmann, K., Sehr, A., Thewes, M., Kleeberg, H., and Tomazic, D., “Potential of the Spray-Guided Combustion System in Combination with Turbocharging”, SAE 2008-01-0139, 2008.
14. Liang, L. and Reitz, R.D., "Spark Ignition Engine Combustion Modeling Using a Level Set Method with Detailed Chemistry", SAE 2006-01-0243, 2006.
15. Liang, L., Reitz, R.D., Iyer, C.O., and Yi, J., "Modeling Knock in Spark-Ignition Engines Using a G-equation Combustion Model Incorporating Detailed Chemical Kinetics", SAE 2007-01-0165, 2007.
16. Reiche, D., Wooldridge, S., et al., “Micro-Stratified Lean Combustion Concept and Development”, Ford R&A Engineering Technical Report SRR-2014-0024, 2014.
17. Richards, K.J., Senecal, P.K., and Pomraning, E., CONVERGE (Version 1.4.1) Manual, Convergent Science, Inc., Middleton, WI, 2012.
18. VanDerWege, B., Han, Z., Iyer, C.O., Munoz, R.H., and Yi, J., "Development and Analysis of a Spray-Guided DISI Combustion System Concept", SAE 2003-01-3105, 2003.
19. Yi, J., Han, Z., Yang, J., Anderson, R., Trigui, N., and Boussarsar, R., "Modeling of the Interaction of Intake Flow and Fuel Spray in DISI Engines", SAE 2000-01-0656, 2000.
20. Yi, J. and Han, Z., "A Methodology of Rapid Mesh Generation and Dynamic Mesh Management with Moving Valves for Engine CFD", SRR-2001-0268, 2001.
21. Yi, J., Han, Z., and Trigui, N., "Fuel-air Mixing Homogeneity and Performance Improvements of a Stratified-Charge DISI Combustion System", SAE 2002-01-2656, 2002.
22. Yi, J., Han, Z., Xu, Z., and Stanley, L.E., "Combustion Improvement of a Light Stratified-Charge Direct Injection Engine", SAE 2004-01-0546, 2004.
23. Yi, J., Wooldridge, S., Coulson, G., Hilditch, J., Iyer, C., Moilanen, P., Papaioannou, G., Reiche, D., Shelby, M., VanDerWege, B., Weaver, C., Xu, Z., Davis, G., and Schamel, A. "Development and Optimization of Ford 3.5L V6 EcoBoost Engine", 09PFL-1069, SAE 2009 World Congress, 2009.